WOODHEAD PUBLISHING IN TEXTILES

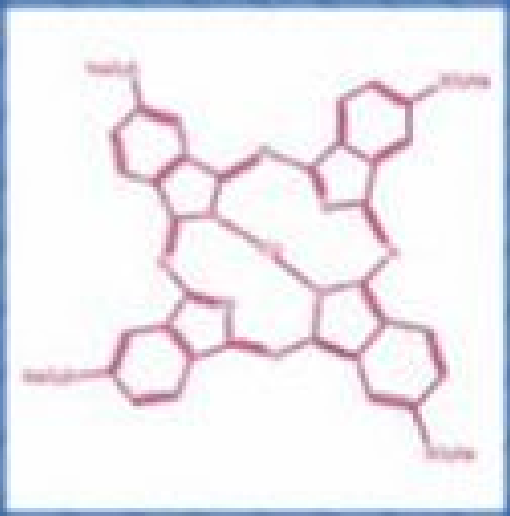

Analytical electrochemistry in textiles

P. Westbroek, G. Priniotakis and P. Kiekens

CRC
The Textile Institute
WP

Analytical electrochemistry in textiles

Related titles from Woodhead's textile technology list:

Chemical finishing of textiles
(ISBN-13: 978-1-85573-905-5; ISBN-10: 1-85573-905-4)

Chemical testing of textiles
(ISBN-13: 978-1-85573-917-8; ISBN-10: 1-85573-917-8)

Medical textiles and biomateials for healthcare
(ISBN-13: 978-1-85573-683-2; ISBN-10: 1-85573-683-7)

Recycling textile and plastic waste
(ISBN-13: 978-1-85573-306-0; ISBN-10: 1-85573-306-4)

Smart textiles for medicine and healthcare materials systems and applications
(ISBN-13: 978-1-84569-027-4; ISBN-10: 1-84569-027-3)

Wearable electronics and photonics
(ISBN-13: 978-1-85573-605-4; ISBN-10: 1-85573-605-5)

Details of these books and a complete list of Woodhead's textile technology titles can be obtained by:

- visiting our web site at www.woodheadpublishing.com
- contacting Customer Services (e-mail: sales@woodhead-publishing.com; fax: +44 (0) 1223 893694; tel.: +44 (0) 1223 891358 ext. 30; address: Woodhead Publishing Limited, Abington Hall, Abington, Cambridge CB1 6AH, England)

Analytical electrochemistry in textiles

P. Westbroek, G. Priniotakis and P. Kiekens

The Textile Institute

CRC

CRC Press
Boca Raton Boston New York Washington, DC

WOODHEAD PUBLISHING LIMITED
Cambridge England

Published by Woodhead Publishing Limited in association with The Textile Institute
Woodhead Publishing Limited
Abington Hall, Abington
Cambridge CB1 6AH, England
www.woodheadpublishing.com

Published in North America by CRC Press LLC,
6000 Broken Sound Parkway, NW
Suite 300, Boca Raton, FL 33487, USA

First published 2005, Woodhead Publishing Limited and CRC Press LLC

British Library Cataloguing in Publication Data
A catalogue record for this book is available from the British Library.

Library of Congress Cataloging in Publication Data
A catalog record for this book is available from the Library of Congress.

Woodhead Publishing ISBN-13: 978-1-85573-919-2 (book)
Woodhead Publishing ISBN-10: 1-85573-919-4 (book)
Woodhead Publishing ISBN-13: 978-1-84569-087-8 (e-book)
Woodhead Publishing ISBN-10: 1-84569-087-7 (e-book)
CRC Press ISBN-10: 0-8493-3485-3
CRC Press order number: WP3485

The publishers' policy is to use permanent paper from mills that operate a sustainable forestry policy, and which has been manufactured from pulp which is processed using acid-free and elementary chlorine-free practices. Furthermore, the publishers ensure that the text paper and cover board used have met acceptable environmental accreditation standards.

Typeset by SNP Best-set Typesetter Ltd., Hong Kong
Printed by TJ International Limited, Padstow, Cornwall, England

Contents

Author contact details

Dr Philippe Westbroek
Ghent University
Department of Textiles
Technologiepark 907
B-9052 Ghent
Belgium
Tel: +32 9 264 54 07
Fax: +32 9 264 58 46
E-mail:
philippe.westbroek@ugent.be

Professor Georgios Priniotakis
Technological Education Institute
of Piraeus
Textile Engineering Department
Thivon & P. Ralli 250
GR-12244 Egaleo, Athens
Greece
Tel: +30 210 538 13 35
E-mail: gprin@teipir.gr

Professor Paul Kiekens
Ghent University
Department of Textiles
Technologiepark 907
B-9052 Ghent
Belgium
Tel: +32 9 264 57 34
Fax: +32 9 264 58 46
E-mail: paul.kiekens@ugent.be

Preface

This book is the result of 13 years of research by the authors in the field of analytical electrochemistry with applications in textiles. However, without the support of many people, we would not have been able to bring this book, and the research explained in it, to a good conclusion. We would therefore like to thank all the people listed below for their help and would ask for forgiveness if anyone is not mentioned in this list.

First of all, we would like to thank our families for all their support and encouragement in our work. Without them, our jobs would be much more difficult.

We thank also the people from Ghent University, Department of Analytical Chemistry, Belgium: Professor Eduard Temmerman, Professor Harry Thun, Joost, Ine, Jan, Karolien, Filip, Fabien, Bart, Severine, Danjiella, Kathleen, Brigitte, Françoise and Michel. From Ghent University, Department of Textiles, Belgium, we should express our gratitude to Professor Lieva Van Langenhove, Emmanuel, Jean, Karen, John, Kyriaki, Vaggelis, Mojca, Jan and Lieve. Special thanks also to Judith for the translation of Chapters 4 and 5. Finally, we would like to thank the researchers from Rhodes University, Department of Chemistry, South Africa for their valuable input through bilateral cooperation: Professor Tebello Nyokong, Joshua, Kenneth, Mozes, Nchinda, Mamothibe, Natasha, Suzanne, Pulane, Sibongiseni, Andre and Rubin.

Finally, we would also like to thank the official bodies for providing us with the necessary financial support to execute our research projects: Ghent University (Belgium), Rhodes University (South Africa), Institute for Promotion of Scientific Research and Technology in Flemish Industry (IWT, Belgium), Vlaams Wetenschappelijke Stichting (VWS, Belgium), European Union (Europe) and the National Research Foundation (NRF, South Africa).

The book is divided into four parts. In the first part, an overview is given of the theory of electrochemistry as well as some practical considerations. The second part covers the development of sensors for the optimisation and

automation of textile-finishing processes. In Part III, after providing an overview of intelligent, or smart, materials, a brief fundamental study is given of textile electrodes that are used in a wide variety of applications but, for reasons of a lack of reproducibility and low electrode stability, are not yet known within the industry. Tentative answers to the questions raised are formulated, and a quality-control method is developed and provided. Finally, the fourth part of the book deals with the functionalisation of fibres through chemical/electrochemical modification, and some applications are given for this type of textile-related electrode.

Part I

Theoretical considerations

1

Fundamentals of electrochemistry

P. WESTBROEK

1.1 Introduction

A system of two electrodes connected to each other with an external circuit providing an electrical current and immersed in an electrolyte solution allows the conversion of chemical energy into electrical energy and vice versa. Conversion of chemical energy into electrical energy is found in batteries, fuel cells and corrosion reactions, while the conversion of electrical energy to chemical energy is obtained in electroanalysis, electrolysis and electroplating.

At the beginning of the twentieth century, there was a significant increase in the use of electrochemical phenomena for electroanalytical purposes, with potentiometry and polarography being the main methods. This growth was based on the development of the electrochemical thermodynamics theory by Faraday. For both methods, the relationships that describe them reveal information from solution thermodynamics by measuring a potential or an electrical current. For polarography (not discussed in detail in this book), an additional phenomenon occurs, namely diffusion of species from solution towards the electrode measuring the potential or electrical current.

In the last four decades, a wide range of electrochemical transient methods have been developed and offered the possibility of studying new applications, chemical reactions and heterogeneous adsorption. In addition, the dynamics and mechanism of electron-transfer processes were investigated with the transition-state theory to the kinetics for electrochemical reactions[1]. This resulted in understanding not only the kinetics of electron transfer, but also the (electro)chemical reaction steps preceding and following the electron-transfer step.

The most significant breakthrough of electrochemistry came with the introduction of modern electronic equipment controlled by a computer with suitable software. This allowed experiments under much more extreme conditions which opened new fields of research and applications:

- study of unstable intermediates and its thermodynamics;
- study of the kinetics of electron transfer, also in non-aqueous solution;
- organic electrosynthesis at the electrode–electrolyte interface;
- bioelectrochemistry;
- studies at inorganic metal complexes towards structure, chemical formula and reactivity;
- (electro)catalysis;
- development of a wide range of sensors for electroanalysis.

The studies and developments described in this book focus on the latter application, which is the development of sensors, with the aim of generating information from textile wet processes by immersing the developed sensor in the process bath and measuring parameters such as temperature, pH and concentration of the active compound. With this information, it is possible to improve and optimise the envisaged processes.

1.2 What is an electrochemical reaction?

Electrochemical methods are useful for the determination of chemical parameters, such as the concentration of analytes, through measurement of electrical parameters (current, potential, resistance, impedance) of an electrochemical cell. In this chapter, the relationship between electrical and chemical parameters will be described qualitatively. In the following chapters, this general approach will be discussed in more detail and applied to specific problems.

An electrochemical reaction can be defined as a chemical reaction involving charge transfer through an interface. The most commonly known form of charge transfer is the transfer of electrons over a solid electrode–liquid electrolyte interface. In the simplest form, electrons can be transferred from the electrode to a chemical substance in solution (reduction), or electrons that were released from the chemical substance by oxidation can be taken up by the electrode. This is generally given by Equation 1.1:

$$\mathrm{O} + n\mathrm{e}^- \leftrightarrows \mathrm{R} \qquad [1.1]$$

with O and R being the oxidant and reductant, respectively and n being the number of electrons transferred over the interface. From this equation, it is clear that charge transfer (in this case, the electrons passing the electrode–electrolyte solution interface) implies chemical transformations (being the transformation of O to R, or the opposite). However, this charge transfer also implies transport of charge or electrons, which in fact is an electrical current – hence the electrical current can provide information about the chemical transformation. This current can be positive or negative depending on the direction of electron transfer (from or to the electrode). It is also possible that two electrode processes occur at the same time in

such a way that their corresponding electrical currents are equal but opposite. This means that no net current will be measured. More generally, it is possible that a net current I_{net} is measured which reflects the excess of charge transfer not compensated by the opposite process (Equation 1.2):

$$I_{net} = I_{ox} + I_{red} \quad [1.2]$$

where I_{ox} is the electrical current of the oxidation reaction (positive sign) and I_{red} is the electrical current of the reduction reaction (negative sign).

The electrical current flowing through an electrical system is carried by electrons. In solution, however, charges are moving through the transport of ions instead of electrons. Making contact with the electrode is no problem when using a conductor and connecting it to the electron-conducting electrode; for the solution, however, this is not possible. To make contact with the solution, a conductor must be immersed in it in order to obtain electrical contact. However, this implies that a second interface is created between the solution and this conductor surface. An interim conclusion is that for electrochemical measurements, at least two electrodes are always necessary to realise and study an electron-transfer reaction.

A basic electrochemical cell always consists of at least two electrodes, schematically shown in Fig. 1.1, where two metallic electrodes are immersed

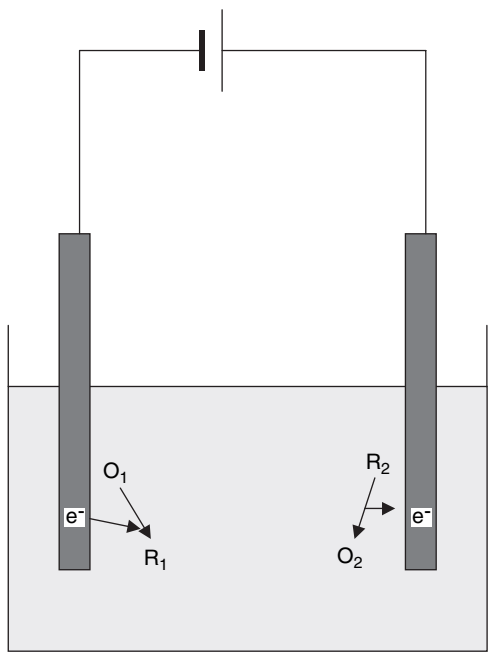

1.1 Scheme of a potentiometric setup with an anode (electrode on the right) at which oxidation reactions occur and a cathode (left electrode) at which reduction reactions take place.

in an electrolyte solution. These electrodes are connected to a direct current (DC) or potential source. Electrons flow from the negative side of this source to the electrode connected at this side. At the interface of this electrode and electrolyte solution, the electrons are taken up by chemical substances. At the other electrode, an equal number of electrons are taken up by the electrode, released by chemicals through oxidation, and then flow to the positive side of the current source. This mechanism implies that electrons enter the electrochemical cell at one electrode and leave the cell at the other. However, between the electrodes, charge transport is carried out by species being reduced (Equation 1.3) at one electrode and oxidised (Equation 1.4) at the other. As a result, an electrochemical process always consists of two steps, each process occurring at one of the two electrodes. It will be further explained as to how the electrochemical cell should be configured to obtain information about only one of these two reactions (the one that the researcher is interested in).

$$O_1 + ne^- \leftrightarrows R_1 \qquad [1.3]$$

$$R_2 \leftrightarrows O_2 + ne^- \qquad [1.4]$$

It should be noted that not only can a species in solution behave as an electroactive substance but also the electrode material itself. Suppose that one of the electrodes is copper which can be oxidised to Cu(II) ions, while releasing two electrons to the electrode. The Cu(II) then dissolves in solution in acidic medium or precipitates at the electrode surface as $Cu(OH)_2$ in alkaline solution.

The total amount of material that is transformed during an electrochemical reaction is in proportion with the electrical current, since both parameters are reflected by the number of electrons that flow through the system. This amount can be obtained by the Faraday equation[2]:

$$Q = \frac{pn\mathrm{F}}{M_\mathrm{m}} \qquad [1.5]$$

where Q is the number of qoulombs, p is the mass of the chemical transformed (g), M_m is the molecular mass of the chemical transformed ($\mathrm{g\,mol^{-1}}$), n is the number of electrons exchanged for each transformed chemical substance, and F is the Faraday constant ($96\,485\,\mathrm{C\,mol^{-1}}$).

The presented electrochemical cell (electrolyte, electrodes and connections to the current or potential source) should meet the basic condition of an electrical circuit, which is that no charge can be lost or can remain and be stored in the system. This leads also to the following conclusions:

- The amount of material oxidised at the anode, in terms of electrons, is perfectly balanced by the amount of reduced material at the cathode.

- A measurement of the current at any level of the cell shows how much reacting substance is transformed at both electrodes.
- To retain the neutrality of charge in the solution, ions should move between the electrodes.

Besides charge transfer, the transport of electroactive substance towards the electrode and the transport of reaction product away from the electrode also play an important role[3]. It is clear that an electrochemical reaction can only occur if the electroactive species is in the vicinity of the electrode surface. However, due to the continuous transformation of electroactive species, this also means that fresh species should be transported towards the electrode surface and that the formed reaction product must be transported away from the surface. The transport conditions and properties will be discussed more in detail in section 1.7.

Furthermore, it should be noted that the electroactive species taking part in an electrochemical reaction at an interface can be:

- organic, inorganic or bio-organic;
- solid (inclusive of the electrode material itself), a dissolved product, the solvent itself or a gas;
- neutral, negatively or positively charged.

The electrode involved in the reaction can be:

- metal or other type of conductor, semi-conductor or insulator;
- homogeneous or heterogeneous;
- a large surface (industrial applications, electrolysis) or a very small surface (sensing);
- a simple configuration (disc, sheet, . . .) or complex.

Finally, the advantages (1–3) and disadvantages (4–6) of electrochemistry are:

1. The methods are well established, and are supported by a well-defined theory, and the equipment used is relatively inexpensive for obtaining information concerning molecules in solution, thermodynamic data and insight in kinetics of reactions.
2. Detection limits are low; with electrochemical methods, it is possible to detect concentrations at nanolevel.
3. These methods are also selective because of control of the electrochemical spectrum through selection of applied potential range. In addition, selectivity can be improved by modification of the electrode surface with membranes, electrocatalysts, etc.
4. All the disadvantages are related to the electrical double layer, which in fact is the region at the electrode–electrolyte interface in which the electrochemical reactions occur. Such a layer behaves like a capacitor.

A first disadvange is that when the electrode potential is changed, some capacitive current will flow, which can influence the measured data.

5. Owing to the small thickness of the double layer and the fact that the experiment causes electrochemical reactions by application of a potential, an electrical field is created over the double layer, which can reach a magnitude of $1 \times 10^9\,\mathrm{V\,m^{-1}}$.
6. With every electrochemical reaction, consumption of electroactive species at the interface is involved. This means that fresh electroactive species should be transported towards the interface by diffusion, convection and/or migration. Migration, in particular, can cause significant problems and is very difficult to interpret and quantify. However, migration can be suppressed by using a supporting electrolyte in the solution.

1.3 Conventions for presentation of electrochemical data

In the past, different sign conventions were used in electrochemistry, which led to difficulty in interpretation of experiments and results. Consequently the electrochemical literature requires an understanding of this problem to avoid confusion. The approach followed in this book is summarised in this section. As pointed out in the previous section, all electrochemical cells are regarded as a combination of two half cells, with each of the latter represented by a half reaction written as a reduction:

$$\mathrm{O} + n\mathrm{e}^- \rightarrow \mathrm{R} \qquad [1.6]$$

As will be explained in more detail further in this book, each half-reaction corresponds to a potential and can be calculated by means of the Nernst equation[3–5]:

$$E = E^0 + \mathrm{R}T \Big/ n\mathrm{F} \ln \frac{a_0}{a_\mathrm{R}} \qquad [1.7]$$

where E is the potential, E^0 is the standard potential, R is the gaseous constant ($8.317\,\mathrm{J\,mol^{-1}\,K^{-1}}$), T is the temperature (K), n is the number of electrons exchanged in the electrochemical reaction, F is the Faraday constant ($96\,485\,\mathrm{C\,mol^{-1}}$), and a is the activity of oxidant (O) and reductant (R). The half cell with the most positive potential will be the anode, with the other one the cathode, and the measurable cell potential will be the difference between the two half-cell potentials.

In addition, in the graphical presentation of data, different conventions are used, giving rise to problems in the interpretation and comparison of results. However, a good convention will not cause any problems. In this book (Fig. 1.2) positive potentials are directed to the right of the origin, and anodic (oxidation) currents are taken as positive (directed upward from the

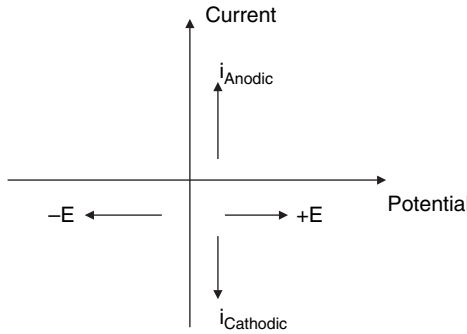

1.2 Sign conventions used in this book.

origin). Whatever convention is used, the axes should be clearly labelled so that, in principle, it should be clear to the reader what is meant and how the data should be converted to other conventions used in the electrochemical literature.

1.4 Classification of electrochemical methods

It is the aim of this chapter to explain the basic requirements for performing electrochemistry, such as equipment, electrodes, electrochemical cells and boundary conditions to be respected. The following chapter focuses on the basic theory of charge transfer at the electrode–electrolyte solution interface and at transport phenomena of the analyte towards the electrode surface. In Chapter 3, a theoretical overview of the electrochemical methods applied in the work described in this book is given.

Essentially, the items mentioned above will be described as a function of the type of electrochemical method. The methods described and used in the work of this book can therefore be divided into three groups:

- ***Potentiometric methods***: in potentiometric methods, the equilibrium potential of the working electrode (see section 2.2) is measured against the potential of a reference electrode. That potential results from an equilibrium established over the electrode–electrolyte interface and provides information about the analyte taking part in this equilibrium.
- ***Voltammetric methods***: in these methods, a potential is applied to the working electrode using a three-electrode setup (see section 1.6). The electrical current, resulting from charge transfer over the electrode–electrolyte interface, is measured and reveals information about the analyte that takes part in the charge transfer reaction. The potential applied can be constant (chronoamperometry, section 2.5), varied linearly (cyclic voltammetry, section 2.3) or varied in other ways (Chapter 2).

- ***Conductometric methods***: in conductometric methods, the conductivity of an electrolyte is assessed by measuring the impedance of this system using two identical electrodes, planarly positioned. However, much more can be done if the impedance is measured as a function of applied frequency, a method that is called electrochemical impedance spectroscopy; more details about this method are given in section 2.3.

1.5 Two-electrode setup

In potentiometry, a two-electrode setup is used and is given schematically in Fig. 1.3. This setup consists of a working and a reference electrode, and it is the aim of this method to measure equilibrium conditions at the surface of the working electrode. Under equilibrium, the Nernst equation is valid:

$$E_{eq} = E^0 + \mathrm{R}T/n\mathrm{F} \ln \frac{a_0}{a_R} = E^0 + 2.3\mathrm{R}T/n\mathrm{F} \log \frac{a_0}{a_R}$$
$$= E^{0'} + 2.3\mathrm{R}T/n\mathrm{F} \log \frac{c_0}{c_R} \qquad [1.8]$$

where E_{eq} is the measured equilibrium potential (V), E^0 is the standard potential (V), $E^{0'}$ is the formal potential (V), R is the universal gas constant (8.317 J mol^{-1} K^{-1}), T is the temperature (K), n is the number of electrons, F

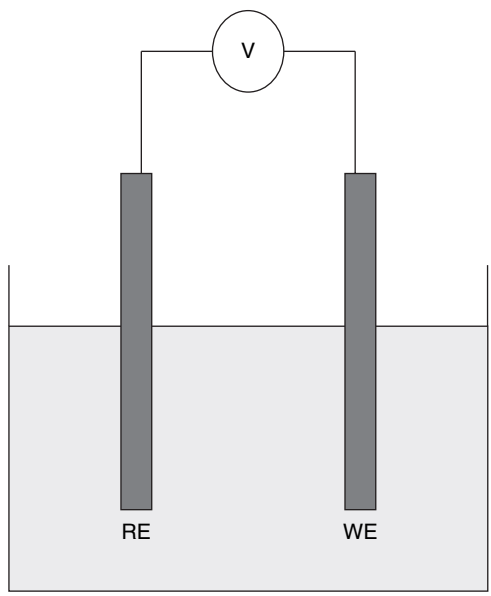

1.3 Scheme of a potentiometric setup, showing reference electrode (RE) and working electrode (WE).

is the Faraday constant and *a* and *c* are the activities and concentration of oxidant O and reductant R, respectively.

Under equilibrium conditions, there is no current flowing through the system. Note that this does not mean that no reaction is occurring. The equilibrium is a dynamic one, which means that the current related to oxidation of R is equal (but opposite in sign) to the reduction current of O, resulting in a zero total current. This equilibrium can be measured by using a voltmeter with high impedance to avoid current flowing through the system. In fact, this type of measurement is similar to the measurement of the open, circuit potential.

In principle, the working electrode can be any material, but strict conditions apply to the reference electrode. This electrode should have a stable potential that is independent of the flux of electrons going through it. This cannot be obtained in practice because a current flowing through such an electrode contributes to the reference potential of this electrode; therefore it is no longer stable, and the potential difference measured between working and reference electrode does not provide information about the equilibrium at the working electrode only. However, in a potentiometric setup, this limitation does not hold because in this type of measurement no electrical current is flowing through the system.

The requirements that need to be met when performing measurement with current flowing through the electrochemical cell will be explained in section 1.6.

The reference electrode used in this work is a silver/silver chloride/saturated chloride electrode (Ag|AgCl)[6] with a reference potential of 0.222 V vs. the Standard Hydrogen Electrode (SHE), an electrode selected as reference point having a potential of zero. This can be compared with the selection of the melting point of water as an arbitrary reference point that is zero degrees in the Celcius temperature scale. A schematic view of the Ag|AgCl electrode is given in Fig. 1.4 with (1) connecting tube, (2) silver wire, (3) silver wire coated with AgCl, (4) KCl solution, (5) cap for replacement of KCl solution and (6) glass frit. A silver wire is positioned in a glass tube filled with saturated potassium chloride solution. Locally, at the surface of the silver wire, silver will dissolve in solution by oxidation (while oxygen also dissolved in the electrolyte solution is reduced by uptake of the electrons released during silver oxidation). The oxidation is given in Equation 1.9:

$$\mathrm{Ag} \leftrightarrows \mathrm{Ag^+} + \mathrm{e^-} \qquad [1.9]$$

The potential of the equilibrium between Ag and Ag^+ in the neighbourhood of the Ag wire surface is given by the Nernst equation, keeping in mind that the activity of a solid (metallic silver) is equal to 1:

$$E_{\mathrm{eq}} = E^0{}_{\mathrm{Ag|Ag^+}} + 2.3 \mathrm{R}T/n\mathrm{F} \log a_{\mathrm{Ag^+}} \qquad [1.10]$$

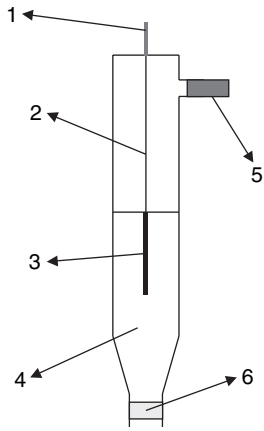

1.4 Scheme of a Ag|AgCl reference electrode with (1) connecting tube, (2) silver wire, (3) silver wire coated with AgCl, (4) KCl solution, (5) cap for replacement of KCl solution and (6) glass frit.

However, this equilibrium is not obtained in practice because the Ag^+ ions form immediately the sparingly soluble AgCl with the chloride ions in solution. Therefore the potential given in Equation 1.10 will be dependent of the presence of Cl^- ions. The unknown parameter is the activity of Ag^+, but this parameter can be calculated through the solubility constant, K_{sp}:

$$K_{sp} = a_{Ag^+} a_{Cl^-} \qquad [1.11]$$

Substitution of Equation 1.11 in Equation 1.10 results in the following equation:

$$E_{eq} = E^0{}_{Ag|Ag^+} + 2.3 R T \Big/ n F \log \frac{K_{sp}}{a_{Cl^-}} \qquad [1.12]$$

which results in Equation 1.13 after reorganisation of the right-hand side of Equation 1.12:

$$E_{eq} = E^0{}_{Ag|AgCl} - 2.3 R T \Big/ n F \log a_{Cl^-} \qquad [1.13]$$

The potential $E^0{}_{Ag|AgCl}$ is equal to $E^0{}_{Ag|Ag^+} + \log K_{sp,AgCl}$. In a saturated chloride solution, the activity of the chloride ions is equal to one, therefore Equation 1.13 simplifies to Equation 1.14, which shows that the potential is constant and not dependent on a dissolved species present in the electrolyte solution:

$$E_{eq} = E^0{}_{Ag|AgCl} \qquad [1.14]$$

Table 1.1 Commonly used reference electrodes which are commercially available

Reference-electrode type	Potential determining ion in solution
Ag|AgCl	Cl^-
$Hg\|Hg_2Cl_2$ (calomel electrode)	Cl^-
Hg|HgO	OH^-
$Hg\|HgSO_4$	SO_4^{2-}

Note that Equation 1.14 remains valid only if the chloride solution is saturated with chloride. This requires that this solution should be separated by the solution in which the compound(s) to be analysed is present. By using glass frits with small pore size that prevent the electrolyte solution from leaking out of the reference electrode, this problem can be solved, but because of the porous structure both solutions are electrolytically in contact, which is an important condition for performing electrochemistry.

Up to 20 years ago, it was difficult to construct a reference electrode because they were not commercially available, and glass frits with small pore sizes did not exist. In those days, electrolytic contact between the chloride solution and the solution to be analysed was obtained by a salt bridge. This is not used anymore, and because of the wide range of reference electrodes commercially available today (Table 1.1) this need not be discussed further.

Further details about the theory of potentiometry are presented in Chapter 3 (section 3.1).

1.6 Three-electrode setup

1.6.1 Introduction

When an electrical current is passing through the electrochemical cell, a two-electrode setup is not possible because the current flowing through the reference electrode has an influence on its reference potential. Indeed, when current is flowing through this electrode, the equilibrium between Ag|AgCl and Cl^- changes, so the potential also related to this equilibrium varies during current passing the electrode. However, this problem is circumvented by using a three-electrode setup[3] as shown in Fig. 1.5. The additional electrode brought into the system is a counter electrode, which in fact is nothing more than a good conductor. With a potential source, a potential is applied over the working and counter electrode in such a way that the desired potential difference between working and reference electrode is obtained.

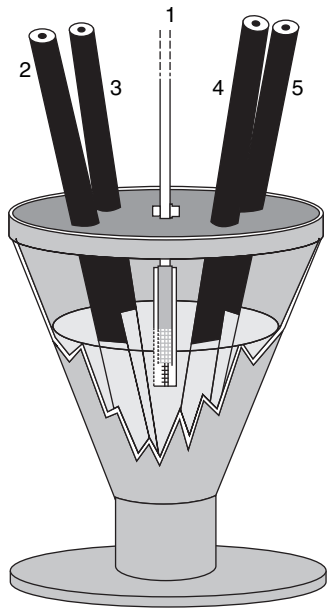

1.5 Scheme of the electrochemical cell consisting of a Teflon container in which the working (1), counter (2) and reference (3) electrode are immersed together with a temperature and pH sensor.

This potential difference is measured with a volt meter; if this potential is not equal to the desired potential, more or less potential difference is applied between the working and counter electrode until the desired potential difference between the working and reference electrode is obtained. At this moment, the potential of the working electrode is known, being a certain potential more positive or negative against the stable reference potential. In this setup, it is clear that the potential is applied between the working and counter electrode, therefore the two half reactions occurring in the electrochemical cell also occur at these electrodes. This implies that the electrical current is flowing between the working and counter electrode (and measured with the ampere meter), so no electrical current is flowing through the reference electrode, and its equilibrium potential remains stable. This three-electrode setup is also known as a potentiostatic setup.

1.6.2 The counter electrode

Several conditions should apply to the counter electrode in order to avoid fouling and errors in the current measured at the electrochemical:

- The surface of the counter electrode should be at least ten times greater than the surface of the working electrode. The aim is to study the half reaction occurring at the working electrode. This means that this half reaction should be the slowest, as otherwise the properties of the half reaction occurring at the counter electrode will determine the characteristics of the measured electrical current. By using a much bigger surface, this problem is circumvented because the reaction rate is dependent on electrode surface. Therefore, a relatively slow half reaction at the counter electrode is occurring much faster still than the one at the working electrode because more species are transformed per time unit owing to the much bigger surface that is available for the half reaction at the counter electrode.
- The counter electrode should be a good electrical conductor. This condition is clear; if the counter electrode is not a good conductor, it means that a poor amount of current can pass the interface at the counter electrode, which will then determine the measured current of the electrochemical cell. Therefore, the measured current will provide information about the properties of the counter electrode and not about the half reaction occurring at the surface of the working electrode.
- The positioning of the counter electrode against the working electrode is very important[3].

1.6.3 The reference electrode

Reference electrodes were discussed in section 1.5, and Table 1.1 presented commonly used and commercially available reference electrodes.

1.6.4 The working electrode

The working electrode is the one where the reaction to be studied occurs and is constructed of an electrically conductive material. The commonly used materials are platinum, gold and glassy carbon, which are available in a wide range of shapes, purity and configuration, and will be discussed in this section.

Materials

Platinum and gold

Platinum[7–11] and gold[12–16] are the most commonly used electrode materials. The reason can be found in their ease of manufacture, variety of configurations and the commercial availability of these configurations (rod, wire, microwire, sheet, woven structures) and on their high purity. Despite their

high resistivity to oxidation, they are not inert as will be shown further in this book (Chapter 8 for platinum and Chapter 10 for gold).

The overpotential for the hydrogen-evolution reaction is much smaller at platinum than at gold, which explains the use of platinum as the electrode material for reversible hydrogen electrodes. In addition to this, platinum adsorbs hydrogen at its surface, which allows estimation of the active surface and comparison with the geometrical surface. Gold does not adsorb hydrogen. The absence of this effect, in combination with the relatively high overpotential for the hydrogen-evolution reaction, makes gold very suitable for studying cathodic processes.

At high positive overpotentials, platinum and gold form an oxide layer, which is reduced back to the metallic phase in the return-scan direction. From the current of these peaks, it is possible to estimate the 'true' active surface, which can be seriously different from the geometrical surface area.

Glassy carbon

Glassy carbon[17–21] is a polymer based on benzene units. It is very hard, chemically inert, not porous and looks like glass at broken surfaces. This type of carbon was first synthesised by Yamada and Sato based on fenolic resins[18]. Today, fenol–formaldehyde mixtures are used for the synthesis of glassy carbon. The mixture is subjected to a thermal treatment with a gradual increase of the temperature. At 670 K, the polymerisation process starts with the formation of N_2 and O_2. A slow and controlled increase of the temperature is crucial to allow the removal of O_2 and N_2 gas by diffusion towards the edge of the mixture. At 870 K, H_2 also is formed and needs to be removed by diffusion. Further increase of the temperature is continued until 1570 K. After that, the temperature is brought back to 298 K (also in a slow and controlled way to allow all the gas to diffuse out of the structure), and the glassy carbon polymer is obtained, which is also called vitreous carbon.

Advantages of using glassy carbon as electrode material are:

- highly resistive to chemical attack (strong acidic and/or alkaline solution);
- gas impermeable;
- pre-treatment by polishing and scanning of the potential;
- improved reversibility for some redox systems;
- larger available potential window;
- low cost compared with platinum and gold.

Pre-treatment of working electrodes[22–43]

The rate of electron transfer at a solid electrode is strongly dependent on the condition of that electrode surface. In this book, several explanations

prove this statement. In order to activate the electrode surface in a reproducible and repeatable way, it should be subjected to mechanical treatment comprising scouring the electrode surface to remove a few micrometers followed by polishing to smoothen the surface. A typical procedure is given here: the electrode surface was scoured briefly on 1200-grit SiC-emery paper to obtain a fresh surface. To smooth this relatively rough surface, it was further subjected to sequential polishing on a polishing cloth covered with alumina (Buehler) powder of 1, 0.3 and 0.05 μm for respectively 5, 10 and 20 min. To remove any adherent Al_2O_3 particles, the electrode surface was rinsed thoroughly with doubly deionised water and cleaned in an ultrasonic bath (Branson 3210) for 2 min. An alternative polishing procedure is the use of diamond paste instead of Al_2O_3 polishing powder.

After the mechanical pre-treatment, the electrode can be subjected to a chemical and/or electrochemical pre-treatement. Chemical treatment consists mainly of etching of a few layers of the metal, including possible contaminants. A well-known etching solution for gold is the so-called 'piranha' solution. Other reported solutions are kali, which is a concentrated KOH solution to remove fats and oils and etch off a layer of platinum.

Finally, electrochemical pre-treatment is performed to obtain a reproducible surface. This is done mainly by cycling the applied potential over the entire potential window limited by the hydrogen and oxygen evolution reaction. Such a treatment has two functions: first, removal of adsorbed species and, second, altering the microstructure of the electrode, the latter being caused by the repetitive dissolution and deposition of a metal monolayer in the scanning procedure.

Electrode configurations

Rotating-disc[3] and ring–disc electrodes[44]

Disc electrodes are commonly used in voltammetry as stationary and as rotating electrodes. The diffusion of electroactive species towards the surface of these electrodes is linear, as shown in Fig. 1.6a. The advantage of the second configuration is that rotation of the electrode causes convection in solution that compensates for the increase of the diffusion layer thickness with time after a period of about 200 ms. This results in a limiting current instead of a peak-shaped current (see also section 3.2) according to the Levich equation[3]:

$$I_{\text{lim}} = 0.62nFAD^{2/3}\upsilon^{-1/6}\omega^{1/2}c \qquad [1.15]$$

where I_{lim} is the limiting current (mA), n is the number of electrons, F is the Faraday constant (C mol^{-1}), A is the surface of the electrode (cm^2), D is the diffusion coefficient (cm^2 s^{-1}), ν is the kinematic viscosity (cm^2 s^{-1}), $\omega = 2\pi N$

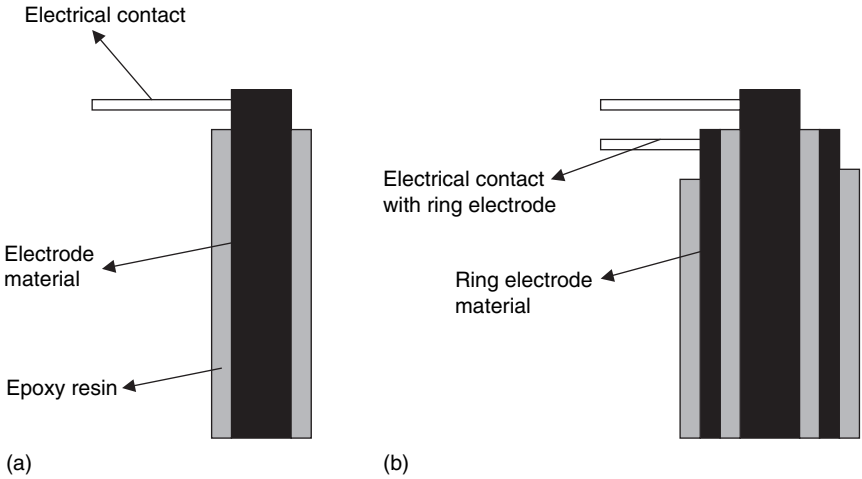

1.6 Scheme of a cross section (in the length of the electrode) of rotating-disc electrode (a) and a rotating-ring–disc electrode (b).

(with N the number of revolutions per second), and c is the concentration of the compound in moll^{-1}.

Different methods are proposed in the literature to construct disc electrodes, but the commonly used way is embedding a rod of the electrode material in an insulating material such as glass, polyamides, acrlyates, epoxy resins or polyvinylchloride. The electrodes used in the work described in this book were constructed by insulating the electrode material in epoxy resin (Fig. 1.7). First, a copper piece was made with a hole for the positioning of the electrode material rod. This was positioned in a PVC holder, which was then filled with epoxy resin. After curing for 48 h, the PVC mantel was removed and the excess of epoxy scoured away on emery paper.

An alternative to disc electrodes is the ring–disc electrode (Fig. 1.6b). In this type of electrode configuration, the disc electrode is surrounded by a ring electrode, which is electrically isolated from the disc electrode. The purpose of such an electrode is to study electrochemical reactions and their mechanisms by detection of intermediates and reaction products at the ring electrode which were formed at the disc surface. Owing to rotation, time-independent limiting currents are obtained, and the radial convection allows the reaction product of the disc to be transported to the ring. However, it may be clear that only a fraction of the reaction product formed at the disc will be transferred at the ring electrode. This fraction N is given by the following equation and is called the collection efficiency[43]:

$$N = I_R / I_D \qquad [1.16]$$

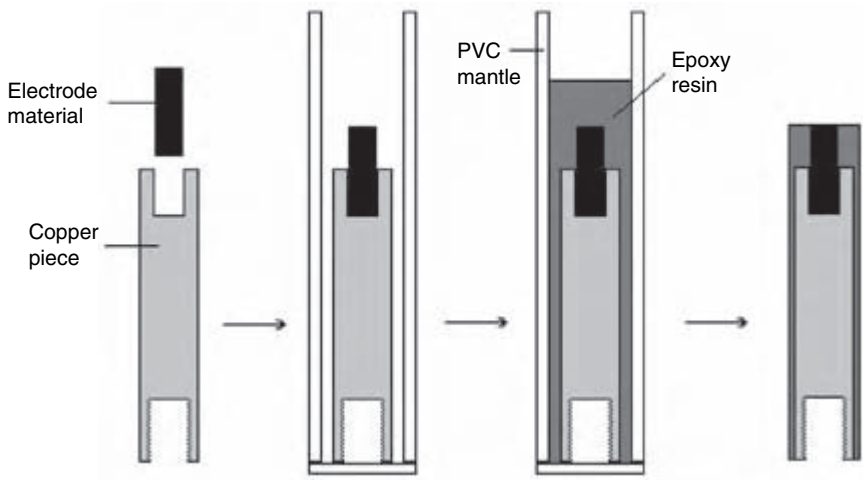

1.7 Scheme of the construction of micro electrodes starting from a rod of the electrode material, a copper base, a PVC moulding and epoxy resin.

where N is the collection efficiency, I_R is the ring current (density), and I_D is the disc current (density). The collection efficiency is dependent on the geometry of the ring–disc electrode (radius of the disc, gap between disc and ring and the thickness of the ring) and can be determined by using a reversible system such as $[Fe(CN)_6]^{4-}|[Fe(CN)_6]^{3-}$. Typical values of N for a well-constructed ring–disc electrode vary around 0.25.

Flow electrodes[45]

Alternatively, the solution can be moved, rather than the electrode, by a solution flow passing a stationary electrode. Flow electrodes are described in different setups and shapes. The main reasons for using these electrodes are that, depending on the flow rate, a steady state will be obtained (time-independent current signal), and that these electrodes are very useful for analysis of continuous flow of solution. A typical scheme for such an electrode setup is shown in Fig. 1.8. A very important condition that needs to be fulfilled in flow electrodes is that there is no turbulent behaviour because this would seriously disturb the measured signal.

Wall-jet disc electrode[46]

Electrodes can also be positioned in a wall-jet disc electrode configuration, a home prepared construction, schematically shown in Fig. 1.9. From a small bath (1) with a capacity of about 3l, solution is taken by an EHEIM pump

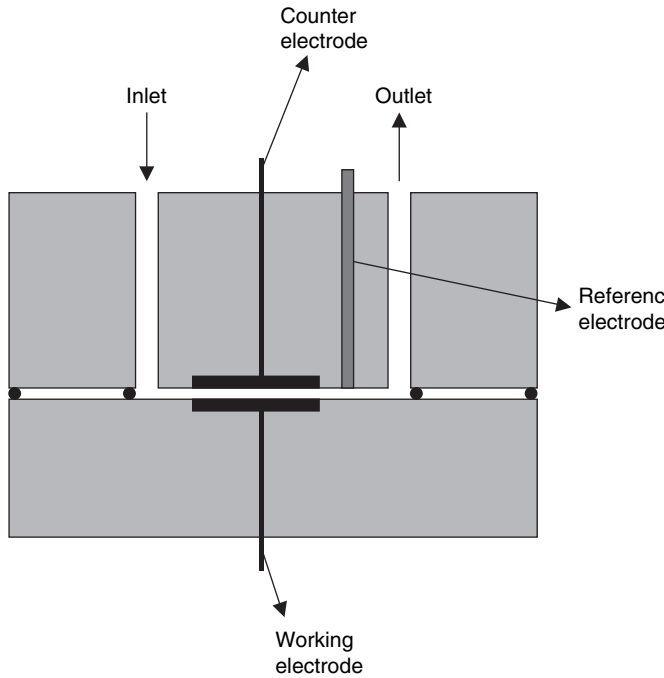

1.8 Scheme of a flow-through electrode configuration.

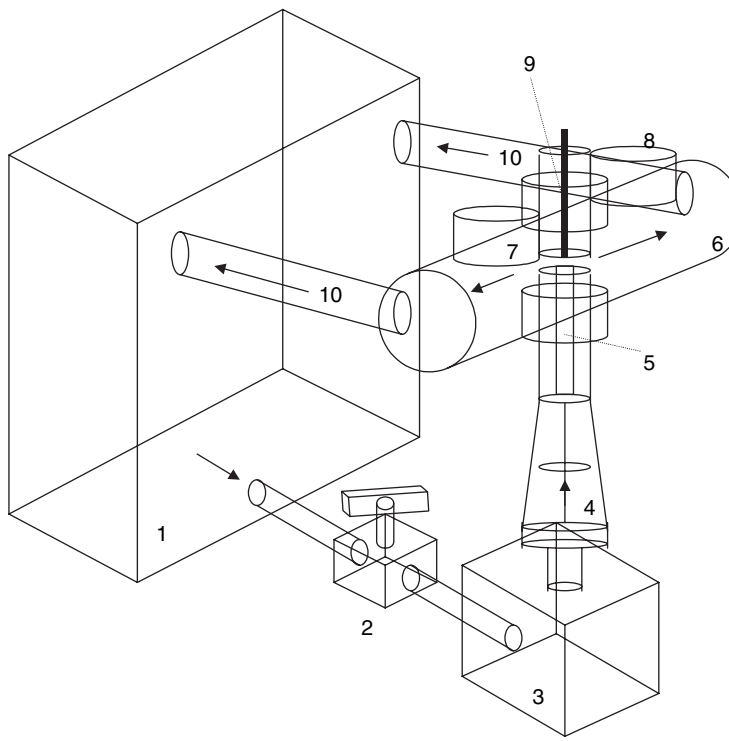

1.9 Scheme of the wall-jet electrode as constructed in our laboratory with (1) solution tank, (2) vessel to control the solution flow rate, (3) pump, (4) flow-rate measuring device, (5) capillary, (6) measuring chamber, (7) counter electrode, (8) reference electrode, (9) working electrode, (10) overflow system to return solution to the solution tank.

(3) over a vessel (2). This valve is used for variation of the flow rate of the solution. The solution is further pumped over a flow meter (4, Cole-Parmer) through a capillary (5, further called the nozzle) made of glass. In a detection cell (6), the solution is pumped onto the surface of the platinum electrode (9). The reference and counter electrode are positioned in (7) and (8) respectively. Finally, the solution flows back to the bath via pipelines (10) due to gravimetric forces. The flow direction of solution in this electrode configuration is similar to the one obtained at rotating disc electrodes. In a wall-jet electrode setup, the diffusion layer thickness is controlled by the flow rate of the solution through the nozzle of the capillary instead of being controlled by the rotation rate of the disc electrode.

Ultramicro electrodes

Ultramicro electrodes are electrodes of any shape with dimensions of the order of a few micrometers and possessing a different electrochemical behaviour compared with its millimetre shaped counterparts. The reason is a different mechanism for the transport of electroactive species towards the electrode (Fig. 1.10). For ultramicro electrodes, the main fraction of electroactive species is transport through a spherical diffusion, where it is a

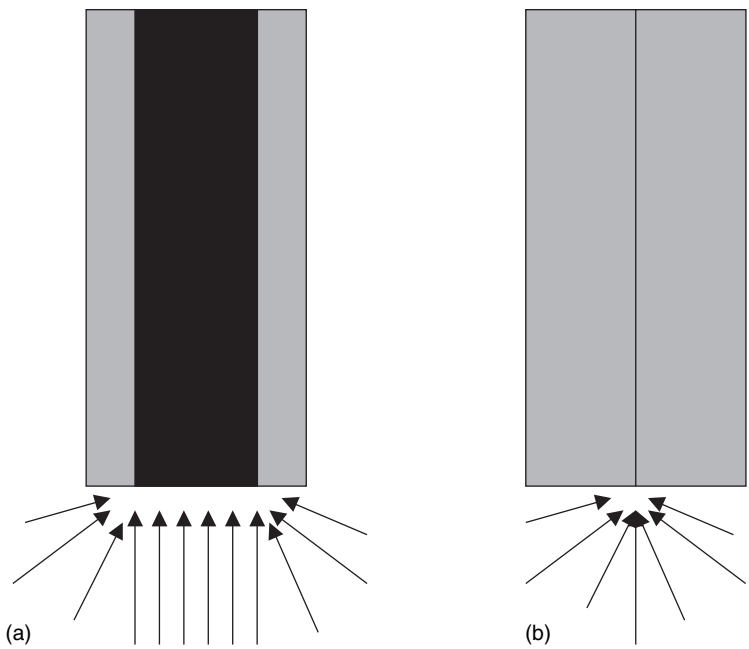

1.10 Schematic representation of transport of electroactive species towards the surface of a micro (a) and an ultramicro (b) electrode.

linear mechanism for micro electrodes. Spherical diffusion at the edge of the micro electrode can be neglected; for ultramicro electrodes, it is the fraction of linear diffusion that can be ignored. This has several advantages:

- Despite much smaller current being recorded, the current density at ultramicro electrodes is much higher.
- Owing to the small current measured, Ohmic drop (also called IR-drop) effects in solution are much less pronounced. This includes that ultramicro electrodes can be used in highly resistive media (including non-aqueous solution) and/or without the use of supporting electrolyte.
- The small area of the electrode also reduces the double-layer capacitance and RC-time constant, which allows experiments to be performed at high scan rates (e.g. $100\,000\,\mathrm{V\,s^{-1}}$).
- Owing to spherical diffusion, a diffusion layer is obtained with constant thickness, therefore resulting in time-independent limiting-current plateaus. This implies that its current is (almost) not affected by convection of the solution, therefore it can be used in flowing streams as long as turbulent behaviour in solution is avoided.
- Converting the small currents measured at ultramicro electrodes results in higher current densities compared with the values obtained at micro electrodes. This is also caused by the spherical diffusion path. This effect improves on the sensitivity and the detection limit for analytical purposes, and the small size of the electrodes in combination with application of high scan rates allow measurement to be performed *in vivo* and with a minimal (negligible) disturbance of the conditions of the system to be analysed.

The current obtained at ultramicro disc electrodes is described in Equation 1.17[47]:

$$I = 4\pi rn\mathrm{F}\mathrm{D}c\left(r\left(\frac{1}{\pi \mathrm{D}t}\right)^{1/2} + 1\right) \qquad [1.17]$$

where I is the measured current, r is the radius of the ultramicro electrode, F is the Faraday constant, D is the diffusion coefficient, c is the concentration and t is the time that the potential is applied. This equation shows that the current becomes independent for longer values of t, which means that a time-independent limiting-current will be obtained. Note also that the time needed to obtain a steady-state condition is dependent on the radius of the electrode.

The main disadvantage of ultramicro electrodes is the need to use equipment that is able to measure very small direct currents (nA) with high precision and low noise (pA–fA). This equipment is fairly expensive, and special precautions should be taken when it is used in an industrial envi-

ronment where numerous sources can have a serious contribution to the noise signal.

Different methods are described to construct ultramicro electrodes[48–62] such as insulation in glass or epoxy resin, the construction of ultramicro electrode arrays (an array of individual ultramicro electrodes to increase the current signal without losing the benefits of ultramicro electrode behaviour) by template synthesis, metal depositions in pores of membranes and by using the connecting wires in microchips. The latter has the advantage that each ultramicro electrode is individually addressable.

Insulation of microfibres of platinum, gold and graphite in glass is the best-known method for the construction of ultramicro electrodes. Ultramicro electrodes used in the work described in this book are also obtained by insulation in glass according to the following procedure (Fig. 1.11): a wire of platinum with $r = 25\,\mu m$ is deposited in a glass capillary with 5 mm outer and 0.5 mm inner diameter. One tip of the glass tube is heated, while the other side of the tube is connected to a vacuum pump. When the glass tube starts to soften during heating, its internal volume reduces because of the vacuum, which results in the insulation of a piece of the platinum, gold or graphite wire. A portion of this sealed tube is analysed under the microscope, and a piece of about 4 mm is cut for further use. Both sides of this small piece are polished on emery paper in order to obtain a smooth surface and to allow electrical contact to the insulated microwire. This small piece is then positioned in a glass tube with an inner diameter of 5 mm and, with

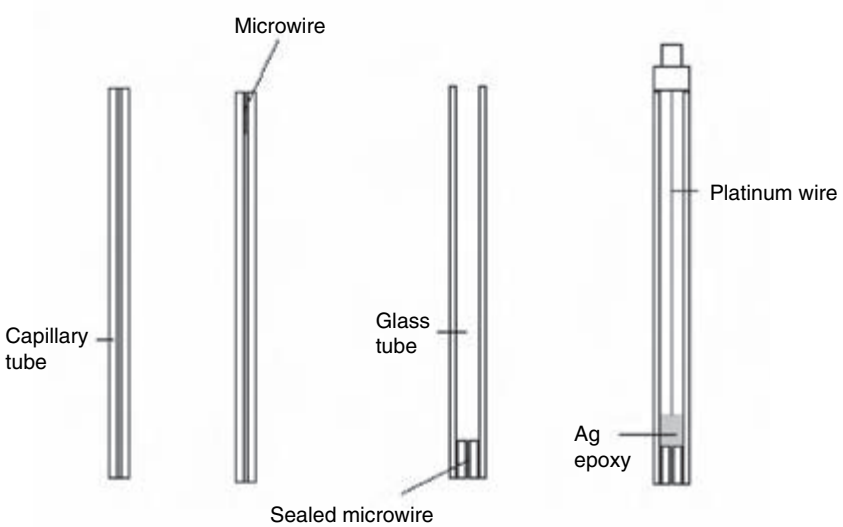

1.11 Scheme of the construction of ultramicro electrodes according to a procedure described in the text.

the same procedure as described before, sealed in this tube. Finally, the electrode is polished until the microwire is in contact with the environment. At the inner side of the tube, electrical contact is made through mercury or Ag paint.

1.6.5 Role of electrolytes[45]

Before ultramicro electrodes became important in voltammetry, a supporting electrolyte always needed to be used and was of more importance than one would think. The role of the supporting electrolyte is summarised here:

- The liquid medium (the solution to be studied) is mainly non- or poor-conductive (H_2O, organic solvents), which makes it practically impossible to pass electrical current between electrodes immersed in that solution. So, the first role of a supporting electrolyte is to provide the solution with some conductive properties by adding an electrolyte.
- Application of a potential difference between electrodes immersed in a solution causes the presence of an electrical field in solution. Negatively charged ions in that solution will move towards the anode, and positively charged ions will move towards the cathode due to this field (this way of species transport is called migration). This process results in charge transport or the flow of an electrical current, and the fraction of this current transported by each species is dependent on its mobility and concentration. However, in voltammetric experiments, this type of charge and species transport is complicated and frequently disturbs the transport properties by diffusion and/or convection so intensively that interpretation of the data becomes very complicated or even impossible. To suppress the migration, an electrolyte is added in excess (10–50 times the concentration of the species to be studied). In this case, mainly the electrolyte will be transported due to the electrical field and not the species to be studied.
- Strong acids in pH range of 0–4, strong bases in pH range of 11–14 and buffer solutions over the entire pH scale can also be used as supporting electrolyte if the concentration is high enough (see above). Besides the role of decreasing the solution resistance and suppression of migration currents, this type of electrolyte can also provide H^+ or OH^- in a solution – a species that is frequently involved in the mechanism of electrochemical reactions. This can have a serious impact on the kinetics of the reaction because less activation energy (read applied overpotential) is needed owing to H^+ or OH^- being directly available in large amounts instead of being delivered from the dissociation reaction of water.
- Besides being a potential source of H^+ or OH^-, the ionic form of the electrolyte can be useful as complexing agent. It is well known in

Table 1.2 Ions used in electrolytes, based on their good solubility in different solvents[63–65]

Ion type	Suitable solvent
H^+	Water, acetone, acetonitrile
Li^+	Acetone, acetonitrile
Na^+	Water, acetone, acetonitrile
K^+	Water, acetone, acetonitrile, DMF
Me_4N^+	Acetone, acetonitrile, DMF, DMSO
Et_4N^+	Acetone, acetonitrile, DMF, DMSO
Bu_4N^+	Acetone, acetonitrile
Cl^-	Water, acetone, acetonitrile, DMF, DMSO
Br^-	Water, acetone, acetonitrile, DMF, DMSO
I^-	Water, acetone, acetonitrile, DMF, DMSO
NO_3^-	Water, acetone, acetonitrile, DMF, DMSO
BF_4^-	Acetonitrile
PF_6^-	Acetonitrile
ClO_4^-	Water, acetone, acetonitrile, DMF, DMSO

voltammetry that complexing a species to a more stable form results in a more difficult reduction of this species (in other words higher negative overpotentials should be applied to reduce the species compared with the non-complexed form). It can be useful that the supporting electrolyte also acts as complexing agent.

Typical supporting electrolytes are given in Table 1.2, including the environment[63–65].

1.7 Charge-transfer and transport phenomena

1.7.1 Introduction

In order to develop an amperometric sensor, voltammetric research is essential, both to find out about the working principle or mechanism of the sensor reaction and to determine the appropriate working conditions (amongst others, the potential of the working electrode). A potential in-line sensor having an output signal which is continuously in proportion to the concentration of the analyte can only be based on a time-independent signal and hence on a voltammetric steady-state method making use of configurations such as rotating disc electrodes, flow-through cells, ultramicro electrodes, wall-jet electrodes or diffusion through membranes. For the development of a sensor on a laboratory scale, predominately rotating-disc voltammetry is used. In order to investigate the mechanism of the occurring oxidation/reduction reactions, rotating-ring–disc voltammetry and non-

steady-state techniques, such as voltammetry with linear potential variation and cyclic voltammetry, were also used.

For industrial applications, other parameters such as ease of implementation and maintenance and investment cost guide the decision as to which electrode configuration will be used. These configurations will be described in the appropriate sections of this book.

1.7.2 General theoretical background of electrochemical reactions

The extensive Butler–Volmer relation for charge transfer

The electrode processes that are dealt with in this work relate to the transfer of electrons at an interface between a conductive material and an aqueous solution. Since it concerns a heterogeneous process, at least three steps can be distinguished:

1. Supply of reacting component from the dissolution phase (transport).
2. Transfer of electron(s).
3. Discharge of reaction product away from the electrode surface (transport)[66].

It will appear later on in this work that other sub-steps will also play a role, namely homogeneous chemical reactions and adsorption processes[67]. The rate of the global process is always determined by the slowest sub-step. Many voltammetric and amperometric analysis methods make use of transport-controlled currents[2,68–70] because this has certain advantages (discussed later on in this book). However, this is not indispensable if a reduction or oxidation current under the appropriate experimental conditions is in proportion to the concentration of the reacting component, regardless of the nature of the rate-determining step.

Besides transport, the most simple electrode process consists of one step in which one electron is transferred:

$$\mathrm{O} + \mathrm{e}^- \leftrightarrows \mathrm{R} \qquad [1.18]$$

The flux of O that is converted into R by reduction is presented as v_c:

$$v_c = \frac{\mathrm{d}(c_O)_0}{A\mathrm{d}t} = \mathrm{k}_c (c_O)_0 = \frac{j_c}{n\mathrm{F}} \qquad [1.19]$$

where v_c is the rate of the cathodic reduction reaction, c_0 the concentration of oxidants, $(c_O)_0$ is the concentration of oxidants at the electrode surface, A is the electrode surface, k_c is the reaction rate constant of the envisaged reduction reaction, and j_c is the current density of the reaction.

Reorganisation of this equation for the application of the potential difference of ΔE results in:

$$j_c = (c_O)_0 n\mathrm{F}(k_c)_{\Delta E=0} e^{\frac{-\alpha n\mathrm{F}\Delta E}{RT}} \quad [1.20]$$

where $(k_c)_{\Delta E=0}$ is the rate constant at equilibrium and α the transfer coefficient ($0<\alpha<1$).

Similarly, an equation for the oxidation reaction can be deduced:

$$j_a = (c_R)_0 n\mathrm{F}(k_a)_{\Delta E=0} e^{\frac{(1-\alpha)n\mathrm{F}\Delta E}{RT}} \quad [1.21]$$

When the cathodic current density (j_c) is equal to the anodic current density (j_a), the net current flowing across the electrode–solution interface is zero, and the net flux of O and R is zero. For this condition, the current densities represent the equilibrium-exchange current density (j_0), given by:

$$j_c : j_a = j_0 \quad [1.22]$$

which is associated with the equilibrium potential difference ΔE_e. The difference between this equilibrium potential ΔE_e and ΔE is called the overpotential, η:

$$\eta = \Delta E - \Delta E_e \quad [1.23]$$

Equations 1.22 and 1.23 can be combined to obtain an expression for the net current when a potential (the overpotential) is applied, which is also known as the Butler–Volmer (BV) equation[71]:

$$j = j_a - j_c = j_0\left[e^{\frac{(1-\alpha)n\mathrm{F}\eta}{RT}} - e^{\frac{-\alpha n\mathrm{F}\eta}{RT}}\right] \quad [1.24]$$

Figure 1.12 illustrates the relationship between current density and applied overpotential expressed in the previous equation.

The BV relation is often used in a form where the electrode potential is referred to by the more accessible equilibrium potential, E_e, and where the exchange current density, j_0, replaces the rate constant $k^{0'}$:

$$j = j_0\left\{e^{(1-\alpha)\frac{n\mathrm{F}}{RT}(\Delta E-\Delta E_e)} - e^{-\alpha\frac{n\mathrm{F}}{RT}(\Delta E-\Delta E_e)}\right\} \quad [1.25]$$

$$j_0 = n\mathrm{F}k^{0'}(c_R^{\infty})^{\alpha}(c_O^{\infty})^{(1-\alpha)} \quad [1.26]$$

where c^{∞} represents a concentration in the middle of the solution. $(\Delta E-\Delta E_e)$, the overpotential, is indicated with the symbol η. To indicate

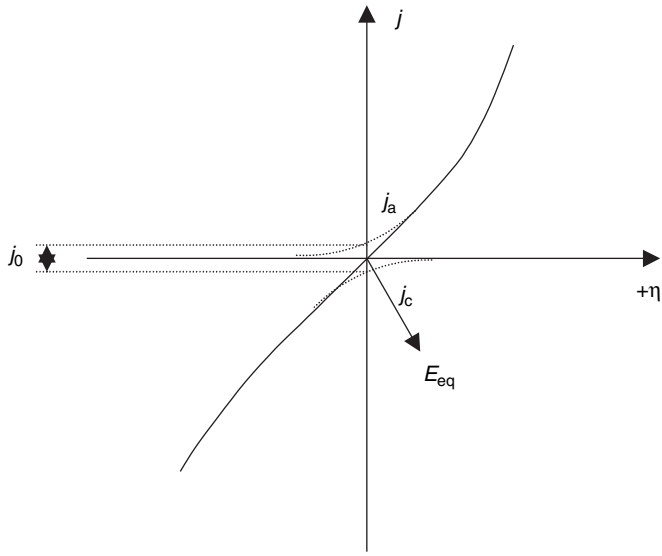

1.12 Relationship between applied over-potential and the measured current for an electrochemical reaction.

that the charge transfer is rate determining, one refers to an activation over-potential η_{act}.

In practice, most of the electrode processes involve, besides the transport steps, more than one stage, and often several electrons are transferred.

Suppose, for example, that a voltammetric wave is due to an electrochemical reaction where n electrons are transferred and which occurs in n one-electron steps:

$$O + e^- \leftrightarrows B \qquad [1.27]$$

$$B + e^- \leftrightarrows C \qquad [1.28]$$

:

$$Q + e^- \leftrightarrows S \qquad [1.29]$$

$$S + e^- \leftrightarrows T \qquad [1.30]$$

$$T + e^- \leftrightarrows U \qquad [1.31]$$

$$Z + e^- \leftrightarrows R \qquad [1.32]$$

where comparison [Equation 1.30] is supposed to be the rate-determining step (RDS), which is preceded by n_{be} other one-electron-transfer steps and followed by n_{af} such steps. Every step has its specific formal rate constant,

and the redox system concerned has its specific formal potential. In that case, the BV relation maintains the same general form as Equation 1.24. Moreover, Bockris[1] has extended the validity of the BV relation to reaction sequences comprising, besides electron-transfer steps, also homogeneous reaction steps – rate-determining ones as well as non rate-determining ones. In the general reaction scheme as above, they can occur anywhere, without a limitation to their number. The BV relation for multistep reactions, including homogeneous chemical reactions, which will be referred to later on as the extended BV relation, is as follows:

$$j = j_0 \left\{ e^{\alpha_a \frac{F}{RT}\eta} - e^{\alpha_k \frac{F}{RT}\eta} \right\} \qquad [1.33]$$

where j_0 depends on the kinetic parameters of every sub-step. For the transfer coefficients, the following applies:

$$\alpha_a = \frac{n_{na}}{v} + \frac{1}{v} - \beta r = \frac{n - n_{vo}}{v} - \beta r \qquad [1.34]$$

$$\alpha_k = \frac{n_{vo}}{v} + \beta r \qquad [1.35]$$

$$\alpha_a + \alpha_k = \frac{n}{v} \qquad [1.36]$$

Here β is the cathodic symmetry factor of the rate-determining step and ν is a positive integral number indicating how many times the RDS is occurring in the global electron-transfer reaction (mostly $\nu=1$). The parameter r takes into account a homogeneous chemical reaction, the rate of which is not dependent on the potential, as RDS: when the RDS is a charge-transfer step, $r=1$ applies, and for a chemical RDS, $r=0$.

The transfer coefficients are the ones determining how the electrode potential influences the electrochemical reaction rate or, in other words, the inclination of the relation between log I and the over-potential, also called the Tafel slope, of a multistep reaction. The coefficients are an important aid when unravelling the electrochemical reaction mechanisms, because the experimentally determined Tafel slope should correspond to the value that is calculated for the postulated sub-step sequence and RDS.

However, this method is not sufficient to validate quickly a possible reaction mechanism because it cannot deliver the reaction order of a component *not* occurring in the global reaction equation. Often H^+ ions or OH^- ions are involved in the sub-steps where an intermediate is formed before the RDS and is re-used in or after the RDS. This causes a pH dependency of the global reaction, despite the fact that not necessarily H^+ or OH^- appears in the overall reaction of the oxidation or reduction.

In order to postulate reaction mechanisms, one needs to know the reaction orders of all components present in the solution and hence to verify experimentally if the current is dependent on their concentration. In order to validate subsequently the postulated mechanisms, one has to assume successively that each of the sub-steps is rate determining and to deduct the resulting BV relation. In order to be able to verify the validity of the latter, it can contain only experimentally accessible concentrations. Accordingly, the non-accessible concentrations of intermediates should be eliminated. This is tried by assuming that all the sub-steps, except for the rate-determining ones, are in balance and by treating the rates of their forward and backward reaction as equivalent. This results in both the Tafel slope (transfer coefficient) and the reaction orders, which are compared with the values obtained experimentally. For the scheme, given by Equations 1.27–1.32, this can be worked out in general terms. This work is rather extensive and moreover is set up in an abstract form. Since the procedure is to be applied on the reaction onto which the hydrogen peroxide and the dithionite/indigo sensor is based (see further in this book), reference is made to the chapters concerned for more insight in the method itself.

Transport phenomena

When there is balance in an electrochemical cell which contains oxidising and reducing agent from one and the same redox system, and the balance is disturbed by, for example, making the working electrode potential more positive, Equation 1.24 predicts a net anodic current. When the potential is made sufficiently positive, the cathodic term in the right part can be neglected in relation to the anodic term. In short and in general, one can write a one-electron reaction as an example:

$$i = \mathrm{k}(E)\mathrm{Fc} \qquad [1.37]$$

where the exponential increase of the current, with the potential becoming more positive, is incorporated in the term $\mathrm{k}(E)$. Since an electrode reaction is a heterogeneous reaction and current continuity is accompanied by conversion of reducing agent at the electrode surface, the exponential current increase will be weakened by a concentration depletion of the reactant at the electrode surface. This leads to a situation where, starting from a certain potential, the current is exclusively determined by the supply rate of the reacting component:

$$i = \mathrm{mF}(c^{\infty} - c) \qquad [1.38]$$

Here m is called the transport coefficient, which in a stationary solution, for example, where transport occurs only by diffusion, is much smaller than in

a rotating-disc configuration. Moreover, a transport-determined current is proportional to the difference between the concentration in solution and the concentration at the electrode surface. When the latter turns zero, the current cannot increase any further and this is termed a limiting-current. This is a simplification arising from the Nernst diffusion-layer concept. Primarily, this applies to transport by diffusion, where the current according to the first law of Fick is proportional to the concentration gradient of the reacting component at the electrode surface. Nernst assumes that the concentration profile is linear in a large part of the depletion layer, bordering the electrode surface. By extrapolating the linearised profile, a thickness of the diffusion layer (depletion layer or enhancement layer for the reacting component and the reaction product, respectively) can be calculated. This notion has no real meaning due to the asymptotical extinguishing of the depletion.

When comparing Equations 1.37 and 1.38, it is clear that it is the relation of two parameters, namely the transport coefficient, m, and the formal reaction rate constant $k^{0'}$ (incorporated in $k(E)$ in Equation 1.37; see also Equation 1.20), that decides whether the current is determined mainly by the BV relation or by transport. In a voltammogram, the potential area in which the BV relation applies decreases when $k^{0'}$ increases relatively in relation to m. In electrochemical terms, one speaks of an increase in the reversible character of the voltammetric wave. When having sufficient positive (negative) potentials for an oxidation (reduction), transport mostly prevails. Providing that the appropriate cell and/or electrode configuration is present, transport-determined currents are very reproducible and suitable for analytical purposes.

When transport is rate determining, the shape of the voltammetric curve can, in a rather simple way, be deducted by means of the Nernst diffusion-layer concept[44]. As an example, a solution is considered that contains oxidising and reducing agent of the same redox system and where *n* electrons intervene in the interconversion. As the potential is varied in a positive or a negative sense starting from the equilibrium potential, the following can be stated:

$$i = nFm(c_R^{\infty} - c_R) \qquad [1.39]$$

$$i = -nFm(c_0^{\infty} - c_0) \qquad [1.40]$$

Transport coefficients of components of the same redox couple usually display only very small differences, hence $m_O = m_R = m$ is assumed. It must be remembered that *c* and m are time-dependent parameters when no steady-state electrode configuration is used.

When the potential sufficiently deviates from the equilibrium potential, $c = 0$ and the current attains a limiting value:

$$i_{\mathrm{L,a}} = n\mathrm{F}\mathrm{m}c_{\mathrm{R}}^{\infty} \quad [1.41]$$

$$i_{\mathrm{L,k}} = -n\mathrm{F}\mathrm{m}c_{0}^{\infty} \quad [1.42]$$

By combining Equations 1.39–1.42, the surface concentrations can be expressed as a function of both the current and the limiting current:

$$c_{\mathrm{R}} = \frac{i_{\mathrm{L,a}} - i}{n\mathrm{F}\mathrm{m}} \quad [1.43]$$

$$c_{0} = \frac{i - i_{\mathrm{L,k}}}{n\mathrm{F}\mathrm{m}} \quad [1.44]$$

Incorporating Equations 1.43 and 1.44 in the Nernst relation results in the desired *I–E* relation for rate-determining transport:

$$E = E^{0'} + \frac{\mathrm{R}T}{n\mathrm{F}} \ln \frac{i - i_{\mathrm{L,k}}}{i_{\mathrm{L,a}} - i} \quad [1.45]$$

Potentiostatic experiments are more often carried out than galvanostatic ones, so that most of the time, for *i*, an expression is desired in function of the potential. Starting from Equation 1.45, one can deduct a comparison for this:

$$i = \frac{i_{\mathrm{L,a}} \mathrm{e}^{\left[n\mathrm{F}\left(E-E^{0'}\right)/\mathrm{R}T\right]} + i_{\mathrm{L,k}}}{\mathrm{e}^{\left[n\mathrm{F}\left(E-E^{0'}\right)/\mathrm{R}T\right]} + 1} = n\mathrm{F}\mathrm{m}\frac{c_{\mathrm{R}}^{\infty} \mathrm{e}^{\left[n\mathrm{F}\left(E-E^{0'}\right)/\mathrm{R}T\right]} - c_{0}^{\infty}}{\mathrm{e}^{\left[n\mathrm{F}\left(E-E^{0'}\right)/\mathrm{R}T\right]} + 1} \quad (1.46)$$

This relationship shows that when transport is the slowest step of a process, the current is completely determined by the working electrode potential and the limiting currents, or alternatively (last part of Equation 1.46) by *E*, c_{O}^{∞}, c_{R}^{∞} and m.

The above discussion showed the relationships for the current measured at the surface of the electrode due to conversion of O to R or R to O when the process is controlled by transport phenomena. In the next paragraphs, the transport of species itself and the resulting concentration profiles in solution are discussed.

The transport of electroactive material towards and away from the electrode can generally be given by Fick's second law:

$$\frac{\delta c_{(x,t)}}{\delta t} = \mathrm{D}\frac{\delta c_{(x,t)}}{\delta x^{2}} \quad [1.47]$$

where D is the diffusion coefficient, *c* is the concentration of material, *x* is the distance away from the electrode surface, and *t* is the time that the concentration gradient exists. Through Laplace transformations with specific boundary conditions, given below:

$$\begin{array}{llll} \text{for} & t = 0 & \text{and} & x \geq 0 \qquad c = c^{\infty} \\ \text{for} & t \geq 0 & \text{and} & x \rightarrow 0 \qquad c \rightarrow c^{\infty} \\ \text{for} & t > 0 & \text{and} & x = 0 \qquad c = 0 \end{array}$$

it is possible to calculate that the variation of the concentration of electroactive material as a function of time at the surface of the electrode:

$$\left(\frac{\delta c}{\delta x}\right)_{(0,t)} = \frac{c^{\infty}}{\pi^{1/2} D^{1/2} t^{1/2}} \qquad [1.48]$$

and the flux of material crossing the boundary of the electrode is obtained by the following equation:

$$I = nFAD\frac{\delta c_{(0,t)}}{\delta x} \qquad [1.49]$$

The concentration–distance profiles predicted by Equation 1.48 and resulting in the current in Equation 1.49 are given in Fig. 1.13. A complete expression for the current that results from semi-infinite diffusion is obtained as follows, which in fact is also called the Cotrell equation for a planar electrode:

$$I = \frac{nFAD^{1/2}}{\pi^{1/2} t^{1/2}} c^{\infty} \qquad [1.50]$$

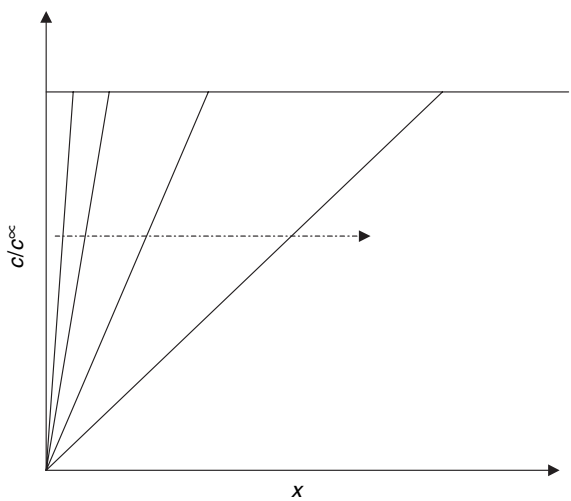

1.13 Concentration profile of the analyte in the vicinity of the electrode and concentration gradient variation as a function of proceeding electrochemical reaction.

In this work, for the research on a laboratory scale, rotating-disc electrodes[72] were used, amongst others. For the transport coefficient of this configuration, the following applies:

$$m = 0.620\left(\frac{d}{\eta}\right)^{1/6} D^{2/3}\omega^{1/2} \qquad [1.51]$$

where (d/η) $(m^2 s^{-1})$ represents the kinematic viscosity of the solution and ω is the angular rate $(rad\,s^{-1})$ of the electrode. This electrode, which permits change in the relation between $k^{0'}$ and m, makes it possible to study, in an efficient way, kinetic and transport parameters of electrode processes, on condition that the value for $k^{0'}$ is not greater than $5.10^{-4}\,m\,s^{-1}$.

The field of predominantly kinetic influence (base of the voltammogram, BV relation valid) and the field of a mixed influence of kinetics and transport are suitable to determine parameters such as rate constant, reaction order and transfer coefficients. The field controlled by transport (Equation 1.51 valid, in practice usually with c_O^{∞} or $c_R^{\infty}=0$) can lead to the diffusion coefficient.

In the field of mixed influence, a combination of the BV relation with the comparison for transport-determined current is valid. A number of variants to these have been described in the literature. The most well known and the most commonly used is presumably the relation deduced by Frumkin and Tedoradze[72]:

$$\frac{1}{i} = \frac{1}{i_{kin}} + \frac{1}{B\omega^{1/2}} \qquad (1.52)$$

The denominator of the first term of the right part represents the BV current. The denominator of the second term represents the transport-controlled current at the rotating-disc electrode; this is Equation 1.41 or 1.42, where m is replaced by the right part of Equation 1.51 and all the terms, except for $\omega^{1/2}$, are incorporated in the parameter B.

1.8 References

1. Bockris J.O'M., Reddy A.K. (eds), *Modern Electrochemistry 2*, Plenum Press, New York, 1970.
2. Kissinger P.I., Heinemann W.R., *Laboratory Techniques in Electroanalytical Chemistry*, Marcel Dekker, New York, 1996.
3. Levich E., *Physicochemical Hydrodynamics*, Prentice Hall, Englewood Cliffs, New Jersey, 1962.
4. Compton R.G, Sanders G.H.W., *Electrode Potentials*, Oxford Science Publications, Oxford, 1996.
5. Monk P.M.S., *Fundamentals of Electroanalytical Chemistry*, Wiley, Chichester, 2001.

6. Brett C.M.A., Oliveira Brett A.M., *Electrochemistry, Principles, Methods and Applications*, Oxford University Press, Oxford, 1993.
7. Angerstein-Kozlowska H., Conway B.E., Sharp W.B.A., *Electroanal. Chem. Interfac. Electrochem*, **43** (1973) 9.
8. Horyani G., *J. Solid State Electrochem.*, **2** (1998) 237.
9. Horyani G., *Electrochim. Acta*, **36** (1991) 1453.
10. Tilak B.V., Conway B.E., Angerstein-Kozlowska H., *Electroanal. Chem. Interfac. Electrochem.*, **48** (1973) 1.
11. Gasana E., Westbroek P., Temmerman E., Thun H.P., Twagiramungu F., *Electrochem. Commun.*, **2** (2000) 727–732.
12. Finklea H., *Electroanal. Chem.*, **19** (1996) 109.
13. Burke L.D., O'Sullivan J.F., *Electrochim. Acta*, **37** (1992) 585.
14. Burke L.D., O'Leary W.A., *J. Appl. Electrochem.*, **19** (1989) 758.
15. Woods R., in Bard A.J. (ed.), *Electroanalytical Chemistry*, **9**, Marcel Dekker, New York, 1976.
16. Sirohi R.S., Gensham M.A., *J. Electrochem. Soc.*, **116** (1969) 910.
17. Van Der Linden W.E., Dieker J.W., *Anal. Chimica Acta*, **119** (1980) 1.
18. Yamada S., Sato H., *Nature*, **193** (1962) 261.
19. Jenkins G.M., Kawamura K., *Nature*, **231** (1971) 175.
20. Mentus Z., Mentus S., Marinkovic N., Lausevic Z., *J. Electroanal. Chem.*, **283** (1990) 449.
21. Hu I., Karweik D.H., Kuwana T., *J. Electroanal. Chem.*, **188** (1985) 59.
22. Grundler P., Zerihun T., Moller A., Kirho A., *J. Electroanal. Chem.*, **360** (1993) 309.
23. Bjelica L.J., Jovanovic L.S., *Electrochimica Acta*, **37** (1992) 371.
24. Yuzhanina A.V., Kokoulina D.V., Mashkovich L.A., Dronseiko L.A., Kuteinikov A.F., *Elektrokhimiya*, **15** (1979) 308.
25. Panzer R.E., Elving P.J., *J. Electrochem. Soc.*, **119** (1972) 864.
26. Gamburtaev S., Iliev I., Kaisheva A., Steinberg G.V., Mokrousov L.N., *Elektrokhimiya*, **16** (1980) 1069.
27. Wang J., Naser N., Angnes L., Wu H., Chen L., *Anal. Chem.*, **64** (1992) 1285.
28. Anjo D.M., Kahz M., Khodabakhsh M.M., Novinski S., Wanger M., *Anal. Chem.*, **61** (1989) 2603.
29. Ricc R., Allred C., McCreery R., *J. Electroanal. Chem.*, **263** (1989) 163.
30. McDermott M.T., McDermott C.A., McCreery R.L., *Anal. Chem.*, **65** (1993) 937.
31. Dribiuskii A.V., Griuberg V.A., Kaneskii L.S., Avdalyan M.B., Yakushev V.V., *Elektrokhimiya*, **28** (1992) 1718.
32. Surmann J.P., Wenders G., *Fres. J. Anal. Chem.*, **346** (1993) 914.
33. Jurgen D., Steckhan E., *J. Electroanal. Chem.*, **333** (1992) 177.
34. Poon M., McCreery R.L., *Anal. Chem.*, **58** (1986) 2745.
35. Ricc R.J., McCreery R.L., *J. Electroanal. Chem.*, **310** (1991) 127.
36. Hance G.W., Kuwana T., *Anal. Chem.*, **59** (1987) 131.
37. Otero L., Vettorazzi N., Barbero C., Miras M.C., Silber J.J., Sereno L., *J. Electroanal. Chem.*, **350** (1993) 251.
38. Upadhyay P.K., *J. Electroanal. Chem.*, **271** (1989) 339.
39. Zhang H., Coury L.A., *Anal. Chem.*, **65** (1993) 1552.
40. Nagadaka T., Yoshino T., *Anal. Chem.*, **58** (1986) 1037.

41. Hoogvliet J.C., Van Der Beld C.M., Van Der Poel C.J., Van Bennekom W.P., *J. Electroanal. Chem.*, **201** (1986) 11.
42. Picq G., Reeves R., Ribourg P., Vennereau P., *J. Electroanal. Chem.*, **162** (1984) 225.
43. Kamau G.N., *Anal. Chimica Acta*, **207** (1988) 1.
44. Bard A.J., Faulkner L.R. (eds), *Electrochemical Methods, Fundamentals and Applications*, Wiley, New York, 1980.
45. Sawyer D.T., Sobkowiak A., Roberts J.L., *Electrochemistry for Chemists*, Wiley, New York, 1995.
46. Gasana E., Westbroek P., Temmerman E., Thun H.P., Kiekens P., *Anal. Chim. Acta*, **486** (2003) 73.
47. Wightman R.M., Wipf D.O., in Bard A.J. (ed.), *Electroanalytical Chemistry*, **15**, Marcel Dekker, New York, 1989.
48. Bixler J.W., Bond A.M., Lay P.A., Thormann W., Van Den Bosch P., Fleischmann M., *Anal. Chim. Acta*, **187** (1986) 67.
49. Baer C.D., Stone N.J., Sweigart D.A., *Anal. Chem.*, **60** (1986) 188.
50. Pendley B.D., Abruma H.D., *Anal Chem*, **62** (1990) 782.
51. Nomura S., Nozaki K., Okazaki S., *Anal. Chem.*, **63** (1991) 2665.
52. Penner R.M., Martin C.R., *Anal. Chem.*, **59** (1987) 2625.
53. Strohben W.E., Smith D.K., Evans D.H., *Anal. Chem.*, **62** (1990) 1709.
54. Cheng I.F., Schimpf J.M., Martin C.R., *J. Electroanal. Chem.*, **284** (1990) 499.
55. Golas J., Osteryoung J., *Analytica Chimica Acta*, **181** (1986) 211.
56. Golas J., Osteryoung J., *Analytica Chimica Acta*, **186** (1986) 1.
57. Kounaves S.P., Deng W., *J. Electroanal. Chem.*, **301** (1991) 77.
58. Lee C., Miller C.J., Bond A.J., *Anal. Chem.*, **63** (1991) 78.
59. Brumlik C.J., Martin C.R., *J. Am. Chem. Soc.*, **113** (1991) 3174.
60. Wipf D.O., Michael A.C., Wightman R.M., *J. Electroanal. Chem.*, **269** (1989) 15.
61. Tabei H., Morita M., Nina O., Horiuchi T., *J. Electroanal. Chem.*, **334** (1992) 25.
62. Steward A.A., Taylor G., Girault H.H., *J. Electroanal. Chem.*, **296** (1990) 491.
63. Robinson R.A., Stokes R.H., *Electrolyte Solutions*, Butterworth Scientific, London, 1955.
64. Janz G.J., Tomkins R.P.T., *Non-aqueous Electrolytes Handbook*, Academic Press, New York, 1972.
65. Kratochvil B., Yeager H.L., *Fortsch. Chem. Forsch.*, **27** (1972) 1.
66. Temmerman E., *Elektrochemische analysemethoden*, cursus 1e licentie Scheikunde, RUG, 1997.
67. Bockris J.O'M., Khan S.U. (eds), *Surface Electrochemistry*, Plenum Press, New York and London, 1993.
68. LaCourse W.R. (ed.), *Pulsed Electrochemical Detection in HPLC*, Wiley, New York, 1997.
69. Wang J. (ed.), *Analytical Electrochemistry*, VCH, New York, 1994.
70. Dahmen E.A. (ed.), *Electroanalysis*, Elsevier, Amsterdam, 1986.
71. Frumkin A.N., Tedoradze G.A., *Z. Elektrochem.*, **62** (1958) 251.
72. Pleskov Y.V., Filinovskii V.Y. (eds), *The Rotating Disk Electrode*, Consultants Bureau, New York, 1976.

2
Electrochemical methods

P. WESTBROEK

2.1 Introduction

Electrochemical methods include potentiometry, cyclic voltammetry and chronoamperometry. These methods as well as other voltammetric methods and the impedance of electrochemical systems are discussed in this chapter.

2.2 Potentiometry

2.2.1 Introduction

A galvanic cell produces a potential which is in relation with the concentration of an electroactive species, given by the Nernst equation. This equation provides a quantitative relationship between potential and the ratio of activities (a_O/a_R) or, in a simplified form, the ratio of the concentrations for a redox couple ([O]/[R]), and is the basis for potentiometry and potentiometric titrations[1–3]. Despite the comparatively late development of potentiometry, the application of potentiometric measurements for analytical purposes was established with the development of the glass electrode in 1909 for a selective potentiometric response to hydronium ion concentrations. A second milestone in the development of potentiometric measurements was the introduction of the hydrogen electrode for the measurement of hydronium ion concentrations, which was also of significant use for other electrochemical methods. The potential of the H_2/H^+ equilibrium at platinised platinum electrodes became the reference point of the potential scale. Subsequent development of special glass formulations has made it possible to have electrodes that are selective to different monovalent cations. This also led to the development of electrodes that are selective for many cations and anions, as well as several gas- and bioselective electrodes[4]. The use of these electrodes and the potentiometric measurement of pH continue to be among the most important applications of electrochemistry. The pH electrode is discussed in more detail in Chapter 3.

At an early date, Nernst also introduced the concept of potentiometry with polarised electrodes[5–7], that went together with the many other specialised forms of potentiometric measurements for a wide range of chemical systems[8].

2.2.2 Fundamentals of potentiometry

Potentiometric measurements are based on the Nernst equation, which was developed from thermodynamic relationships and is therefore valid only under equilibrium (read thermodynamic) conditions. As mentioned above, the Nernst equation relates potential to the concentration of electroactive species. For electroanalytical purposes, it is most appropriate to consider the redox process that occurs at a single electrode, although two electrodes are always essential for an electrochemical cell. However, by considering each electrode individually, the two-electrode processes are easily combined to obtain the entire cell process. Half reactions of electrode processes should be written in a consistent manner. Here, they are always written as reduction processes, with the oxidised species, O, reduced by n electrons to give a reduced species, R:

$$\mathrm{O} + n\mathrm{e}^- \leftrightarrows \mathrm{R} \qquad [2.1]$$

For such a half reaction the free energy is given by the relation:

$$\Delta G = \Delta G^0 + \mathrm{R}T \ln \frac{a_\mathrm{R}}{a_\mathrm{O}} \qquad [2.2]$$

or:

$$-\Delta G = -\Delta G^0 + \mathrm{R}T \ln \frac{a_\mathrm{O}}{a_\mathrm{R}} \qquad [2.3]$$

where $-\Delta G$ is the electromotive force indicating the tendency for the reaction to go to the right; R is the gas constant ($8.317\,\mathrm{J\,mol^{-1}\,K^{-1}}$), T is the temperature (K), and the quantity ΔG^0 is the free energy of the half reaction when the activities of the reactant and product have values of unity and is directly proportional to the standard half-cell potential for the reaction as written. The electromotoric force, also called the free energy of this half reaction, is related to the electrode potential, E, by the expressions:

$$-\Delta G = r\mathrm{F}E \qquad [2.4]$$

$$-\Delta G^0 = r\mathrm{F}E^0 \qquad [2.5]$$

It also is a measure of the equilibrium constant for the half reaction assuming the activity of electrons is unity and under this condition the following equation is valid:

$$-\Delta G^0 = \mathrm{R}T \ln K \qquad [2.6]$$

Beware of the fact that E^0 values are valid only under equilibrium conditions and for $a_O = a_R = 1$. In practice, this condition is, in most cases, not fulfilled.

When Equations 2.2 and 2.4 are combined, the resulting equation relates the half-cell potential to the effective activity of the redox couple:

$$E = E^0 - \frac{\mathrm{R}T}{n\mathrm{F}} \ln \frac{a_R}{a_O} = E^0 + \frac{\mathrm{R}T}{n\mathrm{F}} \ln \frac{a_O}{a_R} \qquad [2.7]$$

a relation better known as the Nernst equation. This quantity is equal to the concentration of the species times a mean activity coefficient:

$$a_{M^{y+}} = \gamma_{\pm} C_{M^{y+}} \qquad [2.8]$$

Although there is no straightforward and convenient method for evaluating activity coefficients for individual ions, the Debye–Hückel relationship permits an evaluation of the mean activity coefficient ($\gamma_\pm$), for ions at low concentrations (usually $<0.01\,\mathrm{mol\,l^{-1}}$):

$$\log \gamma_\pm = -0.509 z^2 \frac{\sqrt{I}}{1+\sqrt{I}} \qquad [2.9]$$

where z is the charge on the ion and I is the ionic strength given by:

$$I = 0.5 \sum c_i z_i^2 \qquad [2.10]$$

The reaction of an electrochemical cell always involves a combination of two redox half reactions such that one species oxidises a second species to give the respective redox products. Thus, the overall cell reaction can be expressed by a balanced chemical equation:

$$a\mathrm{O}_1 + n\mathrm{e}^- \leftrightarrows c\mathrm{R}_1 \qquad E_1 \qquad [2.11]$$

$$\underline{b\mathrm{R}_2 \leftrightarrows d\mathrm{O}_2 + n\mathrm{e}^-} \qquad \underline{E_2} \qquad [2.12]$$

$$a\mathrm{O}_1 + b\mathrm{R}_2 \leftrightarrows c\mathrm{R}_1 + d\mathrm{O}_2 \qquad K \qquad [2.13]$$

However, electrochemical cells are most conveniently considered as two individual half reactions, whereby each is written as a reduction in the form indicated by Equations 2.11 and 2.12. When this is done and values of the appropriate quantities are inserted, a potential can be calculated for each half cell of the electrode system. Then the reaction corresponding to the half cell with the more positive potential will be the positive terminal in a galvanic cell, and the electromotive force of that cell will be represented by the algebraic difference between the potential of the more-positive half cell and the potential of the less-positive half cell:

$$E_{\text{cell}} = E_1 - E_2 \quad (E_{\text{cell}} \text{ being positive}) \qquad [2.14]$$

Insertion of the appropriate forms of Equation 2.7 gives an overall expression for the cell potential:

$$E_{\text{cell}} = E_1^{\,0} - E_2^{\,0} + \frac{RT}{n\text{F}} \ln \frac{a_{O_1}{}^{a} a_{R_2}{}^{b}}{a_{O_1}{}^{a} a_{R_2}{}^{b}} \qquad [2.15]$$

The equilibrium constant for the chemical reaction expressed by Equation 2.15 is related to the difference of the standard half-cell potentials by the relation:

$$\ln K = \frac{n\text{F}}{RT}(E_1^{\,0} - E_2^{\,0}) \qquad [2.16]$$

Equation 2.16 shows that potentiometry is a valuable method for the determination of equilibrium constants. However, it should be borne in mind that the system should be in equilibrium. Some other conditions, which are described below, also need to be fulfilled for use of potentiometry in any application. The basic measurement system must include an indicator electrode that is capable of monitoring the activity of the species of interest, and a reference electrode that gives a constant, known half-cell potential to which the measured indicator electrode potential can be referred. The voltage resulting from the combination of these two electrodes must be measured in a manner that minimises the amount of current drawn by the measuring system. This condition includes that the impedance of the measuring device should be much higher than that of the electrode.

For low-impedance electrode systems, a conventional potentiometer is satisfactory. However, electrochemical measurements with high-impedance electrode systems, and in particular the glass-membrane electrode, require the use of an exceedingly high-input impedance-measuring instrument (usually an electrometer amplifier with a current drain of less than 1 pA). Because of the logarithmic nature of the Nernst equation, the measuring instrumentation must have considerable sensitivity. Another important condition is that the potential response is directly dependent on the temperature of the measuring system. Thus, if the correct temperature is not used in the Nernst expression, large absolute errors can be introduced in the measurement of the activity for an electroactive species. In addition, temperature indirectly has an influence through the activity coefficients, ionic strength and dilution of the solution.

2.2.3 Electrode systems in potentiometry

The indicator electrodes for potentiometric measurements have traditionally been categorised into three separate groups. A first group of electrodes

consist of a metal immersed in a solution which contains ions of the same metal as the electrode, for example, a copper electrode immersed in a Cu(II) solution. These electrode systems provide a direct response to the ion or species to be measured:

$$M^{n+} + n\mathrm{e}^- \leftrightarrows M \qquad [2.17]$$

$$E = E^0 + \frac{\mathrm{R}T}{n\mathrm{F}} \ln a_{\mathrm{M}^{n+}} \qquad [2.18]$$

Therefore, the primary electrode reaction includes the sensed species. Such electrodes give a direct response according to the Nernst equation for the logarithm of the activity of the species.

Electrodes classified in the second group of electrode systems are those in which the metal electrode is coated with a layer of a sparingly soluble salt of the electroactive species and the metal ion of the metal electrode, such that the potentiometric response is indicative of the concentration of the inactive anion species. Thus the silver/silver-chloride electrode system, which is representative of this class of electrodes, gives a potential response that is directly related to the logarithm of the chloride ion activity (see also Chapter 1, section 1.5), even though it is not the electroactive species:

$$\mathrm{AgCl} + \mathrm{e}^- \leftrightarrows \mathrm{Ag} + \mathrm{Cl}^- \qquad [2.19]$$

$$E = E^0 - \frac{\mathrm{R}T}{n\mathrm{F}} \ln a_{\mathrm{Cl}^-} \qquad [2.20]$$

This is true because the chloride ion concentration, through the solubility product, controls the activity of the silver ion, which is measured directly by the potentiometric silver-electrode system.

Finally, there is a third group of electrodes, which are a more specialised case of the electrodes belonging to the second group. They consist of the metal being in direct contact with a sparingly soluble salt of the metal, which is then used to monitor the activity of an electroinactive metal ion in equilibrium with a more soluble salt that includes the same anion as the electrode–salt system. For example, the concentration of calcium ions in equilibrium with solid calcium oxalate may be monitored using a silver/silver oxalate electrode system. The concentration of calcium ion affects the concentration of oxalate ion, which in turn controls the concentration of silver ion; the latter is monitored by the potentiometric silver-electrode system. A rather more important example of this type of electrode is the Hg|Hg(II)–EDTA electrode system, which is used as a sensing system for the potentiometric titration of electroinactive metal ions with EDTA[9–10]. The stability constant of the Hg(II)–EDTA complex is so high that only a

small fraction is dissolved. Hence, when calcium ion is titrated with EDTA, the concentration of calcium ion controls the equilibrium concentration of the EDTA anion in solution, which in turn directly controls the free concentration of Hg(II). The latter is monitored by a Hg electrode system to give a direct measure of the calcium ion concentration. This type of system can be applied to most of the divalent ions that form moderately strong complexes with EDTA.

One of the most important and extensively used indicator electrode systems is the glass-membrane electrode that is used to monitor hydronium ion activity. Although developed in 1909, it did not become popular until reliable electrometer amplifiers were developed in the 1930s. When the outside surface of the glass membrane is exposed to an ionic solution, a response for the hydronium ion activity meets with the Nicholsky equation, which is similar to the Nernst expression. In view of the importance and widespread use of the hydronium or pH electrode, this system is discussed in a separate chapter.

Other potentiometric electrode systems are ion-selective electrodes such as fluoride, calcium, magnesium, sodium, potassium and chloride, selective gas electrodes based on membranes such as O_2, CO_2, CO, NO, NO_2 and SO_2, and enzyme electrodes. These electrodes fall beyond the scope of this book and are not discussed further.

For most potentiometric measurements, either the saturated calomel reference electrode or the silver/silver chloride reference electrode are used. These electrodes can be made compact, are easily produced, and provide reference potentials that do not vary more than a few mV. The silver/silver chloride electrode also finds application in non-aqueous solutions, although some solvents cause the silver chloride film to become soluble. Some experiments have utilised reference electrodes in non-aqueous solvents that are based on zinc or silver couples. From our own experience, aqueous reference electrodes are as convenient for non-aqueous systems as are any of the prototypes that have been developed to date. When there is a need to exclude water rigorously, double-salt bridges (aqueous/non-aqueous) are a convenient solution. This is true even though they involve a liquid junction between the aqueous electrolyte system and the non-aqueous solvent system of the sample solution. The use of conventional reference electrodes does cause some difficulties if the electrolyte of the reference electrode is insoluble in the sample solution. Hence, the use of a calomel electrode saturated with potassium chloride in conjunction with a sample solution that contains perchlorate ion can cause dramatic measurements due to the precipitation of potassium perchlorate at the junction. Such difficulties normally can be eliminated by using a double junction that inserts another inert electrolyte solution between the reference electrode and the sample solution (e.g., a sodium chloride solution).

2.3 Cyclic voltammetry

In cyclic voltammetry, the potential applied to the working electrode is varied linearly (Fig. 2.1) between potentials E_1 and E_2, E_2 being a potential more positive (for oxidation) or negative (for reduction) than the peak maximum observed for the oxidation/reduction reaction concerned. At E_2, the voltage scan is reversed back to E_1 or to another end potential value, E_3. The application of this type of potential ramp can be done in a number of ways, varying the starting potential E_1, the reverse potential E_2, the end potential E_3 and the scan rate. The latter is the rate that is applied to vary the potential as a function of time, commonly represented in $\mathrm{V\,s^{-1}}$ or $\mathrm{mV\,s^{-1}}$.

The resulting current measured while scanning the potential from E_1 to E_2 and back to the initial potential, E_1, is shown in Fig. 2.2 for a reversible redoxsystem as a function of time, and in Fig. 2.3 in the more common way. Note that the scan rate (in this case $10\,\mathrm{mV\,s^{-1}}$) is the main relation between the way of data presentation in Fig. 2.2 and Fig. 2.3.

The voltammogram shown in Fig. 2.3 is characterised by a peak potential E_p, a potential corresponding to the point where the measured current reaches it maximum value I_p. For a reversible system, the peak current is given by:

$$I_\mathrm{p} = 0.4463nFA(\mathrm{D}a)^{1/2}c \qquad [2.21]$$

where I_p is the peak current (A), n is the number of electrons exchanged in the concerned reaction, F is the Faraday constant ($\mathrm{C\,mol^{-1}}$), A is the

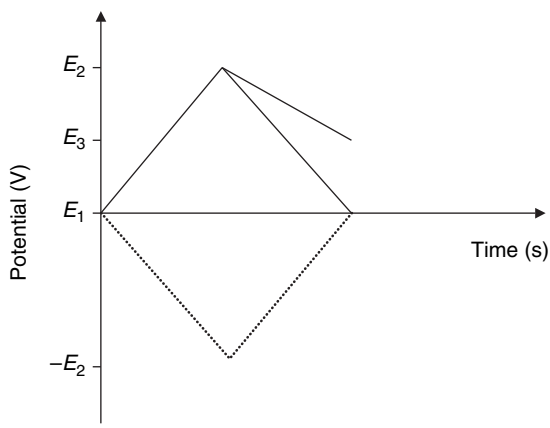

2.1 Variation of the applied potential in cyclic voltammetry. Typical triangle wave between two potentials followed by an opposite triangle (.....) or by another type of potential ramp (_____).

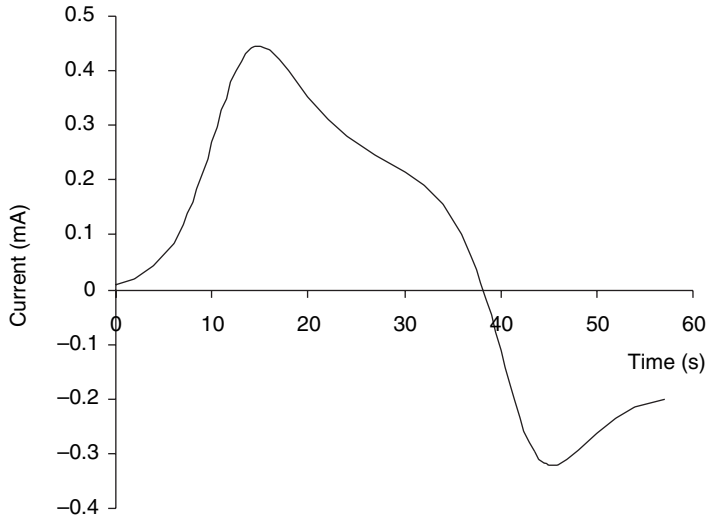

2.2 Cyclic-voltammetry response of a reversible system represented as a function of time.

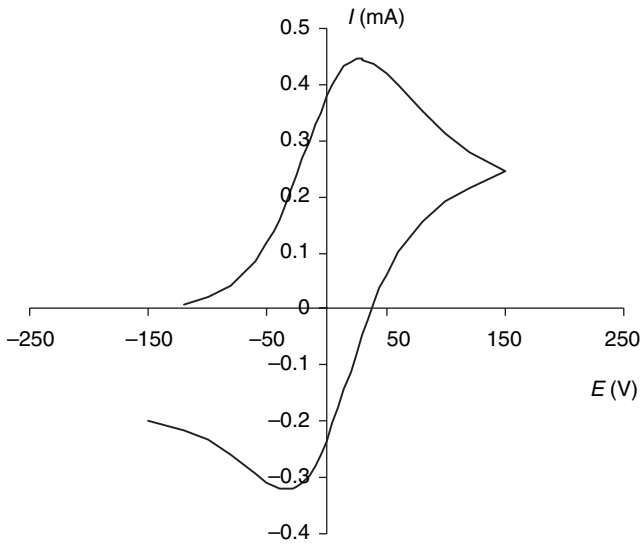

2.3 Cyclic-voltammetry curve for a reversible system in an *E–I* plot. Data are in fact identical to those shown in Fig. 2.2.

surface of the electrode (cm^2), D is the diffusion coefficient of the electroactive species ($cm^2 s^{-1}$), c is the concentration of electroactive species ($mol\,dm^{-3}$), and a is given in Equation 2.22:

$$a = nFv/RT \qquad [2.22]$$

where v is the scan rate ($V s^{-1}$), R is the universal gas constant ($J mol^{-1} K^{-1}$), and T is the temperature (K). Combination of Equations 2.21 and 2.22 at T = 298.0 K results in the Sevcik–Randles equation which expresses the peak current of the forward scan in cyclic voltammetry for a reversible system:

$$I_p = 2.69 \times 10^5 n^{3/2} A D^{1/2} v^{1/2} c \quad [2.23]$$

Several criteria can be used for the analysis of the cyclic voltammetric curve to determine the reversibility of the redox system investigated:

- A clear and well-defined return peak should be observed due to the occurrence of the opposite reaction $O + n\ e^- \rightarrow R$.
- The peak current of the forward and the return peak should be equal $I_{p,a} = I_{p,c}$, of course after correction of $I_{p,c}$ for background current (see Fig. 2.3).
- The peak potential can be related to the half-wave potential $E_{1/2}$, defined as the potential corresponding with a current equal to $I_p/2$, by the following equation:

$$E_p = E_{1/2} - 1.11 RT/nF \quad [2.24]$$

- For a reversible system, only one half-wave potential can be defined being:

$$E_{1/2} = E_{1/2,a} = E_{1/2,c} \quad [2.25]$$

- For a reversible system, a peak separation of the anodic and cathodic peak should apply to the following equation:

$$|\Delta E_p| = |E_{p,a} - E_{p,c}| = 0.059/n$$
with E in V. [2.26]

Besides the peak current and the reversibility of the redox system and its current–potential curve, the inclining part of the forward wave has also been a target for extensive studies and characterisation. Numerous mathematical approaches have been presented in the literature; however, the approach of Nicholson and Shain has been chosen here[11] due to the clarity of the physical–chemical meaning behind the mathematical approach and the ease with which non-electrochemists can understand the shape of the voltammetric curve. In their approach, a current–potential curve of a reversible system is presented as:

$$I = nFAc(Da)^{1/2} \chi_{rev} \quad [2.27]$$

where χ_{rev} is a factor being dependent on applied potential but constant for a constant potential. The relation between the measured current, I, and the applied potential, E, is given through a tabulated relationship of $n(E–E_{1/2})$ and χ_{rev},[12] a relationship that is shown in Table 2.1.

Table 2.1 Tabulated relationship of $n(E-E_{1/2})$ and χ_{rev}[12] for the relation between the measured current, *I*, and the applied potential, *E*, in cyclic voltammetry for a reversible system

$n(E-E_{1/2})$ (mV)	χ_{rev}	$n(E-E_{1/2})$ (mV)	χ_{rev}
5	0.335	–5	0.400
10	0.328	–10	0.418
15	0.298	–15	0.432
20	0.269	–20	0.441
25	0.240	–25	0.445
30	0.211	–30	0.446
35	0.185	–35	0.443
40	0.160	–40	0.438
45	0.138	–45	0.429
50	0.117	–50	0.421
60	0.084	–60	0.399
80	0.042	–80	0.353
100	0.020	–100	0.315
120	0.009	–120	0.280

It will be clear that cyclic voltammetry is a powerful tool for a first analysis of an electrochemical reaction occurring at the surface of an electrode because it will reveal reversibility. Depending on whether the system is reversible, information will be obtained about half wave potential, number of electrons exchanged in the reaction, the concentration and diffusion coefficient of the electroactive species. However, these data can also be obtained for an irreversible system[11,13] but, in this case, the equations describing the current–potential curves differ somewhat from Equations 2.21 to 2.27.

For an irreversible system, the peak current may be expressed in terms of a heterogeneous rate constant, k_h, and the peak potential by the following relation:

$$I_p = 0.227nFAck_h \exp[-\alpha n_a F/RT(E_p - E')] \quad [2.28]$$

where k_h is the heterogeneous rate constant of the concerned process on the condition that the potential of the electrode is equal to the formal potential of the electrode process E'.

The equation that is valid for the peak current of irreversible redox systems is derived from Equation 2.28 and is given in Equation 2.29 (at 298.0 K):

$$I_p = 2.99 \times 10^5 n(\alpha n_a)^{1/2} AD^{1/2}v^{1/2}c \quad [2.29]$$

where n_a is the number of electrons in the rate-determining step and α is the transfer coefficient. These two parameters are related to the kinetics of

the electron transfer, a reaction step that cannot be neglected in Equation 2.29. For reversible systems, these parameters do not appear in the equation, because for reversible systems the kinetics of electron transfer are so high (even at very small overpotentials) that they do not control the experimentally obtained current signal.

Values for α and n_a can be obtained in two alternative ways. First, by studying the difference between peak potential and half-wave potential:

$$E_p - E_{1/2} = -1.857\,RT/\alpha n_a F \qquad [2.30]$$

Second, by performing two identical experiments, except for the scan rate v. From the shift in peak potential obtained in the experiments with scan rates v_1 and v_2, the kinetic parameters can be determined:

$$E_{p,2} - E_{p,1} = RT/\alpha n_a F \ln(v_1/v_2)^{1/2} \qquad [2.31]$$

This shows that for an irreversible process, the peak potential is shifted towards more negative (reduction reaction) or more positive (oxidation reaction) potentials by about 0.03 V per decade of increase in the scan rate. For a totally irreversible reaction, no return peak is observed due to the fact that the kinetics are so slow that the opposite reaction cannot occur. The activation energy, overcome by application of a potential, is so high that it is not possible to apply such a potential under experimental conditions. However, the absence of a return peak does not necessarily imply slow electron transfer, but can also be due to a fast following chemical reaction.

Besides electrochemical reactions, cyclic voltammetry is also very useful in studying electrochemical reactions that are preceded or followed by a chemical reaction and if adsorption of species at the surface of the electrode is involved[14–24]. A short discussion is given below[25–27].

For a process in which a reversible electron-transfer reaction is preceded by a chemical reaction (so-called CE mechanism), the shape of the voltammetric wave and the peak is dependent on the rate of that chemical reaction:

$$A \leftrightarrows O + ne^- \leftrightarrows R \qquad [2.32]$$

- The chemical reaction is very slow: the experimental current is controlled by kinetics because the formation of O is very small, thus not giving the system the chance to build up a diffusion layer. In this case, a broad wave rather than a peak is observed.
- The chemical reaction rate is very fast: this implies that the formation of O is very fast, much faster than its consumption in the following electrochemical step. Therefore, the wave is that for a diffusion-controlled electron transfer. In this case, the depletion of O in the vicinity of the electrode surface is counter-balanced by formation of O in the

chemical step; therefore it is the diffusion of A towards the electrode surface that determines the overall reaction rate, resulting in a diffusion-controlled peak-shaped wave.
- For the intermediate case, the shape of the wave is determined by both diffusion and kinetic parameters resulting in a peak-shaped voltammetric wave with a smaller peak current and a broader peak width compared with a purely diffusion-controlled voltammetric peak.

A second situation is the EC mechanism or the mechanism where the electron-transfer step is followed by a chemical reaction. In addition, different conditions can be defined, resulting in different shapes of the recorded voltammetric waves:

$$\mathrm{O} + n\mathrm{e}^- \leftrightarrows \mathrm{R} \rightarrow \mathrm{B} \qquad [2.33]$$

- The electrochemical step is irreversible. In this case, no return peak will be observed, and R reacts further to B.
- The electrochemical step is reversible. In this case, it depends on the rate of the chemical step. If the chemical step is much faster, then no return peak will be observed as R will react further to B. If the chemical step is not as fast, a return peak will be observed. However, with a smaller peak current as for the peak in the forward scan, because a fraction of R will be transformed into B, the other fraction is oxidised to O, resulting in the return peak with smaller peak current.

Cyclic voltammetry is also very useful for the study of adsorbed species[14,15,28–30]. In the examples discussed above, it was assumed that the electroactive species and its reaction products are soluble in the solution and that surface processes can be neglected. However, if the shape of the peak is unusual (e.g. very sharp), the electrochemical reaction is probably complicated by surface processes, such as adsorption. Usually, adsorption of species favours the electrode reaction taking place at lower potentials; in the case of a deposition, one speaks about under potential deposition. Different ways of adsorption can be obtained:

- Only the adsorbed species, O and R, are electroactive. In this case, the voltammetric peaks are sharp and symmetrical (Fig. 2.4a) due to the fact that a fixed amount of O is adsorbed and oxidised to R, and the same amount of R is reduced in the return scan to O. The values of I_p and E_p and the width of the peak depend on the type of adsorption and the strength of the adsorption of the electroactive species to the electrode surface. For Langmuir adsorption isotherms, the peak potentials of anodic and cathodic reactions are equal, and the peak current is described by Equation 2.34:

$$I_{\mathrm{p,c}} = (n^2\mathrm{F}^2 A\Gamma_\mathrm{O}/4\mathrm{R}T)v \qquad [2.34]$$

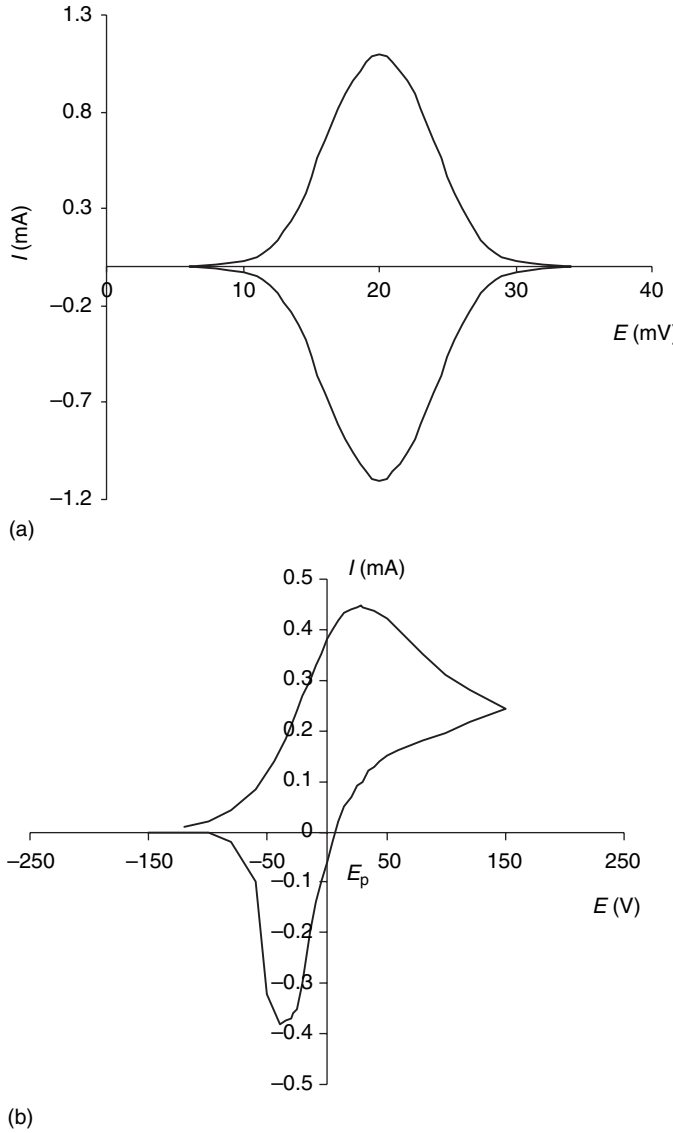

2.4 Cyclic-voltammetry response of adsorbed species if only adsorbed O and R are electroactive (a) and if also the species in solution is electroactive (b).

where Γ_O is the surface excess of O before the potential scan is initiated. From this equation, it might be clear that a distinction between reactions of species from solution and adsorbed species can be made by plotting the peak current as a function of scan rate. For species from solution, a square-root relation is obtained; for adsorbed species, a linear

relationship is obtained. The charge can be calculated from the area under the peak, and if *n* is known, it is possible to calculate the amount of species adsorbed at the electrode surface.

- A more general case is that adsorbed and solution species are electroactive. In this case, symmetrically shaped peaks are observed, corresponding to the electrode reaction of adsorbed species in combination with the normal peak for soluble species.
- In the final scenario, the species in solution is adsorbed in the forward scan and desorbs electrochemically in the reverse scan. This case is frequently observed in the deposition of metals. In the forward scan, a common diffusion-controlled voltammetric wave is observed, but in the reverse scan a sharp return peak is obtained because of the fixed amount of metal deposited in the forward scan (Fig. 2.4b). The metal is already present at the electrode when the reverse scan is started; therefore no diffusion process is observed, and the current drops to zero after the peak because of the fixed and limited amount of deposited metal present at the electrode surface.

2.4 Impedance of electrochemical systems

2.4.1 Introduction

The impedance for the study of materials and electrochemical processes is of major importance. In principle, each property or external parameter that has an influence on the electrical conductivity of an electrochemical system can be studied by measurement of the impedance. The measured data can provide information for a pure phase, such as electrical conductivity, dielectrical constant or mobility of equilibrium concentration of charge carriers. In addition, parameters related to properties of the interface of a system can be studied in this way: heterogeneous electron-transfer constants between ion and electron conductors, or capacity of the electrical double layer. In particular, measurement of the impedance is useful in those systems that cannot be studied with DC methods, e.g. because of the presence of a poor conductive surface coating.

The simplest application of electrochemical impedance spectroscopy (EIS) is the determination of the conductivity of the electrolyte solution, where polarisation of the electrode surfaces is eliminated by choosing an appropriate frequency range for measurement of the conductivity[31].

2.4.2 Definition of impedance

The parameter impedance in electrical alternating-current circuits is the equivalent of resistance in direct-current circuits. If a linear and time-invariant system, L, is considered, then it can be said that:

$$L(au + bv) = aLu + bLv \quad [2.35]$$

with u(t) and v(t) being input signals and complexes of a and b, and

$$u(t) \rightarrow y(t) \text{ so } u(t - t_0) \rightarrow y(t - t_0) \quad [2.36]$$

where y(t) is the output signal and t_0 is an arbitrarily selected real time.

It is well known for such systems that the output signal of a sinusoidal input signal, e.g. a monochromatic signal u(t) with amplitude A, angle frequency $\omega = 2\pi f$ (f in Hz) and phase φ_0 (rad) is also sinusoidal[32]. In the context of this work, the signals can be defined as follows: input signal is an alternating potential $E(t)$, while the output signal is an alternating current $I(t)$, with amplitude E_m (V) and I_m (A) and phases α and β. In principle, each of these signals can be selected as the input signal of which the corresponding phase is defined as zero. The equation of Euler allows both signals to be written as complex e-powers:

$$E(t) = E_m e^{j(\omega t + a)} \quad [2.37]$$

and

$$I(t) = I_m e^{j(\omega t + \beta)} \quad [2.38]$$

with $j^2 = 1$.

The impedance is defined as the ratio of the alternating potential and the alternating-current signal:

$$Z(\omega) = \frac{E(t)}{I(t)} = \frac{E_m}{I_m} e^{j(\alpha - \beta)} = \frac{E_m}{I_m} e^{j\phi} = |Z| e^{j\phi} \quad [2.39]$$

This impedance can be presented as a vector in the complex plane with modulus $|Z| = E_m/I_m$ and argument $\phi = \alpha - \beta$. As a consequence, it is expected to obtain a plane with axes having unit 1 for the real and j for the imaginary axis. However, mainly R^2 is presented, so both axes are real[33]. The projection of the impedance vector at these axes results in the resistance Z' and the reactance Z'', also called the real and imaginary part of the impedance, respectively (Fig. 2.5):

$$Z(\omega) = Z'(\omega) + jZ''(\omega) \quad [2.40]$$

2.4.3 Graphical presentation

Equations 2.37–2.40 result in the commonly used presentation of the impedance, e.g. the Nyquist and the Bode plots. The first one shows the total impedance vector point for different values of ω. The plane of this figure is a complex plane, as shown in the previous section. Electrochemical-related processes and effects result in resistive and capacitive behaviour, so it is common to present the impedance as:

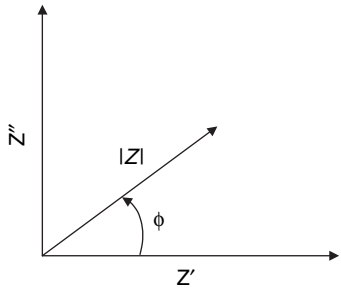

2.5 Scheme of the impedance presentation in the complex plane.

$$\overline{Z} = Z' - jZ'' \qquad [2.41]$$

The Bode plot shows the impedance in pole coordinates as a negative-phase angle and the logarithm of the impedance as a function of the logarithm of the frequency. If the frequency is varied over several decades, advantage is given to the Bode diagram, because in the Nyquist plot the high impedance values can mask important data in the low-frequency range[34]. Besides the Bode and Nyquist plots, other ways of presenting the data also exist, which have more complicated axes such as Z′ as a function of ωZ″. These alternative presentations are intended to show specific electrochemical phenomena, which are not clear in the typical Bode and Nyquist plots.

2.4.4 Electrical models for electrochemical systems

Introduction

An observation which probably gave electrochemical impedance spectroscopy its recognition as being important is the relationship between an electrochemical system that contains a series of independent or interrelating phenomena and an idealised electrical equivalent circuit that is composed of individual electrical components, such as resistors and capacitors. However, a set of conditions and limitations should always be taken into account. Electrical equivalent circuits are seldom unique, which means that additional information (obtained through other methods) is needed to eliminate possible electrical equivalent circuits. Furthermore, the individual components are not exact representations of interfaces, electrolyte resistances or electrochemical reactions, and therefore they apply only in a limited range of experimental conditions. Finally, electrochemical impedance spectroscopy can be performed only with small amplitude of the input signals in order to meet the condition that the studied systems behave as a virtually linear system[35].

An additional complication is the often experimentally detected dependency of the frequency of bulk and interface parameters. Up to now, discussion of this phenomenon has attributed it to causes such as poor uniformity at microscopic scale, but other causes are also possible. More attention is given to this problem on pages 55–56.

Elements and rules for electrical equivalent circuits

The simplest electrical elements that can be part of an electrical equivalent circuit are resistance R, capacity C and induction L, with the following impedance functions:

$$Z_{\mathrm{R}} = R \qquad [2.42]$$

$$Z_{\mathrm{C}} = {}^{1}\!\!\diagup\!\!{}_{j\omega C} \qquad [2.43]$$

$$Z_{\mathrm{L}} = j\omega L \qquad [2.44]$$

where the use of R and C is linked to their classical meaning in electrical sense, being the dissipation of electrical energy for R and charge separation for C. The rules for calculations of impedances are for electrical equivalent circuits with components only in series:

$$Z_{\mathrm{s}} = \sum_{\mathrm{i}} Z_{\mathrm{i}} \qquad [2.45]$$

and with components only in parallel:

$$\frac{1}{Z_{\mathrm{p}}} = \sum_{\mathrm{i}} \frac{1}{Z_{\mathrm{i}}} \qquad [2.46]$$

Model of Ershler–Randles

Figure 2.6 shows an electrical equivalent circuit of an electrode to which a chemical reaction occurs:

$$O + n\mathrm{e}^{-} \leftrightarrows \mathrm{R} \qquad [2.47]$$

In its most simple form, this means without effects such as adsorption or formation of coatings at the electrode surface[36]. The resistance, R_{e}, represents electrical conductivity of the electrolyte and is not a property of the electrode itself. The differential double-layer capacity, C_{dl}, is caused by an excess of charge at the metal surface of the metal–electrolyte interface, which is in equilibrium with an equal excess of charge but opposite in sign at the side of the electrolyte.

In electrochemical impedance spectroscopy, an electrode can be assumed to be in equilibrium because the reaction rate of this equilibrium is not

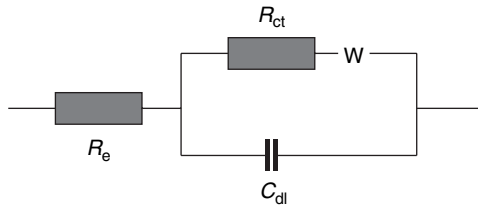

2.6 Electrical equivalent circuit representing the model of Ershler–Randles.

determined by transport phenomena in the electrolyte. This is based on the fact that in electrochemical impedance spectroscopy, the amplitude of the applied signal(s) is(are) small. The charge-transfer resistance for a reaction is given by Equation 2.48.

Suppose that the envisaged reaction is a corrosion reaction, which means that reactions of the type of Equation 2.47 occur simultaneously at the electrode surface but belonging to two different redox systems; then R_{ct} can be defined as a polarisation resistance:

$$R_{ct} = \frac{RT}{nFi_0} \qquad [2.48]$$

where R is the universal gas constant (8.317 J mol^{-1} K^{-1}), T is the thermodynamic temperature in K, n is the number of electrons exchanged in the reaction, F is the Faraday constant (96485 C mol^{-1}), i_0 is the current density at the equilibrium potential (in A m^{-2}).

If the reaction rate is controlled by transport phenomena, then the resulting impedance can be explained by a component that depends on the conditions of transport. The best-known example is the so-called Warburg impedance Z_W, valid for semi-infinite diffusion[37,38]:

$$Z_W = \frac{\sigma}{\sqrt{\omega}}(1 - j) \qquad [2.49]$$

where σ is the Warburg coefficient:

$$\sigma = \frac{RT}{n^2F^2\sqrt{2}}\left(\frac{1}{c_O^{\infty}D_O^{-1/2}} + \frac{1}{c_R^{\infty}D_R^{-1/2}}\right) \qquad [2.50]$$

where, if i represents O and R, c_i^{∞} is the bulk concentration of component I (mol m^{-3}), and D_i is the diffusion coefficient (m^2 s^{-1}).

Another example of a transport-determined impedance is the one for convective diffusion[39], which is not explained here.

Figure 2.7 shows a Nyquist plot corresponding to the electrical equivalent circuit of Fig. 2.6. The slope of the impedance can be explained by a circuit, consisting of different resistive and capacitive components[37]. The

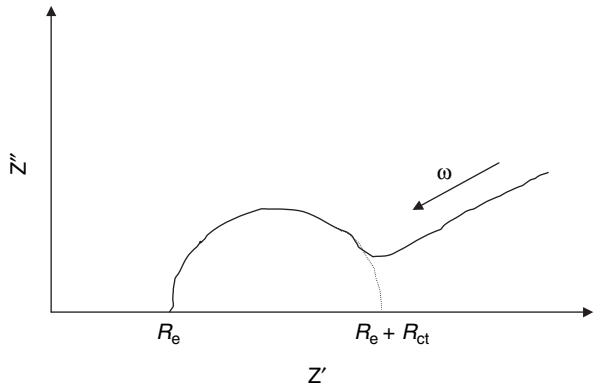

2.7 Idealised Nyquist diagram corresponding to the equivalent circuit of Ershler–Randles (Fig. 2.6).

semi-circle of which the centre point is located at the x-axis correlates with frequencies at which electrolyte properties and/or reaction rates determined by kinetic parameters can be studied, while diffusion limitations can be correlated with the linear part of the curve. This linear part corresponds to a phase angle of π/r (45°) for semi-infinite diffusion. From Fig. 2.7, it is also clear that diffusion limitations are observed in the low-frequency range of the spectrum.

Constant-phase elements

It is often experimentally observed that in the Nyquist plot, semi-circles are obtained with a centre point below the x-axis. Analysis of the situation tells us that the double-layer capacity is not a suitable description of the system occurring and should be replaced by an element with an impedance function given in Equation 2.51:

$$Z_{\mathrm{CPE}} = \frac{1}{Y_0(j\omega)^n} \qquad [2.51]$$

where Y_0 and n are frequency-independent parameters, and n can vary from –1 to +1. This so-called constant-phase element behaves like a pure resistor if $n = 0$, a pure capacitor if $n = 1$, and a pure inductance if $n = -1$. Note also that for $n = 0.5$, a Warburg impedance is found.

Constant-phase elements were first used to explain dielectrical properties of polar liquids and solids, and were attributed to the presence of the investigated material properties as a partitioning between extreme conditions, rather than as constant or uniform parameters[40]. Furthermore in the

case of interface parameters rather than bulk properties (such as capacitive behaviour of the metal–electrolyte interface) an observation can be associated with a lack of uniformity at a microscopic scale. These could include the presence of a rough surface, local inhomogeneities in charge density, adsorbed species and variations in composition amongst other things[41].

In this book, an explanation of capacitive behaviour in similar and comparable systems is not directly possible with constant-phase elements because such a comparison is only possible if n values are equal, particularly in the study of surfaces covered with polymer coatings where a unification of the envisaged parameters is necessary. The impedances measured match with a relatively large amount of samples, of which the structure can be complex, showing many sources of non-idealities (e.g. variations in thickness of the membrane, pore size and pore density[42–47]). A good indication if such non-idealities occur can be found in the values of n. If they are not comparable, non-idealities occur.

A solution to this problem is the use of electrical equivalent circuits without constant-phase elements (note that a good numerical simulation of the experiments can be obtained only by inserting constant-phase elements); only pure capacities are used. This method, although not convincing, results in comparable capacities.

Another possibility is based on the fact that constant-phase elements represent processes that are not purely conservative (charging and discharging of a capacitor is a conservative process), first because of the fact that n is not equal to 1. From such an element, one can isolate the conservative contribution, which can then be further treated as a conservative process and simulated by a pure capacitor. The starting point for this separation is the existence of an angle frequency, ω, for which[48]:

$$Z_{\mathrm{CPE}}(\omega) = Z_{\mathrm{C_{id}}}(\omega) \qquad [2.52]$$

at the inflection point of the Bode diagram, so:

$$\frac{\delta\phi(\omega)}{\delta\omega} = 0 \qquad [2.53]$$

therefore:

$$\frac{1}{Y_0(j\omega)^n} = \frac{1}{j\omega C_{\mathrm{id}}} \qquad [2.54]$$

Since the following equation is valid:

$$j^{-\mathrm{n}} = \cos\left(-n\frac{\pi}{2}\right) + j\sin\left(-n\frac{\pi}{2}\right) \qquad [2.55]$$

2.4.5 Experimental detection of impedance

Electrical stimulation

As described in section 2.4.2, an impedance experiment involves the application of an electrical signal (E or O) and the measurement of an electrical current or a potential. Consider that a potentiostatic experiment (application of a potential) with three types of input signals can be used for determination of the impedance[49].

A first method consists of a measurement of an electrical current as a function of time, while applying a potential step at $t = 0$:

$$E(t) = E_{\text{step}} \text{ for } t \geq 0$$
$$E(t) = 0 \text{ for } t < 0$$

The impedance is obtained using Fourier transformations, on the condition that E_{step} is small enough to obtain a linearly dependent output signal. The simplicity of this experimental approach is one of its advantages. A second method is based on the application of a (continuous) noise signal to the system. Also in this case, Fourier transformations are used to obtain the impedance. An advantage of this method is its short measuring time because only one signal must be applied. Despite the advantages of the previous methods, most researchers use a third method: application of an alternating potential signal with frequency ω and measurement of alternating current. With Equation 2.41 and related equations, the impedance is obtained. The most important reason to use this method is that the existing equipment allows measurements in the frequency range of 1×10^{-4} – 1×10^{6} Hz. This assumes that the frequency range can be chosen and varied according to the type of system being studied.

Impedance of two- and three-electrode systems

Before the introduction of potentiostats in the early 1960s, the study of electrode processes was done mainly with two-electrode systems in which the functions of the reference and the counter electrode were unified in one simple electrode. Such an electrode is a non-polarisable electrode with a relatively large surface to be sure that it can conduct a certain amount of current due to occurring electrochemical processes.

A potentiostatic, three-electrode circuit allows the separation of both functions physically: for the reference potential, a non-polarisable electrode is used (a calomel or Ag|AgCl reference electrode), while the electrical-current conducting electrode is an inert metal electrode. With electrochemical, direct-current methods, the effect of this modification is limited to a reduction of the so-called IR-drop (or ohmic-drop), which is caused by

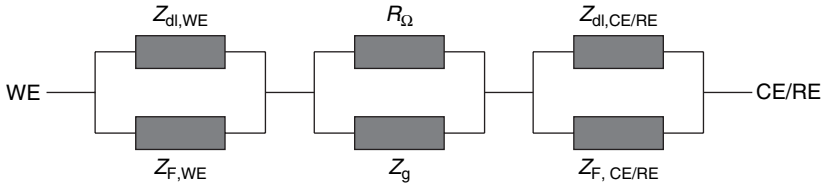

2.8 Equivalent electrical circuit for a two-electrode setup with planar electrodes. (WE: working electrode; CE/RE: counter electrode and reference electrode, respectively, being fulfilled by one single electrode.)

the limited electrical conductivity of the electrolyte. Improvements were found through using a Haber–Luggin capillary, which allows measurement of the working potential very close to the surface of the working electrode. A more fundamental difference is observed when an electrochemical system is studied. Figure 2.8 shows the equivalent electrical circuit of a cell with the two-electrode setup. WE and CE/RE represent, respectively, working electrode, counter electrode and reference electrode, and the latter two are fulfilled by one single electrode.

The resistance of the electrolyte, R_Ω, represents the ohmic resistance of the complete column of electrolyte between both electrodes. Note that in this way of presentation, the Faradaic impedance cannot necessarily be correlated with an occurring process, therefore it is represented by a general symbol Z_F. It can be seen in this case that the total impedance consists of contributions from the working and the counter/reference electrodes, and knowledge of the behaviour of only the working electrode needs manipulation. A simple possibility is to use a CE/RE electrode with much larger surface than the WE. However, in the work presented in this book, this manipulation is not done, because the system used here will be used in applications as a set of two identical electrodes. In addition, one of the parameters that we are interested in is the electrolyte resistance, a parameter that is suppressed when using electrodes of different surface areas.

The equivalent electrical circuit in the case of a three-electrode setup is given in Fig. 2.9. Working and counter electrode are identical as for a two-electrode setup, while the reference electrode, as a non-current conducting electrode, only has the role of potential reference and therefore does not contribute to the impedance. However, the position of the Haber-Luggin capillary determines the contribution of R_e and R_{comp} to R_Ω given by the following equation:

$$R_\Omega = R_e + R_{comp} \qquad [2.56]$$

with R_e and R_{comp}, the uncompensated and compensated resistance, respectively. So, indirectly, the reference electrode plays an important role. The

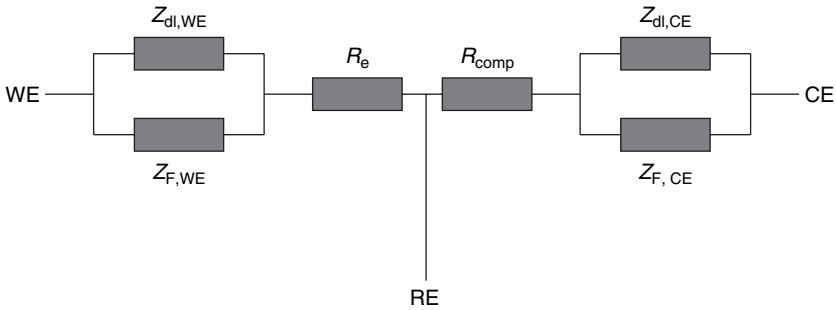

2.9 Equivalent electrical circuit for a three-electrode setup. (WE: working electrode; CE/RE: counter electrode and reference electrode, respectively, being fulfilled by one single electrode.)

advantage of using a three-electrode system is that the potential is measured between the working and reference electrodes and is controlled by application of a suitable potential difference between the working and counter electrode (see also Chapter 1, section 1.6). This occurs independently of what happens at the surface of the counter electrode. Therefore, a three-electrode setup allows us to measure exclusively the behaviour of the working electrode, taking into account that always a certain amount of R_Ω is not compensated (R_e), which in fact is the resistance between the working and reference electrodes. The three-electrode setup will not be used in this work and is not discussed further.

Data analysis

The relevance of a recorded impedance spectrum is not clear, as is the case for experiments done with instrumental methods. A number of potentially occurring errors can give rise to a distortion (small or large) of the impedance spectrum, with a certain impact on the interpretation of the data and the curves. A method to analyse the obtained impedance spectra makes use of so-called Kramers–Kronig transformations[50,51], which are a set of coupled integral equations that describe the relationship between the real and imaginary part of the impedance. For impedance Z:

$$Z'(\omega) - Z'(\infty) = \frac{2}{\pi}\int_0^\infty \frac{xZ''(x) - \omega Z''(\omega)}{x^2 - \omega^2}\,dx \qquad [2.57]$$

$$Z''(\omega) = -\frac{2\omega}{\pi}\int_0^\infty \frac{Z'(x) - Z'(\omega)}{x^2 - \omega^2}\,dx \qquad [2.58]$$

where x is a variable in the integration method. These relations were first used in optical studies with polarised light[52,53], and they were also used in

the analysis of electrical networks[54] before their introduction in electrochemical impedance spectroscopy[55].

Conditions for the envisaged system described in Equations 2.57 and 2.58 are those given in section 2.4.4, e.g. linearity and time-independent systems and further stability and causality. The latter implies that the output signal cannot precede the input signal:

$$\forall t < t_0 : u(t) = v(t) \Rightarrow (Lu)(t) = (Lv)(t) \qquad [2.59]$$

Application of the Kramers–Kronig relations means that the real part of the impedance is calculated from the imaginary part by using Equation 2.57, and vice versa using Equation 2.58. However, in an experiment both parameters are determined so that comparison of the calculated and measured real and imaginary parts of the impedance allows validation or elimination of experimental data. If a discrepancy is found between predicted and measured data of Z' and Z'' it means that at least one of the outlined conditions is not fulfilled. It is clear that for electrochemical reactions such as a corrosion reaction, the condition of time independency is frequently not fulfilled. This can be caused by the continuation of the reaction during the recording of the impedance data. However, for the purpose that electrochemical impedance spectroscopy is used in this work, mainly time-independent systems are obtained[56].

A difficulty in using Kramers–Kronig transformations is that, in principle, the impedance should be known over the entire frequency range, but as long as the impedance spectrum can be explained using equivalent electrical circuits, a simple solution can be proposed. Since this is the case in this work, reference is made to the literature for further details about this topic[55–66]. Basic equivalent electrical circuit elements, such as resistance, R, capacitance, C, inductance, L, and a constant-phase element (CPE), can directly be transformed in Kramers–Kronig relations. For the latter, an additional condition of n lying between –1 and 1 should be fulfilled. From the linearity of the integration of the Kramers–Kronig transformations and the fact that the relations presented in Equations 2.57 and 2.58 are also functions of an electrical circuit with series and/or parallel connected elements, such connections can also be transformed. All the systems studied in this work meet this condition.

2.5 Chronoamperometry

As discussed earlier, the potential is scanned between selected potentials with the measurement of the corresponding electrical current. Another type of electrochemical methods is potential step methods, such as chronoamperometry. In this case, the potential of the working electrode is changed drastically and immediately from a potential E_1 to a potential E_2, at the

same time that the electrical-current response is followed continuously as a function of time. The use and advantages of this approach are multifunctional:

- The method is useful for the evaluation of diffusion coefficients.
- The method enables study of the rate of electrode reactions, and the rates of coupled chemical reactions, as well as the study of adsorption phenomena.
- For analytical purposes, the method can be used to obtain time-independent signals when a constant thickness of the diffusion layer is obtained by convection or using ultramicro electrode configurations.

The latter use is particularly appropriate for the work and results shown and discussed in this book (see Chapters 4, 5 and 6).

2.6 Other voltammetric methods

2.6.1 Introduction

In this chapter, some commonly known electrochemical methods are described to complete the set of methods described in Chapter 1. In contrast to the methods discussed in Chapter 3, the methods described here are not used in the further work considered and evaluated in this book, though they have been included for general information.

2.6.2 Fast direct-current voltammetry

In fast direct-current voltammetry[67], also known as linear sweep voltammetry, scan rates of 0.01–20 $V s^{-1}$ are used and result in a peak-shaped current response at a stationary electrode. The resolving and separating capacity can be up to 40 mV and 1×10^3/1, resulting in a detection limit of 1×10^{-7} mol l^{-1}. However, a drawback of using fast scan rates is the increasing background current due to the capacitive charging effect of the electrical double layer. In practice, this results in a limitation to the Faraday current with increasing scan rate because this current is superponated at an increasing base line. At high scan rates, this increase in capacitive current is larger than the increase of the Faraday current, and therefore an increasing perturbation of the Faraday current is observed having a negative effect on its shape, nature and detection limit.

In fact this method is identical to cyclic voltammetry, except that the potential is swept from a certain starting potential to an end potential without returning to the initial starting potential. In other words, only the forward sweep is recorded in linear sweep voltammetry. However, relationships for the measured current and its relation to applied potential, and

concentration, are identical, and therefore reference is made to section 2.3 for a more quantitative approach.

2.6.3 Potential step voltammetry

In potential step voltammetry, a DC potential window is covered by a DC ramp (linearly increasing applied DC potential) with discrete and symmetrical pulses superponated to this ramp. As an alternative, the pulse amplitude can increase with each pulse, superponated on a constant DC offset. Methods where pulses are involved superponated on a DC signal are generally called potential step methods.

Normal pulse voltammetry

In normal pulse voltammetry[68], rectangular potential pulses with increasing amplitude E_p and constant pulse time τ (10–100 ms) are superponated at a constant DC offset E_b (Fig. 2.10). E_b is equal to a potential smaller than the potential where the oxidation or reduction of the analyte starts to occur. This offset can be situated in the background current region or in a limiting-current region of a preceding oxidation/reduction reaction. The amplitude of the pulses increases with constant time intervals (e.g. 0.5 s) with a value ΔE. The current signal is measured at the end of the applied potential pulse, because under this condition the capacitive current is very small compared with the Faraday response (Fig. 2.11). It may also be clear from Fig. 2.11 that this effect depends on the pulse time, τ. From Fig. 2.10, it can

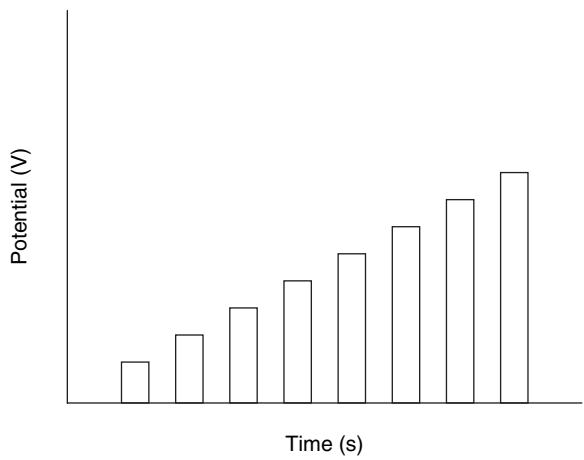

2.10 Variation profile of the applied potential in normal pulse voltammetry.

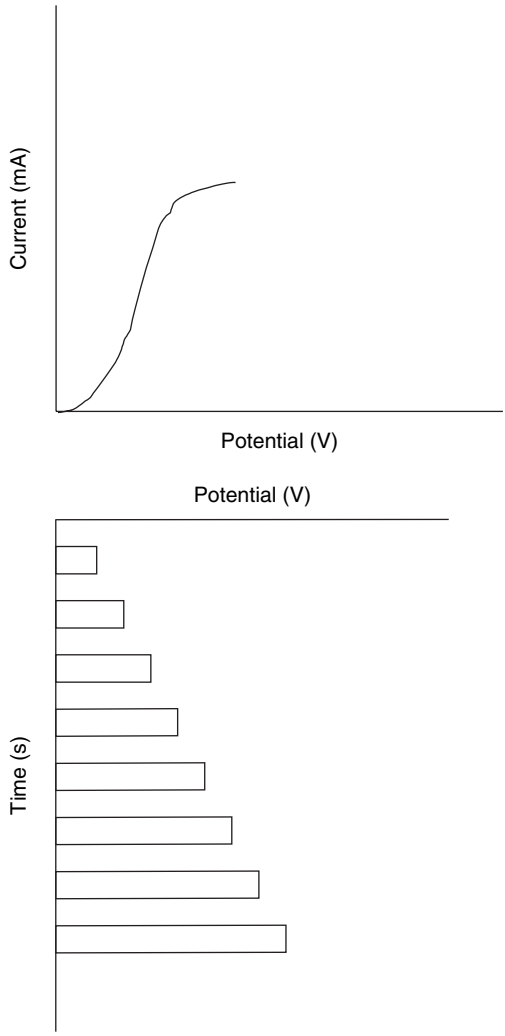

2.11 Electrical-current signal profile in normal pulse voltammetry as a function of applied potential step with increasing amplitude.

be seen that if the pulses are superponated on a DC offset located in the limiting-current region of a preceding wave they can be separated very well because the contribution of the preceding wave to the pulse current is almost zero. Its main contribution is located in the DC offset.

Normal pulse voltammetry is mainly used when the condition of the electrode surface should be kept constant but applying a potential would have a serious effect on this condition. In normal pulse voltammetry, the applied potential to the electrode is always the DC offset, except for those short

periods of time that the pulses are applied. However, after each pulse, the potential returns to its initial potential, giving the electrode surface time to return to its initial condition and to compensate for the changes of surface condition caused by the application of the pulse.

Differential pulse voltammetry

In differential pulse voltammetry (DPV)[69–73], short pulses (τ = 10–100 ms) with limited amplitude (ΔE = 1–100 mV) are superponated to a linearly increasing DC ramp (Fig. 2.12). This means that besides the current of the pulse, a DC current also is obtained due to the inclining DC ramp. Practically, the current is measured before the application of a pulse (I_1) and at the end of the pulse (I_2). The first current is attributed to the DC ramp, while the difference $I_2 - I_1$ reflects the current of the potential pulse. The resulting voltammograms of the pulse current have a differential shape, which is illustrated in Fig. 2.13. In Fig. 2.13a, the common voltammogram is illustrated that would be obtained in linear sweep, cyclic or normal pulse voltammetry, while in Fig. 2.13b, the differential pulse voltammogram is shown. As explained above, the signal in differential pulse voltammetry is the result of the difference between two signals – the signal just before the pulse and the signal at the end of the pulse. Therefore, it can be seen in Fig. 2.13a that the pulses cover a small fraction of the common voltammogram,

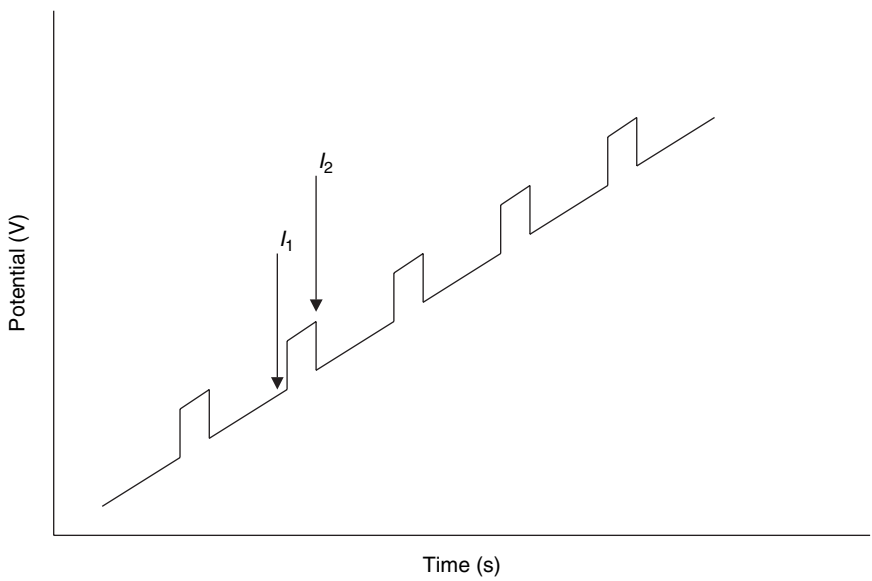

2.12 Variation profile of the applied potential in differential pulse voltammetry.

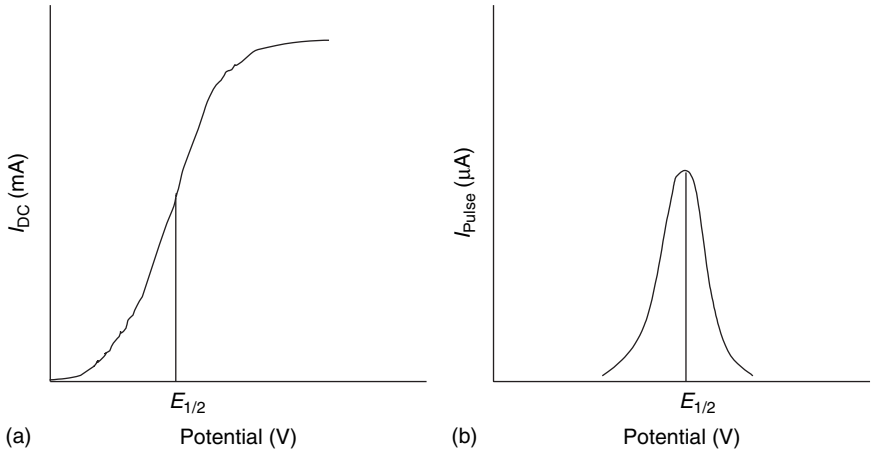

2.13 Electrical-current signal in differential pulse voltammetry with (a) the DC-current signal due to applied and linearly increasing DC ramp and (b) the signal due to the application of potential pulses.

and a maximum in the difference between I_2 and I_1 will be obtained at the inflection point of the voltammetric wave. This point corresponds to the half-wave potential; therefore, the peak potential in DPV is identical to the half-wave potential of the envisaged oxidation or reduction reaction. Typical detection limits obtained in differential pulse voltammetry are 1×10^{-8} mol l^{-1}, with a resolving capacity of 40 mV and a separating capacity of 1×10^5/1.

Square-wave voltammetry

In square-wave voltammetry[74–82], a symmetrical square-wave pulse (Fig. 2.14a) is superponated to a staircase wave (Fig. 2.14b) resulting in the square wave (Fig. 2.14c). The duration of the pulse, τ, is equal to the length of the staircase, and the superponation is obtained in such a way that the forwards pulse of the square wave coincides with the first half of that staircase. Two other important parameters are E_{sw}, the pulse height of the square wave, and E_{sc}, the increase of the staircase for each step.

In square-wave voltammetry, the current signal is the result of a difference between the experimentally measured currents. The first current is measured at the end of the forward square-wave pulse (I_1, Fig. 2.14c), and the second one is measured at the end of the return square-wave pulse (I_2, Fig. 2.14c); the difference results in a larger peak because both individual signals are opposite in sign (Fig. 2.15). This can also be explained as follows, supposing that the following reversible reaction occurs at the electrode surface:

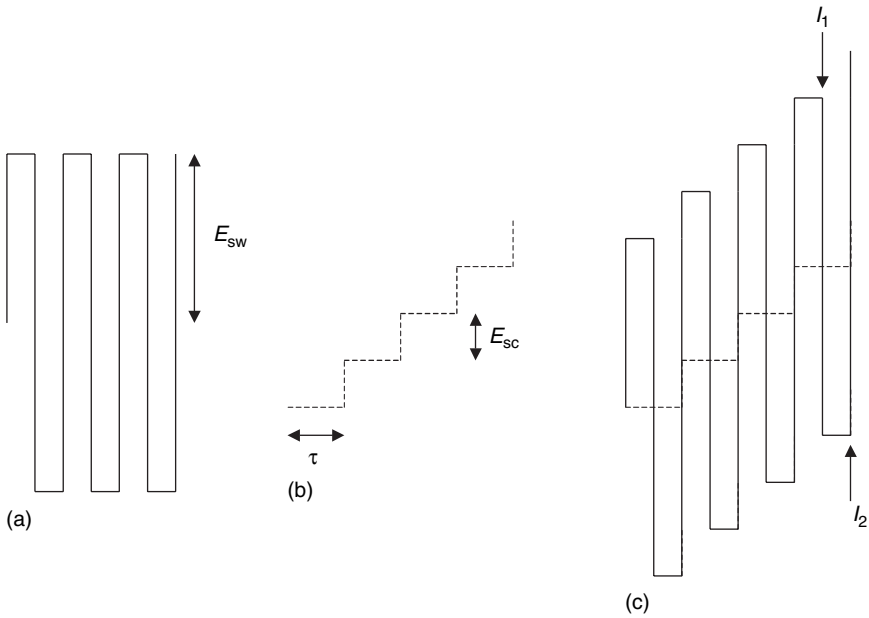

2.14 Variation profile of the applied potential in square-wave voltammetry, with (a) the step potential, (b) the staircase and (c) the combination of (a) and (b) into the square-wave form.

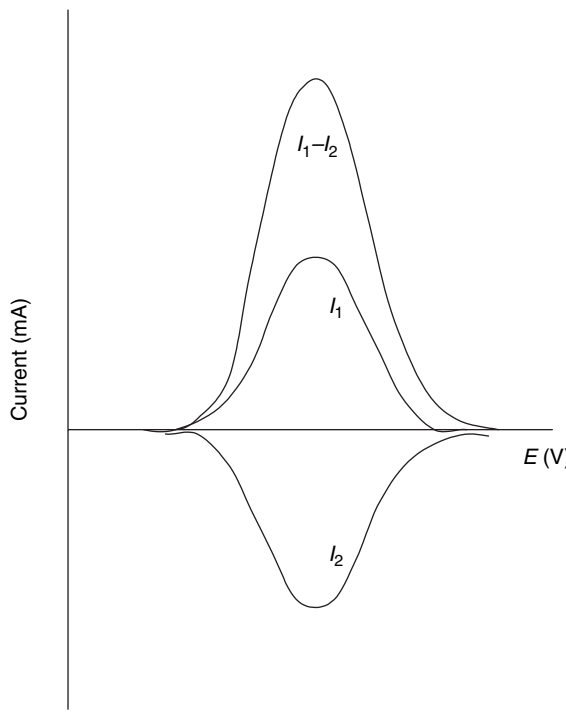

2.15 Electrical-current signal in square-wave voltammetry, resulting in a peak-shaped curve obtained by I_1–I_2.

$$R \leftrightarrows O + ne^- \qquad [2.60]$$

In the forward square-wave step, R is oxidised to O giving rise to a positive current; this assumes that the concentration of the reaction product O in the vicinity of the electrode surface increases. During the reverse square-wave step, this reaction product O is reduced back to its initial form, being R. This results in a measured negative current. The difference $I_1 - I_2$ is a higher signal than I_2 and I_1 individually, because it is the difference between two signals that are opposite in sign. The resulting square-wave voltammogram shows a differential shape with a peak maximum equal to the half-wave potential and located at the same peak potential of the individual signals from the oxidation and reduction reaction. Detection limits in square-wave voltammetry are of the order of 1×10^{-10} mol l^{-1}.

2.6.4 Other methods

Other methods[67] have been proposed and studied, which will not be discussed here. In principle, a large variety of methods can be proposed because of the huge possibilities for variation of the applied potential in a DC mode, AC mode and/or with pulses. For a more detailed overview of voltammetric methods, reference is made to literature[67].

2.7 References

1. Nernst W., *Z. Phys. Chem.*, **4** (1889) 129.
2. Behrend R., *Z. Phys. Chem.*, **11** (1893) 466.
3. Eisenman G, Rudin D.O., Casby I.U., *Science*, **126** (1951) 831.
4. Pranitis D.M., Telting-Diaz M., Meyerhoff M.E., *Crit. Rev. Anal. Chem.*, **23** (1992) 163.
5. Nernst W., Merriam E.S., *Z. Phys. Chem.*, **52** (1905) 235.
6. Ives D.J.G., Janz G.J., *Reference Electrodes*, Academic Press, New York, 1961.
7. Guilbault G.G., *Ion-select. Elect. Rev*., **4** (1982) 187.
8. Kolthoff I.M., Furman N.H., *Potentiometric Titrations*, Wiley, New York, 1931.
9. Reilley C.N., Schmid R.W., Lamsen D.W., *Anal. Chem.*, **30** (1958) 953.
10. Reilley C.N., Schmid R.W., *Anal. Chem.*, **30** (1958) 947.
11. Nicholson R.S., Shain I., *Anal. Chem.*, **36** (1964) 706.
12. Vassos B.H., Ewing G.W., *Electroanalytical Chemistry*, Wiley, New York, 1983.
13. Nicholson R.S., *Anal. Chem.*, **37** (1965) 1351.
14. Bard A.J., Faulkner L.R., *Electrochemical Methods*, Wiley, New York, 1980.
15. Galus Z., *Fundamentals of Electrochemical Analysis*, Ellis Horwood, Chichester, 1994.
16. Saveant J.M., Vianello E., *Electrochim. Acta*, **8** (1963) 905.
17. Saveant J.M., Vianello E., *Electrochim. Acta*, **12** (1967) 629.
18. Saveant J.M., *Electrochim. Acta*, **12** (1967) 753.
19. Saveant J.M., Vianello E., *Electrochim. Acta*, **12** (1967) 1545.
20. Mastragonisto M., Nadjo L., Saveant J.M., *Electrochim. Acta*, **13** (1968) 721.

21. Nadjo L. Saveant J.M., *J. Electroanal. Chem.*, **48** (1973) 113.
22. Saveant J.M., Andrieux C.P., Nadjo L., *J. Electroanal. Chem.*, **41** (1973) 137.
23. Macdonald D.D., *Transient Techniques in Electrochemistry*, Plenum Press, New York, 1977.
24. Greef R., Peat R., Peter L.M., Pletcher D., Robinson J., *Instrumental Methods in Electrochemistry*, Ellis Horwood, Chichester, 1985.
25. Matsuda H., Ayabe Y., *Z. Elektrochem.*, **59** (1955) 494.
26. Nicholson R.S., Shain I., *Anal. Chem.*, **37** (1964) 178.
27. Nicholson R.S., Shain I., *Anal. Chem.*, **37** (1964) 190.
28. Laviron E., *J. Electroanal. Chem.*, **52** (1974) 355.
29. Laviron E., *J. Electroanal. Chem.*, **52** (1974) 395.
30. Srinivasan S., Gileadi E., *Electrochim. Acta*, **11** (1966) 321.
31. Sluyters-Rehbach M., Sluyters J.H., in Bard A.J. (ed.) *Electroanalytical Chemistry 4*, Marcel Dekker, New York, 1970.
32. Beerends R.J., Ter Morsche H.G., Van Den Berg J.C., Van De Vrie E.M., *Fourieren Laplace-transformaties 29*, Educaboek, Culemborg, 1993.
33. Beerends R.J., Ter Morsche H.G., Van Den Berg J.C., Van De Vrie E.M., *Fourieren Laplace-transformaties 31*, Educaboek, Culemborg, 1993.
34. Mansfeld F., *J. Appl. Electrochem.*, **25** (1995) 187.
35. Diard J.P., Le Gorrec B., Montella C., *Electrochim. Acta*, **39** (1994) 539.
36. Randles J.E.B., *Disc. Faraday Soc.*, **1** (1947) 11.
37. Sluyters J.H., *Rec. Trav. Chim.*, **79** (1960) 1092.
38. Warburg E., *Ann. Phys. Chem.*, **67** (1899) 493.
39. Kaufman A.M., *Solartron Instruments*, technical report 017/85.
40. Cole K.S., Cole R.H., *J. Chem Phys.*, **9** (1941) 341.
41. Macdonald J.R., Johnson W.B., in Macdonald J.R. (ed.), *Impedance Spectroscopy*, **13**, Wiley, New York, 1987.
42. Rammelt U., Reinhard G., *Corros. Sci.*, **27** (1987) 373.
43. Nyikos L., Pajkossy T., *Electrochim. Acta*, **35** (1990) 1567.
44. Mulder W.H., Sluyters J.H., *Electrochim Acta*, **33** (1988) 303.
45. Le Mehaute A., Crepy G., *Solid State Ionics*, **9/10** (1983) 17.
46. Rammelt U., Reinhard G., *Electrochim. Acta*, **35** (1990) 1045.
47. De Levie R., *J. Electroanal. Chem.*, **261** (1989) 1.
48. Van Westing E.P.M., *PhD Diss., T.U. Delft*, 1992.
49. Macdonald J.R., Johnson W.B., in Macdonald J.R. (ed.), *Impedance Spectroscopy* **3**, Wiley, New York, 1987.
50. Popkirov G.S., Schindler R.N., *Electrochim. Acta*, **38** (1993) 861.
51. Popkirov G.S., Schindler R.N., *Electrochim. Acta*, **39** (1994) 2025.
52. Kramers H.A., *Phys. Z.*, **30** (1929) 522.
53. Kronig R. de L., *J. Opt. Soc. Am.*, **12** (1926) 547.
54. Bode H.W., *Network Analysis and Feedback Amplifier Design*, van Nostrand, New York, 1945.
55. Van Meirhaeghe R.L., Dutoit E.C., Cardon F., Gomes W.P., *Electrochim. Acta*, **21** (1976) 39.
56. Macdonald J.R., *Electrochim. Acta*, **142** (1995) 1885.
57. Orazem M.E., Esteban J.M., Moghissi O.C., *Corrosion*, **47** (1991) 248.
58. Agarwal P., Orazem M.E., Garcia-Rubio L.H., *J. Electrochem. Soc.*, **142** (1995) 4159.

59. Urquidi-Macdonald M., Real S., Macdonald D.D., *J. Electrochem. Soc.*, **133** (1986) 2018.
60. Boukamp B.A., *J. Electrochem. Soc.*, **142** (1995) 1885.
61. Urquidi-Macdonald M., Real S., Macdonald D.D., *Electrochim. Acta*, **35** (1990) 1559.
62. Boukamp B.A., *Solid State Ionics*, **62** (1993) 131.
63. Agarwal P., Orazem M.E., Garcia-Rubio L.H., *J. Electrochem. Soc.*, **139** (1992) 1917.
64. Boukamp B.A., Macdonald J.R., *Solid State Ionics*, **74** (1994) 85.
65. Morgan F.D., Lesmes P.D., *J. Chem. Phys.*, **100** (1994) 671.
66. Uhlman D.R., Hakim R.M., *J. Phys. Chem. Sol.*, **32** (1971) 2652.
67. Kissinger P.T., Heineman W.R. (eds), *Laboratory Techniques in Electroanalytical Chemistry*, Marcel Dekker, New York, 1996.
68. Norman S.A., *Anal. Chem.*, **54** (1982) 698A.
69. Parry E.P., Osteryoung R.A., *Anal. Chem.*, **37** (1965) 1634.
70. Vassos B.H., Osteryoung R.A., *Chem. Instrum.*, **5** (1973) 257.
71. Christie J.H., Jackson L.L., Osteryoung R.A., *Anal. Chem.*, **48** (1976) 242.
72. Osteryoung J., Hasebe K., *Rev. Polarography*, **22** (1976) 1.
73. Krause M.S., Ramaley L., *Anal. Chem.*, **41** (1969) 1365.
74. Osteryoung J., O'Dea J.J., *Electroanal. Chem.*, **14** (1986) 209.
75. Barker G.C., *Anal. Chim. Acta*, **18** (1958) 118.
76. Ramaley L. Krause M.S., *Anal. Chem.*, **41** (1969) 1362.
77. Christie J.H., Turner J.A., Osteryoung R.A., *Anal. Chem.*, **49** (1977) 1899.
78. Turner J.A., Christie J.H., Vukovic M., Osteryoung R.A., *Anal. Chem.*, **49** (1977) 1904.
79. Osteryoung J, Osteryoung R.A., *Anal. Chem.*, **57** (1985) 101A.
80. Parry E.P., Osteryoung R.A., *Anal. Chem.*, **37** (1965) 1634.
81. O'Dea J.J., Wikiel K., Osteryoung J., *J. Phys. Chem.*, **94** (1990) 3628.
82. Mirceski V., Lovric M., *Electroanal.*, **11** (1999) 984.

Part II

Electrochemistry in textile finishing

3

Probes for pH measurement and simultaneous cellulose removal and bleaching of textiles with enzymes

P. WESTBROEK AND P. KIEKENS

3.1 Introduction

This chapter examines various probes for pH measurement such as ion-selective and glass-membrane electrodes as well as simultaneous cellulose removal and bleaching of textiles with enzymes.

3.2 Ion-selective electrodes

3.2.1 What is an ion-selective electrode?

Ion-selective electrodes belong to the group of potentiometric methods. Many electrode systems, partly well known, partly in development and under investigation, show a Nernstian relationship between the measured electrode potential and the activity of a species in solution. Important conditions to be fulfilled for the development of ion-selective electrodes are the affinity of a membrane surface for a typical ion or molecule and a minimum ion conductivity over the membrane. If possible, but not necessarily, these conditions should be fulfilled at room temperature.

In practice (Fig. 3.1), the potential difference, ΔE, is measured over a membrane:

$$\Delta E = E_2 - E_1 \qquad [3.1]$$

where E_2 is the actual potential of the interface solution 2 (membrane surface 2), and E_1 is the potential of the interface solution 1 (membrane surface 1). This difference is related to the activity of a species in solution according to the following equation:

$$\Delta E = \mathrm{k} \pm \mathrm{R}T/z_\mathrm{i}\mathrm{F}\ln a_\mathrm{i} \qquad [3.2]$$

being a variant of the Nernst equation (Equation 2.7), where k is a constant, R is the gaseous constant, T is the temperature (K), z_i is the charge of the species, F is the Faraday constant, and a_i is the activity of the species.

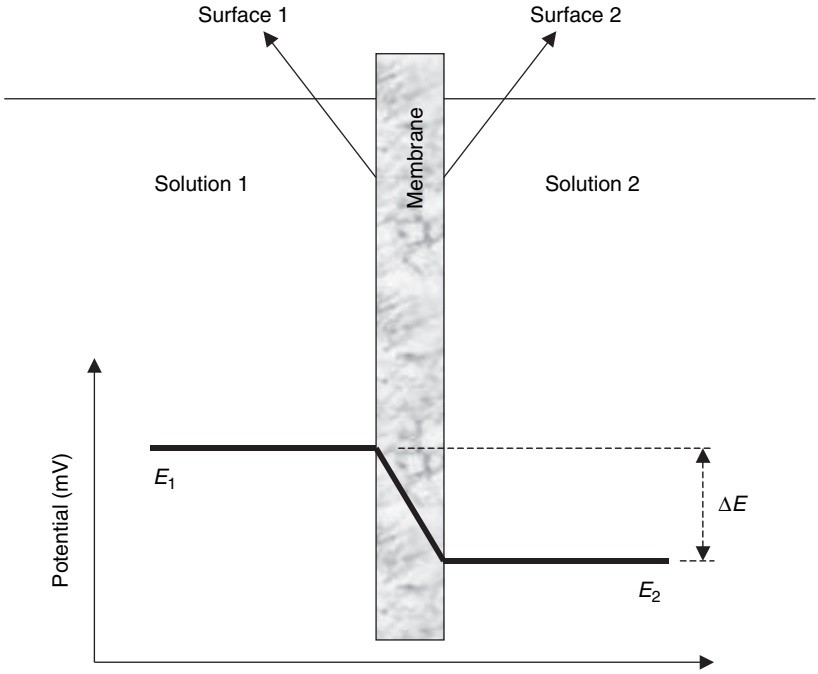

3.1 Scheme of the potential difference over an ion-selective membrane, with both surface sides in contact with a solution containing chemical species.

Typical for ion-selective electrodes is the selective exchange of one or a limited number of species dissolved in solution at the surface of the membrane. This can be obtained through different mechanisms, as will be discussed in the next section of this chapter. The intensity of this exchange determines the values of E_1 and E_2 and is therefore the value of ΔE. As a consequence, the higher the activity of species i in the solution, the higher the value of ΔE will be. This principle can be used for electroanalytical purposes – hence the value of potentiometric sensors.

3.2.2 Types of ion-selective electrodes

A wide range of ion-selective electrodes were developed and can be classified in subgroups of the following main groups:

- solid-membrane electrodes;
- liquid-membrane electrodes.

Subgroups for the solid-membrane electrodes are mainly:

- Glass-membrane electrodes, such as pH electrodes. In this type of electrode, a glass body acts as a membrane and shows affinity for different

ions, such as H^+, Na^+ and K^+. This type of electrode will be discussed more in detail in section 3.3[1].

- Crystal-membrane electrodes, such as the fluoride electrode. Here a crystal is responsible for the exchange of ions; in the case of the fluoride electrode, it is a LaF_3 crystal. The advantage of this type of electrode is their high selectivity towards one single species because of the unique affinity of the ion in solution (e.g. fluoride) for the crystal (e.g. LaF_3)[2].
- Homogeneous and heterogeneous precipitation membranes[3].
- Oxygen-conductive electrodes for use at high temperatures. The most well-known electrodes of this type are the ZrO_2/O_2^- interfaces, used as the oxygen-measuring electrode and/or reference electrode in studies in molten glass[4–8].

The second group of ion-selective electrodes can be subdivided into:

- membranes of liquid ion-exchanging systems[9];
- membranes with organic complexing agents[10];
- enzyme membranes[11].

3.2.3 Selectivity of ion-selective electrodes

The selectivity of an ion-selective electrode for a specific species in solution is given by the following equation, which in fact is an extension of Equation 3.2[12]:

$$E = \mathrm{k} \pm \frac{\mathrm{R}T}{z_\mathrm{i}\mathrm{F}} \ln\left(a_\mathrm{i} + \sum_\mathrm{i}^{\infty} \mathrm{K}_{\mathrm{i},\mathrm{i}+1} a_{\mathrm{i}+1}^{\,z_\mathrm{i}/z_{\mathrm{i}+1}} \right) \qquad [3.3]$$

where k is a constant, R is the gaseous constant, T is the temperature (K), z_i is the charge of the species to be analysed, $z_{\mathrm{i}+1}$ is the charge of the signal-disturbing species, $\mathrm{K}_{\mathrm{i},\mathrm{i}+1}$ is the constant related to the power of contribution to the signal of the signal-disturbing species, F is the Faraday constant, a_i is the activity of the species to be analysed, and $a_{\mathrm{i}+1}$ is the activity of the signal-disturbing species.

3.3 Glass-membrane electrodes

3.3.1 Principles of a glass-membrane electrode

At the surface of a glass membrane (Fig. 3.2) that is in contact with an aqueous solution, a layer, called the Haber–Haugaard layer, is established with a thickness of about 100 nm. In this layer, a fraction of the positive ions, typical for the glass structure, are exchanged by hydrogen ions (H^+). Owing

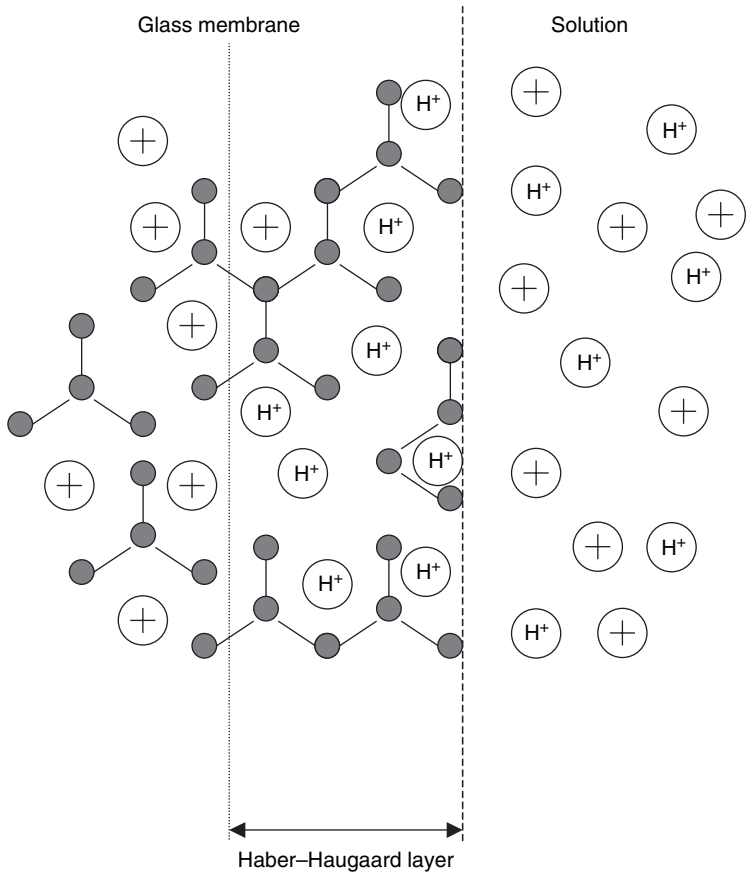

3.2 Scheme of the exchange mechanism of hydrogen ions (H^+) with ions from the glass structure (+) at the interface of the membrane surface with the solution containing hydrogen ions.

to this exchange, a potential, E_1, is obtained, which is dependent on the activity of hydrogen ions in the thin layer. The latter is determined by the hydrogen-ion activity of the solution in contact with this layer.

At the other side of the membrane, a similar hydrogen-ion exchange is obtained (not shown in Fig. 3.2). At both interfaces, a potential is obtained (E_2 and E_1, respectively), and the potential difference over the entire membrane is defined as $\Delta E = E_2 - E_1$ (Equation 3.1). This potential difference, which is related to the hydrogen-ion acitivity in solution (see also Equation 3.3), can be used for analytical purposes to measure the hydrogen-ion activity in solution and thus to determine the pH. The relation between pH and hydrogen-ion solution is given by:

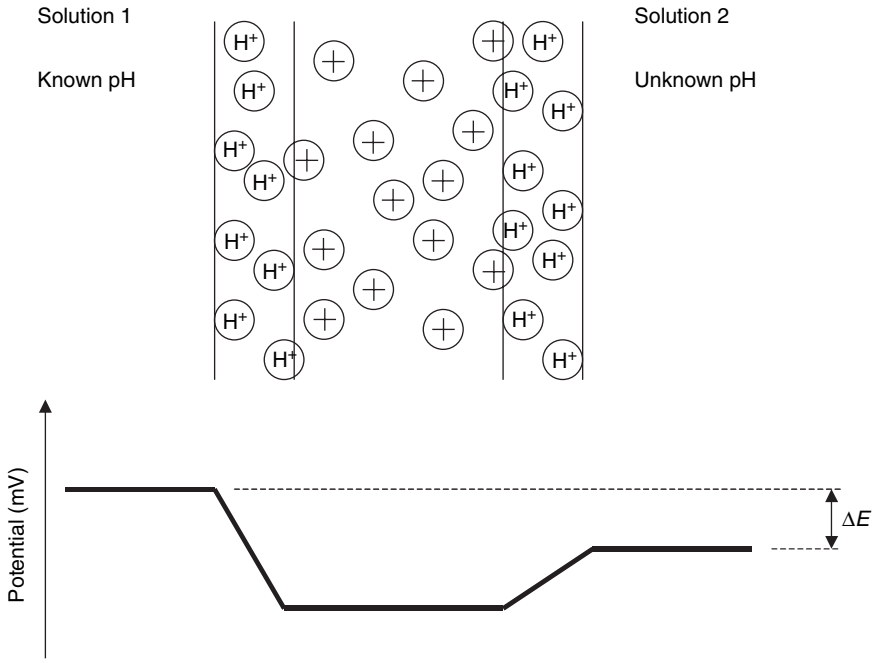

3.3 Potential variation over a glass membrane in contact with two solutions of different composition, one being of constant and known hydrogen-ion activity.

$$\mathrm{pH} = -\log a_{\mathrm{H^+}} \qquad [3.4]$$

In practice, the trick to obtain the pH is to use a membrane that is on one side exposed to a solution of known and constant hydrogen-ion activity (e.g. a buffer solution) and on the other side is exposed to the solution of unknown pH (Fig. 3.3). On the first side of the membrane, an exchange of H^+ occurs, but because of the constant composition of the buffer solution 1, this will result in a constant potential, E_1. On the other side of the membrane, a potential, E_2, is established which is determined by the activity of hydrogen ions in the solution of unknown pH. Therefore, ΔE is dependent only on E_2, and thus the pH of this solution can be determined using a glass membrane.

Of course, before such a glass membrane can be used, the measured potential, ΔE must be linked to the pH. This can be done through calibration by measuring the potential differences when the membrane surface is immersed in buffer solutions of known pH. In that case, E_2 is linked to the pH of the buffer and a calibration curve. Finally, a solution of unknown pH can be analysed by measuring ΔE and calculating the pH using the calibration curve.

3.3.2 Practice

Practically, ΔE is calculated by measuring the potential over two reference electrodes (e.g. Ag|AgCl electrodes), each electrode being positioned at one side of the glass membrane (Fig. 3.4a). The potential of both reference electrodes is the same because they are identical, so if a difference in potential is measured over these electrodes, this difference should be related to the presence of the glass membrane. As explained above, the contribution of E_1 is constant, so the potential difference measured over the entire cell system is related to E_2, or to the hydrogen-ion activity of the solution of unknown pH.

In order to make this type of measurement practically possible in a relatively easy way, pH electrodes were developed (Fig. 3.4b), which consist of a glass tube (1) ending in a ball or other symmetrical shape (2) and filled with a buffer solution (3). It is the ball-shaped part of the tube that acts as the measuring zone for hydrogen-ion activity-monitoring and thus will be in direct contact with the solution of unknown pH. Inside this compartment and immersed in the buffer solution, a Ag|AgCl electrode is positioned (4). The glass tube (1) is surrounded by a second tube (5), filled with a Cl^- solution (6) of identical concentration as the one used for the inner part (3) of the electrode. Also in this tube, a Ag|AgCl reference electrode (7) is immersed, which is in contact with the solution of unknown pH through a diaphragm (8). The potential difference measured over the two reference electrodes is related to the hydrogen-ion activity of the solution of unknown

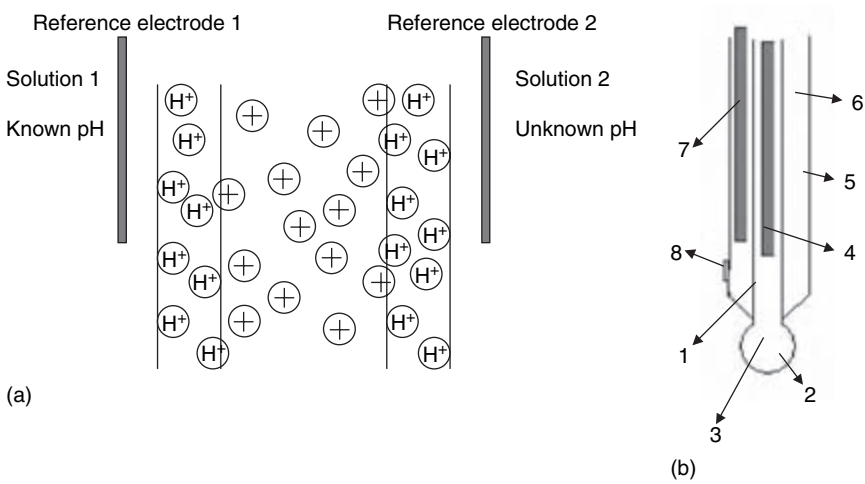

3.4 (a) Scheme of the setup for measurement of pH with a glass membrane and (b) scheme of (a) incorporated into a suitable electrode system that allows simple and user-friendly handling.

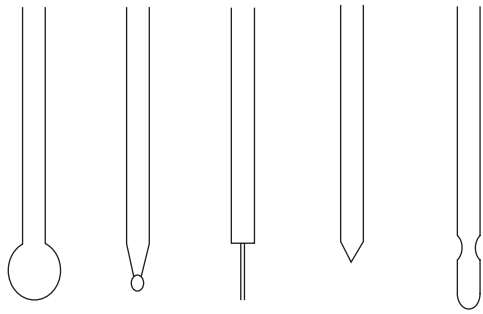

3.5 Alternative shapes of the measuring zone of glass-membrane electrodes.

pH, and this pH can be determined after calibration of the electrode in buffer solutions of known pH.

Finally, in Fig. 3.5, different possible shapes of the glass membrane that is in contact with the solution to be analysed are proposed. Note that all of them have a high degree of symmetry.

3.3.3 Limitations of pH electrodes

The main limitation of glass electrodes is the fact that they should always be in contact with an aqueous solution, e.g. 3 mol l^{-1} KCl. If these electrodes become dry, their properties for pH measurement will drop. It is possible to recover pH electrodes after they have been dry for some time. However, it will be noted that these electrodes have longer reaction times, show a decrease of the slope of the ΔE–pH calibration curve, and display increased impedance of the membrane and a shift of the zero point.

Besides the fact that pH electrodes should always be kept in solution, their lifetime can also be shortened by using the electrodes at high temperatures (their lifetime ranges from 1 to 3 years at room temperature, up to 6 months at 323 K and only a few weeks at 373 K) and/or in poisoning or chemically aggressive solutions. Some cleaning procedures for the latter sources of life-time shortening are proposed, but with limited success, and are based on ultrasonic and/or electromagnetic treatment or treatment in an etching solution[13].

Another important source of errors for pH electrodes is the alkali error[14]. At high pH (>11), the concentration of H^+ is smaller than 1×10^{-11} mol l^{-1}, which indicates that at these levels the influence of other components, such as sodium and potassium ions, becomes important. Under such conditions, positive ions in the glass membrane are not only exchanged with H^+ but also with Na^+ and K^+. The latter ions also contribute to E_2, giving rise to an

incorrect calculation of the pH. Over the past 10 years, this problem has been drastically reduced and circumvented by using glass membranes of special composition. An example is the membrane with high Li^+ content. In this case, Li^+ is exchanged with H^+ but not with K^+ and Na^+, because the latter ions are too big to fit in the small holes left by Li^+ in the membrane.

In addition, other sources of errors can occur owing to imperfections in the glass-membrane construction or due to limitations related to the reference electrodes and the diaphragm. Temperature also plays an important role in pH measurement. However, for these sources of errors reference is made to the literature for more detailed information[15].

The influence of temperature on the glass electrodes used in this work is explained below. On the basis of the inclination RT/z_iF, and the knowledge of k, the pH of unknown solutions can be determined starting from the measured potential. In practice, these parameters are obtained via calibration of the glass electrode on the basis of two or more buffer solutions. However, since both the inclination and factor k are functions of temperature, and the activity of the protons in the buffer also changes with a varying temperature (chemical equilibrium), the measurement of the pH of unknown solutions is, in principle, only correct with the calibration temperature. Hence, it would be necessary for measuring the pH with different temperatures to recalibrate the glass electrode with every change in temperature. An alternative is to derive an empirical relation which takes into account the occurring changes. Manufacturers of glass electrodes often offer an equation with the glass electrode which can be used in this relation. An example of such a relation is given in Equation 3.5, which applies for the Schott glass electrode used in this research and which is based on calibration of the electrode at 298.0 K:

$$pH_T = \frac{298 pH_m + 7(T_m - 273) - 175}{T_m} \qquad [3.5]$$

in which pH_T represents the corrected pH; in fact this is the pH at 298.0 K and pH_m is the pH measured with a temperature T_m, which is different from the calibration temperature of 298.0 K. So this pH_m is not correct because, on the one hand, it was calculated on the basis of an incorrect inclination; (namely the one valid with 298.0 K) and, on the other hand, because of the temperature dependency of the pH on the calibration buffers. Equation 3.5 corrects both effects. In order to verify the correctness of this equation, the pH_m of unknown solutions was measured, and from this the pH_T was calculated, and, simultaneously, the pH_m of the same solution was measured after the glass electrode was calibrated with the temperature T_m. This means that for the latter no temperature correction is needed or that $pH_m = pH_T$. From this, it appeared that Equation 3.5 is valid in the temperature area T_m ±10 K. Deviations between the pH values obtained via the above-

mentioned methods are smaller than 0.5%. Outside this area, this deviation quickly increases, presumably because of effects (such as asymmetry potentials in the glass membrane) which were not taken into account in Equation 3.5.

Finally, it should be mentioned that the impedance of a glass membrane is reasonably high. Therefore the impedance of the measuring device (potentiometer) should be higher[16], as otherwise the applied electrical current will also flow through the potentiometer and result in error signals. A typical potentiometer used for ion-selective electrodes has impedance of about $1\times10^{12}\,\Omega$, which is sufficient for pH measurement with glass electrodes.

3.4 Simultaneous cellulose removal and bleaching with enzymes

3.4.1 Introduction

During spinning and weaving of textiles (cotton, wool, bast fibres, etc.) breakdown of the textile yarn is frequently observed[17]. This has an influence not only on the quality of the textile product but also on the production cost, since the machines have to be stopped every time that the yarn is broken. To avoid or reduce the incidence of these harmful consequences, the textile yarn is strengthened with a layer of cellulose. Less than 5% of the breakages that occur with an untreated yarn still occur when the yarn is treated with cellulose.

The quality of the subsequent wet processes like bleaching, caustification, mercerisation and dyeing[18–21] is strongly dependent on affinity, reactivity and time of the interaction between the textile and the used chemicals. Therefore, the cellulose layer must be removed from the textile before applying the wet treatments to the textile product. This can be achieved by using sodium persulphate, which oxidises the cellulose, or by enzymes called cellulases, which are able to transform the cellulose into glucose. New approaches in the textile industry have been developed not only to transform cellulose into glucose, but also to use this glucose for the *in situ* formation of hydrogen peroxide with the aid of glucose oxidases by the following reaction:

$$\text{glucose} + 2H_2O + O_2 \xrightarrow[\text{oxidase}]{\text{glucose}} \text{gluconic acid} + H_2O_2 \qquad [3.6]$$

The hydrogen peroxide formed *in situ* can be used for bleaching[22] of the textile fabric (wool, cotton), and its concentration is an important parameter concerning the quality of the bleached product. Cotton is mostly

bleached in strongly alkaline medium in which oxidative products, such as sodium persulphate, potassium persulphate or ammonium persulphate, are used to remove cellulose from the fabric. However, wool is bleached in an acidic or slightly alkaline environment[21] by the use of hydrogen peroxide, which acts only as oxidising agent for acetic acid anhydride, the reaction product that possesses the necessary bleaching properties[22]. The hydrogen peroxide formed in Equation 3.6 can oxidise the acetic acid anhydride to reaction products that bleach the cellulose-free textile. The main problems to be solved in order to allow industrial use of the method are related to the concentration of hydrogen peroxide obtained from the oxidation process, the optimal pH and temperature for enzyme activity and the method used for measuring the process parameters and controlling them at optimal values for the best quality of cellulose-free and bleached product.

Dyeing on a cellulose layer is totally different to dyeing directly on the textile, because the structure of the textile is different from the structure of cellulose. Depending on the type of dye used, there is either a chemical, an electrochemical[18], an ionic[18], an electrostatic[19] or an adsorptive[20] interaction with the textile structure. It is clear that this interaction would be totally different if the dye were to be used directly on the cellulose layer. The interaction could be weaker, or even zero, or could be based on a different mechanism.

In this chapter, a method is described to remove simultaneously cellulose and bleach fibre products in the same bath with an acidic medium. An account is also given of a sensor system for measuring and controlling the hydrogen peroxide concentration. For the first purpose, enzymes are used that catalyse the oxidation of the cellulose-structure. In this cellulose-removal process oxygen, dissolved in the process liquid, is consumed and hydrogen peroxide is formed (Equation 3.7):

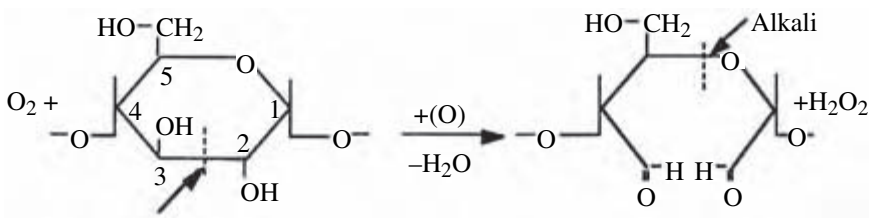

[3.7]

As can be seen from Equation 3.7, a strongly alkaline medium initiates a break of the bonding between the oxygen and the fifth carbon atom of the ring structure. The opening of this structure gives the cellulose the opportunity to react chemically with the wool structure and results in its fixation to the wool structure. This is a second reason why wool is not bleached and/or treated to remove cellulose in strongly alkaline solutions.

As shown in Equation 3.7, oxygen is consumed in the enzymatic process. In order to control the latter, it would be interesting to utilise a sensor able to measure both dissolved oxygen and hydrogen peroxide concentrations. The development of such a sensor is the subject of the present study. In addition, this sensor could indirectly give information on the enzymatic activity in the reactor solution, which in turn is dependent on pH, temperature and solution composition. Of course, the concentration of glucose can also be monitored, e.g. with the aid of a biosensor[23–30]. As glucose is only an intermediate in the coupled cellulose removal and bleaching processes, this approach seemed less useful and was not followed.

3.4.2 Sensor system for simultaneous oxygen and hydrogen peroxide detection

In Fig. 3.6, current–potential curves are shown recorded in a buffer solution (pH = 5.2 curve 1) and in the presence of hydrogen peroxide (curves 2–5) at room temperature on a glassy-carbon disc electrode, which was rotated at 1000 rpm. Two reduction waves can be observed, with a limiting-current plateau at around –0.5 V vs. Ag|AgCl, and a second one at around –1 V vs.

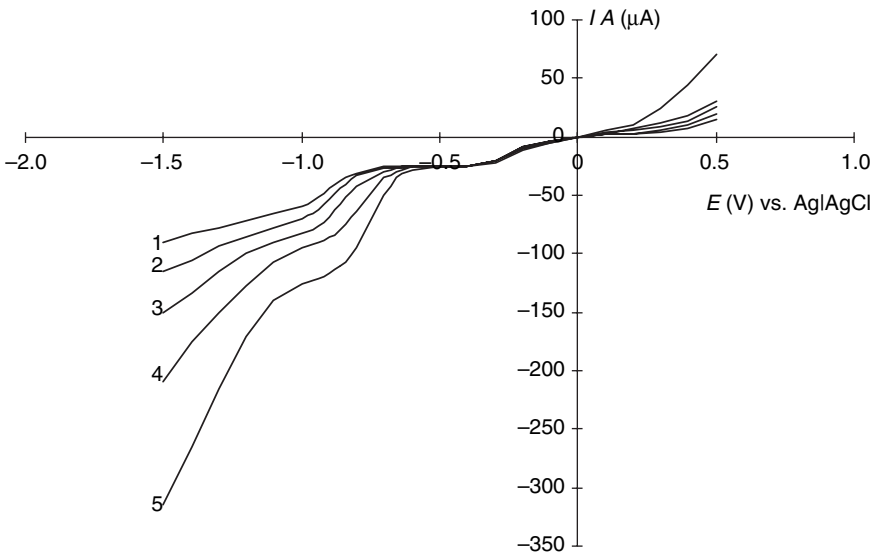

3.6 Current–potential curves of the reduction of oxygen in the absence (1) and presence of 0.008 (2), 0.022 (3), 0.037 (4) and 0.058 (5) mol l^{-1} hydrogen peroxide at a glassy-carbon rotating-disc electrode at pH = 5.2, T = 303 K and a rotation rate of 1000 rpm. (From Sensor system for simultaneous measurement of oxygen and hydrogen peroxide concentration during glucose oxidase activity in *Electroanalysis Journal*, 1999. Reprinted by permission of Wiley-VCH)

Ag|AgCl. Both waves can be attributed to the reduction of oxygen to water (Equation 3.8), which occurs in two steps. The fact that the second wave increases with hydrogen peroxide concentration reveals that this wave is associated with the reduction of hydrogen peroxide according to Equation 3.9. This also indicates that the intermediate product formed in the first step of the oxygen reduction (at 0.5 V vs. Ag|AgCl), which is also the reaction product of the first wave in the oxygen reduction, is hydrogen peroxide. Therefore Equation 3.10 shows the reaction corresponding to the first reduction wave:

$$O_2 + 4H^+ + 4e^- \leftrightarrows 2H_2O \quad [3.8]$$

$$H_2O_2 + 2H^+ + 2e^- \leftrightarrows 2H_2O \quad [3.9]$$

$$O_2 + 2H^+ + 2e^- \leftrightarrows H_2O_2 \quad [3.10]$$

The two limiting-current plateaus formed at –0.5 and –1 V vs. Ag|AgCl can be used for analytical purposes to detect hydrogen peroxide and oxygen simultaneously. The limiting-current corresponding to the plateau at –1 V vs. Ag|AgCl (given by the Levich equation [Chapter 1, Equation 1.15]) is the sum of the limiting-currents of the reduction of oxygen (Equation 3.8) and the reduction of hydrogen peroxide (Equation 3.9)[30–32]. To separate the measured current signal at –1 V vs. Ag|AgCl into two individual signals corresponding to oxygen and hydrogen peroxide, respectively, an independent measurement of the oxygen signal is needed. This can be obtained in two ways. The first possibility involves the measurement of the current at a potential of E=0.5 V vs. Ag|AgCl (see Fig. 3.6).This corresponds to the limiting-current of the wave of the reduction reaction of dissolved oxygen to hydrogen peroxide[32–33] (uptake of two electrons for each molecule of oxygen, Equation 3.10).

In practice, a repetitive double potential-step chronoamperometric method will be used. Potentials of –1 and –0.5 V vs. Ag|AgCl were applied alternately, for 300 ms. During each potential step, the currents (I_1 at –0.5 V and I_2 at –1 V, see Fig. 3.6) were measured 200 ms after the application of the step. This delay was used to ensure that the steady-state surface concentration of hydrogen peroxide at E=–0.5 V vs. Ag|AgCl is established at the time that the current is measured at E=–1 V vs. Ag|AgCl and that the concentration gradient of hydrogen peroxide established at –1 V vs. Ag|AgCl has vanished at the next measurement at –0.5 V vs. Ag|AgCl. Typically, this takes some 200 ms. The current corresponding to the hydrogen peroxide reduction reaction (I_3) can be calculated by Equation 3.11:

$$I_3 = I_2 - 2I_1 \quad [3.11]$$

where I_1 is the limiting-current of the plateau at –0.5 V vs. Ag|AgCl. This current is counted twice, because I_1 corresponds to the reduction of oxygen to hydrogen peroxide with the exchange of two electrons. However, the same oxygen reduction also contributes to the second plateau, but in this case it is the reduction to water with exchange of four electrons. Therefore, the contribution of I_1 to the current I_2 has to be counted twice. I_2 is the limiting-current at –1 V vs. Ag|AgCl, corresponding to the sum of the reduction reactions of oxygen (Equation 3.8) and hydrogen peroxide (Equation 3.9).

To link I_2 to the hydrogen peroxide concentration, first a calibration curve was obtained by measuring I_2 in a series of solutions with known hydrogen peroxide concentrations and in the absence of dissolved oxygen (Fig. 3.7). From this curve, it is possible to obtain the hydrogen peroxide concentration by measuring the experimental limiting-current, I_2, compensate it for I_1 and calculate the hydrogen peroxide concentration using Equation 3.12:

$$c_{hp} = kI_3 \qquad [3.12]$$

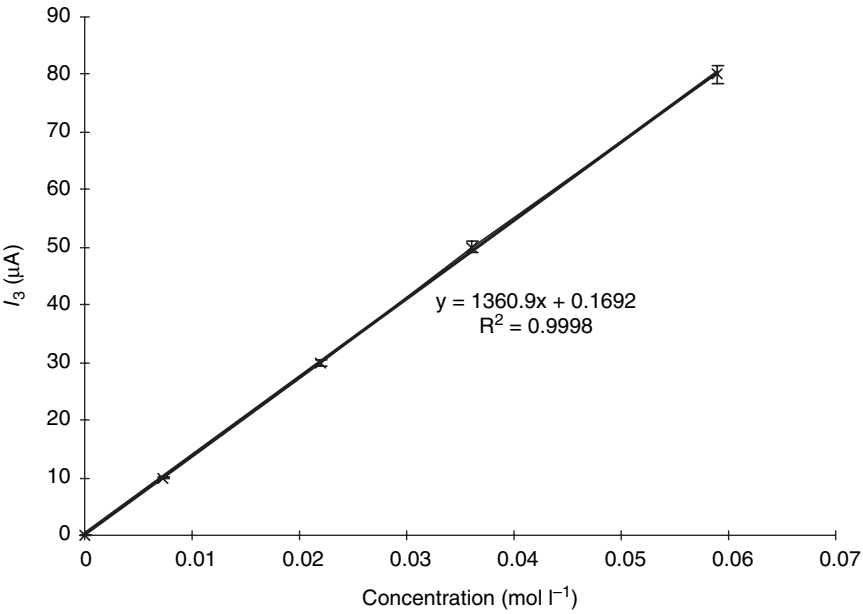

3.7 Calibration plot of the reduction of hydrogen peroxide at a glassy-carbon rotating-disc electrode in the absence of dissolved oxygen. pH = 5.2, T = 303 K, E = –1 V vs. Ag|AgCl and N = 1000 rpm. (From Sensor system for simultaneous measurement of oxygen and hydrogen peroxide concentration during glucose oxidase activity in *Electroanalysis Journal*, 1999. Reprinted by permission of Wiley-VCH)

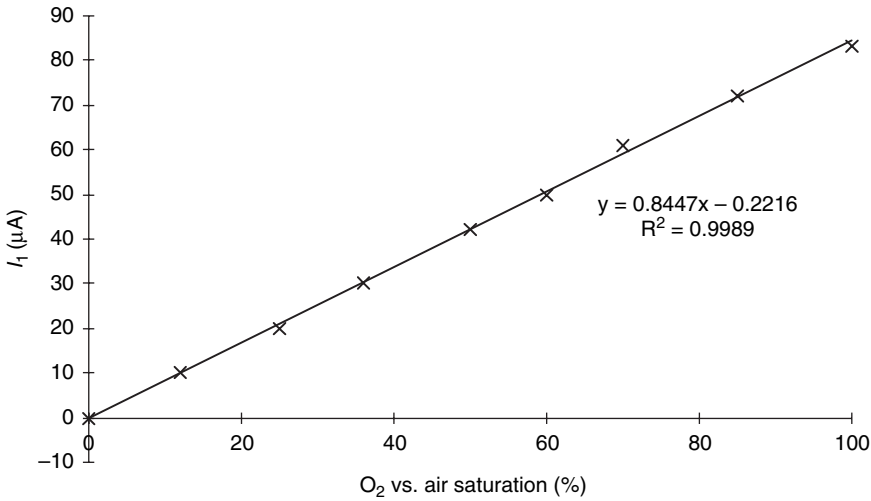

3.8 Calibration plot of the reduction of oxygen at a glassy-carbon rotating-disc electrode in the absence of hydrogen peroxide. pH = 5.2, T = 303 K, E = –1 V vs. Ag|AgCl and N = 1000 rpm. Oxygen was measured with Clark electrode. (From Sensor system for simultaneous measurement of oxygen and hydrogen peroxide concentration during glucose oxidase activity in *Electroanalysis Journal*, 1999. Reprinted by permission of Wiley-VCH)

As with hydrogen peroxide, a calibration curve for oxygen can be obtained based on I_1 and the known oxygen concentration in absence of hydrogen peroxide. This plot is shown in Fig. 3.8.

A second method of obtaining the hydrogen peroxide and oxygen signals separately is to measure the current signal at the glassy-carbon electrode at E = –1 V vs. Ag|AgCl, and to correct this signal for the influence of dissolved oxygen by measuring its concentration with a Clark sensor. For this purpose, the signal of the Clark electrode has to be linked to the current signal for oxygen of the glassy-carbon electrode. Primarily, the output of the Clark sensor is a current, but common commercial measuring devices often express results as oxygen, in percent, versus a calibration standard. The relationship between the output signals of the Clark cell and the glassy-carbon electrode can easily be established by performing measurements with both techniques in the same solution containing equal concentrations of dissolved oxygen. For this purpose, the calibration plot shown in Fig. 3.8 is also used.

The disadvantage of using a Clark cell is that it needs a larger instrument, because of the additional electrode and measuring device that are necessary, but it has the advantage of high selectivity. Another advantage is that the reduction of oxygen occurring in two steps at the glassy-carbon electrode is an important condition for this method, but such a two-step reduc-

tion of oxygen is not often observed. This reduction reaction occurs in two steps only at a few materials, such as mercury and glassy carbon. An additional reason for using a Clark electrode is that many electrode materials (platinum, palladium, gold, silver, copper, etc.) are catalysts for the decomposition of hydrogen peroxide into oxygen (Equation 3.13). This means that the current measured for the reduction of dissolved oxygen, which is proportional to the concentration of oxygen in the neighbourhood of the electrode surface, is not representative of the oxygen concentration in the bulk of the solution when hydrogen peroxide is present. In the latter case, the oxygen concentration in the vicinity of the electrode will be higher compared with the bulk concentration owing to decomposition of hydrogen peroxide at this electrode surface (Equation 3.13):

$$2H_2O_2 \leftrightarrows O_2 + 2H_2O \qquad [3.13]$$

Both proposed methods of separating I_2 into I_1 and I_3 were used to follow the concentration of hydrogen peroxide and dissolved oxygen, and thus indirectly the enzyme activity, in a solution of glucose contained in a semi-industrial setup (flow-through pipeline configuration). The enzyme used was glucose oxidase from *Aspergillus niger* with low catalase activity (catalase destroys hydrogen peroxide). pH and temperature of the solution were measured continuously. The results are shown in Fig. 3.9. At a pH value of 5.2 and a temperature, T, of 298.0 K (section 1 of the curves in Fig. 3.9), the concentration of dissolved oxygen is zero, which limits the hydrogen peroxide concentration to approximately 0.05 mol l^{-1}. The formation rate of hydrogen peroxide is controlled by the rate at which oxygen is taken up from the air. Indeed, in an additional experiment (results not shown here), it was possible to obtain higher hydrogen peroxide concentrations when convection through the solution was forced and when oxygen was purged in the solution.

When the pH value is increased to 10.5 by addition of caustic soda, a substantial oxygen reduction current is measured, and the concentration of hydrogen peroxide drops to ca. 0.01 mol l^{-1}, apparently controlled by the lowered enzyme activity at this pH (section 2 of both curves in Fig. 3.9). When again at a pH of 10.5, but with the temperature raised to 310 K, the oxygen current is that of a nearly saturated solution, while the concentration of hydrogen peroxide becomes low (section 3 of both curves in Fig. 3.9). It might be clear that the enzyme activity under these conditions is very low, explaining the fact that no hydrogen peroxide is formed and that the oxygen concentration returns to its initial value because it is not consumed at these conditions of pH and temperature.

The proposed method can be used in textile processes given below:

- Bleaching processes with relatively low hydrogen peroxide concentration (up to 5 g l^{-1}).

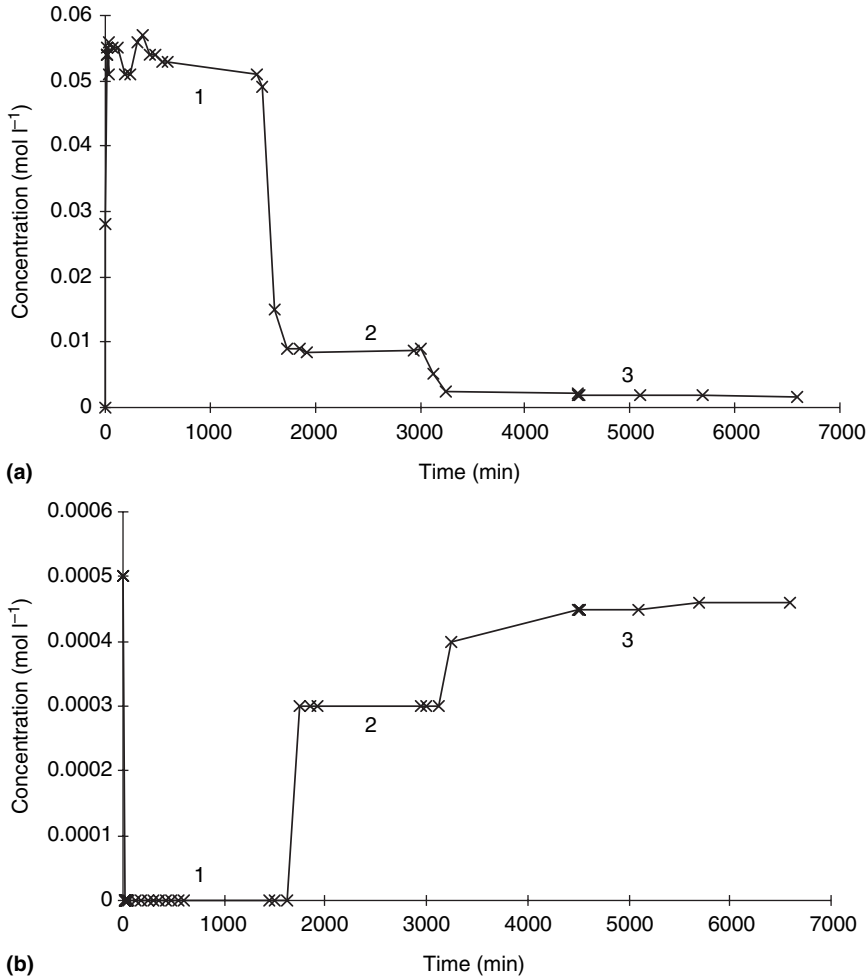

3.9 Variation of the hydrogen peroxide concentration (a) and oxygen concentration (b) as a function of time in a solution containing an excess of glucose and 0.2 g l^{-1} of *Aspergillus niger* at a (1) pH=5.2 and T=298 K, (2) pH=10.5 and T=298 K and (3) pH=10.5 and T=310 K. (From Sensor system for simultaneous measurement of oxygen and hydrogen peroxide concentration during glucose oxidase activity in *Electroanalysis Journal,* 1999. Reprinted by permission of Wiley-VCH)

- Simultaneous removal of cellulose and bleaching. The cellulose-removal process is a source of cellulose, removed from the fabric, which is transformed by cellulose while producing hydrogen peroxide from dissolved oxygen. The hydrogen peroxide formed can be used for bleaching. However, cellulose removal must be executed as otherwise the hydrogen peroxide cannot attack the fabric for bleaching.

- Washing processes involving enzymes that attack specific impurities in the fabric and simultaneously produce small amounts of hydrogen peroxide up to concentrations of about $1\,g\,l^{-1}$. Such concentrations are not high enough for bleaching, but have disinfecting properties.

As an example of these possible applications, a semi-industrial test was performed, simulating a washing process with the involvement of enzymes that produce hydrogen peroxide *in situ* by reduction of dissolved oxygen. The experiment was performed at room temperature in a tank through which cotton fabric was pulled. The tank was filled with an aqueous solution containing 1% of enzyme at near-neutral pH (pH of about 7). The convection obtained in the solution owing to the movement of the cotton fabric allowed the establishment of a steady state in the uptake rate of dissolved oxygen, and a sensor determined this uptake rate. The result is shown in Fig. 3.10, curve 1. Initially, the concentration of hydrogen peroxide increases as a function of time over a period of about 2 min because a large amount of oxygen is present in solution. After these 2 min, the oxygen uptake starts to determine the overall rate of hydrogen peroxide formation, and at the same time hydrogen peroxide is consumed in the disinfection reaction. It can be seen that after about 3 min a steady state is obtained, which means that,

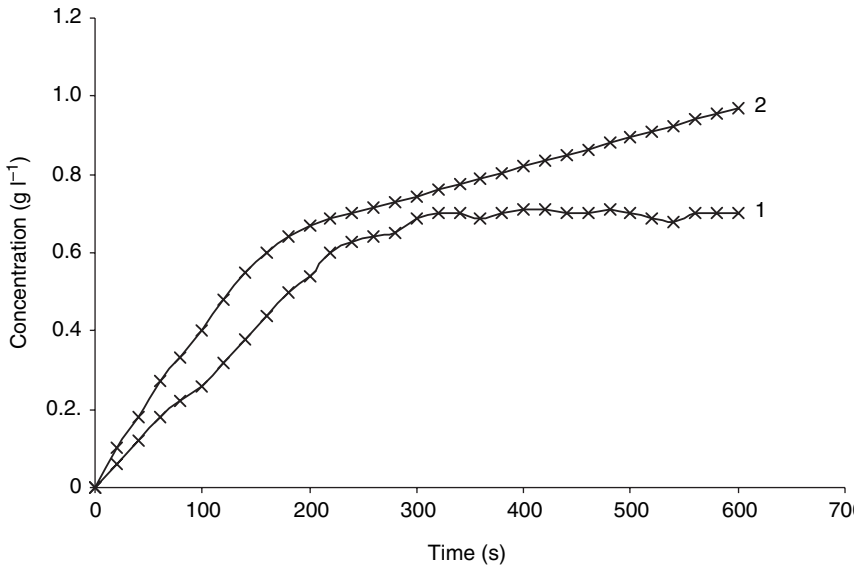

3.10 Variation of hydrogen peroxide concentration during a disinfection process in a semi-industrial setup at $T = 298.0\,K$ and pH = 7 using (1) cotton fabric and (2) prior-disinfected cotton fabric. (From Sensor system for simultaneous measurement of oxygen and hydrogen peroxide concentration during glucose oxidase activity in *Electroanalysis Journal,* 1999. Reprinted by permission of Wiley-VCH)

from that moment, the rate of formation of hydrogen peroxide (by enzymatic reduction of oxygen taken up from the air) is equal to the rate of consumption (in the disinfection reaction).

In order to ascertain the amount of hydrogen peroxide that was consumed in the disinfection reaction, the experiment was repeated with prior-disinfected cotton fabric. In this case, the hydrogen peroxide consumption should be very low because the disinfection reaction has already been completed. This is shown in Fig. 3.10, curve 2. In this case, a linearly increasing curve is obtained, indeed because the hydrogen peroxide concentration increases owing to enzymatic transformation of oxygen. From the slope, it can be seen that the hydrogen peroxide concentration increases with a value of $7.1 \times 10^{-4}\,g\,l^{-1}\,s^{-1}$. The experiment shows very clearly that hydrogen peroxide can be determined continuously, and that it is possible to obtain industrially interesting concentrations by using enzymes for *in situ* production of hydrogen peroxide. The key parameters in these processes are pH and temperature to control the activity of the enzymes. The temperature must not be too low, as otherwise insufficient hydrogen peroxide is produced, but also it must not be too high, in order to avoid de-naturation of the enzyme catalyst.

3.5 References

1. Sawyer D.T., Sobkowiak A., Roberts J.L., *Electrochemistry for Chemists*, Wiley, New York, 1995.
2. Frant M.S., Ross J.W., *Science*, **154** (1966) 1553.
3. Lundgrun D., Woermann D., *Z. Phys. Chem.*, **207** (1998) 245.
4. De Strycker J., Westbroek P., Temmerman E., *J. Electroanal. Chem.*, **565** (2004) 149.
5. De Strycker J., Westbroek P., Temmerman E., *Glass Sci. Technol.*, **75** (2002) 175.
6. De Strycker J., Westbroek P., Temmerman E., *Elec. Commun.*, **4** (2002) 41.
7. De Strycker J., Westbroek P., Temmerman E., *J. Non-Cryst. Solids*, **289** (2001) 106.
8. De Strycker J., Gerlach S., Von Der Gonna G., Russel C., *J. Non-Cryst. Solids*, **272** (2000) 131.
9. Smith P.J.S., Hammar K., Porterfield D.M., Sanger R.H., Trimarchi J.R., *Microsc. Res. Techn.*, **46** (1999) 398.
10. Qin Y., Bakker E., *Talanta*, **58** (2002) 909.
11. Simonian A.L., Grimsley J.K., Flounders A.W., Schoeniger J.S., Cheng T., De Frank J.J., Wild J.R., *Anal. Chim. Acta*, **442** (2001) 15.
12. Schollmeyer E, Knittel D., Hemmer E.A., *Betriebsmesstechnik in der Textilerzeugung und-veredlung*, Springer-Verlag, Heidelberg, 1988.
13. Morf W.E., *Electroanal*, **7** (1995) 852.
14. Evans A., *Potentiometry and Ion-Selective Electrodes*, Wiley, Chichester, 1987.
15. Covington A.K., *Ion-Selective Electrode Methodology 1*, CRC Press, Boca Raton, 1979.

16. Covington A.K., *Ion-Selective Electrode Methodology 2*, CRC Press, Boca Raton, 1979.
17. Kong L.X., Flatfoot R.A., Wang X., *Text. Res. J.*, ***66*** (1996) 30.
18. Yoshida M., *Progress in Organic Coatings*, **31** (1997) 63.
19. Condamone M., Bao G.P., Marmer W.N., Dudley R.L., Bulanbrady J., *Textile Chemist and Colorist*, **28** (1996) 19.
20. Akrman J., Prikryl J., *J. Appl. Polymer Sci.*, **62** (1996) 235.
21. Cleve E., Bach E., Deneter U., Duffner H., Schollmeyer E., *Text. Res. J.*, **67** (1997) 701.
22. Cori Y., David S.K., *Text. Res. J.*, **67** (1997) 459.
23. Ekinci E., Karagozler A.A., Karagozler A.E., *Electroanalysis*, **8** (1996) 571.
24. Chut S.L., Li J., Tan S.N., *Anal. Lett.*, **30** (1997) 1993.
25. Liu H.Y., Ying T.L., Sun K., Li H.H., Qi D.Y., *Anal. Chim. Acta*, **344** (1997) 187.
26. Li J., Tan S.N., Ge H.L., *Anal. Chim. Acta*, **335** (1996) 137.
27. Ruan C.M., Yang R., Chen X.H., Deng J.Q., *J. Electroanal. Chem.*, **455** (1998) 121.
28. Xu J.J., Zhou D.M., Chen H.Y., *Electroanalysis*, **10** (1998) 713.
29. Garcia M.A.V., Blanco P.T., Ivaska A., *Electrochim. Acta*, **43** (1998) 3533.
30. Diaz A.N., Peinado M.C.R., Minquez M.C.T., *Anal. Chim. Acta*, **363** (1998) 221.
31. Jacq J., Bloch O., *Electrochim. Acta*, **9** (1964) 551.
32. Brezina M., *Ber. Bunssen-gesellschaft*, **77** (1973) 849.
33. Westbroek P., Temmerman E., Kiekens P., *Anal. Comm.*, **35** (1998) 21.

4

Electrochemical behaviour of hydrogen peroxide oxidation: kinetics and mechanisms

P. WESTBROEK AND P. KIEKENS

4.1 Introduction

Hydrogen peroxide is used in a large number of applications such as bleaching, disinfecting and oxidation processes. It is such an attractive oxidising chemical because its reaction products are oxygen and water. For this reason, its valuable oxidising properties are also advantageous from an environmental point of view. Consequently, there has been an increase in the industrial use of hydrogen peroxide over the past 15 years. In the textile industry, hydrogen peroxide is used in the bleaching of cotton, linen, polyester and polyurethane fibres. Cellulose, in the wood and paper industry, is another example of bleaching with hydrogen peroxide.

In the chemical industry, hydrogen peroxide is used in the production of peroxide substances, such as sodium perborate, sodium percarbonate and percarboxylic acid[1]. In the field of organic chemistry, hydrogen peroxide is used in epoxidation reactions, oxidation reactions and as initiator of polymerisation reactions[2–5]. Finally, hydrogen peroxide is also used as a cleaning and etching chemical and, in ultra-pure form (which is a very explosive form) in the production of semi-conductor chips. The use of hydrogen peroxide in environmental applications has grown tremendously, particularly in waste-water purification[6–7] and in the purification of cyanide-containing waste-water from galvanisation lines[8–9]. In relatively small concentrations, it can also be used as a disinfecting chemical in swimming pools. Finally, hydrogen peroxide is also used for bleaching human hair.

Owing to the textile-related topics which are covered in this book, this chapter is devoted to a description of a sensor which has been developed to measure and control high hydrogen peroxide concentrations in bleaching processes, and its extension with a flow-injection system to adopt it for use in disinfecting processes.

4.2 Use of hydrogen peroxide in textile-bleaching processes

4.2.1 Hydrogen peroxide and sodium hydroxide

As mentioned earlier, the importance of hydrogen peroxide as a bleaching agent[10] in the textile industry has increased significantly in recent years due to the environmentally friendly reaction products – oxygen and water. These are in strong contrast to the harmful or environmentally damaging chlorine compounds that are released during bleaching processes based on chlorite or hypochlorite[11].

Hydrogen peroxide in itself has weak bleaching properties[12] as opposed to its conjugated base, HO_2^-. Since hydrogen peroxide belongs to the category of weak acids, a highly alkaline medium will be necessary to obtain significant concentrations of HO_2^- in solution (Equations 4.1 and 4.2). Hence, in practice, bleaching processes on the basis of hydrogen peroxide are performed at a pH of 12–12.5. In order to establish this pH, sodium hydroxide is used[13].

$$H_2O_2 \leftrightarrows HO_2^- + H^+ \qquad [4.1]$$

$$\log \frac{[HO_2^-]}{[H_2O_2]} = -11.63 + \text{pH} \qquad [4.2]$$

Specific research, including with radical scavengers, showed that it is not the HO_2^- particle that participates in the bleaching reaction, but a radical oxygen anion O_2^-[14]. It is presumed that this particle is formed from HO_2^- which, owing to the localised charge on the terminal oxygen, is unstable and further decomposes:

$$HO_2^- \leftrightarrows O_2^{\bullet -} + \text{reaction products} \qquad [4.3]$$

The mechanism of this reaction is still not completely understood. The radical dioxygen anion, which is formed in the process, finally reacts with the chromophore groups of the material that is to be bleached. According to the pH of the solution and the potential, E^0, of the system to which the chromophore group belongs, it will be oxidised (the hydrogen peroxide anion being reduced to water) or, rather seldom, it will be reduced (the hydrogen peroxide anion being oxidised to oxygen). Owing to the absorption or release of electrons, the absorption wavelength of the chromophore groups will move outside the visual range of wavelengths, causing them to lose the colour of the treated fabric. However, the radical dioxygen anion has little selectivity in relation to the chromophore groups, and, when extensively present, it can also affect the textile structure itself. This effect should be avoided, since it will weaken the structure of the fabric[15], which can lead

to tears and holes during after-treatments (for example dyeing, mercerising, thermofixation).

Apart from the basic products, hydrogen peroxide and sodium hydroxide, an industrial bleaching bath contains many additives, the most important of which are discussed below. From an analytical point of view, it is evident that, for the development of a sensor for hydrogen peroxide, each of the additives used must be investigated to determine whether and to what extent they can interfere.

4.2.2 Stabilisation of hydrogen peroxide

Already at a pH of 11, the balance of Equation 4.1 is situated too far to the right because too much of the radical dioxygen anion is formed[12]. Besides activation (with sodium hydroxide), hydrogen peroxide should also be stabilised by shifting the balance of Equation 4.3 more to the left. This means that HO_2^- should be made more stable, which can be achieved by spreading the strongly localised charge present at the terminal oxygen atom. This can be realised by inserting a cation in solution with a high charge density. This ion will tend to associate with HO_2^- since it is relatively unstable itself. An ion that qualifies for this task is Mg(II), which is brought into the bleaching solution in the form of magnesium sulphate[16]. Even though it is correct that such ions are stabilised by solvation (with water), formation of complexes with HO_2^- creates even more stable configurations[12].

In a strongly alkaline solution, magnesium ions will immediately precipitate. Therefore, they are first dissolved in an aqueous solution of waterglass. Waterglass is a sodium silicate, having the six-chain structure as its main component. The magnesium ions are bound to the waterglass on the terminal $–O^-–$ groups. In fact, an exchange reaction between the sodium ions and the magnesium ions occurs, resulting in improved stabilisation of sodium ions in solution by hydration, so that Mg(II) is able to replace Na(I) in the waterglass structure. The magnesium ions are now bound to the waterglass in such a way that, when they are dissolved in the alkaline bleaching solution, they will not precipitate; however, they will still be able to stabilise HO_2^- (Fig. 4.1).

Waterglass also has a second advantageous property – the stabilisation of hydrogen peroxide[16]. It masks metal ions and their oxides and hydroxides (such as those from iron, copper and manganese). The latter compounds can strongly catalyse the decomposition of hydrogen peroxide to water and oxygen. During this decomposition, the radical dioxygen anion is formed as an intermediate, and hence it can occur in a highly increased concentration in the presence of metal ions, metal oxides and metal hydroxides. Cotton that is to be bleached always contains small amounts of metal ions, the quantity being dependent on the place of origin and the climato-

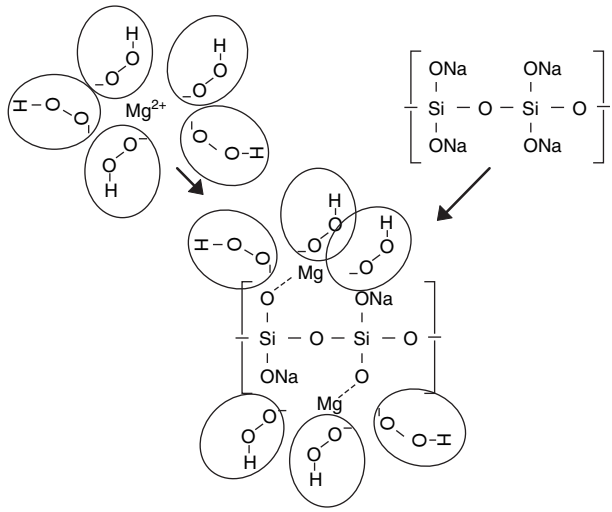

4.1 Schematic representation of the role of waterglass to keep magnesium ions in solution and of the stabilisation of hydrogen peroxide by magnesium ions.

logical circumstances. Owing to the bleaching process, metal ions diffuse into solution, which can lead to a relatively higher concentration of the radical anion, O_2^-, at the textile fabric–solution interface, which can affect and damage its structure because of the low selectivity of O_2^-. This effect, known as catalytic damage[15], can cause attenuations in the textile structures and, in extreme cases, even visible holes. Waterglass is capable not only of complexing components with such catalytic properties, but because of this complexity, it can also make them inactive for catalytic reactions (called masking).

However, waterglass also has a considerable disadvantage. At high temperatures (>273 K) and/or in relatively high concentrations, it tends to dehydrate and form polymers. This precipitated product forms a hard and transparent deposit on the fabric and the machines, which is very difficult to remove. To avoid this, stabilisers are used based on the structure of EDTA. They have similar, but less powerful, stabilising properties as waterglass, except for the disadvantageous property of polymerisation. For this reason, these products cannot be a substitute for waterglass, but rather are used to supplement waterglass, enabling it to be used in lower concentrations, strongly reducing the risk of dehydration.

4.2.3 Composition of a bleaching solution

In practice, two types of bleaching process are used, namely the dry–wet and the wet–wet bleaching treatments. In this way, the condition of the

fabric is described when entering the bleaching bath, and when leaving the bath, respectively. Particularly with the dry–wet treatment, the surface energy barrier between fabric and bleaching solution is high, so that the humidification rate restricts the rate of the process. To avoid this, tensio-active substances are added to the bleaching solution, as these substances decrease the surface energy barrier[17–18]. This facilitates the penetration of hydrogen peroxide (over a smaller energy barrier) in the fabric and oxidises or reduces the chromophore groups. Adding tensio-active substances can even double the daily production. However, many tensio-active products have one considerable disadvantage: namely, the intense formation of foam due to turbulent streaming profiles present in a bleaching bath.

In order to control this disadvantageous effect, de-foamers and de-aeraters are added[19]. The defoamer's task is to control the foam formation due to the tensio-active substances, while the de-aerater removes gas bubbles, in solution and in the fibre structure. In this way, the contact surface between fabric and bleaching solution is kept maximal, which can only favour the rate of the process. By adding the de-aerater, lower quantities of tensio-active substances are needed, which helps to minimise foam formation.

Finally, sodium persulphate is added in order to weaken the fibre. Before the cotton is spun to a thread, this thread is reinforced with a layer of cellulose to reduce the incidence of failures during the spinning process. Obviously, the cellulose layer will have to be removed later, and this can be achieved either by means of enzymes in a process preceding the bleaching, or with sodium persulphate simultaneously with the bleaching process.

The various producers launching the above-mentioned additives onto the market use trade names that nearly always relate to mixtures of reagents, of which neither the identity nor the concentration is made public because of corporate propriety. A comparative analysis has shown that the various additives contain similar products; a minor modification to the structure common to all the stabilisers is the EDTA structure, although the terminal groups on the amine positions can be different[11].

4.3 Determination methods of hydrogen peroxide

The most commonly used technique for the determination of hydrogen peroxide in an industrial environment is the classical manual titration of a bath sample with potassium permanganate after acidification with sulphuric acid. In the past, numerous attempts have been made to perform the determination by means of an instrumental technique; however, disadvantages were always encountered, which, up to now, have hindered the breakthrough of an alternative method.

Originally, attempts were made to replace the manual titration[20] by an automatic titration unit where the equivalence point was no longer determined by visual colour changes but via a potential change at redox electrodes. The MnO_4^-/Mn^{2+} system, as well as the Ce^{4+}/Ce^{3+} system[21–23], was investigated as a titration reagent. The most serious drawbacks, which explain why this method is seldom applied in industry, are the relatively high investment costs for such an automatic system and the excessively long response times (of the order of minutes). Moreover, cerium (IV) is a rather expensive reagent. The arsenite system (AsO_2^-) was also investigated. However, this method was more used for bleaching processes on the basis of chlorite and hypochlorite.

Calorimetric, potentiometric[24] and conductometric[25] methods of determination appeared to be insufficiently precise and/or accurate. However, the sensitive spectrophotometric determination was discontinuous with relatively long response times (a few minutes). A continuously measuring variant of this method, based on the flow injection analysis (FIA) principle, did have a short response time (a few seconds, depending on the length of the delivery pipe), but a lower precision and stability, due to the frequent congestion of the small pipes through which the bath solution is pumped. Furthermore, the purchase of a spectrophotometric apparatus appeared to be relatively expensive. Research groups (in Germany[26–27] and the Netherlands[25]) have recently worked on methods to measure hydrogen peroxide in a continuous way.

4.4 Voltammetric behaviour

In the development of an amperometric sensor, voltammetric research is of utmost importance. In literature, much information can be found on the voltammetric behaviour of hydrogen peroxide with numerous electrode materials. This behaviour can be divided into two large groups, namely oxidation and reduction of hydrogen peroxide. The largest group of publications deals with the reduction on platinum[28–33], palladium[34], gold[35–37], silver[38–43], several carbon forms[35,39,44], iron[45–47], and others[48–51], and this in an acid as well as an alkaline medium. The fact that more attention is paid to the reduction reaction is partly due to the fact that hydrogen peroxide is formed as an intermediate product in the oxygen reduction[52–56]. The latter is one of the most studied electrode reactions, amongst others, because of the importance in corrosion and in research regarding batteries[57]. In this research, no attention was paid to the oxygen reduction itself. The oxidation reaction of hydrogen peroxide was studied to a more limited extent[58–60].

Since hydrogen peroxide can decompose faster under the influence of catalysts, this so-called catalyst decomposition was also studied by means of voltammetric methods applied to the oxidation and reduction reactions

of hydrogen peroxide with the catalyst as electrode material, to clarify the mechanism of this decomposition[61–68]. Finally, it can be mentioned that the reduction of hydrogen peroxide was also investigated with semiconductors[69–70]. In none of the above-mentioned publications was a study performed into the relatively high hydrogen peroxide concentrations that are used in bleaching baths.

4.5 Detection of high hydrogen peroxide concentrations with amperometric method

4.5.1 Preliminary research

In this part of the work, electrode configurations were searched that qualify to be submitted to a thorough further investigation with regard to the possibility to measure high concentrations of hydrogen peroxide in a continuous way. A necessary condition is that the electrode signal is independent of time. In this respect, the rotating-disc electrode is a suitable configuration because the limiting current is independent of time and well described by the equation of Levich (Chapter 1, Equation 1.15). This limiting current is proportional to the bulk concentration of the reacting component.

With numerous electrode materials (Pt, Pd, Ni, Sn, Rh, Ir, Cr, Cu, Au, Ag, Fe, vitreous carbon, graphite, Re, Ti and Zr), current–potential curves were registered for 8–10 different hydrogen peroxide concentrations in the full potential range, limited by the oxygen and hydrogen evolution reactions. With none of the examined materials did the transport-controlled oxidation or reduction current of hydrogen peroxide appear to qualify for further investigation. Certain materials have specific disadvantages, such as an unfavourable position of the wave, interference of reactions from the electrode material itself, an excessively high or excessively low limiting current plateau and strongly irreversible behaviour of hydrogen peroxide. Nevertheless, besides these disadvantages, which they all demonstrate, for the oxidation as well as the reduction wave of hydrogen peroxide, it was also found that the linearity between the limiting current and the hydrogen peroxide concentration was limited to approximately $15\times10^{-3}\,\mathrm{mol\,l^{-1}}$ (Fig. 4.2), whereas the concentrations used in bleaching processes can increase to $2\,\mathrm{mol\,l^{-1}}$.

This effect apparently could be ascribed to the occurrence of the so-called ohmic potential drop (IR-drop)[71] with concentrations higher than ca. $15\times10^{-3}\,\mathrm{mol\,l^{-1}}$. This ohmic potential drop is the product of the electrical resistance of the cell solution between working electrode and reference electrode and the electrical current, resulting in a high value of the last-mentioned parameter in a potential loss that cannot be neglected. Consequently, the effective potential of the working electrode compared

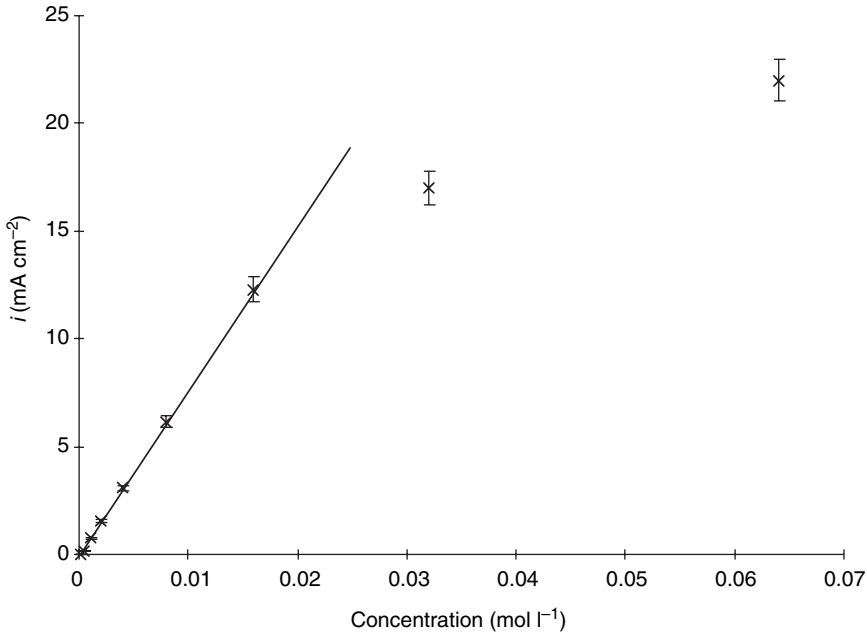

4.2 Nature of the relation between current density and hydrogen peroxide concentration observed for different rotating-disc electrode materials with a rotation speed of 16.67 rotations per second.

with the reference electrode is smaller than the potential applied by the potentiostat.

This ohmic potential drop can be reduced in two ways: either by lowering the cell resistance or by decreasing the measured electrical current. The resistivity or specific resistance cannot be modified in this research because it is set according to the composition of the bleaching solution. The absolute resistance can be diminished in principle by putting the working electrode and the reference electrode (using a so-called Luggin capillary tube) closer to each other. Applying this has led in practice to a slight improvement, yet totally insufficient to solve the problem.

The current signal, on the other hand, can be reduced drastically. A first, obvious, method is reducing the working electrode surface. A second possibility involves reducing the amount of reacting electroactive component which is transported to the electrode surface, e.g. by means of a membrane or a porous wall. When the working electrode, the reference electrode and the counter electrode are positioned at the same side of the membrane, the resistance of the solution between the electrodes is not influenced by the membrane, which is not the case when the electrodes are positioned at different sides of the membrane, and the influence on the IR voltage drop can

be positive or negative as the effect of the decrease in electrical current or the increase in resistance predominates.

A third possibility is based on the presence of small current densities due to high coverage of the electrode surface. Frequently, current–potential curves show multiple waves or peaks which cannot immediately be explained. These are due to more complicated reaction mechanisms where phenomena such as adsorption/desorption, homogeneous chemical reactions in solution and slow balances play a role. These phenomena can strongly depend on the environment and the electrode material. The literature, in this respect, often refers to pre (after)-waves or pre (after)-peaks, which can have a considerably lower current density than the normal transport-limited reaction. On condition of proportionality with the bulk concentration, these currents are useful for analytical purposes and give occasion to a lower ohmic voltage drop. With a glassy-carbon electrode, hydrogen peroxide shows two oxidation waves. The second wave is transport-controlled and, because of IR-drop or ohmic-drop effects, it is not suitable for the determination of the high hydrogen-peroxide concentrations in this research. In the literature, nothing was found on the prewave, probably because it is easily overlooked due to the relatively low current density. For this reason, the wave is noticed only with relatively high concentrations, whereas the majority of published papers deal with the lowering of detection limits and the measuring of very small concentrations.

On the basis of the results obtained in the preliminary research, three potentially useful electrode configurations were investigated further:

- ultramicro-electrodes having a diameter of the order of μm;
- electrodes modified with membranes;
- the rotating glassy-carbon electrode in consideration of a more profound research of the oxidation prewave.

Various experiments and procedures were performed to investigate the possibilities using ultramicro-electrodes and membranes to lower the IR-drop effects and to increase the linearity of the relationship between electrode signal and concentration to higher hydrogen peroxide concentrations. This led to limited success, inhibited by low accuracy and precision and poor long-term stability. The third option, based on glassy carbon, showed much better results and is described more in detail below and in the following sections of this chapter. Figure 4.3 shows the current–potential curves of hydrogen peroxide with a glassy-carbon electrode for different hydrogen peroxide concentrations.

It is possible to distinguish clearly two waves in the oxidative area. The second wave, occurring at a potential more positive than ca. 0.6 V vs. saturated calomel electrode (SCE), is of no use in attaining this aim, since the S-shaped character (and the related linear connection between the limiting

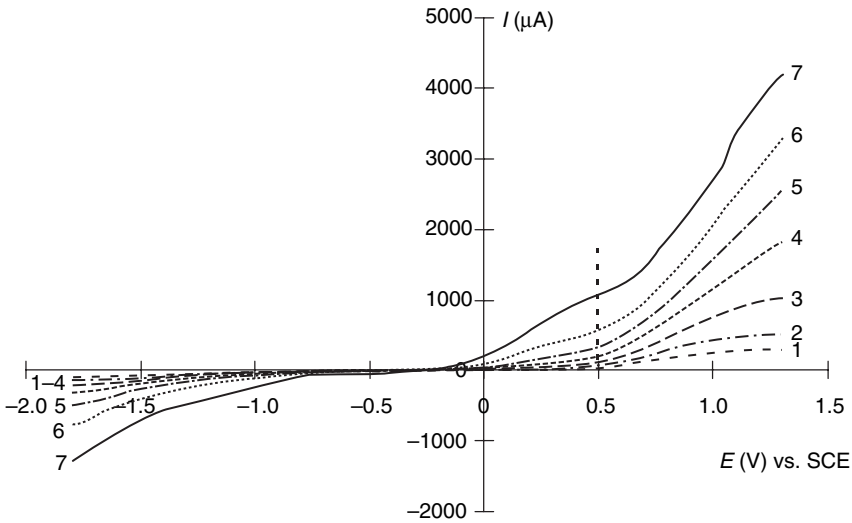

4.3 Current–potential curves of hydrogen peroxide with a glassy-carbon electrode at pH = 11.45 and $T = 298.0$ K. The concentrations equal (1) 0.012, (2) 0.025, (3) 0.05, (4) 0.1, (5) 0.2, (6) 0.4 and (7) 0.8 mol l^{-1}.

current and hydrogen peroxide concentration) disappears with higher concentrations owing to the IR-drop effects. This effect remains absent in the first wave, which occurs at ca. –0.2 V vs. SCE, and this wave is further called the 'prewave'. A remarkable characteristic of the prewave is that it does not represent a common limiting-current plateau, since the ideal transport-limited current, in the presence of sufficient indifferent electrolyte to keep transport by migration sufficiently low, shows small or no variations with the potential. At the most positive potentials in the prewave, the inclination of the current–potential curve is considerably smaller than for more negative potentials in the wave; however, the current still varies considerably with applied potential. By means of variation of the cell geometry, it could be determined that this was not due either to IR voltage drop or to migration, and this was verified by variation of the electrolyte concentration. The potential range in the prewave, where the inclination of the current–potential curve is the lowest, cannot be correlated with a classical limiting current, since it still notably increases with the potential. Discussion of this type of current will frequently return in the following section, and to avoid mix up with other currents, it is called the pseudo-limiting current, with symbol I_{Lp}. Figure 4.4 shows a calibration curve of the pseudo-limiting current measured at a potential of 0.45 V vs. SCE as a function of the hydrogen peroxide concentration.

In principle, the findings offer the possibility of determining hydrogen peroxide at sufficiently high concentrations. However, the presented

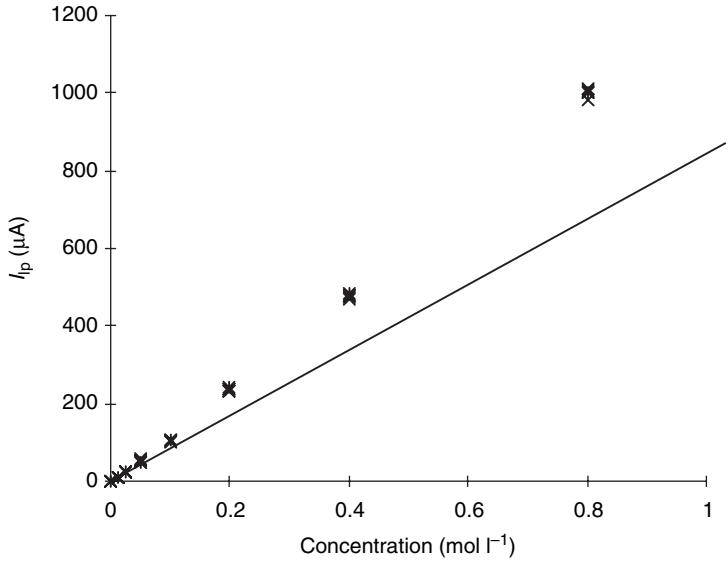

4.4 Calibration curve of the hydrogen peroxide oxidation with a glassy-carbon electrode at $E = 0.45$ V vs. SCE. pH = 11.45 and $T = 298.0$ K.

relation is not linear, and the deviation of the linear behaviour increases as the hydrogen peroxide concentration increases. Moreover, it was established that the voltammetric signal is strongly pH-dependent and that the relation between the current and the hydrogen peroxide concentration is also dependent on the pH. Although the possible causes for such behaviour are not obvious, the prewave in the anodic voltammetric curve of hydrogen peroxide with glassy carbon also offers perspectives to serve as a basis of a hydrogen peroxide sensor. Therefore, a detailed study was necessary, described in the next sections.

4.5.2 Electrode behaviour at high hydrogen peroxide concentrations

From the preliminary research described in the previous section, it appears that the small oxidation wave with half-value potential ($E_{1/2}$) of ca. 0.21 V vs. SCE offers favourable perspectives for the amperometric determination of relatively high hydrogen peroxide concentrations. In contrast to the second oxidation wave with $E_{1/2}$=0.76 V vs. SCE, the pseudo-limiting currents obtained in the prewave do not satisfy the relation of Levich (Chapter 1, Equation 1.15). However, they are almost completely independent of the rotation rate of the electrode, revealing that these limiting currents are not controlled by transport of electroactive species but by (an)other process(es). This is illustrated in Fig. 4.5.

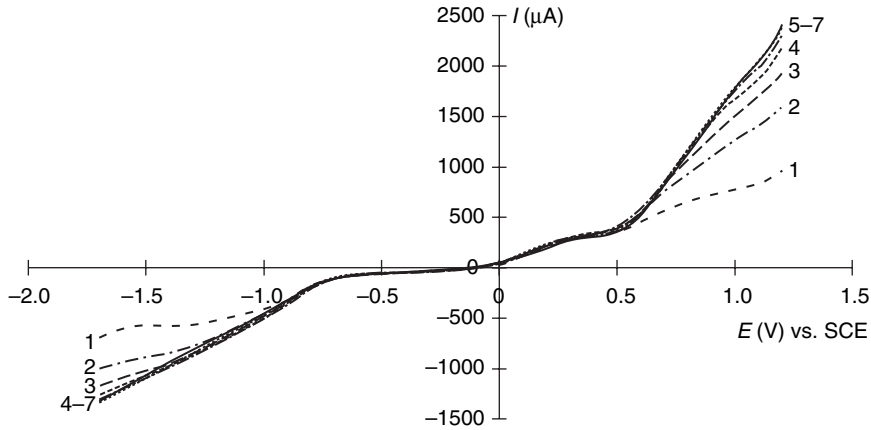

4.5 Current–potential curves of hydrogen peroxide with a glassy-carbon electrode at pH = 11.72 and $T = 298.0\,K$, with rotation rates of (1) 100, (2) 400, (3) 900, (4) 1600, (5) 2500, (6) 3600 and (7) 4900 revolutions per minute; C_{per} (hydrogen peroxide concentration) = $0.11\,mol\,l^{-1}$.

Apparently, the current in the ascending part of the wave and the pseudo-limiting current are mostly determined by transport-independent, kinetic factors. The limiting current of the second wave, obtained after correction for the IR voltage drop, satisfies the Levich relation (Chapter 1, Equation 1.15) and is hence determined by the transport rate of hydrogen peroxide to the electrode surface. This wave will not be further discussed since it is of no use for the aim of this investigation.

If one wishes to verify whether the prewave can form the basis for an amperometric sensor, one would preferably dispose of as much information as possible concerning the nature and the properties of this wave. An obvious technique for diagnosis is cyclic voltammetry. Hydrogen peroxide can be oxidised as well as reduced at glassy-carbon electrodes; however, the potential ranges within which the reactions occur are situated relatively distant from each other, as can be seen in Fig. 4.3 and Fig. 4.5.

When varying the hydrogen peroxide concentration, pH and polarisation rate (v) in a broad range, in no case could a reduction reaction connected with the oxidation wave be detected in cyclic voltammograms. With a lower polarisation rate, the same S-shaped curve was described in the opposite potential variation as in the departing potential variation. With higher v-values, hysteresis effects were observed; however, this did not provide any relevant information. This behaviour strongly reduces the diagnostic possibilities. The effectiveness of cyclic voltammetry as a diagnostic instrument depends considerably on the voltammetric signal obtained in the opposite potential variation, because this signal contains information about the reaction product that has arisen from the forward potential variation.

Ring-disc voltammetry (glassy-carbon disc/glassy-carbon ring) did not provide a deeper insight either: except for oxygen, no electroactive reaction products, generated in the disc reaction, could be detected on the ring. We tried to detect intermediates by means of ring electrodes constructed from precious metals. This provided no results either and, moreover, the catalytic decomposition of hydrogen peroxide strongly interfered at some of these materials (such as platinum).

A classical approach[72] to unravelling the mechanism of electrochemical reactions and to identifying the rate-determining step (RDS) is based on testing the validity of possible sequences of reaction stages according to the elementary theory of electron transfer. As opposed to disc voltammetry, one does not look for direct evidence such as the presence of intermediate components. As a consequence, more reaction sequences appear to be theoretically possible, which in the ideal case can be dismissed, all but one on the basis of experimental evidence. It should be pointed out that neither does the identification of intermediates by means of electrochemical or non-electrochemical techniques automatically lead to the 'true' reaction mechanism. It is only an aid in the sense that identified intermediates must occur in a postulated reaction mechanism and that hence the number of possible mechanisms can be reduced.

In order to apply the method, one needs to have a number of data, first of all, the reacting component, the reaction product and the number of electrons interfering in the global reaction. As to the global reaction in the prewave, it is clear that the reaction product is molecular oxygen. The only reaction product that could be detected with ring-disc voltammetry is precisely oxygen. Moreover, one can visually detect the formation of a gas in the reaction. Considering the composition of the solution (H_2O, H_2O_2 and NaOH), it is logical that, for an oxidation reaction, oxygen is the resulting reaction product. Hence, in a sufficiently alkaline environment, the global reaction is:

$$HO_2^- + OH^- \leftrightarrows O_2 + H_2O + 2e^- \qquad [4.4]$$

A key element in the analysis is the correspondence between the observed and the theoretical dependence of the current on the potential. In other words, one compares the theoretical Tafel slope for the postulated mechanisms, or the transfer coefficients which are derived from these, to the experimentally obtained values.

The experimental Tafel slope does not appear to deviate significantly from 120 mV/decade, which corresponds to a transfer coefficient of 0.5, and this over the complete investigated range of hydrogen peroxide concentration and pH (Fig. 4.6). This Tafel slope is found within a potential range restricted from ca. –0.10 to 0.20 V vs. SCE. Above $E = 0.20$ V vs. SCE, the inclination of the current–potential curve appears to decrease. In Fig. 4.7,

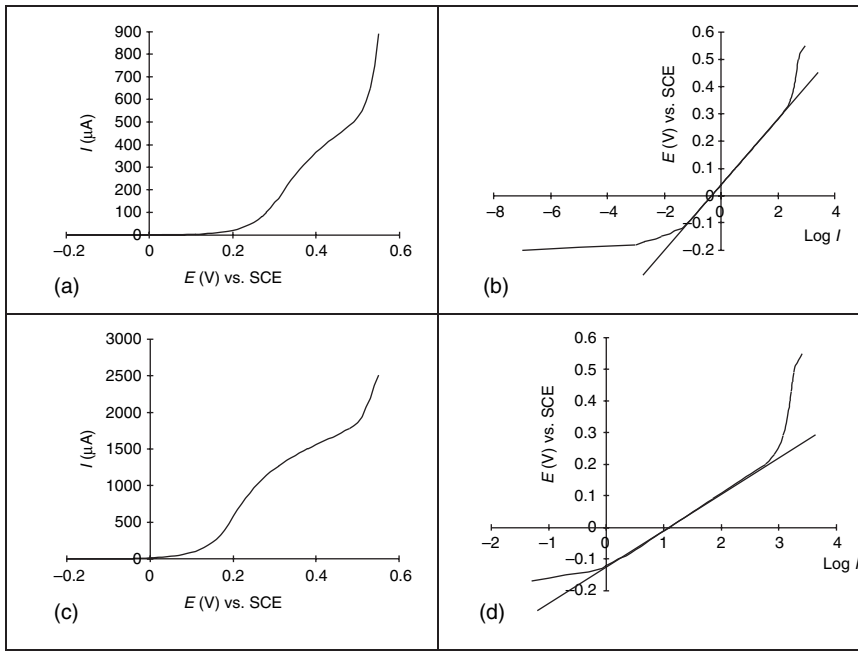

4.6 Current–potential curves of the oxidation of hydrogen peroxide with a vitreous-carbon electrode in an alkaline environment with a hydrogen peroxide concentration of (a) 0.15 mol l^{-1} and pH = 12.04 and (c) 0.44 mol l^{-1} and pH = 12.80, and their corresponding table graphs with (b) an inclination of 0.50 and (d) an inclination of 0.48.

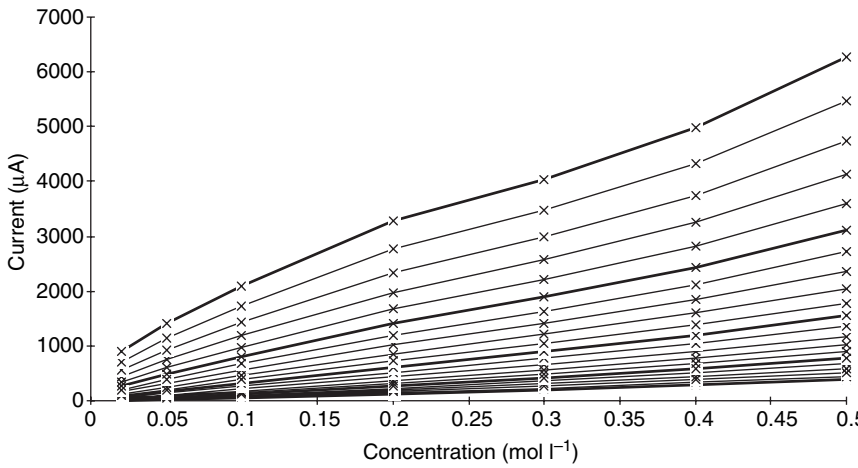

4.7 Relationship between pseudo-limiting-current of the pre-wave at $E = 0.45$ V vs. SCE and the hydrogen peroxide concentration for various pH values, recorded at a glassy carbon electrode rotating at 16.67 Hz. The numbered curves correspond to pH values of (1) 10, (2) 11, (3) 12, (4) 13 and (5) 14; other curves correspond to each increment of 0.2 pH units.

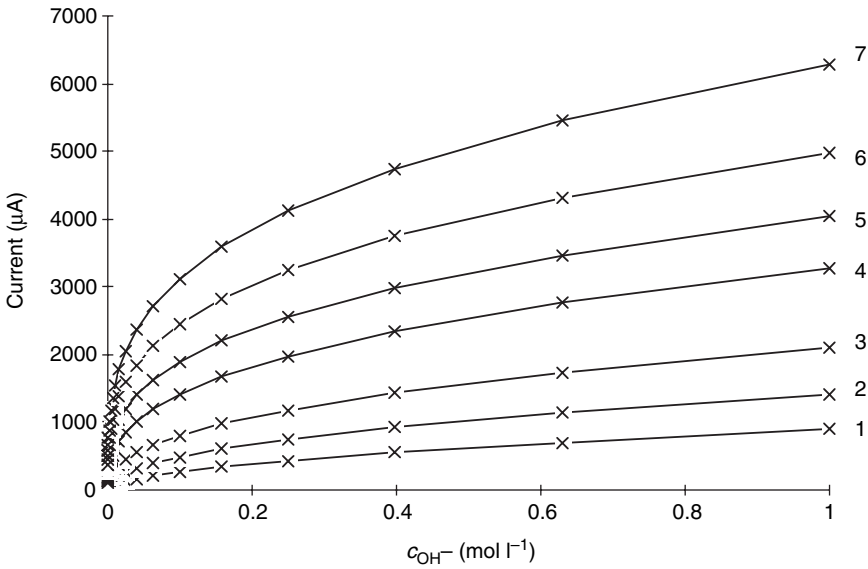

4.8 Relationship between pseudo-limiting-current of the prewave at E = 0.45 V vs. SCE and the hydroxide concentration (pH) for various hydrogen peroxide concentrations, recorded at a glassy-carbon electrode rotating at 16.67 Hz. The numbered curves correspond to hydrogen peroxide concentrations of (1) 0.02, (2) 0.05, (3) 0.1, (4) 0.2, (5) 0.3, (6) 0.4 and (7) 0.5 mol l^{-1}.

the relation is represented between the current signal at 0.45 V vs. SCE, situated in the pseudo-limiting-current plateau, and the hydrogen peroxide concentration for a large number of pH values in the range of 10–14. Remarkable characteristics are the non-linear relation between the oxidation current and the hydrogen peroxide concentration, which is more pronounced when the pH is higher, and the strong increase of the current with an increasing pH. The latter is an indication that there is a high probability of hydroxide ions in the reaction sequence. The pH dependency is displayed more directly in Fig. 4.8, which shows the relation between the oxidation current in the pseudo-limiting-current plateau of the prewave and the concentration of the hydroxide ions [$(1\times10^{-4}$–1 mol l^{-1}) area] for different hydrogen peroxide concentrations in the 0.02–0.5 mol l^{-1} range.

The fact that the relation between the hydrogen peroxide concentration and the oxidation current measured at E=0.45 V vs. SCE is not linear with all pH values could be due to the changes in the nature of the rate-determining step, in the mechanism itself or in the reaction orders of the components involved in the reaction.

The calibration curves in Fig. 4.7, registered at a constant pH, can be divided into three groups. With the lowest pH values (10 to ca. 11.6), the slope of the I_{LP} vs. c relation increases with an increasing hydrogen perox-

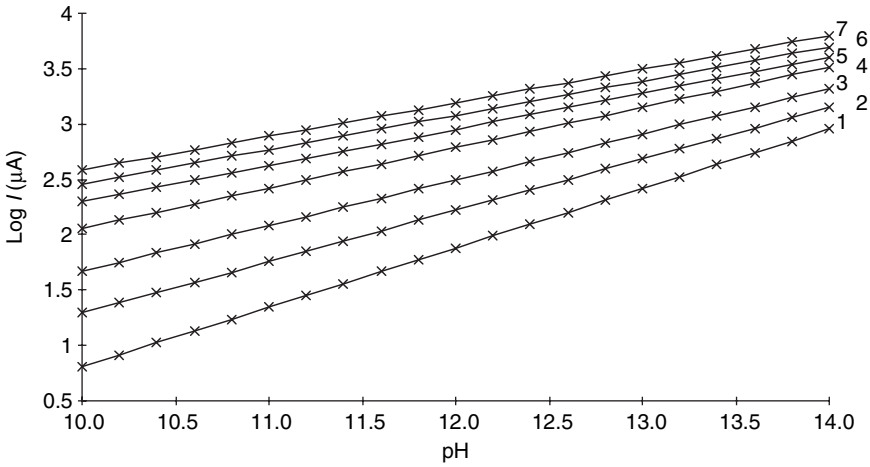

4.9 Logarithmic relationship between pseudo-limiting-current of the prewave at $E = 0.45$ V vs. SCE and the hydroxide concentration (pH) for various hydrogen peroxide concentrations, recorded at a glassy-carbon electrode rotating at 16.67 Hz. The numbered curves correspond to hydrogen peroxide concentrations of (1) 0.02, (2) 0.05, (3) 0.1, (4) 0.2, (5) 0.3, (6) 0.4 and (7) 0.5 mol l^{-1}.

ide concentration; with the highest pH values (ca. 12.6–14), the slope of the calibration curves initially decreases with an increasing hydrogen peroxide concentration, and the concentration range where this applies increases when the pH is higher. After this initial decrease, the slope of the calibration curve increases again with higher hydrogen peroxide concentrations. A third group of curves, with intermediate pH values, can be considered as a transition between both curves mentioned above.

When the data of Fig. 4.8 (I_{lp} vs. c_{OH^-}) are set out logarithmically, Fig. 4.9 is obtained. Although the relationships are linear, their slope, which one expects to reflect the reaction order of the OH^- ions, varies with the hydrogen peroxide concentration. The inclination varies from 0.5365 to 0.3035 with hydrogen peroxide concentrations of 0.02 and 0.5 mol l^{-1}, respectively. When the data of Fig. 4.7 are also displayed logarithmically, which results in Fig. 4.10, no linear relations are obtained.

All the relationships mentioned above were obtained from measurement of the current in the pseudo-limiting-current range at $E = 0.45$ V vs. SCE (Figs. 4.7, 4.8, 4.9 and 4.10). They were also found when the current was measured in the ascending part of the prewave at $E = 0.15$ V vs. SCE, with the difference that the absolute value of the currents is smaller. An important implication here is that the reaction orders, of hydrogen peroxide as well as hydroxyl ions, are the same in the ascending part of the prewave and in the pseudo-limiting-current range. Since the potential of $E = 0.45$ V

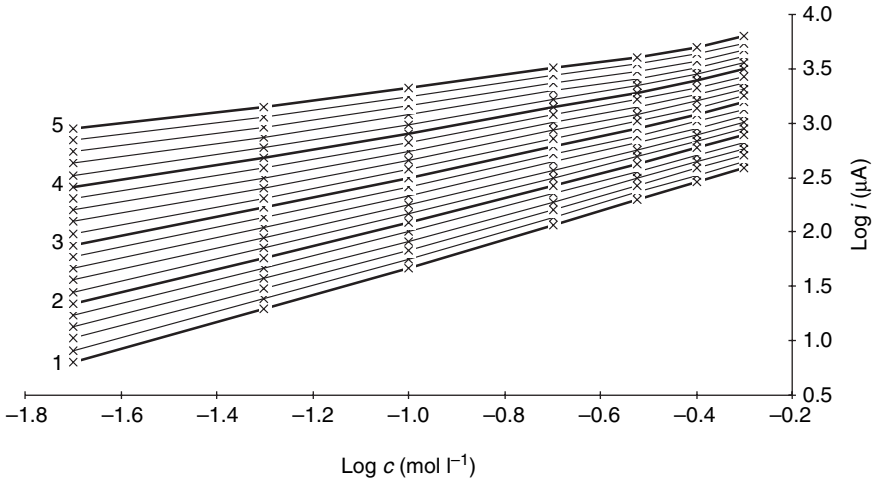

4.10 Logarithmic relationship between pseudo-limiting-current of the prewave at $E = 0.45$ V vs. SCE and the hydrogen peroxide concentration for various pH values, recorded at a glassy-carbon electrode rotating at 16.67 Hz. The numbered curves correspond to pH values of (1) 10, (2) 11, (3) 12, (4) 13 and (5) 14; other curves correspond to each increment of 0.2 pH units.

vs. SCE is important for the possible analytical application of the prewave, we will work with the results obtained with this potential.

A rough qualitative analysis tells us that, for the highest hydrogen peroxide concentrations, the slope of all log I_{LP} vs. c-curves, obtained for the different pH values, appears to strive towards the same value of ca. 1.28 with the highest hydrogen peroxide concentrations. With lower hydrogen peroxide concentrations, the slope varies from 1.22, with the lowest pH value, to 0.49 at pH=14.

If the experimental observations are summarised, a constant finding is the value of 0.5 for the transfer coefficient of the oxidation reaction, with all the combinations of hydrogen peroxide concentration and pH. Obviously, this is valid only in the potential range in which this transfer coefficient was experimentally determined. With potentials outside this range, the transfer coefficient cannot be used as a criterion. This value of the transfer coefficient is a primary requirement which every postulated reaction mechanism should meet theoretically. Furthermore, it is certain that hydroxide ions interfere in the oxidation reaction.

What is confusing at first sight is the conclusion that the reaction orders of hydrogen peroxide and of OH^- have a different value for each hydrogen peroxide concentration. A possible explanation could be found in the hypothesis that in the prewave at least two reaction mechanisms are simul-

taneously operational with all the hydrogen peroxide concentrations investigated, that these mechanisms are competing with each other, and that the relative fraction of each mechanism in the global reaction depends on the hydrogen peroxide concentration. If one supposes for the time being that the number of operational mechanisms equals two, this hypothesis implies that the variation of the hydrogen peroxide concentration involves a transition in the relative predominance of one mechanism in relation to the other. With sufficiently high or low hydrogen peroxide concentrations, respectively, this should, in principle, lead to a situation where one or the other mechanism, respectively, has only a negligible influence.

When examining Fig. 4.9 and Fig. 4.10, it seems that these extreme situations have not yet been reached, neither with the highest nor with the lowest hydrogen peroxide concentrations. Hence, the search for a global reaction mechanism becomes rather complicated and potentially time-consuming: it is not only necessary to combine two mechanisms, but, moreover, little support is found in the reaction orders of hydrogen peroxide and OH^- in both submechanisms. For hydrogen peroxide, the experimentally obtained orders vary between 0.49 (highest pH) and 1.22 (lowest pH) with the lowest hydrogen peroxide concentrations applied, and between 1.05 (highest pH) and 1.28 (lowest pH) with the highest hydrogen peroxide concentrations applied. For the OH^- ions, reaction orders of ca. 0.54 and 0.30, respectively, are obtained. For the sake of clarity, it should be emphasised that what we call 'experimentally obtained orders' are apparent, and there are no real reaction orders when, as is mentioned above, two reaction mechanisms are operational. Hence mechanisms belonging to mechanism pairs postulated in the framework of the above hypothesis need to imply reaction orders that are, respectively, higher or lower than the experimental limit values mentioned earlier in this paragraph. In addition, both of them should lead to a transfer coefficient of 0.5 within the potential range of ca. $E = -0.10\,V$ to $E = 0.20\,V$ vs. SCE.

There is no routine procedure for determining hypothetical reaction mechanisms. Normally, one starts with the obvious, simple sub-stage reaction sequences which should contain the components that are known to interfere in the overall reaction. In this research, it appeared totally impossible to explain the experimentally observed relations if only the components already mentioned (H_2O, H_2O_2 or HO_2^-, O_2 and OH^-) were to occur in the reactions of the postulated mechanism pairs. In such a case, possible intermediates need to be inserted. Hydrogen peroxide is an intermediate product itself in the oxygen–water system in an alkaline environment. Together with the hydrogen system, these are largely the most investigated redox systems. Hence, an extensive literature is available in order to verify which of the possible intermediates show sufficient evidence. Table 4.1 presents a number of particles which display a considerable evidence for their

Table 4.1 Possible species in solution and adsorbed at the surface of a glassy-carbon electrode that can occur and take part in the oxidation of hydrogen peroxide in alkaline solution

In solution	Adsorbed at the electrode surface
H_2O	$OH^{\cdot}$
HO_2^-	HO_2^-
OH^-	$HO_2^{\cdot}$
O_2	$O_2^{\cdot -}$
	$O^{\cdot}$
	O^-

presence in homogeneous and electrochemical reactions of hydrogen peroxide in a sufficiently alkaline environment[73–81].

It is generally accepted that, except for HO_2^-, none of the particles represented in the right-hand column of the table occur in the solution; it generally concerns somewhat reactive or unstable short-living components. Since they are present only in the vicinity of the electrode–solution interface, they are considered to be adsorbed components.

The following step examines the reactions that are theoretically possible when making use of the reacting and reaction products presented in Table 4.1, including decomposition reactions of every particle separately and reactions where identical particles react with each other. In this work, a number of restrictions will be observed. First, it was presumed that no more than two particles react with each other. Furthermore, it was assumed that no intermediary reduction steps occur in the global oxidation reaction considered, and that no more than one electron is transferred in every sub-stage.

Under these conditions and making use of the components from Table 4.1, mechanism pairs were tentatively established, logically starting with the simplest pair possible. Subsequently, in both mechanisms, every sub-stage of the postulated reaction sequences is considered as the RDS, and it is verified if the theoretically predicted transfer coefficient equals 0.5 and if the reaction orders of hydrogen peroxide and OH^- are situated in the range required by the assumed hypothesis. As has already been mentioned, the value of the transfer coefficient can serve as a criterion only in the potential range limited by ca. $E=-0.10$ V and $E=0.20$ V vs. SCE. If the postulated conditions are met, it is verified if a combination of both mechanisms can lead to an explanation of the experimental evidence.

Initially, it was assumed that the reaction sequence had to start with the reaction:

$$HO_2^- + O_2 \leftrightarrows (HO_2^{\bullet})_{ads} + (O_2^-)_{ads} \qquad [4.5]$$

where the reaction products are adsorbed at the surface of the electrode. Owing to its instability, the obtained peroxide radical disintegrates into an oxygen (O) and a hydroxyl radical (OH), which each further react. In order to identify at least a partial correspondence between the predicted and the experimental behaviour, it soon became clear that an atomic oxygen anion (O^-) needed to occur in both sub-stage sequences. In literature, it is often assumed that such an anion is formed by the reaction:

$$(OH^\bullet)_{ads} + OH^- \leftrightarrows (O^-)_{ads} + H_2O \qquad [4.6]$$

However, the introduction of the component O^- in the sub-stage sequences, which happened exclusively through Equation 4.6, resulted repeatedly in incompatibility between observation and theoretical prediction. Tens of mechanism pairs which seemed possible on paper a priori had to be rejected, and, for a certain time, the feeling prevailed that it would not be possible to find a combination of two reaction mechanisms with which all the experimental details would be compatible. The mechanisms verified and rejected are neither listed nor elaborated here in order to keep the size of this work within reasonable proportions.

A turning point in the compatibility between theory and experiment was reached by inserting, in both mechanisms, a sub-stage which directly produces the O^- anion:

$$(HO_2^-)_{ads} \leftrightarrows (O^-)_{ads} + (OH^\bullet)_{ads} \qquad [4.7]$$

A stage preceding this reaction is the adsorption of hydrogen peroxide from the solution. The OH radical formed reacts into a second O^-, after which both of them can react into oxygen in two stages, each time by emitting an electron. The sequence of stages from Equation 4.8 to 4.12 will be referred to as mechanism 1.

$$HO_2^- \leftrightarrows (HO_2^-) \qquad k_1/k_{-1} \qquad [4.8]$$

$$(HO_2^-)_{ads} \leftrightarrows (O^-)_{ads} + (OH^\bullet)_{ads} \qquad k_2/k_{-2} \qquad [4.9]$$

$$(OH^\bullet)_{ads} + OH^- \leftrightarrows (O^-)_{ads} + H_2O \qquad k_3/k_{-3} \qquad [4.10]$$

$$(O^-)_{ads} + (O^-)_{ads} \leftrightarrows (O_2^-) + e^- \qquad k_4/k_{-4} \qquad [4.11]$$

$$(O_2^-)_{ads} \leftrightarrows O_2 + e^- \qquad k_5/k_{-5} \qquad [4.12]$$

where the global reaction is given in Equation 4.4.

The O^- ions formed can react not only with each other but also with hydrogen peroxide. In a competitive relation with mechanism 1, a second mechanism occurs which will be referred to as mechanism 2 (Equations 4.8–4.10, 4.13 and 4.12, in this order):

$$HO_2^- \leftrightarrows (HO_2^-) \qquad k_1/k_{-1} \qquad [4.8]$$

$$(HO_2^-)_{ads} \leftrightarrows (O^-)_{ads} + (OH^\bullet)_{ads} \qquad k_2/k_{-2} \qquad [4.9]$$

$$(OH^\bullet)_{ads} + OH^- \leftrightarrows (O^-)_{ads} + H_2O \qquad k_3/k_{-3} \qquad [4.10]$$

$$(O^-)_{ads} + HO_2^- \leftrightarrows (O_2^-)_{ads} + OH^- \qquad k_4/k_{-4} \qquad [4.13]$$

$$(O_2^-)_{ads} \leftrightarrows O_2 + e^- \qquad k_5/k_{-5} \qquad [4.12]$$

Mechanism 2 is obtained from the same stages as mechanism 1, except for stage 4 (Equation 4.13). Hence, the reaction rate constants of stage 4 have been given a different symbol. In the global reaction:

$$3HO_2^- \leftrightarrows 2O_2 + H_2O + OH^- + 2e^- \qquad [4.14]$$

and sub-stages in Equations 4.13 and 4.12 occur twice.

Sections 4.6 and 4.7 of this chapter provide calculations as to which current–potential relations are theoretically expected for both mechanisms. Section 4.8 then attempts to unify these relations into one single relation and to verify the validity of this current–potential relation against the experimentally obtained data.

4.6 Theoretical *I–E* relationship for mechanism 1

In the first instance, equations need to be formulated for the reaction rate of the different sub-stages in the postulated mechanism. To keep the equations and calculations as simple and as clear as possible, a number of abbreviated notations will be used. For example, a rate constant $k_n(E)$ means that it is potential dependent. Hence, the exponential potential-dependent factor of the rate equation is integrated here. The rate constants of the reactions in forward (from left to right) sense – i.e. in anodic sense for the electrochemical reactions – are represented by k_1, k_2, up to k_n. The constants for the reactions in the opposite sense are k_{-1}, k_{-2}, up to k_{-n}. For the components, which do not occur in the bulk of the solution, the reaction rate cannot be expressed as a function of a concentration. Here, the degree of coverage of the electrode surface (symbol θ) is used. The reaction rates of the five sub-stages (Equations 4.15–4.19) of mechanism 1 can be written as follows (for easy reference, the reactions involved are noted once again):

$$HO_2^- \leftrightarrows (HO_2^-) \qquad [4.8]$$

$$v_1 = k_1 c_{HO_2^-}\left(1 - \theta_{HO_2^-}\right) - k_{-1}\theta_{HO_2^-} \qquad [4.15]$$

$$(HO_2^-)_{ads} \leftrightarrows (O^-)_{ads} + (OH^\bullet)_{ads} \quad [4.9]$$

$$v_2 = k_2\theta_{HO_2^-}(1-\theta_{O^-})(1-\theta_{OH^\bullet}) - k_{-2}\theta_{O^-}\theta_{OH^\bullet}\left(1-\theta_{HO_2^-}\right) \quad [4.16]$$

$$(OH^\bullet)_{ads} + OH^- \leftrightarrows (O^-)_{ads} + H_2O \quad [4.10]$$

$$v_3 = k_3\theta_{OH^\bullet}c_{OH^-}(1-\theta_{O^-}) - k_{-3}\theta_{O^-}(1-\theta_{OH^\bullet}) \quad [4.17]$$

$$(O^-)_{ads} + (O^-)_{ads} \leftrightarrows (O_2^-) + e^- \quad [4.11]$$

$$v_4 = k_4(E)\theta_{O^-}{}^2\left(1-\theta_{O_2^-}\right) - k_{-4}(E)\theta_{O_2^-}(1-\theta_{O^-})^2 \quad [4.18]$$

$$(O_2^-)_{ads} \leftrightarrows O_2 + e^- \quad [4.12]$$

$$v_5 = k_5(E)\theta_{O_2^-} - k_{-5}(E)c_{O_2}\left(1-\theta_{O_2^-}\right) \quad [4.19]$$

The factors $(1-\theta)$ express that the reaction involved can take place only on the fraction of the electrode surface that is not covered.

In order to determine whether mechanism 1 is compatible with the experimental evidence and to indentify which of the five sub-stages is the rate-determining one, Equations 4.15–4.19 are of no use in practice, because the degrees of coverage are not experimentally accessible. If one of the sub-stages is assumed to be rate-determining step, it is then possible to transform the rate equation of the stage involved into the form:

$$v \cong k_a c_{A'} e^{r\frac{\alpha_a F}{RT}E} - k_k c_{B'} e^{r\frac{\alpha_k F}{RT}E} \quad [4.20]$$

where c is the concentration of a bulk component (hydrogen peroxide, hydroxide ion or oxygen), k_a and k_k are reaction rate constants with the reference potential, and E is the working electrode potential versus the same reference potential. The value of r is either zero or one. If no chemical reaction stages occur in the sequence of sub-reactions, $r = 1$ always applies, and the potential dependence is represented by classical Butler–Volmer exponents. If chemical stages are present, the anodic or cathodic term of Equation 4.20 can be potential-independent ($r = 0$). The transformation is possible by assuming that the four sub-stages which are not rate-determining are in virtual balance, and their net reaction rate can be set equal to zero. This is a realistic assumption: being not rate-determining supposes sufficiently high k, c or θ values, or in other words, for electrochemical reactions, a relatively high i_0 and hence a relatively small overpotential or a quasi-equilibrium situation. In what follows, the sign of approximate equality (Equation 4.20) is replaced by the equals sign.

Hence, the followed procedure involves subsequently considering every sub-stage of a postulated mechanism as the rate-determining stage and

confronting the resulting rate equation with the experimental data. This is elaborated in detail in section 4.6.1, in the case where stage 1 is assumed to be the RDS of mechanism 1. This elaboration will serve at the same time as an illustration of the procedure, since this method was deliberately not discussed in detail in Chapter 1 under section 1.7.2 addressing, in general terms, formulated mechanisms (Equations 1.27–1.32).

4.6.1 Stage 1 as RDS

The rate equation of stage 1 is given by:

$$v_1 = \mathrm{k}_1 c_{\mathrm{HO_2^-}} \left(1 - \theta_{\mathrm{HO_2^-}}\right) - \mathrm{k}_{-1} \theta_{\mathrm{HO_2^-}} \qquad [4.15]$$

By assuming a virtual balance for the other stages, it is possible to eliminate the unknown, experimentally inaccessible parameters θ and $(1-\theta)$ in Equation 4.15 by equalising, in Equations 4.16 to 4.19, the two terms of the right part ($\nu = 0$).

$$\mathrm{k}_2 \theta_{\mathrm{HO_2^-}} (1 - \theta_{\mathrm{O^-}})(1 - \theta_{\mathrm{OH^\bullet}}) = \mathrm{k}_{-2} \theta_{\mathrm{O^-}} \theta_{\mathrm{OH^\bullet}} \left(1 - \theta_{\mathrm{HO_2^-}}\right) \qquad [4.21]$$

$$\mathrm{k}_3 \theta_{\mathrm{OH^\bullet}} c_{\mathrm{OH^-}} (1 - \theta_{\mathrm{O^-}}) = \mathrm{k}_{-3} \theta_{\mathrm{O^-}} (1 - \theta_{\mathrm{OH^\bullet}}) \qquad [4.22]$$

$$\mathrm{k}_4(E) \theta_{\mathrm{O^-}}{}^2 \left(1 - \theta_{\mathrm{O_2^-}}\right) = \mathrm{k}_{-4}(E) \theta_{\mathrm{O_2^-}} (1 - \theta_{\mathrm{O^-}})^2 \qquad [4.23]$$

$$\mathrm{k}_5(E) \theta_{\mathrm{O_2^-}} = \mathrm{k}_{-5}(E) c_{\mathrm{O_2}} \left(1 - \theta_{\mathrm{O_2^-}}\right) \qquad [4.24]$$

By combining Equations 4.21 and 4.22, it is possible to deduce an expression for $\theta_{\mathrm{O^-}}$ from which $\theta_{\mathrm{OH}}^{\bullet}$ is eliminated. A second expression for $\theta_{\mathrm{O^-}}$ results from the combination of Equations 4.23 and 4.24, in which the coverage fraction of O_2^- is eliminated. Equalising these two expressions for $\theta_{\mathrm{O^-}}$ results in an expression in which, besides the coverage of HO_2^- and the non-covered surface fraction $(1-\theta)$, only accessible concentrations occur:

$$\frac{\theta_{\mathrm{HO_2^-}}}{\left(1 - \theta_{\mathrm{HO_2^-}}\right)} = \frac{1}{\mathrm{K}_2 \mathrm{K}_3} \frac{\mathrm{k}_{-4}(E) \mathrm{k}_{-5}(E) c_{\mathrm{O_2}}}{\mathrm{k}_4(E) \mathrm{k}_5(E) c_{\mathrm{OH^-}}} \qquad [4.25]$$

where K ($\mathrm{K}_n = \mathrm{k}_n / \mathrm{k}_{-n}$) is an equilibrium constant of a chemical reaction of the corresponding substage. The $(1-\theta)$ term of HO_2^- can be equalised to 1 if the degree of coverage of HO_2^- is sufficiently small. Since stage 1 of the reaction sequence is considered as the speed-determining one, all the other stages of the sequence will be faster. This means that the HO_2^- formed from stage 1 can continue to react rapidly through these faster stages, and it can be assumed that the degree of cover of HO_2^- will be minimal. When combining Equations 4.15 and 4.25 under this condition, the following is obtained:

$$v_1 = \mathrm{k}_1 c_{\mathrm{HO_2^-}} - \frac{1}{\mathrm{K_2K_3}} \frac{\mathrm{k_{-1}k_{-4}}(E)\mathrm{k_{-5}}(E) c_{\mathrm{O_2}}}{\mathrm{k_4}(E)\mathrm{k_5}(E) c_{\mathrm{OH^-}}} \qquad [4.26]$$

In order to express explicitly the dependence of the reaction rate on potential, it is necessary to re-introduce this dependence for every electrochemical reaction-speed constant. These constants concern reactions where one electron is transferred and to which Equation 4.20 applies. In this relation, the potential of the redox system involved is referred to as the formal potential, so that the anodic and cathodic subcurrent can be expressed as a function of the same rate constant, $\mathrm{k}^{0'}$. This is not possible in Equation 4.26 because there are rate constants of different redox systems, or because formal potentials of intermediary redox systems are not known.

However, Equation 4.20 can easily be transformed into a form where the potential is referred to any other potential than $E^{0'}$. Therefore, the desired reference potential, E_{ref}, is added up with and subtracted from the present potential difference, which results after rearranging into:

$$i = \mathrm{F}\left\{ c_{\mathrm{R}} \left[\mathrm{k}_a{}^0 \mathrm{e}^{(1-\beta)\frac{\mathrm{F}}{\mathrm{R}T}\left(E_{\mathrm{ref}} - E^{0'}\right)} \right] \mathrm{e}^{(1-\beta)\frac{\mathrm{F}}{\mathrm{R}T}(E - E_{\mathrm{ref}})} + c_{\mathrm{O}} \left[\mathrm{k}_k{}^0 \mathrm{e}^{-\beta\frac{\mathrm{F}}{\mathrm{R}T}\left(E_{\mathrm{ref}} - E^{0'}\right)} \right] \mathrm{e}^{-\beta\frac{\mathrm{F}}{\mathrm{R}T}(E - E_{\mathrm{ref}})} \right\} \qquad [4.27]$$

or in general:

$$i_n = \mathrm{F}\left\{ c_{\mathrm{R},n} \mathrm{k}_n'' \mathrm{e}^{(1-\beta_n)\frac{\mathrm{F}}{\mathrm{R}T}(E - E_{\mathrm{ref}})} + c_{\mathrm{O},n} \mathrm{k}_{-n}'' \mathrm{e}^{-\beta_n\frac{\mathrm{F}}{\mathrm{R}T}(E - E_{\mathrm{ref}})} \right\} \qquad [4.28]$$

In order to calculate the theoretically predicted dependence of the global reaction rate on potential, the value of the symmetry factor β is missing. In many one-electron transfer reactions, β approximates a value of 0.5. A reminder should be given here that the intention is to find out whether a postulated reaction mechanism is possible or should be rejected. In this perspective, it is not necessary to have an exact value for β, and it is not indefensible to presuppose that β = 0.5.

Introducing in Equation 4.26 the explicit dependence of the electrochemical reaction rate constants (cf. Equation 4.28) on potential and equalising β to 0.5 results in:

$$v_1 = \mathrm{k}_1 c_{\mathrm{HO_2^-}} - \frac{1}{\mathrm{K_2K_3}} \frac{\mathrm{k_{-1}k_{-4}}'' \mathrm{k_{-5}}''}{\mathrm{k_4}'' \mathrm{k_5}''} \frac{c_{\mathrm{O_2}}}{c_{\mathrm{OH^-}}} \mathrm{e}^{-2\frac{\mathrm{F}}{\mathrm{R}T}(E - E_{\mathrm{ref}})} \qquad [4.29]$$

For the current, the following applies:

$$I = Ai = AnFv_1$$
$$= AnF\left(k_1 c_{HO_2^-} - \frac{1}{K_2 K_3} \frac{k_{-1} k_{-4}'' k_{-5}''}{k_4'' k_5''} \frac{c_{O_2}}{c_{OH^-}} e^{-2\frac{F}{RT}(E-E_{ref})} \right) \quad [4.30]$$

This is the steady-state current which is theoretically predicted if stage 1 is the rate-determining step in the sub-stages sequence represented in Equations 4.8–4.12. An important parameter to compare both in theory and experimentally is the Tafel slope or the transfer coefficient which results from it. Therefore, Equation 4.30 has to be written in a form that contains only one exponential term. Since the considered *I–E* curve is an oxidation wave, the effect of the reduction (second term in the right-hand part of Equation 4.30) will be negligible with potentials that are situated sufficiently far away from the equilibrium potential, and for the anodic current the following applies:

$$I = AnFk_1 c_{HO_2^-} \quad [4.31]$$

Mechanism 1, with sub-stage 1 as the RDS, can be rejected because, contradictory to the experiment, the theory predicts a current that is not dependent on potential and pH.

In the following parts of this chapter, subsequently the remaining stages of the sequence (Equations 4.9–4.12) are supposed to be rate determining. Since the reasoning to come to a Butler–Volmer relation remains the same, a number of explanations from this part of the chapter will not be repeated further on.

4.6.2 Stage 2 as RDS

Similarly to section 4.6.1, the speed equation is calculated for mechanism 1 with stage 2 of the reaction sequence as the RDS, starting from the rate equation and the equilibrium equations below:

$$v_2 = k_2 \theta_{HO_2^-} (1-\theta_{O^-})(1-\theta_{OH^\bullet}) - k_{-2} \theta_{O^-} \theta_{OH^\bullet} \left(1-\theta_{HO_2^-}\right) \quad [4.16]$$

$$k_1 c_{HO_2^-} \left(1-\theta_{HO_2^-}\right) = k_{-1} \theta_{HO_2^-} \quad [4.32]$$

$$k_3 \theta_{OH^\bullet} c_{OH^-} (1-\theta_{O^-}) = k_{-3} \theta_{O^-} (1-\theta_{OH^\bullet}) \quad [4.22]$$

$$k_4(E) \theta_{O^-}{}^2 \left(1-\theta_{O_2^-}\right) = k_{-4}(E) \theta_{O_2^-} (1-\theta_{O^-})^2 \quad [4.23]$$

$$k_5(E) \theta_{O_2^-} = k_{-5}(E) c_{O_2} \left(1-\theta_{O_2^-}\right) \quad [4.24]$$

Equation 4.16 contains three experimentally inaccessible degrees of coverage, i.e. from HO_2^-, O^- and $OH^\bullet$. All three of them occur once separately and once in the form $(1-\theta)$. The latter will be left as such for the time being.

The coverage fraction of HO_2^- can simply be substituted by means of Equation 4.32. Analogously, the degree of coverage of $OH^\bullet$ is calculated from Equation 4.22 and substituted in Equation 4.16. However, Equation 4.22 also contains the degree of coverage of O^- which is substituted by its value obtained from Equations 4.23 and 4.24 after elimination of the coverage fraction of O_2^-. This results in the following equation:

$$v_2 = \mathrm{K_1 k_2} c_{\mathrm{HO_2^-}} \left(1-\theta_{\mathrm{HO_2^-}}\right)(1-\theta_{\mathrm{O^-}})(1-\theta_{\mathrm{OH^\bullet}}) - \frac{1}{\mathrm{K_3}} \frac{\mathrm{k_{-2} k_{-4}}(E)\mathrm{k_{-5}}(E) c_{\mathrm{O_2}} \left(1-\theta_{\mathrm{HO_2^-}}\right)(1-\theta_{\mathrm{O^-}})(1-\theta_{\mathrm{OH^\bullet}})}{\mathrm{k_4}(E)\mathrm{k_5}(E) c_{\mathrm{OH^-}}} \qquad [4.33]$$

The terms $(1-\theta)$ for O^- and $OH^\bullet$ can be equalised to 1, since these particles are formed from the slowest stage and react further through the faster stages. Eliminating the degree of coverage of HO_2^- in Equation 4.33 by means of Equation 4.32 is not a problem from an algebraic point of view. However, it gives rise to two anodic terms in the final equation for the current, so that the Tafel slope cannot be used as a criterion of correspondence between theory and experiment. In the $(1-\theta)$ term for HO_2^-, θ can also be eliminated by introducing an additional condition i.e. $k_{-1} >> k_2$. This means that the adsorbed HO_2^- that does not immediately react through the rate-determining stage will further react in a considerable way back into its dissolved form through the stage preceding the RDS. Under this condition, the degree of coverage of HO_2^- is small and $(1-\theta) \approx 1$. After elaborating the potential terms of Equation 4.33 in a completely analogous way as in the previous part, the following is obtained:

$$v_2 = \mathrm{K_1 k_2} c_{\mathrm{HO_2^-}} - \frac{1}{\mathrm{K_3}} \frac{\mathrm{k_{-2} k_{-4}''} \mathrm{k_{-5}''}}{\mathrm{k_4''} \mathrm{k_5''}} \frac{c_{\mathrm{O_2}}}{c_{\mathrm{OH^-}}} \mathrm{e}^{-2\frac{\mathrm{F}}{\mathrm{RT}}(E-E_{\mathrm{ref}})} \qquad [4.34]$$

Providing that $k_{-1} >> k_2$, on the same grounds as under section 4.6.1, the predicted anodic current is completely incompatible with the experimental evidence, from which it can be concluded that mechanism 1 with stage 2 as RDS as a possibility should also be rejected.

4.6.3 Stage 3 as RDS

Once more, the speed equation is calculated as in sections 4.6.1 and 4.6.2, starting from the basic equations below:

$$v_3 = \mathrm{k_3} \theta_{\mathrm{OH^\bullet}} c_{\mathrm{OH^-}} (1-\theta_{\mathrm{O^-}}) - \mathrm{k_{-3}} \theta_{\mathrm{O^-}} (1-\theta_{\mathrm{OH^\bullet}}) \qquad [4.17]$$

$$\mathrm{k_1} c_{\mathrm{HO_2^-}} \left(1-\theta_{\mathrm{HO_2^-}}\right) = \mathrm{k_{-1}} \theta_{\mathrm{HO_2^-}} \qquad [4.32]$$

$$\mathrm{k_2} \theta_{\mathrm{HO_2^-}} (1-\theta_{\mathrm{O^-}})(1-\theta_{\mathrm{OH^\bullet}}) = \mathrm{k_{-2}} \theta_{\mathrm{O^-}} \theta_{\mathrm{OH^\bullet}} \left(1-\theta_{\mathrm{HO_2^-}}\right) \qquad [4.21]$$

$$k_4(E)\theta_{O^-}{}^2\left(1-\theta_{O_2^-}\right)=k_{-4}(E)\theta_{O_2^-}(1-\theta_{O^-})^2 \quad [4.23]$$

$$k_5(E)\theta_{O_2^-}=k_{-5}(E)c_{O_2}\left(1-\theta_{O_2^-}\right) \quad [4.24]$$

In a similar way as in both previous parts, the following rate equation for mechanism 1 with stage 3 as RDS is obtained:

$$v_3=K_1K_2\frac{k_3k_4{}^{1/2}(E)k_5{}^{1/2}(E)c_{HO_2^-}c_{OH^-}(1-\theta_{OH^\bullet})(1-\theta_{O^-})}{k_{-4}{}^{1/2}(E)k_{-5}{}^{1/2}(E)c_{O_2}{}^{1/2}}$$
$$-\frac{k_{-3}k_{-4}{}^{1/2}(E)k_{-5}{}^{1/2}(E)c_{O_2}{}^{1/2}(1-\theta_{O^-})}{k_4{}^{1/2}(E)k_5{}^{1/2}(E)} \quad [4.35]$$

Even though the O^- particle is formed in the stage preceding the RDS, it reacts further in a stage that is faster than the RDS (stage 4 of the sequence). It is expected that the surface coverage of O^- will be extremely small so that the $(1-\theta)$ term is equal to 1. $OH^\bullet$, which is also formed in stage 2, reacts further by means of the RDS so that the $(1-\theta)$ term cannot be neglected as such. To do this anyway, an additional condition $k_{-2} >> k_3$ is needed, where the formed $OH^\bullet$ which does not immediately react by means of the RDS mainly reacts back to adsorbed HO_2^-. After inserting the potential terms, rate equation (4.35) looks as follows:

$$v_3=K_1K_2\frac{k_3k_4''{}^{1/2}k_5''{}^{1/2}}{k_{-4}''{}^{1/2}k_{-5}''{}^{1/2}}\frac{c_{HO_2^-}c_{OH^-}}{c_{O_2}{}^{1/2}}e^{\frac{F}{RT}(E-E_{ref})}-\frac{k_{-3}k_{-4}''{}^{1/2}k_{-5}''{}^{1/2}}{k_4''{}^{1/2}k_5''{}^{1/2}}c_{O_2}{}^{1/2}e^{\frac{F}{RT}(E-E_{ref})} \quad [4.36]$$

Although the anodic term is dependent both on the hydrogen peroxide concentration and on the hydroxide ions concentration, the theoretically predicted value of the anodic transfer coefficient, i.e. 1, is twice that at the experimentally observed value. Moreover, Equation 4.36 predicts that the anodic current depends on the concentration of dissolved oxygen, which is not observed experimentally. When $k_{-2} >> k_3$ is assumed, this mechanism also should consequently be rejected.

4.6.4 Stage 4 as RDS

By means of the equations below, the rate equation is calculated for mechanism 1 with stage 4 as RDS:

$$v_4=k_4(E)\theta_{O^-}{}^2\left(1-\theta_{O_2^-}\right)-k_{-4}(E)\theta_{O_2^-}(1-\theta_{O^-})^2 \quad [4.18]$$

$$k_1c_{HO_2^-}\left(1-\theta_{HO_2^-}\right)=k_{-1}\theta_{HO_2^-} \quad [4.32]$$

$$k_2\theta_{HO_2^-}(1-\theta_{O^-})(1-\theta_{OH^\bullet})=k_{-2}\theta_{O^-}\theta_{OH^\bullet}\left(1-\theta_{HO_2^-}\right) \quad [4.21]$$

$$k_3\theta_{OH\bullet}c_{OH^-}(1-\theta_{O^-}) = k_{-3}\theta_{O^-}(1-\theta_{OH\bullet}) \quad [4.22]$$

$$k_5(E)\theta_{O_2^-} = k_{-5}(E)c_{O_2}\left(1-\theta_{O_2^-}\right) \quad [4.24]$$

The resulting rate equation is:

$$v_4 = K_1K_2K_3k_4(E)c_{HO_2^-}c_{OH^-}(1-\theta_{O^-})^2\left(1-\theta_{O_2^-}\right) - \frac{k_{-4}(E)k_{-5}(E)c_{O_2}(1-\theta_{O^-})^2\left(1-\theta_{O_2^-}\right)}{k_5(E)} \quad [4.37]$$

The $(1-\theta)$ term for O_2^- can be neglected since the component reacts further into stage 5, which is faster than the RDS from which O_2^- is formed. However, in order to be able to neglect the term $(1-\theta)$ of O^-, the condition $k_{-3} >> k_4''$ and/or $k_{-2} >> k_4''$ must be introduced so that the formed O^- that does not immediately react away by means of the RDS can react back into its starting product by means of stages 2 and 3. The resulting rate equation is as follows:

$$v_4 = K_1K_2K_3k_4''c_{HO_2^-}c_{OH^-}e^{0.5\frac{F}{RT}(E-E_{ref})} - \frac{k_{-4}''k_{-5}''}{k_5''}c_{O_2}e^{-1.5\frac{F}{RT}(E-E_{ref})} \quad [4.38]$$

When $k_{-3} >> k_4''$ and/or $k_{-2} >> k_4''$ is assumed, the transfer coefficient of the anodic current corresponds to the one obtained experimentally. For the reaction orders of hydrogen peroxide and OH^-, a value of 1 is predicted. These orders, predicted by one of the postulated competing mechanisms, should not be compared to the experimentally obtained orders, which are also influenced by both the orders in the second sub-mechanism and by the other parameters in the rate equations concerned. Only the orders resulting from a combination of two not rejected mechanisms are to be compared with the experimentally obtained orders. Hence, mechanism 1 with substage 4 as RDS qualifies as a possible sub-mechanism in the complete wave.

4.6.5 Stage 5 as RDS

The following equations were used to calculate the rate equation:

$$v_5 = k_5(E)\theta_{O_2^-} - k_{-5}(E)c_{O_2}\left(1-\theta_{O_2^-}\right) \quad [4.19]$$

$$k_1c_{HO_2^-}\left(1-\theta_{HO_2^-}\right) = k_{-1}\theta_{HO_2^-} \quad [4.32]$$

$$k_2\theta_{HO_2^-}(1-\theta_{O^-})(1-\theta_{OH\bullet}) = k_{-2}\theta_{O^-}\theta_{OH\bullet}\left(1-\theta_{HO_2^-}\right) \quad [4.21]$$

$$k_3\theta_{OH\bullet}c_{OH^-}(1-\theta_{O^-}) = k_{-3}\theta_{O^-}(1-\theta_{OH\bullet}) \quad [4.22]$$

$$k_4(E)\theta_{O^-}{}^2\left(1-\theta_{O_2^-}\right) = k_{-4}(E)\theta_{O_2^-}(1-\theta_{O^-})^2 \quad [4.23]$$

which has the following form:

$$v_5 = K_1K_2K_3 \frac{k_4(E)k_5(E)c_{HO_2^-}c_{OH^-}\left(1-\theta_{O_2^-}\right)}{k_{-4}(E)} - k_{-5}(E)c_{O_2}\left(1-\theta_{O_2^-}\right) \quad [4.39]$$

In order to be able to neglect the $(1-\theta)$ term, an additional condition must be introduced since the O_2^- particle in the RDS is consumed. This condition is $k_{-4}'' >> k_5''$. The rate equation becomes:

$$v_5 = K_1K_2K_3 \frac{k_4''k_5''}{k_{-4}''}c_{HO_2^-}c_{OH^-}e^{1.5\frac{F}{RT}(E-E_{ref})} - k_{-5}''c_{O_2}e^{-0.5\frac{F}{RT}(E-E_{ref})} \quad [4.40]$$

Under the condition $k_{-4}'' >> k_5''$, the confrontation of the predicted consequences of the anodic term with the experimental evidence leads us to the conclusion that mechanism 1 of which stage 5 is the RDS cannot explain the experimental observations in the foot of the prewave because of the diverging transfer coefficient. Since with more positive potentials, the transfer coefficient cannot be used as a criterion, mechanism 1 with stage 5 as RDS should not be rejected with these potentials, because the predicted anodic current depends on the hydroxide ions concentration and the hydrogen peroxide concentration, as is experimentally observed.

From the calculations presented in sections 4.6.1 to 4.6.5, it can be concluded that, by comparing experimentally obtained and theoretically predicted transfer coefficients and reaction orders, mechanism 1 with stage 4 of the reaction sequence as the RDS, under the additional condition that $k_{-3} >> k_4''$ and/or $k_{-2} >> k_4''$, qualifies as a possible partial reaction mechanism over the complete potential range. With potentials more positive than ca. 0.20 V vs. SCE, the same applies for stage 5 as RDS under the additional condition that $k_{-4}'' >> k_5''$.

In the next stage, the above conclusions need to be combined with the conclusions drawn from the following section of the chapter, where the second postulated mechanism will be analysed and confronted with the experimental evidence in the same way as the first mechanism.

4.7 Theoretical *I–E* relationship for mechanism 2

By analogy with the calculation of the theoretical *I–E* relation for the first postulated mechanism, the rate equations for mechanism 2 are calculated, where subsequently each of the sub-stages is supposed to be the RDS. Because of the analogy with mechanism 1, i.e. five stages in total, which are identical except for the fourth stage, only the final results will be presented in this section. Below are presented the reactions concerned with their rate equation, which applies in case they act as RDS, and the

equilibrium relation which is presumed to apply when the stage is not rate-determining.

$$HO_2^- \leftrightarrows (HO_2^-) \qquad [4.8]$$

$$v_1 = k_1 c_{HO_2^-}\left(1-\theta_{HO_2^-}\right) - k_{-1}\theta_{HO_2^-} \qquad [4.15]$$

$$k_1 c_{HO_2^-}\left(1-\theta_{HO_2^-}\right) = k_{-1}\theta_{HO_2^-} \qquad [4.32]$$

$$(HO_2^-)_{ads} \leftrightarrows (O^-)_{ads} + (OH^\bullet)_{ads} \qquad [4.9]$$

$$v_2 = k_2\theta_{HO_2^-}(1-\theta_{O^-})(1-\theta_{OH^\bullet}) - k_{-2}\theta_{O^-}\theta_{OH^\bullet}\left(1-\theta_{HO_2^-}\right) \qquad [4.16]$$

$$k_2\theta_{HO_2^-}(1-\theta_{O^-})(1-\theta_{OH^\bullet}) = k_{-2}\theta_{O^-}\theta_{OH^\bullet}\left(1-\theta_{HO_2^-}\right) \qquad [4.21]$$

$$(OH^\bullet)_{ads} + OH^- \leftrightarrows (O^-)_{ads} + H_2O \qquad [4.10]$$

$$v_3 = k_3\theta_{OH^\bullet} c_{OH^-}(1-\theta_{O^-}) - k_{-3}\theta_{O^-}(1-\theta_{OH^\bullet}) \qquad [4.17]$$

$$k_3\theta_{OH^\bullet} c_{OH^-}(1-\theta_{O^-}) = k_{-3}\theta_{O^-}(1-\theta_{OH^\bullet}) \qquad [4.22]$$

$$(O^-)_{ads} + HO_2^- \leftrightarrows (O_2^-)_{ads} + OH^- \qquad [4.13]$$

$$v_4' = k_4' c_{HO_2^-}\theta_{O^-}\left(1-\theta_{O_2^-}\right) - k_{-4} c_{OH^-}\theta_{O_2^-}(1-\theta_{O^-}) \qquad [4.41]$$

$$k_4 c_{HO_2^-}\theta_{O^-}\left(1-\theta_{O_2^-}\right) = k_{-4}' c_{OH^-}\theta_{O_2^-}(1-\theta_{O^-}) \qquad [4.42]$$

$$(O_2^-)_{ads} \leftrightarrows O_2 + e^- \qquad [4.12]$$

$$v_5 = k_5(E)\theta_{O_2^-} - k_{-5}(E)c_{O_2}\left(1-\theta_{O_2^-}\right) \qquad [4.19]$$

$$k_5(E)\theta_{O_2^-} = k_{-5}(E)c_{O_2}\left(1-\theta_{O_2^-}\right) \qquad [4.24]$$

On the basis of Equations 4.15, 4.21, 4.22, 4.42 and 4.24, the rate equation was calculated with stage 1 of the reaction sequence as RDS:

$$v_1' = k_1 c_{HO_2^-} - \frac{1}{K_2 K_3 K_4''^2}\frac{k_{-1}k_{-5}''^2}{k_5''^2}\frac{c_{OH^-}{c_{O_2}}^2}{{c_{HO_2^-}}^2}\left(e^{-\frac{F}{RT}(E-E_{ref})}\right)^2 \qquad [4.43]$$

It is clear that the anodic term does not meet the experimental observations and this over the entire potential area. Through Equations 4.16, 4.32, 4.22, 4.42 and 4.24, the rate equation was calculated with stage 2 of the reaction sequence as RDS under the additional condition that $k_{-1} >> k_2$:

$$v_2' = K_1 k_2 c_{HO_2^-} - \frac{1}{K_3 K_4'^2} \frac{k_{-2} k_{-5}''^2}{k_5''^2} \frac{c_{O_2}^2 c_{OH^-}}{c_{HO_2^-}^2} \left(e^{-\frac{F}{RT}(E-E_{ref})} \right)^2 \quad [4.44]$$

The anodic term is independent of the potential, which is contrary to the experimental evidence. Moreover, the established relation between current and pH does not arise from this rate equation. To calculate the rate equation for stage 3 as RDS, Equations 4.17, 4.32, 4.21, 4.42 and 4.24 were used, and, under the additional condition $k_{-2} >> k_3$, the following applies:

$$v_3' = K_1 K_2 K_4' \frac{k_3 k_5''}{k_{-5}''} \frac{c_{HO_2^-}^2}{c_{O_2}} e^{\frac{F}{RT}(E-E_{ref})} - \frac{1}{K_4'} \frac{k_{-3} k_{-5}''}{k_5''} \frac{c_{O_2} c_{OH^-}}{c_{HO_2^-}} e^{-\frac{F}{RT}(E-E_{ref})} \quad [4.45]$$

Equation 4.45 cannot explain the experimentally observed influence of the pH and predicts a Tafel slope of 1 and an influence of the oxygen concentration, which was not experimentally observed. The rate equation for a rate-determining fourth stage of the reaction sequence was calculated with Equations 4.41, 4.32, 4.21, 4.22 and 4.24, and, under the additional condition $k_{-3} >> k_4'$ and/or $k_{-2} >> k_4'$, the following applies:

$$v_4' = K_1 K_2 K_3 k_4' c_{HO_2^-}^2 c_{OH^-} - \frac{k_{-4}' k_{-5}''}{k_5''} c_{O_2} c_{OH^-} e^{-\frac{F}{RT}(E-E_{ref})} \quad [4.46]$$

This rate equation does not correspond to the experimental evidence in the bottom of the wave since the anodic term is independent of the potential. With potentials which are more positive than ca. 0.2 V vs. SCE, Equation 4.46 is not taken into consideration as a possible reaction rate equation due to the fact that the reaction order of the hydroxide ions is the same as in Equations 4.38 and 4.40, the reaction rate equations of the first mechanism which are to be considered further on. The experimentally observed variation of the reaction order of the hydroxide ions with the hydrogen peroxide concentration can result only from two sub-mechanisms, in case in the resulting rate equations the reaction order of the hydroxide ions is different and the values are situated outside the range where the experimentally obtained values are situated, i.e. 0.30 to 0.54 (section 4.5.2). For the reaction order of the hydroxide ions in the postulated competing mechanisms, this condition can be put because the order does not depend on the hydroxide ion concentration itself, but only on the hydrogen peroxide concentration. Hence, this condition cannot be put for the reaction order of hydrogen peroxide, which depends on the hydrogen peroxide concentration itself. So excluding Equation 4.46 is not based on absolute grounds, but on the fact that in the five rate equations derived for mechanism 1, no reaction orders for hydroxide ions occur smaller than 0.30.

For the fifth stage of the reaction sequence as RDS, the following rate equation was calculated, making use of Equations 4.19, 4.32, 4.21, 4.22 and 4.42, and, under the additional condition $k_{-4}' >> k_5''$, the following applies:

$$v_5' = K_1^{1/2} K_2^{1/2} K_3^{1/2} K_4' k_5'' \frac{c_{HO_2^-}^{3/2}}{c_{OH^-}^{1/2}} e^{0.5\frac{F}{RT}(E-E_{ref})} - k_{-5}'' c_{O_2} e^{-0.5\frac{F}{RT}(E-E_{ref})} \quad [4.47]$$

When comparing the experimental Tafel slopes and the dependency of the current of hydroxide ions and hydrogen peroxide concentration to what Equation 4.47 theoretically predicts, mechanism 2 with stage 5 as RDS can be considered as a correct sub-mechanism and this over the entire potential area. The predicted reaction orders amount to 3/2 and –1/2 for hydrogen peroxide and OH^-, respectively. In section 4.9, it is verified whether a combination of mechanism 1, where stage 4 or 5 is the RDS, with mechanism 2, where stage 5 is the RDS, corresponds to the experimental data.

4.8 The pseudo-limiting-current

As discussed in sections 4.6 and 4.7, mechanism 1 with stage 4 as RDS and mechanism 2 with stage 5 as RDS are taken into consideration as possible mechanisms within the potential area limited by ca. –0.1 V and 0.2 V vs. SCE. With potentials that are more positive than ca. 0.2 V vs. SCE, the current increases less significantly than predicted by the anodic exponential term in Equations 4.38 and 4.47. The best known, most commonly occurring cause of such a phenomenon is the depletion of the reacting components at the electrode surface, in the case considered hydrogen peroxide and/or hydroxyl ions. This, however, can be left out of consideration here because the pseudo-limiting-current of the prewave is influenced minimally by convection in the solution.

Another obvious possible explanation can be found in sub-stages that are becoming rate-determining, sub-stages of which the rate of the anodic reaction is independent of potential. In the postulated sub-mechanisms, the rate-determining supposition of five stages in total (two in mechanism 1, see Equations 4.31 and 4.34 and three in mechanism 2, see Equations 4.43, 4.44 and 4.46) appeared to lead to potential-independent reaction rates. However, they should all be excluded, because the reaction orders predicted for hydrogen peroxide or hydroxyl ions are not compatible with the experimental data.

It is clear that rate Equations 4.38, 4.40 and 4.47 do not appear to be able to explain the deviation of the experimental current–potential relation occurring with the more positive potentials in the prewave. However, these relations apply only under restrictive conditions ($k_{-3} >> k_4''$ and/or $k_{-2} >> k_{-4}''$ for Equation 4.38, $k_{-4}'' >> k_5''$ for Equation 4.40 and $k_{-4}' >> k_5''$ for Equation 4.47), which have only been introduced to eliminate $(1-\theta)$ terms from

the equations. The only purpose was to obtain the simplest possible rate equations, allowing verification if the theoretically predicted Tafel slopes and reaction orders correspond to the experimentally obtained values.

A possible explanation for the pseudo-limiting-current formation is as follows: considering the global rate equations of stages 3 and 4 of mechanism 1 (without restrictions, only anodic terms):

$$v_{3,a} = K_1 K_2 k_3 \frac{k_4''^{1/2} k_5''^{1/2}}{k_{-4}''^{1/2} k_{-5}''^{1/2}} c_{HO_2^-} c_{OH^-} c_{O_2}^{-1/2} (1-\theta_{O^-}) e^{\frac{F}{RT}(E-E_{ref})} \quad [4.48]$$

$$v_{4,a} = K_1 K_2 \frac{k_3}{k_{-3}} k_4'' c_{HO_2^-} c_{OH^-} (1-\theta_{O^-})^2 (1-\theta_{O_2^-}) e^{0.5\frac{F}{RT}(E-E_{ref})} \quad [4.49]$$

Since stage 4 is the RDS, the $(1-\theta)$ term of O_2^- is equal to 1. However, this is not the case for the $(1-\theta_{O^-})$ term. What can be considered is that $k_{-3} < k_4''$ so that formed O^- particles react only in a very restricted way back into the $OH^\bullet$ radical. In order to clarify the rate difference between stages 3 and 4, the rate relation can be examined, without the relation of the exponents being simplified:

$$\frac{v_{3,a}}{v_{4,a}} = \frac{\frac{k_5''^{1/2}}{k_{-4}''^{1/2} k_{-5}''^{1/2}} c_{O_2}^{-1/2} e^{\frac{F}{RT}(E-E_{ref})}}{\frac{k_4''^{1/2}}{k_{-3}} (1-\theta_{O^-}) e^{0.5\frac{F}{RT}(E-E_{ref})}} \quad [4.50]$$

With a potential that becomes more positive, one expects from the potential dependency an increase in the rate relation. However, one should also take into account the oxygen concentration and the $(1-\theta)$ term. Oxygen is the reaction product of the hydrogen peroxide oxidation reaction which is considered here. This means that the oxygen concentration in the vicinity of the electrode surface increases with the potential becoming more positive, which will oppose the above-mentioned increase in rate of stage 3 and hence also the increase in the O^- surface coverage, with the result that the value of the $(1-\theta_{O^-})$ term varies very little. This corresponds to the experimental observation in the potential area of ca. $E = -0.1$ V to $E = 0.2$ V vs. SCE. The fact that, with more positive potentials, the current bears off can be explained by considering that the degree of saturation of dissolved oxygen is attained in the vicinity of the electrode surface. The excess of oxygen that is formed will turn into the gas phase (oxygen bubbles) and will therefore not have any further influence on the dissolved oxygen concentration. This means that the oxygen concentration in the rate equation of stage 3 becomes constant and no longer acts as a rate inhibitor. This will result in the fact that the rate of stage 3 will increase much more strongly

than that of stage 4, and that the surface coverage of O^- particles increases, with a resultant decrease of the current.

Returning to Fig. 4.6, it can be seen that the potential range in which the transfer coefficient applies amounts to ca. $E = 0.3\,V$ vs. SCE for low hydrogen peroxide concentrations. This can be explained on the basis of the degree of saturation since, with lower hydrogen peroxide concentrations, less oxygen is formed (lower current density), and so the degree of saturation is attained only with more positive potentials. Analogously, the pseudo-limiting-current can be explained for mechanism 2 by comparing the rate of stage 3 (Equation 4.51) and 5 (Equation 4.52) on the basis of the relation of the speed equations (Equation 4.53):

$$v_{3,a}' = K_1 K_2 k_3 \frac{k_4'}{k_{-4}'} \frac{k_5''}{k_{-5}''} c_{HO_2^-}^2 c_{O_2}^{-1} (1-\theta_{O^-}) e^{\frac{F}{RT}(E-E_{ref})} \quad [4.51]$$

$$v_{5,a}' = K_1^{1/2} K_2^{1/2} \frac{k_3^{1/2}}{k_{-3}^{1/2}} \frac{k_4'}{k_{-4}'} k_5'' c_{HO_2^-}^{3/2} c_{OH^-}^{-1/2} \left(1-\theta_{O_2^-}\right) e^{0.5\frac{F}{RT}(E-E_{ref})} \quad [4.52]$$

$$\frac{v_{3,a}'}{v_{5,a}'} = \frac{\frac{K_1^{1/2} K_2^{1/2} K_3^{1/2}}{k_{-5}''} c_{HO_2^-}^{1/2} c_{O_2}^{-1} e^{\frac{F}{RT}(E-E_{ref})}}{\frac{1}{k_{-3}^{1/2}} c_{OH^-}^{-1/2} \left(1-\theta_{O_2^-}\right) e^{0.5\frac{F}{RT}(E-E_{ref})}} \quad [4.53]$$

It can be concluded that the combination of sub-mechanism 1 with stage 4 as RDS and sub-mechanism 2 with stage 5 as RDS qualifies for a possible global mechanism to explain the experimentally observed evidence.

In section 4.6.5, stage 5 of mechanism 1 as a possible RDS with potentials more positive than ca. $E = 0.2\,V$ vs. SCE was not excluded. Based on the above-mentioned arguments, this stage as RDS can be excluded. Moreover, the relation of the rate equations of stages 4 and 5 of mechanism 1 cannot explain that stage 5 would become slower than stage 4:

$$\frac{v_{4,a}}{v_{5,a}} = \frac{(1-\theta_{O^-})^2 e^{0.5\frac{F}{RT}(E-E_{ref})}}{\frac{k_5''}{k_{-4}''} e^{1.5\frac{F}{RT}(E-E_{ref})}} \quad [4.54]$$

unless $(1-\theta_{O^-}) \approx 1$ and $k_{-4}'' >> k_5''$. However, this seems very unlikely since both conditions predict much higher current densities than was experimentally observed. In the next stage, it should be verified whether the current or rate equations which resulted from both postulated sub-mechanisms can be combined, and, if so, if this combination can explain the experimentally obtained data and connections.

4.9 Combination of rate equations of both mechanisms

In consideration of a sensor based on the prewave, the highest ascending part of this wave is not important from an analytical point of view. In a possible analytical application, the pseudo-limiting-current needs to be applied, because the current is higher and because it is less sensitive to variations in the potential of the reference electrode.

Before attempting to combine the two postulated mechanisms with each other, it is useful to examine them in the light of the experimental data presented in Fig. 4.9. Here, the inclination of the log I vs. pH relation decreases with an increasing hydrogen peroxide concentration, and this from 0.54 to 0.30. Stages 4 and 5 as RDS of mechanisms 1 and 2 in the pseudo-limiting-current range predict for OH^- reaction orders of 1 and –0.5, respectively. Qualitatively, this means that with an increasing hydrogen peroxide concentration, the relative fraction of mechanism 2 in the total current increases. Physically, this reasoning can be explained by means of the fourth stage in the reaction sequence of both postulated mechanisms. In mechanism 1, the adsorbed O^- particles react with each other (Equation 4.11) while in mechanism 2 these particles react with fresh hydrogen peroxide (Equation 4.13). Therefore it is logical that, with an increasing hydrogen peroxide concentration, more O^- particles will react with hydrogen peroxide, resulting in an increase of the fraction of mechanism 2 in the total current.

In order to quantify this effect of a shifting relative contribution of mechanisms 1 and 2 as a function of the hydrogen peroxide concentration, a factor, x, is introduced. This factor depends only on the hydrogen peroxide concentration and is equated to 1 if only mechanism 1 would occur and is equated to zero if only mechanism 2 would occur. By means of this parameter, x, it appears possible to combine Equation 4.49 with Equation 4.52 and to transform it into the same relation.

$$I = nFA{K_1}^{(1/2x+1/2)}{K_2}^{(1/2x+1/2)}{K_3}^{(1/2x+1/2)}{K_4''}^{(1-x)}{K_4''}^{x}{K_5''}^{(1-x)}$$
$$c_{HO_2^-}{}^{(3/2-1/2x)}c_{OH^-}{}^{(3/2x-1/2)}(1-\theta_{O^-})^{2x}(1-\theta_{O_2^-})e^{0.5\frac{F}{RT}(E-E_{ref})} \qquad [4.55]$$

or:

$$\log I = \log G(x,E) + (3/2 - 1/2x)\log c_{HO_2^-} + (3/2x - 1/2)\log c_{OH^-} \qquad [4.56]$$

In the parameter G, all factors are incorporated from the right-hand part of Equation 4.55, except for the bulk concentrations of hydrogen peroxide and hydroxyl ions. With $E = 0.45$ V vs. SCE, the parameter is defined as G′.

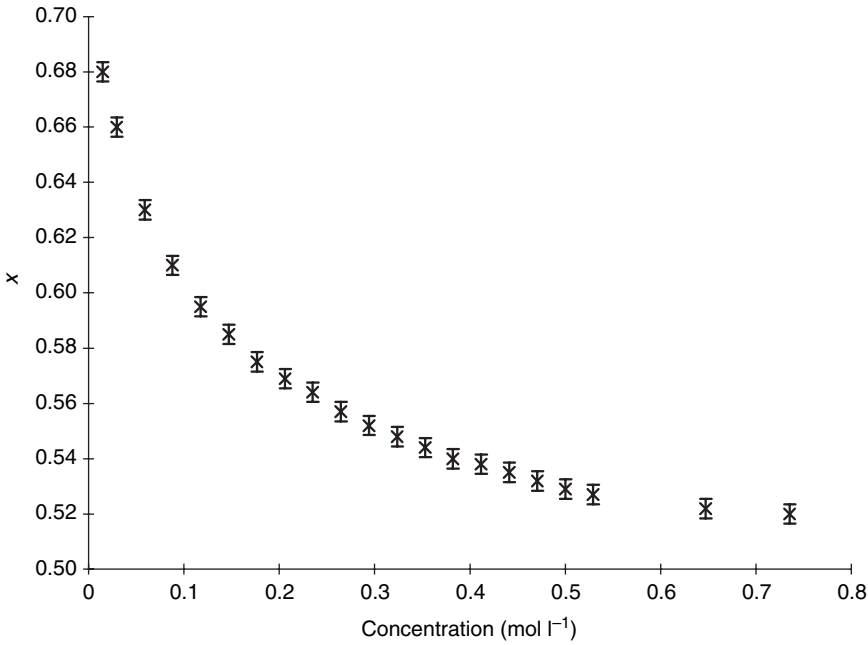

4.11 Relation between the factor x and the hydrogen peroxide concentration valid for the mechanism pair described in sections 4.6 and 4.7; $E = 0.45\,V$ vs. SCE.

In order to check this theoretically predicted current with the experimentally observed currents, it is necessary to know the relation between x and the hydrogen peroxide concentration. Since the value of x depends exclusively on the latter and not on the pH, it can be determined for every desired concentration by measuring the amperometric current with a number of different OH^- concentrations and setting log I vs. pH. For $E = 0.45\,V$ vs. SCE, the relation of Equation 4.56 is shown in Fig. 4.9 and Fig. 4.10 with, *in abscissa*, the logarithm of either concentration as a variable, for a selected number of constant values of the other concentration. From the inclination of the straight lines in Fig. 4.9, it is possible to determine x. This was applied at 21 different hydrogen peroxide concentrations situated between 2.45×10^{-2} and $0.74\,mol\,l^{-1}$ and the resulting x values are shown in Fig. 4.11. In the examined hydrogen peroxide concentration area ($2.45\times10^{-2}-0.74\,mol\,l^{-1}$) x appears to vary between ca. 0.52 and 0.68.

It is indirectly clear from Fig. 4.11 as to why it was necessary to search for a relatively long time for a mechanism pair which can explain the experimental evidence. The first mechanism pair, where x equals zero, does not correspond with an experimentally accessible situation, since it applies only within existing very high hydrogen peroxide concentrations. The second

mechanism, where $x = 1$, can correspond exclusively to the situation of an extremely low hydrogen peroxide concentration, which is in practice also unreal, because the electrode signals for concentrations smaller than ca. 1×10^{-4} mol l^{-1} become very small and unmeasurable owing to disturbing factors such as capacitive current, presence of impurities or noise.

Plotting the data presented in Fig. 4.11 in a logarithmic way results in a linear relation; from this, it is possible to deduce the following relation between x and the hydrogen peroxide concentration:

$$x = 0.5071 c_{HO_2^-}^{-0.0791} \quad [4.57]$$

As appears from Equation 4.55, in the factor G of Equation 4.56, the product of a number of equilibrium constants and reaction-rate constants is elevated to a power in which x occurs. The values of these constants are not known, so that G can be determined only experimentally. Figure 4.12 represents the relation between G' and the hydrogen peroxide concentration with a working electrode potential of 0.45 V vs. SCE, where G' was obtained by using Equation 4.56 from current data for a number of selected hydrogen peroxide concentrations where pH and x are known. From a combination of the data of Fig. 4.11 and Fig. 4.12, the relation between G' and x follows, with $E = 0.45$ V vs. SCE, represented in Fig. 4.13. In general, this relation can be written as follows:

$$G' = 9.3 \times 10^5 x^{6.607} \quad [4.58]$$

Equations 4.55 and 4.56, combined with the knowledge of the relations between G' and x, respectively, and the hydrogen peroxide concentration,

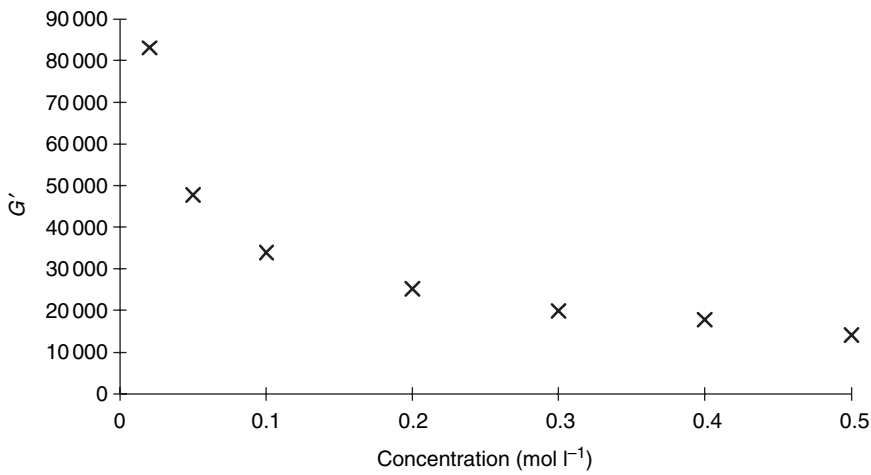

4.12 Relation between the factor G and the hydrogen peroxide concentration; $E = 0.45$ V vs. SCE.

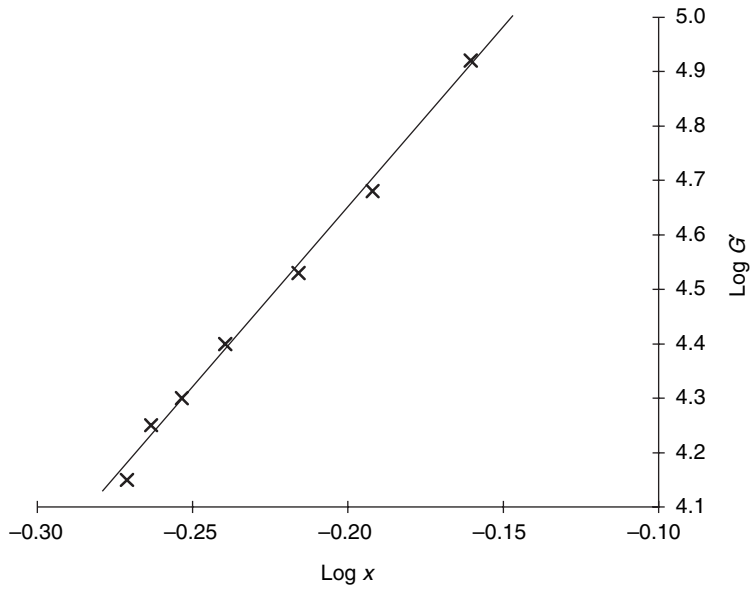

4.13 Logarithmically set relation between the factors G and x; $E = 0.45$ V vs. SCE.

make it possible to clarify the experimental relations represented in Figs 4.7–4.10 in a qualitative way. Since G' and x both depend on the hydrogen peroxide concentration, the linearly or logarithmically set calibration curves (Fig. 4.7 and Fig. 4.10) are bent with all the pH values. The significant influence of the pH itself follows immediately from Equations 4.55 and 4.56, as well as the fact that this influence varies with the hydrogen peroxide concentration, once again because of the dependency of G' and x on this concentration.

From what precedes, it appears that the postulated reaction-mechanism pair can explain all the experimentally observed relations. This was repeatedly verified in the course of further research work, in which, as will appear in the following chapter, many experiments were carried out in the framework of the industrial realisation of a hydrogen peroxide sensor which is based on the reaction described in this chapter. In the unified current relation (Equation 4.55), the factor x is a key element. Hence, the relation between x and the hydrogen peroxide concentration was determined again in three additional, mutually independent series of experiments with a limited number of hydrogen peroxide concentrations. By using average x values, the relation between the theoretically predicted and the experimental current course was again repeatedly verified in the further research. From this, it can be concluded that the postulated model in which two

mechanisms are combined applies and is able to explain the experimentally obtained evidence.

As was done earlier for the pseudo-limiting-current area, unified relations can be derived for the potential area in the steeper ascending part of the prewave. Since this derivation is highly analogous to the above-mentioned treatment, it will not be repeated here. It appears that the conclusions are analogous, and that only the numerical values of factor G are different. With the knowledge of the mechanism and its rate equation, one can start with the development of an analytical method. This will be explained in detail in Chapter 5.

4.10 References

1. Weigert W.M., *Chem. Ztg.*, **99** (1975) 106.
2. Interox Chemicals, *FR Patent 2 379 519* (1978).
3. Degussa, *US Patent 4 137 242* (1978).
4. Bayer A.G., *BE Patent 841 208* (1978).
5. Olin Corp., *GB Patent 1 520 821* (1978).
6. Degussa, *GE Patent 2 511 432* (1975).
7. Ebara-Infilco Co., *JP Patent 76 35 672* (1976).
8. Fuji Sekiyu K.K., *JP Patent 75 8 369* (1975).
9. Knorre H., *Galvanotechnik*, **66** (1975) 374.
10. Weck M., *Textil Praxis International*, **53** (1991) 144.
11. Rösch G., *Textil Praxis International* (1988) 384.
12. Ney W., *Textil Praxis International* (1974) 1392.
13. Wurster P., *Textilveredlung*, **22** (1987) 230.
14. Dannacher J., Schlenker W., *Textilveredlung*, **25** (1990) 205.
15. Schliefer K., Heidemann G., *Melliand Textilberichte*, **70** (1989) 856.
16. Ney P., *Textil Praxis International*, **11** (1974) 1552.
17. Henkel GmbH, DIN-Sicherheitsdatenblatt 003167 DE (1988) 1.
18. Henkel GmbH, DIN-Sicherheitsdatenblatt 001251 DE (1987) 1.
19. Henkel GmbH, DIN-Sicherheitsdatenblatt 005901 DE (1989) 1.
20. Schumb W.C., Satterfield C.N., Wentworth R.L., *Hydrogen Peroxide*, Reinhold, New York, 1955.
21. Oehme F., Laube K., *Melliand Textilberichte*, **46** (1965) 616.
22. Laube K., Zollinger H., *Melliand Textilberichte*, **46** (1965) 727.
23. Jola M., *Melliand Textilberichte*, **61** (1980) 931.
24. Eisele J., Hafenrichter S., *Melliand Textilberichte*, **25** (1954) 756.
25. Brugman Machinefabriek, *Bleach-O-Matic Product Bulletin*, Almelo, Nederland, 1993.
26. Knittel D., Wei Q., Schollmeyer E., *Fresenius J. Anal. Chem.*, **348** (1994) 820.
27. Prominent, *PEROX 20*, *www.H2O2.com*, 1998.
28. Damjanovic A., Gensher M.A., Bockris J. O'M., *J. Phys. Chem.*, **70** (1966) 3761.
29. Vitvitskaya G.V., Strakhova V.V., *Elektrokhimiya*, **7** (1971) 1361.
30. Bowen R.J., Urbach H.B., *J. Chem. Phys.*, **49** (1968) 1206.
31. Urbach H.B., Bowen R.J., *Electrochimica Acta*, **14** (1969) 927.

32. Prabhu V.G., Zarapkar L.R., Dhaneshwar R.G., *Electrochimica Acta*, **26** (1981) 725.
33. Pletcher D., Sotiropoulos S., *J. Electroanal. Chem.*, **356** (1993) 109.
34. Chang C., Wen T., Tien H., *Electrochimica Acta*, **42** (1997) 557.
35. Jacq J., Bloch O., *Electrochimica Acta*, **9** (1964) 551.
36. Strbac S., Adzic R.R., *J. Electroanal. Chem.*, **337** (1992) 355.
37. Wu B., Lei H., Cha C., Chen Y., *J. Electroanal. Chem.*, **377** (1994) 227.
38. Merkulova N.D., Zhutaeva G.V., Shumilova N.A., Bagotzky V.S., *Electrochimica Acta*, **18** (1973) 169.
39. Brezina M., *Berichte der Bunsen-gesellschaft*, **77** (1973) 849.
40. Bianchi G., Caprioglio G., Mazza F., Mussini T., *Electrochimica Acta*, **4** (1961) 232.
41. Hurlen T., Sandler Y.L., Pantier E.A., *Electrochimica Acta*, **11** (1966) 1463.
42. Iwakura C., Matsuda Y., Tamura H., *Electrochimica Acta*, **16** (1971) 471.
43. Brezina W., Koryta J., Musilova M., *Coll. Czech. Chem. Comm.*, **33** (1968) 3397.
44. Yeager E., Krouse P., Rao K.V., *Electrochimica Acta*, **9** (1964) 1057.
45. Zecevic S., Drazic D.M., Gojkovic S., *Electrochimica Acta*, **36** (1991) 5.
46. Vago E.R., Calvo E.J., *J. Electroanal. Chem.*, **339** (1992) 41.
47. Calvo E.J., Schiffrin D.J., *J. Electroanal. Chem.*, **163** (1984) 257.
48. Lowry J.P., O'Neill R.D., *Anal. Chem.*, **64** (1992) 456.
49. Van Den Meerakker J.E., *Electrochimica Acta*, **35** (1990) 1267.
50. Vazquez M.V., de Sanchez S.R., Calvo E.J., Schiffrin D.J., *J. Electroanal. Chem.*, **374** (1994) 179.
51. Jianzhong Z., Xiaohui L., Jiali W., Deren L., Guoxiong Z., *Fres. J. Anal. Chem.*, **348** (1994) 277.
52. Sepa D.B., Vojnovic M.V., Damjanovic A., *Electrochimica Acta*, **26** (1981) 781.
53. Linek V., Benes P., Vacek V., *J. Electroanal. Chem.*, **169** (1984) 233.
54. Damjanovic A., Dey A., Bockris J. O'M., *Electrochimica Acta*, **11** (1966) 791.
55. Damjanovic A., 'Progress in the studies of oxygen reduction during the last thirty years' in Murphy O.J., Srinivasan S., Conway B.E. (eds), *Electrochemistry in Transition*, Plenum Press, New York and London, 1992.
56. Appleby A., *J. Electroanal. Chem.*, **357** (1993) 117–179.
57. Mukerjec S., Srinivasan S., *J. Electroanal. Chem.*, **357** (1993) 201.
58. Hall S.B., Khudaish E.A., Hart A.L., *Electrochimica Acta*, **43** (1998) 579.
59. Zhang Y., Wilson G.S., *J. Electroanal. Chem.*, **345** (1993) 253.
60. Gojkovic S.L., Zecevic S.K., Drazic D.M., *Electrochimica Acta*, **37** (1992) 1845.
61. Honda M., Kodera T., Kita H., *Electrochimica Acta*, **28** (1983) 727.
62. Koryta J., Brezina M., Kriz N., *Rev. Roumaine Chim.*, **17** (1972) 171.
63. Bianchi G., Mazza F., Mussini T., *Electrochimica Acta*, **7** (1962) 457.
64. Tarasevich N.R., Radyushkina K.A., *Elektrokhimiya*, **6** (1970) 376.
65. Sheblovinskii V.M., Kicheev A.G., Yanchuk B.N., *Elektrokhimiya*, **15** (1979) 1279.
66. Yang Y., Tseung A.C., Lin Z.G., *J. Electroanal. Chem.*, **370** (1994) 159.
67. Sousa J.P., *J. Electroanal. Chem.*, **372** (1994) 151.
68. Kanungo S.B., Parida K.M., Sant B.R., *Electrochimica Acta*, **26** (1981) 1157.
69. Koper M.T., Meulenkamp E.A., Vanmaekelbergh D., *J. Phys. Chem.*, **97** (1993) 7337.
70. Ferrer I.J., Muraki H., Salvador P., *J. Phys. Chem.*, **90** (1986) 2805.

71. Scribner L.L., Taylor S.R., *The Measurement and Correction of Electrolyte resistance in Electrochemical Tests*, ASTM Publication, STP 1056, Philadelphia, 1990.
72. Bockris J. O'M., Reddy A.K. (eds), *Modern Electrochemistry 2*, Plenum Press, New York, 1970.
73. Legrini O., Oliveros E., Braun A.M., *Chem. Rev.*, **93** (1993) 671.
74. Lunak S., Sedlak P., *J. Photochem. Photobiol. A: Chem.*, **68** (1992) 1.
75. Taube H., *Trans. Faraday Soc.*, **53** (1957) 656.
76. Eckenfelder W.W., Bowers A.R., Roth J.A. (eds), *Chemical Oxidation: Technologies for the Nineties*, Technomic Publishing, Lancaster, 1992.
77. Christensen H., Sehested K., Corfitsen H., *J. Phys. Chem.*, **86** (1982) 1588.
78. Rajeshwar K., Ibanez J.G. (eds), *Environmental Electrochemistry*, Academic Press, New York, 1997.
79. Gall B.L., Dorfman L.M., *J. Am. Chem. Soc.*, **91** (1969) 2199.
80. Bard A.J., Parsons R., Jordan J. (eds), *Standard Potentials in Aqueous Solution*, Marcel Dekker, New York and Basel, 1985.
81. Janata J. (ed.), *Principles of Chemical Sensors*, Plenum Press, New York, 1989.

5

Amperometric detection of hydrogen peroxide in bleaching and washing processes

P. WESTBROEK AND P. KIEKENS

5.1 Introduction

In this chapter, the development of an amperometric sensor will be explained and discussed. The principle of the analysis method will be based on the results described in Chapter 4; this means that use will be made of the oxidation reaction of hydrogen peroxide in the prewave, and that the concentration will be determined using the rate equation. In addition to measurement of the electrical current response, temperature and pH will therefore also be measured. Accordingly, it is interesting to start with an investigation of the temperature influence.

5.2 Influence of temperature

5.2.1 Introduction

All the experimental results and the derived data obtained in the previous sections apply with a temperature of 298.0 K. Since the temperature in bleaching processes can vary considerably (working temperature of ca. 288–323 K), it is necessary to verify the way in which the electrode signal depends on the temperature.

Most factors in parameter G (Chapter 4, Equations 4.55 and 4.56) and the potential of the reference electrode are temperature-dependent; this is possibly also the case for factor x. Equation 4.56 also represents the concentration of the hydroxide ion. This means that a potential sensor based on the prewave will also have to contain a pH sensor. The hydroxide ion concentration derived from the output signal of this additional sensor needs to be introduced in the algorithm for the calculation of the hydrogen peroxide concentration. As an additional sensor, a glass electrode is an obvious choice, with a temperature-dependent potential, which is the case also for the potential of the reference electrode associated with the glass electrode and for the pH of the buffers. In this research work, the influence of

temperature on the current signal in the pseudo-limiting-current plateau was first verified. In prospect of developing a sensor, based on the examined electrode reaction, the influence of the temperature was examined on the measured pH.

5.2.2 Relation between current signal and temperature

Initially it was verified, by recording log I vs. pH relations with different temperatures, whether the reaction order of the hydroxide ions was changing as a function of the temperature. This appeared not to be the case, from which it could be concluded that factor x is independent of temperature. The influence of temperature on the current signal can consequently be found by measuring this current signal with constant hydrogen peroxide concentration and pH at different temperatures. This means that the terms $(3/2–1/2x) \log c_{HO_2^-}$ and $(3/2x–{}^1/_2) \log c_{OH^-}$ in Chapter 4, Equation 4.56 remain almost constant. Experimentally, a linear relation was found between the logarithm of the current signal and the temperature, except for relatively high hydrogen peroxide concentrations in combination with a high pH and temperature (Fig. 5.1). Equation 4.56 can consequently be transformed into:

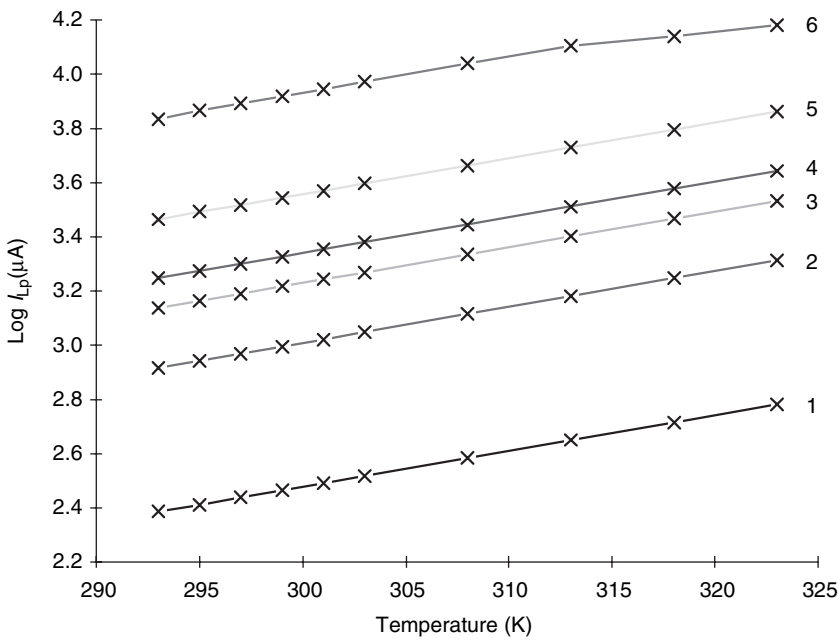

5.1 Relation between the current signal of the oxidation of hydrogen peroxide with a glassy-carbon electrode and the temperature, with E=0.45 V vs. SCE. The hydrogen peroxide concentration and pH are (1) 0.1 mol l^{-1} and 11.0, (2) 0.3 mol l^{-1} and 11.05, (3) 0.1 mol l^{-1} and 12.88, (4) 0.6 mol l^{-1} and 10.97, (5) 0.3 mol l^{-1} and 12.74, (6) 0.6 mol l^{-1} and 12.98, respectively.

$$\log I_{Lp} = \log G' + (3/2 - 1/2x)\log c_{HO_2^-} + (3/2x - 1/2)\log c_{OH^-} + 0.013\,24T \quad [5.1]$$

or after anti-logarithming:

$$I_{Lp} = G' c_{HO_2^-}^{(3/2-1/2x)} c_{OH^-}^{(3/2x-1/2)} e^{0.03049T} \quad [5.2]$$

5.3 Behaviour of the sensor electrode at the laboratory scale

5.3.1 Influence of bleaching additives on the current signal

Introduction

In the previous sections, the investigated solutions contained only sodium hydroxide and hydrogen peroxide. Apart from these basic ingredients, industrial bleaching baths also contain a number of commercial 'additives' (in reality, mainly mixtures of several active components, see Chapter 4, section 4.2.) aiming at optimisation of the bleaching process. It is evident that these additives can also contribute to the voltammetric behaviour of hydrogen peroxide. Hence, it is clearly necessary to investigate in the next stage the influence of additives on the prewave of the oxidation of hydrogen peroxide with glassy carbon and to examine the implications on the possible development of a sensor for the pseudo-limiting-current of the prewave.

The role that each of the different classes of bleaching additives plays was elaborated in Chapter 4, section 4.2. Considering the wide variety of additives, and classes of additive, available on the world market, and in order to be able to control the number of variable parameters in the planned research work, it was necessary to make a selective choice between the numerous commercially available products. Therefore it was decided to use products from Henkel, with at least one representative from each class of additives. These are tensio-active agents in Cottoclarin® SV, Cottoclarin® BF and Seclarin® 540; auxiliary stabilisers in Stabilol® K and Stabilol® HN; and de-aeraters and de-foamers in Defindol® E. For reasons of control, a limited number of additives from Sandoz were also investigated – notably Sandopan with tensio-active agents and auxiliary stabilisers and Sandozin with de-aeraters and de-foamers. By means of tests in different companies, with products from several other manufacturers of additives and under different working conditions[1], it can be shown that a generalisation of the results obtained with the Henkel and Sandoz additives is appropriate. The choice of additives from Henkel and Sandoz was based on the fact that

these products were used in two companies with which agreements had been made to perform experiments in an industrial environment. Apart from the commercial additive mixtures, the generally used products, such as water glass, magnesium sulphate and sodium persulphate were also studied as single substances.

Each selected additive was investigated in the presence and absence of hydrogen peroxide. Based on these experiments, it was verified as to whether or not the additive has electroactive properties and whether it interferes with the hydrogen peroxide signal, which can be possible in an electrochemical way or through another route. Once the behaviour of the different groups of additives is known, they are combined into real bleaching solutions, where, once again, a number of experiments are performed for reasons of control. In these, it is not only the concentration of the additives that is varied but also the hydrogen peroxide concentration and the pH. The aim is to verify whether the sensor works correctly, whether a possibly occurring interference was intercepted and/or eliminated in an appropriate way, and whether Equation 5.2, obtained in absence of additives, needs to be adapted.

Inorganic additives

Sodium hydroxide is the most important inorganic additive in solution, not only to obtain optimal bleaching effects but also because this particle is pH-determining and the latter parameter strongly influences the current signal. This interference, which was thoroughly investigated in the absence of other additives (as was described in the previous sections of this chapter), appears not to be influenced by the presence of these other additives. Consequently, the influence of the sodium hydroxide concentration as is represented in Equation 5.2 is still valid. Besides an activator (sodium hydroxide), a stabiliser is also required, as is indicated in Chapter 4, section 4.2.2. To this end, mainly $MgSO_4$ in combination with water glass is used. These components do not appear to have electroactive properties in the studied potential area, and do not perceptibly influence the hydrogen peroxide signal.

Sodium persulphate (desizing agent) does, however, appear to have electroactive properties. However, these are manifested only in the sensor not the relevant reduction region. In an oxidation region, sodium persulphate behaves indifferently. It does not display electroactive properties, and it does not influence the hydrogen peroxide signal in a non-electrochemical way either. It can be concluded that the inorganic additives do not interfere with the electrode signal originating from the hydrogen peroxide oxidation reaction, with the exception of sodium hydroxide. Considering the importance of this reagent in the bleaching process, its influence was thor-

oughly investigated and incorporated in the relation for the pseudo-limiting-current of the prewave (Equation 5.2).

Organic additives

Organic additives, as described in Chapter 4, section 4.2, are divided into classes according to their role in the bleaching process. Several additives per class were investigated, and the first type of organic additive to be studied was the class of complexing agents. Complexing agents cause the inactivation of metal ions and prevent the associated damage of the catalyst. Although these additives did not appear to have electroactive properties, they do interfere in the potential area of the prewave with the hydrogen peroxide signal by drastically lowering the pseudo-limiting-current. This presumably means that adsorption occurs of one or more components of the additives at the glassy-carbon surface, leading to a decrease of the free surface and a lowering of the current. To verify whether this effect is connected with the nature of the electroactive component, it was examined whether the additives also influence the reaction of components other than hydrogen peroxide. Experiments based on the hexacyano ferrate system ($K_4[Fe(CN)_6]/K_3[Fe(CN_6)]$), displayed an identical signal-lowering effect both for the oxidation reaction and the reduction reaction. This leads us to conclude that the current-lowering effect of this class of additives is very likely to be ascribed to a decrease of the active free surface of the working electrode.

Characteristic for the commercial complexing agents investigated in this work is the fact that the maximum current-lowering effect is already attained in the presence of additive concentrations that are much lower than those used in practice, and this is illustrated in Fig. 5.2. The manufacturers of the additive mixtures all refused to communicate the identity and concentration of the complexing agent in the mixtures. In the case of what is here called in short ‘adsorption of an additive’, it most likely concerns complex adsorption equilibria, where synergist effects between the different components can play a part.

The fact that the electrode surface is not completely blocked by adsorption of complexing agent can be explained by means of the hypothesis of sterical hindrance: the complexing agents are relatively large organic molecules, and substances that are already adsorbed can prevent further adsorption. Smaller components, e.g. hydrogen peroxide, can still penetrate through the adsorbed layer towards the surface of the electrode. To verify this hypothesis, it was checked how the oxidation of a larger molecule, notably an indanthrene dye, is influenced by the presence of complexing agents. The relatively low complexing agent concentration, which is enough to obtain the maximum current-lowering effect on the hydrogen peroxide

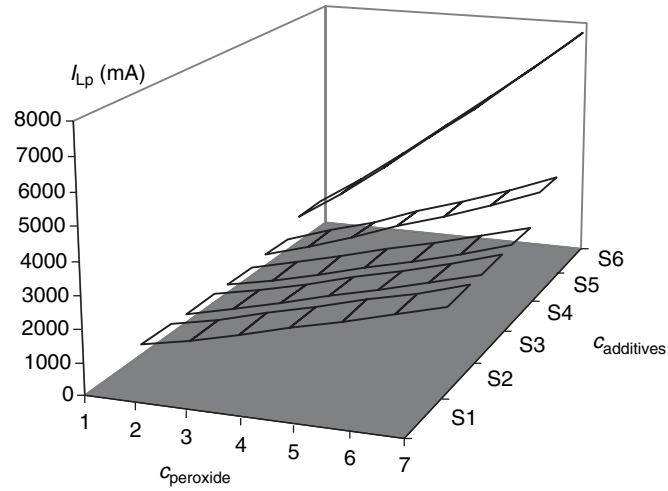

5.2 Influence of increasing concentration of complexing agent Cottoclarin® SV (Henkel) on the current signal of the glassy-carbon electrode onto which hydrogen peroxide is oxidised, with $E = 0.45$ V vs. Ag|AgCl. Hydrogen peroxide concentration increased from 0 mol l^{-1} (series 1) to 0.8 mol l^{-1} (series 7); additive concentration in series S6 is 100 times lower than the lowest concentrations used in bleaching processes; additive concentration in series S2 corresponds to the minimally used concentration in bleaching processes.

prewave, causes complete disappearance of the oxidation/reduction peak of the indanthrene dye. This leads to the conclusion that sterical hindrance of adsorbed complexing agent additives is responsible for the fact that the working electrode surface is still accessible, in a limited way, by relatively smaller molecules, such as hydrogen peroxide.

The adsorption of the additive at the electrode surface is achieved quickly, since after adding an additive to a solution that contains hydrogen peroxide, the signal almost immediately decreases and a new stable condition occurs after a few seconds (Fig. 5.3). The adsorption leading to maximal shielding of the electrode surface is reached in a few seconds with an additive concentration that is 100 times lower than the minimal concentrations used in bleaching processes. An important consequence is that the signal-lowering effect is constant during the bleaching process, even if the additive concentrations vary.

A second and third class of additive are the de-foamers and de-aerators, respectively, which are always integrated together in one commercial product. They also display a current-lowering effect, which strongly resembles that of the complex formers. Here as well, the effect occurs quickly and already reaches a maximum with extremely low additive concentrations. Everything indicates that here steric hindrance is also responsible for not

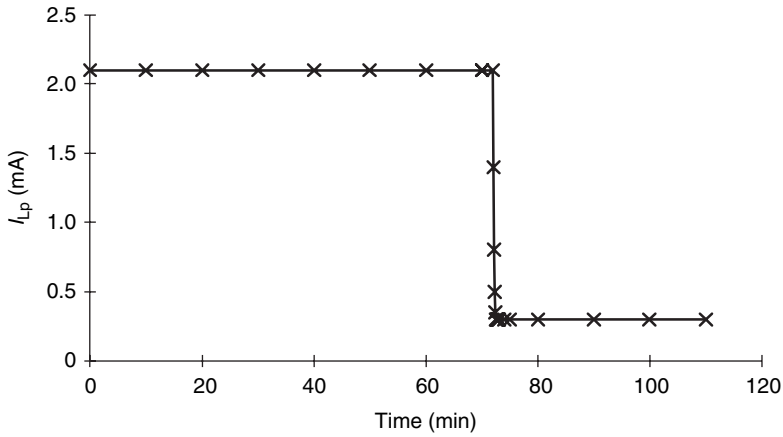

5.3 Signal-lowering effect of complexing agents in organic bleach additives added to the solution 72 min after the start of the current measurement; solution contains 0.4 mol l^{-1} H_2O_2, pH = 12.14 and T = 298.0 K.

completely blocking the electrode surface. Furthermore, the mechanism of oxidation of hydrogen peroxide in the prewave appears to remain unaltered. Finally, the stabilisers, which partially take over the role of water glass, do not appear to interfere perceptibly with the electrode signal.

Combination of additives

With the exception of the stabilisers, all organic additives that were tested manifest an interference that is ascribed to adsorption phenomena at the electrode surface. Whereas synergist effects within one additive cannot be tested because of the unknown composition, it becomes possible when more additives are brought together.

In the next experiment, in an alkaline solution containing hydrogen peroxide, the pseudo-limiting-current of the prewave was measured before and after adding the complexing agent mixture (Cottoclarin® SV). Subsequently, the de-foamer and de-aerater Defindol® E was added and the current measured again. As can be deduced from Fig. 5.4, the addition of Defindol® E does not seem to have an influence on the signal.

This indicates that no synergist effects occur with regard to the pseudo-limiting-current of the prewave of hydrogen peroxide. To verify that the wrong conclusions had not been drawn because of slow setting in adsorption equilibria, the experiment was repeated, adding both additives in reverse direction. Hence, in a second experiment, of which the results are also presented in Fig. 5.4, first Defindol® E was added and subsequently

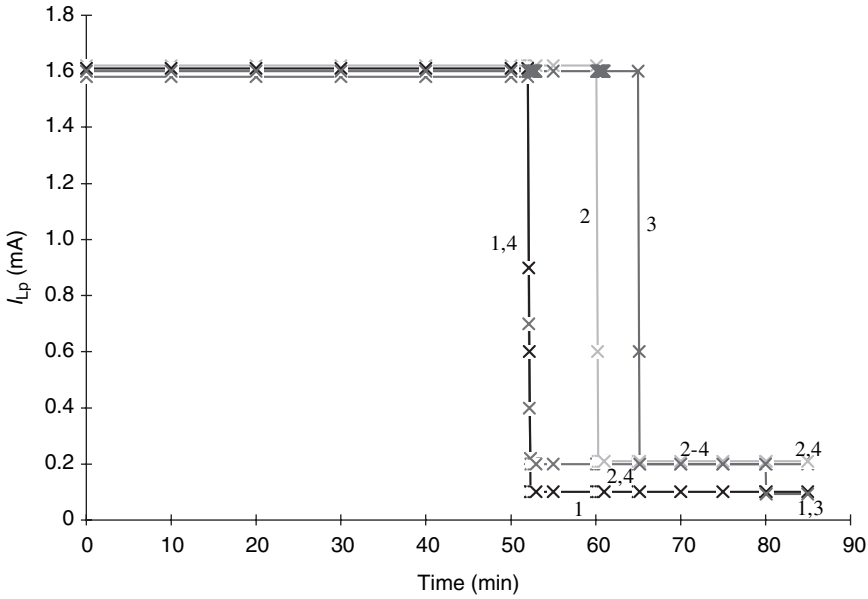

5.4 Effect of the adding order of additives on the pseudo-limiting-current. (1) Addition of Cottoclarin® SV after 52 min and Defindol® E after 75 min; (2) addition of Defindol® E after 60 min and Cottoclarin® SV after 75 min; (3) addition of Cottoclarin® BF after 65 min and Defindol® E after 80 min; (4) addition of Defindol® E after 52 min and Cottoclarin® BF after 82 min.

Cottoclarin® SV. As can be observed in Fig. 5.4, the final value of the current is the same as in the first experiment.

A similar experiment was carried out with Cottoclarin® BF instead of Cottoclarin® SV. The manufacturer of the additives does not report anything concerning the differences in composition, only that the former is more suitable for applications with higher temperatures. The result is also represented in Fig. 5.4. Cottoclarin® SV manifests a slightly stronger current-lowering effect than its BF variant, where the current also does not vary any further when Defindol® E is added as a second additive. When adding in reverse order, the current is lowered when adding Cottoclarin® BF to the solution that contains Defindol® E, notably to the level obtained in the presence of only Cottoclarin® BF.

From this, it can be concluded that the adsorption equilibria occur quickly. However, the pseudo-limiting-current of the prewave of hydrogen peroxide is not further influenced by the addition of a second additive to a solution that already contains an additive, unless the most recently added additive mixture contains components with a stronger current-lowering effect than the first.

Amperometric determination of hydrogen peroxide in the presence of additives

An important question is whether the above-mentioned influence of additives on the pseudo-limiting-current could jeopardise the use of the prewave of the oxidation of hydrogen peroxide with glassy carbon for analytical purposes. To investigate this, a number of experiments with varying hydrogen peroxide concentrations and pH, which have already been performed in the absence of additives, were carried out again in their presence. The results indicated that the reaction orders of the reagents involved and the oxidation mechanism in the prewave remained the same as in the absence of additives. This is an additional argument in favour of the hypothesis that the drastic decrease in current in the presence of additives is due to the decrease of the active surface of the working electrode. In Equation 5.2, the presence of additives is manifested in the decrease of the value of parameter *G*.

In practice, the effect of the additives could easily be overcome by calibrating the sensor in the presence of the additives. This means that the sensor needs to be calibrated in the bleaching solution of the process, which is favourable from an industrial point of view since it is not necessary to remove the sensor from its working environment and no standard solutions need to be made or bought. In the next part, it is explained how this calibration needs to be done.

5.3.2 Calibration of the sensor electrode

To be able to use a sensor in practice, it must always be calibrated. All variable parameters should be known at the time of calibration (in this case, current signal, pH, temperature and hydrogen peroxide concentration) and hence should be measured. The current signal is measured by means of the amperometrical circuit, the pH by means of the glass electrode and the temperature by means of a PT100 thermometer. The hydrogen peroxide concentration needs to be determined by means of an independent method, e.g. titration of a sample of the bleaching solution on potassium permanganate in an acidic medium. In the event that the mutual relations between these variable parameters are known (which is the case in this system and is translated in Equation 5.2), it is possible for every other sample to calculate the unknown hydrogen peroxide concentration after measurement of the amperometrical current, temperature and pH. Based on Equation 5.2, formulated for the conditions where the calibration (Equation 5.3) and the measurement (Equation 5.4) occur, respectively, a general deduction can be made for the measurement of the hydrogen peroxide concentration, represented in Equation 5.5:

$$I_{\text{cal}} = G_{\text{cal}}' c_{\text{HO}_{2,\text{cal}}^-}^{(3/2-1/2x_{\text{cal}})} c_{\text{OH}_{\text{cal}}^-}^{(3/2x_{\text{cal}}-1/2)} \text{e}^{0.03049T_{\text{cal}}} \quad [5.3]$$

$$I_{\text{m}} = G_{\text{m}}' c_{\text{HO}_{2,\text{m}}^-}^{(3/2-1/2x_{\text{m}})} c_{\text{OH}_{\text{m}}^-}^{(3/2x_{\text{m}}-1/2)} \text{e}^{0.03049T_{\text{m}}} \quad [5.4]$$

$$c_{\text{HO}_{2,\text{m}}^-} = \left[c_{\text{HO}_{2,\text{cal}}^-}^{(3/2-1/2x_{\text{cal}})} \frac{I_{\text{m}}}{I_{\text{cal}}} \frac{G_{\text{cal}}'}{G_{\text{m}}'} \frac{c_{\text{OH}_{\text{cal}}^-}^{(3/2x_{\text{cal}}-1/2)}}{c_{\text{OH}_{\text{cal}}^-}^{(3/2x_{\text{m}}-1/2)}} \text{e}^{0.03049(T_{\text{cal}}-T_{\text{m}})} \right]^{1/(3/2-1/2x_{\text{m}})} \quad [5.5]$$

Equation 4.58 in Chapter 4 represents the relationship between the term G' and factor x. Moreover, a relationship was derived between the hydrogen peroxide concentration and factor x, so that by substituting Equation 4.57 in Equation 4.58, a relationship is found for G' in which only the unknown hydrogen peroxide concentration occurs. Substituting the resulting relation in Equation 5.5 leads to:

$$c_{\text{HO}_{2,\text{m}}^-} = \left[c_{\text{HO}_{2,\text{cal}}^-}^{\left[3/2-1/2\left(0.05071 c_{\text{HO}_{2,\text{cal}}^-}^{-0.0791}\right)\right]} \frac{I_{\text{m}}}{I_{\text{cal}}} \frac{\left(c_{\text{HO}_{2,\text{cal}}^-}^{-0.0791}\right)^{6.607}}{\left(c_{\text{HO}_{2,\text{m}}^-}^{-0.0791}\right)^{6.607}} \frac{c_{\text{OH}_{\text{cal}}^-}^{\left[2/3\left(0.05071 c_{\text{HO}_{2,\text{cal}}^-}^{-0.0791}\right)-1/2\right]}}{c_{\text{OH}_{\text{m}}^-}^{\left[3/2\left(0.05071 c_{\text{HO}_{2,\text{m}}^-}^{-0.0791}\right)-1/2\right]}} \text{e}^{0.03049(T_{\text{cal}}-T_{\text{m}})} \right]^{1/\left[3/2-1/2\left(0.05071 c_{\text{HO}_{2,\text{m}}^-}^{-0.0791}\right)\right]} \quad [5.6]$$

Since the missing hydrogen peroxide concentration cannot be isolated from this in a simple way, iteration procedures are used in the sensor algorithm, in which the unknown hydrogen peroxide concentration at first is equated with the value at calibration. After calculating and comparing the left-hand and right-hand parts, it is possible to check whether the introduced concentration needs to be adapted for a subsequent calculation or sufficiently approximates the correct concentration.

In a limited number of experiments, in which six different hydrogen peroxide concentrations were examined with four different pH values, the validity of the procedure used was checked by comparing the results obtained with the sensor electrode to those obtained by means of titration. The results obtained with the sensor electrode have a maximum divergence of 3% compared with the concentrations obtained by titration. The final aspect of the amperometrical detection method that was examined at laboratory scale is the stability in time of a calibrated sensor electrode.

5.3.3 Stability of the sensor electrode in time

In this part of the research work, the stability was checked of the amperometric signal of a calibrated sensor electrode in the presence of additives as a function of time. To this end, during a longer period of time, without re-calibrating the sensor electrode, the amperometric pseudo-limiting-current was measured continuously, and the hydrogen peroxide concentration was periodically determined by means of titration of a sample of the cell solution. In the course of the experiment, the hydrogen peroxide concentration deteriorates by catalytic decomposition, and the concentration was either periodically reduced by means of dilution of the cell solution, or increased by addition of hydrogen peroxide. Two different bleaching solutions were selected that contain products from Henkel and Sandoz as can be seen below.

Bleaching solution 1:

- 20 ml l^{-1} 10 mol l^{-1} NaOH solution
- 50 ml l^{-1} 11 mol l^{-1} H_2O_2 solution
- 15 ml l^{-1} commercial water-glass solution
- 12 ml l^{-1} Cottoclarin® SV (Henkel)
- 1 ml l^{-1} Defindol® E (Henkel)
- 5 g l^{-1} $Na_2S_2O_8$

Bleaching solution 2:

- 20 ml l^{-1} 10 mol l^{-1} NaOH solution
- 50 ml l^{-1} 11 mol l^{-1} H_2O_2 solution
- 12 ml l^{-1} Sandopan® 540 (Sandoz)
- 2 ml l^{-1} Sandozin® (Sandoz)
- 5 g l^{-1} $Na_2S_2O_8$

Some of the results obtained with bleaching solution 1 are represented in Fig. 5.5. The first point of the curve corresponds to the calibration point. It is observed that the concentrations obtained by means of Equation 5.6 (full line) on the one hand and titration on the other (discrete measuring points, represented by small crosses) correspond with each other very well. The deviations are limited to less than 2%, which is sufficient for a possible application as a sensor in industry. During this experiment, water was added at different stages (1–3 on Fig. 5.5) in order to modify pH as well as hydrogen peroxide and additive concentration. In stage 4, the hydrogen peroxide concentration was increased and the pH reduced to its starting value, and Stabilol® K, which serves as auxiliary stabiliser for water glass, was progressively added (spread over stage 5). No interference by this additive was observed. In between the dilutions and additions, the decrease of the hydrogen peroxide concentration is to be ascribed to natural deterioration and,

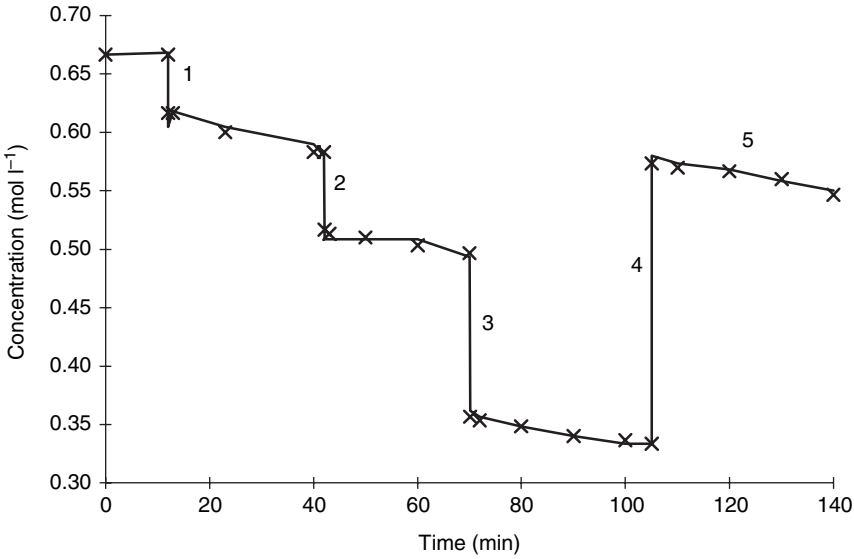

5.5 Amperometric determination of the hydrogen peroxide concentration with a glassy-carbon electrode, with E=0.45 V vs. Ag|AgCl. Hydrogen peroxide concentration obtained by means of Equation 5.6 (fluent line) and by means of titration (crosses); regions 1, 2 and 3: dilutions with water; region 4: addition of hydrogen peroxide; region 5: progressive addition of additive Stabilol® K (Henkel).

moreover, in area 5 by dilution of the solution owing to addition of Stabilol® K. A similar experiment was carried out with bleaching solution 2, which led to similar results. As a consequence, these are not represented here.

5.4 Behaviour of the sensor in an industrial environment

5.4.1 Introduction

In order to use the sensor on an industrial scale, an appropriate housing is needed in which the required electrodes and temperature sensor are positioned in the scientifically and technically most considered and logical way. Additional requirements imply that the system should be robust and offer good protection against blows and/or other possible causes of defects. The system should be easy to handle, electrodes and other components should be straightforward to replace, the calibration of the electrodes should be accomplishable in a quick and particularly simple way, and the system must

conform to the regulations concerning safety. Finally, the data processing aspects and the output panel should be orderly, simple and clear for the workers who are responsible for the good development of the process.

Broadly, the sensor contains, apart from the glassy-carbon working electrode, a reference electrode, a counter electrode, a temperature sensor and a pH glass electrode with associated reference electrode. As to the auxiliary sensor and electrodes, in the experiments on a laboratory scale, described in the previous chapters, types commonly used in research were employed. Here these need to be replaced by types which satisfy the above-mentioned requirements, which are discussed in the next section.

5.4.2 Description of the housing

The concept and design of the sensor configuration received much attention, although it is partially a technical matter. The working electrode, the counter electrode and the reference electrode have to be positioned as close to each other as possible, because the measured current must flow between the working and the counter electrode, and because the electrical resistance between the working and the reference electrode should be kept as low as possible. If the reference electrode were to be positioned too far away, a non-negligible voltage drop occurs, leading to IR-drop or ohmic-drop effects. When the counter electrode is positioned further away, it is easier for stray currents to interfere, something which should be taken into account in industrial installations. For these reasons, it was decided to put the electrodes under an angle of 80° in relation to the pipeline as is schematically represented in Fig. 5.6–5.8.

Furthermore, a choice had to be made with regard to the relative mutual positioning of the electrodes and the temperature sensor in relation to the direction of the liquid current. As the electrodes represent barriers in the fluid current, they influence the convection pattern of electrodes that are situated further downstream. For this reason, it was decided to put the working electrode separately in the most upstream position. Next, the reference and counter electrode are positioned, then finally the temperature sensor and the glass electrode (Fig. 5.6 and Fig. 5.7). The prototype of the housing constructed in the laboratory, the form of which is represented in Fig. 5.6, was manufactured from polypropylene. The electrodes and the sensor were fixed by means of screw thread. Leakage through this thread was avoided by using sealing rings. Finally, some photographs are shown of the sensor system (Fig. 5.9) in order to give an impression of the working conditions of a sensor system in an industrial environment.

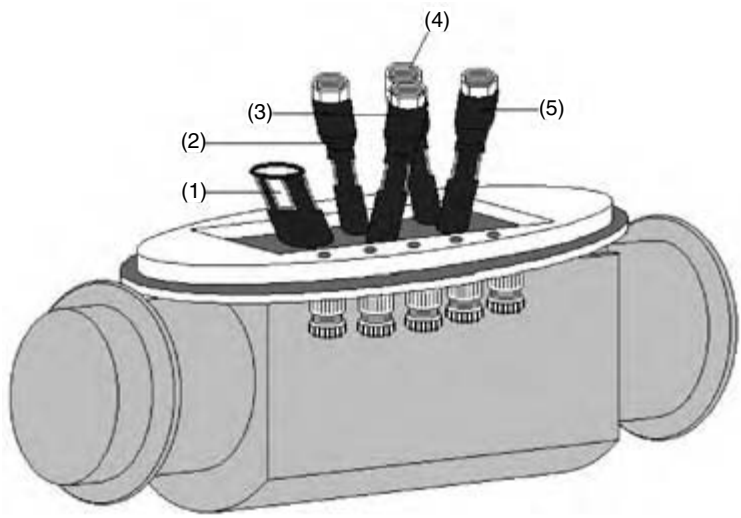

5.6 Schematic representation of the sensor housing. (1) Working electrode, (2) reference electrode, (3) counter electrode, (4) glass electrode with incorporated reference electrode and (5) PT100.

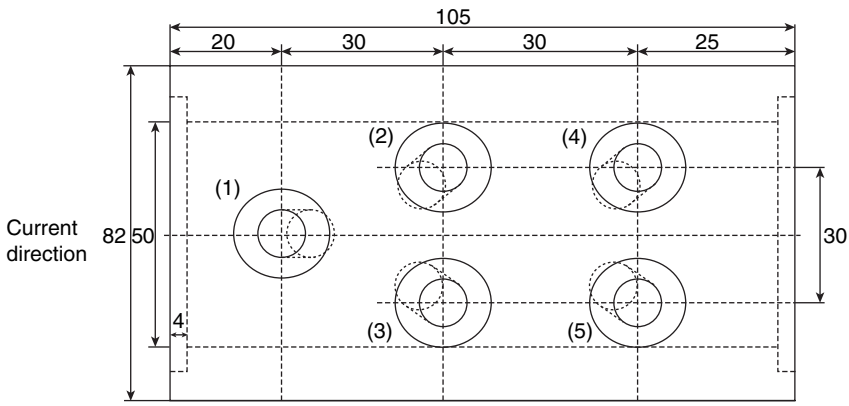

5.7 Top view of the sensor housing. Dimensions are given in mm. (1) Working electrode, (2) reference electrode, (3) counter electrode, (4) glass electrode with incorporated reference electrode and (5) PT100.

5.4.3 Evaluation of the sensor system in an industrial environment

The first tests were performed in machines at two German companies. Chronologically, the first evaluation experiments were carried out in a

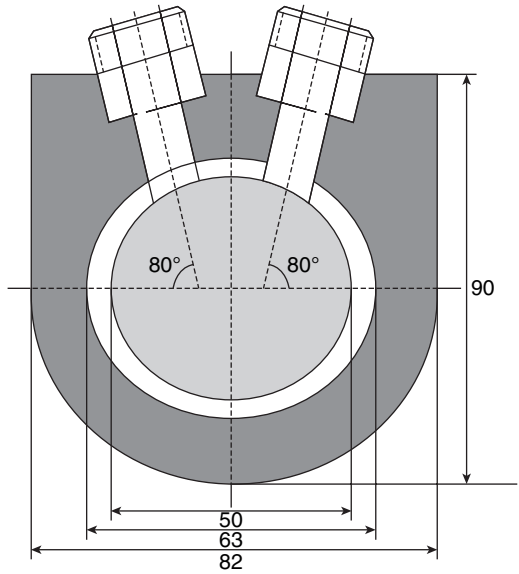

5.8 Cross-section of the sensor housing. Dimensions are given in mm.

company where a maximum bleaching time of 3 h was respected (semi-continuous bleaching activity). The results are presented in Figs 5.10–5.14 and concern five measurement series over a period of 83 days. It is important to note that the sensor was calibrated only once, notably at the first point of the first series of measurements. It must be pointed out that the sensor remained in bleaching solution when no bleaching activity was occurring in the company. Those results are represented in Fig. 5.10 (test 1). Hence, the time axes of Figs 5.11–5.14 are fragments of a continuous time axis. An important condition that needs to be fulfilled to compare the results of the subsequent tests (test 2 to test 5, after 6, 15, 57 and 82 days, respectively), mutually as well as with those of the first test, is that the sensor is continuously maintained in a bleaching solution. It should also be noted that for the control of the bath composition, particularly for determination of the hydrogen peroxide concentration, this company adopts a simple method. Titration is performed occasionally and then the metering pumps are manually operated, where timing of the titrations and the added quantities of reagents are based on experience. It is to be noted here that the titrations indicated in Figs 5.10–5.14 are all analyses that we performed ourselves.

The results given in Figs 5.10–5.13 indicate that wide fluctuations occur in the hydrogen peroxide concentration of the bleaching bath, and that the pattern of the concentration variation changes with the time of the measurements. This suggests a poorly efficient bleaching process; however, it is

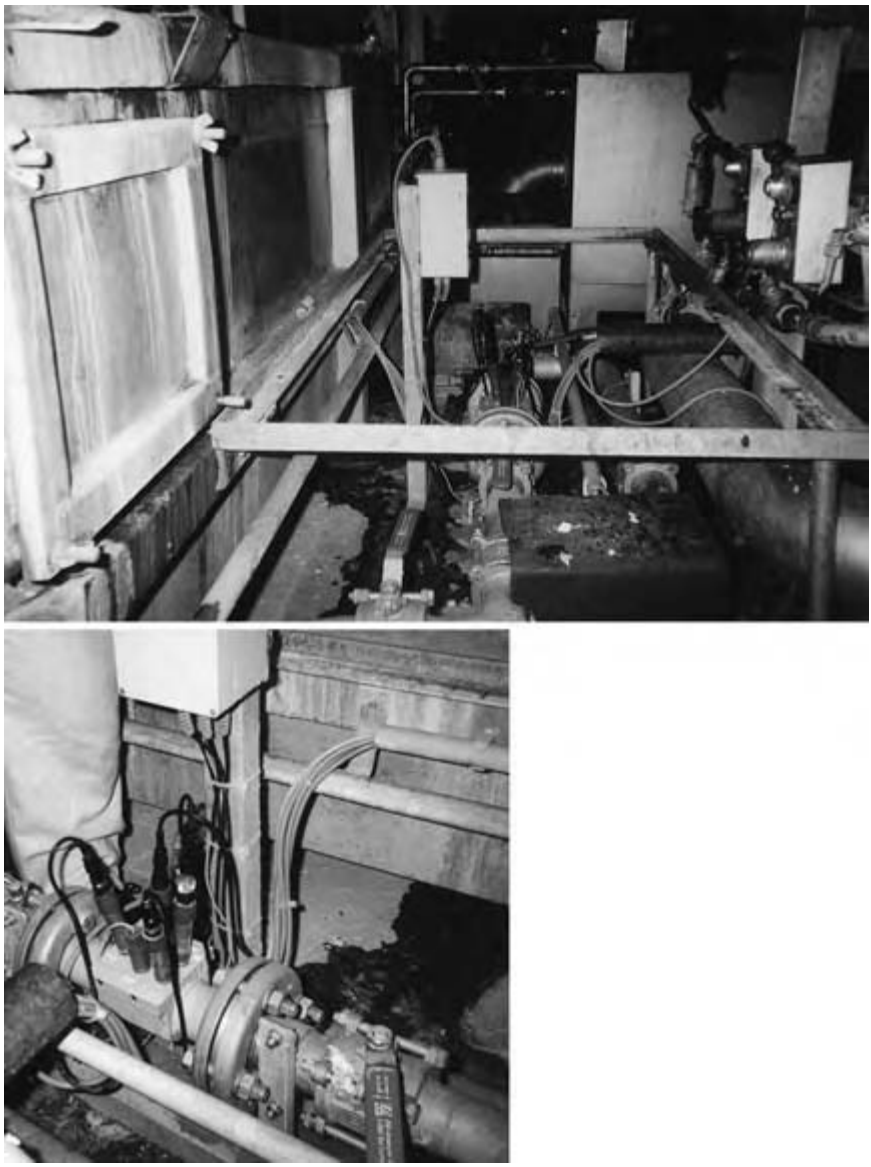

5.9 Photographs of the sensor system.

favourable for the evaluation of the sensor. In all these tests, performed over a period of 82 days, the hydrogen peroxide concentration indicated by the sensor diverges less than 4% from the value obtained by titration. Besides the accuracy, the stability of the sensor is also manifested with time. The fluctuations in the bath that are not under control have an important

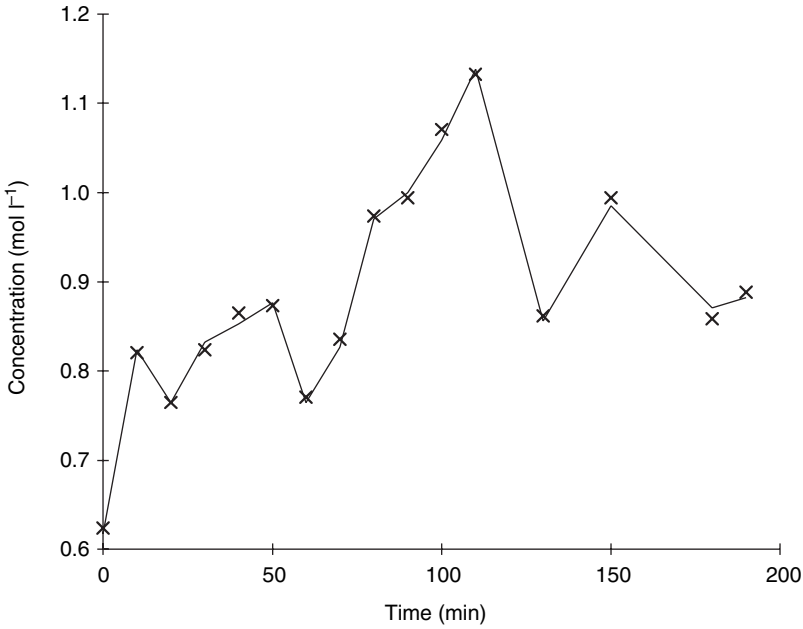

5.10 Test 1, the first point being the calibration point. Concentration obtained through the sensor system (—) and through titration (×).

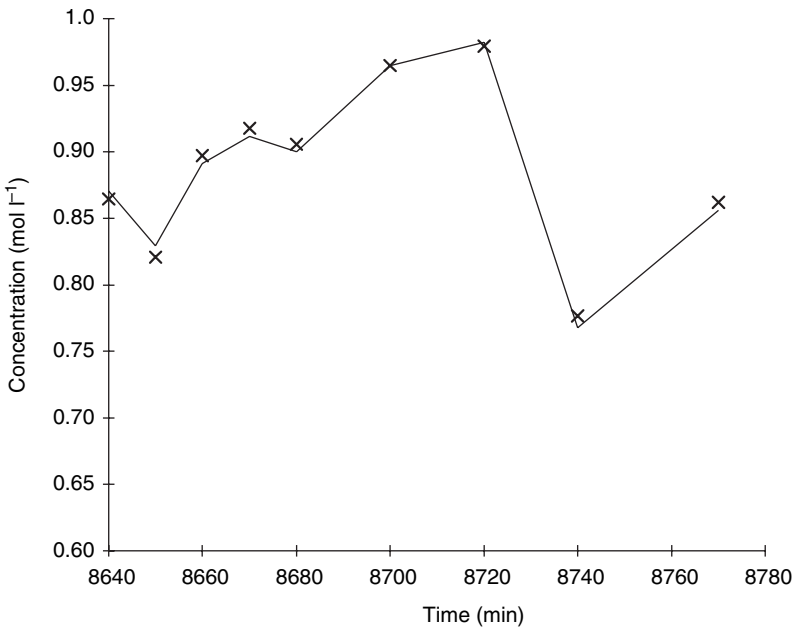

5.11 Test 2 after 6 days. Calibration point is first point of test 1. Concentration obtained through the sensor system (—) and through titration (×).

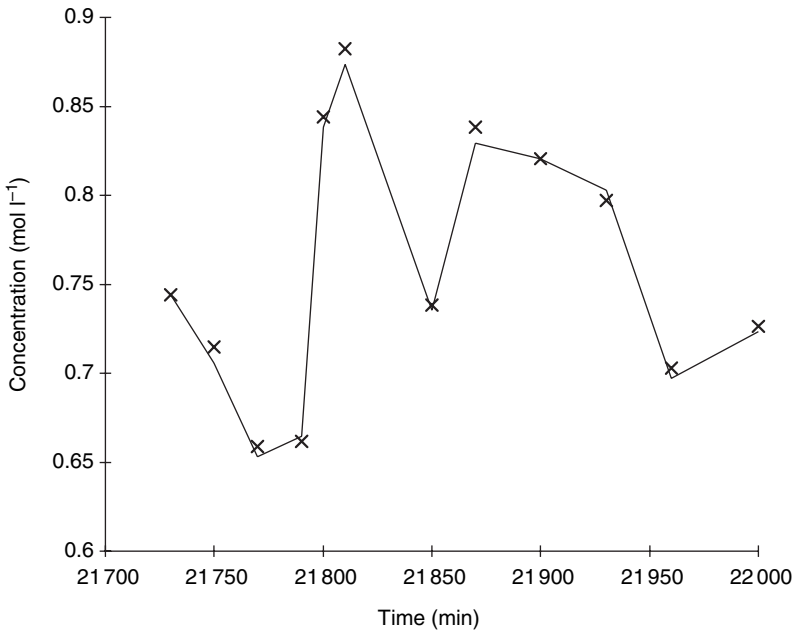

5.12 Test 3 after 15 days. Calibration point is first point of test 1. Concentration obtained through the sensor system (—) and through titration (×).

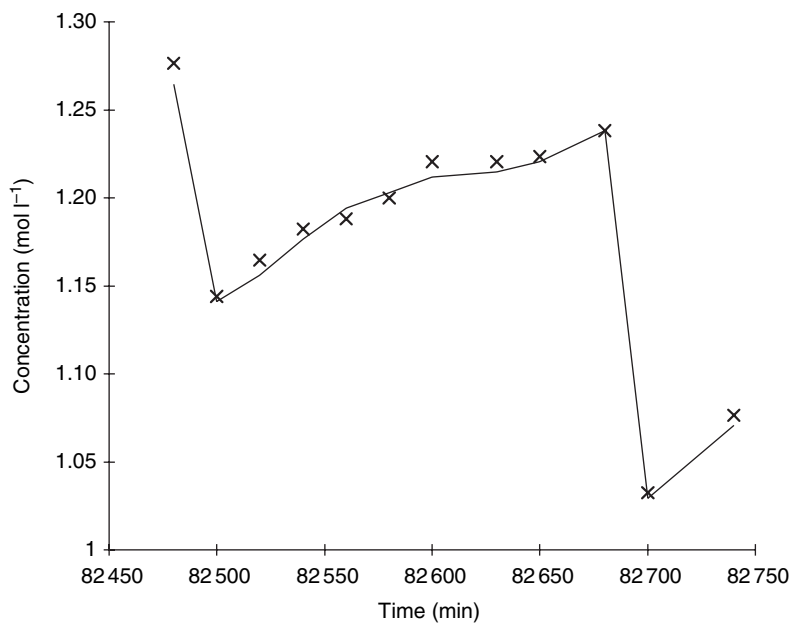

5.13 Test 4 after 57 days. Calibration point is first point of test 1. Concentration obtained through the sensor system (—) and through titration (×).

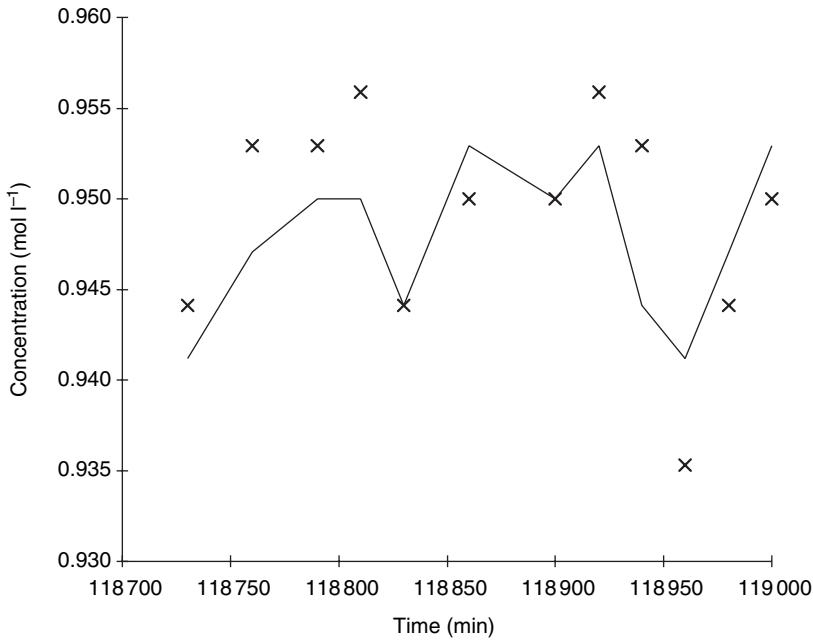

5.14 Test 5 after 82 days. Calibration point is first point of test 1, hydrogen peroxide concentration is measured and controlled. Concentration obtained through the sensor system (—) and through titration (×).

influence on the quality of the bleached product. Already, at this stage of the development, it became clear that a sensor system monitoring the hydrogen peroxide concentration continuously offers significant improvements to the process.

In the fifth and final test, of which the results are shown in Fig. 5.13, the metering pumps (until then manually operated) are coupled to the regulating unit of the sensor system. It can be observed that the hydrogen peroxide concentration during the measuring period of 5 h is maintained between 0.940 and 0.955 mol l^{-1} with error margins between sensor output and titration of less than 2%, which demonstrates the advantages and the possible applications of the sensor.

Similar tests were performed at a second German company. These tests led to analogous conclusions, namely that the sensor system is capable not only of measuring hydrogen peroxide concentrations with sufficient accuracy, but also that the process can be directed to an optimal hydrogen peroxide concentration which is set in advance. Finally, the sensor was tested in a third company, also located in Germany. An additional asset of this 50-day test is that it can be performed mainly by employees at the company.

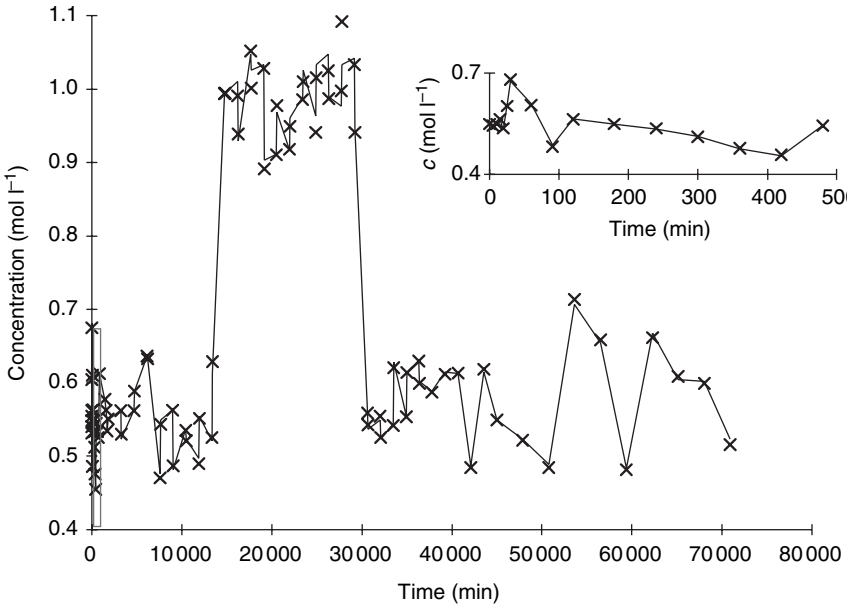

5.15 Measurement of the hydrogen peroxide concentration during bleaching processes determined by means of the sensor system (—) and titration (×). The smaller figure represents the measured data during the first 500 min.

The results of the test are given in Fig. 5.15, confirming the conclusions from the tests described above.

5.5 Expanding the sensor system for processes occurring at pH <10.5

5.5.1 Introduction

As indicated in Chapter 4 (section 4.1), the applications of hydrogen peroxide are not limited to the bleaching of cotton. Other application areas, such as the use of hydrogen peroxide in the paper industry, in processes involving the synthesis of inorganic and organic products, and as a disinfectant in swimming pools and in waste-water purification, are situated outside the pH area in which the sensor can be used directly. In these applications as well, the continuous measuring and adjusting of the hydrogen peroxide concentration by means of a sensor system is regarded as useful. Considering the environmentally friendly character of hydrogen peroxide, its use has increased strongly; in the future no doubt, further application areas will arise in which the use of a sensor system will be crucial.

At the beginning of this research, one of the aims was to develop a hydrogen peroxide sensor that would be useful in the complete pH area. When, after the preliminary study, the glassy-carbon electrode was chosen for further research but was limited for pH values in the envisaged high hydrogen peroxide concentration range, several attempts were made to use the sensor system also in the lower pH area. Modifying the pre-treatment method of the glassy-carbon electrode, adjusting the electrode configuration and even investigating other electrode materials did not lead to a solution to the problem. When research is limited to the vitreous-carbon electrode, it appears in the oxidation reaction mechanism on which the sensor is based that a minimal concentration of hydroxyl ions is required. Inevitably, it has to be concluded that the developed hydrogen peroxide sensor cannot be adjusted to mediums with pH <10.5 in combination with the detection of high hydrogen peroxide concentrations.

Hence, other strategies were considered, e.g. a system where the sensor is in permanent contact with an alkaline solution, which is separated from the measurement solution by means of a membrane which sufficiently conducts hydrogen peroxide. In such configurations, the fast response time and advantages of this system obviously disappear. In general, this strategy boils down to influencing the medium in which the measurements take place instead of adjusting the sensor system itself to the medium. A possible mechanism for achieving this strategy in practice is the so-called FIA (flow-injection analysis) system. For further research, this method was preferred because the advantage of the short response time was not lost. This study is more exploratory than exhaustive and should be considered as a pre-research investigation, aiming at figuring out whether the system qualifies for further research.

FIA systems are used to investigate the kinetics of homogeneous chemical reactions and for the analytical determination of many components by means of spectrophotometric detection, amongst other applications. In the latter method, a certain concentration of reagent (component forming a coloured complex with the component to be determined) is added (injection), to a constant liquid flow of the solution in which the component to be determined is situated (flow). The resulting solution subsequently passes a reaction chamber, after which detection occurs by means of a spectrophotometer (analysis).

The aimed use of the FIA principle in the hydrogen peroxide sensor system is similar. More specifically, the aim of this part of the research was to verify whether the following approach could lead to the desired result. A constant flow of a bleaching solution (flow) is mixed with a constant flow of a solution with a known sodium hydroxide concentration (injection). This concentration depends on the final pH of the process solution to be established and is chosen in such a way that, after homogenising the two liquid

flows, a pH value is obtained situated between 11.5 and 13. Within this pH area, the sensor system is useable in its actual configuration, and it is the basis of the measuring system of the complete setup (analysis).

Some disadvantages are associated with this system. A first disadvantage is the disappearance of the continuous character of the sensor since a certain period of time elapses between the measurement of electrical current at the sensor surface and the moment in time when the sample to be analysed leaves the process bath. Whereas the developed sensor is intrinsically a continuous working system, it is clear that a basically discontinuous system can be considered as virtually continuous when the duration of the measurement is situated below a specific critical threshold, the 'dead time' for every considered application. One of the tasks of the research is to keep the dead time as short as possible, and if necessary take this into account when the global process is directed by means of the output signal of the sensor expanded with a FIA system.

Another problem is waste generation. Since, after detection, the solution has a pH of 11.5–13, it cannot, depending on the application, be sent back to the bath where the process occurs at a lower pH. This means that the waste quantity created by the system must be kept as low as possible and that one should miniaturise the sensor configuration as much as is practicable. According to a limited survey realised with the users of hydrogen peroxide, a waste volume of 1 l/h is considered as acceptable. Finally, a dilution factor should be taken into account, which depends on the volumes of both liquid flows mixed in the injection area of the FIA system.

5.5.2 The FIA system

The principle of the constructed FIA system is shown in Fig. 5.16. A tank with a 15 l volume replaces the bath where the actual industrial process occurs. By means of a peristaltic pump, the process solution is tapped from the bath and sent to the mixing chamber through flexible tubes having an inside diameter of 1 mm. In the same way, a constant liquid flow of a sodium hydroxide solution is pumped to the mixing chamber with the same peristaltic pump. The concentration of this solution is such that, after mixture with the process solution, a pH of 12.5 is obtained. The concentration of the sodium hydroxide solution is hence adjusted to the pH of the process solution.

The mixing chamber is a T-junction having a 1-mm inside diameter and, as a result, the two liquid flows (process solution and sodium hydroxide solution) meet each other under a 90° angle. Subsequently, the mixed solution is sent to the detection cell (Fig. 5.17). The dimensions of the working electrode and auxiliary sensors are adjusted in such a way that they strongly decrease (ca. 50%) the internal volume actually taken in by the solution. The actual volume of the detection cell amounts to ca. 7 ml. In this config-

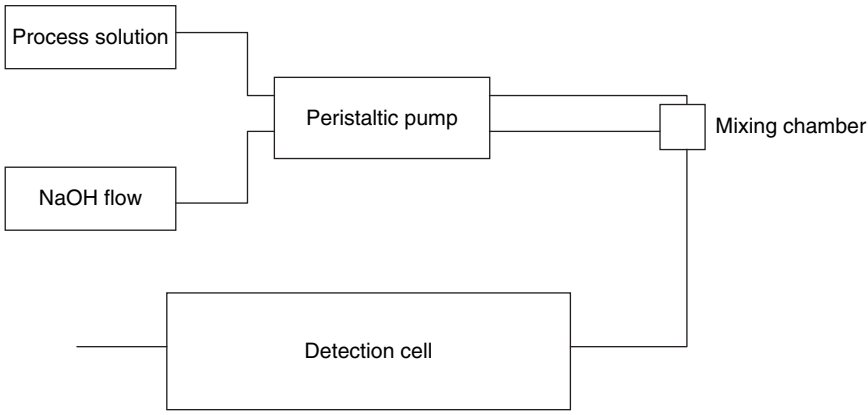

5.16 Schematic representation of the FIA system with the existing sensor system for the determination of hydrogen peroxide or a variant incorporated in the detection cell.

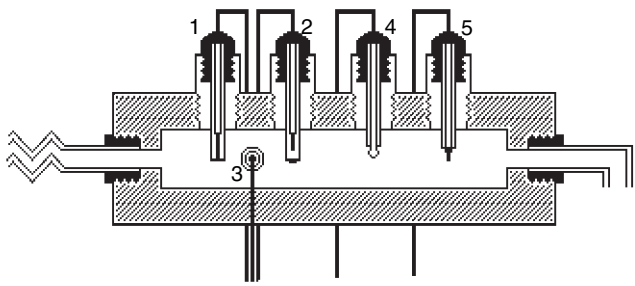

5.17 Scheme of the detection cell of the hydrogen peroxide sensor expanded with the FIA system. The inner chamber has a 20-cm length and a 1-cm diameter; (1) working electrode, (2) reference electrode, (3) counter electrode, (4) combined glass electrode, and (5) temperature sensor, surface of the working electrode equals 7 mm^2.

uration, the electrodes have to be put after each other in the detection cell. Naturally, the mutual angle of the positioning can differ (e.g. the counter electrode situated between the working electrode and the reference electrode is located under an angle of 90° in relation to the other electrodes). Finally, the liquid flow coming from the detection cell is carried away. Since the pH is too high, the solution cannot be brought back to the process tank. The total distance to be covered between bath and exit of the detection cell amounts to approximately 1 m.

In the initial phase of this pre-research, the configuration of the FIA system was examined and, because of practical and financial considerations, only one peristaltic pump was used to obtain the constant liquid flows. The flow of the process solution as well as that of the sodium hydroxide

solution are coupled to this peristaltic pump, so that it is expected that the dilution of the process solution equals a factor two. The exact value of this factor has to be verified experimentally.

An initial series of measurements concerned the accurate determination of the dilution factor. As is represented in Fig. 5.16, the absolute position of the tubes of the process solution and of the sodium hydroxide solution over the rollers of the pump is different. One tube is situated higher on the roller than the other, which can lead to a small difference in flow rate. By determining the hydrogen peroxide concentration by means of titration of a sample taken from the bath and a sample taken at the exit of the detection cell (diluted solution), the dilution factor can be determined. Table 5.1 presents the results of 23 measurements of the hydrogen peroxide concentration, performed at a liquid flow rate of 1 l/h. It is concluded that the dilution factor equals 1.9773 ± 0.0014, which in fact is very close to 2.

In a second series of experiments, the dead time is examined by means of the sensor signal at a liquid flow of 1 l/h. It is clear that when modifying, for example, the hydrogen peroxide concentration in the bath, this change will only be observed in the detection cell after a period of time. The length and the diameter of the tubes and the actual internal volume of the detection cell play an important part here. After changing the hydrogen

Table 5.1 Determination of the dilution factor of the FIA system

$c_{process}$ (mol l^{-1})	$c_{detection\ cell}$ (mol l^{-1})	Dilution factor
0.009948	0.005024	1.98
0.01700	0.008586	1.98
0.2301	0.1168	1.97
0.9801	0.4950	1.98
0.5600	0.2828	1.98
0.08146	0.04135	1.97
0.4000	0.2010	1.99
0.05520	0.02788	1.98
0.7699	0.3869	1.99
0.6150	0.3105	1.98
0.04100	0.02092	1.96
0.02800	0.01414	1.98
0.03479	0.01766	1.97
0.1200	0.06061	1.98
0.06500	0.03283	1.98
0.3900	0.1970	1.98
0.8100	0.4091	1.98
0.07908	0.04014	1.97
0.06600	0.03333	1.98
0.1500	0.07614	1.97
0.8060	0.4112	1.96
0.4354	0.2188	1.99
0.7800	0.3939	1.98

peroxide concentration in the bath (e.g. by addition of hydrogen peroxide or water), the peristaltic pump was started, and the time necessary for the measurement of the newly established hydrogen peroxide concentration in the detection cell was established. From approximately 30 measurements, it was concluded that the dead time of the sensor expanded with the FIA system amounts to around 30 s for an actual volume of ca. 7 ml, a 1-mm inside diameter of the tubes and a ca. 1-m length between bath and detection cell.

This means that one should bear in mind that the values of the process parameters detected at the sensor correspond to a situation which occurred in the bath of the process 30 s earlier. This is extremely important if one wishes to control the hydrogen peroxide concentration in the considered process. Though the dead time can be shortened by increasing the flow rate, the problem arises then that higher flow rates generate more waste-water and turbulent behaviour in the detection cell which affects the sensor signal. Similarly, the dead time of the same sensor expanded with the FIA system was verified with different flow rates (Fig. 5.18). With a flow rate of, for example, 2 l/h, the dead time amounts to ca. 23 s.

Another important element that should be taken into account is that, in certain processes, relatively low hydrogen peroxide concentrations are used. This means that the sensor's detection limit can be a crucial parameter for these applications. As a criterion, one speaks of useful measurements when the sensor signal is three times higher than the noise observed in the absence of hydrogen peroxide. As appears from the data shown in Fig. 4.9, the sensor signal increases with increasing pH. Hence, it is interesting to

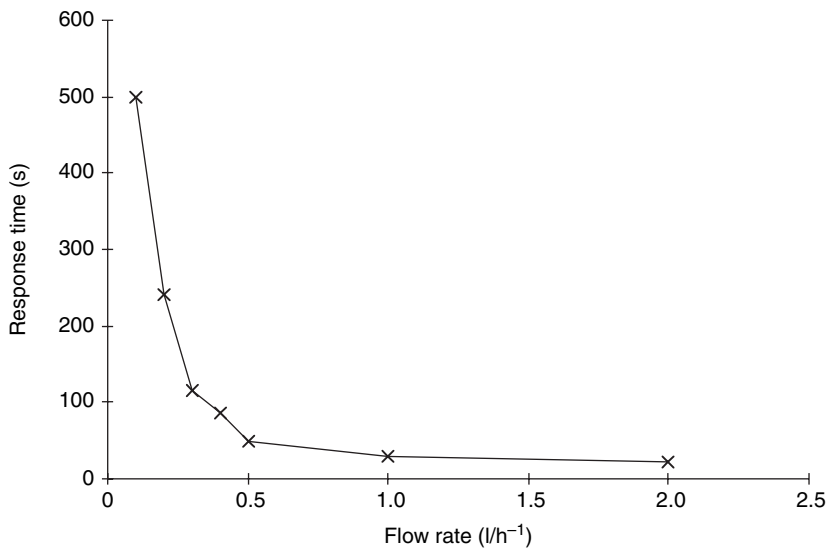

5.18 Development of the dead time as a function of the liquid flow rate.

establish a high pH in the detection cell in order to obtain the detection limits as low as possible. Experiments have been performed to determine these detection limits analogously as in Chapter 4, section 4.5.2 (Figs 4.7–4.10) and with a pH of ca. 12.5; the lowest detectable concentration equals 5×10^{-4} mol l^{-1} ($\approx$10 ppm). This concentration corresponds to a sensor signal of ca. 8 μA, which is more than three times higher than the signal in the absence of hydrogen peroxide (2.5 μA). The deviation in relation to the result obtained through titration of a solution with this hydrogen peroxide concentration amounts to ca. 10%, and is clearly wider than the error obtained when determining higher concentrations. The upper limit of the hydrogen peroxide concentration, which can be determined with the classical sensor system (2 mol l^{-1}) is maintained when using the FIA system.

For the calculation of the concentration, it appeared that the same equation can be used as the one used for the sensor which was directly applied (Equation 5.6) if the dilution factor was taken into account. A first possible approach to take the dilution factor into account is the following: Equation 5.6 is connected to the hydrogen peroxide concentration in the process through sampling of process-bath solution, and the obtained hydrogen peroxide concentration should be divided by the dilution factor, 1.98. The hydrogen peroxide concentration simultaneously obtained via titration has to be connected to the sensor signal which is obtained in the detection cell ca. 30 s after the sampling, which can cause errors, even with an efficient timing.

Hence another strategy was followed, where the calibration is done by means of a solution from the detection cell. With this solution, the sensor signal, as well as the concentration of hydrogen peroxide through titration, was obtained. In order to be able to calculate subsequently the original concentration in the bath where the process occurs, the dilution factor should be taken into account, and for the control of the hydrogen peroxide concentration one should bear in mind a 30-s delay. In this way, a possible difference in process-bath composition is eliminated. The equation for the calculation of the hydrogen peroxide concentration in the process bath is:

$$c_{HO_{2m}^-} = 1.98\left[c_{HO_{2,cal}^-}^{\left[3/2-1/2\left(0.05071 c_{HO_{2,cal}^-}^{-0.0791}\right)\right]} \frac{I_m}{I_{cal}} \frac{\left(c_{HO_{2,cal}^-}^{-0.0791}\right)^{6.607}}{\left(c_{HO_{2,m}^-}^{-0.0791}\right)^{6.607}} \frac{c_{OH_{cal}^-}^{\left[2/3\left(0.05071 c_{HO_{2,cal}^-}^{-0.0791}\right)-1/2\right]}}{c_{OH_m^-}^{\left[3/2\left(0.05071 c_{HO_{2,m}^-}^{-0.0791}\right)-1/2\right]}} e^{0.03049(T_{cal}-T_m)} \right]^{1/\left[3/2-1/2\left(0.05071 c_{HO_{2,m}^-}^{-0.0791}\right)\right]} \quad [5.7]$$

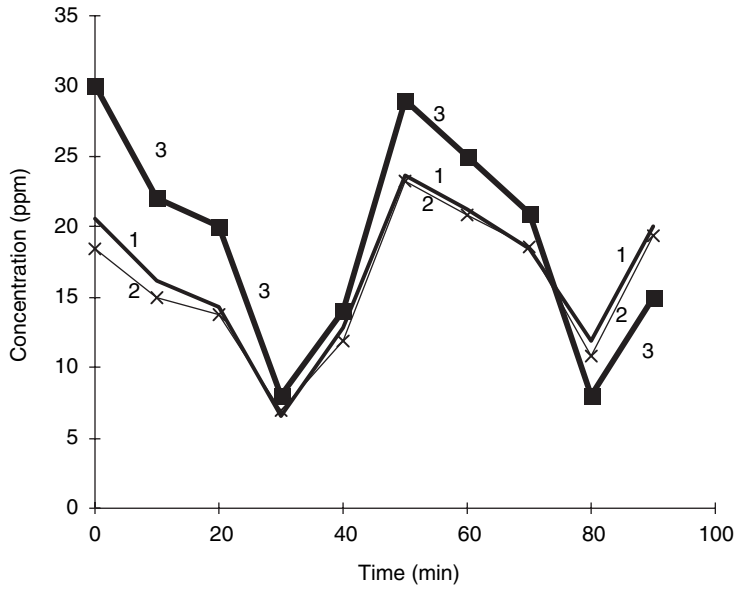

5.19 Development of the hydrogen peroxide concentration in a solution containing paper pulp with a pH of ca. 8. The concentrations were determined by means of a sensor system with (1) FIA-expansion, (2) titration, and (3) strips.

At a laboratory scale, some preliminary experiments were performed to determine hydrogen peroxide concentrations in solutions with pH <10.5. To this end, hydrogen peroxide solutions from a paper pulp process (pH ca. 8) were used, which were obtained from a French company. The results are displayed in Fig. 5.19. Here, mainly relatively low hydrogen peroxide concentrations were examined, with output signals that were never higher than 35 μA. The pH in the detection cell was ca. 12.5, and the temperature fluctuated around 318 K.

From Fig. 5.19, it appears that the hydrogen peroxide concentrations obtained by means of the sensor system and through titration correspond relatively well with each other (deviations always <10%), and that the system qualifies both to measure the hydrogen peroxide concentration and to control it. To illustrate, Fig. 5.19 also shows the hydrogen peroxide concentrations obtained by means of strips (Merck), which are frequently used in the paper industry. It is clear that the strips are rather inaccurate, compared with the results obtained with the sensor system.

5.5.3 Conclusion

Using the previously described sensor system expanded with the FIA system, and in a miniaturised configuration, hydrogen peroxide concentrations of 5×10^{-4} mol l^{-1} to 2 mol l^{-1} can be determined over the complete pH area. Obviously, the FIA setup is incorporated only if the pH is lower than ca. 10.5. When the pH is higher than 10.5, the classic flow-tube system can be used, which is faster, simpler and cheaper, unless the hydrogen peroxide concentration to be determined is so low that it cannot be detected with, for example, a pH of 10.5, but instead requiring a pH of 12.5. Expanding the sensor with a FIA system can also be considered in such applications.

5.6 References

1. Granwald W., *Zeitschrift Ges. Textilind.*, **63** (1961) 285.

6

Simultaneous detection of indigo and sodium dithionite for control of dyeing processes

P. WESTBROEK AND P. KIEKENS

6.1 Introduction

Dyeing processes with indigo are carried out all over the world[1–6]. However, dyeing of textiles with indigo in a reproducible way is complicated. Several reasons for errors and irreproducible dyeing can be found, including a lack of quality control during the dyeing itself and also in the preceding textile-finishing processes. Ab- and adsorption of dyestuff by the textile is strongly dependent on the nature, source and properties of the fibre and its surface activity. These properties are determined by the preceding textile-finishing processes such as bleaching and mercerisation. Optimisation of these processes can result in a vast improvement of the dyeing process. In this context, the authors of this book developed a sensor for the continuous and online detection and control of hydrogen peroxide concentrations in textile bleaching baths, as described in references 5–9, in order to improve the quality and reproducibility of the bleached textile fabric.

Another problem faced by the dyeing industry is the inability to maintain the concentration of leuco-indigo (reduced, water-soluble form of indigo) at a constant level. Indigo is reduced to leuco-indigo by adding a reducing agent (sodium dithionite)[1,10–12], so, indirectly, the actual concentration of leuco-indigo is dependent not only on the initial indigo concentration but also on the concentration of reducing agent. Finally, quality control of the dyed product is scarce, and in about 60% of the companies in the world it is non-existent[13]. However, even if quality control is performed, it is done at the dyed product, which means that if errors occurred earlier they cannot be corrected[14–19].

The aim of an indigo sensor is to keep the leuco-indigo concentration in the solution at a constant value. In the past, different methods were developed for detection of the indigo and sodium dithionite concentration, but up to now with limited success. The sodium dithionite concentration can be determined by volumetric titration with iodine[20–22] or with $K_3[Fe(CN)_6]$[23]. The endpoint detection of these titrations can be done visually[22,24–25] or

potentiometrically[24–25]. Besides utilising a photometric or spectrophotometric reflectance method[26–27], indigo can be determined by potentiometric titration[23]. The difference in standard potential of indigo and sodium dithionite is about 150 mV, which allows determination of both concentrations in the same titration[23]. Most of these methods are not continuous, which means that control of the indigo and sodium dithionite concentration cannot be done properly. Automation of these methods (e.g. with titration equipment) also resulted in only limited success owing to poisoning of the detection system (e.g. potentiometric electrodes) and blocking of the valves and the peristaltic pumps used for pumping the dyeing solution to the analysis cell. Finally, photoacoustics were also investigated as a possible method for determining the concentration of dyestuff[28].

In this chapter, a sensor system is described, based on multistep chronoamperometry, that makes it possible to measure the indigo and sodium dithionite concentration simultaneously, on line and in line and with high precision, accuracy and long-term stability. This system allows the quality and reproducibility of the dyeing process to be improved, because the indigo and sodium dithionite concentration are measured and controlled at a fixed value. In the following sections, the different steps that were undertaken in order to develop this sensor are described in detail and not only show the development strategy, but also give insight into the working principle, advantages, disadvantages and properties of the sensor system.

6.2 Basic electrochemical reactions of dithionite and sulphite

A necessary pre-requisite to starting the development of a sensor system is knowledge of the reactions that occur at the surface of the sensor electrode and result in the response signal delivered by the sensor system. In this section, the pathway of how the sensor reaction is found and studied is described.

In a first set of experiments, the voltammetric behaviour of sodium dithionite was investigated in alkaline solution (pH around 12.5), by variation of the rotation rate of the platinum-disc electrode for different concentrations of sodium dithionite. In Fig. 6.1, current–potential curves are shown, obtained at different rotation rates of the electrode in a solution with constant sodium dithionite concentration. Two anodic waves are observed. In principle, sodium dithionite is the only electroactive species in solution, therefore it is supposed that both well-separated waves can be attributed to the oxidation of sodium dithionite with formation of a relatively stable intermediate product in the first wave.

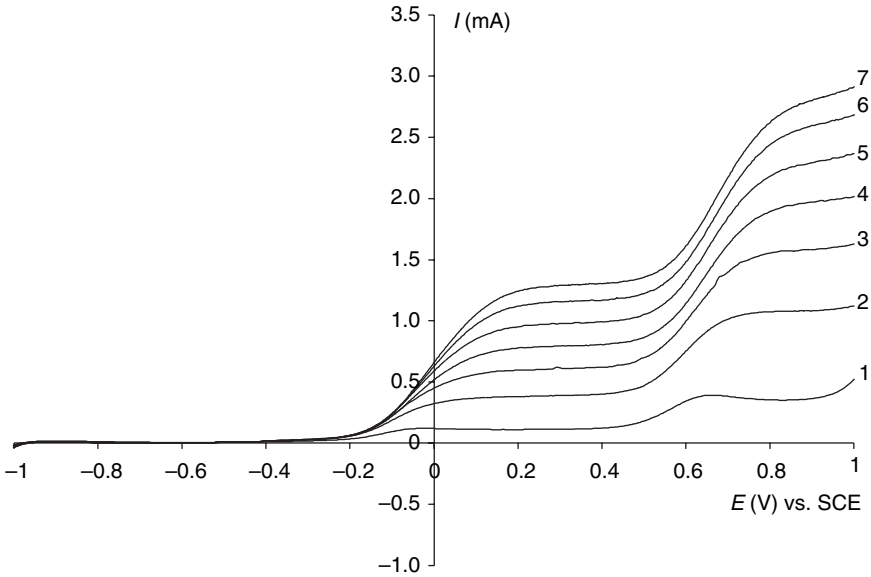

6.1 Current–potential curves recorded in a solution containing 5.747×10^{-3} mol l^{-1} sodium dithionite at pH = 12.5 (NaOH) at a platinum rotating-disc electrode with rotation rates of (1) 100, (2) 400, (3) 900, (4) 1600, (5) 2500, (6) 3600 and (7) 4900 rpm; $T = 298$ K.

In the literature[29–30], sulphite is mentioned as a possible reaction product in the decomposition reaction of sodium dithionite. Therefore, it is quite possible that sulphite is the intermediate product. Experimental proof is given by repeating the described experimental series in an alkaline solution containing only sodium sulphite (7.9×10^{-3} mol l^{-1}) at 16.67 Hz. Five successively recorded scans are shown in Fig. 6.2. The difference between the first and other scans will be explained further in section 6.3.2. In this case, it was found that the first oxidation wave, observed in Fig. 6.1, was not obtained, while the second wave occurred clearly. This oxidation wave occurs at identical potentials as the second oxidation wave observed when sodium dithionite is present in solution. These results indicate that the relatively stable intermediate formed in the first oxidation wave of the sodium dithionite oxidation is sulphite. In the second wave, sulphite is presumably further oxidised to sulphate.

Assuming that the first oxidation wave in Fig. 6.1 corresponds to the oxidation of sodium dithionite to sulphite, two possible oxidation reactions can be considered in alkaline solution:

$$S_2O_4^{2-} + 4OH^- \leftrightarrows 2SO_3^{2-} + 2H_2O + 2e^- \quad [6.1]$$

$$S_2O_4^{2-} + 6OH^- \leftrightarrows SO_3^{2-} + SO_4^{2-} + 3H_2O + 4e^- \quad [6.2]$$

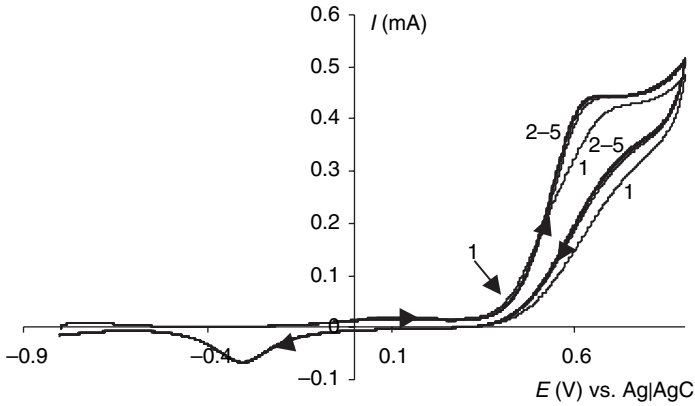

6.2 Five successively recorded current–potential curves at a platinum rotating-disc electrode in a solution containing 7.94×10^{-3} mol l^{-1} sulphite at 298.0 K, N = 16.67 Hz and pH = 12.43 after initial polarisation at –0.5 V vs. Ag|AgCl for 5 min. (Reprinted from *Electrochemistry Communications*, Vol 2, No 10, Gasana *et al.*, 'Influence of changes of . . .' pp 727–732, Copyright 2000, with permission from Elsevier.)

Other particles like $S_2O_6^{2-}$ and $S_4O_6^{2-}$ are not considered, because in the literature no evidence can be found of them being stable in alkaline solution[31]. In the second oxidation wave, sulphite is further oxidised according to:

$$SO_3^{2-} + 2OH^- \leftrightarrows SO_4^{2-} + H_2O + 2e^- \qquad [6.3]$$

The ratio of the number of electrons totally exchanged in the first and the second oxidation wave of dithionite is 3.0 for the combination of reactions 1 ($2e^-$) and 3 ($6e^-$), and 1.5 for reactions 2 ($4e^-$) and 3 ($2e^-$). Note that for these ratios, the electrons exchanged in the first oxidation wave are also taken into account in the second wave. A choice between both hypotheses can be made because in principle the number of electrons n_1 and n_2 transferred in both waves can be obtained theoretically from the postulated reaction scheme and experimentally from the ratio of the limiting-currents ($I_{L,2}/I_{L,1}$) of both waves. An important condition is that the currents $I_{L,1}$ and $I_{L,2}$ are true limiting-currents, which means that the corresponding reaction rate should be controlled by transport of electroactive species only. This can be verified by plotting the logarithm of the plateau currents vs. log ω. If the reaction rate is controlled by transport only, a slope of 0.5 must be obtained according to the Levich equation (Chapter 1, Equation 1.15):

$$I_{lim} = 0.62nFAD^{2/3}\nu^{-1/6}\omega^{1/2}c \qquad [1.15]$$

where I_{lim} is the limiting-current (mA), n is the number of electrons, F is the Faraday constant (C mol^{-1}), A is the surface of the electrode (cm^2), D is the diffusion coefficient ($cm^2 s^{-1}$), ν is the kinematic viscosity ($cm^2 s^{-1}$), $\omega = 2\pi N$

(with N the number of revolutions per second), and c is the concentration of the compound in mol l^{-1}.

However, before plotting this relationship, another consideration must be made. As already mentioned, one of the reaction products of the decomposition reaction of sodium dithionite is sulphite, and the solid form of sodium dithionite contains approximately 15% (m/m) of decomposition products. By the preparation, dilution, storage and manipulation of sodium dithionite solutions, some further decomposition of sodium dithionite into sulphite cannot be avoided.

When comparing limiting-currents of the first and second oxidation waves, it is important to know the proportion of dissolved commercial product that is present as sulphite, and the quantity that is still present as dithionite. To check this, a selective titrimetric determination of dithionite and sulphite in solutions prepared and preconditioned for voltammetric analysis showed that approximately 13% of the sum of sodium dithionite and sulphite concentration could be attributed to sulphite. Taking into account that in the second oxidation wave, sodium dithionite is oxidised to sulphate with the exchange of six electrons and sulphite is oxidised with the exchange of two electrons, a 5% contribution from sulphite to the total limiting-current in the plateau of the second oxidation wave in Fig. 6.1 was calculated. This means that all the limiting-currents of the second plateau in Fig. 6.1 must be reduced by 5% to obtain the limiting-currents corresponding to the oxidation reaction of sodium dithionite to sulphate, without the influence of sulphite (about 5%) that is also present in the solution as a decomposition product of sodium dithionite.

Figure 6.3 shows the logarithmic relationship between the rotation rate of the electrode and the limiting-current of the first wave. The slope of the curves is 0.47 ± 0.02, which is near to 0.5 as predicted by the Levich equation (1.15). It can therefore be concluded that the limiting rate of the oxidation reaction of sodium dithionite corresponding to the first wave is controlled by transport only (diffusion and convection). A similar analysis for the second wave shows that the $\log I$ vs. $\log \omega$ relationship is not linear and that its slope increases with decreasing values of $\log \omega$ (Fig. 6.4). It can also be seen that the slopes decrease with increasing sodium dithionite concentration. Looking at a constant sodium dithionite concentration, however, it can be seen that the curves become more linear at the lower rotation rates, where their slope tends towards 0.5 for all the investigated sodium dithionite concentrations. This suggests that the limiting rate of the oxidation reaction of sodium dithionite corresponding with the second oxidation wave is controlled by transport only at small rotation rates.

The reason for the changes in slope can be found in limiting-current that is not purely transport controlled. Some contribution of charge transfer kinetics is supposed to be responsible for this effect. In section 6.3, more

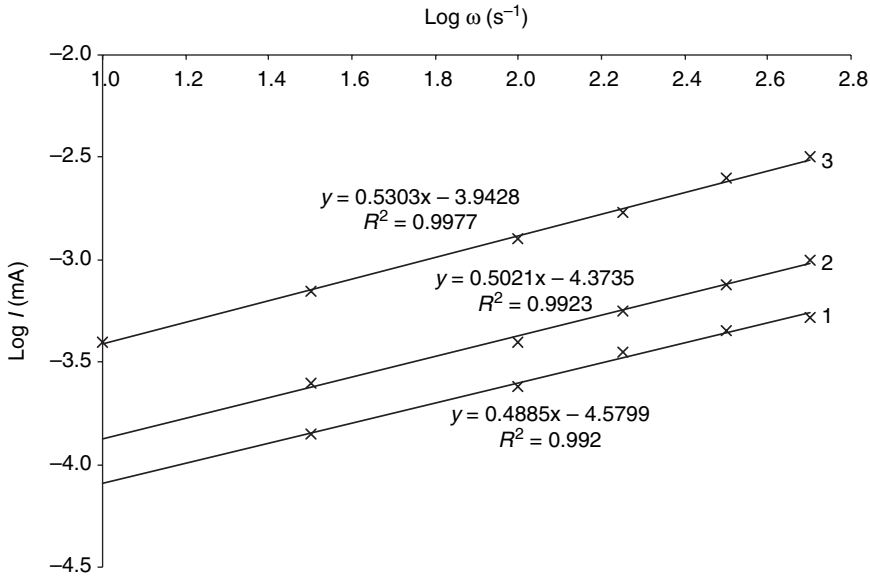

6.3 Logarithmic plot of the relationship between rotation rate of the electrode and limiting current for the first wave of the oxidation of sodium dithionite in alkaline solution at a platinum-disc electrode as a function of sodium dithionite concentration: (1) 2.9×10^{-3}, (2) 5.8×10^{-3} and (3) 1.2×10^{-2} mol l^{-1}.

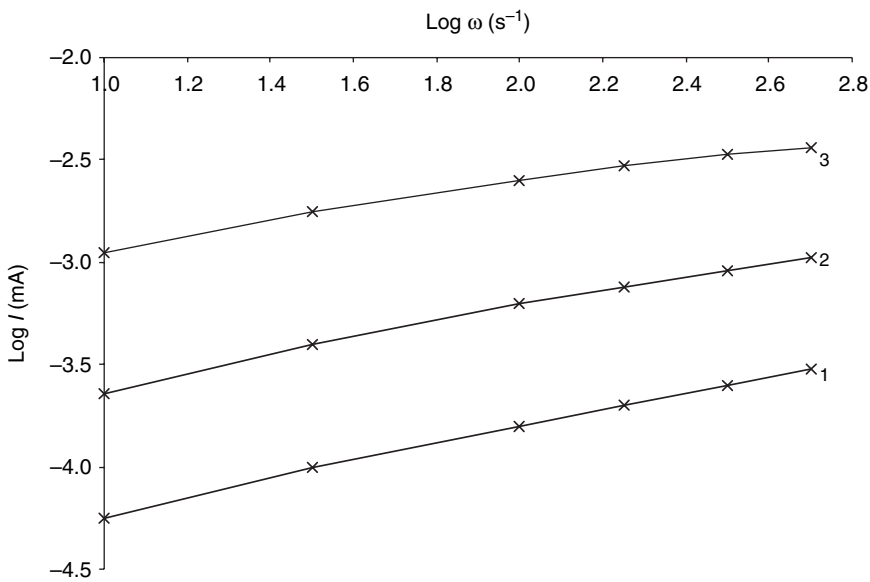

6.4 Logarithmic plot of the relationship between rotation rate of the electrode and limiting current for the second wave of the oxidation of sodium dithionite in alkaline solution at a platinum-disc electrode as a function of sodium dithionite concentration: (1) 5.8×10^{-4}, (2) 2.9×10^{-3} and (3) 1.2×10^{-2} mol l^{-1}. Slopes at slow rotation rates are (1) 0.50, (2) 0.48 and (3) 0.41.

attention is given to the nature of this kinetic influence. The contribution of kinetic parameters can also be observed from the curves in Fig. 6.1. For the second oxidation wave, a weak inclination of the limiting-current in the limiting-current plateau is observed. For a purely transport-controlled reaction, a potential-independent limiting-current should be obtained as is the case for the limiting-current of the first oxidation wave.

In a general form, the voltammetric current measured for a system that is not reversible, which is the case for the dithionite and sulphite reactions concerned (no return peak is observed), can be expressed by[32–33]:

$$\frac{1}{I} = \frac{1}{I_K} + \frac{1}{I_L} \qquad [6.4]$$

where I_K and I_L are the kinetic current and the limiting-current, respectively. If the rate of the electrochemical reaction is controlled only by the rate of electron transfer, which means that $I_L \gg I_K$, then Equation 6.4 simplifies into $I = I_K$. In Fig. 6.1, this situation approximately corresponds with the potential region from $E = -0.45$ to -0.15 V vs. SCE at the onset of the first oxidation wave of sodium dithionite. However, if the rate of the electrochemical reaction is controlled only by transport phenomena, then $I = I_L$, and this current is independent of potential.

The relationships between $\log I_L$ and $\log \omega$ for the first (Fig. 6.3) and second (Fig. 6.4) dithionite oxidation wave (Fig. 6.1) do not allow the derivation of the number of electrons exchanged in the electrochemical reaction from the ratio of the limiting-currents, because the second one, $I_{L,2}$, is not purely controlled by transport of electroactive species. However, an indirect method can be used. Extrapolation of the relationship between $I_{L,2}/I_{L,1}$ and the rotation rate of the electrode (ω) to very low rotation rates allows the number of electrons to be obtained. As outlined earlier, it is presuming that, at these slow rotation rates, the velocity of the second oxidation reaction is controlled by transport only. The driving force in this case is that at very slow rotation rates of the electrode, the transport rate is much slower than the one for charge transfer and becomes rate determining.

It should be mentioned that this situation is experimentally not accessible and is therefore performed by an extrapolation method. The value of $I_{L,2}/I_{L,1}$ at these slow rotation rates is equal to the value of n_2/n_1. The relationship between the logarithm of $\log \omega$ and $\log[\log(I_{L,2}/I_{L,1})]$ was plotted for various concentrations of sodium dithionite and revealed that all the curves tend towards a value of -0.33 for $\log[\log(I_{L,2}/I_{L,1})]$ at slow rotation rates (e.g. $\omega = 10$). This corresponds to a $I_{L,2}/I_{L,1}$ ratio of approximately 3. In the Levich equation (Chapter 1, Equation 1.15), I_L is proportional to n; thus it can be concluded that the combination of Equations (6.1) and (6.3) can explain the experimentally obtained results.

6.3 Kinetic limitations in oxidation of dithionite and sulphite

As described in the theoretical section of this book, an electrochemical reaction consists of different steps, and each of these steps (transport and/or charge-transfer steps) can be rate determining. In this section, it is explained why it is not possible to obtain a purely transport-controlled oxidation reaction for sulphite as outlined in the previous section. This is caused by the platinum electrode surface condition that has a large influence on the electron-transfer rate. Therefore, the electrochemical behaviour of the electrode surface itself is described first and limited to observations made during oxidation of dithionite and sulphite.

6.3.1 Electrochemical behaviour of platinum electrode surface

First, the electrochemical behaviour of the substrate material, which is platinum, was investigated as a function of applied potential by cyclic voltammetry. For that, the potential was swept in positive direction from –0.5 V vs. Ag|AgCl to a first vertex potential of 0.9 V vs. Ag|AgCl, followed by a scan in reversed direction to a second vertex potential of –0.8 V and back to –0.5 V vs. Ag|AgCl. The curves obtained in solutions of different pH values are shown in Fig. 6.5. Similarly shaped curves were obtained by variation of

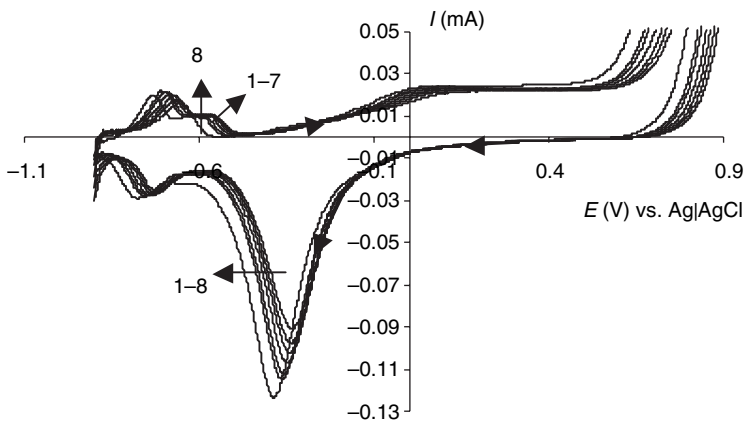

6.5 Current–potential curves recorded at a platinum-disc electrode rotating at $N = 16.67$ Hz. The pH of the solution is (1) 11.79, (2) 12.04, (3) 12.13, (4) 12.29, (5) 12.42, (6) 12.61, (7) 12.76 and (8) 13.11. (Reprinted from *Electrochemistry Communications*, Vol 2, No 10, Gasana *et al.*, 'Influence of changes of . . .' pp 727–732, Copyright 2000, with permission from Elsevier.)

the vertex potentials to more negative and positive values. However, the absolute values of the different peak heights obtained were not the same, and a small shift towards more negative values of the peak potential of the reduction peak was observed as a function of increasing anodic vertex potential.

In the potential region from –0.8 to –0.5 V vs. Ag|AgCl, two reversible peak currents can be observed at –0.7 V and –0.6 V vs. Ag|AgCl. Under ultrapure conditions, a third reversible peak (not observed in these experiments) can be obtained in this region[34]. These peaks can be attributed to hydrogen adsorption/desorption reactions[35]. At potentials below –0.8 V vs. Ag|AgCl, the hydrogen-evolution reaction takes place. In the anodic potential scan direction, a 'double layer' region[35] from –0.5 to –0.4 V vs. Ag|AgCl can be observed, which is frequently strongly affected by anion adsorption[36–37]. Sweeping the potential in anodic direction from –0.4 V vs. Ag|AgCl, a broad and flattened peak is observed resulting in a more or less steady-state current. The flattened peak is composed of three oxidation peaks defined as O_{A1}, O_{A2} and O_{A3}[35,38] and is attributed to electrosorption of OH^- at the platinum surface. Notice that the OH^- electrosorption to PtOH is dependent on pH. The more or less steady-state current observed at potentials more positive than 0.25 V vs. Ag|AgCl is the result of further oxidation of electrosorbed OH^- to O species[35,38].

Despite the involvement of hydrogen ions in this further oxidation, the limiting-current does not show a change with pH. This means that in the mechanism of this oxidation reaction, the elementary pH-dependent step(s) are preceded by a slower rate-determining step. Finally, the oxygen-evolution reaction starts to occur from a potential of 0.5 V vs. Ag|AgCl. In the cathodic polarisation direction, a well-defined reduction peak is observed between –0.1 and –0.5 V vs. Ag|AgCl and is attributed to the reduction of the oxides formed in the anodic-approaching profile.

However, the mechanism and kinetics of reduction are more complicated than a single peak would suggest and were studied by Tilak *et al.*[38] They came to the conclusion that the oxidation/reduction of PtO/PtOH is an irreversible process, and the further reduction of PtOH is reversible although the mechanism is relatively complicated. They suggested that a shift of the reduction peak potential to more negative values as a function of increasing anodic vertex potential can occur through rearrangements of the platinum surface (such as PtOH→OHPt). This means that the fraction of rearrangement is higher at higher oxide coverage of the platinum surface. To eliminate the hypothesis that strongly adsorbed molecular oxygen, formed during the oxygen-evolution reaction, is responsible for the observed reduction peak, the anodic vertex potential was limited to 0.5 V vs. Ag|AgCl. At this potential, no molecular oxygen is formed, but the reduction peak is still obtained, which confirms

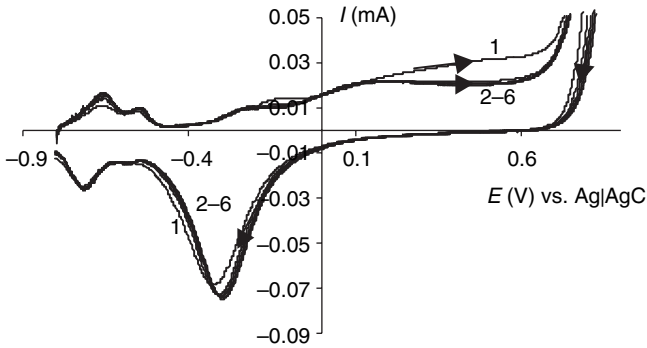

6.6 Six successively recorded current–potential curves at a platinum rotating-disc electrode with $N = 16.67$ Hz and pH = 12.20, after pre-treatment of the surface by polarisation at –0.5 V vs. Ag|AgCl for 5 min. (Reprinted from *Electrochemistry Communications*, Vol 2, No 10, Gasana *et al.*, 'Influence of changes of . . .' pp 727–732, Copyright 2000, with permission from Elsevier.)

the conclusion that the reduction peak is attributed to reduction of oxides[35,38].

In a second series of experiments, the electrochemical behaviour of the platinum surface was investigated at a rotation rate of 100 rpm and a pH of 12.2. First, a cathodic pre-treatment with a duration of 5 min was performed at a potential situated in the double-layer region (e.g. –0.5 V vs. Ag|AgCl). In this pre-treatment, a reproducible hydrogen and oxide-free platinum surface was obtained. After the pre-treatment, six scans were recorded between a starting potential of –0.8 and 0.9 V vs. Ag|AgCl (Fig. 6.6). It can be seen that the first and second scans are different from the other curves. The first scan shows smaller peaks for the hydrogen oxidation, which is expected because the surface is at least partly free of hydrogen after the cathodic pre-treatment. For the second and other scans, higher peaks are observed, because it is assumed that the surface is covered with hydrogen formed at the end of the preceding scan.

Looking towards the oxide layer formation (anodic–potential range), a remarkably higher current is obtained in the first scan. However, the reduction peak (I_p at –0.3 V vs. Ag|AgCl) of the first scan is not much higher than for the other scans. This suggests that once PtO is formed, it possibly is not totally reduced during the cathodic sweep of the scan. Evidence that some PtO or PtOH (possibly in rearranged form) may remain at the surface was found in an additional experiment where the potential was swept from –0.5 to –0.8 V vs. Ag|AgCl after 5 min of cathodic pre-treatment at –0.5 V vs. Ag|AgCl. In this case, hydrogen reduction takes place at a hydrogen- and oxide-free surface. The obtained curve differs from the scan segment

between –0.5 and –0.8 V vs. Ag|AgCl of the curves shown in Fig. 6.6, which indicates a different condition of the platinum surface, possibly due to the presence of an oxide or hydroxide layer. Arvia *et al.*[39] also suggested that some oxide and/or hydroxide coverage remains at the surface of platinum and gold during the cycling procedure, with vertex potentials located in the region of the hydrogen- and oxygen-evolution reaction.

It can be concluded from the curves in Fig. 6.6 that a reproducible platinum surface is obtained after three consecutive scans, which allows use of the electrode for the study of the oxidation reactions of sodium dithionite and sulphite. However, before going into quantitative measurements, first a qualitative analysis was performed for the oxidation of sulphite and dithionite.

6.3.2 Oxidation of sulphite

In section 6.3.1, it was shown that for the second oxidation wave of sodium dithionite (sulphite oxidation to sulphate), an influence of electron-transfer rate (kinetics) is observed that cannot be neglected. Therefore, first the oxidation of sulphite is studied and described, followed by the oxidation reaction of sodium dithionite.

In Fig. 6.2, five successively recorded current–potential curves are shown, obtained at a platinum rotating-disc electrode (N=1000 rpm) in a 7.9×10^{-3} mol l^{-1} Na_2SO_3 solution. The platinum surface was previously pre-treated at –0.5 V vs. Ag|AgCl for 5 min in the electrolyte solution (0.6 mol l^{-1} $NaClO_4$, pH=12.5), and the following observations were made. First, it is clear that the oxidation reaction of sulphite occurs in the potential region where the oxidation of chemisorbed OH^- to platinum oxide proceeds (see Fig. 6.5 and Fig. 6.6). The fact that sulphite is not oxidised at platinum or at platinum covered with chemisorbed OH^- indicates that the electron transfer between sulphite and electrode surface is determined by a PtO–SO_3 interaction and not by PtOH–SO_3, PtOH–OSO_2, Pt–SO_3, Pt–OSO_2 or HOPt–SO_3 and HOPt–OSO_2. Second, the oxidation reaction of sulphite appears at initial potentials somewhat less positive in the first scan compared with the current signals of the other scans, but the slope of the transient is smaller than the one for the subsequent scans. This is an indication of slower oxidation kinetics in the first scan. It can also be seen that the limiting-current plateau of the first scan is not as flat as it should be for a transport-controlled reaction. This also indicates that even in the limiting-current plateau, some kinetic influence is still present, despite a relatively high overpotential.

These slow kinetics can be explained by the following hypothesis. In the first scan, it is presumed that the relative amount of PtO sites present (necessary for sulphite oxidation) is small compared with the Pt and PtOH sites (not favourable for sulphite oxidation) owing to the pre-treatment of the

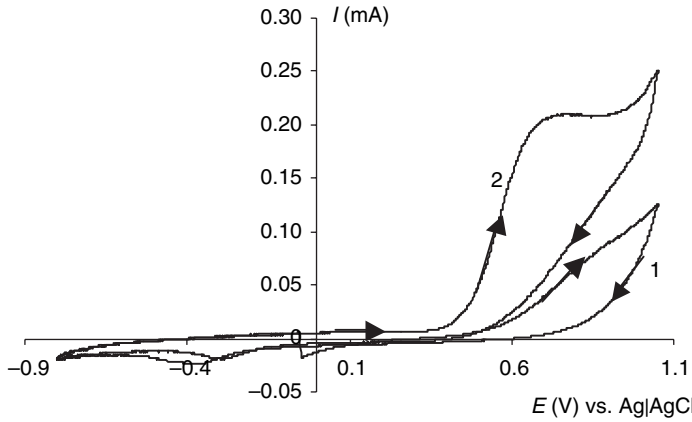

6.7 Two successively recorded current–potential curves at a platinum rotating-disc electrode containing 7.94×10^{-3} mol l^{-1} sulphite at 298.0 K, $N = 16.67$ Hz and pH = 12.43, after pre-treatment at 1.2 V vs. Ag|AgCl for 5 min. (Reprinted from *Electrochemistry Communications*, Vol 2, No 10, Gasana *et al.*, 'Influence of changes of . . .' pp 727–732, Copyright 2000, with permission from Elsevier.)

platinum surface. In the cathodic sweep direction, platinum oxide is reduced to hydroxide, which in its turn is not totally reduced to platinum[39], as was already concluded in the previous section. This means that in the second and further scans, the amount of $(Pt)_xOH$ sites (with $1 < x < 4$[39]) ready for further oxidation to PtO has increased. It is presumed that this causes an acceleration of the sulphite-oxidation reaction, resulting in well-defined and flat limiting-current plateaux (transport much slower than electron transfer).

Finally, a hysteresis effect is observed when comparing the forward and backward oxidation wave of sulphite. A possible and likely explanation for this effect is adsorption of a reaction product at the PtO sites. This species can be sulphate (reaction product of sulphite oxidation), oxygen (reaction product of the oxygen-evolution reaction) or possibly other species. Although it could not be determined clearly which species is responsible for the hysteresis effect, additional experiments (Fig. 6.7) revealed the important role of oxygen. A remarkable difference between the first and second scan is obtained after a 5-min anodic pre-treatment of the platinum surface at 1.2 V vs. Ag|AgCl. This way of pre-treatment has an adverse influence on the kinetics of the sulphite oxidation (first scan) despite the anodic potential used in the pre-treatment. At this potential not only is platinum oxidised, but also the oxygen-evolution reaction occurs. Therefore, it is presumed that molecular oxygen is adsorbed at the PtO sites and blocks these sites for the oxidation reaction of sulphite. In the reverse scan direction,

this oxygen is removed from the surface by reduction and desorption. Notice that in these experiments the hysteresis effect is much more pronounced, indicating a blocking effect of the electrode at relatively high overpotentials – overpotentials that coincide with the occurrence of the oxygen-evolution reaction.

6.3.3 Oxidation of dithionite

In the same way as was done for sulphite, current–potential curves were recorded successively, containing 3.5×10^{-2} mol l^{-1} $S_2O_4^{2-}$ at pH=12.4 at a platinum electrode surface that was pre-treated cathodically at –0.5 V vs. Ag|AgCl for 5 min. It could be seen from these experiments that, in the first scan, three oxidation waves were observed, while, in the second and further scans, only two waves were obtained. Again, the difference between the first and other scans can be explained by considering the changes in the condition of the platinum electrode surface. At the initial potential of the first scan (E=–0.5 V vs. Ag|AgCl), an oxide and hydrogen-free electrode surface is obtained due to the pre-treatment procedure. From the first scan, it is clear that dithionite can be oxidised at a pure platinum surface. Around –0.05 V vs. Ag|AgCl, the current tends towards the formation of a limiting-current plateau. However, it is not a common limiting-current plateau, because its plateau shape is not determined by transport of dithionite but by a continuous decrease of the available Pt sites. This was verified by a chronoamperometric experiment at a stationary platinum electrode with a constant potential of –0.1 V vs. Ag|AgCl. No linear segment could be observed in the I vs. $t^{-1/2}$ plot, typical for transport-controlled reactions, which means that the formation of a limiting-current plateau could not be explained by transport of dithionite.

In the further scans, this first wave is not observed because in the aforementioned potential region, the electrode surface is no longer a pure platinum one but is a rearranged platinum hydroxide surface[39]. The results described in section 6.2 showed that the limiting-current plateau of the second oxidation wave (first scan) is controlled by transport of dithionite. This indicates that electron transfer from dithionite to PtOH and/or PtO is a much faster process than transport of dithionite towards the electrode. This is confirmed by the fact that in the further scans an identical limiting-current is obtained. The third oxidation wave in the first scan (second wave for the other scans) is attributed to the oxidation of sulphite described earlier. It is formed as a reaction product of the sodium dithionite oxidation and also of the homogeneous decomposition of sodium dithionite. Also in this case, a hysteresis effect is observed for the sulphite forward/backward sweep oxidation wave.

In the backward-sweep direction, a limiting-current plateau for dithionite is obtained, with limiting-current values that are almost equal to those obtained in the forward-sweep direction (second oxidation wave of the first scan, first wave of the other scans). This again is proof that the electron transfer of dithionite at PtOH and PtO is fast compared with the rate of transport. In addition, for the first wave (second and following scans) of dithionite, a hysteresis effect is observed. At a potential of about 0.25 V vs. Ag|AgCl, the reduction of PtO to PtOH starts to occur. Owing to the simultaneously occurring rearrangement of PtOH to OHPt, a dissimilar surface condition is present compared with the PtOH condition prevailing in the forward-scan direction. Slow kinetics for the oxidation of dithionite at rearranged platinum hydroxide can possibly explain the kinetically controlled decrease of dithionite signal leading to the observed hysteresis effect.

From what is described in this section, it can be concluded that the kinetics of the oxidation reaction of sulphite and dithionite at a platinum electrode in alkaline solution are strongly affected by the nature of the platinum surface. This is important when a platinum electrode is used for a quantitative investigation of the kinetics of the oxidation of sodium dithionite and/or sulphite or as electrode material in the development of a sensor for the measurement and/or control of dithionite and/or sulphite concentrations. However, for sodium dithionite, it has no serious consequences because the limiting-current at 0.45 V vs. SCE does not change as a function of scan number. However, this oxidation is still irreversible (no return peak observed) which means that, in the onset of the voltammetric wave, the current is controlled by charge-transfer kinetics. Therefore, it is possible to investigate and obtain the mechanism of the oxidation of sodium dithionite, which is explained in the next section.

6.4 Mechanism of the charge-transfer kinetics of dithionite oxidation

As mentioned in the previous section, the onset of the first oxidation wave of sodium dithionite is determined by kinetic parameters, and therefore it is possible to study the reaction rate and the mechanism of this oxidation reaction. In practice, a hypothesis will be formulated and compared with the experimental evidence. As long as there is no contradiction between the experimental evidence and the results predicted by the hypothesis, the defined hypothesis remains valid.

6.4.1 Experimental evidence

In Fig. 6.1, current–potential curves are shown of the oxidation of sodium dithionite at a platinum rotating-disc electrode in alkaline solution for dif-

ferent rotation rates of the electrode. Irreversible but well-defined waves are obtained, in which three distinctive regions can be observed:

- a first region from –0.5 to –0.2;
- a second region from –0.2 to 0;
- a third region from 0 to 0.4 V vs. Ag|AgCl.

In the first region, the current is completely independent of rotation rate of the electrode and increases exponentially, which means that in this region the current (or reaction rate) is mainly controlled by electron transfer and not by transport phenomena. This allows a study of the kinetics and the mechanism of the electron-transfer reaction of the oxidation of dithionite. The third region shows a well-defined limiting-current plateau. This indicates that in this region, electron transfer is so fast that the overall reaction rate is controlled by transport only. This is confirmed by a linear relationship between limiting-current and square root of the rotation rate of the electrode. In this region, it is not possible to study the kinetics and the mechanism, but such conditions are suitable for electroanalytical purposes and sensor development (see sections 6.5 and 6.7).

The second region is the mixed kinetic transport-controlled region, and the most negative part of it can also be used for kinetic and mechanistic studies of the electron-transfer reaction after the experimental currents have been compensated for transport limitations. Finally, a second wave is observed at potentials higher than 0.5 V vs. Ag|AgCl, which can be attributed to the oxidation of sulphite to sulphate. However, this wave is not further considered because the oxidation mechanism of sulphite showed poor reproducibility (see section 6.3), and sulphite detection in dyeing processes is not of great importance compared with dithionite detection.

Figure 6.8 shows the relationship between applied potential and logarithm of the kinetic current in the region from –0.35 to –0.05 V vs. Ag|AgCl for different concentrations of sodium dithionite. For each concentration, it was verified that the currents in this potential region are independent of the rotation rate of the electrode to be sure that kinetic parameters control the overall rate of the reaction. From the linear relationships shown in Fig. 6.8 (potential range between the dotted lines), the charge-transfer coefficient, α, could be determined[33] and was found to be 0.43 ± 0.07. The relatively high standard deviation for this type of determination is remarkable, which results in a relatively great uncertainty on the value of α.

Three other methods were used to obtain a value for the charge-transfer coefficient. The coefficient can be obtained from the difference between peak (E_p) and half-wave potential ($E_{p/2}$) in cyclic voltammetry at a stationary-disc electrode[40,41]:

$$|E_p - E_{p/2}| = (48/\alpha n_a) \qquad [6.5]$$

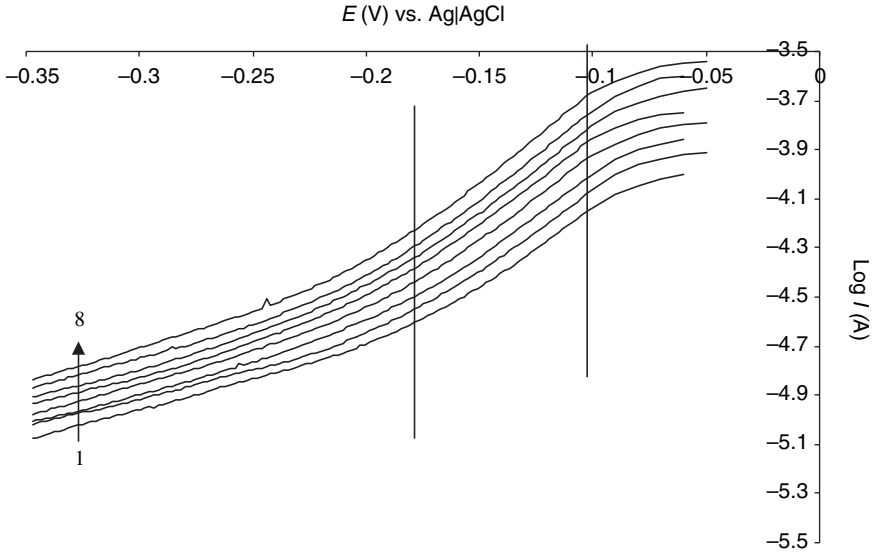

6.8 Relationship between potential and logarithm of the kinetic current for the oxidation of sodium dithionite at the surface of a platinum-disc electrode in alkaline solution (pH = 12.5) at a rotation rate of 1000 rpm. Sodium dithionite concentrations are (1) 6.0×10^{-4}, (2) 1.2×10^{-3}, (3) 1.8×10^{-3}, (4) 2.4×10^{-3}, (5) 3.6×10^{-3}, (6) 4.8×10^{-3}, (7) 6.0×10^{-3}, (8) 7.2×10^{-3} mol l^{-1}. (Reprinted from *Journal of Electroanalytical Chemistry*, Vol 553, Gasana *et al.*, 'Kinetics and mechanism of . . .', pp 35–42, Copyright 2003, with permission from Elsevier.)

with n_a the number of electrons exchanged in the rate-determining step. It is assumed here that no more than one electron is transferred in each of the elementary steps in the oxidation of sodium dithionite. The results obtained are summarised in Table 6.1. A second method is based on the shift of peak potential as a function of polarisation rate that obeys the following equation[40,41] recorded at stationary electrodes:

$$|E_j - E_i| = (30/\alpha n_a)\log(v_j/v_i) \qquad [6.6]$$

where E is the peak potential and v is the polarisation rate of curves i and j. Numerical data are shown in Table 6.2. Tables 6.1 and 6.2 show the analysis of the data, and values for the charge-transfer coefficient are obtained with $\alpha = 0.46 \pm 0.04$ if n_a is assumed to be 1. A final method, based on the currents obtained in the second potential region of the voltammetric wave, cannot be used at this stage of the analysis, because correction of the experimental current for transport effects necessitates knowledge of the order of the electron-transfer reaction in respect to sodium dithionite, which is not yet the case. However, the data obtained in the first potential region allow

Table 6.1 Values for αn_a calculated from the difference between peak and half-wave potential for the oxidation of sodium dithionite at a platinum-disc electrode

v (mV s^{-1})	E_p (mV)	$E_{p/2}$ (mV)	$\alpha\ n_a$
50	–76	–175	0.48
100	–56	–159	0.46
200	–38	–147	0.44
400	–26	–141	0.42
750	–4	–127	0.40
1000	8	–113	0.40

Table 6.2 Values for αn_a calculated from the shift of peak potential as a function of polarisation rate for the oxidation of sodium dithionite at a platinum-disc electrode

v_i (mV s^{-1})	v_j (mV s^{-1})	E_{Pj} (mV)	E_{Pi} (mV)	$\alpha\ n_a$
50	100	–76	–56	0.45
50	200	–76	–38	0.48
100	200	–56	–38	0.50
100	750	–56	–4	0.50
100	1000	–56	8	0.47
200	750	–38	–4	0.50
200	1000	–38	8	0.46

the determination of this order directly from the experimental currents by variation of the sodium dithionite concentration.

In Fig. 6.9, current–potential curves are shown for different sodium dithionite concentrations at a constant pH of 12.5 and a rotation rate of the electrode of N=6.67 Hz. In the third potential region, it is expected and found that the limiting-current is proportional to the concentration according to the Levich equation (1.15). When the reaction rate of the oxidation of dithionite is controlled by electron transfer only in the first potential region from –0.5 to –0.2 V vs. Ag|AgCl, the changes of experimental current as a function of sodium dithionite concentration should give information about the electrochemical reaction order in respect to sodium dithionite. A logarithmic plot of the relation between the experimental current and sodium dithionite concentration is shown in Fig. 6.10. A reaction order of 0.50±0.02 is obtained at different applied potentials. With this knowledge, a value of the electrochemical rate constant can be obtained by plotting $1/I^2$ as a function of $1/I\omega^{1/2}$ with experimental currents obtained in the first and second region of the voltammetric wave of sodium dithionite. Extrapolation

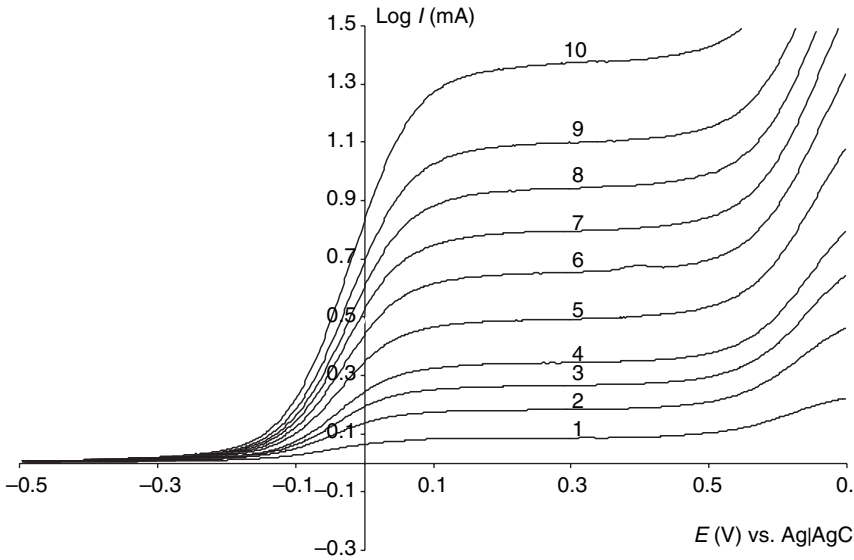

6.9 Current–potential curves recorded at a rotating platinum-disc electrode in an alkaline solution (pH = 12.5) at a rotation rate of 400 rpm for dithionite concentrations of (1) 6.0×10^{-4}, (2) 1.2×10^{-3}, (3) 1.8×10^{-3}, (4) 2.4×10^{-3}, (5) 3.6×10^{-3}, (6) 4.8×10^{-3}, (7) 6.0×10^{-3}, (8) 7.2×10^{-3}, (9) 8.4×10^{-3} and (10) 1.08×10^{-2} mol l^{-1}. (Reprinted from *Journal of Electroanalytical Chemistry*, Vol 553, Gasana *et al.*, 'Kinetics and mechanism of . . .', pp 35–42, Copyright 2003, with permission from Elsevier.)

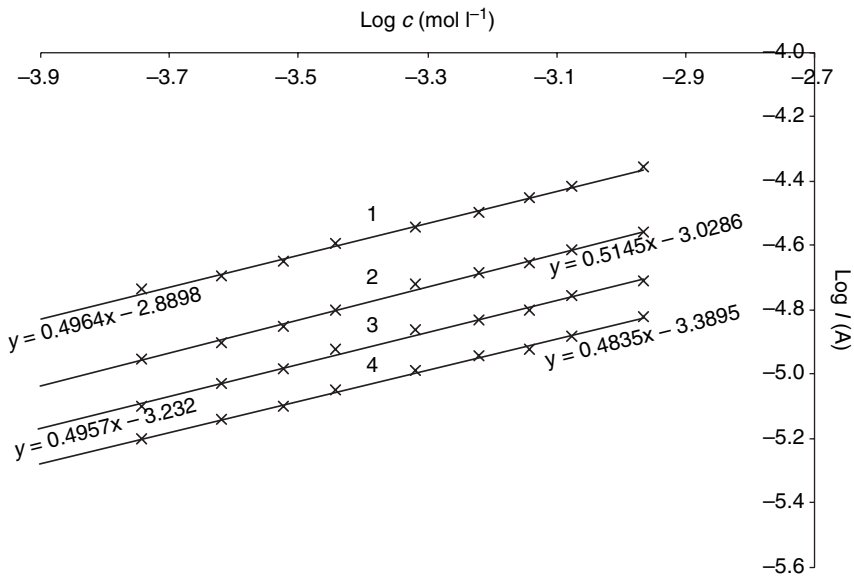

6.10 Logarithmic plot between the sodium dithionite concentration and the kinetic current obtained at applied potentials of (1) –0.2, (2) –0.25, (3) –0.3 and (4) –0.35 V vs. Ag|AgCl. (Reprinted from *Journal of Electroanalytical Chemistry*, Vol 553, Gasana *et al.*, 'Kinetics and mechanism of . . .', pp 35–42, Copyright 2003, with permission from Elsevier.)

of the linear parts of these curves to $1/I\omega^{1/2}=0$ results in a current controlled by the kinetics of electron transfer. Plotting the logarithm of these currents versus the applied potential results in the Tafel slope and a value for the charge-transfer coefficient. A value of 0.45 ± 0.03 was obtained, which is in agreement with the values obtained by the other methods.

Finally, the pH dependency of the current signals was investigated. Voltammetric curves were recorded obtained at a platinum rotating-disc electrode for different pH values in the 11.65–12.95 range at constant electrode-rotation rate. These experiments were repeated at other sodium dithionite concentrations. It was found that the measured current in all three regions of the voltammetric waves did not vary with pH.

6.4.2 Determination of the mechanism of dithionite oxidation reaction

Before considering and proposing mechanisms that consist of several elementary steps, some assumptions need to be made. From a statistical point of view, two general rules were taken into account:

- No more than two particles react with each other in one elementary reaction step at the same time.
- A maximum of one electron is exchanged in each elementary reaction step.

Specifically for the oxidation of dithionite, three additional rules were defined:

- No elementary reduction step(s) was included in the mechanism because no experimental evidence was found for it.
- In the first voltammetric wave of the reaction (see Fig. 6.1), sodium dithionite is oxidised to sulphite at a platinum electrode, and two electrons are exchanged in this reaction (see section 6.2).
- The condition of the platinum electrode surface can play an important role in the kinetics of electrochemical reactions, but for the kinetics of dithionite oxidation it was found that the platinum surface condition did not seriously interfere (see section 6.3).

Proposing a mechanism also necessitates knowledge of the compounds that can participate in the overall reaction. For an electrochemical reaction at the surface of an electrode, adsorbed species not present in the bulk of the solution should also be taken into account as a possible (intermediate) species. Species potentially present or formed in solution and/or at the surface of the electrode in the global oxidation reaction of dithionite to sulphate are summarised in Table 6.3.

Table 6.3 Species potentially present or formed during the oxidation of sodium dithionite at a platinum-disc electrode in alkaline solution

Species in solution and/or adsorbed at the electrode surface		Species adsorbed at the electrode surface	
$S_2O_4^{2-}$	SO_3^{2-}	$S_2O_4^{\bullet-}$	$SO_2^{\bullet}$
SO_4^{2-}	H_2O	SO_2^{-}	SO^{-}
OH^{-}	HSO_3^{-}	$OH^{\bullet}$	
SO_3^{-}	SO_2		

As a starting point, the experimental values of ca. 0.5 and 2 obtained for the charge-transfer coefficient and the number of electrons transferred in the first oxidation wave of dithionite, respectively, were linked to the theoretical expression for the transfer coefficient:

$$\alpha = [(n-\gamma)/\nu] - r\beta \qquad [6.7]$$

where γ is the number of electrochemical elementary steps preceding the rate-determining step (RDS), ν is the number of times that the rate-determining step occurs in the overall reaction, and β is the symmetry factor presumed to be equal 0.5; $r=1$ if the rate-determining step is electrochemical, and $r=0$ if the rate-determining step is chemical. It is clear that the rate-determining step of the proposed mechanism should be electrochemical, otherwise a value of 0.5 cannot be obtained with $n=2$. Therefore two possibilities remain, namely that the rate-determining step occurs once ($\nu=1$), preceded by another electrochemical step ($\gamma=1$) or that the rate-determining step occurs twice ($\nu=2$). The latter implies that an intermediate species should be formed twice in one or two elementary chemical steps preceding the rate-determining step. Preference was given to the second possibility because it would be compatible with the experimental reaction order with respect to dithionite being 0.5. Assuming that the final electrochemical step is rate-determining and that this step occurs only once can never explain a dithionite reaction order of 0.5. Therefore it is presumed that the following dissociation reaction is the initial step of the proposed mechanism:

$$S_2O_4^{2-} \leftrightarrows SO_2^{-} \qquad [6.8]$$

Evidence that this reaction occurs in homogeneous acidic solution was found in the literature[42]. However, the present study was carried out in alkaline solution, and therefore it is assumed that this dissociation reaction occurs only at the surface of the electrode. If that is the case, the initial step of the mechanism, equation 6.8 is replaced by:

$$S_2O_4^{2-} \leftrightarrows (S_2O_4^{2-})_{ads} \qquad [6.9]$$

$$(S_2O_4^{2-})_{ads} \leftrightarrows 2(SO_2^{-})_{ads} \qquad [6.10]$$

where the suffix *ads* means that the species is adsorbed at the electrode surface. Equations 6.9 and 6.10 are compatible with the fact that two SO_2^- particles are formed in one step preceding the electrochemical rate-determining step. However, again two possibilities can be proposed for adsorbed SO_2^- reacting further. A first possibility is the release of an electron in Equation 6.11 followed by reaction with hydroxide (Equation 6.12):

$$(SO_2^-)_{ads} \leftrightarrows (SO_2^{\bullet})_{ads} + e^- \quad [6.11]$$

$$(SO_2^{\bullet})_{ads} + OH^- \leftrightarrows (HSO_3^-)_{ads} \quad [6.12]$$

or reaction with hydroxide and release of an electron in one step (Equation 6.13):

$$(SO_2^-)_{ads} + OH^- \leftrightarrows (HSO_3^-)_{ads} + e^- \quad [6.13]$$

As is known from the results given above, an electrochemical step must be rate-determining. This inference means that all steps after the rate-determining one are faster and therefore do not contribute to the overall rate. This latter conclusion means that a distinctive choice between steps (Equations 6.11 and 6.13) can be made by recognising that if Equation 6.13 were to occur, a clear pH-dependence should be observed for the overall reaction. This is, however, not observed, and therefore Equation 6.13 can be eliminated as possible step. Equation 6.11 is compatible with the observed pH-dependence. The rate-determining step and all steps preceding it are not dependent on pH. OH^- is involved only in step(s) that follow the rate-determining step and therefore do not contribute to the overall reaction rate. As a conclusion, the following mechanism can be proposed:

- *Step 1*: $S_2O_4^{2-} \leftrightarrows (S_2O_4^{2-})_{ads}$ [6.9]
- *Step 2*: $(S_2O_4^{2-})_{ads} \leftrightarrows 2(SO_2^-)_{ads}$ [6.10]
- *Step 3*: $(SO_2^-)_{ads} \leftrightarrows (SO_2^{\bullet})_{ads} + e^-$ [6.11]
- *Step 4*: $(SO_2^{\bullet})_{ads} + OH^- \leftrightarrows (HSO_3^-)_{ads}$ [6.12]
- *Step 5*: $(HSO_3^-)_{ads} + OH^- \leftrightarrows SO_3^{2-} + H_2O$ [6.14]

The general rate equation valid for this proposed mechanism can be calculated and verified by experimental evidence. It is clear that if there is one contradiction between calculated results and experimental evidence, the proposed mechanism cannot be valid. Step 3 of the mechanism is proposed as RDS because it is the only electrochemical step in the reaction scheme. Its rate equation can be written as:

$$i = 2F\left[k_3\theta_{SO_2^-}(1-\theta_{SO_2^{\bullet}})e^{(1-\beta)FE/RT} - k_{-3}\theta_{SO_2^{\bullet}}(1-\theta_{SO_2^-})e^{-\beta FE/RT}\right] \quad [6.15]$$

where θ expresses the surface coverage by the respective compound (SO_2^- or $SO_2^{\bullet}$), F is the Faraday constant, R is the gas constant, *T* is the

temperature, β is the symmetry factor, E is an applied potential, and k_3 and k_{-3} are the rate constants of the forward and backward reactions, respectively.

The other steps in the mechanism are assumed to be in quasi-equilibrium because of their much higher rate then step 3. Therefore, the following equation is valid for steps 1, 2, 4 and 5:

$$k_i c_{\text{reagents}} = k_{-i} c_{\text{products}} \qquad [6.16]$$

By using the quasi-equilibrium equations of steps 1, 2, 4 and 5, it is possible to eliminate the unknown θ parameters in the rate equation (6.15). The surface coverage of SO_2^- can be eliminated by using step 2:

$$k_2 \theta_{S_2O_4^{2-}} \left(1 - \theta_{SO_2^-}\right)^2 = k_{-2} \theta_{SO_2^-}^2 \left(1 - \theta_{S_2O_4^{2-}}\right) \qquad [6.17]$$

or

$$\theta_{SO_2^-} = \sqrt{\frac{k_2 \theta_{S_2O_4^{2-}} \left(1 - \theta_{SO_2^-}\right)^2}{k_{-2}\left(1 - \theta_{S_2O_4^{2-}}\right)}} \qquad [6.18]$$

The surface coverage of $S_2O_4^{2-}$ in Equation 6.18 can be substituted using Equation 6.15 for step 1:

$$k_1 c_{S_2O_4^{2-}} \left(1 - \theta_{S_2O_4^{2-}}\right)^2 = k_{-1} \theta_{S_2O_4^{2-}} \qquad [6.19]$$

or

$$\theta_{S_2O_4^{2-}} = \frac{k_1 c_{S_2O_4^{2-}} \left(1 - \theta_{S_2O_4^{2-}}\right)}{k_{-1}} \qquad [6.20]$$

Substitution of Equation 6.22 in Equation 6.20 results in an expression for the surface coverage of SO_2^-:

$$\theta_{SO_2^-} = \sqrt{\frac{k_1 k_2 c_{S_2O_4^{2-}} \left(1 - \theta_{SO_2^-}\right)^2}{k_{-1} k_{-2}}} \qquad [6.21]$$

After substitution of the coverage fraction of SO_2^- into the general rate equation (6.15), the following equation is obtained:

$$i = 2F\left[k_3 \left(\frac{k_1 k_2}{k_{-1} k_{-2}} \right)^{1/2} c_{S_2O_4^{2-}}^{1/2} \left(1 - \theta_{SO_2^-}\right)\left(1 - \theta_{SO_2^\bullet}\right) e^{(1-\beta)FE/RT} \right.$$
$$\left. - k_{-3} \theta_{SO_2^\bullet} \left(1 - \theta_{SO_2^-}\right) e^{-\beta FE/RT} \right] \qquad [6.22]$$

In this equation, the second term of the right-hand side can be neglected because it expresses the rate of the reduction of dithionite. No evidence was found for this reaction in the potential region studied in this work. In the first term of the right-hand side of Equation 6.22, the $(1 - \theta)$ expression for

$SO_2^{\bullet}$ equals 1, because $SO_2^{\bullet}$ is formed in the rate-determining step and therefore reacts further in much faster elementary steps. This implies that the surface coverage of $SO_2^{\bullet}$ equals zero or $(1 - \theta)$ equals 1. The $(1 - \theta)$ for SO_2^{-} cannot be eliminated in the same way. However, its elimination is possible when an additional condition is taken into account in the proposed mechanism. If it is presumed that $k_{-2} \gg k_3$, this means that most of the SO_2^{-}, formed in step 2, that does not react in the RDS, will react to adsorbed dithionite via the backward reaction of step 2. When Equation 6.18 is modified, taking into account the above assumptions, the following final rate equation for the oxidation of sodium dithionite at a platinum electrode is obtained:

$$i = 2F\sqrt{\frac{k_1 k_2}{k_{-1} k_{-2}}} k_3 c_{S_2O_4^{2-}}^{0.5} e^{0.5(FE/RT)} \qquad [6.23]$$

This equation is fully compatible with the experimental evidence:

- The anodic current depends on the potential applied at the working electrode.
- The current density is not dependent on pH.
- The reaction order for dithionite is 0.5.
- The charge-transfer coefficient is 0.4. Equation 6.23 predicts a value of 0.5 because this value was presumed when deriving the equation, but the symmetry factor can vary from 0 to 1.

6.5 Detection of sodium dithionite

In the preceding sections, it was mentioned several times that the limiting-current of the first wave of the sodium dithionite oxidation is suitable for electroanalytical purposes because of the transport-controlled nature of this limiting-current. Indeed, it was proven earlier that this limiting-current can be correlated with the Levich equation (1.15), showing a linear relationship between limiting-current and sodium dithionite concentration.

However, it is not ideal to use cyclic or linear-sweep voltammetry as a method for analytical purposes. A more suitable method is chronoamperometry, which in fact is the application of a constant potential located in the limiting-current plateau and measurement of the limiting-current as a function of time. With this method, it is possible to measure continuously, and the required equipment setup becomes much more simplified.

Figure 6.11 shows the result of such a chronoamperometric experiment, where a constant potential of 0.45 V vs. Ag|AgCl is applied to the platinum electrode rotating at 6.67 Hz in a pH of 12.5. The sodium dithionite concentration was increased in ten consecutive steps. It can be seen that the limiting-current corresponds to the values obtained with linear-sweep

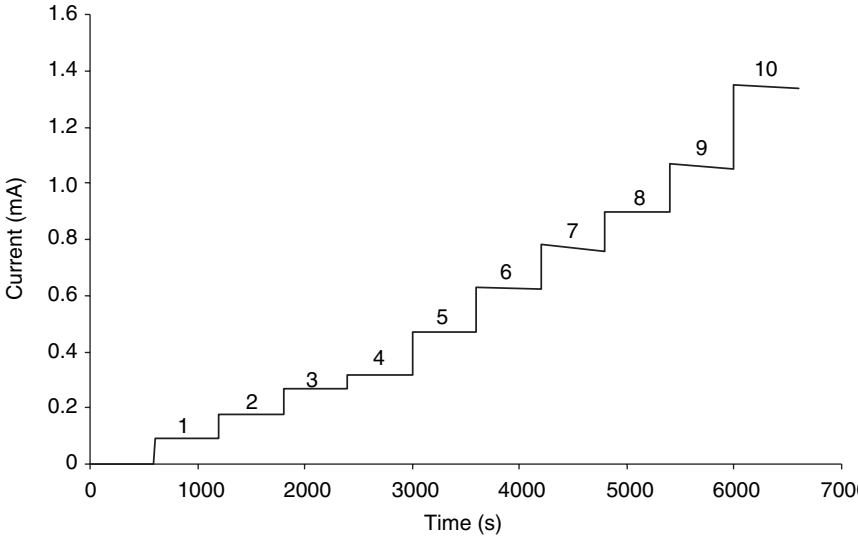

6.11 Chronoamperometric experiment at $E = 0.45$ V vs. Ag|AgCl recorded at a rotating platinum-disc electrode in an alkaline solution (pH = 12.5) at a rotation rate of 400 rpm for dithionite concentrations of (1) 6.0×10^{-4}, (2) 1.2×10^{-3}, (3) 1.8×10^{-3}, (4) 2.4×10^{-3}, (5) 3.6×10^{-3}, (6) 4.8×10^{-3}, (7) 6.0×10^{-3}, (8) 7.2×10^{-3}, (9) 8.4×10^{-3} and (10) 1.08×10^{-2} mol l^{-1}.

voltammetry and shown in Fig. 6.9, and that these currents do not change, which means that the electrode behaves in a stable manner as a function of time; continuous detection of dithionite is possible with this setup. From the data in Fig. 6.11, it could be concluded that the limiting-current is proportional to the dithionite concentration following the next given equation:

$$I(mA) = 122.6c + 0.032 \quad (R^2 = 0.9993) \qquad [6.24]$$

6.6 Detection of indigo

Indigo can be oxidised and reduced according to the following equation and behaves as a reversible system:

$$C_{16}H_{10}N_2O_2 + 2H_2O + 2e^- \leftrightarrows C_{16}H_{12}N_2O_2 + 2OH^- \qquad [6.25]$$

The oxidised form of indigo is only sparingly soluble in aqueous solution, which has serious consequences for electroanalytical purposes. Indeed, oxidising the reduced and water-soluble form of indigo to its insoluble oxidised form results in the formation of a deposited layer of the oxidation product. This causes blocking of the electrode surface and prevents it from further use in electroanalytical applications. However, this problem can be cir-

cumvented because the insoluble product formed as a deposited layer in the forward (oxidative) sweep direction is reduced in the backward-sweep direction. This means that the formed layer is dissolved again in solution by reducing the oxidised, initially deposited, layer of insoluble indigo to its soluble form. Use will be made of this '*in situ*' cleaning property further in this work (see section 6.7.4).

6.7 Simultaneous detection of sodium dithionite, sulphite and indigo at a wall-jet electrode

6.7.1 Introduction

In this section, the aim is to explain how the previously discussed results can be implemented in an industrially acceptable setup, taking into account parameters such as long-term stability, selectivity, reproducibility, simplicity and low cost. Therefore, it was the intention of the authors not to use the rotating-disc electrode, but rather to implement a so-called wall-jet electrode, which possesses similar characteristics but with a long-term stability, simplicity and cost effectiveness that are much more favourable than for a rotating-disc electrode. The setup of the wall-jet electrode is discussed in Chapter 1, pages 19–21.

6.7.2 Characterisation of the wall-jet disc electrode

Prior to use for analytical purposes, the developed wall-jet electrode should first be characterised and calibrated. This is described here, where the wall-jet disc electrode is optimised by making use of a reversible, one-electron exchanging, redox system ($[Fe(CN)_6]^{4-}/[Fe(CN)_6]^{3-}$) in order to obtain the most favourable conditions for the determination of sodium dithionite, sulphite and indigo.

A first parameter that was investigated is the distance between nozzle and working-electrode surface, further called NES gap. Current–potential curves showed that, for different NES-gap values, the limiting current of the $[Fe(CN)_6]^{3-}$ reduction is almost independent of NES-gap value in a range of 1–6 mm. In addition, this range can be selected as a good working range because, for smaller NES-gap values, the risk of blocking of the capillary (e.g. by textile fibres) becomes high. Larger NES gaps are, from an economical point of view, not favourable. Therefore, a NES-gap value of between 1 and 6 mm is used, with an electrode diameter of 3 mm.

A second parameter that was varied is the flow rate of the solution. This was done in the same solution as was used in the previous section with the same nozzle and electrode. The NES gap was fixed at 2.14 mm, the flow rate

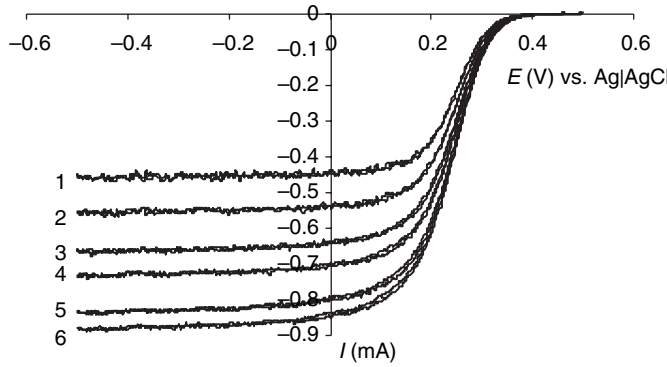

6.12 Current–potential curves of the reduction of 2.0×10^{-3} mol l^{-1} $K_3[Fe(CN)_6]$ in 0.8 mol l^{-1} KNO_3 recorded at a wall-jet platinum-disc electrode with a diameter of 3.0 mm, a nozzle diameter of 2.0 mm, a NES gap of 2.1 mm and a flow rate of (1) 0.5, (2) 1.0, (3) 1.6, (4) 2.0, (5) 2.7 and (6) 3.0 l min^{-1}. (Reprinted from *Analytica Chimica Acta*, Vol 486, No 1, Gasana *et al.*, 'A wall-jet disc . . .' pp 73–83, Copyright 2003, with permission from Elsevier.)

was changed by variation of the vessel opening (see Chapter 1, pp 19–21) and was measured with a flow meter (again, see Chapter 1, pp 19–21). The results of these experiments are shown in Fig. 6.12. It can be seen that the limiting current of the Fe(III) reduction increases with flow rate. A logarithmic plot of the limiting current versus the flow rate proved that the limiting current is proportional to the square root of the flow rate. Note also that for smaller flow rates a larger noise signal is detected.

Finally, the diameter of the platinum electrode and the diameter of the nozzle were varied. Similarly shaped curves were obtained as shown in Fig. 6.12, and therefore they are not given. A linear relationship between limiting current I_L (μA) and electrode area A (cm^2) was obtained.

Investigation of the influence of the diameter of the nozzle was not simple. The nozzle diameter was varied from 1.25 to 3.0 mm, and the obtained results were not always reproducible. This can possibly be explained by the fact that diminishing the nozzle diameter also has an influence on the flow rate. With the smallest nozzle diameter, the maximum flow rate that could be obtained was 0.5 l min^{-1}. As can be seen from the results in Fig. 6.12, this is not an optimal value for the flow rate, resulting in relatively small signals with a weak signal-to-noise ratio. From a qualitative analysis, it was found that the limiting current increases with decreasing nozzle diameter. This can be explained by the fact that a smaller nozzle diameter in combination with a constant flow rate causes a jet of solution under higher pressure. This gives rise to smaller values for the thickness of the diffusion layer.

Determination of the optimal values for the parameters investigated in the first part of the research, and which will be used as fixed values in the following sections, resulted in a flow rate of 1.5 l min^{-1}, an electrode diameter of 3.0 mm and a nozzle diameter of 2.0 mm. The relatively large nozzle diameter is used to avoid blocking by fibres. For the same reason, a NES gap of 2.5 mm is used. A second reason is that in the region of 1–3 mm, the limiting current is almost independent of the NES-gap distance, therefore some deviation is allowed without distortion of the electrode signal. An electrode diameter of 3.0 mm is used to obtain a large signal without the risk of IR-drop effects at large currents associated with large sodium dithionite concentrations. For the same reason, a flow rate of 1.5 l min^{-1} is selected. The obtained optimal parameter values resulted in satisfactory signal-to-noise ratios.

6.7.3 Detection of sodium dithionite and sulphite concentrations

Linear-sweep experiments recorded in solutions containing sodium dithionite or sulphite were discussed in sections 6.2 and 6.3 using rotating-disc electrodes. With these electrodes, well-shaped limiting-current plateaux were obtained for the oxidation of dithionite to sulphite, while the second plateau shows some kinetic influence. This could be explained by changes in electrode surface conditions, which inevitably have an effect on the kinetics of sulphite oxidation. Despite this disadvantage, it is still possible to measure sulphite concentrations based on the plateau currents of the second oxidation wave. Therefore, the investigation in this section is started immediately with a double potential step chronoamperometric experiment in order to measure the limiting current $I_{0.45\,V}$ of sodium dithionite oxidation at a first applied potential E_{dit}=+0.45 V vs. Ag|AgCl. It will also measure the step related to the sum of sodium dithionite and sulphite oxidation ($I_{0.8\,V}$) at a second applied potential E_{sul}=+0.8 V vs. Ag|AgCl using the wall-jet electrode setup. Each potential is alternately applied for 5 s, and the resulting current signal is measured at the end of each potential step.

In Fig. 6.13, the variation of the limiting currents of the oxidation of sodium dithionite and sulphite is shown as a function of time during decomposition of sodium dithionite in an alkaline solution. In the oxidation of dithionite corresponding to the first potential, two electrons are exchanged, while at the second potential, six electrons are released. This means that the current contribution of sulphite ($I_{L,sul}$) present in solution, also shown in Fig. 6.13, can be calculated as:

$$I_{sul} = I_{0.8V} - 3I_{0.45V} \qquad [6.26]$$

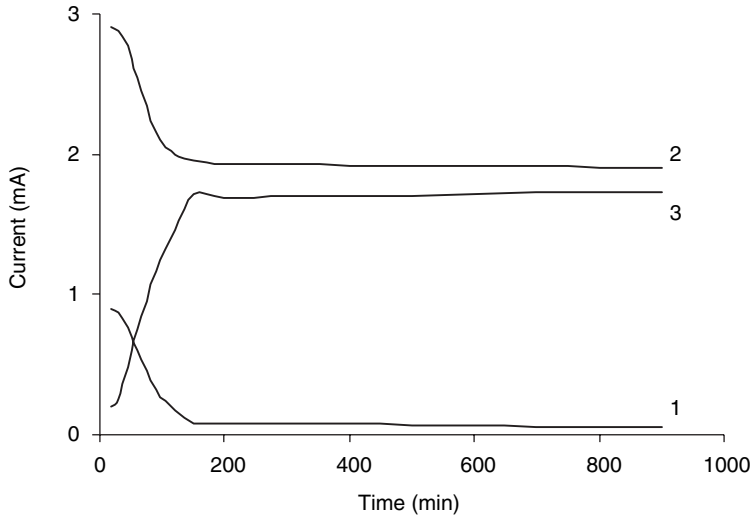

6.13 Variation of experimental currents measured at a potential of (1) 0.45 V showing decomposition of sodium dithionite, and (2) 0.8 V vs. Ag|AgCl showing the decomposition of dithionite and formation of sulphite as reaction product of dithionite decomposition. (3) Current contribution of sulphite calculated according to Equation 6.28. (Reprinted from *Analytica Chimica Acta*, Vol 486, No 1, Gasana *et al.*, 'A wall-jet disc . . .' pp 73–83, Copyright 2003, with permission from Elsevier.)

From the data shown in Fig. 6.13, the concentrations of sodium dithionite and sulphite can be calculated by Equations 6.27 and 6.28 after calibration (determination of B and B′). This is achieved by measuring the limiting current in a solution with known dithionite and sulphite concentration (determined by titration). It was found that B and B′ were equal to 0.75 ± 0.01 and 0.74 ± 0.04 A l mol^{-1}:

$$c_{\text{dit}} = \text{B}I_{0.45\text{V}} \qquad [6.27]$$

$$c_{\text{sul}} = \text{B}'(I_{0.8\text{V}} - 3I_{0.45\text{V}}) \qquad [6.28]$$

The results of this calculation for the above-mentioned decomposition experiment are given in Fig. 6.14 by the continuous lines. The crosses illustrate the variation of the concentration of dithionite and sulphite in solution obtained by titration of samples taken at fixed times. It can be seen that the concentrations obtained by calculation from the experimental currents (continuous line) are in good agreement with the ones obtained by titration (crosses). Note also that the increase of the concentration of sulphite is twice as high as the drop of the sodium dithionite concentration. Indeed, for each dithionite ion that is decomposed, two sulphite ions are

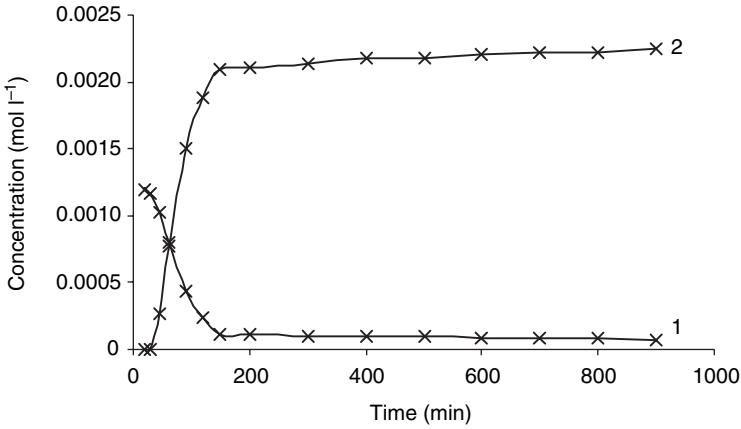

6.14 Variation of the concentrations of dithionite (curve 1) and sulphite (curve 2) during dithionite decomposition obtained by measuring limiting currents at 0.45 and 0.8 V vs. Ag|AgCl at a platinum wall-jet electrode (data of Fig. 6.13). A flow rate of 1.5 l min^{-1}, a diameter of the electrode of 3.0 mm, a diameter of the nozzle of 2.0 mm and a NES gap of 2.5 mm were used. The crosses indicate concentrations determined by titration. (Reprinted from *Analytica Chimica Acta*, Vol 486, No 1, Gasana *et al.*, 'A wall-jet disc . . .' pp 73–83, Copyright 2003, with permission from Elsevier.)

formed (Equation 6.1). Detection limits for dithionite and sulphite were found to be 5×10^{-5} mol l^{-1}, while the upper limit of linearity of the calibration line was located around 1×10^{-2} mol l^{-1}.

6.7.4 Detection of sodium dithionite, sulphite and indigo

Previous investigations (discussed in section 6.6) demonstrated that indigo is soluble in water in the reduced form only. Oxidation of the reduced form at the surface of an electrode inevitably causes deposition of the sparingly soluble reaction product, even in the presence of sodium dithionite concentrations that are common in the textile dyeing industry. The deposition of indigo at the electrode surface during oxidation cannot be prevented completely by reduction with dissolved sodium dithionite because of limitations in transport of dithionite towards the electrode surface. Therefore, the electrode surface should be cleaned in an alternative way after each measurement of a limiting current by applying a potential where indigo is reduced electrochemically. Preliminary experiments proved that suitable potentials for oxidation of leuco-indigo or reduction of indigo in alkaline solutions are located between –0.7 and –0.3 V and –0.5 and –0.8 V vs. Ag|AgCl, respectively. However, a fraction of the usable potential range for

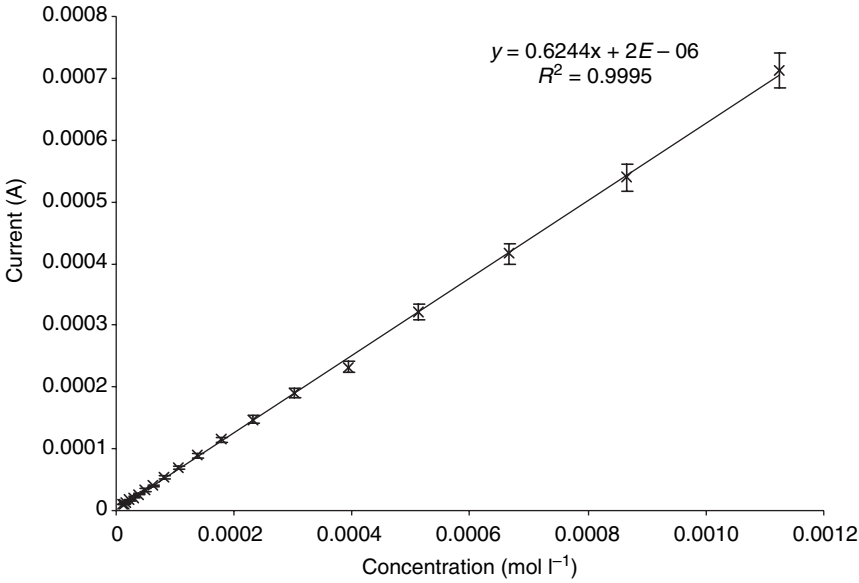

6.15 Calibration plot of indigo at a platinum electrode positioned in a wall-jet with a flow rate of 1.5 l min^{-1}, a diameter of the electrode of 3.0 mm, a diameter of the nozzle of 2.0 mm and a NES gap of 2.5 mm. Currents are measured at –0.55 V vs. Ag|AgCl. (Reprinted from *Analytica Chimica Acta*, Vol 486, No 1, Gasana *et al.*, 'A wall-jet disc . . .' pp 73–83, Copyright 2003, with permission from Elsevier.)

indigo oxidation overlaps with the onset of the oxidation wave of sodium dithionite. Therefore, first the interference signal of sodium dithionite on the indigo oxidation signal was investigated. It was found that the amperometric signal of indigo is independent of dithionite concentration in the region from –0.6 to –0.45 V vs. Ag|AgCl. Therefore, indigo can be detected selectively in this potential range.

Figure 6.15 shows a calibration plot obtained by repeated additions of indigo and dithionite to the cell solution, keeping the dithionite/indigo concentration ratio constant (to guarantee that all added indigo is in the reduced form). A linear relationship was found with satisfactory sensitivity and reproducibility at a potential of E=–0.55 V vs. Ag|AgCl. The reproducibility was studied by repeating the calibration experiment eight times, resulting in the error flags shown in Fig. 6.15. Note that this plot was obtained by measuring the signal for reduced indigo during 1 s at –0.55 V vs. Ag|AgCl, followed by a cleaning step of 10 s at –0.9 V vs. Ag|AgCl.

For the simultaneous detection of sodium dithionite, sulphite and indigo, a multistep amperometric method was worked out and optimised, as outlined in Table 6.4. It is clear that after each measuring step, the electrode surface should be cleaned to remove indigo that is oxidised at all applied

Table 6.4 Sequence of applied potentials for simultaneous detection method

Solution detected	Applied potential (vs. Ag|AgCl)	Applied time(s)
Cleaning	–0.90	10
Indigo	–0.55	1
Cleaning	–0.90	10
Dithionite	0.45	1
Cleaning	–0.90	10
Sulphite	0.80	1

oxidation potentials. The times applied for measurement of the current signals are the shortest times possible in order to obtain a steady state without a drop of the output signal due to indigo precipitation. However, the period to clean the surface is made 5 s longer than the shortest time observed to be necessary to clean the surface completely. Figure 6.16 shows the results of such a potential multistep amperometric experiment obtained with a cell solution in which the concentrations of indigo and dithionite were increased periodically by repeated additions of the reagents. In Fig. 6.16a, the experimental current signals for sodium dithionite (1), sulphite (2) and indigo (3) are shown. After each period of about 240 s, the concentration of these compounds was increased by the addition of a solution of indigo and dithionite with a concentration ratio of 1:2. After reduction of indigo in this solution, a ratio of about 1:1 was obtained. The current signals of the cleaning steps are not shown for clarity of the figure and because they do not contribute to the analytical purpose of the method. The concentrations of the appropriate compounds could be calculated from these data using Equations 6.29, 6.30 and 6.31 and are shown in Fig. 6.16b (continuous line). The symbols in the same figure represent the concentration of dithionite, sulphite and indigo obtained by titration after withdrawing an aliquot from the solution at appropriate times. It can be seen that there is no significant discrepancy between the results of both methods. From Fig. 6.16b, it can also be seen that after reduction of indigo in the stock solution, a ratio of about 0.8 is obtained for c_{ind}/c_{dit}. This is sufficiently close to 1 regarding the continuous decomposition of dithionite as a function of time:

$$c_{ind} = B'' I_{-0.55V} \quad [6.29]$$

$$c_{dit} = B(I_{0.45V} - I_{-0.55V}) \quad [6.30]$$

$$c_{sul} = B'(I_{0.8V} - 3I_{0.45V} - I_{-0.55V}) \quad [6.31]$$

where B″ is 0.62 A l mol^{-1}.

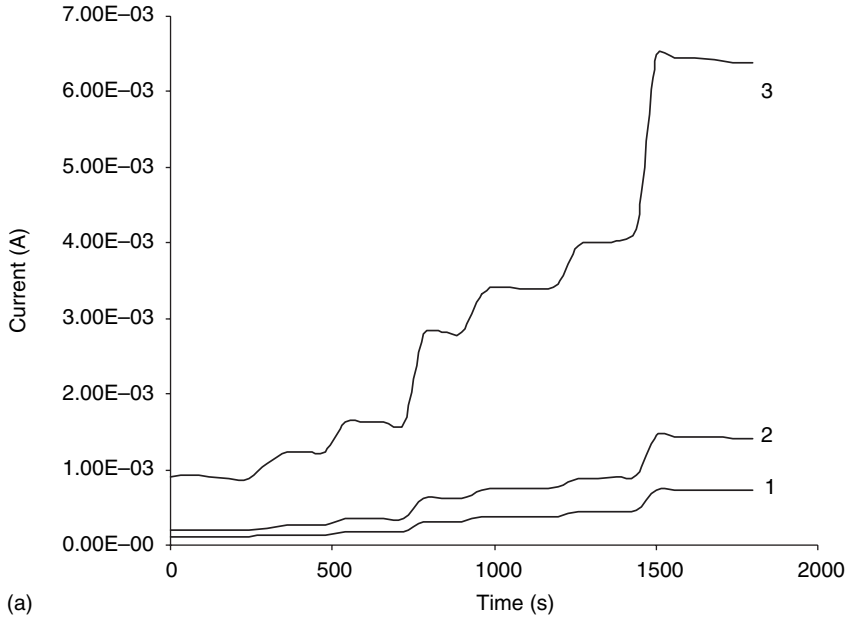
7.00E–03
6.00E–03
5.00E–03
4.00E–03
3.00E–03
2.00E–03
1.00E–03
0.00E–00
Current (A)
0
500
1000
1500
2000
Time (s)
3
2
1

(a)

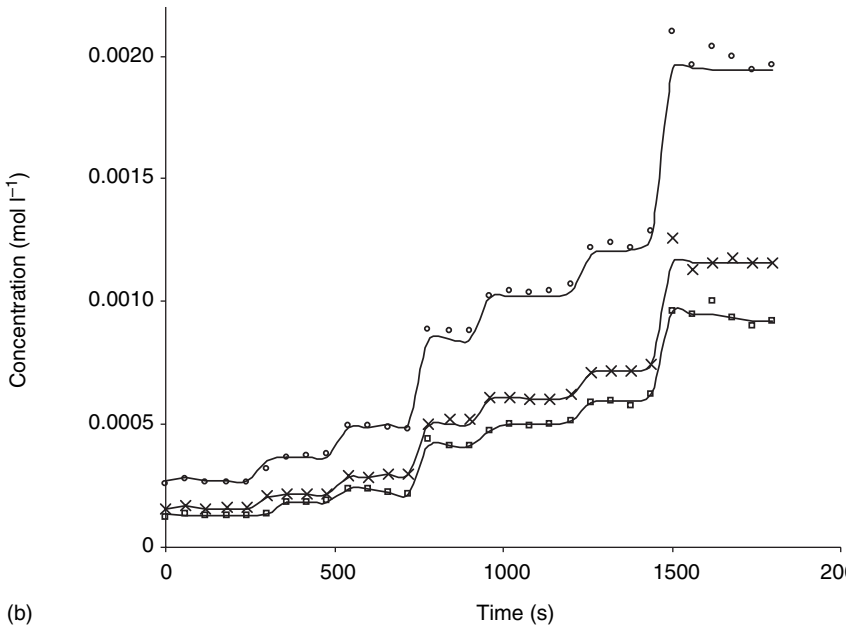
0.0020
0.0015
0.0010
0.0005
0
Concentration (mol l^{-1})
0
500
1000
1500
2000
Time (s)

(b)

6.7.5 Dyeing-process behaviour with and without sensor system

In this section, the use of a wall-jet electrode (with optimal values for its parameters as described in section 6.7.2) and the method to detect simultaneously sodium dithionite, sulphite and indigo (see section 6.7.4) are evaluated as a function of reproducible dyeing processing. In order to evaluate this, a spectrophotometric method was used to measure the amount of dye absorbed and/or adsorbed by the dyed fabric.

The first section of Fig. 6.17 and Fig. 6.18 shows the changes of indigo and sodium dithionite concentration (measured in the bath solution with the developed sensor) and of absorbance and wavelength of the dye taken up by the fabric (measured off-line, spectrophotometrically), respectively. The experiment was performed in a continuous dyeing line with a similar step as the one for bleaching described in Chapter 5, section 5.4.2. The data of Fig. 6.18 show that the concentration of dye stuff decreases as a function of time, which can easily be understood as the uptake of indigo by the fabric without a considerable change in volume of the bath solution. This means that dilution of indigo occurs measured as a concentration decrease. It can be seen that the concentration of dithionite also decreases. This can be explained by the fact that, besides uptake by the fabric, dithionite is also consumed in the bath. Convection in the bath causes uptake of oxygen in the bath solution that can oxidise dithionite and indigo easily.

The second sections of Fig. 6.17 and Fig. 6.18 represent the same parameters as in the first section, but this time the concentrations of indigo and sodium dithionite are not only measured but are also row controlled. This

6.16 Variation with time of amperometric currents, resulting concentrations and concentrations obtained by titration of indigo, dithionite and sulphite, obtained from a cell solution in which the concentrations of dithionite and indigo were increased periodically by recurrent additions. (a) Variation of the experimental currents measured at a platinum wall-jet electrode with a flowrate of 1.5 l min^{-1}, a diameter of the electrode of 3.0 mm, a diameter of the nozzle of 2.0 mm and a NES gap of 2.5 mm and at a potential of (1) –0.55 V, (2) 0.45 V and (3) 0.8 V vs. Ag|AgCl. (b) Variation of the concentrations of indigo (×), dithionite (□) and sulphite (○), obtained by titration and from limiting-currents (continuous lines) measured at a platinum wall-jet electrode with a flow rate of 1.5 l min^{-1}, a diameter of the electrode of 3.0 mm, a diameter of the nozzle of 2.0 mm and a NES gap of 2.5 mm and by using Equations 6.29–6.31 (full lines). (Reprinted from *Analytica Chimica Acta*, Vol 486, No 1, Gasana *et al.*, 'A wall-jet disc . . .' pp 73–83, Copyright 2003, with permission from Elsevier.)

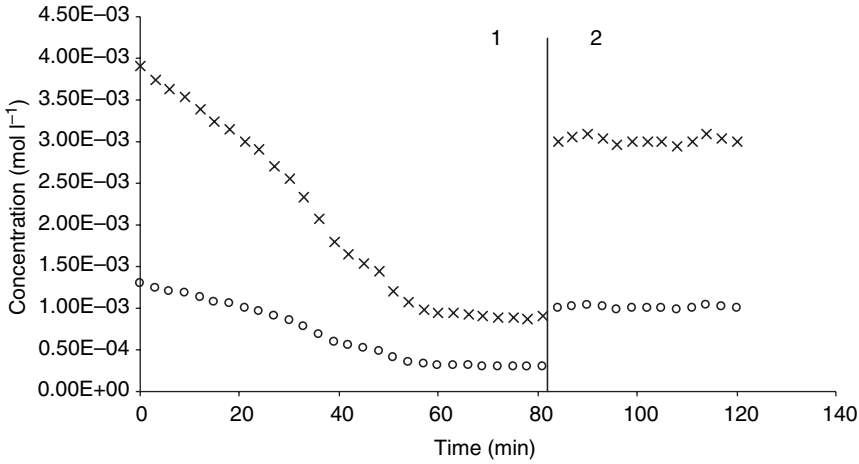

6.17 Changes in (○) indigo and (×) sodium dithionite concentration during a laboratory-scale dyeing process with indigo. Current signals, proportional to those concentrations, are obtained by using the described multi-step chronoamperometric method at a wall-jet platinum-disc electrode. The concentrations are calculated using Equations 6.29 and 6.30. Section (1) measurement of concentrations; section (2) measurement and control of concentrations. (Reprinted by permission of *Textile Research Journal*.)

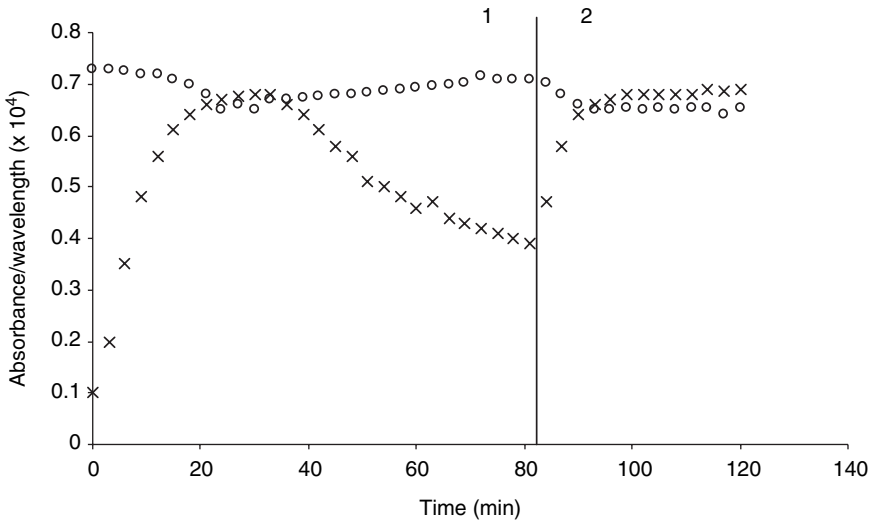

6.18 Changes in spectrophotometric characteristics of an indigo-dyed fabric in a laboratory-scale pilot line with (1) measurement and (2) control of the concentrations of indigo and sodium dithionite. Characteristics are (×) absorbance and (○) wavelength at maximal absorbance. (Reprinted by permission of *Textile Research Journal*.)

is obtained by addition (automatic opening and closing of valves dependent or the electrode signal) of concentrated indigo and dithionite solution to the dyeing bath.

With this setup, the advantage of using the developed sensor during dyeing is shown. In the first section of the curves in Fig. 6.18, it can be seen that some deviation occurs in the reproducibility of the dyed product for wavelength as well as for colour intensity. In relation to this, indigo and dithionite concentration decrease during this same time-section (Fig. 6.17). The decrease of the indigo concentration can be explained by fabric that ab- and adsorbs indigo from the solution. This assumes that the amount of dye taken up by the fabric is dependent on the actual concentration of indigo and is observed in Fig. 6.18 as a time effect.

Additional proof for the relation between indigo concentration and uptake of indigo by the fabric was obtained when the concentrations of indigo and dithionite were controlled. It can be seen clearly from the second section of Fig. 6.17 and Fig. 6.18 that if the concentration of indigo is kept constant, the quality and reproducibility of the dyed product improves remarkably. In addition, the spectrophotometric data results remain constant, indicating that a reproducible dye result is obtained for the fabric.

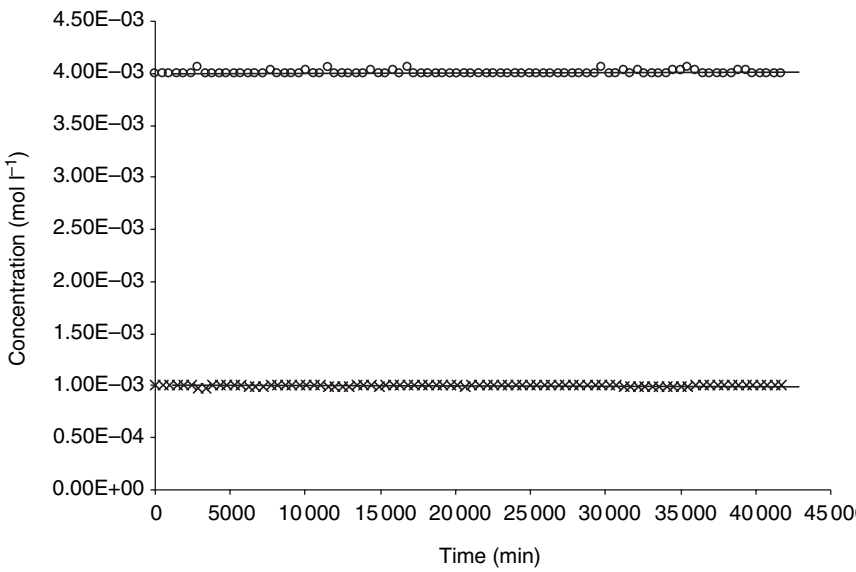

6.19 Long-term stability test of sensor system over a period of 1 month during continuous dyeing of textile in a pilot, laboratory-scale, dyeing line. Concentrations of indigo (×) and dithionite (○) obtained by titration are equal to those measured by the sensor system (continuous lines). (Reproduced by permission of *Textile Research Journal*.)

This result shows clearly that the developed sensor system is useful in the textile dyeing industry.

Finally, the long-term stability of the sensor system was tested during a dyeing process where the concentrations of indigo and dithionite were controlled at a fixed value of 1.0×10^{-3} and 4.0×10^{-3} mol l^{-1}, respectively. Simultaneously, aliquots were taken from the bath solution and titrated according to the established method. The results are shown in Fig. 6.19, and it can be seen that the concentration of indigo and dithionite is constant in the bath due to the good long-term stability of the sensor. A poor long-term stability would have resulted in a shift of the concentration of these compounds, which in turn would have resulted in a deviation between indigo and dithionite concentration obtained by the sensor and by titration. This is not the case.

6.8 References

1. The Merck Index, 12th ed., Merck and Co, New Jersey, 1996.
2. Othmer K., *Encyclopedia of Chemical Technology*, 3rd edn., **8** (1979) 313.
3. *Ullmann's Encyclopedia of Industrial Chemistry*, 5th edn., **A14** (1989) 149.
4. Yost D.M., Russel H., *Systematic Inorganic Chemistry of the Fifth and Sixth Group Nonmetalic Elements*, Prentice Hall, New York, 1946.
5. Westbroek P., Van Haute B., Temmerman E., *Fres. J. Anal. Chem*., **354** (1996) 405–409.
6. Westbroek P., Temmerman E., Kiekens P., *Anal. Commun*., **35** (1998) 21–23.
7. Westbroek P., Temmerman E., Kiekens P., Govaert F., *J. Autom. Chem*., **20** (1998) 185–188.
8. Westbroek P., Temmerman E., Kiekens P., *Anal. Chim. Acta*, **385** (1999) 423–428.
9. Westbroek P., Temmerman E., *J. Electroanal. Chem*., **482** (2000) 40–47.
10. Bauer H., Kowski K., Kuhn H., Luttke W., Rademacher P., *J. Mol. Structure*, **445** (1998) 277–286.
11. Miliani C., Romani A., Favaro G., *Spectrochim. Acta*, **54** (1998) 581–588.
12. *Ullmann's Encyclopedia of Industrial Chemistry*, 5th edn., **A9** (1989) 74.
13. Huang C.C., Yu W.H., *Text. Res. J*., **69** (1999) 914–918.
14. Choi H.T., Jeong S.H., Kim S.R., Juang J.Y., Kim S.H., *Text. Res. J*., **71** (2001) 563–573.
15. Church J.S., O'Neill J.A., Woodhead A.L., *Appl. Spectr*., **52** (1998) 1039–1046.
16. Jordan D.M., *AATCC Rev*., **1** (2001) 76–80.
17. Kazmi S.Z., Grady F.L., Mock G.N., Hodge G.L., *ISA Trans*., **35** (1996) 33–43.
18. Paulsson N., Stocklassa B., *Foren. Sc. Int*., **103** (1999) 37–59.
19. Reininger D.S., *Text. Chem. Col*., **29** (1997) 13–17.
20. Brown L., Szekeres L., *Talanta*, **26** (1979) 414–416.
21. Kilroy W.P., *Talanta*, **27** (1980) 343–347.
22. Kilroy W.P., *Talanta*, **30** (1983) 419–422.
23. Baumgarte U., *Mell. Textilber*., **68** (1987) 189–195.
24. Bard A.J., Parsons R., Jordan J., *Standard Potentials in Aqueous Solution*, Marcel Dekker, New York, 1985.

25. Serjeant E.P., *Potentiometry and Potentiometric Titrations*, Wiley, Chichester, 1984.
26. Bechtold T., Butscher E., Bobleter O., *Textil. Praxis. Int*., **47** (1992) 44–49.
27. Denney R.C., Sinclair R., *Visible and Ultraviolet Spectroscopy*, Wiley, Chichester, 1987.
28. Schlosser U., Bahners T., Schollmeyer E., *Melliand. Textilber*., **78** (1997) 622–625.
29. Camacho F., Paez M.P., Jimenez M.C., Fernandez M., *Chem. Eng. Sci.*, **52** (1997) 1387–1391.
30. Shaikh A.A., Zaidi S.M.J., *J. Chem. Technol. Biotechnol.*, **56** (1993) 139–145.
31. Bard A.J., *Encyclopedia of Electrochemistry of the Elements*, Marcel Dekker, New York, 1975.
32. Brett C.M.A., Oliveira Brett A.M., *Electrochemistry: Principles, Methods and Applications*, Oxford University Press, New York, 1993.
33. Bockris J.O'M., Reddy A.K.N., *Modern Electrochemistry 2*, Plenum Press, New York, 1970.
34. Jaaf-Golze K.A., Kolb D.M., Scherson D., *J. Electroanal. Chem*., **200** (1986) 353–362.
35. Angerstein-Kozlowska H., Conway B.E., Sharp W.B.A., *Electroanal. Chem. Interfac. Electrochem.*, **43** (1973) 9–36.
36. Horanyi G., *J. Solid State Electrochem.*, **2** (1998) 237–241.
37. Horanyi G., *Electrochim. Acta*, **36** (1991) 1453–1463.
38. Tilak B.V., Conway B.E., Angerstain-Kozlowska H., *Electroanal. Chem. Interfac. Electrochem.*, **48** (1973) 1–23.
39. Arvia A.J., Salvarezza R.C., Triaca W.E., *Electrochim. Acta*, **34** (1989) 1057–1071.
40. Weissberger A., Rossiter B., *Physical Methods for Chemistry 1*, Wiley Interscience, New York, 1971.
41. Southampton Electrochemistry Group, *Instrumental Methods in Electrochemistry*, Wiley, New York, 1985.
42. Camacho F., Paez P., Jimenez C., Fernandez M., *Chem. Eng. Sci.*, **52** (1997) 1387–1391.

7

Advantages of electrocatalytic reactions in textile applications: example – electrocatalytic oxidation of sodium dithionite at a phthalocyanine and porphyrin cobalt(II)-modified gold electrode

P. WESTBROEK

7.1 Introduction

Sodium dithionite has several applications as a reducing agent, for example in the reduction of textile dyes for dyeing processes. This reduction is crucial for the process because the oxidised form of most of these dyes (indigo, indanthrenes, etc.) is virtually insoluble in aqueous solutions. However, sodium dithionite is relatively unstable and reacts with oxygen, potentially causing a rapid decline in its concentration during processing[1,2]. This can have a serious influence on the actual reduced dye concentration and on the quality and reproducibility of the dyed textile product.

In Chapters 3–6, the development of sensors to measure concentrations of chemical components important in the textile industry is discussed for hydrogen peroxide in bleaching[3–6], sodium dithionite[7–10] and sulphite[8,10] in dyeing, as well as the dyes themselves such as indigo[10] and indanthrenes[7,9]. These investigations focused primarily on voltammetric and amperometric detection of these components using rotating-disc[3–9], ultramicro[5] and wall-jet electrodes positioned in flow-through cells[10]. To support the insight into the analytical determination of the concentration of the above-mentioned chemicals, the mechanism[11–13], kinetics[11–14] and reagent transport properties[8,11–14] of the oxidation/reduction reactions used for their analytical detection was also discussed in those chapters. The reason for initiating the above-mentioned investigations on sodium dithionite and associated dye sensor development was that the poor detection limit of about 5×10^{-4} mol l^{-1} is not low enough to use this sensor in waste-water monitoring. For that purpose, the sensor should be able to detect lower concentrations, which can be obtained by electrocatalysis.

In this chapter, it will be shown that the detection of sodium dithionite on bare gold electrodes can be improved by electrocatalysis using a cobalt(II)tetrasulphonated phthalocyanine, sodium salt (CoTSPc) or a 5,10,15,20-tetrakis-(4-sulphonatophenyl)porphyrin cobalt(II), tetrasodium salt (CoTSPor) as catalyst. The selection of these catalysts was based on

their well-described behaviour in the literature[15–17] (but not in combination with gold), the knowledge concerning the electrodeposition of these compounds on gold surfaces and their good water solubility, making it possible to perform electrodeposition in aqueous (read 'environmentally friendly') solutions.

7.2 Electrodeposition of Co(II)TSPc at gold electrodes

7.2.1 General observations

Figure 7.1 shows the first 20 cyclic voltammetric scans recorded at a gold electrode in a pH=12 buffer solution (curve 1) and a solution containing 8.07×10^{-3} mol l^{-1} Co(II)TSPc (curves 2–7). In the first scan (curve 1), a well-defined oxidation wave, I_a, at 0.38 V vs. SCE and a reduction peak, I_c, at 0.13 V vs. SCE can be observed, attributed to the oxidation of the gold surface and reduction of the gold oxide formed during surface oxidation[18–22]. In curves 2–7, it can be seen that two new oxidation peaks, at –0.05 V vs. SCE (II_a) and at 0.24 V vs. SCE (III_a), occur and that the peak attributed to gold oxide formation (I_a) decreases markedly. Another three

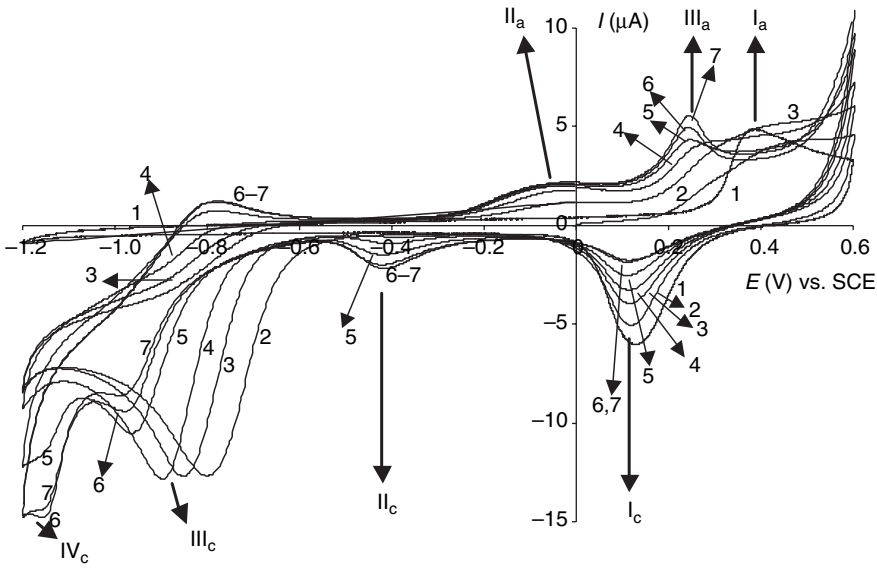

7.1 Current–potential curves recorded at a gold-disc electrode in a pH= 12 buffer solution in the absence (curve 1) and presence (curves 2–7) of 8.07×10^{-3} mol l^{-1} Co(II)TSPc at a scan rate of 50 mV s^{-1} and a temperature of 298.0 K as a function of scan number. Scan numbers are (2) 1, (3) 2, (4) 5, (5) 10, (6) 15 and (7) 20. (Reprinted from *Journal of Electroanalytical Chemistry*, Vol 567 No 2, De Wael et al, 'Study of the deposition of . . .', pp 167–73 (2004), with permission from Elsevier.)

reduction peaks are observed: the first one at –0.41 V vs. SCE (II_c) and a third peak at –1.15 V vs. SCE (IV_c) grow with increasing scan number; the second reduction peak around –0.8 V vs. SCE (III_c) decreases, and its peak maximum shifts towards more negative potentials.

The increase of the oxidation peaks, II_a and III_a, and the reduction peaks, II_c and IV_c, and the decrease of the gold oxide reduction peak, I_c, continue until scan 20. Continuation of the scanning beyond scan 20 results in different behaviour. It is remarkable for scan 20 that the charge related to the two oxidation waves (II_a and III_a) and the charge related to reduction wave II_c is almost the same and equal to 4.1±0.3 μC. For peak I_c, a charge of 5.0±0.2 μC is obtained. Assuming this is due to gold oxide reduction, it would correspond to a Co(II)TSPc coverage of 70%, which is somewhat low and rather unexpected. Therefore, it is presumed that peak I_c at scan 20 is not only due to a fraction of the gold surface that is still uncovered and able to be oxidised and reduced, but also that this peak is the return peak of the second oxidation peak (III_a). An additional indication that peak I_c in scan 20 is not exclusively associated with gold oxide reduction can be found in the shift of the peak maximum towards less positive potentials with increasing scan number, despite the fact that the peak intensity is decreasing. An opposite effect would be expected if peak I_c in scan 20 was due to gold oxide reduction only.

Taking account of the charge associated with peak III_a, this implies that about 1 μC of the 5 μC of peak I_c measured in scan 20 is still due to gold oxide reduction, corresponding to 95% CoTSPc coverage. Therefore, it can be concluded that peaks I_c and III_a in scan 20 are related to the same reversibly behaved redox system. Reversibility can be proven by the fact that the half-wave potentials for both waves are the same, and that the peak potential for the anodic wave (III_a) does not shift with scan number.

It is also important to note that for peak III_c, the peak potential shifts towards more negative potentials without a decrease in peak current in the first scans. Only after a few scans does the peak height start to decrease and, simultaneously, peak IV_c starts to grow. This indicates that the decrease of peak III_c and increase of peak IV_c are related to each other. The increase with scan number of the previously mentioned peaks is due to the deposition of Co(II)TSPc at the gold surface. With each scan, the fraction of deposited Co(II)TSPc increases, which results in higher peaks because more adsorbed Co(II)TSPc is present at the surface in the next scan. This feature also explains the gradual decay of peak I_c. Covering the gold surface with Co(II)TSPc prevents its oxidation and reduction, and therefore the gold oxide formation and reduction peaks (I_a and I_c) decrease.

The second reduction peak due to CoTSPc (III_c) is reasonably large and shifts towards more negative potentials with scan number. This shift also ends with scan 20. Therefore, it is presumed that this peak is to be attributed to the reduction of Co(II)TSPc in solution (not adsorbed) and that the

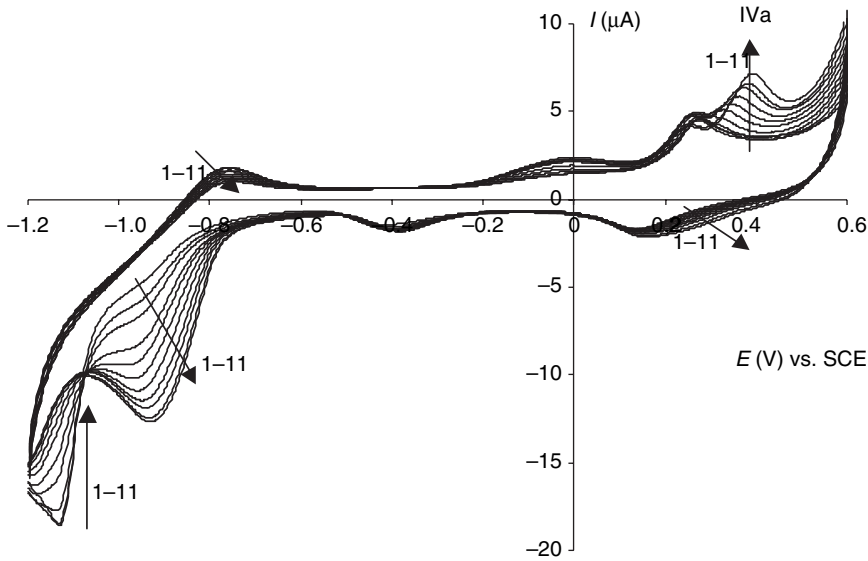

7.2 Current–potential curves recorded at a gold-disc electrode in a pH = 12 buffer solution in the absence (curve 1) and presence (curves 2–7) of 8.07×10^{-3} mol l^{-1} Co(II)TSPc at a scan rate of 50 mV s^{-1} and a temperature of 298.0 K as a function of scan number. Scan numbers are (1) 20, (2) 30, (3) 40, (4) 50, (5) 60, (6) 70, (7) 80, (8) 90, (9) 100, (10) 110 and (11) 120. (Reprinted from *Journal of Electroanalytical Chemistry*, Vol 567 No 2, De Wael et al, 'Study of the deposition of . . .', pp 167–73 (2004), with permission from Elsevier.)

charge-transfer kinetics are faster at gold than at a Co(II)TSPc-modified gold electrode. As the coverage of the gold electrode increases, the kinetics of Co(II)TSPc reduction slow down, which results in the observed shift of the reduction wave. In addition, note that the peak current decreases with scan number – an additional indication that changes in charge-transfer kinetics are occurring.

Figure 7.2 shows curves obtained during the following 100 scans, from scan 20 (curve 1) to scan 120 (curve 11). It can be seen that both oxidation peaks (II_a and III_a) and reduction peak (II_c), and the associated charges, decrease with increasing scan number, with a maximum decline of 27%. This indicates that Co(II)TSPc initially adsorbed at the electrode surface is again released. A possible explanation is a reorganisation of the deposited layer(s) to obtain a thermodynamically more stable condition. At the same time, a third oxidation peak (IV_a) is observed which increases with scan number. Its peak potential is initially dependent on scan number, but eventually the peak potential becomes independent of scan number. This can be explained by the fact that, initially, at lower scan numbers, there is an overlap between peaks III_a and IV_a. As soon as there is no more interference from peak III_a,

the peak potential of peak IV_a becomes independent of scan number. However, the magnitude of this peak is too large to be explained by oxidation of adsorbed Co(II)TSPc only. Therefore, it is believed that it corresponds to the electrocatalytic oxidation of Co(II)TSPc, because when the modified electrode is put into a blank pH 12 solution, this peak disappears. The small increase of the reduction peak (I_c, Fig. 7.2) is probably due to the return peak corresponding with the newly formed oxidation peak, IV_a. The fact that the onset of peak I_c is shifted to more positive potentials reveals that, for scan numbers higher than 20, I_c is the result of two overlapping peaks.

Another observation in Fig. 7.2 is that the reduction peak (III_c) increases markedly, combined with a shift of peak potential towards less negative potentials. It can be seen that, simultaneously with the increase of peak III_c, the fourth peak (IV_c) decreases, which in fact is the opposite effect of that observed in the first 20 scans. This confirms the interrelationship between the increase/decrease of peaks III_c and IV_c. With continued scanning, eventually reduction peak IV_c disappears completely. For all data obtained in Fig. 7.1 and Fig. 7.2, it should be noted that the same potential region was used. The reason for this is that, by using smaller potential regions, no electrodeposition of Co(II)TSPc at gold was observed. By scanning only in the positive or negative region, no marked immobilisation of Co(II)TSPc species was observed, nor when potential regions smaller than those shown in Fig. 7.1 and Fig. 7.2 were used. This indicates that both the negative and positive regions are important in the electrodeposition reaction. In addition, it was observed that if the whole potential window was used and the potential was first varied from 0 to –1.2 V vs. SCE, no changes were observed in the negative region. When the potential was first varied from 0 to 0.6 V and then to –1.2 V vs. SCE, peaks II_c and III_c started to occur. This means that the first adsorption of Co(II)TSPc occurs in the positive region (probably because in this region, the electrode behaves as an anode and Co(II)TSPc is negatively charged), while a stronger immobilisation is obtained in the negative region.

7.2.2 Scan-rate study

In order to find out whether a peak is due to adsorption of species or to a diffusion-controlled reaction of species, the influence of the peak current on the scan rate was investigated. If a slope of 0.5 was found between log I_p and log v, the reaction corresponded to diffusion of Co(II)TSPc towards the electrode surface, while for a slope equal to 1 the reaction corresponded to oxidation or reduction of Co(II)TSPc adsorbed at the electrode surface. It was found that peaks II_a, III_a, I_c and II_c correspond to adsorbed Co(II)TSPc, while peaks III_c and IV_c are attributed to diffusion of

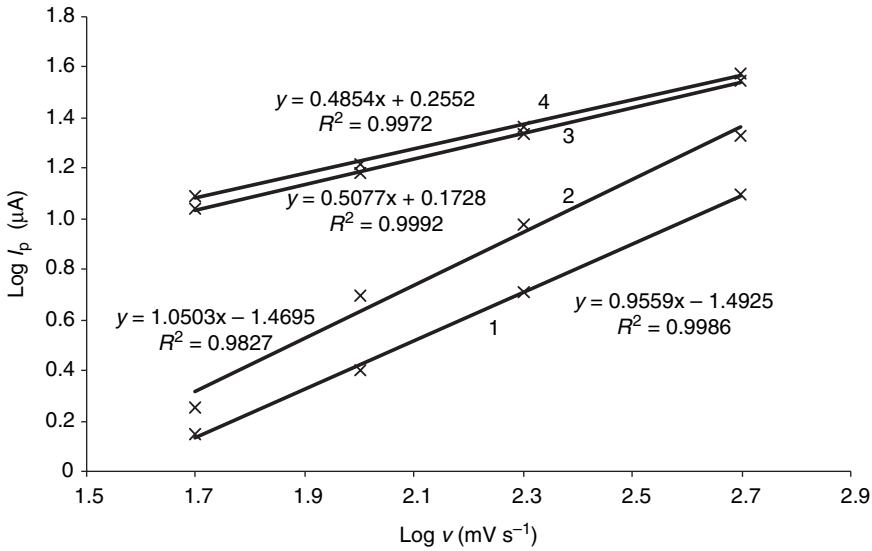

7.3 Logarithmic plot of the peak current observed in the curves in Fig. 7.2 as a function of scan rate. Curve (1) peak I_c, (2) peak III_a, (3) peak III_c and (4) peak IV_c. (Reprinted from *Journal of Electroanalytical Chemistry*, Vol 567 No 2, De Wael et al, 'Study of the deposition of . . .', pp 167–73 (2004), with permission from Elsevier.)

Co(II)TSPc. Figure 7.3 shows the relationship for some peak currents observed in Fig. 7.2.

7.2.3 Concentration study

The experiments described in section 7.2.1 were repeated for other Co(II)TSPc concentrations, and qualitatively similar results were obtained. The same peaks were observed and they also appeared/disappeared as a function of scan number, but the number corresponding with the break in the trend of the behaviour depends on Co(II)TSPc concentration. Figure 7.4 shows the scan number as a function of Co(II)TSPc concentration where the peaks do not increase further with continued scanning and where new peaks appear while existing peaks disappear. These results indicate clearly that Co(II)TSPc is electrodeposited at the electrode surface and the time (or scan number) needed to obtain maximum coverage is dependent on the Co(II)TSPc concentration in solution. This is expected because more Co(II)TSPc in solution means more of it is transported towards the electrode surface per time unit. The fact that the charges of the peaks II_a, III_a, I_c and II_c at the scan number of maximum coverage are not dependent on Co(II)TSPc concentration shows that the electrodeposition is controlled by kinetics. The fact that at the scan number of maximum coverage, the other

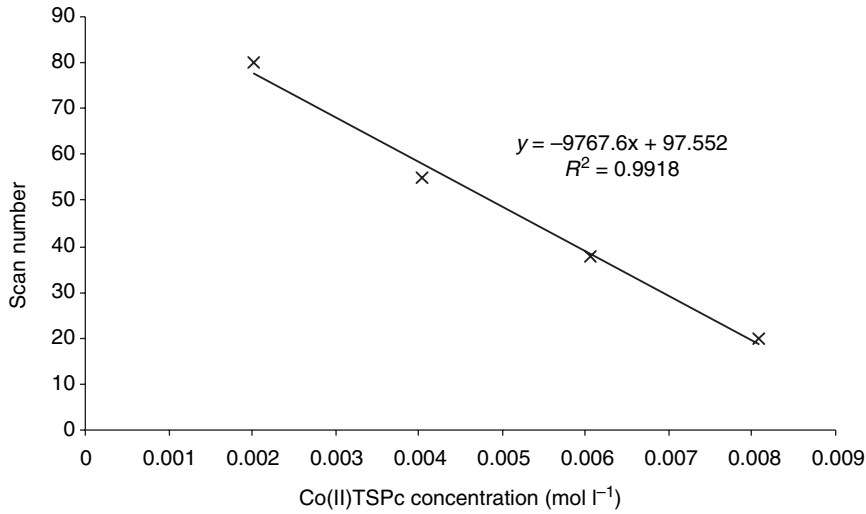

7.4 Relationship between scan number and Co(II)TSPc concentration at which different behaviour of the Co(II)TSPc layer formation is observed at a gold-disc electrode in a pH=12 buffer and at T=298.0 K. (Reprinted from *Journal of Electroanalytical Chemistry*, Vol 567 No 2, De Wael et al, 'Study of the deposition of . . .', pp 167–73 (2004), with permission from Elsevier.)

peaks III_c and IV_c show a linear relationship with the Co(II)TSPc concentration in solution indicates that these peaks correspond to the reduction of Co(II)TSPc at gold electrodes modified with Co(II)TSPc.

7.3 Analysis of the data

In correlation with data found in the literature, the oxidation and reduction peaks II_a and II_c (Fig. 7.2) are attributed to the Co(II)/Co(I) redox system[23–25], while the oxidation and reduction peaks III_a and I_c correspond to Co(III)/Co(II)[26,27]. The first system behaves quasi-reversibly, while the second one is a reversible redox system. The charge under these peaks associated with Co(II)TSPc (taken at scan 20, when deposition is virtually complete) is equal to $4.1 \pm 0.3\,\mu C$. Knowing that the charge of one electron is 1.6×10^{-19} C, it follows that 2.56×10^{13} electrons are exchanged in each reaction. For a deposited Co(II)TSPc, one electron is exchanged per molecule in each peak, and thus 2.56×10^{13} molecules or 4.26×10^{-11} mol of Co(II)TSPc is deposited at the gold surface. This amount was also found for other Co(II)TSPc concentrations but, as mentioned previously, the time needed to reach this maximum coverage is different (Fig. 7.4).

Assuming a monolayer to be present would mean that each Co(II) TSPc covers 7.8 Å^2. However, literature results[28] show that a Co(II)TSPc

molecule, deposited in a flat configuration at the electrode surface (so-called octopus configuration) covers about 200 $Å^2$. This means that the Co(II)TSPc is deposited perpendicularly (with some freedom to bend) and/or that a multiplayer is formed. Preference is given to the latter because even if the molecules were orientated perpendicularly, it is difficult to believe that only 7.8 $Å^2$ is covered by one molecule. CoTSPc in solution is negatively charged, so there will be a repulsive effect between CoTSPc particles adsorbed at the electrode surface and also steric hindrance will play an important role. Therefore, a multilayer situation is assumed instead of extremely close packing within the dimensions of a monolayer.

The variations of the charges of peaks II_a, III_a and II_c, which first increase with increasing scan number, then become constant around scan 20 (Fig. 7.2) and then decrease again, are attributed to changes in the adsorption configuration of the molecule. While the layers are formed, it is presumed that a mixture of flat and perpendicularly oriented molecules are deposited. This process is kinetically controlled, explaining the relatively chaotic orientation of the Co(II)TSPc molecules. However, from a thermodynamic point of view, flat oriented molecules (columnar aggregates) are more stable. Once saturation of deposited Co(II)TSPc is obtained (in scan 20), a reorganisation of the layer takes place from a mixture of flat and perpendicularly oriented molecules towards flat-orientated molecules only. To obtain this situation, a fraction of initially adsorbed Co(II)TSPc molecules should desorb from the surface to allow others to obtain the flat configuration, explaining the decrease of the exchanged charge under the peaks from $4.1 \pm 0.3\,\mu C$ to $3.0 \pm 0.4\,\mu C$.

This reorganisation also explains the decrease of the current of reduction peak IV_c and the formation of the third oxidation peak (IV_a). However, both peaks and also peak III_c are too large to be explained by reduction or oxidation of adsorbed Co(II)TSPc only. It is assumed that this is the result of an electrocatalytic reaction, such as reaction with Co(II)TSPc in solution. This is confirmed by the fact that these peaks disappear when the Co(II)TSPc-modified gold electrode is scanned in a pH 12 buffer in the absence of Co(II)TSPc in solution. In addition, the peak currents of peak III_c in the first scan and peaks III_c and IV_c at the scan of maximum coverage vary linearly with Co(II)TSPc concentration (Fig. 7.5). Note that small peaks are observed at the same potentials where peaks III_c and IV_c occurred with solutions containing Co(II)TSPc. Electrochemical measurements of TSPc without Co show also a reduction wave at these potentials, explaining the ring reduction of CoTSPc in solution. This confirms the fact that Co(II)TSPc is adsorbed at the surface of the electrode and electrocatalyses the oxidation/reduction of Co(II)TSPc transported from solution towards the electrode surface.

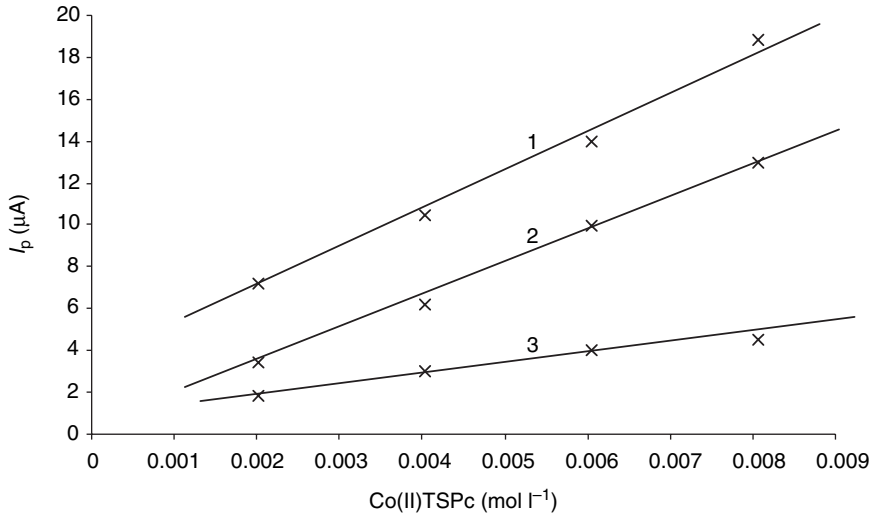

7.5 Relationships between peak current and Co(II)TSPc concentration of peak III_c (curve 1) at scan number 1 (see Fig. 7.1) and peaks III_c and IV_c (see Fig. 7.1) for the scan number where the deposition behaviour changes (curves 2 and 3, respectively), obtained at a gold-disc electrode in a pH = 12 buffer solution at T = 298.0 K. (Reprinted from *Journal of Electroanalytical Chemistry*, Vol 567 No 2, De Wael et al, 'Study of the deposition of . . .', pp 167–73 (2004), with permission from Elsevier.)

7.4 Electrocatalysis with modified gold electrodes towards sodium dithionite

Common possible steps in an overall electrochemical reaction are electron transfer, chemical reaction, transport and ad(de)sorption steps, the slowest one being rate determining. It is known that depositing a catalyst at the surface of an electrode can increase the reaction rate, in general by accelerating the charge transfer or chemical reaction kinetics. This means that if improvement of the overall electrochemical reaction rate is the goal, such a kinetic step should be rate determining at the unmodified electrode. This also means that for redox systems behaving reversibly at the unmodified electrode, electrocatalysis is not useful because, for reversible systems, transport controls the overall rate of the reaction at all potentials.

Despite the fact that, for the oxidation of sodium dithionite at unmodified gold electrodes, well-defined voltammetric waves are obtained[12], the reaction still behaves irreversibly[12–14]. Therefore, it is in principle possible to improve the oxidation rate of this reaction by using an appropriate catalyst immobilised at the gold electrode surface. The modified electrode used here was obtained by a 100-fold scanning experiment between –1.2 and

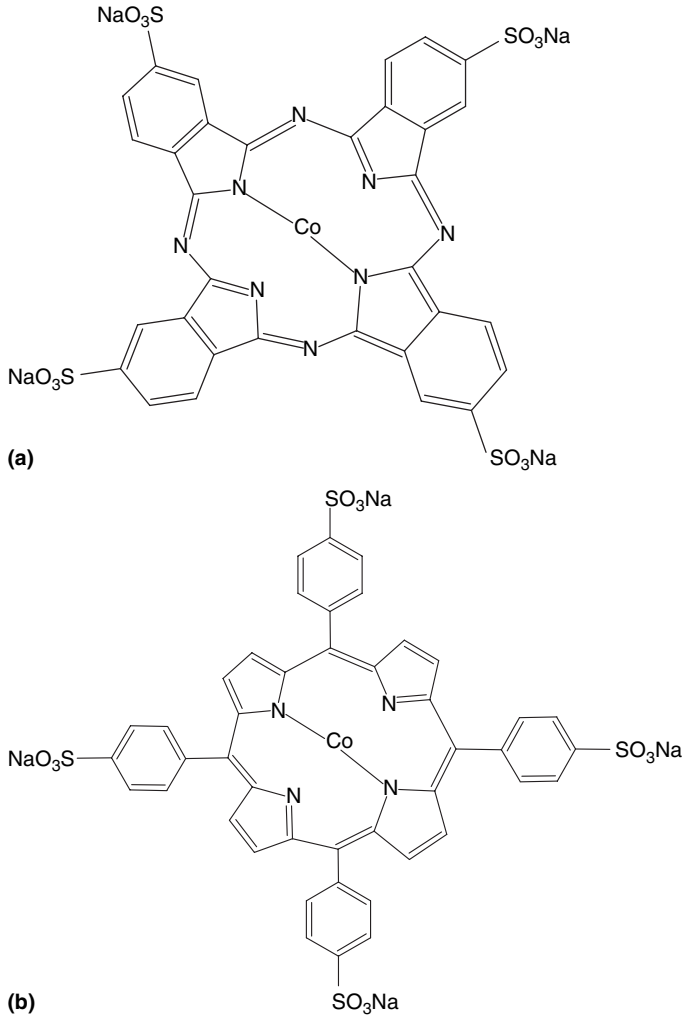

7.6 (a) Molecular structure of cobalt(II)tetrasulphonated-phthalocyanine, sodium salt; (b) 5,10,15,20-tetrakis-(4-sulphonatophenyl) porphyrin cobalt (II), tetrasodium salt.

0.6 V vs. Ag|AgCl in a pH=12 buffer containing 8×10^{-3} mol l^{-1} Co(II)TSPc or Co(II)TSPor (for structures, see Fig. 7.6a and Fig. 7.6b, respectively).

In Fig. 7.7, cyclic voltammetric curves are shown of the oxidation of sodium dithionite at a gold electrode (curves 1, 4), at a CoTSPc-modified gold electrode (curves 2, 5) and at a CoTSPor-modified gold electrode (curves 3, 6) for two different sodium dithionite concentrations. Several observations indicate electrocatalytic behaviour. First, the voltammetric waves are shifted towards less-positive potentials. This means that less

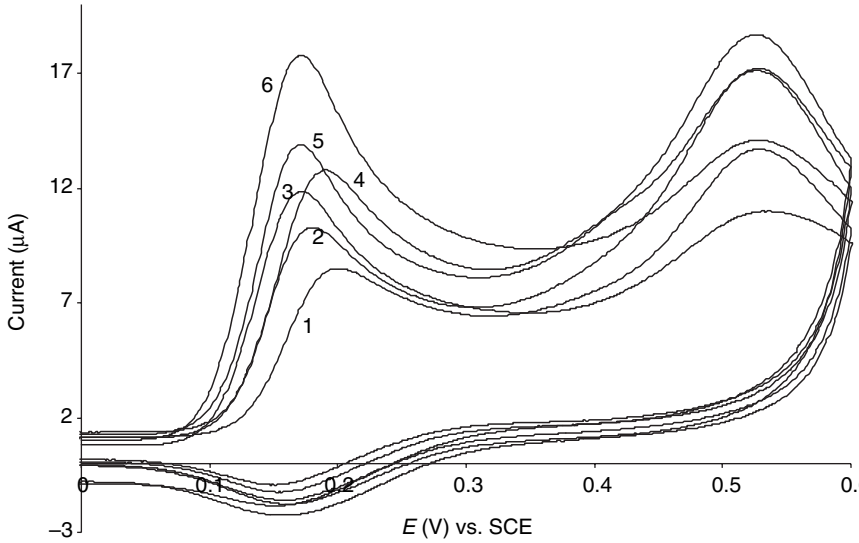

7.7 Voltammetric curves of sodium dithionite at a bare gold electrode (curves 1 and 4), at a CoTSPc-modified gold electrode (curves 2 and 5) and at a CoTSPor-modified gold electrode (curves 3 and 6), in pH = 12 buffer solution containing 9.85×10^{-4} (curves 1, 2 and 3) and 1.46×10^{-3} mol l^{-1} (curves 4, 5 and 6) of sodium dithionite. T = 298.0 K; v = 50 mV s^{-1}.

overpotential (or generally activation energy) should be applied to the system because of the presence of CoTSPc that provides an alternative, less energy demanding, oxidation reaction path for sodium dithionite. Secondly, the slope of the inclining part of the wave is higher at the modified electrodes, revealing faster charge-transfer kinetics. Thirdly, the shape of the voltammetric wave is better defined (more peak-shaped wave), and the peak currents are higher compared with the peak currents obtained at an unmodified electrode. Finally, experiments with varying concentrations of sodium dithionite at gold electrodes and CoTSPc-modified gold electrodes (Fig. 7.8) showed that the peak current shift towards more positive potentials is much more expressed at unmodified gold electrodes than is the case at the modified ones. This again indicates that, for the modified electrodes, the influence of the charge-transfer kinetics in the overall oxidation rate is smaller. Important to note is that the oxidation of sodium dithionite at the modified gold electrodes is still behaving irreversibly, so charge-transfer kinetics still play a role in the overall rate, particularly at low overpotentials.

Another remark is the relatively mild electrocatalytic effect resulting in a shift of the wave of 20 mV and an increase of the peak currents by approx-

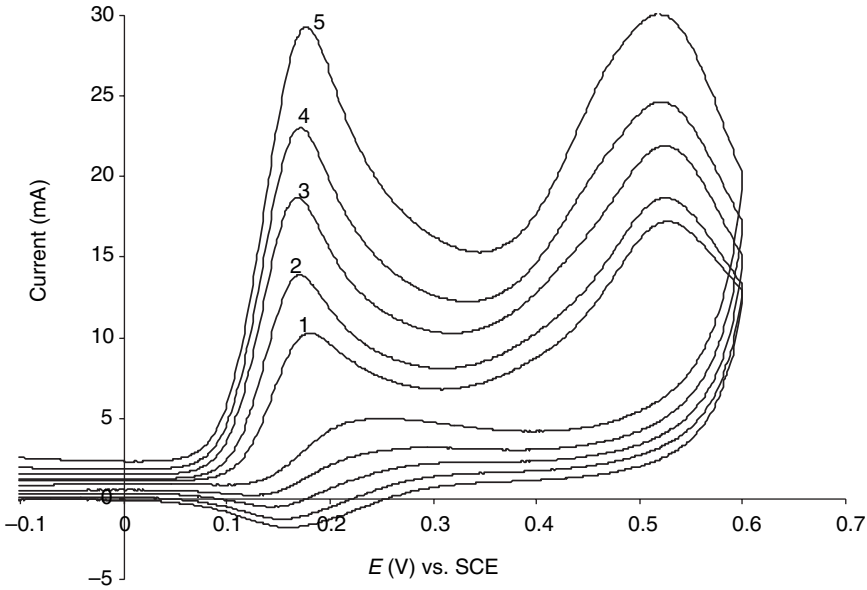

7.8 Oxidation of sodium dithionite at a CoTSPc-modified gold electrode in a pH = 12 buffer solution containing (1) 9.85×10^{-4}; (2) 1.46×10^{-3}; (3) 1.93×10^{-3}; (4) 2.39×10^{-3} and (5) 2.84×10^{-3} mol l^{-1} of sodium dithionite. $T = 298.0$ K; $v = 50$ mV s^{-1}.

imately 17%. This can be explained by the fact that the dithionite oxidation at bare gold occurs with relatively fast kinetics (well-defined, transport-controlled peak), despite the irreversible behaviour of this reaction. Therefore, it may be clear that it is not possible to improve significantly on the kinetics. This partly explains the relatively mild electrocatalytic effect of CoTSPc. Another reason is that the oxidation of dithionite is performed at Co(III)TSPc, a species that first needs to be formed at the electrode surface. From Fig. 7.2, it can be seen that its formation is complete around 0.1 V vs. Ag|AgCl, the same potential where the oxidation of dithionite at CoTSPc starts to occur.

Electrocatalysing the oxidation of sodium dithionite has advantageous consequences for its analytical application, particularly in sensor development to monitor the sodium dithionite concentration during processing. Calibration curves obtained at gold electrodes and CoTSPc-modified gold electrodes (Fig. 7.8) are shown in Fig. 7.9. The peak currents of these calibration plots are the net peak currents, obtained by subtracting the background current recorded at $E = 0$ V vs. SCE from the experimental peak current. Note that this background current is dependent on the dithionite concentration (see Fig. 7.8) for both modified and unmodified electrodes.

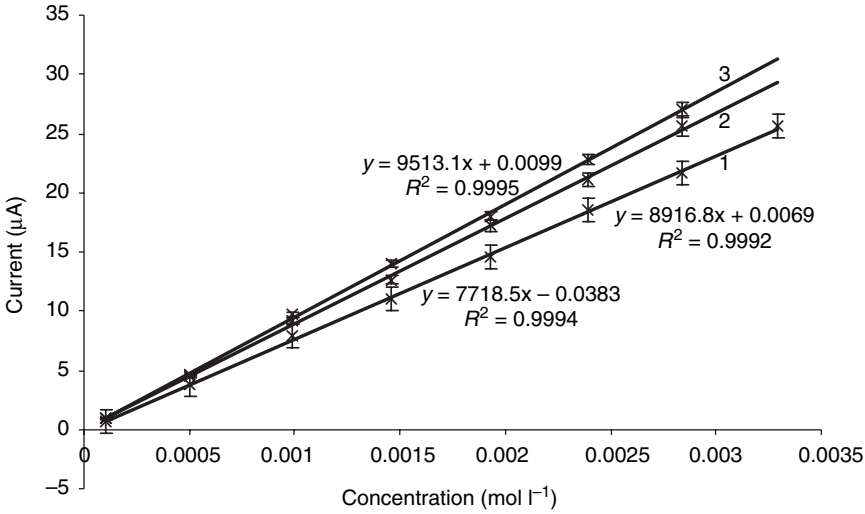

7.9 Calibration plot between peak current of the sodium dithionite oxidation reaction and its concentration at a bare gold electrode (curve 1) and at a CoTSPc-modified (curve 2) and CoTSPor-modified (curve 3) gold electrode. T=298.0 K.

However, repetition of the concentration studies demonstrated that this current is highly reproducible for the modified electrodes, which is not the case for the unmodified ones. This explains why the error margins (Fig. 7.9) for unmodified electrodes were relatively high, particularly for low concentrations.

The large difference in error margin observed at the bare gold and modified gold electrode, also has consequences on the detection limit. Taking into account the criterion that the detection limit corresponds to twice the standard deviation results in a detection limit of about 2×10^{-4} mol l^{-1} for the unmodified gold electrode, which was also found in the literature[10], and 8×10^{-6} mol l^{-1} for the modified electrode. As mentioned above, this is mainly due to a much more stable and reproducible background current. From Fig. 7.9, it can also be seen that the sensitivity of the detection of sodium dithionite has improved on the modified gold electrode because a higher slope is obtained for the calibration curve. Finally, it can be observed from the curves in Fig. 7.7 that the second oxidation peak of dithionite (due to oxidation of sulphite to sulphate[7,8,10,12,13]) does not shift to less-positive potentials at modified gold electrodes. In other words, this reaction is not electrocatalysed. This means that an improved peak separation will be obtained at the modified electrode, or a higher selectivity for dithionite will be obtained.

7.5 References

1. Camacho F., Paez P., Jimenez C., Fernandez M., *Chem. Eng. Sci*., **52** (1997) 1387.
2. Shaikh A.A., Zaidi S.M.J., *J. Chem. Technol. Biotechnol*., **56** (1993) 139.
3. Westbroek P., Temmerman E., Kiekens, P., *Anal. Commun*., **35** (1998) 21.
4. Westbroek P., Temmerman E., Kiekens, P., *Anal. Chim. Acta*, **385** (1999) 423.
5. Westbroek P., Van Haute B., Temmerman, E., *Fres. J. Anal. Chem*., **354** (1996) 405.
6. Westbroek P., Temmerman E., Kiekens P., Govaert F., *J. Autom. Chem*., **20** (1998) 185.
7. Govaert F., Temmerman E., Westbroek P., *Anal. Commun*., **35** (1998) 153.
8. Gasana E., Westbroek P., Temmerman E., Thun H.P., *Anal. Commun*., **36** (1999) 387.
9. Govaert F., Temmerman E., Kiekens P., *Anal. Chim. Acta*, **385** (1999) 307.
10. Gasana E., Westbroek P., Temmerman E., Thun H.P., Kiekens P., *Anal. Chim. Acta*, **486** (2003) 73.
11. Westbroek P., Temmerman E., *J. Electroanal. Chem*., **482** (2000) 40.
12. Westbroek P., De Strycker J., Van Uytfanghe K., Temmerman E., *J. Electroanal. Chem*., **516** (2001) 83.
13. Gasana E., Westbroek P., De Wael K., Temmerman E., De Clerck K., Kiekens P., *J. Electroanal. Chem*., **553C** (2003) 35.
14. Gasana E., Westbroek P., Temmerman E., Thun H.P., Twagiramungu F., *Electrochem. Commun*., **2** (2000) 727.
15. Gupta S., Huang H., Yeager E., *Electrochim. Acta*, **36** (1991) 2165.
16. Oni J., Nyokong T., *Anal. Chim. Acta*, **434** (2001) 9.
17. Lucho A.M.S., Oliveira E.C., Pastore H.O., Gushikem Y., *J. Electroanal. Chem*., **573** (2004) 55.
18. Burke L.D., O'Sullivan J.F., *Electrochim. Acta*, **37** (1992) 585.
19. Burke L.D., O'Leary W.A., *J. Appl. Electrochem*., **19** (1989) 758.
20. Sirohi R.S., Genshaw M.A., *J. Electrochem. Soc*., **116** (1969) 910.
21. Schmid G.M., Curley M.E., in Bard A.J. (ed.), *Encyclopedia of Electrochemistry of the Elements 4*, Marcel Dekker, New York, 1975.
22. Woods R., in Bard A.J. (ed.), *Advances in Electroanalytical Chemistry*, Marcel Dekker, New York, 1997.
23. Ozoemena K., Westbroek P., Nyokong T., Porphyr. J. *Phthalocya.*, **6** (2002) 98.
24. Lever A.B.P., Milaeva A., Speier G., in Leznoff C.C., Lever A.B.P. (ed.), *Phthalocyanines: Properties and Applications*, VCH, New York, 1989.
25. Ozkaya A.R., Hamuryudan E., Bayir Z.A., Bekaroglu O., *J. Porphyr. Phthhalocya*., **4** (2000) 689.
26. Leznoff C.C., Lever A.B.P., *Phthalocyanines, Properties and Applications 3*, VCH, Weinheim, 1993.
27. Ozoemena K., Westbroek P., Nyokong T., Electrochem. *Comm*., **3** (2001) 529.
28. Zagal J., Sen R.K., Yeager E., *J. Electroanal. Chem*., **83** (1977) 207.

Part III

Textile electrodes

8

Intelligent/smart materials and textiles: an overview

G. PRINIOTAKIS

8.1 Introduction

Since the nineteenth century, revolutionary changes which have had a profound impact on human life have been seen in many fields of science and technology. The invention of electronic chips, computers, the Internet and the discovery and complete mapping of the human genome have transformed the entire world. The past century also brought about tremendous advances in the textile and clothing industry, particularly the past 20 years, in which new and innovative developments were reported, including the development of a wide range of synthetic fibres, microfibres, and nanofibres, as well as in the field of intelligent textiles and materials. In addition, the increasing importance of nanotechnology and the development of equipment to manipulate at the nanolevel will soon allow the development of supercomputers that can be deposited at the surface of a fibre/yarn/clothing and the development of medical nanorobots smaller than a human cell to eliminate cancers, infections and clogged arteries. Intelligent technology for materials and structures is the future and will keep the textile industry on the right track. The driving force for these changes in the textile industry is mainly the shift from developing and producing textiles purely for clothing purposes to more advanced applications such as heating, cooling and protection (shielding, anti-radar, flame-retardant properties, sensing and actuating amongst other applications).

Despite the many reports that can be found in the literature regarding intelligent textiles, it is difficult to find a good overview of the subject. This chapter endeavours to provide a good overview of intelligent textiles, their production methods and properties. However, it is first essential to formulate a clear definition of intelligent textiles in order to avoid confusion and ambiguity. The definition of intelligent textiles has changed over the past decade, because textiles that were named intelligent 10 years ago now appear in everyday life and are therefore regarded as conventional[1]. By the time some readers access this book, the intelligent textiles discussed could well be part of everyday life.

Starting from smart materials in general, intelligent textiles can be formulated as textile structures that are made of 'smart' materials. They can have the ability to perform sensing and actuating functions, such as the ability to mimic living systems (actuator)[2]. They can also measure a signal related to a specific parameter (pressure, temperature, pH, concentration, heart beat, respiration rate) or even sense environmental parameters or stimuli of a mechanical, thermal, chemical, electrical or magnetic nature[3]. Intrinsically, a textile structure that acts as housing for a conventional sensor or actuator is not an intelligent textile because the textile structure itself is not responsible for the measuring/actuating activity. For a similar reason, advanced textiles, such as those with breathing or fire-retardant properties, or ultra-strong fabrics, are also not considered as intelligent, no matter how highly technological they may be[4–6], because these properties do not reflect a sensing or actuating activity. Smart textiles are therefore those textiles with a sensing and/or actuating function, which conventional textiles do not have. Additionally, very often smart textiles cannot be produced by conventional methods[7].

As is the case for smart materials, intelligent textiles have the property to respond to their environment, sometimes in a clearly perceptible way, but sometimes at the molecular level, completely invisible to the observer. They cover a wide range of technologies, from materials with shape-memory properties or sensing and actuating properties, to entire systems based on information technology[5].

In principle, at least two components need to be present in an intelligent textile structure in order for it to actually be called an intelligent textile: first, a textile structure that possesses sensing and/or actuating properties and second, a processing unit that controls the actuating textile or measures the signals provided by the textile structure[5]. The actuator acts according to a signal that is applied by the processing unit in a preset way or that is provided by the processing unit based on measured signals at a 'sensing' textile structure. This can be the same structure as the actuating one or a different one. At higher levels of intelligence (predominantly theoretical at present), another, more intelligent, processing unit, with cognition, reasoning and activating capacities awaits development. Such intelligent systems could be possible through the successful interaction of research and development activities in traditional textiles/clothing technology, materials science, structural mechanics, sensor and actuator technology, advanced processing technology, communication, artificial intelligence and biology.

8.2 Smart materials

Intelligent textiles are frequently based on smart materials that are transformed into the shape of a fibre, yarn and/or textile structure (woven, nonwoven or knitted).

8.2.1 Phase-change materials

Phase-change materials can absorb heat, resulting in an increase in the temperature of the material. In reverse, the temperature of the material will decrease during a cooling process. For typical textile materials, energy of about one kilojoule per kilogram of heat is absorbed while its temperature rises by one degree Celsius. Comparing heat absorption during the melting process of a phase-change material (PCM) with those in a normal heating process, a much larger amount of heat is absorbed if a PCM melts. A paraffin-PCM, for example, absorbs approximately 200 kilojoules per kilogram of heat if it undergoes a melting process. In order for a textile to absorb the same amount of heat, its temperature would need to be raised by 200 K. The heat absorbed by the paraffin in the melting process is released into the surrounding area in a cooling process which starts when the PCMs reach their crystallisation temperature. After comparing the heat-storage capacities of textiles and PCMs, it is obvious that by applying a paraffin-PCM to textiles; the heat-storage capacities can be substantially enhanced.

In textiles developed for temperature-balance control using the PCM principle, the PCM material is either present in a solid or a liquid form in the textile structure and immobilised in a specific way. Active wear needs to provide a thermal balance between the heat generated by the body and the heat released into the environment. Only by using PCMs can the wearer remain at a constant temperature. In other words, a steady state should be obtained in heat exchange between the body and the textile structure. Normal active-wear garments do not always fulfil this requirement. The heat generated by the body during strenuous activity is often released into the environment too slowly, thus resulting in a thermal-stress situation due to heat accumulation in the body. However, during periods of rest, the body generates less heat. Owing to this insufficient heat-exchange rate, hypothermia is likely to occur in extreme situations.

In order to ensure a suitable and durable active thermal-insulation effect, a phase-change material should be incorporated in the textile material in the correct way and in appropriate quantities. The selected PCM is normally incorporated in a textile substrate by micro-encapsulation. Another possibility is deposition of the phase-change material at the textile surface, but this results in poorer mechanical stability and lifetime. Selecting a suitable substrate requires consideration of whether the textile structure is able to carry the necessary PCM quantity to provide the required heat transfer rate to and from the microcapsules. Further requirements of the textile substrate in a garment application include sufficient breathability, high flexibility and mechanical stability; in other words, the advantageous properties of conventional textiles should not be lost. The substrate with incorporated PCM-microcapsules needs to be suitably integrated into the garment design. Certain design principles need to be taken into account[5].

8.2.2 Shape-memory materials

Shape-memory materials are those materials that return to a specific shape after being exposed to specific temperatures. In other words, these materials are able to 'remember' their initial shape. This process of changing the shape of the material can be repeated several times. The shape-memory effect has been observed in different materials, such as metallic alloys, ceramics, glasses, polymers and gels.

Shape-memory alloys (e.g. Cu–Zn–Al, Fe–Ni–Al, Ti–Ni alloys) are already in use in biomedical applications such as cardiovascular stents, guidewires and orthodontic wires. The shape-memory effect of these materials is based on a martensitic phase transformation. Shape memory alloys, such as nickel–titanium, are used to provide increased protection against sources of (extreme) heat. A shape-memory alloy possesses different properties below and above the temperature at which it is activated. Below this temperature, the shape of the alloy is easily deformed due to its flexible structure. At the activation temperature, the alloy can be changed by applying a force, but the structure resists this deformation and returns back to its initial shape. The activation temperature is a function of the ratio of nickel to titanium in the alloy. In contrast with Ni–Ti, copper–zinc alloys are capable of a two-way activation, and therefore a reversible variation of the shape is possible, which is a necessary condition for protection purposes in textiles used to resist changeable weather conditions.

In products, a shape-memory alloy is usually in the shape of a spring. The spring is flat below the activation temperature but becomes extended above it. By incorporating these alloys between the layers of a garment, the gap between the two layers can be substantially increased above the activation temperature. The increased amount of air between the textile layers forms additional insulation, and as a consequence, provides considerably improved protection against changes in external temperature. Shape-memory polymers have the same effect as the Ni–Ti alloy but, being polymers, they have the potential to be more compatible with textiles. However, a limitation of polymers with shape-memory properties (polyurethanes) is that they have a relatively low melting point. The shape-memory effect is observed when a plastic deformed to a specific shape returns to its initial shape at a particular temperature. For clothing applications, the desirable temperatures for the shape-memory effect to occur will be close to body temperature. Established applications for shape-memory alloys also include domestic appliances (e.g. shower mixer valves, coffee makers and rice cookers) and utility applications (e.g. safety shut-off valves for fuel lines in the event of fire, and air-conditioning systems). The shape-memory alloys can also contribute to the miniaturisation of equipment and systems, and

can decrease the number of parts required and extend the life expectancy due to the favourable fatigue properties of the alloy[5].

8.2.3 Chromic materials

The term chromic materials is a general one relating to materials that radiate, lose or change colour because of an induction caused by the external stimuli. Chromic is a suffix that means colour. Depending on the stimuli affecting the chromic materials, they can be classified as:

- *photo-chromic:* external stimuli energy is light;
- *thermo-chromic:* external stimuli energy is heat;
- *electro-chromic:* external stimuli energy is electricity;
- *piezo-chromic:* external stimuli energy is pressure;
- *carsol-chromic:* external stimuli energy is an electron beam.

Organic materials are specifically used in products having chromic properties because of the wide variety of colours due to the presence of small or large chromoforic groups (conjugated electron systems). Thermo-chromic materials are the most common. Two types of thermo-chromic system that have been used successfully in textiles are liquid-crystal and molecular rearrangement[5]. Thermo-chromic textiles are also called chameleon fibres because of their colour change as a function of ambient temperature.

8.2.4 Electroactive polymers

Materials that have actuating properties are based mainly on polymers. Since these materials respond to a stimulus signal, they can be defined as intelligent textiles. Historically, actuator materials have been investigated with mainly inorganic compounds[8]. However, with the development of polymers, this field of R&D has grown intensively, despite the initial limitation of polymer materials as actuators, because they generate much lower strain than inorganic materials. Despite this, however, polymer materials, such as polymer gels, generate a large strain by variation of triggers, such as solvent exchange, pH and temperature, though their response and durability is rather poor, and they have not really been used in actuators.

A polymer gel is an electroactive material which differs in various ways from solid polymer materials[9]. The polymer chains in the gel are usually considered to be chemically or physically cross-linked and form a three-dimensional network. The gels also have various actuating modes, such as change of volume due to swelling and de-swelling, symmetric deformation and asymmetric deformation. Various triggers for actuating polymer gels have been described. Triggers are classified into two categories: chemical and physical triggers. A well-known example of a chemical trigger is a

solvent exchange that causes a change in solvent polarity[10], pH[11] and ionic strength[12]. An example of a physical trigger is an electrical field, which is one of the most attractive triggers for use. Polyelectrolyte gels contain ionic species. These species can move inside the gel by diffusion (due to a concentration gradient) and/or by migration (due to the presence of an electrical field). A reorganisation of positively and negatively charged ions occurs to resist against the presence of the electrical field. A drawback of ionic species is that they are not only sensitive to an electrical field but are also electrochemically active if they are in contact with the electrodes used for the application of the electrical field. Such electrochemical reactions are often undesirable if an actuating property is wanted.

The main electroactive polymers, known for their actuating properties, are listed below:

- Polyacrylic acid gel was the first polyelectrolyte investigated as an electroactive polymer gel. Polyacrylic acid gel can be deformed by a DC electrical field application[13]. A polyacrylic acid gel rod was immersed in a saline aqueous solution while a DC field was applied at both sides of the gel, using platinum electrodes in contact with the gel. A slow bending motion was observed in the gel with the magnitude being dependent on the type and concentration of the salt. An asymmetric deformation of the gel occurs when the electrical field is applied at both cross sections of the gel rod. This is because the gel shrinks at one end and swells at the other. The negatively charged ions move to one end and positively charged ions to the other. The positively charged ions take a considerable amount of solvent with them because of their solvated form. This explains why the mass is moved more with the positive ions than with the negative ions, resulting in the asymmetrical deformation mentioned above.
- Poly(2-actylamido-2-methylpropanesulphonic acid) (PAMPS) gel was found to undergo worm-like mobility[14]. The principle of deformation is based on an electrokinetic molecular assembly reaction of surfactant molecules in the hydrogel, caused by both electrostatic and hydrophobic interactions and resulting in anisotropic contraction to give bending towards the anode. In order to have a complex formation ratio at less than 1×10^{-3}, surfactants like *N*-dodecylpyridinium chloride (Cl_2PyCl) were used. This low ratio value explains that mainly surface complex formation occurs to bend the gel in an electrical field[15].
- The hydrogel of perfluorosulphonate ionomer is also an effective electroactive material. This material already shows actuating properties as a film of 0.2 mm in a DC field, with application of only 3 V[16]. The principle of the deforming mechanism is similar to that for other polyelectrolyte gels. The response time and durability are much better than for

other gel materials, and the actuating process is not seriously affected by disturbing electrochemical reactions, mainly because of the relatively small potential difference that needs to be applied[17].

- Non-ionic polymer gel, swollen with dielectric solvent, can be extremely deformed as is the case for non-ionic polymer plasticised with non-ionic plasticiser. Instead of the 'charge-injected solvent drag' as a mechanism of the gel actuation, the principle is based on local asymmetrical charge distribution at the surface of the gel[18]. The mechanism can also be applied to non-ionic elastomers in which the motion of the polymer chain is relatively free. In spite of their many difficulties for practical actuators, polyelectrolyte gels and related materials are the most interesting electroactive polymer materials.

8.3 Intelligent/smart textiles

8.3.1 Introduction

Advances in polymer and fibre science and in the manufacturing technologies of fibres, yarns and fabrics have been the driving force behind the development of smart textiles and innovative products that fulfil customer expectations. In contrast with the situation that existed 20 years ago, these products now find applications primarily in sectors outside the textile field. Therefore, fibre, yarn and clothing producers are in constant pursuit of developing new materials in order to meet the demands for both traditional and technical textiles to be used for applications outside the textile industry.

Smart textiles can be divided into three categories, based on their reaction to the environment:

- *passive smart textiles* can only sense the environmental conditions or stimuli.
- *active smart textiles* can sense the stimuli from the environment and also react to these stimuli.
- *very smart textiles* can sense and react to the environmental conditions in such a way that their reaction is an adaptation to the environment[3,19].

8.3.2 Fibre-optic sensors, a passive smart textile

Optical-fibre grating (OFG) sensors respond to stain and temperature by a shift in their optical wavelength. Many optical-fibre grating sensors can be manufactured onto a single optical fibre, and then analysed independently to provide distributed measurements over large structures such as civil infrastructure. The technology of optical-fibre grating sensors is classified in three groups, based on the measurement principle:

- *How sensing is accomplished*. In this category, the sensors can measure a change in intensity of one or more light beams or phase changes in the light beam(s) caused by an interaction between these beams. Therefore, these sensors are categorised as intensity and interferometric sensors, respectively.
- *The physical extent of the sensing.* This category is based on whether sensors operate only at a single point or over a distribution of points. Thus, sensors in this category are categorised as either point-measuring sensors or distribution-measuring sensors. In the case of a point sensor, the transducer may be at the end of the fibre, where its role is to transport a light beam to and from the transducer. Examples of this type of sensor are interferometers-immobilised at the tip of fibres to measure temperature and/or pressure. In the case of a distributed sensor, the sensing is performed all along the fibre length. Examples of this type of sensor are fibre Bragg gratings distributed along a fibre length to measure strain or temperature.
- *The role of the optical fibre in the sensing process.* Further distinction is often made as to whether measurements act externally or internally to the fibre. Where the transducers are external to the fibre and the fibre merely registers and transmits the sensed quantity, the sensors are termed extrinsic sensors. Where the sensors are embedded in, or are part of, the fibre – and for this type there is often some modification to the fibre itself – the sensors are termed internal or intrinsic sensors. Examples of extrinsic sensors are moving gratings to sense strain, fibre-to-fibre couplers to sense displacement, and absorption cells to sense chemistry-related effects. Examples of intrinsic sensors are those that use microbending losses in the fibre to sense strain, modified fibre claddings to make spectroscopic measurements, and counter-propagating beams within a fibre coil to measure rotation.

Several recent examples of sensor networks have been reported. Arrays of fibre Bragg grating sensors have been deployed for sensing strain in bridges and other structures. It was demonstrated that these sensors can measure the change in internal strain within the girders associated with both static and dynamic loading of the bridge with a truck. The sensor arrays are used to test both steel and carbon composite tendons within the concrete deck of support girders. This was performed on the first bridge using carbon-fibre composite tendons.

8.3.3 Specialty fibres for sensors

As a large percentage of current optical sensors involve optical fibres in certain shapes, it is important to discuss the status of fibre R&D. Glass fibres

are mainly used to develop optical-fibre sensors because of their availability, low price, high-volume production and high-volume use in telecommunications. The transmission and fluorescence properties of plastic compounds used as optical fibre complicate the spectral response, as such glass fibres are favoured instead of plastic fibres for many spectroscopic-type sensors. Polarised light transmission is important for a number of sensors (e.g., the fibre-optic gyroscope); many fibre devices are designed to retain this property along the length of the fibre and in the presence of macro- and micro-bending of the fibre. In the case of fibre-optic gyroscopes, the requirements are for a small coil of fibre for which the bending loss must be small; the polarisation properties of the light must be maintained, and the physical strength of the fibre should not be lost. For many of the chemical sensors, it is important for the lightwave to interact with its surroundings. Therefore, fibres have been produced where the core is close to the cladding–external interface. An example of this type of fibre is the 'D-fibre'.

8.3.4 Super-absorbing textiles

Other functional materials address the problems associated with the discomfort experienced by using impermeable materials in close proximity to the skin. This problem is minimised by primarily maintaining a vapour atmosphere or microclimate between the skin and the fabric. 'Stomatex' textiles are based on closed-cell foam materials such as neoprene. 'Hydroweave' is a performance-enhancing fabric that consists of three layers and offers a cooling effect through evaporation. When immersed in water, the centre layer absorbs and retains moisture. As the water evaporates from this layer, the fabric cools the wearer while its shell and lining keep the wearer dry. The principle of hydroweave starts with a super-water-absorbing polymer fibre that is blended to form a layered mat structure. This mat is positioned between a breathable exterior shell and a conductive, waterproof inner-fabric layer. Upon evaporation, water vapour can only escape through the breathable exterior layer and cannot affect the conditions of the wearer's surface because of a waterproof interior layer. The main features and advantages of the hydroweave structure are:

- cooling effect over the entire fabric;
- flexible fabric can be easily manufactured into a wide range of products;
- wearer remains dry;
- rugged and machine-washable;
- re-usable;
- easily reactivated[5].

8.3.5 Bioprocessing for intelligent textiles

Synthetic materials used in surgery have demonstrated important progress in this area since the 1970s. Such materials consist of poly(α-hydroxyacid)s like polyglycolide and the copolymers of L,L-dilactide and diglycolide[20]. Polyanhydrides are an example of a group of materials that have been introduced for clinical applications. Gliadel® (Guilford Pharmaceutical Co, Baltimore, USA) and Septicin® (Abbott Laboratories, Illinois, USA) are textiles applied for the treatment of brain cancer, filling cavities caused by the surgical treatment of brain tumours, and also for curing chronic bone infections[21].

Biodegradable, stimuli-sensitive polymers have great potential in minimal invasive surgery. Degradable implants can be inserted into the body through a small incision in a compressed or stretched temporary shape. Upon heating to body temperature, they revert back to their memorised shape (see section 8.2.2). As the materials are biodegradable, they do not need to be removed by a second surgical operation. To be degradable, a biomaterial needs bonds that are cleavable under physiological conditions. In the case of aliphatic polyesters and polyanhydrides, these are hydrolysable bonds. There are two mechanisms for degradation involving water: bulk degradation and surface erosion. Both mechanisms differ in the rate of diffusion of water in the polymer matrix and the rate of hydrolysis of a cleavable bond. If the rate of diffusion is higher than the rate of hydrolysis, water uptake is substantial; typically, a 1–3% uptake by weight can be observed. The hydrolysable bonds within the bulk will degrade almost homogeneously. This mechanism is called bulk degradation.

For hydrophobic polymers, the rate of diffusion of water into the polymer matrix is significantly lower than the rate of cleavage of the hydrolysable bonds. Here, the degradation is only taking place within a thin surface layer of the implant. In the case of surface erosion, the degradation rate depends on the surface area of a device. While polyanhydrides show surface erosion, poly-hydroxy acids undergo bulk degradation[21].The number of potential applications for biodegradable implant materials is constantly increasing. The growing confidence from the clinical environment in the use of degradable biomaterials, in addition to the new therapeutic methods, which have been developed taking advantage of the concept of biodegradable polymers such as tissue engineering, make such materials very popular[22].

8.3.6 Textile scaffolds in tissue engineering

Tissue engineering is an interdisciplinary approach aiming at the generation of new functional living tissue. The new tissue should be fabricated using living cells associated with a degradable porous scaffold. The scaffold

should determine the three-dimensional shape of the resulting tissue, and should degrade while the cells are growing and replacing the artificial structures. The need for scaffolds in tissue engineering is undisputed as cells cannot survive on their own; cells need a substrate on which to grow. The choice of scaffold for tissue depends on its characteristics. Besides the mechanical properties, the optimum design of a scaffold for a specific tissue application requires consideration of microstructural, chemical and biological aspects. In surgical applications, a number of requirements need to be fulfilled such as surface biocompatibility (chemical structure, topography, etc.), mechanical compatibility (elastic modulus, strength, stiffness, etc.), non-toxicity, durability conditions and sterilising properties. Owing to recent advances in textile engineering and biomedical research, the use of textiles in surgery is growing, and they have been used in some situations to replace the functions of living tissues of the human body[23].

Polymers reinforced with textiles, called polymer composite materials, are also considered in tissue replacements or with implants such as dental posts, bone grafts, bone plates, joint replacements, spine rods, inter-vertebral discs and spine cages[24]. Synthetic biomaterials are reasonably successful, but have drawbacks compared with living tissues, including a higher risk of infection, loosening, failure and finally rejection. In a currently developing field of tissue-engineering, mammalian cells and certain synthetic biodegradable materials are being combined to produce living (vital) synthetic tissue substitutes or replacement tissues[25,26]. Tissue engineering already has applications in engineering skin[27], blood vessels[28], heart valve[29] cartilage[30] and nerve[31] for applications such as replacement of burned skin and restoring of vital heart functions.

The basic concept of tissue engineering is to regenerate or grow new tissues by culturing isolated cells from the damaged body on porous biodegradable scaffolds or templates. A new and innovative step further in this field is to grow complete organs in such an artificial environment. The scaffold acts as an extracellular matrix for cell adhesion and growth and/or regeneration. They can be processed into various shapes and microstructures, such as desired surface area, porosity, pore size and pore-size distribution. Recent progress in electrospinning[32–36] allows scaffolds of nano-dimensioned structure with a large surface/volume ratio to be obtained, promoting the adhesion of cells. These aspects are vital, as they provide the optimal spatial and nutritional conditions for the cells, and determine the successful integration of the natural tissue and the scaffold.

Fibro-vascular tissues require a pore size greater than 500 μm for rapid vascularisation, whereas the optimal porosity for bone-bonding materials is considered to be between 70 and 200 μm. Textile structures have the potential to be tailored in such a way as to provide the required porosity in terms of size, quantity and distribution pattern. For example, in a typical textile

scaffold, three levels of porosity can be achieved. The arrangement of fibres in the yarn determines the accessible space for cells. The inter-fibre space may be considered as the first level of porosity. This inter-fibre space or first level of porosity can be controlled by varying the number of fibres in the yarn and also the yarn packing-density. Further variations in porosity can be achieved by using twisted, untwisted, textured, untextured, continuous or spun yarns. At this level, the dimensions are only a few micrometers, and it is at this level that electrospinning can make the difference in the production of scaffolds with nano-dimensioned gaps between individual fibres. The gap or open space between the yarns forms the second level of porosity.

In the case of knitted scaffolds, the porosity can be varied selectively by changing the stitch density and stitch pattern, or, in case of woven scaffolds, by controlling the inter-yarn gaps. Furthermore, a third kind of porosity can be introduced by subjecting the textile structures to secondary operations such as crimping, folding, rolling and stacking. In other words, the flexibility of microstructural parameters is very important for applications such as scaffold engineering[37]. Similar to the microstructural aspects, the mechanical aspects of scaffolds, such as structural stability, stiffness and strength, have considerable influence on the cellular activity. In tissues like bone, cell shape is influenced by the cellular activity, and in blood-vessel applications, the scaffold needs to be strong enough to resist physiologically relevant pulsatile pressures and, at the same time, match the elasticity values of a native blood vessel[38]. Textile structures are particularly attractive for tissue engineering because of their ability to tailor a broad spectrum of scaffolds with a wide range of properties.

8.3.7 Heat storage and thermo-regulated textiles and clothing

Since the dawn of evolution, man has been trying to keep body temperature at a constant level, around 37 °C, by wearing clothes. Before the development of intelligent textiles, body temperature was maintained by adding or removing layers of clothing. If clothing could automatically change its thermal resistance according to body temperature, it could provide control over the rate of heat uptake or release and thereby regulate body temperature. The first thermo-regulated heat-insulating materials appeared in the late 1980s. The solar-ray selective absorbing textile can absorb the near infra-red wavelengths of the sunlight spectrum and convert it to heat, thus enhancing the inner temperature of the clothing. The far-infrared textile can absorb the body's irradiated far-infrared ray and turn it into heat, enhancing thermal resistance. Ultra-violet absorbing fabric can absorb the ultraviolet wavelengths of the light spectrum and reflect the near-infrared rays

of this spectrum, resulting in a decrease in the inner temperature of the clothing and thus indirectly of the body temperature (cooling effect). All these new functional textiles are in one way (heating or cooling) thermo-regulated heat-insulating materials[39].

More interesting are those materials that show two-way thermo-regulated properties. Such textiles are obtained by impregnation, coating, development of composite materials or microencapsulation. The active material for the thermoregulation is often a phase-change material (see section 8.2.1.), such as polyethylene glycol; this is one of the most important phase-change materials.

Heat storage and thermo-regulated textiles can be manufactured by filling hollow fibres or impregnating non-hollow fibres with phase-change materials and plastic crystals. They can also be manufactured by coating fabric surfaces with phase-change materials, plastic crystals or microcapsules. Embedding the microcapsules directly within the fibre increases durability as the phase-change material is protected by a dual wall, the first being the wall of the microcapsule and the second being the surrounding fibre itself. Thus the phase-change material is less likely to leak from the fibre during its liquid phase, enhancing its life and the repeatability of the thermal response. Additionally, the PCM-coated fabrics can gain anti-bacterial properties as is the case for polyethylene glycol-coated fibres[40]. If particles of ZrC are added to a heat-storage and thermo-regulated textile, they can absorb near infra-red rays of sunlight and convert it into heat, which allows phase-change materials to melt (to change phase)[41]. So, in this way, an excess of energy uptake is compensated for by using it for the melting process of the phase-change material, thereby ensuring that the inner clothing temperature (and thus the body temperature) remains almost constant.

8.4 Electrotextiles

8.4.1 Introduction

Electrotextiles are a novel category of textiles, offering a unique way to fabricate flexible clothing for use in military and medical applications as well as for novel large-area, commercial systems. For that reason, there is unique research and development in basic yarn components, textile circuits, CAD device manufacturing and simulation, fabric-based system simulation, design and modelling. The term electrotextiles encompasses a very important condition – the possibility of conducting an electrical current. In this section, different methods of producing such fibres, yarns and garments will be discussed.

However, electrotextiles are not expected to compete with high-density, high-performance electronic systems typified by current computer or

telecommunications products because of higher resistance, and thus slower electrical-charge transport (data transport). Electrotextiles can have other unique applications that are determined by the need for flexible and conformable systems or systems that require large surface areas. Distribution of elementary sensors, actuators, logic, and power sources combined with reconfigurable network architecture with fault tolerance and operational long-term stability is needed. It is expected that lower production costs for these types of applications will be achieved through the use of textile manufacturing processes that are appropriately modified and optimised to incorporate electronic components (conventional or yarn based).

Textile structures are characterised by their high strength, flexibility, and conformability to almost any desired shape. They can be manufactured continuously at high speed with extremely low production costs. Textiles structures are produced and used in forms such as fibres, yarns, twisted structures, braided, woven, knitted, non-woven, or a combination thereof. They can be modified and structured with piles, spaces and multi-layers to accommodate inserts and devices. They exist almost everywhere in many forms. There are numerous end uses of textile structures for small surface areas (such as apparel, seat covers, and seat belts) large surface area (such as rugs, parachutes, weather balloons, and parafoils) and exceptionally large surface areas (such as carpets, wall covers, wraps, geo-textiles, scientific balloon, air structures and tensioned structures)[42]. It is the aim to develop electrotextiles that keep the advantages of conventional textiles but allow electrical charge transport through its structure.

8.4.2 Electrotextile structure and production methods

There are a wide variety of structures in electrotextiles, which are mainly based on the technology used to produce such fibres:

- Production of pure metallic fibres. The structure is of the metal, and charge conduction is obtained through the entire fibre.
- Metallisation is a process in which a metal ion is absorbed by a conventional fibre, followed by chemical reduction of the absorbed metal ions to its metallic phase. In this case, conduction is also obtained through the entire fibre but with a limited rate, dependent on the density of metal ion absorbed in the fibre and adsorbed at the surface of the fibre.
- In the method of chemical deposition, conductive materials are deposited through chemical methods, thus the conductivity properties are obtained exclusively at the surface of the fibre.
- Inclusion of conductive material, such as carbon particles, during melt spinning in the production of the fibres.

Fibres obtained by these methods are then further manufactured in yarns, clothing and garments. The production methods are described in more detail below.

Melt-spinning process

One of the cost- and process-effective methods is blending common plastics with conductive fillers, such as carbon black or metal powders, during the melt-spinning production of fibres. The method is still experimental, and there are several efforts to develop conductive fibres with melt-spinning process. Ikkala *et al.*[43] described the development of conductive polymer blends by blending thermoplastic bulk polymers, such as polyolefins, polystyrene or a polyaniline salt complex; in their report, 1–20 S/cm of conductivity has been achieved in the range of 1–30% by weight of the polyaniline complex. Kim *et al.*[44] prepared conductive composite fibres by mixing polyaniline emeraline salt, polypyrrole and graphite with polypropylene or low-density polyethylene using a co-rotating twin-crew extruder. Low polyaniline concentrations (6–10% by weight) were used for polyaniline particle dispersion in polypropylene via melt blending.

Dall'Acqua *et al.*[45] reported the development of conductive fibres made by cellulose-based fibres embedded with polypyrrole. Several efforts with cotton, viscose, cupro and lyonell have followed. The conductivity is directly related to the amount of polypyrrole, oxidant ratio and fibre structure with significant differences between viscose and lyonell. Polymerisation occurs uniformly inside the fibre bulk, by producing a coherent composite polypyrrole/cellulose. The mechanical and physical properties of cellulose fibres were not significantly modified as they are the best available[45].

A serious remark should be made here about the difference between electroconductivity and ion conductivity. Electroconductivity means that charge is conducted by electrons that move freely through the conductive fibre. This mechanism is present in metal fibres, those fibres obtained through metallisation if enough metal is dispersed in the fibre and through modification of fibre surfaces with metallic coatings. Ion conductivity also enables conduction of charge, but in this case it is not an electron that moves freely but electrons that jump from one place to another leaving a positive gap behind, and it is the movement of that positive gap that allows conduction. This is the mechanism present in conductive polymers, such as polypyrrole and polyaniline. This type of conduction is inferior to the electroconductive mechanism because of a much smaller rate of charge transfer and a limited capacity to conduct charge.

Conductive fibres obtained through chemical deposition of coatings

Chemical deposition of different polymers, such as polyaniline, polypyrrole and polythiophene that possess conductive properties is obtained through deposition of the monomer followed by polymerisation in the presence of an initiator (e.g. $FeCl_3$). In this method, the surface to be coated is enriched either with a monomer, or an oxidising agent (through spontaneous deposition, using auxiliary reagents that promote the adsorption), followed by treatment with a solution of either oxidising agent or monomer, respectively. A major advantage of this process is that the polymerisation occurs almost exclusively at the surface, and there is no bulk polymerisation in the solution. The enrichment of the surface by an oxidiser can occur either by ion-exchange mechanism, or by the deposition of an insoluble layer of oxidiser. The process is limited by materials that can be covered or enriched with a layer of either monomer or oxidiser in a separate stage, preceding the surface polymerisation[46–51].

An alternative to chemical polymerisation for coating is electro-polymerisation of monomers at electrodes performed either in aqueous, or in organic solutions. However, electro-polymerisation is strongly restricted by the use of conducting materials because an activation potential needs to be applied, and an electrical current should be able to flow in the electrodes. This implies that the initial fibre to be coated should already have conductive properties which limits the use of this method[52]. Frequently, electro-polymerisation is used as a finishing touch after fibres have been treated with a chemical deposition, the latter providing the conductive properties to the fibre necessary to perform electro-polymerisation.

Spraying a solution containing the polymer onto the surface of a textile, followed by solvent evaporation, is an alternative method, but is not discussed here because of its poor reproducibility, poor adhesion of the polymer to the substrate, inhomogeneous distribution of the polymer on the fibre surface, large fluctuations in layer thickness and co-deposition of impurities present in the solution[53]. Another method, also limited in use, is bulk polymerisation of the monomer to form insoluble polymers, which precipitate on the surface of the fibres. In this case, it is the insolubility of the polymer that is the driving force for precipitation and not the strength of the bonding and type of bonding (adsorption, covalent bonding) that determines the stability of the deposited polymer onto the fibre. A strong bonding is not necessarily obtained, and this could seriously limit the possible applications of such a modified fibre[54–66].

8.4.3 The electrotextile challenges

Textiles offer a unique combination of attributes to facilitate the fabrication of electrotextile systems. They are lightweight, flexible and con-

formable. Two- and three-dimensional fabrication techniques are available to provide a preformed network to incorporate and connect a large number of nodes. Also available are a large number of crossover points that can be exploited for fault-tolerance in signal routing and low-level computing. Multilayered textile systems can be made to mimic film transistors and printed wiring-board structures. Textile market economics drive manufacturing towards large-area, high-throughput and cost effective technologies. There is a broad spectrum of functions that may be incorporated into textiles:

- *sensing*: large areas, simple modification methods, large number of sensors, platform modular sensors (acoustic, chemical/biochemical, thermal, optical, etc.);
- *actuation*: multiple nano/micro actuation to achieve macro effect, shaping, conforming, variable porosity, affecting surrounding environment/fluid;
- *power sources/generation*: fibre batteries/ fuel cells/solar cells;
- *communication*: connectivity, fibre optics.

8.4.4 Production of electrotextiles

Despite the potential of creating innovative electrotextile products from each fabric-production methodology, weaving is the most promising technology for producing electrotextiles, owing to the combined advantages of weaving and woven structures that cannot be found with any other process. Woven fabrics are characterised by their lightweight, conformability, flexibility, durability, high tensile and tear strength, possibility for obtaining multilayers, high thread density, dimensional stablility, easy recovery from high stresses and high fabric width of up to 12 m. Weaving technology is good for short runs as well as long runs; it is highly automated, and versatile, being capable of handling a wide range of yarn types including ribbon yarns, as well as a broad range of yarn size, highly twisted yarns, and rigid rods. Additional advantages that are relevant to the formation of electrotextiles by the weaving process are:

- Weaving zone is spacious and can accommodate additional devices to automate the formation of interconnections/disconnections while weaving.
- Different yarns of different physical and mechanical properties can be woven into the same fabric by adding creel behind the weaving machine or by adjusting filling yarn feeders.
- Woven fabrics have ordered structure in which warp and filling yarns are precisely addressed and controlled.

8.4.5 Flexibility in conductive fibres and yarns

Unlike textile fibres, many conductive fibres have a clear Young's modulus. Consequently, Finlayson's equation for the flexibility of fibres can be essential in understanding the sewability of yarns made from conductive fibres[67]. For instance, metal fibres in yarns may have a Young's modulus between 80 GPa (Au) and 200 GPa (steel). In contrast, a spider's dragline has a modulus of 2.7–4.4 GPa and nylon a modulus of 3 GPa[67]. Finlayson makes an important comparison between flexibility in fibres and the standard physics of both the deflection of a cantilever beam under stress, and the bending modulus of a beam supported in the center with deflected ends. Finlayson derives this equation for inherent filament and fibre flexibility from the equation for deflection in a cantilever beam loaded at the end. Note that this equation has some unusual notation:

$$f = (f)\frac{FlR^3}{\mathrm{E}W^4} \qquad [8.1]$$

where f is the deflexion, l is the length of cantilever, E is Young's modulus of fibre (isotropic material), F is the applied load modulus, R is the eccentricity of cross section, or major axis width/minor axis width, and W is the average diameter.

According to Finlayson, this demonstrated that the flexibility of a filament is directly proportional to its flatness, as measured by the ratio of major to minor axis of the elliptical cross section, and is inversely proportional to its elasticity and the fourth power of its diameter. Although the equation describes the flexibility of individual fibres, it can also be relevant for yarns. Yarns are composite materials made from the twisting of fibres, which are held together by the forces between these fibres. As a yarn is tensioned, these fibres slide past each other allowing strain in the yarn to occur. This strain is non-Hookian and anisotropic. The twist of most yarns imparts a far more complex geometric and mechanical relationship between fibres. The movement of fibres during the straining of a yarn may render the stiffness of the individual fibres irrelevant to overall fabric and yarn stiffness[68].

The width and shape of non-textile fibres is also significant to its flexibility. In general, textile fibre widths can vary from 15 μm in fine cotton, to 50 μm for ramie. Wool fibres, which possess a width of 25 μm, a low tensile strength, and a circular cross-section are far less flexible than cotton and are therefore never used for machine sewing thread. Comparing wool with the drawn stainless-steel fibres that are incorporated into yarns, stainless-steel fibres have a diameter larger than 35 μm, and a generally circular cross section. Thus, looking at the diameter, cross-sectional shape and Young's modulus of stainless-steel fibres may lead to the assumption that these

fibres may simply be too inflexible to be incorporated into machine-sewable yarns. However, it is important to remember that individual fibres are part of an overall yarn geometry. Experiments with stainless-steel yarns have shown that both yarn geometry and the percentage of conductor incorporated into a yarn also play a significant role in a yarn's flexibility, and therefore its sewability.

8.4.6 Electrotextile applications

For the past 20 years, the textile industry has provided simple electrotextile products. Several novel uses of electrotextiles have been developed for laboratory testing, while others have been utilised in products on the commercial market, as well as in items used in space science[69,70]. The ability to integrate electrical functionality into textile garments is becoming increasingly desirable for consumer devices, military applications and for companies with large distributed workforces. This technology has the potential to facilitate the transfer of information and increase efficiency in many areas. Nevertheless, these products should be electrically conductive, but must also exhibit superior flexibility, enhanced wearability, and the ability to withstand multiple washing environments. The electrotextiles should be tested and evaluated accordingly[71].

Clothes are worn for long periods and next to the skin and are therefore convenient hosts for physiological monitoring of a person. Integration of sensors onto clothes would enable comfortable monitoring. Conductive and pressure-sensitive textiles have been incorporated in the advanced development of space suits (I-Suit), as switch controls for lights and as signal-transmission cables. Conductive fibres have been used in several stitched applications for electrostatic charge dissipation, including large pharmaceutical containment enclosures where fine powders are being captured for transfer between manufacturing facilities, as well as impact-attenuation airbags used in landing spacecraft on the surface of Mars. In both cases, conductive threads are uniquely located in seams and panel locations[72]. Electrically conductive and semi-conductive fabrics have been used in applications such as electromagnetic interference and microwave attenuation.

Electromagnetic interface shielding is the most common application. Conductive fibres braided into a shield or sock offer superior performance against electromagnetic interference, and they present the following advantages:

- *More uniform coverage*: the large number of very fine fibres, together with the tendency of yarn bundles to flatten and spread, makes it easy to obtain high coverage.

- *Improved high-frequency shielding*: the fine fibres provide a very high surface-to-volume ratio. Together with the excellent coverage, the extra surface yields improved high-frequency electromagnetic interface-shielding performance.
- *Reduced weight*: weight savings can be particularly important in aerospace and similar applications where every milligram saved is important.
- *Flexibility*: braid made from these fibres has successfully replaced copper braid in military applications where freedom of movement and durability are critical.
- *Compatibility*: yarns of conductive fibres are fully compatible with standard braiding equipment[5].

Battlefield acoustic sensors are required to detect, localise, track, and classify or identify targets of interest, which typically include vehicles, aircraft and personnel[73].

More advanced electrotextile products such as thermal blankets for human and animal use, computer keyboard and smart shirts to monitor physiological conditions have appeared on the market in the past few years. Researchers are conducting research and development in electrotextiles to come up with a new generation of multi-functional and active 'smart textiles' that are able to harvest energy for self-powering, sense, response, and adjustment to stimuli such as pressure, temperature and/or electrical charge. Examples of large deployable structures featuring very thin, large flexible circuits for use in space include synthetic aperture radar (SAR) antennae, communications antenna reflectarrays, and active variable reflectance solar sails.

In order to improve volume efficiency and reduce payload weight for earth-orbital remote-sensing applications, low-mass membrane-based synthetic aperture radar array concepts are being developed. One such system is an inflatable deployable SAR consisting of thin fabrics or membranes that are deployed for L-band operation with dual polarisation. The entire assembly is flexible before employment and is rolled up onto the spacecraft bus. The antenna comprises three membranes positioned vertically over one another: the ground plane, the radiation patch, and the microstrip transmission line membranes[74].

The increasing desire for localisation of soldiers on the battlefield requires a new approach for their garments. This includes the implementation of communications systems through electrotextiles. Conductive fibres are used in a conformal sensitive liner garment for the detection of wound locations and medical sensor signal transmission for soldier health monitoring while on the battlefield. Textile-based antennae have already been introduced in similar products, providing some key features including high

efficiency combined with small size, consumption of 15 times less power than conventional antenna technology and synthesising their own radiation, therefore requiring no power amplifier[75]. In some other cases, there are electrotextiles in which the stiffness or colour of the fibres can be controlled by applying an electrical load[76].

8.4.7 Electrotextile research for the future

Basic yarn component development

Functional fibres, filaments and yarns are the basic building blocks of electrotextiles. The textile industry has demonstrated a remarkable capability to incorporate both natural and man-made filaments into yarns and fabrics to satisfy a wide range of physical parameters which survive the manufacturing process and are tailored to specific application environments. Electronic components can be fabricated within and/or on the surface of filaments and can subsequently be processed into functional yarns and woven into fabrics. Passive components such as resistors, capacitors and inductors can be fabricated in several different manners. Diodes and transistors can be made on long, thin, flat strands of silicon or formed in a coaxial way. Progress has been made in the development of fibre batteries and fibre-based solar cells. In addition, a variety of actuated materials (piezoelectric, etc.) can be made into multiple long strands (filaments) and subsequently be woven into fabric.

Textile circuits

Basic yarn components along with conventional filaments/yarns constitute the feedstock of the weaving process. Selectively fed into a loom and manipulated through an advanced textile manufacturing process, this feedstock can be woven into a complex variety of designs that result in a structurally sound, environmentally compatible fabric that provides electrical and mechanical functionality. Electronic circuits can be formed from the selective interconnection of fibre components during the weaving process.

Device manufacturing computer-aided design

The electronics industry has demonstrated a remarkable ability to develop computer-aided design (CAD) tools for developing complex integrated circuits and printed wiring-board products. The textile industry has demonstrated a similar computer-aided design capability for the design and development of advanced fabrics. Tailoring of existing electronic CAD and textile CAD tools is required for the development of new electronic

textiles manufacturing processes. Device and circuit characterisation (both electrical and mechanical parameters) can be used to develop macros and design libraries and be incorporated into the tailored electronic textiles design tools. Such a database could be used as a basis for developing device and circuit simulations.

8.5 Intelligent clothing

8.5.1 Introduction

The important function of intelligent clothing is to monitor specific parameters without disturbing the wearer's day-to-day activities. This is achieved in the most comfortable way by using textile electrodes incorporated in the structure of the clothing, which is able to measure a parameter, transmit the measured data through a conductive wire or wireless as an infrared signal, and a device that is able to convert and analyse the data into a value for the desired parameter. Independent of the use of intelligent clothing, five functions can be distinguished:

- sensing with textile electrodes;
- data processing through electroconductive fibres and yarns;
- actuating with textiles based on electroactive polymers;
- storage of data;
- communication through electroconductive fibres and yarns.

Each item has a specific role, although intelligent suits do not need to contain all those functions[6,77]. They all require appropriate materials and structures and must be compatible with the function of clothing: comfortable, durable and resistant to regular textile maintenance processes[19].

8.5.2 Sensors

The definition of a sensor is that it reacts to a parameter (for example, the volume of the mercury pool in a thermometer increases with temperature), and the intensity of the reaction is in relation to the parameter – for example, the measurement of an electrical current that is in relation to the concentration of the analyte oxidised or reduced at the electrode surface. The parameter to be investigated is the concentration of the analyte, while the parameter measured is an electrical current. As for the real devices, ultimately most signals are being transformed into electric ones. Electroactive materials are consequently of utmost importance with respect to intelligent textiles. Of course, apart from technical considerations, concepts, materials, structures and treatments must focus on the appropriateness for use in or

as a textile material. This includes criteria such as flexibility, water (laundry) resistance, durability against deformation and radiation[19]. Materials that have the capacity of transforming signals into electric ones include:

- *thermocouple*: transforms thermal signal into electrical signals;
- *the soft-switch technology*: from mechanical (pressure) signals to electrical signal;
- *fibre Bragg grating (FBG) sensors*: from mechanical signals over optical to electrical signals.

Signals are transformed through a variety of methods:

- The soft-switch technology uses a so-called quantum tunneling composite (QTC). This composite has a remarkable characteristic that enables it to be an isolator in its normal condition and to change into a metal-like conductor when pressure is being exercised on it[77].
- Fibre Bragg grating sensors are a type of optical sensor that has received considerable attention in recent years. They are used for monitoring the structural condition of fibre-reinforced composites, concrete constructions or other construction materials.
- FBG sensors look like normal optical fibres, but inside they contain diffraction grid at a certain place that reflects the incident light at a certain wavelength (principle of Bragg diffraction) in the direction where the light is coming from. The value of this wavelength linearly relates to a possible elongation or contraction of the fibre. In this way, the Bragg sensor can function as a sensor for deformation[19].

8.5.3 Data processing

Data processing is one of the item components that needs attention only when active processing is necessary. Textile sensors could provide a huge amount of data, but many practical problems need to be overcome before real computing fibres will be on the market[19,78]. The problems include:

- large variations of signals between patients;
- complex analysis of stationary and time-dependent signals;
- lack of objective standard values;
- lack of understanding of complex interrelationships between parameters.

Apart from this, the textile material itself does not have any computing skills. Electronics are still necessary. However, they are available in miniaturised and even in a flexible form. They can be embedded in water-proof materials, but durability can be limited[78].

8.5.4 Actuators

Actuators respond to an applied impulse and can force a displacement or release substances. Shape-memory materials are the best-known examples in this area. They transform thermal energy into motion. Because of their ability to react to a temperature change, a shape-memory alloy can be used as an actuator and links up perfectly with the requirements imposed on smart textiles. Shape-memory alloys exist in the form of threads – hence their interest and use in textile materials. Although shape-memory polymers are cheaper, they are less frequently applied. This is due to the fact that they cannot be very heavily loaded during the recovery cycle. Until now, few textile applications of shape-memory alloys were known. The Italian firm, Corpo Nove, in co-operation with d' Appolonia, developed the Oricalco smart shirt. The shape-memory alloy is woven with traditional textile material, resulting in a fabric with a pure textile aspect. The trained memory shape is a straight thread. When heated, all the creases in the fabric disappear, meaning that the shirt can be ironed with a hair dryer[19]. Real challenges in this area are the development of very strong mechanical actuators that can act as artificial muscles – muscle-like materials, however, are something for the future. Another type of actuators are chemical actuators that release specific substances in predefined conditions. The substances can be stored in 'containers' or chemically bound to the fibre polymer. Thermal actuators can be considered as the third type in this series. Conductive materials can act as an electric resistance and can consequently be used as a heating element[78].

8.5.5 Storage

Smart suits often need some storage capacity. Storage of data or energy is the most common. Sensing, data processing, actuation and communication functions all usually need energy – mostly electrical power. Efficient energy management will consist of an appropriate combination of energy supply and energy storage capacity. Sources of energy that are available to a garment are, for instance, body heat, mechanical motion (elastic from deformation of the fabrics, kinetic from body motion), radiation and some others. Infineon had the idea of transforming the temperature difference between the human body and the environment into electrical energy by means of thermo-generators. The prototype is a rigid, thin micro-module that is discreetly incorporated into the clothing. The module itself is not manufactured out of textile material. At the University of California, Berkeley, USA, a flexible solar cell has been developed which can be applied to any surface[19,78].

8.5.6 Communication

For intelligent textiles, communication has many options:

- within one element of a suit;
- between the individual elements within the suit;
- from the wearer to the suit;
- from the suit to the wearer or his environment.

Within the suit, communication is currently realised by either optical fibres or conductive yarns. They both clearly have a textile nature and can be seamlessly built into the textile. Communication with the wearer is possible, for instance, by the following technologies:

- A flexible textile screen of optical fibres. Nevertheless, these clothes are raised to a first generation of graphical communication means.
- Pressure-sensitive textile material, allow input of information, provided a processing unit can interpret the commands.

For communication over longer distances, a wireless connection is favoured. This can be achieved by integrating a textile material antenna, data conversion and infrared transmission systems[79]. Such a wireless network can be developed based on CANBus, which enables performance at high-speed data transmission and the use of a high number of devices, connected with Bluetooth wireless modules[79]. The advantage of integrating antennae in clothing is that a large surface can be used; indeed the whole clothing device can be an antenna. In the summer of 2002, a prototype was presented by Philips Research Laboratories, UK, and Foster Miller, USA, at the International Interactive Textiles for the Warrior Conference (Boston, USA)[19,78].

8.6 References

1. Kolkmann A., Gries Th., *'Smart Textiles – New Chances for Technical Applications' Techtextil Symposium Proceedings*, Germany, 7–10 April 2003.
2. Newnham R.E., Amin A., 'Smart materials acting as both sensors and actuators can mimic biological behavior' *Chem. Tech.*, **29** (12) (1999) 38–46.
3. Xiang Z.X., Ming X., 'Smart textiles (1): Passive smart' *Textile Asia* (2001), 28–29.
4. Van Hinte (ed.) *Smart Design*, Netherlands Design Institute, 1998, 5.
5. Xiaoming Tao (ed.) *Smart Fibres, Fabrics and Clothing*, Woodhead Publishing, Cambridge, 2001.
6. Van Langenhove L., Hertleer C., 'Smart Textiles, an overview' *Proc. 3rd Textile Conf.*, 25–27 June 2003.
7. Schlosser M., Ziegler M., Fraser D.M., 'Biocompatibility of active implantable devices' in *Biosensors in the Body: Continuous* in vivo *Monitoring*, John Wiley, Weinheim, 1997, 140–157.

8. Uchiko K., *Piezo/Electrostrictive Materials*, Morikita Publishing Co. Ltd., Tokyo, 1986.
9. Bar-Cohen Y., 'Electroactive polymer actuators and devices' *Proc. SPIE*, 1999, 3669.
10. Suzuki M., 'Nonlinear mechanochemical systems' *Nippon Comu Kyokaishi*, **60** (1987) 702.
11. Osada Y., 'Chemical valves and gel actuators' *Adv. Mater.*, **3** (1991) 107.
12. Hirai T., Asada Y., Suzuki T., *et al*., 'Studies on elastic hydrogel membrane. I. Effect of preparation conditions on the membrane performance' *J. Appl. Polymer S.*, **38** (1989) 491.
13. Shiga T., Hirose Y., Okada A., *et al*., 'Bending of high-strength polymer gel in a electric field' *Kobunshi Ronbunshu*, **46** (1989) 709.
14. Gong J.P., Kawakami I., Sergeyev V.G., *et al*. 'Electroconductive organogel. 3. Preparation and properties of a charge-transfer complex gel in an organic solvent' *Macromolecules*, **24** (1991) 5246.
15. Osada Y., Okuzaki H., Hori H., 'A polymer gel with electrically driven mobility' *Nature*, **355** (1992) 242.
16. Ogure K., Kawami Y., Takanama H., 'An actuator element of polymer electrolyte gel-membrane-electrode composite' *Bull. Government Industrial Research Institute Osaka*, **43** (1992) 21.
17. Shahipoor M., 'Electro-mechanics of ion-elastic beams as electrically-controllable artificial muscles' *Proc. SPIE, Electroactive Polymer Actuators and Devices*, **3669** (1999) 109.
18. Hirai T., Zheng J., Watanabe M., 'Electrically active polymer materials – application of non-ionic polymer gel and elastomers for artificial muscles' in Tao X. (ed.) *Smart Fibres, Fabrics and Clothing*, Woodhead Publishing, Cambridge. 2001.
19. Kiekens P., Van Langenhove L., Hertleer C., 'Smart clothing: a new life' *Proc. 19th IAF World Apparel Convention*, 2003.
20. Lendlein A., 'Polymere als Implantatmaterialien' *Chemie in unserer Zeit*, **33** (1999) 279–295.
21. Shalaby S.W., Johnson R.A., 'Synthetic absorbable polyesters' in Shalaby S.W. (ed.) *Biomedical Polymers*, Hanser Publishers, Munich, 1994.
22. Lendlein A., 'Tailor-made intelligent polymers for biomedical applications' in Tao X. (ed.) *Smart Fibres, Fabrics and Clothing*, Woodhead Publishing, Cambridge, 2001.
23. Planck H., 'General aspects in the use of medical textiles for implantation' in Planck H., Dauner M., Renardy M. (eds) *Medical Textiles for Implantation*, Spinger-Verlag, Heidelberg, 1991, 1–16.
24. Ramakrishna S., Ramaswamy S., Teoh S.H., *et al*., 'Application of textiles and textile composites concepts for biomaterials development' *Int. Conf. New Textiles for Composites, TEXCOMP 3 Conference Series*, Aachen, Germany, 1996, 1–27.
25. Peppas N.A., Langer R., 'New challenges in biomaterials' *Science*, **263** (1994) 1715–1720.
26. Langer R., Vacanti J., 'Artificial organs' *Sci. Amer.* (1995), Sept. 100–103.
27. Naughton G.K., Bartel R., Mansbridge J., 'Synthetic biodegrable polymer scaffolds' in Attala A., Mooney D.J., Vacanti J.P., Langer R. (eds) *Synthetic Biodegradable Polymer Scaffolds*, Birkhauser, Boston, 1997, 121–147.

28. Nerem R.M., Braddon L.G., Seliktar D., Ziegler T., 'Tissue engineering and the vascular system' in Attala A., Mooney D.J., Vacanti J.P., Langer R. (eds) *Synthetic Biodegradable Polymer Scaffolds*, Birkhauser, Boston, 1997, 165–185.
29. Shinoka T., Mayer J.E., 'New frontiers in tissue engineering–tissue engineering-heart valves' in Attala A., Mooney D.J., Vacanti J.P., Langer R. (eds) *Synthetic Biodegradable Polymer Scaffolds*, Birkhauser, Boston, 1997, 188–198.
30. Cao Y., Ibarra C., Vacanti J.P., 'Tissue engineering of cartilage and bone' in Attala A., Mooney D.J., Vacanti J.P., Langer R. (eds) *Synthetic Biodegradable Polymer Scaffolds*, Birkhauser, Boston, 1997, 199–214.
31. Dunn R.L., 'Clinical applications and update on the poly(α-hydroxy acids)' in Hollinger J.O. (ed.) *Biomedical Applications of Synthetic Biodegradable Polymers*, CRC Press Inc., Boca Raton, 1995, 17–31.
32. Deitzel J.M., Kosik W., McKnight S.H., Beck Tan N.C., De Simone J.M., Crette S., *Polymer*, **43** (2002) 1025–1029.
33. Guan H., Shao C., Chen B., Gong J., Yang X., *Inorg. Chem. Commun.* **6** (2003) 1409–1411.
34. Diaz-de Leon M.J., *Proc. National Conference on Undergraduate Research*, March 15–17, 2001, Lexington, Kentucky.
35. Buchko C.J., Kozloff K.M., Martin D.C., *Biomater*, **22** (2001) 1289–1300.
36. Deitzel J.M., Kleinmeyer J.D., Hirvonen J.K., Beck Tan N.C., *Polymer*, **42** (2001) 8163–8170.
37. Ramakrishna S., 'Textile scaffolds in tissue engineering' in Tao X. (ed.) *Smart Fibres, Fabrics and Clothing*, Woodhead Publishing, Cambridge, 2001, 299.
38. Wintermantel E., Bruinick A., Eckert C.L., *et al*., 'Tissue engineering supported with structured biocompatible materials: goals and achievements' in Speidel M.O., Uggowitzer P.J. (eds) *Materials in Medicine*, VDF Hochschulvelag AG an der ETH, Zurich, 1998, 1–136.
39. Zhang X., 'Heat-storage and thermo-regulated textiles and clothing' in Tao X. (ed.) *Smart Fibres, Fabrics and Clothing*, Woodhead Publishing, Cambridge, 2001.
40. Jickins R.S., Leonas K.K., 'Influence of a polyethylene glycol treatment on surface, liquid barrier and antibacterial properties' *Textile Chemist Colorist*, **26** (12) (1994) 25–29.
41. Oji Shunsako, Fujimoto, Masanori Furata, 'Thermally insulating synthetic fibres with selective solar absorpting', JK1-132816.
42. Seyam A.M., 'Formation of textiles structures for giant-area applications' in Shur M., Wilson P., Urban D. (eds) *Electronics on Unconventional Substrates – Electrotextiles and Giant Area Flexible Circuits 736*, Materials Research Society, Warrendale, 2003, 25–36.
43. Ikkala O.T., Laakso J., Vakiparta K., *et al*., *Synth. Met.*, **69** (1995) 97–100.
44. Kim B., Koncar V., Devaux E., *et al*., 'Electrical and morphological properties of PP and PET conductive polymer fibres' *Synthetic Metals*, **146** (2004) 167–174.
45. Dall'Acqua L., Tonin C., Peila R., *et al*., 'Performances and properties of intrinsic conductive cellulose-polypyrrole textiles' *Synthetic Metals*, **146** (2004) 213–221.
46. Gospodinova A., Terlemezyan L., *Prog. Polymer Science*, **23** (1998) 1443–1481.

47. Cvetkovska M., Grchev T., Obradovic T., *J. Appl. Polymer Sci.*, **60** (1996) 2049–2058.
48. Tan S.N., Ge H.L., *Polymer*, **37** (1996) 965–968.
49. Tan S.N., Ge H.L., *New Polymer Materials*, **5** (1998) 169–176.
50. Cho J.W., Jung H., *J. Material Sci.*, **32** (1997) 5371–5376.
51. Xu C.C., Wang P., Bi X.T., *J. Appl. Polymer Sci.*, **58** (1995) 2155–2159.
52. Huang J.C., *Advanced Polymer Technology*, **14** (1995) 137–150.
53. De Jesus M.C., Fu Y., Weiss R.A., *Polymer Eng. Sci.*, **37** (1997) 1936–1943.
54. Anand J., Palaniappan S., Sathyanarayana D.N., *Prog. Polymer Science*, **23** (1998) 993–1018.
55. Bhattacharya A., De A., *J. Macromol Sci. Rev. Macromol. Chem. Phys.*, **C39** (1999) 17–56.
56. Saurin M., Armes S.P., *J. Appl. Polymer Sci.*, **56** (1995) 41–50.
57. Li H.H., Shi C.Q., Ye W., *et al*., *J. Appl. Polymer Sci.*, **64** (1997) 2149–2154.
58. Anbarasan R., Vasudevan T., Kalaignan G.P., *et al*., *J. Appl. Polymer Sci.*, **73** (1999) 121–128.
59. Yin X.H., Kobayashi K., Yoshino K., *Synth. Met*., **69** (1995) 367–368.
60. Kuhn H.H., Child A.D., Kimbrell W.C., *Synth. Met.*, **71** (1995) 2139–2142.
61. Kuhn H.H., *Text. Chem. Color.*, **29** (1997) 17–21.
62. Boutrois J.P., Jolly R., Petrescu C., *Synth. Met.*, **85** (1997) 1405–1406.
63. Child A.D., Kuhn H.H. *Sunth. Met.*, **84** (1997) 141–142.
64. Bhadami S.N., Sen Gupta S.K., Sahu G.C., *et al*., *J. Polymer Material*, **13** (1996) 61–67.
65. Bhadami S.N., Sen Gupta S.K., Sahu G.C., *et al*., *J. Appl. Polymer Sci.*, **61** (1996) 207–212.
66. Bhadami S.N., Kumari M., Sen Gupta S.K., *et al*., *J. Appl. Polymer Sci.*, **64** (1997) 1073–1077.
67. Orth M., 'Defining flexibility and sewability in conductive yarns' *Proc. Materials Research Society Symposium 736*, 2003, 47.
68. Kaswell E., *Textile Fibres, Yarns and Fabrics*, Reinhold Publish, New York, 1953.
69. Anderson, K., Seyam, A.M., 'The road to true wearable electronics' '*Proc. TI 82nd World Conference*', The Textile Institute, Cairo, Egypt, March 2002.
70. McAdams E.T., McLaughlin J., Anderson J. McC., 'Wearable and implantable monitoring systems: 10 years experience at University of Ulster' *Proc. Wearable Electronic and Smart Textiles Conf.*, Leeds, UK, 2004.
71. Slade, J., *et al*., 'Washing of Electrotextiles' in Shur M., Wilson P., Urban D. (eds) *Electrotextiles and Giant Area Flexible Circuits 736*, Materials Research Society, Warrendale, 2003, 91–97.
72. Catogan D., Sandy C., Grahne M., 'Development and evaluation of the Mars Pathfinder Inflatable Airbag Landing System' *Proc. 49th International Astronautical Congress*, 1998.
73. http://www.rpi.edu/dept/NewsComm/Renss_news/NYTShur.html.
74. Catogan D., Grahne M., Mikulas M., 'Inflatable space structures – a new paradigm for space structure design' *Proc. 49th International Astronautical Congress*, 1998.
75. Slade J., *et al*., 'Textile-based antennas' in Shur M., Wilson P., Urban D. (eds) *Electrotextiles and Giant Area Flexible Circuits 736*, Materials Research Society, Warrendale, 2003, 91–97.

76. Gough P., 'Electronic and clothes: Watt to wear?' *Proc. Wearable Electronic and Smart Textiles Conf.*, Leeds, UK, 2004, 3.
77. Van Langenhove L., Hertleer C., 'Smart clothing: A new life' *Proc. Int. Textile Design and Engineering Conf: Fibrous Assemblies at the Design and Engineering Interface*, Edinburgh, 22–24 September 2003.
78. Van Langenhove L., Hertleer C., 'Smart textiles for medical purposes' *Proc. Med Tex 03 Conf.*, Dolton Institute, 8–9 July 2003.
79. Stylios G.K., Lyo L., 'A SMART wireless vest system for patient rehabilitation' *Proc. Wearable Electronic and Smart Textiles Conf.*, Leeds, UK, 2004.

9

Characterisation of electrochemical cell for textile electrode studies and quality control

G. PRINIOTAKIS, P. WESTBROEK AND P. KIEKENS

9.1 Introduction

In this chapter, an attempt is made to characterise an electrochemical cell and to describe a method for quality control of textile electrodes by investigating the behaviour of textile electrodes and comparing the obtained results.

9.2 Characterisation of an electrochemical cell

9.2.1 Introduction

The characterisation of an electrochemical cell is discussed in order to understand the parameters that are important and the relationships according to which they contribute to the output signal of the electrochemical cell. This characterisation will be done with electrodes made of palladium, which is a precious metal and enables the electrodes to behave in a relatively inert manner, owing to their stability and the fact that they do not significantly complicate the behaviour of the electrochemical cell. The method of concern is electrochemical impedance spectroscopy (EIS), which is explained in Chapter 2 section 2.3[1].

Relationships between output signal, which in fact is an impedance (R) of the system, and concentration of electrolyte (c), electrode surface area (A) and distance between electrodes (d) will be investigated in order to produce an equation which shows the interrelationships between these parameters. At this moment, a general equation can be formulated as follows:

$$R = f(c, d, A) \qquad [9.1]$$

9.2.2 Description of the electrochemical cell

The electrochemical cell consists essentially of two PVC plates, as shown schematically in Fig. 9.1. The electrodes are positioned at the inner side of

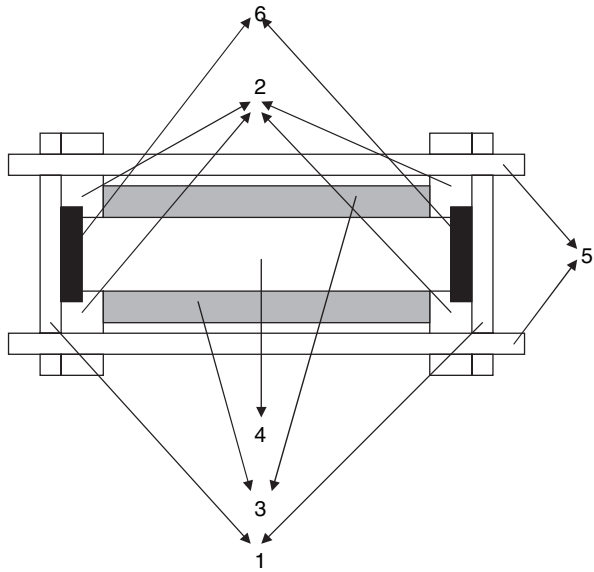

9.1 Scheme of the electrochemical cell described in section 9.2.2, consisting of (1) PVC plates, (2) rubber-ring fittings, (3) PVC tube, (4) electrolyte solution, (5) screws to tighten the cell parts and avoid leaking of electrolyte solution and (6) palladium sheet or textile electrodes.

the plates (1) with rubber fittings (2), having a hole of a specified diameter. The distance between the electrodes (6) is determined by the length of the tube (3) positioned between the plates, which is filled with electrolyte solution (4). The complete structure is held together with screws (5). The metal sheets, with a thickness of about 0.25 mm are used to characterise the electrochemical cell consisting of 99.995% pure palladium metal obtained from Goodfellow (Cambridge, UK). The palladium surface was polished on 1200-grid emery paper to obtain a fresh surface and then further polished with Al_2O_3 polishing powder on polishing cloth; to smooth the surface, Al_2O_3 powder of 1.0, 0.3 and 0.05 µm was used consecutively for 5, 10 and 20 min, respectively. Finally, the surface was subjected to ultrasonic cleaning for 1 min. The textile electrodes comprised stainless-steel fibres. Knitted, woven and non-woven structures were tested.

9.2.3 Study of the influence of the electrolyte concentration

For this study, the composition of the electrolyte was limited to sodium chloride dissolved in de-ionised water in such a way that concentrations of 1×10^{-1}, 1×10^{-2}, 1×10^{-3} and 1×10^{-4} mol l^{-1} were obtained. These solutions were

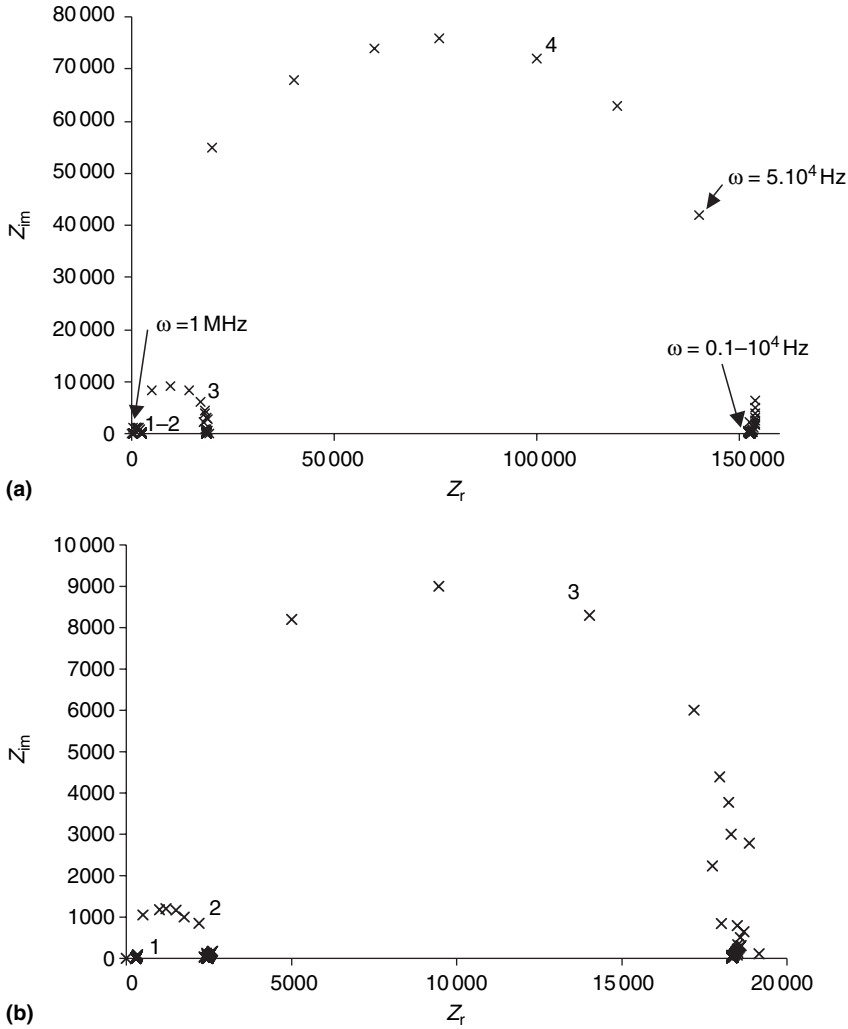

9.2 Nyquist plot recorded at an electrochemical cell with palladium electrodes of 314 mm^2 at a distance of 112 mm for a NaCl concentration of (1) 1×10^{-1}, (2) 1×10^{-2}, (3) 1×10^{-3} and (4) 1×10^{-4} mol l^{-1} at T=298.0 K. Figure 9.2b is an enlargement of Fig. 9.2a.

put in the electrochemical cell, already containing the palladium electrodes, and the electrochemical impedance of the cell was obtained by applying an alternating potential and measuring the resulting alternating current in the frequency domain of 0.1–1 MHz. In order to investigate the contribution of the electrolyte solution to the impedance only, the other parameters were kept constant at values of A=314 mm^2 and d=112 mm. Nyquist and Bode plots of these experiments are shown in Fig. 9.2 and Fig. 9.3. The data show

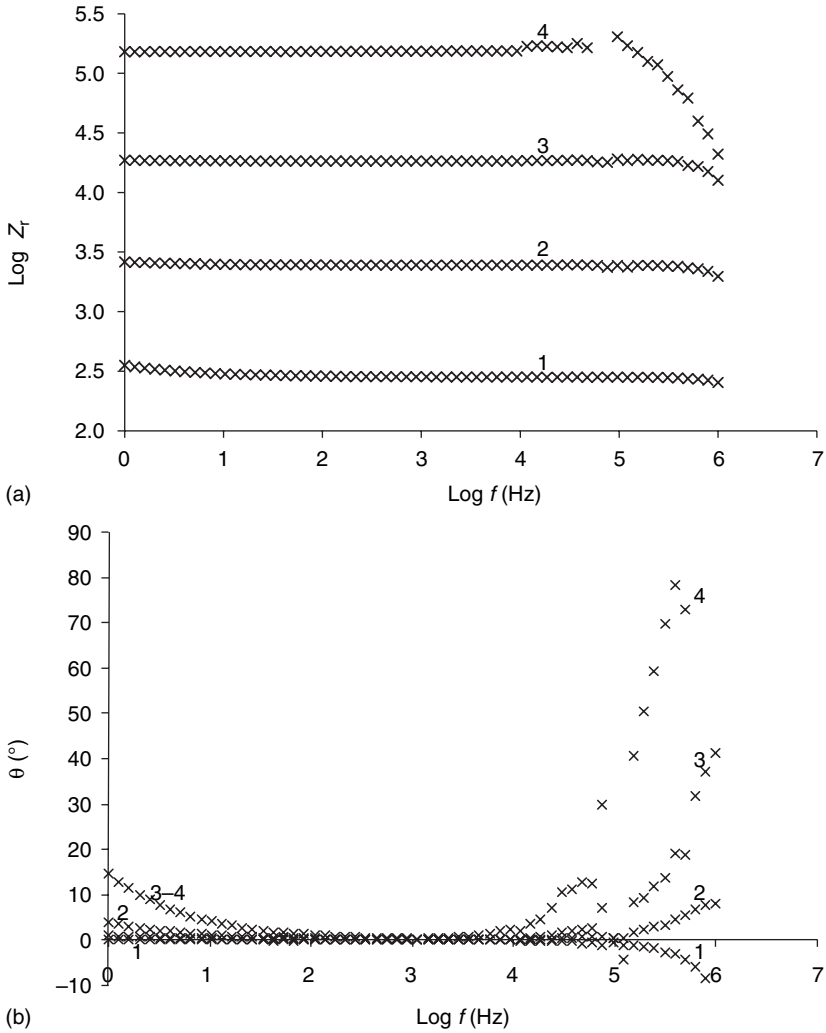

9.3 Bode plot showing the (a) real impedance and (b) phase-angle shift as a function of applied frequency, recorded at an electrochemical cell with palladium electrodes of 314 mm^2 at a distance of 112 mm for a NaCl concentration of (1) 1×10^{-1}, (2) 1×10^{-2}, (3) 1×10^{-3} and (4) 1×10^{-4} mol l^{-1} at T=298.0 K. Figure 9.2b is an enlargement of Fig. 9.2a.

the behaviour of a typical conductivity cell consisting of two electrodes positioned in a planar configuration and in electrical contact with each other through an electrolyte solution. The equivalent electrical circuit corresponding to such a system is given in Fig. 9.4 and consists of a resistor and a capacitor in parallel. The resistor represents the resistive behaviour of the electrochemical cell, which is determined by the resistance of the electrolyte

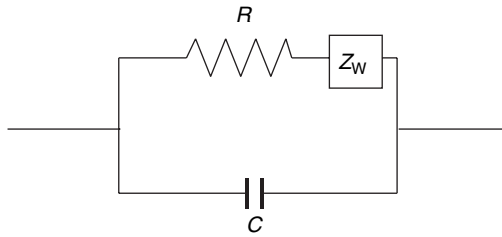

9.4 Equivalent electrical circuit for the electrochemical cell described in section 9.2.2 with palladium electrodes of 314 mm^2, electrically in contact with each other through an electrolyte solution over a distance of 112 mm at T = 298.0 K.

solution; the capacitor represents the capacity of the electrode–electrolyte interface. Finally, there is also the Warburg Impedance (Z_W) in series with the resistance and in parallel with the capacitance. This element represents the diffusion of Na^+ and Cl^- ions in solution.

From Fig. 9.2, it can be seen that in the high-frequency range the imaginary impedance and real impedance are small at the onset of the experiment. By decreasing the frequency, the imaginary impedance first starts to grow, reaches a maximum and then decreases again to zero. The real impedance increases with decreasing frequency and ends up at a constant value. These changes of real and imaginary impedance result in a typical semicircle corresponding to the equivalent electrical circuit shown in Fig. 9.4. Despite the fact that the imaginary impedance is small at the onset of the experiment, it is the main parameter because the phase angle shift shows a value around 90° for an electrolyte concentration of 1×10^{-4} mol l^{-1}, which is typical for pure capacitive behaviour. This result indicates that the electrical current going through the electrochemical cell is flowing exclusively through the capacitive part. Indeed, this element behaves as a good conductor at high frequencies because its charge and discharge rate is extremely high.

At lower frequencies (range of 1 MHz–5×10^4 Hz) its conductive behaviour decreases because of decreasing charge and discharge rate; therefore a competition between the capacitive and the resistive element in the equivalent electrical circuit starts to occur, and a fraction of the current flows through the resistor element. This is in correlation with the increase of the real impedance, but is also in correlation with an increase of the imaginary impedance because the capacitor becomes less conductive with decreasing frequency. In addition, curve 4 in Fig. 9.3.b shows that an increasing fraction of the electrical current is flowing through the resistive element because the phase angle shift is decreasing, indicating an increase in resistive behaviour.

At frequencies lower than 5×10^4 Hz, it can be observed in the Nyquist plot (Fig. 9.2) that no variation of the data is observed. This indicates that from a frequency of about 1×10^4 Hz, the electrical current going through the electrochemical cell flows exclusively through the resistive element, resulting in a constant real impedance value, while the imaginary part is negligible. This is confirmed in Fig. 9.3b, where there is either a zero or a small phase-angle shift observed between the applied alternating potential and the measured current. In addition, the data in Fig. 9.3a show this result; starting from about 1×10^4 Hz, the real impedance is no longer dependent on the frequency, which means that the total impedance is equal to the real impedance. The value of the real impedance, when no imaginary impedance is contributing to the total impedance, or when the phase-angle shift is near to zero, is of major importance to this work. This value shows us the resistive impedance behaviour of the electrochemical cell and provides us with information about the electrolyte concentration, because this is the main resistive part in the cell, determining the overall (experimentally measured) resistance or, more correctly, impedance.

However, before going into this analysis, let us also analyse the other curves in Fig. 9.2a, at higher electrolyte concentrations. It can be seen that the semi-circle is smaller, which can be explained by the fact that the resistor in the equivalent electrical circuit is smaller, resulting in a lower value for the real impedance, when no phase-angle shift is observed. Remember that the value of this resistor element is determined by the resistance of the electrolyte solution, which decreases with increasing electrolyte concentration. Interestingly also, at the onset of the experiment, a much smaller phase-angle shift is observed, and this shift decreases further with increasing electrolyte concentration. This can be explained by the fact that the resistance of the element R in the equivalent electrical circuit at the onset of the experiment decreases with increasing electrolyte concentration. Therefore, the competition between R and C for the fraction of the electrical current flowing through these elements has already started at the beginning of the experiment. This is confirmed in Fig. 9.3a, where the real impedance becomes independent of applied frequency at higher values for the frequency with increasing electrolyte concentration.

Note also that in the low-frequency range, the phase-angle shift increases with decreasing electrolyte concentration, which is explained through the Warburg impedance. This impedance will only become important at low frequencies, because at high frequencies the charge of the two electrodes switches so fast from plus to minus, and vice versa, that the ions remain in their initial position and no diffusion occurs. Typical for a pure Warburg behaviour is a phase-angle shift of 45°. From Fig. 9.3b, it can be seen that pure Warburg impedance is not observed; however, for low electrolyte concentration, the phase-angle shift tends toward this behaviour. The fact that

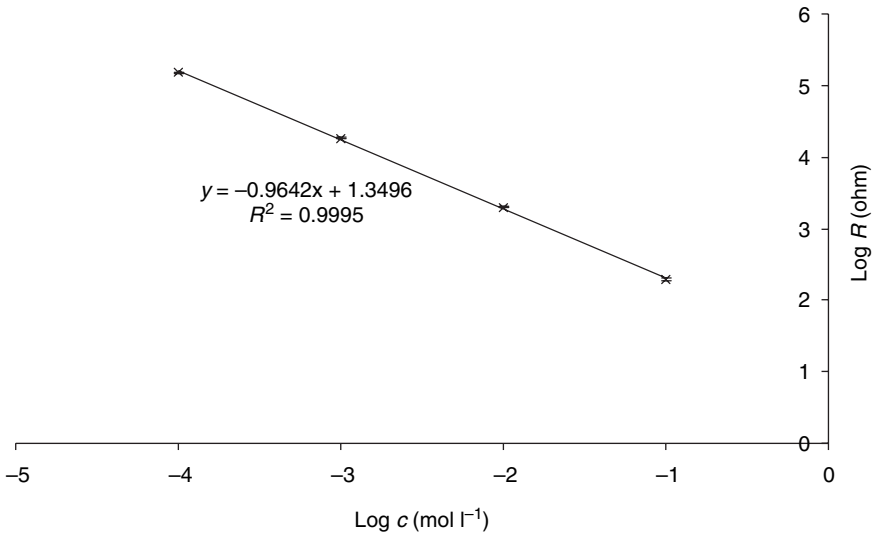

9.5 Logarithmic plot of the impedance at zero phase-angle shift as a function of electrolyte concentration obtained from the electrochemical cell with $A = 314\,mm^2$, $d = 112\,mm$ and $T = 298.0\,K$.

this effect is less pronounced at higher concentrations can be explained by interactions between the ions, which are much closer to each other at higher electrolyte concentrations, thus making free diffusion towards the anode (for Cl^-) and the cathode (for Na^+) more difficult.

Figure 9.5 shows the relationship between the logarithm of the obtained impedance at the completion of the semi-circle (right-hand side of the semi-circle in Fig. 9.2) as a function of the logarithm of the sodium chloride concentration. A linear relationship is observed with good correlation coefficient and a slope of –1, indicating that the relationship between the impedance (R) and the electrolyte concentration (c) is reciprocal. Therefore Equation 9.1 can be re-defined to:

$$R = k_1(d, A) \cdot c^{-1} \qquad [9.2]$$

where k_1 is a factor containing the unknown parameters and relationships. In Equation 9.2, the value of k_1 is 20.0 ± 0.8, taking into account a temperature of 298.0 K and knowing that this factor is dependent on A and d, two parameters that need to be investigated further in this work. The value of $k_1 = 20.0$ is valid for $A = 314\,mm^2$ and $d = 112\,mm$.

9.2.4 Study of the influence of the electrode surface area

Similar to the experiments described in the previous section, but this time with various surface areas of the palladium electrodes and at each elec-

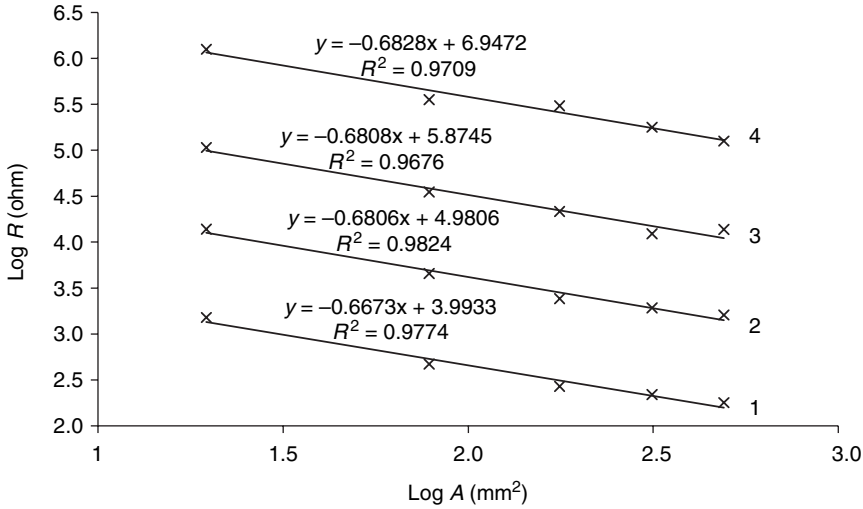

9.6 Logarithmic plot of the impedance at zero phase-angle shift as a function of electrode surface area obtained from the electrochemical cell d=112 mm, T=298.0 K and an electrolyte concentration of (1) 1×10^{-1}, (2) 1×10^{-2}, (3) 1×10^{-3} and (4) 1×10^{-4} mol l^{-1}.

trolyte concentration (1×10^{-1}–1×10^{-4} mol l^{-1}), values for the impedance were obtained as a function of electrode surface area, while keeping in mind that the distance between the electrode was kept constant at a value of d= 112 mm. As also mentioned above, the impedance, when no phase-angle shift is observed, is the most important factor for this research. It is obtained at the cross-section of the x-axis and the completion of the semi-circle. The data obtained are shown in Fig. 9.6 as a logarithmic plot for electrode surfaces of 19.63, 78.5, 176.6, 314 and 490.6 mm^2 (corresponding to diameters of 5, 10, 15, 20 and 25 mm, respectively).

It can be seen that linear relationships with a slope around –0.68 are obtained for all electrolyte concentrations. However, the correlation coefficients are rather poor. This can be explained by the presence of edge effects, which become more important when the electrode surface decreases (electrode surface area decreases with r^2; edge effects decrease with r). Indeed, not taking into account the data of the smallest electrode surface area (with r=2.5 mm) results in correlation coefficients in the range of 0.980–0.995 and a slightly lower slope of –0.65. However, in order to cover a wide range of electrode surface areas, it is preferred to use all the data given in Fig. 9.6, even for those electrodes with small surface area. The relationship between impedance and electrode surface area can be inserted in Equation 9.2 to produce Equation 9.3:

$$R = k_2(d)\cdot A^{-0.68}\cdot c^{-1} \qquad [9.3]$$

Table 9.1 Data for factor k_1 in Equation 9.2 as a function of electrode surface area (A) for a constant distance between the electrodes of $d = 112$ mm

Electrode surface area (mm^2)	k_1
19.63	136.0
78.50	53.0
176.60	30.5
314.00	20.6
490.60	15.3

where k_2 is a factor containing the unknown parameters and relationships and

$$k_1 = k_2 \cdot A^{-0.68} \quad [9.4]$$

From the data in Fig. 9.6, it is possible to calculate the value of k_1 for various electrode surface areas as was done in the previous section for a surface area of 314 mm^2. In addition, with the knowledge of these values, it is possible to obtain the value of k_2 using Equation 9.4. The values for k_1 are summarised in Table 9.1, while for k_2 a value of 1030 ± 40 was obtained, with A in mm^2. It can be seen that the value for k_1 at $A = 314$ mm^2 is in acceptable correlation with the value obtained in the previous section.

9.2.5 Study of the influence of the distance between the electrodes

In this section, the influence of the distance between the electrodes is investigated as a function of NaCl concentration (1×10^{-1}–1×10^{-4} mol l^{-1}) and as a function of electrode surface area (19.6–490.6 mm^2). The distance between the electrodes was varied from 27 to 112 mm by inserting PVC pipes of different lengths into the cell. Additionally in this case, the impedance of the cell was measured as a function of applied frequency, and the impedance of importance for this work is the one at the completion of the semi-circle in Fig. 9.8 (or values corresponding to the observation of no phase-angle shift between applied potential and measured current). As an example of these experiments, Fig. 9.7 shows the logarithmic plot of the relationship between obtained impedance and distance between the electrodes for the four different concentrations of electrolyte and at a fixed value for the electrode surface area (490.6 mm^2).

It can be seen that linear relationships are obtained with a slope very close to 1, indicating that the impedance is proportional to the distance

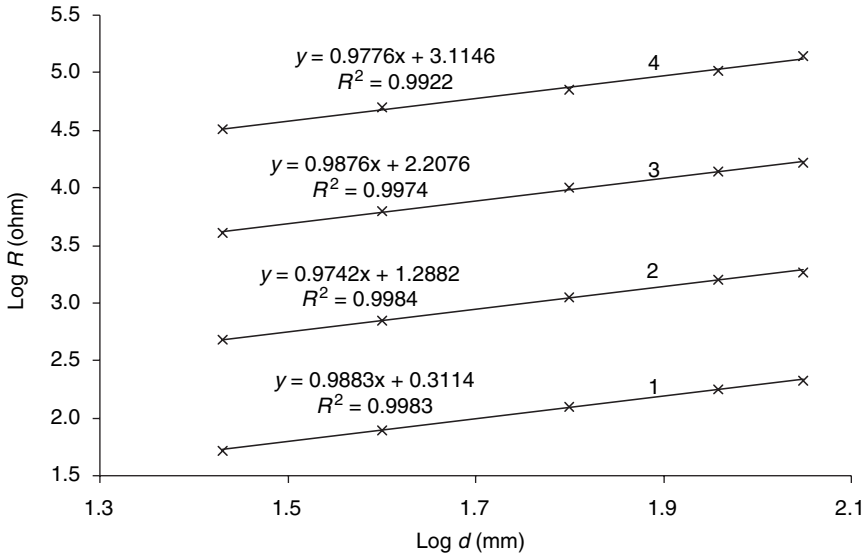

9.7 Logarithmic plot of the impedance at zero phase-angle shift as a function of distance between the electrode (d) obtained from the electrochemical cell with $A = 490.6\,mm^2$, $T = 298.0\,K$ and an electrolyte concentration of (1) 1×10^{-1}, (2) 1×10^{-2}, (3) 1×10^{-3} and (4) $1\times10^{-4}\,mol\,l^{-1}$.

between the electrodes. Therefore, Equation 9.3 can be modified by implementation of a new factor (k_3) and taking into account the relationship obtained in Fig. 9.7:

$$R = k_3 d A^{-0.68} c^{-1} \qquad [9.5]$$

with k_3 a factor which is independent of A, d and c, and d being the distance between the electrodes. Equation 9.6 shows the interrelationships between the different factors used:

$$k_1 = k_2 A^{-0.68} = k_3 A^{-0.68} d \qquad [9.6]$$

and

$$k_2 = k_3 d \qquad [9.7]$$

Using Equations 9.6 and 9.7, it is possible to calculate the values for k_1, k_2 and k_3 for different values of A, d and c, and the values for k_2 and k_1 previously obtained can be verified. These values are given in bold in Tables 9.2 and 9.3 and can be compared with the values obtained in the previous sections. From the data shown in Fig. 9.7, a value for k_3 of 9.5 ± 0.3 is obtained. With this value, it is possible to calculate k_2 as a function of distance between the electrodes according to Equation 9.7, and these results

Table 9.2 Data for factor k_2 in Equation 9.7 as a function of distance between the electrodes (d)

Distance between the electrodes (mm)	k_2
27	256.5
40	380.0
63	598.5
91	864.5
112	**1064.0**

Table 9.3 Data for factor k_1 in Equation 9.6 as a function of electrode surface area (A) and distance between the electrodes (d)

A (mm^2)	Distance between the electrodes, d (mm)				
	27	40	63	91	112
19.63	33.9	50.2	79.1	114.2	**140.5**
78.5	13.2	19.6	30.8	44.5	**54.8**
176.6	7.61	11.3	17.7	25.6	**31.6**
314	5.14	7.62	12.0	17.3	**21.3**
490.6	3.80	5.62	8.86	12.8	**15.7**

are summarised in Table 9.2. The bold value for $d = 112$ mm is in acceptable correlation with the value obtained in the previous section. In addition, with the knowledge of the data of k_2 from Table 9.2, it is possible to calculate the results for k_1 as a function of electrode surface area A and distance between the electrodes d (Table 9.3). Again, it can be seen that there is good correlation between the values in bold and those obtained in the previous sections under the same experimental conditions.

9.3 Method for quality control of textile electrodes

9.3.1 Introduction

For the experiments described in this chapter, use was made of textile electrodes of stainless steel instead of palladium sheets, which were used for the characterisation of the electrochemical cell. The aim of this section is to investigate the behaviour of these textile electrodes in the electrochemical cell and to compare the results obtained with those described in section

9.2. For this purpose, the starting situation in this section is reflected by Equation 9.1 and, depending on the results obtained, will show whether this equation is still valid and, if so, under which conditions. Possible differences in results between those described in this section and those in section 9.2 need to be explained by the fact that a textile structure is used as electrode material, since this is the only modification of the electrochemical cell characterised in section 9.2 and used for the studies described here in section 9.3.

In this investigation, a set of two identical electrodes (same material, type of textile structure and geometrical surface area) will always be used. In principle, it can be interesting to vary these parameters and to use two different electrodes in the electrochemical cell in order to gain information about the properties of one single electrode (e.g. by using an electrode with a small surface area and another with a large surface area). As will be seen further in this work, this approach will have both advantages and disadvantages; where appropriate, its advantages will be exploited in order to derive further insight into the behaviour, although this will not be the standard procedure. Therefore, preference is given to the study of textile electrodes in electrochemical cells with identical electrodes.

9.3.2 Characterisation of the electrochemical cell with textile electrodes

Introduction

Similar to the experiments carried out at palladium electrodes and described in Chapter 3, the concentration of electrolyte (c), the electrode surface area (A) and the distance between the electrodes (d) will be studied as a function of type of textile structure. In this work, three structures will be studied: knitted, woven and non-woven textile structures, all obtained from stainless-steel fibres. To complete the data of this work, palladium sheets will also be inserted in the study as a fourth set of electrodes. Therefore, for palladium electrodes, the work described in section 9.2 will actually be repeated here in order to have a direct comparison between results obtained with palladium electrodes and textile electrodes. Of course, correlation with the data obtained in section 9.2 will be verified.

Electrolyte concentration study

A first parameter to be investigated is the concentration of the NaCl solution. Electrochemical cells with electrolyte concentrations of 1×10^{-1}, 1×10^{-2}, 1×10^{-3} and 1×10^{-4} mol l^{-1} NaCl were prepared. Impedances at these

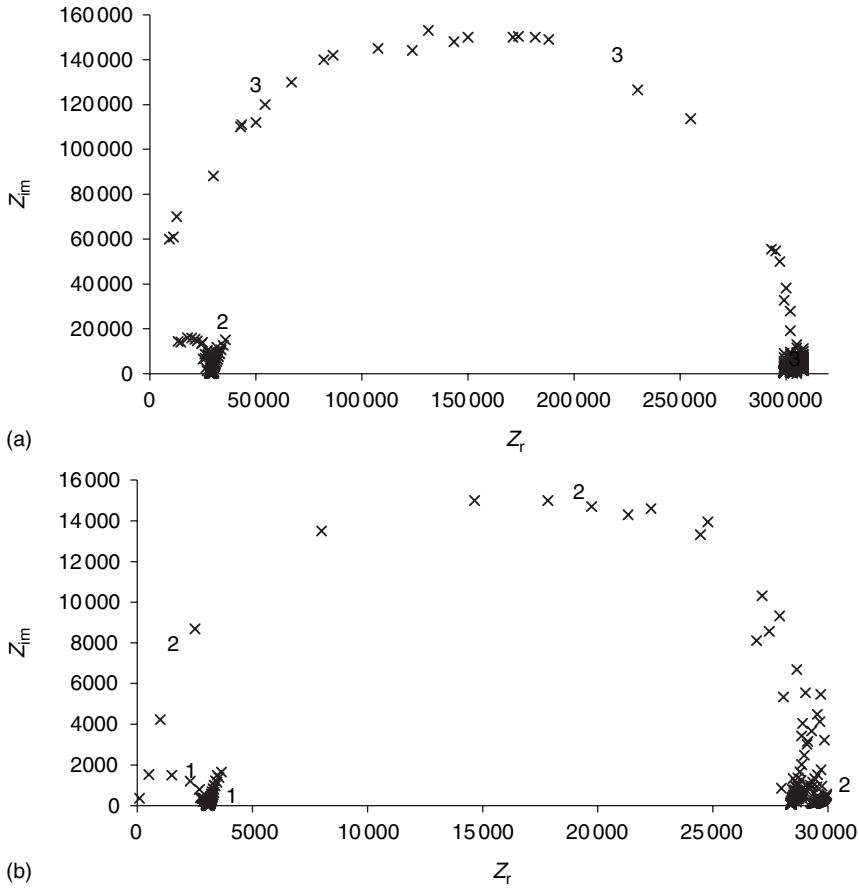

9.8 Nyquist plots recorded at an electrochemical cell with palladium electrodes or woven, non-woven or knitted textile electrodes with $A = 180\,mm^2$ and $d = 103\,mm$ for a NaCl concentration of (1) 1×10^{-2}, (2) 1×10^{-3} and (3) $1 \times 10^{-4}\,mol\,l^{-1}$ at T = 298.0 K. Part b is an enlargement of part a.

cells were measured as a function of frequency in the range of 0.1–1 MHz with $A = 180\,mm^2$ and $d = 103\,mm$. Some curves are shown in Fig. 9.8 and Fig. 9.9. It can be seen that the Nyquist plot corresponding to the textile electrodes is almost identical to those obtained for the palladium electrodes. Well-shaped semi-circles are obtained, and a value for Z_r without phase-angle shift can be determined clearly at the completion of the semi-circle. In principle, it is possible to take account of the different values of the electrolyte resistance obtained in this section and those obtained in section 9.1 because d is different. This can be done using Equation 9.5, but at this stage of the study it is not known whether the behaviour of the textile electrodes

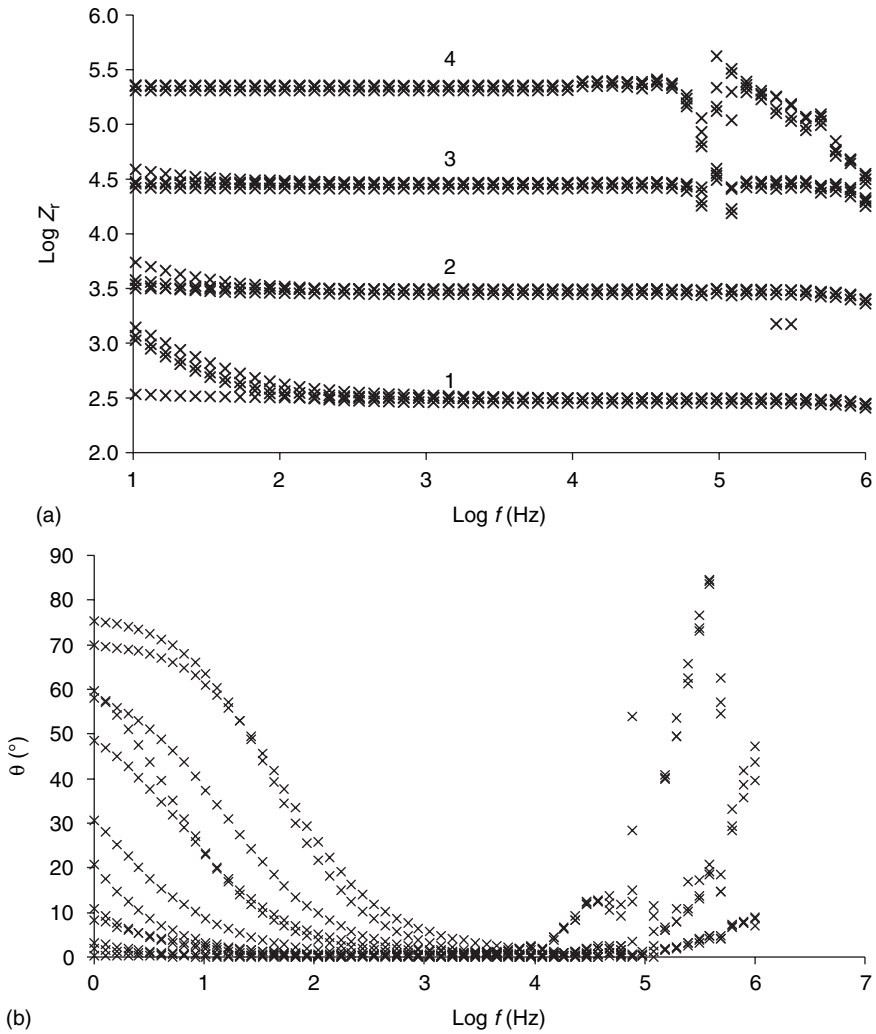

9.9 Bode plot showing the (a) real impedance and (b) phase-angle shift as a function of applied frequency, recorded at an electrochemical cell with palladium electrodes or woven, non-woven and knitted textile electrodes for $A = 180\,mm^2$, $d = 103\,mm$ and an NaCl concentration of (1) 1×10^{-1}, (2) 1×10^{-2}, (3) 1×10^{-3} and (4) $1 \times 10^{-4}\,mol\,l^{-1}$ at $T = 298.0\,K$.

as a function of distance between the electrodes is the same as for the palladium electrodes. Therefore, it is not certain that Equation 9.5 will also be valid for textile electrodes, and thus it is better to compare the results obtained in this section for the textile electrodes and the palladium electrodes and not to compare these results with those obtained in section 9.2.

However, some differences are also observed between the plots obtained for palladium and those obtained for the textile electrodes. Three observations result in the same conclusion, which is that at lower frequencies (<1000 Hz), a capacitive effect plays a role when using textile electrodes, which was not observed for the palladium electrodes. First, the Nyquist plots (Fig. 9.8) show that for textile electrodes a capacitive contribution is observed, after which the semi-circle is completed. This effect corresponds to low frequencies and is much less pronounced at palladium electrodes. Secondly, the capacitive effect observed in the Nyquist plot is confirmed in the Bode plot (Fig. 9.9b). The plots resulting in a high phase-angle shift in the low-frequency range were obtained with the non-woven structures, which are in fact the structures with the roughest and most irregular surface. This is probably the cause of the observed effect.

Finally, it can be seen from Fig. 9.9a that the real impedance does not remain constant at low frequencies for the textile electrode, and this effect is more pronounced at higher electrolyte concentrations. Probably, Z_r is influenced by other effects only occurring in the low-frequency range. This effect is frequently observed and described in the literature and is caused by non-uniformity of surfaces at the micro-scale, which in fact is the case for the textile electrodes. It is also not possible to explain this effect by a pure resistor or a pure capacitor in the electrical equivalent circuit. For this purpose, constant-phase elements are implemented as described in the theoretical discussion of electrochemical impedance spectroscopy (presented in Chapter 2, section 2.4).

In Fig. 9.10, the impedances obtained from Fig. 9.8, where the semi-circle is completed, are plotted logarithmically against the logarithm of the electrolyte concentration. Similar to the result obtained in section 9.2, a linear curve is obtained with a slope equal to approximately –1. From Fig. 9.10, it is also clear that there are no systematic differences observed between the behaviour of the textile electrode and the palladium electrodes. This means that Equation 9.2 is also valid in this case, but of course with another value of k_1 because of the differently used distance between the electrodes. From the data shown in Fig. 9.10, k_1 is calculated, and a value of 30.3 ± 1.8 was obtained, which is in good correlation with the value 29.2 ± 0.8 obtained from the data shown in Table 9.3, with $A = 180\,\text{mm}^2$ and $d = 103\,\text{mm}$. Two important remarks should be made concerning the data in Fig. 9.10, but they are not immediately obvious in Fig. 9.10 because of limited resolution, and therefore the values of the impedance corresponding to each concentration at the calibration curves is given in Table 9.4. First, it can be seen that the error margins for the non-woven structure are wider than for the other structures and palladium. Secondly, the calibration curve for the knitted electrode is shifted over about 1% to smaller impedance values and for the woven electrode over about 1.5% to higher impedance values compared

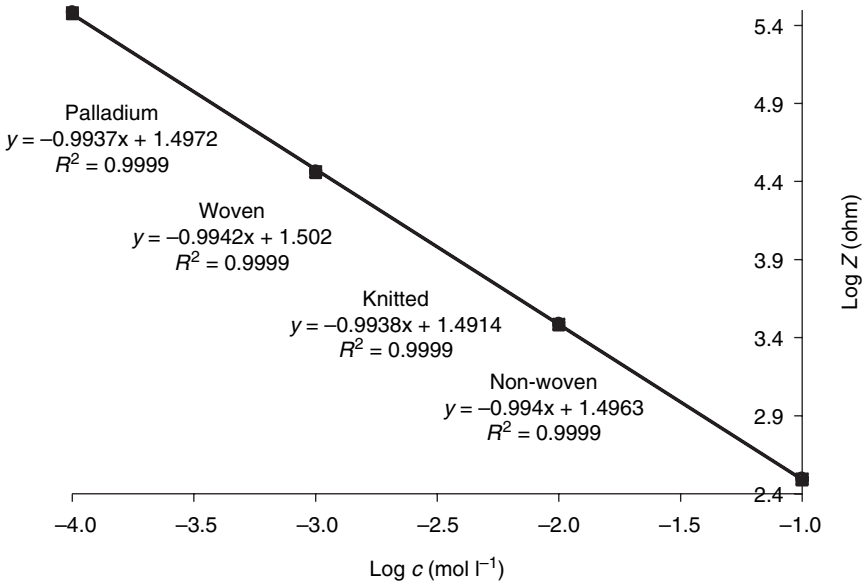

9.10 Logarithmic plot of the impedance at zero phase-angle shift as a function of electrolyte concentration obtained from the electrochemical cell with palladium electrodes, woven, knitted and non-woven electrodes for $A = 180\,\text{mm}^2$, $d = 103\,\text{mm}$ and $T = 298.0\,\text{K}$.

Table 9.4 Impedance data in ohm for the calibration curves shown in Fig. 9.10

c (mol l^{-1})	Electrode type			
	Palladium	Woven	Knitted	Non-woven
10^{-1}	312±2	316±2	308±2	311±7
10^{-2}	3073±70	3113±79	3030±78	3060±205
10^{-3}	29 000±700	29 400±700	28 700±800	29 100±1900
10^{-4}	303 000±5000	308 000±6000	299 000±6000	303 000±13 000

with the calibration curve obtained at palladium electrodes. From Table 9.4, the shift becomes clear when comparing impedances obtained at different types of electrodes. The experiments undertaken to obtain the data in Fig. 9.10 were repeated several times, and the same observation could always be made in a reproducible way.

In order to explain the two remarks described above, it is necessary to look at the structure of the textile electrodes and compare them with the flat palladium sheet electrodes. The measured impedance is in fact an average of a very large number of individual impedances at different

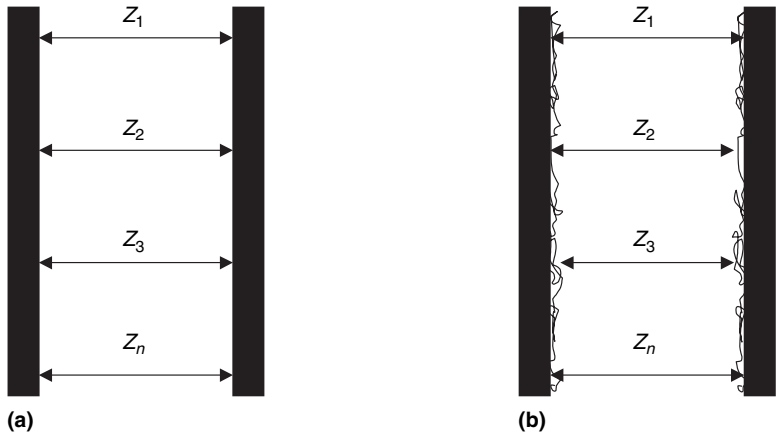

9.11 Schematic representation of two sets of electrodes of palladium (a) and textile electrode (b) and the influence of roughness of the electrode surface on the measured impedance (Z).

locations at the electrode surfaces. This is shown schematically and in a somewhat simplified form in Fig. 9.11. Contrary to the palladium electrodes, the surface of textile structures is not flat, particularly for the non-woven structures. Therefore, the experimental impedance is the sum of the individual local impedances:

$$Z = \sum_{n}^{1} Z_n \qquad [9.8]$$

is not equal to n times Z_1 or Z_2 or Z_n because of differences in local distances between the textile electrodes. This is not the case for the flat palladium electrode where $Z_1 = Z_2 = Z_3 = Z_n$. Larger differences in the values of Z_1, Z_2, Z_3, to Z_n result in wider error margins, an effect that is clearly observed for the non-woven structure and is related to the high degree of roughness compared with the knitted and woven structure and to the flat palladium electrode surfaces.

The cause of the second observation should be sought by examing the way in which the electrodes are positioned in the electrochemical cell. In Fig. 9.12, the positioning of a palladium electrode (a) and a woven (b) and knitted (c) textile electrode at one side of the electrochemical cell is presented. Note that these drawings represent cross-sections. It must also be mentioned that the structure of the knitted electrode is relatively elastic, which is typical for knitted structures, while the structure of the woven electrode is tight and rigid. This effect can explain the shifts of the calibration curves. For a woven structure, the measurement of Z will be somewhat higher compared with the palladium electrode, because a large fraction of

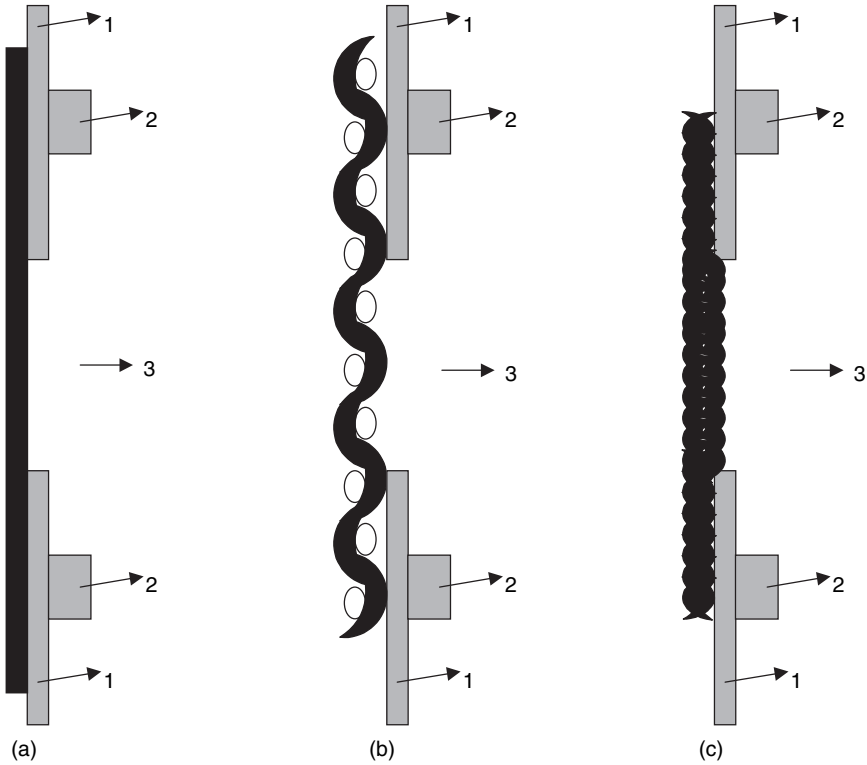

9.12 Scheme showing the positioning of a palladium electrode (a) and a woven (b) and knitted (c) textile electrode in the cell, and the influence on the configuration of the electrodes due to positioning. (1) Rubber fittings, (2) part of the PVC tubing filled with electrolyte and (3) electrolyte solution.

the surface of the woven structure lies somewhat deeper in the cell, as is clearly shown in Fig. 9.12b. In fact with woven electrodes, the actual distance between the electrodes (d') is a little larger than the geometrical distance (d) determined by the electrochemical cell geometry. For palladium electrodes d and d' are equal. This effect explains a small shift in the calibration curves to somewhat higher values; in fact a shift of about 1% is observed, which means that d' is approximately 1% bigger than d. From this conclusion, it is possible to obtain d', which is about 104 mm, or for each woven electrode in the electrochemical cell, the real virtually smoothened surface of the electrode lies about 0.5 mm deeper compared with the flat palladium electrodes.

For the knitted structure, the opposite effect is observed. Because of its elastic structure, the knitted electrode will adapt to the shape of the holders and fittings used in the electrochemical cell. At the surface of the knitted

structure, where the holders of the cell are positioned (Fig. 9.12c), pressure is applied (to avoid leakage of electrolyte solution), which causes a suppression of the knitted structure. The latter is not obtained in the opening of the electrochemical cell (to make contact with the electrolyte solution), and the structure adapts to this opening as shown in Fig. 9.12c. In this case, the actual distance between the knitted electrodes in the electrochemical cell is smaller compared with the geometrical distance, explaining the shift of the calibration curve to somewhat smaller impedance values than the curve obtained for palladium electrodes. From the shift of about 1.5%, it was possible to obtain the actual distance between the electrode being $d' = 101\,\text{mm}$ instead of $d = 103\,\text{mm}$.

Study of the electrode surface area

In this section, the influence of the electrode surface area of woven, nonwoven and knitted textile electrodes at the impedance of the electrochemical cell was studied. This was done for various electrolyte concentrations and a constant distance between the electrodes of 103 mm. Note that this is the geometrical distance (d), which can vary over a range of 1–2% depending on the type of textile electrode that is used. The data in Fig. 9.13 show the relationship between the logarithm of the electrolyte resistance, which is in fact the measured impedance of the cell, and the logarithm of the electrode surface area recorded at palladium and textile electrodes. It can be seen that good correlation is obtained between the different electrodes, except for the smallest electrode surface area. This can be explained by the non-ideal behaviour of textile electrodes with regard to the behaviour of palladium sheet electrodes. For each electrode, edge effects should be taken into account, which are much more expressed at textile electrodes, because of their rough structure. However, if the surface of the electrode is large enough, the bulk properties determine the overall signal, and edge effects can be neglected. This is the reason why edge effects only start to play a role at the smallest electrode surface. The data in Fig. 9.13 (and additionally obtained data) show that edge effects cannot be neglected for the textile electrodes if the ratio of electrode surface area to loop is <2.5 mm, obtained from following equation:

$$\frac{A}{\text{loop}} = \frac{\pi r^2}{2\pi r} = \frac{r}{2} \qquad [9.9]$$

It should be taken into account that this is only valid for the textile electrode investigated in this work, because this parameter is also dependent on the roughness of the surface. The roughness is definitely the cause of this edge effect, because it is absent when using smooth palladium electrodes.

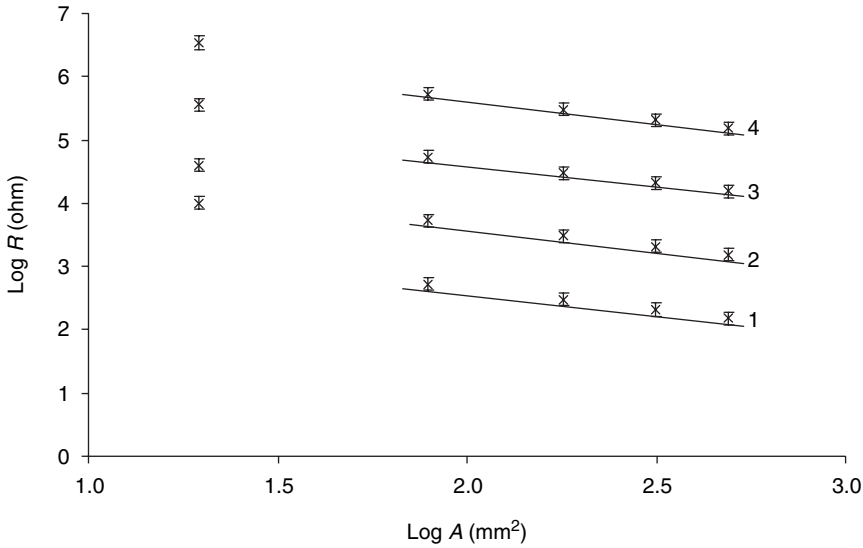

9.13 Logarithmic plot of the impedance at zero phase-angle shift as a function of electrode surface area obtained from the electrochemical cell with palladium and textile structure electrodes, $d = 103$ mm, $T = 298.0$ K and an electrolyte concentration of (1) 10^{-1}, (2) 10^{-2}, (3) 10^{-3} and (4) 10^{-4} mol l^{-1}.

Leaving out the data obtained with the smallest electrode surface area, for further analysis good correlation was obtained for all electrodes with a slope of about –0.68. This is also in correlation with the slope obtained in section 9.2. In principle, as was done in section 9.2, values for k_1 and k_2 (Equations 9.2–9.4) can be calculated, but because these values will be repeated in the next section, where they will have more scientific meaning, they are not calculated here.

Study of the distance between the electrodes

In this section, the distance between the electrodes is studied for different electrolyte concentrations and distances between the electrodes at a constant electrode surface area of $A = 180$ mm^2. The obtained impedances are plotted logarithmically against the distance between the electrodes (d) as shown in Fig. 9.14. Relationships obtained for the textile electrodes are identical to those for the palladium electrodes if the smallest distance between the electrodes is not taken into account. Additionally in this case, the roughness of the textile electrodes is responsible for this effect and can be neglected for distances longer than $d = 40$ mm – an effect that increases with decreasing distance between the electrodes. Of course, also in this case,

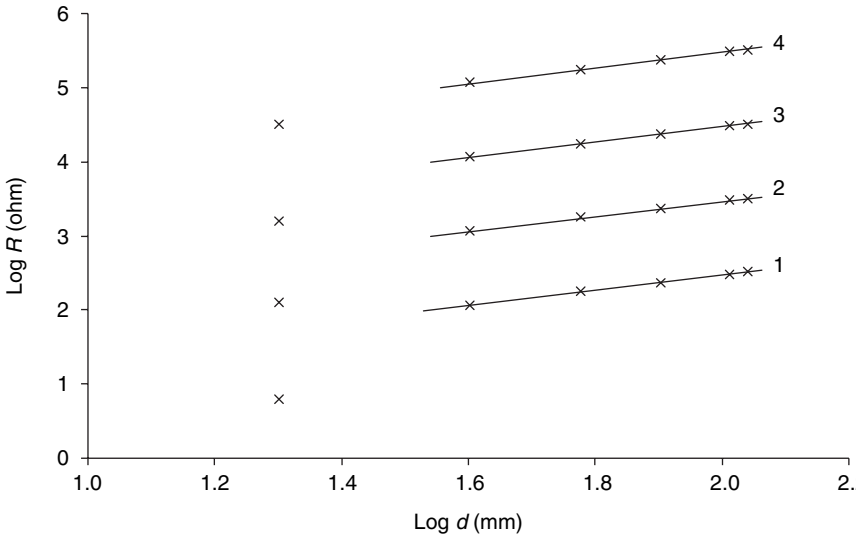

9.14 Logarithmic plot of the impedance at zero phase-angle shift as a function of distance between the electrode (d) obtained from the electrochemical cell with palladium and textile electrodes, A= 490.6 mm^2, T=298.0 K and an electrolyte concentration of (1) 1×10^{-1}, (2) 1×10^{-2}, (3) 1×10^{-3} and (4) 1×10^{-4} mol l^{-1}.

the defined conditions of d_{min} are valid only for the three investigated structures because of its dependency on the surface roughness. The cause of this effect can be explained easily using Fig. 9.11b. The roughness of textile electrodes has an influence on the measured impedance because of small differences between Z_1, Z_2, to Z_n. However, these differences should be related to the distance between the electrodes because the roughness introduces locally different distances between the electrodes.

The smaller the geometrical distance between the electrodes, the more important the local differences in distance become, which causes a drift away from linearity for the relationship between $\log Z$ and $\log d$. In addition, from the experimental data, it could be seen that this drift is slightly more expressed for the non-woven structure, which is in fact the structure with the roughest surface. From additional experiments, it was found that Equations 9.5–9.7, obtained with the palladium electrodes, are also valid for the textile electrodes on the condition that $d_{min}>40$ mm and $A_{min}>75$ mm^2.

From the data introduced in Figs 9.10, 9.13 and 9.14, values for k_1, k_2 and k_3 can be calculated and are presented in Tables 9.5, 9.6, 9.7 and 9.8. It can be seen that the values for the textile electrodes are slightly higher compared with those obtained in section 9.2. However, comparison of the data obtained in this chapter for palladium and textile electrodes did not reveal

Table 9.5 Data for factors k_1, k_2 and k_3 for knitted textile-structure electrodes according to Equations 9.2–9.7

k_1 d (mm) A (mm^2)	20	40	60	80	103	110
19.63	24.8 ± 3.0	52.8 ± 3.1	79.5 ± 5.5	106.5 ± 6.3	136.7 ± 9.8	146.3 ± 10.9
78.5	9.67 ± 1.0	20.6 ± 0.8	31.0 ± 1.2	41.5 ± 1.5	53.3 ± 2.2	57.0 ± 2.2
180	5.50 ± 0.50	11.7 ± 0.4	17.6 ± 0.7	23.6 ± 0.9	30.3 ± 1.2	32.4 ± 1.3
314	3.77 ± 0.39	8.02 ± 0.30	12.1 ± 0.5	16.2 ± 0.7	20.8 ± 0.8	22.2 ± 0.9
491	2.78 ± 0.41	5.91 ± 0.26	8.91 ± 0.32	11.9 ± 0.5	15.3 ± 0.6	16.4 ± 0.7
k_2	188 ± 12	400 ± 15	602 ± 25	806 ± 34	1035 ± 42	1108 ± 45
k_3	10.05 ± 0.4	10.05 ± 0.4	10.05 ± 0.4	10.05 ± 0.4	10.05 ± 0.4	10.05 ± 0.4

Table 9.6 Data for factors k_1, k_2 and k_3 for woven textile-structure electrodes according to Equations 9.2–9.7

k_1 d (mm) A (mm^2)	20	40	60	80	103	110
19.63	24.4 ± 3.1	53.0 ± 3.6	80.3 ± 5.8	108.0 ± 6.1	140.3 ± 9.4	152.0 ± 12.0
78.5	9.60 ± 0.8	21.0 ± 0.8	31.4 ± 1.3	42.1 ± 1.3	53.9 ± 2.1	57.8 ± 2.0
180	5.46 ± 0.50	11.9 ± 0.4	18.1 ± 0.6	23.9 ± 0.9	30.4 ± 1.2	32.8 ± 1.2
314	3.71 ± 0.27	8.08 ± 0.29	12.4 ± 0.5	16.8 ± 0.7	21.3 ± 0.9	22.8 ± 0.8
491	2.77 ± 0.38	6.00 ± 0.25	8.99 ± 0.34	12.2 ± 0.7	15.6 ± 0.8	17.0 ± 0.7
k_2	192 ± 12	401 ± 16	606 ± 25	820 ± 33	1034 ± 40	1118 ± 40
k_3	10.06 ± 0.42	10.06 ± 0.42	10.06 ± 0.42	10.06 ± 0.42	10.06 ± 0.42	10.06 ± 0.42

Table 9.7 Data for factors k_1, k_2 and k_3 for non-woven textile-structure electrodes according to Equations 9.2–9.7

k_1 d (mm) A (mm^2)	20	40	60	80	103	110
19.63	24.6 ± 3.1	52.9 ± 3.4	80.0 ± 6.0	106.9 ± 6.3	137.9 ± 9.9	148.2 ± 10.4
78.5	9.63 ± 0.9	20.6 ± 0.8	31.2 ± 1.2	41.7 ± 1.4	53.7 ± 2.3	57.4 ± 2.1
180	5.50 ± 0.52	11.9 ± 0.4	17.7 ± 0.6	23.5 ± 0.9	30.5 ± 1.1	32.8 ± 1.3
314	3.71 ± 0.30	8.03 ± 0.31	12.2 ± 0.5	16.4 ± 0.7	21.0 ± 0.9	22.4 ± 0.9
491	2.60 ± 0.44	5.94 ± 0.24	8.90 ± 0.32	12.0 ± 0.6	15.4 ± 0.6	16.5 ± 0.7
k_2	187 ± 14	404 ± 14	606 ± 25	818 ± 34	1033 ± 42	1110 ± 46
k_3	9.99 ± 0.40	9.99 ± 0.40	9.99 ± 0.40	9.99 ± 0.40	9.99 ± 0.40	9.99 ± 0.40

Table 9.8 Data for factors k_1, k_2 and k_3 for palladium electrodes according to Equations 9.2–9.7

k_1 d (mm) A (mm^2)	20	40	60	80	103	110
19.63	24.6 ± 0.7	53.0 ± 1.5	80.1 ± 2.5	110.0 ± 3.2	135.0 ± 4.0	142.9 ± 4.5
78.5	9.64 ± 0.29	21.0 ± 0.5	31.1 ± 1.1	42.1 ± 1.3	53.6 ± 1.5	57.3 ± 1.6
180	5.54 ± 0.16	11.8 ± 0.4	17.5 ± 0.5	23.6 ± 0.7	30.1 ± 1.0	32.3 ± 1.1
314	3.72 ± 0.12	7.97 ± 0.14	12.1 ± 0.4	16.4 ± 0.5	20.9 ± 0.6	22.6 ± 0.6
491	2.75 ± 0.11	5.95 ± 0.18	8.96 ± 0.22	12.0 ± 0.4	15.5 ± 0.5	16.0 ± 0.5
k_2	187 ± 4	402 ± 10	608 ± 16	806 ± 21	1038 ± 26	1111 ± 29
k_3	9.81 ± 0.29	9.81 ± 0.29	9.81 ± 0.29	9.81 ± 0.29	9.81 ± 0.29	9.81 ± 0.29

a systematic error. This is probably due to the fact that the error margins for textile electrodes are higher, which explains the consistency between the data obtained for different electrode structures.

9.3.3 Long-term stability of textile electrodes

In this section, the behaviour of the textile electrodes when used for a longer period in the electrochemical cell is investigated. It is expected that this behaviour can change as a function of time because of uptake of electrolyte solution by the textile electrodes and possible corrosion reactions that can occur. Additionally in this case, the data and results obtained for the textile electrodes will be compared with those obtained for palladium electrodes. Bode and Nyquist plots are recorded for the four types of electrodes and the electrolyte resistance was measured as a function of time for electrolyte concentrations of 1×10^{-1}, 1×10^{-2}, 1×10^{-3} and 1×10^{-4} mol l^{-1}. The values for A and d are 180 mm^2 and 103 mm, respectively. For all these concentrations, the resistances are summarised in Tables 9.9–9.12.

From the data in Tables 9.9–9.12 and from Fig. 9.15, it can be seen that the resistance of the system decreases as a function of time when textile electrodes are used. This behaviour is contradictory to the behaviour of the palladium electrodes, the resistance of which is constant within the previously obtained error margins (see Table 9.4). Only at $t=0$ is comparison of the resistances obtained at textile and palladium electrodes possible.

A possible explanation for this effect can be found in the 3D structure of textile electrodes and its permeability for liquids. While slowly soaking electrolyte solution, the contact surface between textile electrode and electrolyte increases. The latter effect gives rise to a decrease in the resistance because of a larger value for A. As this process is occurring reasonably

Table 9.9 Electrolyte-resistance (Ω) data obtained for different electrodes at an electrolyte concentration of 1×10^{-4} mol l^{-1}

Time (h)	Palladium (Ω)	Woven (Ω)	Knitted (Ω)	Non-woven (Ω)
0	303 000	308 000	299 000	303 000
1	301 000	301 000	298 000	301 000
2	304 000	295 000	294 000	299 000
4	304 000	288 000	291 000	296 000
8	301 000	280 000	286 000	291 000
16	299 000	271 000	283 000	286 000
24	304 000	264 000	281 000	284 000
30	302 000	259 000	281 000	283 000
36	301 000	257 000	279 000	282 000
48	304 000	252 000	278 000	281 000
60	303 000	250 000	277 000	283 000
72	300 000	248 000	276 000	281 000
96	301 000	246 000	275 000	282 000
120	303 000	246 000	275 000	282 000

Table 9.10 Electrolyte-resistance (Ω) data obtained for different electrodes at an electrolyte concentration of 1×10^{-3} mol l^{-1}

Time (h)	Palladium (Ω)	Woven (Ω)	Knitted (Ω)	Non-woven (Ω)
0	29 020	29 400	28 600	29 050
1	29 020	28 420	28 200	28 610
2	29 010	28 010	28 050	28 200
4	29 040	27 200	27 900	27 820
8	29 000	26 490	27 420	27 560
16	28 980	25 600	27 000	27 200
24	29 040	24 920	26 900	27 050
30	29 040	24 480	26 790	27 010
36	29 020	24 190	26 750	27 000
48	29 000	23 950	26 700	27 000
60	29 030	23 710	26 610	26 980
72	29 040	23 600	26 550	27 010
96	29 010	23 520	26 510	27 000
120	29 000	23 520	26 500	27 020

slowly, it can most likely be explained by air bubbles trapped in the textile structure. These bubbles can escape only by a slow dissolution process in the surrounding electrolyte solution. Another indication that supports this hypothesis is the fact that, after some time, the system obtains an equilibrium condition, probably because all trapped air is removed, giving rise to

Table 9.11 Electrolyte-resistance (Ω) data obtained for different electrodes at an electrolyte concentration of 1×10^{-2} mol l^{-1}

Time (h)	Palladium (Ω)	Woven (Ω)	Knitted (Ω)	Non-woven (Ω)
0	3079	3103	3015	3058
1	3050	3051	3001	3016
2	3093	3022	2973	2985
4	3062	2900	2957	2951
8	3065	2801	2900	2933
16	3078	2688	2882	2902
24	3052	2618	2835	2881
30	3055	2574	2831	2870
36	3059	2547	2821	2863
48	3064	2524	2810	2857
60	3069	2508	2804	2846
72	3069	2496	2800	2841
96	3049	2486	2793	2836
120	3060	2480	2790	2840

Table 9.12 Electrolyte-resistance (Ω) data obtained for different electrodes at an electrolyte concentration of 1×10^{-1} mol l^{-1}

Time (h)	Palladium (Ω)	Woven (Ω)	Knitted (Ω)	Non-woven (Ω)
0	310	315	308	310
1	311	311	306	308
2	312	307	305	307
4	312	299	302	304
8	312	288	299	300
16	311	275	295	296
24	310	268	292	294
30	312	263	290	292
36	310	260	290	291
48	312	261	291	292
60	311	260	292	293
72	311	261	292	295
96	312	262	294	297
120	311	263	295	298

a constant contact surface between textile electrode and electrolyte solution. Furthermore, it was observed that the resistance-decreasing effect is completed much faster for the non-woven structures, which also supports the hypothesis. The non-woven structure has a much higher solution-soaking capacity, and, due to its more regular microscopic structure, air bubbles can be removed much more easily.

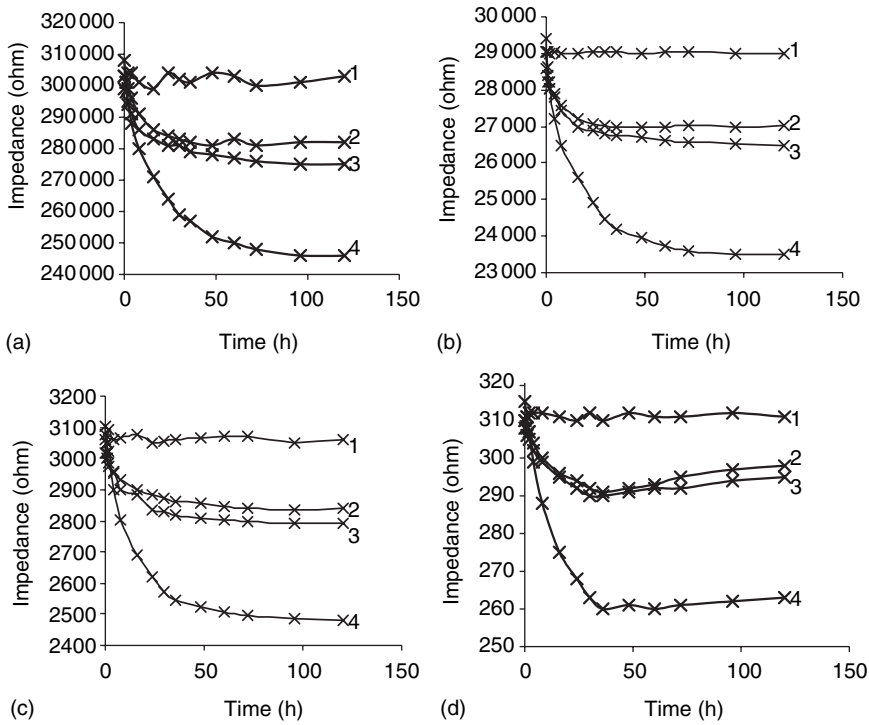

9.15 Long-term stability tests of (1) palladium sheet electrodes and (2) woven, (3) knitted and (4) non-woven textile electrodes, obtained by measurement of R as a function of time in the electrochemical cell for NaCl electrolyte concentrations of (a) 1×10^{-4}, (b) 1×10^{-3}, (c) 1×10^{-2} and (d) 1×10^{-1} mol l^{-1}.

Experimental proof for the above-described hypothesis was found by taking microscopic photographs of the textile structures in dry and wet conditions using a fluorescent solution. From these images, it could be seen that air bubbles were indeed trapped in the wet structures, but due to the more regular structure of the non-woven fabrics compared with woven and knitted fabrics, much less air was trapped. Confirmation for the dissolution of these bubbles is found by the absence of air when the textile electrodes were immersed for about 3 days in the fluorescent solution.

The decrease of resistance from $t=0$ until an equilibrium condition is obtained is about 20% for the woven structure and about 7% for the knitted and non-woven structure, except for the highest electrolyte concentration (1×10^{-1} mol l^{-1}). In that case, the decrease is less pronounced. Extrapolation of the onset of the curve (covering the first 2 days of the experiment) showed that the equilibrium condition is obtained at about 10 Ω higher than expected by this extrapolation. The cause of this can be found in a

corrosion reaction introduced by high concentrations of chloride. This ion is well known for its penetrating properties in metallic layers and for promoting the formation of Cl^- deposits and oxide formation. This mainly results in an increase of the electrode resistance, which becomes important in the behaviour of the system.

The fact that this reaction is observed only at 1×10^{-1} mol l^{-1} does not mean that it does not occur at other electrolyte concentrations. The corrosion rate is probably lower at lower electrolyte concentrations, and this results in an increase of the resistance by a value smaller than 10Ω. At concentrations lower or equal to 1×10^{-2} mol l^{-1}, the increase in resistance will not be detected owing to high resistances measured for the electrolyte and error margins that are much higher than the shift of resistance caused by the corrosion reaction. In addition, the contribution of the corrosion reaction to the cell resistance at electrolyte concentrations lower than 1×10^{-2} mol l^{-1} decreases with chloride concentration, because the intensity and rate of that reaction is determined by different parameters, among them the chloride concentration.

9.3.4 Type of electrolyte used

Initially, sodium chloride was selected as electrolyte for this study, because it is the main component in human sweat which contributes to the conductivity of this solution. However, an important drawback of sodium chloride is that chloride ions (Cl^-) are known for their very strong penetration properties in metallic and alloy surfaces[2]. Such a penetration promotes corrosion of the material – an effect that should be avoided in this work. Therefore, it is necessary also to study other types of electrolytes to avoid this corrosion reaction. Suitable alternatives are potassium nitrate (KNO_3) and sodium perchlorate ($NaClO_4$) – two types of electrolytes that are commonly used in electrochemical experiments owing to their inert nature. These electrolytes also dissociates in 1+ and 1– charged ions (K^+/NO_3^-, Na^+/ClO_4^-); the only different contribution to the conductivity of a solution is their relative ability to diffuse/migrate in the solution. However, these differences will be reasonably small and unimportant compared with the problem of having an important corrosion reaction when using Cl^--containing electrolytes.

The availability of an inert electrolyte is of the utmost importance for the development of a quality-control system for textile electrodes. In such a system, it is the aim to test the quality of textile electrodes; therefore the condition and properties of the electrode should not be changed or influenced during this quality-control experiment. This condition cannot be fulfilled by using NaCl as electrolyte solution, because during the quality testing, the chloride will affect the properties of the textile electrode tested.

Long-term stability experiments described in the previous section were repeated with KNO_3 and $NaClO_4$ as electrolyte solutions at different concentrations. It was observed that, for relatively low concentrations, curves similar to those shown in Figs 9.15a, 9.15b and 9.15c are obtained. Deviations remain within the experimental error margin (less than 3%). However for the highest concentration (0.1 mol l^{-1}) a clear difference is observed. At the initial phase of the experiment, the KNO_3 and $NaClO_4$ electrolyte solution behaves in a similar way as NaCl (curves in Fig. 9.15d). However, after approximately 20 h, the resistance measured in KNO_3 and $NaClO_4$ drifts away from the curve of NaCl to lower values. Indeed, this can be explained by the fact that for KNO_3 and $NaClO_4$, the textile electrodes are not affected by a corrosion reaction; therefore the resistance of the textile electrodes does not increase, affecting the total cell resistance as was observed for NaCl (Fig. 9.15d). It can be concluded that for quality-control testing KNO_3 or $NaClO_4$ electrolyte solutions should be used and not NaCl.

9.3.5 Quality control of textile electrodes

In this section, an application of the obtained results will be described by using the electrochemical cell for quality control of textile electrodes. For this purpose, fixed values of the cell geometry and other parameters will be defined in order to work under standard conditions and to obtain reproducible results. For this purpose, the values for the different parameters to be fixed are summarised in Table 9.13. From the results obtained in the previous section, it is obvious that a value for d of 103 mm and for A of 180 mm^2 will be used. The concentration of electrolyte should be high, because a lower value of R will result in an improved detection of reduced quality because of the larger fraction of R_{el} of the electrode to the overall resistance measured in the cell. A $NaClO_4$-containing electrolyte will be used in this section. It is also not necessary to record the complete impedance plot, but rather it is sufficient to obtain the impedance at one single frequency

Table 9.13 Values for the different parameters involved in the quality control of textile electrodes

Parameter	Value
c (mol l^{-1})	0.1
A (mm^2)	180
d (mm)	103
T (K)	298.0
pH	7.0
Electrolyte	$NaClO_4$

Table 9.14 Resistance, R (Ω) measured in the electrochemical cell at certain time, t (h). Between the short R measurements, the textile electrodes were immersed in NaCl, artificial sweat, waste-water solutions or water. (Knit: knitted; wov: woven; nonw: non-woven.)

Time (h)	NaCl (0.2 mol l^{-1})			Artificial sweat			Waste-water solution			Water		
	Knit	Wov	Nonw	Knit	Wov	Nonw	Knit	Wov	Nonw	Knit	Wov	Nonw
20	300	301	259	298	301	254	510	476	810	298	300	261
25	302	301	258	306	309	258	897	1013	1249	301	301	258
30	304	306	254	309	314	271	1584	1644	1874	306	302	259
35	303	309	259	315	320	286	2241	2200	2584	304	306	261
40	310	314	271	328	331	299	3036	2978	3456	307	305	260
45	317	321	288	337	346	317	3986	3874	4243	299	304	264
50	329	328	301	356	358	346	4196	4003	4316	306	308	267
70	341	339	315	381	378	371	4288	4185	4377	300	309	266
100	350	347	332	403	410	395	4284	4274	4401	298	304	268
200	358	358	336	415	425	403	4298	4345	4425	299	305	264
500	370	369	349	430	436	410	4308	4392	4463	302	307	268

on the condition that at this frequency no phase-angle shift ($\theta=0°$) is observed between the applied potential and measured current that is obtained. From Fig. 9.9b, it can be seen clearly that a frequency of 10 000 Hz is the most optimal value to fulfill this condition.

Textile electrodes were immersed in solutions of NaCl (0.2 mol l^{-1}) in artificial sweat solutions with a similar NaCl concentration, in waste-water from a textile-finishing company and in water. The first three solutions were expected to affect the textile electrodes intensively due to chemical attack, adsorption phenomena, etc. The fourth solution was not expected to have a serious influence. At certain time intervals, the electrodes were inserted in a test cell (see section 9.2.2) for the determination of the cell resistance when using a 0.1 mol l^{-1} $NaClO_4$ solution; and then placed back in the NaCl, artificial sweat, waste-water or water solution. The data are shown in Table 9.14. It can be seen that only the electrodes immersed in water remain at their initial value, and therefore their quality remains constant. For the electrodes immersed in NaCl and artificial sweat, a slow and continuous increase of the resistance is observed due to the attack on the textile electrode surface by chloride. This initiates a corrosion reaction with the formation of metal oxide, metal hydroxide and metal chloride depositions that are less conductive than the metal, thus contributing to the resistance of the cell. An increase of 10% of the resistance can be seen as substantial and outside the limit of twice the standard deviation; thus for a resistance increase of 10% against the initial value of a new (not used) electrode, it can be concluded that the quality is no longer guaranteed and the electrode

should be replaced. The increase of the resistance for the electrodes immersed in artificial sweat is somewhat higher, probably because this solution is more complicated. In addition, other ions play a role and can affect the condition of the textile electrodes.

The electrodes immersed in waste-water from a textile-finishing plant show completely different behaviour. The resistance of the electrodes increases fairly rapidly in the first part of the experiment and then becomes relatively constant. In this case, a chemical present in the waste-water solution adsorbs strongly (possibly a sulphide-containing component) at the surface of the electrode, blocking it completely. Once the adsorption process is finished, the resistance does not change drastically.

9.4 Conclusion

All these tests show that quality control is important, and that the method developed and described in this chapter is useful and interesting for that purpose.

9.5 References

1. Kissinger P.I., Heinemann W.R., *Laboratory techniques in electroanalytical chemistry*, Marcel Dekker, New York, 1996.
2. Kear G., Barker B.D., Walsh F.C., *Corrosion*, **60** (2004) 561–575.

10

Electroconductive textile electrodes for detection and analysis of sweat and urine

P. WESTBROEK, G. PRINIOTAKIS AND P. KIEKENS

10.1 Introduction

The electrode setup described in Chapter 9, section 9.2.2 is, in principle, very useful for detecting the resistance of an electrolyte solution. This also means that liquids such as sweat and urine can be analysed in this way, because they contain a relatively high level of salts – species that dissociate into ions when dissolved in a solvent. These ions contribute to the conductivity of the solution so, indirectly, unknown ion concentrations can be ascertained from measurement of the electrolyte resistance. The principle described above can be used for applications in the field of incontinence detection, diabetes early-warning systems and in diagnosis of cystic fibrosis (muco-viscidosis). Prompt detection of urine for elderly people suffering from incontinence in a hospital environment will improve the comfort of the patient drastically. When a patient has urinated, this is detected by a large increase in the conductivity between the electrodes (or a decrease in the cell resistance); a signal can then be sent to the nurses' room to relieve the patient from his or her discomfort. A patient suffering from diabetes often starts to sweat heavily when the blood sugar level drops. If nothing is done, the patient will collapse and, in worst case, fall into a coma. A textile electrode system, carried by the patient as part of regular clothing (textile electrodes incorporated in clothing), can be able to detect the sweat formation, which is useful as an early warning system to avoid more harm for the diabetes patient.

Muco-viscidosis is one of the most underestimated genetic diseases. In contrast with the fact that about 0.02% of the world's population suffer from this disease, more than 5% of the population are carriers of damaged genes causing muco-viscidosis[1]. Moreover, the physical and psychological discomfort that accompanies this disease is considerable and affects the quality of life not only of the patient but also of those in their direct surroundings. Mainly, the mucus present in the lungs and the colon is responsible for moistening and cleaning these organs, but for children with

muco-viscidosis this mucus has a high viscosity. This causes frequent infections of the bronchea and limited uptake of food, vitamins and vital components by the colon. Despite considerable research that has been carried out on this matter, life expectancy is still limited to about 30 years[2]. A child suffering from muco-viscidosis needs physiotherapy for about 3 h per day and continuous medical treatment. This again seriously limits the quality of life.

Several studies have proved that it is very important to detect muco-viscidosis at an early stage (preferably within the first weeks or months of the baby's life)[3–6]. Except for DNA analysis[7], no reliable methods are available for detection of muco-viscidosis and to assist the diagnosis following it, owing to limited precision and accuracy combined with poor reproducibility. A DNA test is not done commonly, however, because there are about 1000 variations of genes that cause muco-viscidosis and, at present, a DNA analysis is still expensive and time consuming. The following tests are commonly undertaken:

- Detection of specific proteins in the meconium of babies[8]. The presence of these proteins can be an indication for muco-viscidosis. Owing to limited precision and accuracy, however, if the test is positive, further experiments should be carried out before a diagnosis is made.
- A second test, also suffering from poor precision and accuracy, is a blood test, done a few days after the baby's birth[9]. The presence of relatively high concentrations of immuno-reactive trypsine is an indication for muco-viscidosis. In this case also, further investigations should be carried out prior to formulation of the diagnosis.
- A third and most common test is the sweat test[10,11]. Children suffering from muco-viscidosis produce sweat with an electrolyte concentration that is 3–5 times higher than for normal children. Collecting a certain amount of sweat and analysing the electrolyte content by a standard method can reveal muco-viscidosis. However, this test has a fairly poor reproducibility and should be repeated two or three times before a diagnosis is possible. Since the time between the first, second and third test is at least 24 h, it can cause considerable psychological trauma for the parents during this period, particularly if the first test gave a positive result.

A method for the detection of the salt content in sweat with high accuracy and reproducibility would improve the reliability of diagnosis and help the parents at a very difficult time. Such a method can be found in the use of textile electrodes, because the obtained signal (an impedance) is reciprocal to the salt concentration.

10.2 Description of the cell configuration

Owing to the perpendicular orientation of the electrodes, the electrode configuration discussed in Chapter 9 cannot be used for the type of analysis discussed in this section. Therefore, an alternative configuration needs to be developed, which is much flatter and easy to use at the surface of the human body or to implant in a nappy. This can be achieved by using two yarns instead of two sheets, positioned linearly against each other (Fig. 10.1). In practice, two yarns of stainless steel were used for this investigation. To immobilise them for performing a characterisation study, these yarns were put on a PVC sheet with some glue as schematically presented in Fig. 10.1. According to the theory, this type of electrode generates errors because the surfaces of these yarns are not flat; thus the local distance between the yarns will vary from position to position giving rise to variation in local electrolyte resistance. The actual resistance measured will be dependent on the magnitude of the difference between highest and lowest local resistance and therefore the resistance will be dependent on the diameter of the yarns and their regular structures. However, this effect can be minimised by optimising the values for the distance between the electrodes (d) and the diameter of the electrodes ($2r$). The difference (ΔR) between the highest and lowest local impedance will decrease for decreasing yarn diameter and increasing distance between the electrodes (Fig. 10.2). Therefore, it can be assumed that for a certain maximum value of $2r/d$, the system behaves like a system with flat electrodes, because the errors generated caused by imperfections are smaller than the experimental error of the sensor system itself.

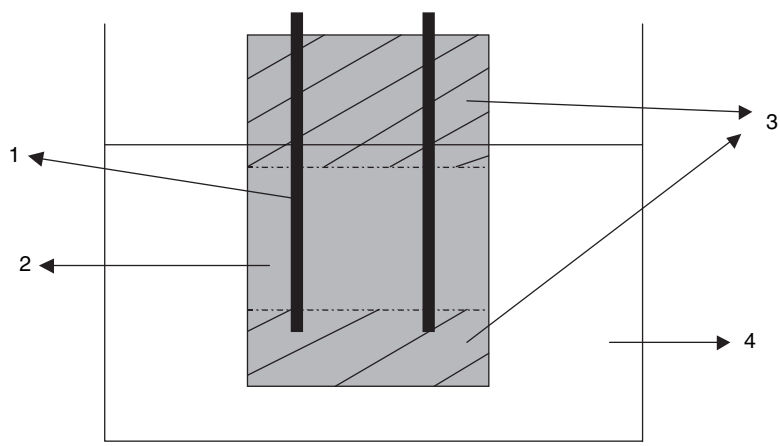

10.1 Scheme of the electrode configuration and the electrical equivalent circuit: (1) electrode, (2) PVC sheet, (3) area protected by glue and (4) electrolyte solution.

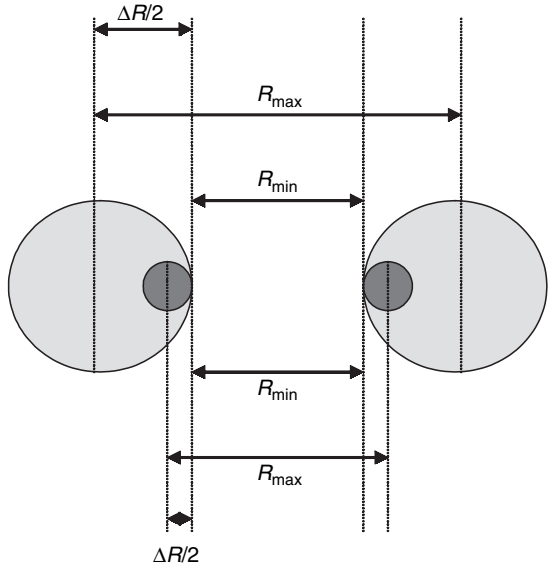

10.2 Schematic representation of the influence of electrode diameter on the value of ΔR.

10.3 Conditions for using yarn electrodes

The described electrode configuration was studied, initially with sodium chloride (NaCl) electrolytes as a function of measured impedance, at frequencies where no phase-angle shift between applied alternating potential and measured alternating current was obtained, while the distance between the yarn electrodes, the length and diameter of the yarn electrodes and the electrolyte concentration were varied in order to identify the optimal values for these parameters for analytical purposes. The distance between the electrodes was varied from 5 to 40 mm, the length of the electrodes from 20 to 80 mm, the diameter of the electrodes from 0.2 to 2 mm and the electrolyte concentration from 1×10^{-1} to 1×10^{-6} mol l^{-1}. EIS spectra were recorded and explained in the same way as was done for the data in Chapter 9, and the impedance was determined at phase-angle shifts between applied potential and measured current near zero. The values of these resistances are plotted logarithmically against the electrolyte concentration (Fig. 10.3), the length of the electrodes (Fig. 10.4) and the distance between electrodes (Fig. 10.5). For all logarithmic relationships, a linear curve was obtained, resulting in the following equation:

$$R = \mathrm{k}\frac{d^{0.68\pm0.02}}{L^{0.62\pm0.03}c^{0.83\pm0.01}} \qquad [10.1]$$

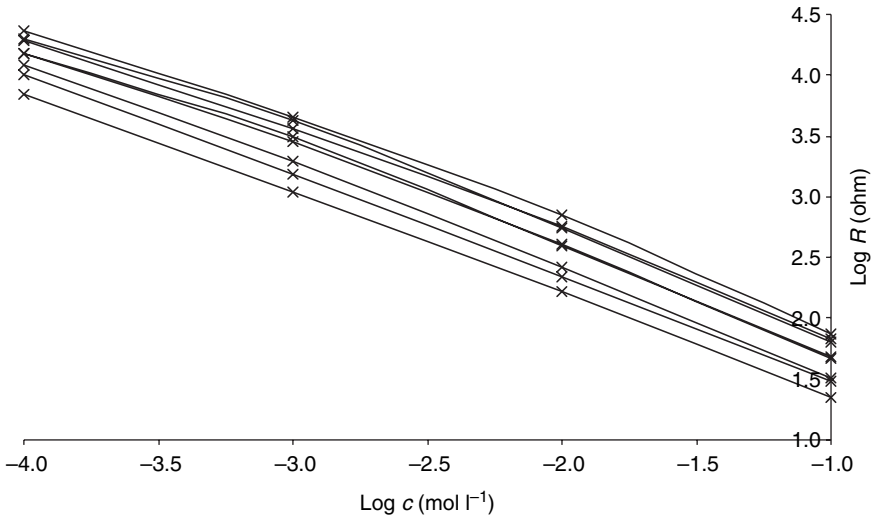

10.3 Logarithmic relationship between measured impedance at a phase-angle shift of zero and electrolyte concentration measured at yarn electrodes of different length and diameter and with varying distances between the yarn electrodes.

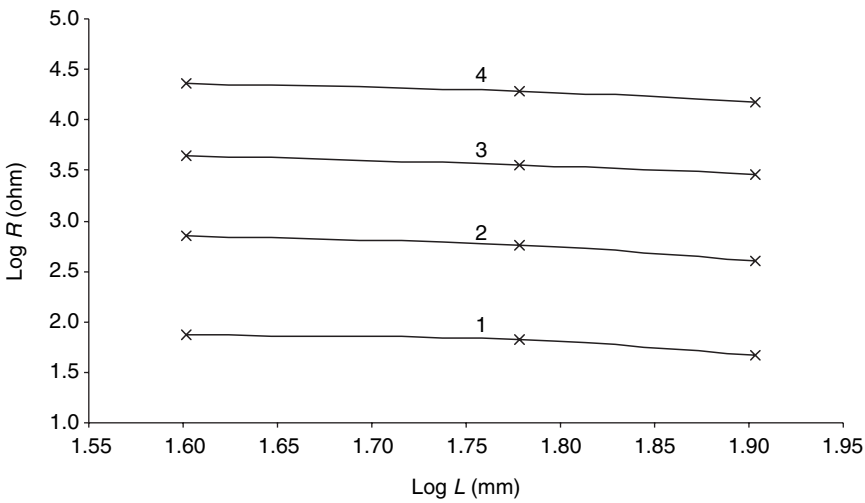

10.4 Logarithmic relationship between measured impedance at phase-angle shift of zero and the length of the electrodes for constant distance between the electrodes (20 mm) and diameter of the electrodes (0.2 mm) and different electrolyte concentrations: (1) 1×10^{-1}, (2) 1×10^{-2}, (3) 1×10^{-3} and (4) 1×10^{-4} mol l^{-1}.

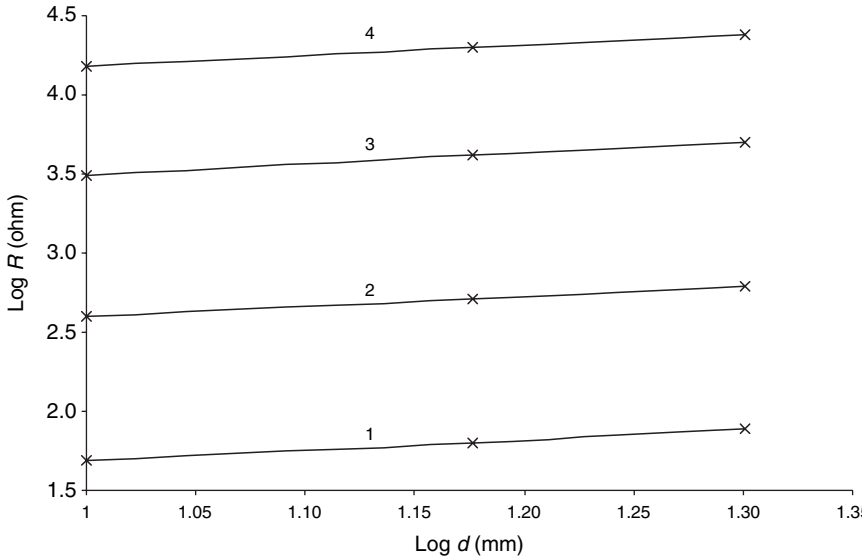

10.5 Logarithmic relationship between measured impedance at phase-angle shift of zero and the distance between the electrodes for constant length of the electrodes (60 mm) and diameter of the electrodes (0.2 mm) and different electrolyte concentrations: (1) 1×10^{-1}, (2) 1×10^{-2}, (3) 1×10^{-3} and (4) 1×10^{-4} mol l^{-1}.

where R is the measured resistance (Ω), d is the distance between two textile electrodes (mm), L is the length of the textile electrodes exposed to the electrolyte solution (mm), c is the concentration of the electrolyte (mol l^{-1}), and k is a constant factor at constant temperature.

The standard deviations given in Equation 10.1 are valid in the following ranges of the investigated parameters:

- c: 1×10^{-1}–1×10^{-4} mol l^{-1}
- L: 20–80 mm
- r: 0.1–1 mm
- d: 5–40 mm on the condition that a maximum value of 0.03 for the ratio r/d is respected.

For all values beyond these limits, it is still possible to use the electrodes in applications but standard deviations increase. This will inevitably have a negative influence on the precision, sensitivity and reliability of the method. This increase is explained as follows: the experimental signals become too small (high c and L) or too large (low c and L) to have a reliable impedance, and the maximum ratio for $2r/d$ of 0.02 should be respected in order to have a planar-like electrode configuration. For $2r/d$ values larger than 0.02, this planar-like configuration is no longer attained, which will result in

larger standard deviations. Finally, the value of the constant k is not specified further because it needs to be obtained by calibration. Calibrating the electrode cell in a setup with known values for c, L, d and r allows calculation of the value for k using Equation 10.1 after measurement of R.

10.4 Cell configuration with immobilised electrolyte solution

An important condition to be fulfilled in order to use the method for detection of sweat formation and its composition is that the electrodes are electrolytically in contact with each other. This is not a strict condition for urine detection and as an early-warning system for diabetes, because in these applications a qualitative detection is enough, and therefore one can start with dry electrodes. For diagnosis of cystic fibrosis, this is not possible because here a quantitative detection of salt concentration is expected. Therefore, one needs to start from a system with electrodes that are electrolytically in contact with each other right from the start of the experiment. For this purpose, water is immobilised in high-density cotton in which the conductive stainless-steel yarn electrodes are implemented.

In order to evaluate the electrode configuration, similar experiments were performed as described in the previous section, and the results were compared in order to determine whether the electrodes behave identically in the absence and presence of cotton. As expected, similar results were obtained concerning the relationships: Equation 10.1 is also valid for electrodes immersed in cotton that act as an immobilising substance for the electrolyte, but the value of k is different. Indeed, all experimentally obtained curves are shifted towards higher resistive behaviour, which can be explained by the fact that the presence of cotton forms a barrier for the conductivity of ions through the electrolyte solution. However, as explained in the previous section, k can be obtained by calibrating the electrode setup, so calibration in the presence of cotton circumvents the problem of different results in the absence and presence of cotton.

10.5 Experiments with artificial sweat and under real-time conditions

Finally, the electrode configuration was tested with artificial sweat instead of sodium chloride-containing electrolyte solutions. No shifts of relationships or different results were found between the experiments performed with artificial sweat and those with sodium chloride solutions (section 10.4). From these results, the following conclusions can be drawn:

- Chemicals like ureum, present in sweat do not interfere by possible adsorption at the electrode surface.
- Other electrolytes like sulphates, potassium and calcium are present in much lower concentrations than sodium chloride, and therefore their contribution to the conductivity can be neglected.
- Sodium chloride in sweat determines the overall conductivity of the sweat.

For each application envisaged in this chapter, tests were performed to evaluate the behaviour of the sensor system in its performance for sweat and urine detection. For this purpose, stainless-steel yarns were incorporated in baby nappies for detection of urine. Figure 10.6 shows the results of some of these tests. It can be seen clearly that the detection of urine is marked by a large change in resistance between the electrodes of the sensor system. In addition, the value of R after urine detection is an indication of how much urine has been formed. However, the latter is not really of scientific relevance, and is therefore not considered further here.

For the detection of low sugar levels in the blood, the sensor system was less successful. Despite its possible use as an early-warning system for diabetes patients, it shows serious limitations owing to interference from other

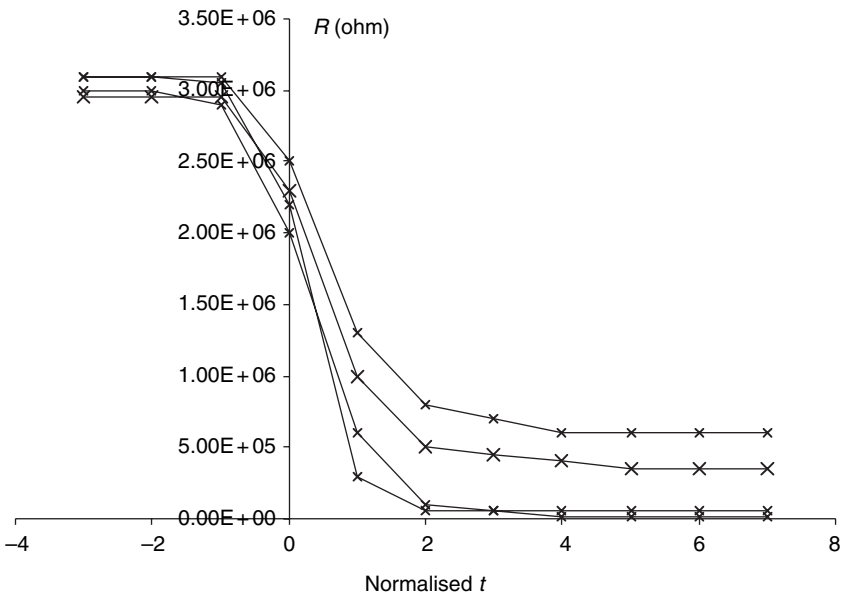

10.6 Resistance measured between two yarn electrodes implemented in a baby's nappy as a function of time, with $t=0$ the moment that urine formation occurs.

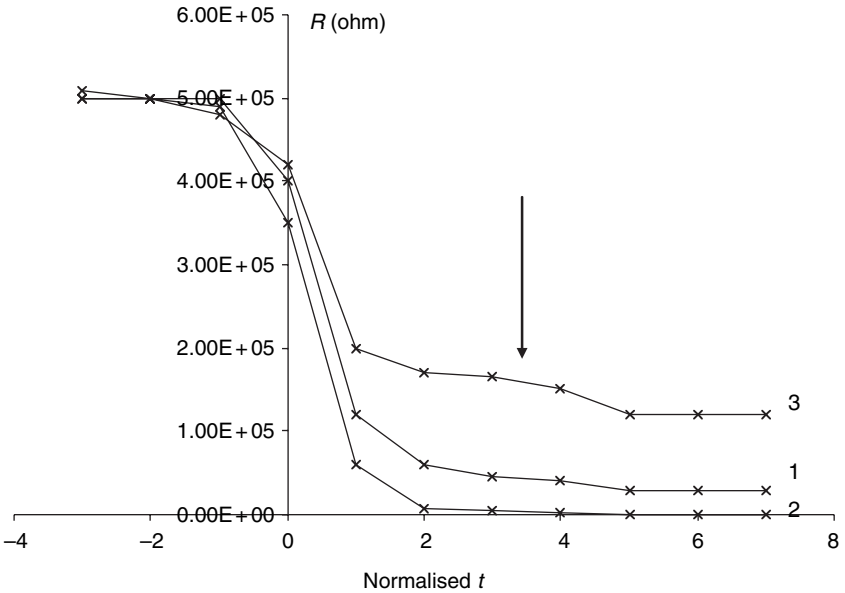

10.7 Resistance measured between two yarn electrodes implemented in an electrochemical cell positioned at the leg of a human body as a function of time. Sweat formation rate for (1) a diabetes patient at the moment of low sugar level, (2) an athlete exercising and (3) a diabetes patient walking in hot severe conditions; arrow indicates the point at which the sugar level becomes low.

sources that promote sweat formation. Results are shown in Fig. 10.7. Curve 1 is an example of the curves obtained from people who are suffering from diabetes and were allowed (with close monitoring) to come very close to a low sugar level in the blood. Intense perspiration occurs at a certain moment, which is very well detected by the sensor system, with a decrease of the cell resistance. However, analysing curve 2 and comparing it with curve 1, it seems that in curve 2 the sweat formation is much more pronounced. Curve 2 was obtained from an athlete during exercise and has nothing to do with diabetes, and it is therefore clear that the sensor system is not able to detect the difference between a curve obtained from a person sweating normally and the one obtained for a diabetes patient who is entering the condition of low sugar level.

In addition, a pleasant walk in the sun during summer (303–308 K) will result in a rate of sweat formation such that the system detects a large decrease of the cell resistance. In view of these findings, the accuracy in detection of a possible occurrence of low sugar level in the diabetes patient's blood is poor or even undetectable. As an example, a laboratory test was carried out with a diabetes patient walking under strict conditions

at an ambient temperature of 303 °C (curve 3). Due to walking, the patient started sweating and, at the same time, his sugar level dropped. Despite the fact that after about 25 min the person was not feeling well (the need for sugar became apparent), an increase in sweat formation could not be detected because it was masked by the actual sweat formation due to walking exercise. This experiment shows very clearly that the system is not reliable as an early-warning system for diabetes unless special precautions are taken to eliminate the possible sources of interference; for example, use of the system in a hospital environment could be possible.

For the detection of cystic fibrosis, which is a quantitative analysis, the situation is different because such an analysis is performed only in the hospital environment. This requires that the conditions to execute such a test with the sensor system can be chosen and controlled in such a way that possible interference is avoided. In addition, for cystic fibrosis detection, the analyst is interested in the electrolyte concentration of the sweat, regardless of how this sweat formation was obtained (high temperature, exercise), with the implication that the sources of interference are much less for cystic fibrosis detection than was the case for the detection of low sugar level in the blood. The complication in this type of analysis is that it is not enough to

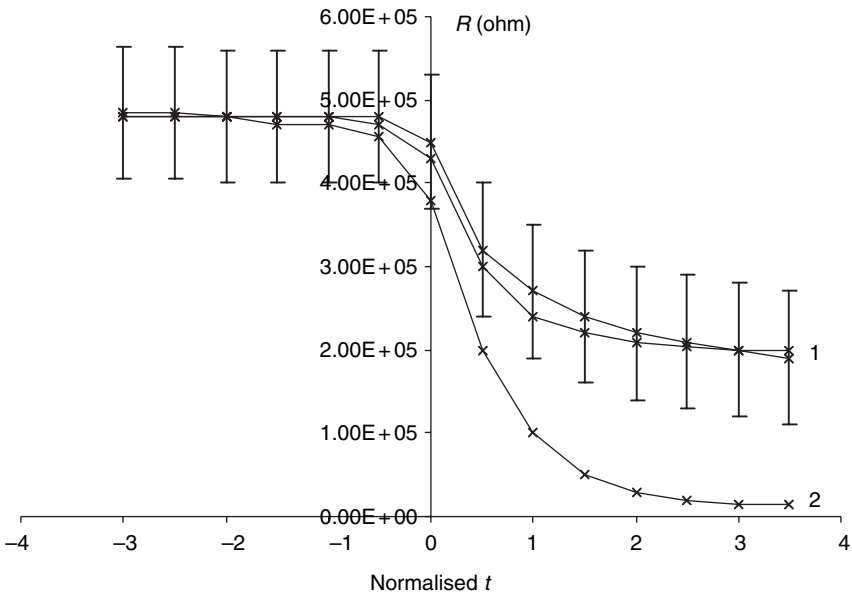

10.8 Resistance measured between two yarn electrodes implemented in an electrochemical cell positioned at the leg of a human body as a function of time. Sweat formation rate (1) for normal people under strict conditions and (2) for cystic fibrosis patient.

detect sweat formation, but it also needs to detect how much. Therefore, the conditions for performing this experiment must be well identified in order to obtain reproducible results, and this matter is still under investigation.

Preliminary results (Fig. 10.8) showed that there is a clear difference in the slope of the decrease of the resistance, and the resistance value after the first strong declining part of the curve is much smaller for the cystic fibrosis patient (up to now, there is only one curve of a positive cystic fibrosis patient). From curve 2, which is recorded from a cystic fibrosis patient, and the other curves (1), which are recorded from healthy people, it can be seen that a clear systematic difference is obtained, even though an error margin of more than 50% was allowed for the curves obtained from healthy people. This can be explained by the much higher electrolyte concentration in the sweat of the cystic fibrosis patient. First the slope is higher because, for an equal sweat-formation rate, more electrolyte is excreted by the cystic fibrosis patient and, due to this same effect, the concentration of the electrolyte in the sweat formed during a certain and preset time is higher, thus giving rise to a lower electrolyte cell resistance.

10.6 References

1. http://www.muco.be/illnes/nl/index_1.html.
2. Stern M., Picard C., Grevet D., *Presse Med*, **31** (2002) 263–270.
3. Feigelson J., Pecau Y., *Sem de Hopitaux* **51** (1975) 741–744.
4. Gottscha B., Fabriciu E.M., Patzug U., *Padiatrie und Padologie* **9** (1974) 48.
5. Travert G., Mustin C., Fernandez Y., *J Gen Humaine* **28** (1980) 141–144.
6. Lenoir G., Michalewski A., Moyse D., Madras M.B., Richardot P.M., Sorin M., Hennequet A., *Clin Invest Med* **10** (1987) A49.
7. Livshits L.A., Gorovenko N.G., Ivashchenko T.E., Buzhiyevskaya T.I., *Vrachebnoe Delo* **4** (1990) 101–103.
8. Pajon A., Aguilaniu B., *Rev Maladies Resp* **9** (1992) 564–566.
9. Bachmann K.D., *Med Welt* **25** (1974) 249–252.
10. Moser H., Liechtigallati S., Braga S., *J Clin Chem Clin Biochem* **26** (1988) 724–725.
11. Rasche K., Poller W., Fisselereckhoff A., Wiebe V., *Deutsche Med Wochenschr* **114** (1989) 1566–1570.

Part IV

Modified fibres and their applications

11

Chemical metallisation and galvanisation as a method for development of electroconductive polyacrylonitrile fibres

P. WESTBROEK AND P. KIEKENS

11.1 Introduction

The synthesis[1,2], characterisation[3–5] and applications[3–6] of conductive polymers and fibres are an attractive and extensive field of research[6]. However, for the purposes of this book, discussion of research on conductive fibres with possible textile applications is limited to fibres obtained by chemical metallisation. Different methods are available to obtain electroconductive fibres. A first method is synthesis of a conductive fibre similar to the synthesis of conductive polymers. Despite the good conductivity of this type of fibre, it is not commonly used as a conductive fibre in textile applications, owing to its limited flexibility which restricts the number of possible applications. A second method is blending common non-conductive fibres with electroconductive fibres. The advantage of this method is that the conductive yarn has the same mechanical properties as a yarn fabricated from pure nonconductive fibre. Frequently, fibres of polyaniline[7,8], polyamide-11[8], polyvinylalcohol[9] and nylon-11[7] are used in the production of mixed electroconductive and non-conductive fibres. A third method is the synthesis of polymers that have a carbon inclusion[10]. This method also results in limited mechanical properties of the fibre and is therefore not used as it is.

A final method is metallisation[11] of fibres, which is most related to the technology described in this chapter. In this method, metal salts are taken up by the fibre and reduced to their metallic conductive form. Metallisation can be achieved in different ways. A first way is by a vacuum metal spray. However, this results in very poor defined metallisation. In addition, galvanic coating is used in the production of conductive fibres, but this type of coating requires a fibre that is already conductive.

The main applications of electroconductive fibres and textiles are for shielding effects[11] and discharge purposes[12,13]. Textile clothing acts as a Faraday cage for personnel and/or equipment that should be protected, while electroconductive carpets avoid charging of the carpet and/or the material that rubs onto it.

Chemical metallisation is one of the more promising methods for obtaining electroconductive fibres; the chemical coating is very flexible, and it is suitable for almost any substrate. Its main advantage is that it allows fibres to obtain high conductivity without significantly altering other properties such as density, flexibility and handling of the substrate. Thanks to these characteristics, this type of fibre can be easily processed by standard textile technologies, and the chemically metallised fibres can be subjected to additional galvanic metallisation. However, the actual production of electroconductive fibres by chemical methods is a complex multistage process that requires expensive chemicals. Furthermore, after each stage, the fibres are carefully washed, yielding a large volume of effluent that requires intensive waste-water treatment. In order to obtain an electroconductive fabric, three different methods can be exploited:

- Impregnation with anti-static agents, although this is not a feasible solution if high and permanent conductivity is required.
- Direct coating of fabrics and non-woven textiles is more appealing, as it allows the separation of the most expensive and difficult operation from the rest of the production cycle. However, it also has serious limitations; it does not result in a permanent conductivity, and the colour is determined by the type of coating. The most important drawback is that the bridges formed by the coating at the crossings between fibres tend to break when the fabric is subjected to movement, which can cause a significant drop in its conductive performance.
- Chemical coating is very flexible and permits high surface conductivity without significantly altering other properties.

In this chapter, a relatively simple method is described to metallise polyacrylonitrile (PAN) fibres with a two-step process (ab/adsorption and reduction of Ni(II) in one bath solution followed by galvanisation), and making use of relatively cheap chemicals in order to offer a simple and economically feasible metallisation method and related metallised product.

11.2 Optimisation of process parameters in polyacrylonitrile production for metallisation with nickel

11.2.1 Introduction

The aim of the investigation and development described in this chapter is the development of electroconductive polyacrylonitrile fibres. In this first section, a preliminary study is described to optimise the common poly-

acrylonitrile fibre-production parameters for further treatment by metallisation to obtain electroconductive polyacrylonitrile.

11.2.2 Metallisation of different types of fibres

Metallisation of fibres is not only a physical process determined by absorption capacity of the fibres for the metal and diffusion capacity of the metal in the fibre structure, but also depends on chemical parameters such as chemical structure of the fibres, presence of functional groups, reactivity of the fibre and the metal, oxidation state of the metal and the presence, necessity and reactivity of supporting chemicals (e.g. reducing agent). Therefore, it was necessary first to study metallisation at different types of fibres in order to investigate which structure is most useful for further research. In this respect, viscose, cotton, natural silk and polyacrylonitrile fibres were investigated because of their different structure and properties and their availability in the New Independent States of the former Soviet Union (Uzbekistan, Kazakhstan, Kyrgyzstan).

Metallisation of these fibres was performed in a single-step process by immersing the fibre for both 5 and 15 min in a bath containing either 0.3 mol l^{-1} sodium dithionite and 0.06 mol l^{-1} $NiCl_2$ or 1.5 mol l^{-1} rongalite and 0.5 mol l^{-1} $NiCl_2$ at both 283 K and 363 K, respectively. Analysis of the fibres obtained was carried out according to methods described in the literature,[14] together with the methods explained below, with the results presented in Table 11.1.

- The content of Ni and NiS (and similar for Co species) present in the fibre was determined in three steps:

Table 11.1 Nickel absorption and reduction by sodium dithionite and rongalite for different types of fibres and their electroconductive capacity

Fibre type	Reducing agent: sodium dithionite				Reducing agent: rongalite			
	Amount of Ni, ww%			Specific electrical resistance (Ω m)	Amount of Ni, ww%			Specific electrical resistance (Ω m)
	Ni_t	Ni_S	Ni_M		Ni_t	Ni_S	Ni_M	
Viscose	3.92	3.11	0.81	10^7	4.90	4.00	0.90	10^7
Cotton	2.28	2.00	0.28	10^7	3.68	2.84	0.84	10^7
Silk	4.30	3.12	1.18	1.3	4.60	3.30	2.30	1.0
PAN, fresh	5.10	1.37	3.73	2×10^{-4}	5.80	2.30	3.50	2×10^{-4}
PAN, thermofix	4.62	2.12	2.50	5×10^{-3}	4.80	2.60	2.20	7×10^{-3}

Step 1. Dry metallised fibre (0.1 g) was immersed in 50 ml of H_2O and 10 ml of 1.5% H_2O_2 was added. It was then boiled for 20 min. Buffer solution (1 ml, pH = 10) was added, and the amount of Ni(II) was determined by titration with 0.01 moll^{-1} EDTA using Hg(II) as end-point detection. Based on Equation 11.1, the amount of NiS extracted from the fibre can be calculated with Equation 11.2:

$$NiS + H_2O_2 \leftrightarrows NiSO_4 + 2H_2 \quad [11.1]$$

$$c_{NiS}(\text{in } \%) = (V \times 58.69 \times c_{EDTA} \times 100)/(1000 \times g) \quad [11.2]$$

where c_{NiS} is the concentration of NiS, V is the volume of the sample, c_{EDTA} is the concentration of EDTA, and g is the weight of the fibre.

Step 2. Same as in step 1, but after 20 min of boiling, add 1 ml of HNO_3 and boil for another 10 min. Then proceed with the addition of the buffer solution and the titration. The total amount of Ni + NiS is determined by Equation 11.4 based on Equation 11.3:

$$NiS + Ni + 2HNO_3 + 2H_2O_2 \leftrightarrows NiSO_4 + Ni(NO_3)_2 + 3H_2 \quad [11.3]$$

$$c_{Ni+NiS}(\text{in } \%) = (V \times 58.69 \times c_{EDTA} \times 100)/(1000 \times g) \quad [11.4]$$

Step 3. Finally, the amount of Ni is determined using Equation 11.5:

$$c_{Ni} = c_{Ni+NiS} - c_{NiS} \quad [11.5]$$

- Prior to the use of these methods, it was verified that extraction occurs for 100%. This was done by dissolving 0.1 g of dry metallised fibre in DMF and another 0.1 g of dry metallised fibre according to the methods described above. In both cases, the same result for Ni or Co content was obtained, showing that extraction occurs for 100%.
- The diffusion coefficient in Table 11.2 is determined using the Krenk equation:

$$c_\tau / c_\infty = (4/r) \times (D\tau/\pi)^{1/2} \quad [11.6]$$

where c_τ and c_∞ are the concentration of absorbed metal at time τ and after equilibrium, respectively, r is the fibre radius, τ is the time of metallisation, and D is the diffusion coefficient.

The results of this analysis are shown in Table 11.1. It is clear that absorption of nickel in all fibres is reasonably high, but the amount of metallic nickel is considerably higher in PAN fibres and, to a lesser extent, in natural silk. This indicates that the structure of the fibres (pore size and permeability as well as functional groups) plays an important role. Sodium dithionite and rongalite are known as good reducing agents, but their stability is fairly limited. One of their decomposition products (particularly in acidic solutions) is sulphide, which explains why an important fraction of

Table 11.2 Nickel and cobalt absorption capacity and their diffusion coefficient as a function of precipitation-bath parameters during PAN-fibre production

Parameters	Concentration of NaCNS in precipitation bath C_{pB}, % (B=700%, T=10°C)			Temperature of precipitation bath, K (C_{pB}=12%, B=700%)			Plasticisation drawing, B, % (C_{pB}=12%, T=10°C)			
	8	12	16	273	283	293	500	700	900	1100
Ni(II) diffusion coefficient, $D\times10^{13}$, m^2/s	7.40	19.00	30.00	14.00	18.50	16.00	22.00	18.00	7.80	5.40
Quantity of sorbed Ni(II), %	0.80	1.00	1.04	0.94	1.00	0.92	1.06	1.05	0.89	0.89
Co(II) diffusion coefficient $D\times10^{13}$, m^2/s	8.00	18.00	27.50	23.20	18.20	15.50	21.00	17.50	7.50	5.60
Quantity of absorbed Co(II), %	0.81	0.97	1.03	0.93	0.97	0.91	1.02	0.98	0.88	0.86

nickel is absorbed in the fibre structure as NiS. Sulphide produced by decomposition of the reducing agent forms NiS, which is sparingly soluble in water and precipitates. The amount of NiS in PAN and silk fibres is much lower than in the other fibres, probably due to the presence of functional groups in its structure. These groups are able to coordinate with the reducing agent, resulting in a more stable complex. As a consequence, this diminishes the decomposition rate of the reducing agent.

Despite the fact that the Ni content and the fractions of NiS and Ni in silk and PAN fibres (after thermofixation) are comparable if rongalite is used as a reducing agent, a considerable difference in specific electrical resistance is observed. This indicates that the amount of nickel absorbed by the fibres and by the functional groups present at the fibre structure is not enough to explain the results. In addition, the distribution of the Ni particles is important. First, with scanning election microscope (SEM) it was found that the distribution of Ni in silk was not uniform, while in PAN fibres the distribution is uniform within the fibre and at the surface. The latter is due to adsorption of nickel on the functional groups of the PAN chemical structure. The non-uniform distribution of nickel in silk can be explained

by the random chemical structure of silk (only a limited number of amino acids in the sequence are able to adsorb nickel), resulting in areas that contain nickel while other areas are nickel-free. Secondly, variation of the relative amounts of carboxylic, cyanide and keto groups in the structure of the PAN resulted in an increased uptake of nickel. This observation also indicates that the presence of functional groups and their distribution in the chemical sequence of the polymeric fibre affects the uptake and distribution of nickel. A non-uniform distribution of the functional groups able to coordinate with nickel in the silk structure probably explains a non-uniform nickel distribution at the surface of and in the fibre, which explains the relatively high specific electrical resistance.

From the above results, it can be concluded that PAN fibres resulted in the desired conductive behaviour and will be used further in this investigation. Microscope images of the cross-section of PAN fibres treated with $NiCl_2$ show that after thermofixation of the fibre, no swelling is obtained. Therefore thermofixation will be an important step in the production process and will also be taken into account in the following steps of this investigation. Finally, it should be pointed out that similar absorption behaviour of PAN fibres for Co and CoS was observed but, contrary to Ni, this led to much weaker electroconductive properties of the metallised fibres.

11.2.3 Optimisation of the PAN-fibre production

PAN fibres are produced mainly from acrylonitrile copolymers processed in water-rhodanate, dimethylformamide or other solvents. It was found that fibres produced by the first of these methods show the highest porosity (higher capacity for metal uptake) and, as this process is performed in water, there is less pollutant. Therefore, it was chosen to use this type of processing for parameter optimisation. Mainly three parameters of the precipitation bath determine the structure of the PAN fibres: concentration of NaCNS, temperature and plasticisation drawing. The formation of the fibre itself, before entering the precipitation bath is performed on a laboratory wet-spinning device using a 12% solution of co-polymer (92.4% acrylonitrile, 6% methylacrylate and 1.6% itaconic acid) in 51.5% NaCNS. In order to determine the optimal values for the parameters of the precipitation bath, PAN fibres were produced under different conditions and were subsequently treated with a $1.0\,mol\,l^{-1}$ $NiCl_2$ or $CoCl_2$ solution, containing $1.5\,mol\,l^{-1}$ of rongalite. The treatment process was interrupted at different times, an excess of liquor was removed, and the fibre was dried, thermofixated at 413 K for 20 min and washed until negative reaction was observed against metal ions of Ni or Co.

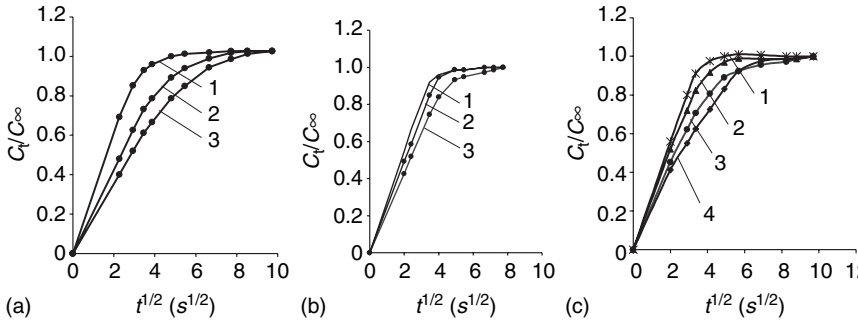

11.1 Profiles of absorption rate of cobalt in PAN fibres as a function of precipitation bath parameters: (a) NaCNS concentration being (1) 6%, (2) 8% and (3) 10%; (b) temperature being (1) 273 K, (2) 283 K and (3) 293 K; and (c) plasticisation drawing being (1) 500%, (2) 700%, (3) 900% and (4) 1100%. (Reprinted by permission of *Textile Research Journal*.)

The metal ion uptake profiles are shown in Fig. 11.1 for variations of NaCNS concentration (Fig. 11.1a), temperature (Fig. 11.1b) and plasticisation drawing (Fig. 11.1c) of the precipitation bath for Co uptake. Similar curves were obtained with Ni. Table 11.2 shows the data for different parameters related to a fully metallised fibre obtained after metallisation of PAN fibres, produced under different experimental conditions of the precipitation bath. Despite the fact that the uptake profiles are considerably different and the data obtained (diffusion coefficient) confirms this, no remarkable changes are observed in the total amount of metal absorbed by the fibre. This means that saturation for metal uptake is obtained independently of the precipitation bath parameters. The role of these parameters is limited to the rate of metal uptake, and a choice for the optimal value of these parameters should be based on economic reasons; first the consumption of chemicals and energy and, secondly, the processing time. Taking these two criteria into account, a NaCNS concentration of about 12%, a temperature of 283 K and a plasticisation drawing of 500% are further used.

11.2.4 Physico-mechanical properties of the metallised PAN fibres

Freshly produced PAN fibres, obtained under optimal conditions for metallisation, were treated with $NiCl_2$ and $CoCl_2$ solutions for different immersion times. After treatment, an excess of liquor was removed and the fibres were dried, thermofixated at 413 K for 20 min and washed until negative reaction against Ni and Co ions was observed. Finally, the physico-mechanical properties of the fibres were determined and are shown in Table

Table 11.3 Physico-mechanical properties of metallised PAN fibres as a function of metal content for freshly formed PAN fibres

ww% M_t in PAN fibre	Linear density (tex)	Strength (g/tex)	Elongation (%)	Preservation of strength (%)
Nickel-containing PAN fibres				
0	0.354	25.2	33.3	NA
0.31	0.371	23.5	37.0	93.4
0.70	0.355	26.3	35.0	104.0
1.20	0.372	22.3	36.0	88.6
1.52	0.278	24.6	38.0	97.8
Cobalt-containing PAN fibres				
0	0.354	25.2	33.3	NA
0.33	0.349	24.8	35.2	98.5
0.69	0.363	26.5	32.6	105.0
1.14	0.378	23.4	40.4	93.5
1.44	0.440	21.7	44.4	86.0

11.3, from which it can be seen that the physico-mechanical properties of the fibres obtained are only weakly dependent on the amount of nickel or cobalt taken up in their structure. A remarkable fact is that for a metal content of about 0.7%, the values for linear density, strength, elongation and preservation of strength are only slightly different between the two metals investigated.

The unchanged mechanical properties of the PAN fibre before and after metallisation indicate that swelling of the fibre is limited, which is confirmed by microscope images at cross-sections of a PAN fibre, a $NiCl_2$-treated PAN fibre and a $NiCl_2$-treated PAN fibre after thermofixation. These experiments were repeated with Fe(II) and showed an important swelling behaviour of the fibre resulting in large shifts of the physico-chemical properties. These properties were so disadvantageous that, in combination with the limited conductivity of Fe(II)-treated PAN fibres, they were not taken into consideration for further research.

The fibres produced according to the above procedure, which resulted in the data presented in Table 11.3, were further subjected to heat treatment. These fibres were exposed to 473 K for approximately 2 h, and again the physico-mechanical properties were investigated (Table 11.4). It can be seen that an important decrease of the mechanical parameters is obtained; however, this reduction is not due to the fact that these fibres are metallised, because the unmetallised PAN fibres showed a similar shift in physico-mechanical properties.

Table 11.4 Physico-mechanical properties of metallised PAN fibres as a function of metal content for thermofixated PAN fibres

ww% M_t in PAN fibre	Strength (g/tex)	Elongation (%)	Preservation of strength (%)
Nickel-containing PAN fibres			
0	11.2	21.4	44.4
0.31	13.6	17.7	54.0
0.70	13.5	21.8	53.0
1.20	14.5	16.6	57.6
Cobalt-containing PAN fibres			
0	11.2	21.4	44.4
0.69	14.6	18.3	58.0
1.14	14.1	18.3	56.0
1.44	14.1	16.6	56.0

11.3 Optimisation of electroconductive PAN-fibre production

11.3.1 Introduction

In this section, the process required to modify PAN fibres into electroconductive PAN fibres is described. Mainly, it is executed by a two-step process. First the fibres are metallised with Ni, but its electroconductive properties are not sufficient, so, in order to improve that property, an electrochemical deposition (galvanisation) is then performed at a second step to add a Ni layer of a few micrometers on top of the metallised fibres.

11.3.2 Stability of the reducing agent in aqueous solution

Prior to stability experiments, a preliminary metallisation of PAN fibres was performed using different types of reducing agent. The metallisation itself was performed in solutions of pH 5.5, containing 0.3 mol l^{-1} of Ni(II) and 0.6 mol l^{-1} of reducing agent. It was found that from sodium hypophosphite, hydroquinone, hydrazinesulphate, hydroxylamine, sodium dithionite and rongalite, only the latter two gave satisfactory results and were able to reduce Ni(II) to its metallic form. Only with these two reducing agents were PAN fibres modified into conductive fibres. Therefore, it is clear that at this stage only sodium dithionite and rongalite will be further used in the investigation.

First of all the stability of rongalite and sodium dithionite in solution was investigated. From the literature, it is clear that sodium dithionite is relatively unstable over the entire pH range[15–19]. This experiment, conducted at a pH of 5.5, showed that sodium dithionite indeed decomposes relatively fast, while rongalite remained stable at room temperature. At elevated temperatures (>330 K), rongalite decomposed very slowly, with a rate of 0.005 $mol\,l^{-1}\,h^{-1}$, which was independent of the rongalite concentration, indicating that this rate is only an apparent value. It is expected that the oxygen uptake rate in the solution determines this apparent rate, because oxygen is a compound taking part in the reaction and its concentration in solution is low owing to limited solubility.

11.3.3 Reduction rate of Ni(II) to metallic Ni in presence of rongalite

In this section of the research, the aim is to investigate the optimal composition of the Ni(II)-containing solution as a function of the Ni(II) reduction rate, the total amount of Ni reduced, the fraction of NiS formed and PAN-fibre properties, such as specific electrical resistance. In Fig. 11.2, data are shown for the variation of Ni(II) and rongalite concentration as a function of time and temperature starting from a constant initial Ni(II) concentration, while the initial rongalite concentration was increased. It must be pointed out that in this section of the research, no fibre was immersed in the solution, so the pure kinetic parameters of the reduction reaction of Ni(II) by rongalite is studied. Similar experiments were performed with different initial Ni(II) concentrations.

First, the initial reduction rate (slope of the decreasing Ni(II) curves during the first 15–30 min) is high. In all cases, the reaction finished after about 60 min, independently of the ratio of rongalite/Ni(II). This is explained by the formation of formaldehyde in solution, owing to the decomposition of rongalite into formaldehyde and sulphite. Formaldehyde is an inhibitor of the Ni(II) reduction reaction by rongalite. As formaldehyde is formed by the compound that reduces Ni(II), this type of inhibition is also called ‘auto-inhibition’. Secondly, the reaction rate of the Ni(II) reduction increases with temperature. In addition, it can be seen that at room temperature the rate of reduction is somewhat limited and too low for practical use. Higher temperatures should be used in order to obtain higher reduction rates and relatively shorter production times. The fact that the linear section in the initial decreasing Ni(II) reduction curves shortens with increasing temperature confirms the fact that formaldehyde inhibits further reduction. At elevated temperatures, a higher decomposition rate for rongalite is observed, resulting in higher formaldehyde concentrations

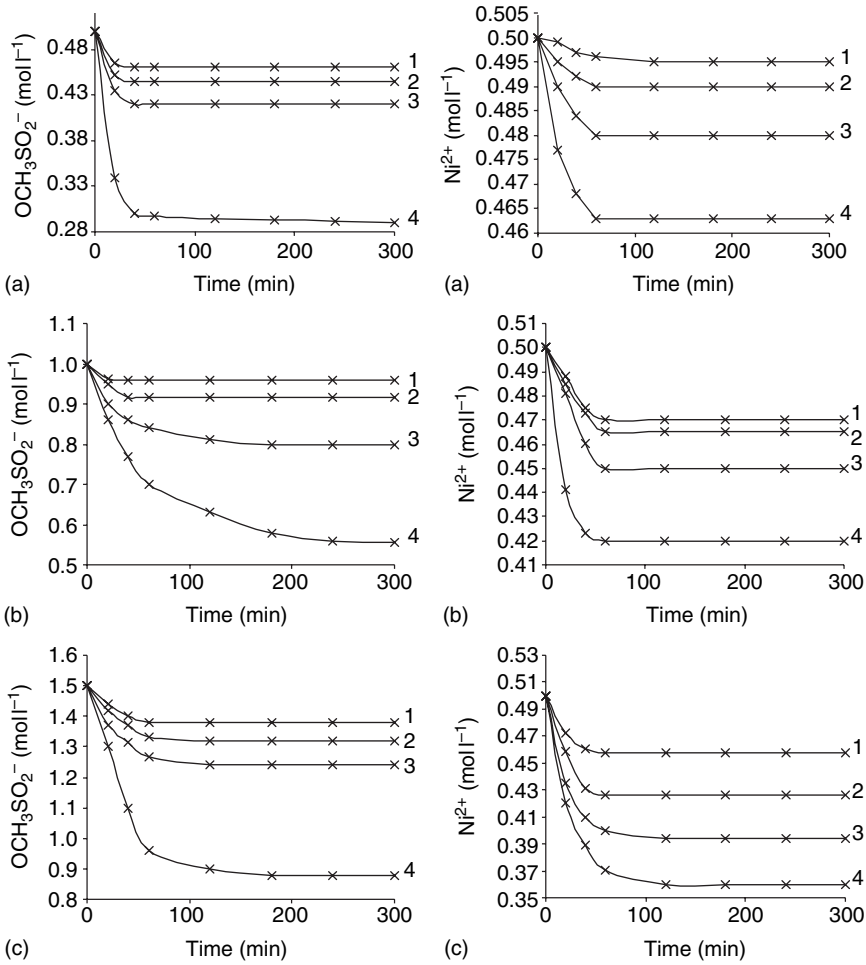

11.2 Changes of solution concentration of Ni(II) and rongalite as a function of time, with concentration ratio rongalite/Ni(II) of (a) 0.5/0.5; (b) 1.0/0.5; and (c) 1.5/0.5 and temperatures of (1) 298 K, (2) 313 K, (3) 333 K and (4) 353 K.

in solution. These higher concentrations cause a greater inhibition effect, and therefore the linear part of the initial decrease of the Ni(II) reduction curve is shorter at higher temperatures.

Thirdly, the absolute amount of Ni(II) reduced in the reaction increases with increasing rongalite concentration. From the complete set of data, it was found that an optimum was obtained for $c_{\text{Rongalite}}/c_{\text{Ni(II)}} = 3$, and the optimal value for the absolute concentrations was 0.5 mol l^{-1} of Ni(II) and 1.5 mol l^{-1} of rongalite. A low ratio is not favourable because of limited Ni(II) in solution, while a ratio higher than 3 results in the formation of too

Table 11.5 Kinetic data for A and B in Equation 11.7 of the reduction of Ni(II) by rongalite for different concentration ratios of rongalite/Ni(II)

c ratio mol l^{-1}	A 10^2				B 10^2				K			
	298 K	313 K	333 K	353 K	298 K	313 K	333 K	353 K	298 K	313 K	333 K	353 K
1.5/0.1	–0.41	–6.65	–9.34	–10.4	8.79	2.85	2.17	2.25	0.999	0.997	0.998	0.998
1.5/0.3	–3.34	–6.61	–8.91	–13.1	3.19	5.80	3.66	3.00	0.996	0.999	0.999	0.998
1.5/0.5	–5.42	–9.00	–11.7	–13.6	5.95	3.14	3.51	3.76	0.998	0.999	0.999	0.999
1.5/0.7	–3.24	–5.13	–11.0	–13.5	4.69	4.20	3.62	2.27	0.995	0.999	0.999	0.999
0.5/0.5	–0.87	–1.01	–2.45	–4.03	3.85	3.22	6.35	5.86	0.994	0.999	0.999	0.999
0.7/0.5	–1.40	–1.81	–4.22	–8.06	8.50	5.12	2.82	6.80	0.999	0.999	0.999	0.999
1.0/0.5	–4.36	–4.83	–5.98	–8.45	2.45	2.98	4.08	8.52	0.995	0.999	0.999	0.999

much formaldehyde. The reaction rate for the reduction of Ni(II) by rongalite can be correlated with the following equation:

$$c = c_0 + \mathrm{A}\frac{\mathrm{B}\tau}{1+\mathrm{B}\tau} \qquad [11.7]$$

where c and c_0 are the actual and initial Ni(II) concentrations in solution, respectively, τ is the time (s), and A and B are constants. From the data obtained in this set of experiments, A and B can be calculated with good correlation coefficients for the first 20 min of the reaction. At longer reaction times, the equation no longer expresses the kinetics owing to inhibiting influences of formaldehyde. Table 11.5 shows the results of A and B for different rongalite/Ni(II) concentration ratios. Differentiation of Equation 11.7 allows information about the reaction rate itself to be obtained:

$$-\frac{\mathrm{d}c}{\mathrm{d}\tau} = \frac{\mathrm{AB}}{(1-\mathrm{B}\tau)^2} \qquad [11.8]$$

This equation was used to calculate the reaction rates as a function of temperature and rongalite/Ni(II) concentration ratio, and Table 11.6 shows the results for a ratio of 1.5/0.5. The data in this table confirm the previous conclusion that a temperature of about 333 K should be used in order to have an economical and technologically acceptable reaction rate for the reduction of Ni(II) by rongalite and to avoid the large influence of autoinhibition by formaldehyde, an unfavourable effect that increases with temperature.

11.3.4 Ni(II) reduction by rongalite in presence of PAN fibre

During the production of cation-containing PAN fibres, it was found that absorption of Ni(II) in the fibre structure and adsorption at the surface of the fibre through formation of complexes with cyanide and carboxylic acid

Table 11.6 Reaction rates for the reduction of Ni(II) by rongalite in solution at different temperatures using Equation 11.8

Temperature, K	Reaction rate, $V \times 10^4$ mol l^{-1} min^{-1}
298	6.72
313	10.66
333	14.18
353	16.70

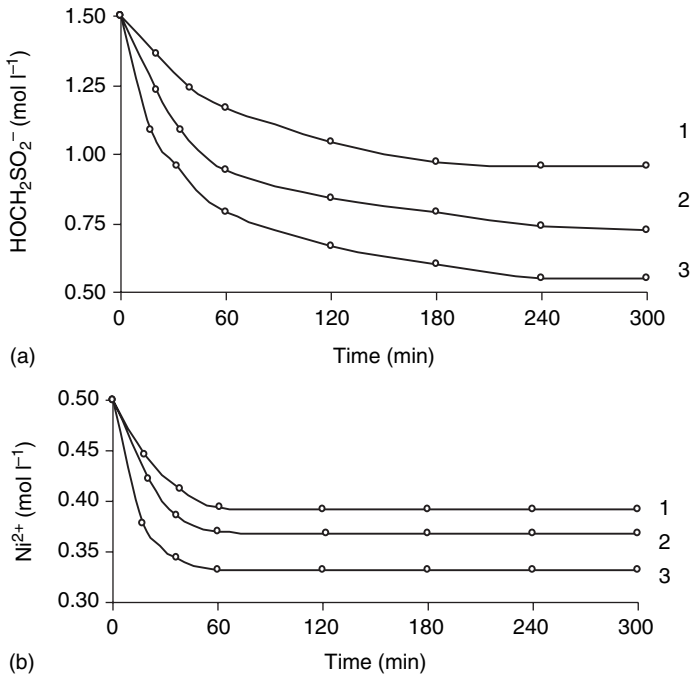

11.3 Changes in solution concentration of Ni(II) and rongalite for an initial concentration ratio rongalite/Ni(II) of 1.5/0.5 as a function of time containing (1) only Ni(II) and rongalite, (2) thermofixated PAN fibre and (3) freshly formed PAN fibre.

groups of the PAN-fibre structure was controlled by kinetic parameters (see section 11.2). In order to investigate the influence of active surface of fibre on the kinetics of interaction of Ni(II) with rongalite, the following experiment was performed: the Ni(II) and rongalite concentration in solution were followed by titration in equivalent amounts of freshly formed and thermofixed PAN fibre and in PAN-fibre precursors such as itaconic acid and acrylonitrile. The data are shown in Fig. 11.3 and Fig. 11.4.

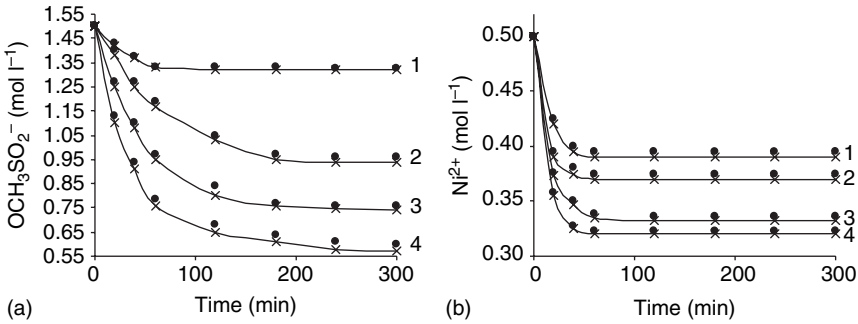

11.4 (a) and (b) Changes in solution concentration of Ni(II) and rongalite for an initial concentration ratio rongalite/Ni(II) of 1.5/0.5 as a function of time and at 313 K, containing (1) only Ni(II) and rongalite; (2) 4.6 g L^{-1} freshly formed PAN fibre; (3) 20.0 g L^{-1} freshly formed PAN fibre; (4) 29.6 g L^{-1} freshly formed PAN fibre (×) and equivalent amounts of PAN-fibre precursors. Data from the modelling using Equations 11.1 and 11.2 are given in bullets (•).

First, it can be seen that the content of Ni(II) in solution is much lower when the PAN fibre or its precursors are present in solution. This is very clear because, apart from the reduction of Ni(II) by rongalite in solution, chelate formation also occurs between Ni(II) and PAN-active groups (cyanide, carboxylic acid), resulting in a decrease of free Ni(II). In addition, the drop in the concentration of rongalite is much more pronounced in the presence of PAN fibre and its precursors. It is well known in the literature that Ni(II) complexes formed with cyanide (e.g. $Na_2[Ni(CN)_4]$) are excellent catalysts for the decomposition of rongalite. Therefore, formation of complexes between Ni(II) and PAN fibre through cyanide results in the formation of similar complexes, and they are responsible for the continuing drop in the rongalite concentration.

Secondly, the drop in Ni(II) concentration is even more pronounced in the presence of the PAN fibres compared with the fact that equivalent amounts of PAN precursors are dissolved. By equivalent amounts, it is meant that an equivalent amount of functional groups are dissolved in solution. This difference can be explained by two effects:

- Using precursors, Ni(II) concentration drops because of reduction by rongalite and complex formation with the functional groups of the PAN precursors, followed by reduction.
- Using fibres, the first effect also applies but, in addition, absorption of Ni(II) in the fibre structure (not only on the surface) occurs. It should also be noted that in the fibre, the functional groups are close to each other, which means that complex formation can occur much faster com-

Table 11.7 Changes of A and B as a function of PAN-fibre quantity in solution for an initial rongalite/Ni(II) concentration ratio of 1.5/0.5 at 313 K for 20 min

PAN-fibre quantity ($g\,l^{-1}$)	A 10^2		B 10^2		K		V$\times 10^4$, $mol\,l^{-1}\,min^{-1}$	
	Fibre	Model	Fibre	Model	Fibre	Model	Fibre	Model
4.6	–0.155	–0.164	–0.084	–0.097	0.999	0.999	18.2	18.3
20.0	–0.166	–0.175	0.083	0.106	0.999	0.999	19.5	19.1
29.6	–0.177	–0.180	0.081	0.096	0.999	0.999	21.1	21.2

pared with the use of PAN precursors, particularly if the concentration of functional groups in solution is low.

Finally, a difference in reduction, absorption and adsorption rate of Ni(II) can be observed between freshly formed and thermofixated PAN fibre. Proof was not found for this effect, but probably the absorption capacity of the thermofixated fibre is reduced, resulting in a decrease in the absorption of Ni(II) in the PAN-fibre structure.

In a second experiment, the kinetics of Ni(II) decrease was followed as a function of time in solutions containing different amounts of freshly formed PAN fibre. The experimental results were also calculated using Equations 11.7 and 11.8, and an acceptable correlation was found between both methods (Table 11.7). Note also from Table 11.7 that the amount of fibre present in the solution does not affect B; only A is dependent on the amount of fibre in solution. Figure 11.4 shows the experimental data and the data from the modelling. It can be seen that the kinetics increase when more PAN fibre is present in solution. This is very clear, because more PAN fibre means a higher capacity to ad- and absorb Ni(II), and also the concentration of rongalite drops faster because more catalytic decomposition occurs through interaction with Ni–cyanide complexes.

Several cables of PAN fibres, obtained through an optimised wet-spinning process followed by chemical metallisation in a pH = 5.5 solution at 333 K and containing 1.5 $mol\,l^{-1}$ of rongalite and 0.5 $mol\,l^{-1}$ $NiCl_2$, resulted in fibre with a specific electrical resistance of $2.5 \times 10^{-4}\,\Omega m$. These fibres contain about 5.5% Ni, consist of about 40 000 elementary fibres and have a weight of 15.3 $g\,m^{-1}$. The specific electrical resistance of these fibres is still much higher than for a metallic conductor. However, because of the adsorption capacity of PAN fibres for Ni(II), through its cyanide and carboxylic acid groups, a relatively large fraction of Ni is present at the surface of the fibres. These Ni centres form a sort of 'seed' layer that can be used as a substrate layer for growing a Ni layer using an electrodeposition method in a

plating bath, also known as galvanisation. This is described in the following section.

11.3.5 Galvanisation of Ni-metallised PAN fibres

For the galvanisation of PAN fibres, a standard galvanisation setup is used as shown in Fig. 11.5. Two cathodic rollers (1, 2) are used to feed the cables of fibre (3) through the electrolyte solution (4) in the bath (5). Anodes (6) are positioned in the bath in order to be able to apply a potential difference between anode and cathode, which results in the deposition of Ni at the fibre surface. The composition of the electrolyte solutions used in this investigation for the galvanisation of the PAN fibres is given in Table 11.8.

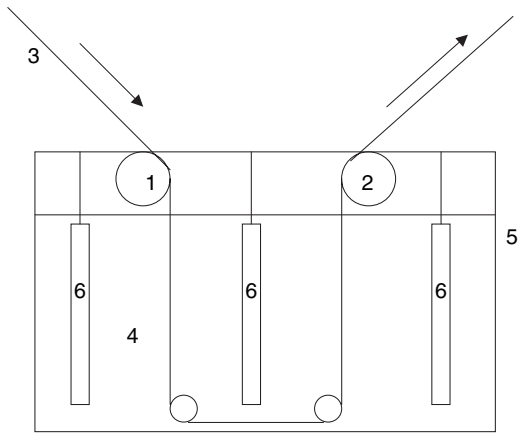

11.5 Scheme of the galvanisation setup with (1, 2) rolling cathodes, (3) chemically metallised yarn, (4) electrolyte solution, (5) galvanisation bath and (6) anodes.

Table 11.8 Composition of the electrolyte solutions used for the galvanisation of the PAN fibres

Composition ($g\,l^{-1}$) and parameters of electrolyte	Electrolyte solution		
	Number 1	Number 2	Number 3
$NiSO_4$	72	145	290
Na_2SO_4	45	45	—
$MgSO_4$	—	27	55
H_3BO_3	22	22	27
NaCl	7	7	4
NaF	—	—	2
pH	5.6–5.8	5.0–5.5	3–5

Galvanisation of the metallised fibre will improve its properties as electrical conductor because of the formation of a continuous metallic coating at the surface of the fibre. In this respect, the 'seed' layer formed during metallisation is crucial for a good adhesion between the metal layer and the PAN-fibre structure.

In galvanisation, it is the electrolyte solution used for this experiment which determines the final properties of the coating and the textile fibre and yarn. Important properties include surface coverage, continuity and uniformity of the layer, thickness and homogeneity of the layer, and specific electrical resistance. These parameters will be determined from the electrical current measured during galvanisation as a function of applied potential difference between anodes and cathodes and with spectroscopic methods to study the structure of the deposited layer. However, the measured current is not only dependent on electrochemical parameters such as type of electrolyte solution and applied potential, but also on geometrical parameters. In order to keep the latter constant, only one electrode setup (see experimental section) is used in this investigation.

A first parameter to be studied is the applied potential difference between anode and cathode. This potential is not necessarily equal to the actual potential difference between the electrodes because ohmic drop contributions decrease the tension applied between the electrodes. Examples are anode polarisation, tension failure, IR-drop or ohmic-drop effects of the electrolyte solution and the specific electrical resistance of the fibres and yarns. This means that relatively high potential differences should be applied (a few volts) in order to obtain an optimal potential difference over the anode and cathode. Figure 11.6 shows the evolution of the measured electrical current between anode and cathode as a function of time for several applied potential differences in three electrolyte solutions. It can be seen that for applied potential differences of less than 6 V, an increase in the electrical current is detected; for potentials great than 6–8 V, first an increase, followed by a decrease, is observed. The increase in current at low applied potentials (<6 V) is caused by the electrodeposition of Ni(II) at the fibre surface, resulting in an increase of its conductive properties; therefore more electrical current can pass the cable per time unit. After approximately 15 min, it reaches a constant value; at that moment, the surface is fully covered (confirmed with X-ray photo/electron spectroscopy (XPS) analysis) with Ni. Further deposition continues but no longer affects the conductive properties of the deposited layer.

At a higher potential difference, the electrical current reaches maximum. The decrease of electrical current is caused by different effects. It is necessary to bear in mind that applying higher potential differences brings with it the risk of side reactions such as decomposition of water, with formation of oxygen at the anode and hydrogen at the cathode. These two compounds

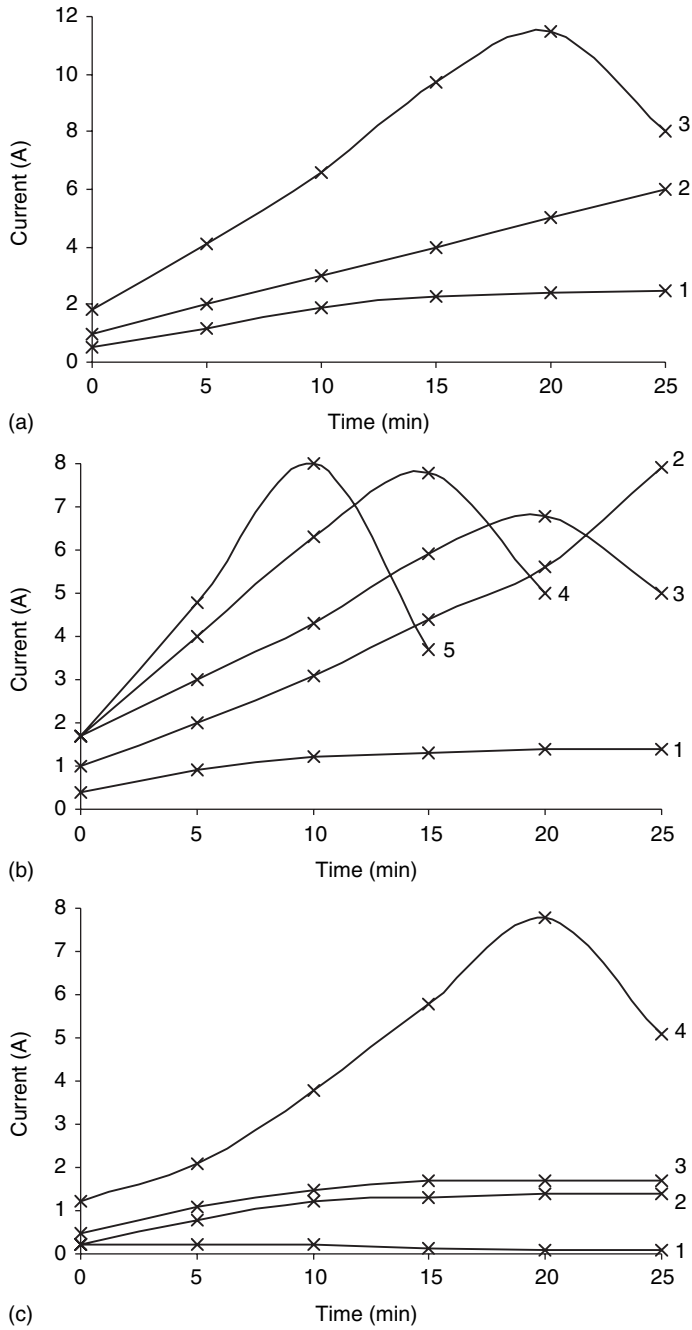

11.6 Current–potential curves recorded in the galvanisation bath shown in Fig. 11.5 during deposition of Ni(II) on metallised PAN-fibre surfaces in electrolyte solution (a) number 1, (b) number 2 and (c) number 3 for applied potential differences of (1) 4 V, (2) 6 V, (3) 8 V, (4) 10 V and (5) 12 V at 298 K.

have a limited solubility in water; therefore they form oxygen and hydrogen gas bubbles at the surface of the anode and the yarn, resulting in an increase of the specific resistance of the system. In addition, reduction of water to hydrogen consumes hydrogen ions in the vicinity of the cathodes; therefore the pH increases locally at that level causing precipitation of Ni(II) as $Ni(OH)_2$ at the surface of the cable and cathodes. This effect also increases the specific resistance of the cables because of deposition of a non-conductive $Ni(OH)_2$ layer. The presence of this compound at the surface of the fibres is confirmed by Raman spectroscopy, and this is only when a maximum is observed in the current–potential curves. This also confirms the fact that at lower applied potentials, the decomposition of water does not occur.

Minor differences between the three electrolyte solutions are also observed. First, electrolyte number 3 only shows a peak maximum in the current–potential curves at potentials higher than 8 V. However, this is very clear because its pH value is smaller, indicating that this electrolyte solution possesses a higher buffer capacity against consumption of hydrogen ions in the vicinity of the fibre surface, avoiding hydrogen gas formation and $Ni(OH)_2$ precipitation. Secondly, at a potential of 4 V, no deposition occurred in electrolyte solution number 3, indicated by the absence of an increase in the measured electrical current and confirmed by XPS data. Additionally in this case, the lower pH plays an important role; because of the lower pH value, the applied potential difference does not overlap with the potential window in which the reduction of Ni(II) occurs. Therefore no deposition is observed.

In an industrial galvanisation line, it is not the potential difference applied between anode and cathode that counts but the current that is measured, because this current reveals information about how much of the compound is deposited. Therefore in industry, a constant electrical current is applied instead of a potential difference. However, one has to take into account the fact that the applied electrical current does not cause high potential differences, as otherwise the unfavourable effects of increase of specific electrical resistance of the PAN fibres will appear. This was verified in an additional experiment, and it was found that a current density of about 0.025 A dm^{-2} could be applied at the first cathodic roller (1 in Fig. 11.5). This does not seem particularly large, but can be explained by the relatively high resistance of the fibres at the initial stage of the process. At the second cathodic roller (2 in Fig. 11.5), a current density of 0.5 A dm^{-2} could be applied, which is much larger because at this roller the electrical resistance of the cables should be taken into account, resulting in a large ohmic drop.

Finally, experiments were performed using current densities of 0.025 A dm^{-2} and 0.2 A dm^{-2} applied at the first (1 in Fig. 11.5) and second (2 in Fig. 11.5) cathodic rollers respectively. Galvanisation time was

Table 11.9 Relative variations of amount of nickel and specific electrical resistance in individually cut PAN-fibre pieces obtained through chemical metallisation and galvanisation

Index of electrolyte	K_{Ni} (%)	$K\rho_v$ (%)
Number 1	31.8	66.1
Number 2	20.0	62.3
Number 3	76.0	82.6

expected to be 12 min; after this time, the galvanised cables were cut into 100 pieces, each of 10 cm, and the variation factors of the contents of nickel in fibre (K_{Ni}) and of specific electric resistance of fibre (K_{ρ_v}) were determined. The variations between the individual pieces of galvanised PAN cable are summarised in Table 11.9 for the different types of electrolyte solution. From this table, it can be seen that differences of 60% were obtained in specific electrical resistance. However, this is acceptable because for all the individual pieces a specific electrical resistance in the order of $1 \times 10^{-6}\,\Omega$m was obtained, which reveals good conductive properties. More important is the variation of the amount of Ni deposited.

These values show clearly that using electrolyte number 2, a much better uniformity and homogeneity is obtained in the deposited layer compared with the other electrolyte solutions. This can be explained by the fact that the concentration of Ni(II) in electrolyte solution 3 is much too high, resulting in too much Ni(II) deposited in a short time, while for electrolyte solution 1, the concentration of Ni is too small, resulting in concentration polarisation (to a large local drop of the concentration) in the vicinity of the cable surface. Additional experiments with shorter galvanisation times revealed that after about 5 min the minimal value for the specific electrical resistance was obtained having deposited about $8\,g\,m^{-1}$ of Ni. Therefore it could be concluded that the galvanisation process should be executed with the following parameters:

- current density of first cathodic roller: $0.025\,A\,dm^{-2}$;
- current density of second cathodic roller: $0.2\,A\,dm^{-2}$;
- electrolyte composition: number 2 (Table 11.8) with $c_{Ni(II)} = 150\,g\,l^{-1}$ and pH = 5;
- temperature: 298 K.

This results in PAN fibres obtained by chemical metallisation and galvanisation with the following properties:

- $23 \pm 1\,g\,m^{-1}$ of weight (after metallisation and galvanisation);
- specific electrical resistance = $5.8 \pm 1.8 \times 10^{-6}\,\Omega$m.

11.4 References

1. Aljumah K., Fernandez J.E., *Macromol*., **20** (1987) 1177.
2. Whang Y.E., Han J.H., Nalwa H.S., Watanabe T., Miyata S., *Synth. Met*., **43** (1991) 3043.
3. Beltsios K.G., Carr S.H., *Abst. Pap. Am. Chem. Soc*., **197** (1989) 45.
4. Dao L.H., Cote R., Gauthier R., *J. Electrochem. Soc*., **134** (1987) C130.
5. McNaughton T.G., Horch K.W., *J. Neur. Methods*, **70** (1996) 103–110.
6. Toyo Boseki K.K., Miramura H., Yoshida F., Shimura T., US Pat. 5 248 486 (1993).
7. Zhang QH., Jin H.F., *Acta Polym. Sin*., (2000) 250–252.
8. Zhang Q.H., Jin H.F., Wang X.H., Jing X.B., *Synth. Met*., **123** (2001) 481–485.
9. Lee B.O., Woo W.J., Kim M.S., *Macromol. Mat. Eng*., **286** (2001) 114–118.
10. Schmitt C., Lebienvenu M., *Mec. Ind. Mat.* **50** (1997) 224–227.
11. Halperin S.A., *EE-Eval Eng.* **33** (1994) 68.
12. Maclaga B., Fisher W.K., *Text. Res. J*., **71** (2001) 281–286.
13. Nelson M.A., Rogers R.L., Gilmartin B.P., *J. Electrostat*., **30** (1993) 135–147.
14. Akbarov D., 'Determination of Ni and Co in fibre' *Nitron, Express Information, Ser: Methods of Analysis and Control of Product Quality*, Moscow, NIITECHIM, 1984, 12–15.
15. Gasana E., Westbroek P., Temmerman E., Thun H.P., *Anal. Commun*., **36** (1999) 387–389.
16. Gasana E., Westbroek P., Temmerman E., Thun H.P., Kiekens P., *Anal. Chim. Acta.*, **486** (2003) 73–83.
17. Govaert F., Temmerman E., Westbroek P., *Anal. Commun*., **35** (1998) 153–156.
18. Makarov S.V., Polenov Y.V., Aleksandrova A.N., Budanov V.V., *Izvestiya Vysshikh Uchebnykh Zavedenii Khimiya I Khimicheskaya Tekhnologiya*, **26** 1983) 1231–1234.
19. Westbroek P., De Clerck K., Gasana E., Kiekens P., Temmerman E., *Tex. Res. J*., **73** (2003).

12

Textile fibres used as electrode materials in analytical applications

P. WESTBROEK

12.1 Introduction

In this chapter, three topics of research will be described in which textile fibres and structures are used as electrodes to detect and determine chemical compounds, concentration to optimise the detection conditions and to use such systems to follow and control polymerisation reactions.

12.2 A platinum-fibre electrode for detection of Cu(II) and Cu(I) in non-aqueous solution

12.2.1 Introduction

The Cu(II)/Cu(I) redox system added as bromide has recently been used to prepare well-defined polymers (controlled molecular weight, reduced poly-dispersity, terminal functionalities). One of the most successful methods to make well-defined polymers is atom transfer radical polymerisation (ATRP)[1–8]:

$$R_n - X + M^{n+1}/\text{ligand} \rightleftharpoons R_n\bullet + X - M^{n+1} \xrightarrow{+R} R_{n+1} \qquad [12.1]$$

A wide range of monomers, including styrene, can be polymerised in this way. Cu(I)/ligand is a commonly used metal complex which can act as a catalyst. These metal complexes must have the ability to be oxidised to a higher oxidation state. In the case of copper, the oxidised form of the metal is Cu(II), the deactivator of the process. The dynamic equilibrium of this method is responsible for the well-defined behaviour of these kinds of polymerisations. This equilibrium can, in its turn, be controlled by the ratio of concentrations of both the metal-complex forms. In this chapter, preliminary research results are described concerning the voltammetric determi-

nation of Cu(I) and Cu(II) concentrations in styrene. Electrochemical methods to determine copper ion concentrations in aqueous solution or in organic solutions with a higher dielectric constant than styrene have been described before[9–12].

Electrochemical measurements are useful for determining concentrations of electroactive species in solution. Playing the role of solvent, the monomer studied in this chapter is styrene. One of its most remarkable characteristics is the low dielectric constant (ε=2.43 at 298.0 K) compared with that of water (ε=78 at 298.0 K). A solvent with a low dielectric constant is a highly resistive medium, in which voltammetric measurements are not evident. Voltammetric measurements in styrene as solvent have not been described before. Papers describing an electrochemical method for the determination of styrene in more polar organic solvents can be found in the literature[13–17].

Voltammetric measurements in highly resistive media became possible by using ultramicro electrodes, which should have dimensions in the range of micrometers or less. One of their most claimed advantages is that the electrode processes are commonly associated with low currents in the range of nano- or picoamperes. As a result, the ohmic 'IR'drop, even in organic solvents with high resistance, can be kept sufficiently low and voltammetric experiments can be performed. Furthermore, ultramicro electrodes have an excellent signal ratio of Faraday-to-background current and enable low concentrations of electroactive species to be determined in high-resistance media. The ability of measuring in low conducting media opens up new perspectives, particularly for electroanalytical purposes in monitoring polymer reactions[18].

12.2.2 Determination of solution resistance

In Fig. 12.1, a Nyquist (Fig. 12.1a) and a Bode (Fig. 12.1b) plot are shown, obtained by electrochemical impedance spectroscopy (EIS) using a standard conductivity cell, in a styrene solution with different concentrations of tetra hexyl amino phosphate (THAP). From the semi-circle (Fig. 12.1a) and the wide range of frequencies where only resistive effects are observed (Fig. 12.1b, range where phase-angle shift is near zero), it can be deduced that the electrical equivalent circuit consists of a resistor and a capacitor in parallel. However, the semi-circle for pure styrene could not be obtained experimentally (and is not shown in the figure) because of an excessively high solution resistance. As expected, this resistance drops by adding THAP and was obtained from Fig. 12.1a through the diameter of the semi-circle, which is equal to the resistance of the solution in the conductivity cell. This resistance can also be obtained from Fig. 12.1b in the plateau of the log Z vs. log$f$ plot, if, in the same region of frequencies, no phase-angle shift

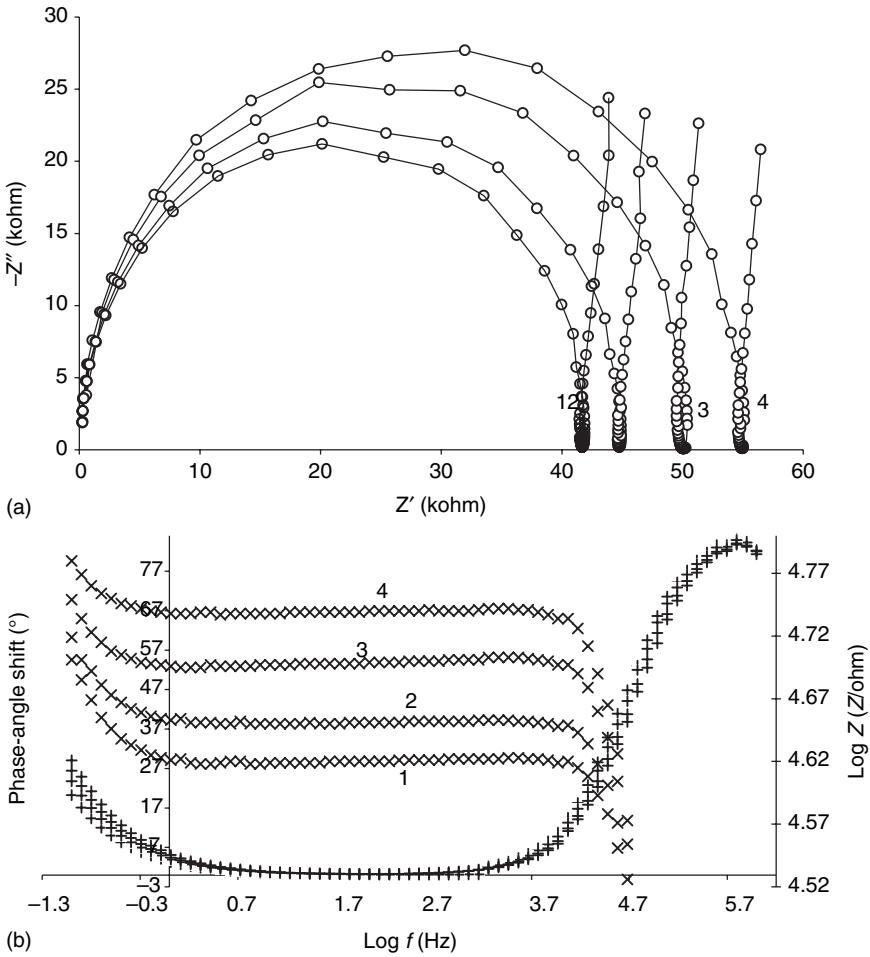

12.1 (a) Nyquist and (b) Bode plots recorded in styrene containing (1) 1.43×10^{-4}, (2) 1.32×10^{-4}, (3) 1.21×10^{-4} and (4) 1.10×10^{-4} mol l^{-1} THAP using a platinum conductivity cell with K = 1 at 298.0 K. (Reprinted from *Microchemical Journal*, Vol 77, De Wael et al, 'Electrochemical detection . . .', pp 85–92 (2004), with permission from Elsevier.)

between applied potential and measured current is observed. Despite the decrease of the resistance, it remains very high (40–60 kohm) compared with aqueous solutions where typical values for R with electrolyte concentrations of 1×10^{-2} mol l^{-1} are a few hundreds of an ohm. This is about 200 times less than the resistance obtained in styrene solutions containing THAP, and the effect can be explained by the very low dielectricity constant (ε=2.43 at 298.0 K) compared with water (ε=78 at 298.0 K), which

implies that styrene is a poor stabiliser of dissolved ions by solvation. As a consequence, clusters of electrolyte are formed explaining the much lower conductivity in styrene than in water.

The results of Fig. 12.1 explain the reason for using ultramicro electrodes instead of commonly used millimeter-sized electrodes. A solution resistance that is about 200 times larger than the one observed in water means that ohmic-drop effects will influence the recorded voltammetric waves at current signals about 200 times smaller than is the case if the experiment were to be performed in aqueous solution. However, using an ultramicro electrode with a diameter of 100 µm reduces the current signal significantly, allowing voltammetric measurements in the styrene/THAP system. Therefore, the investigation was continued with ultramicro electrodes, which explains the presence of limiting-current plateaux instead of peak-shaped voltammetric waves (except for the anodic dissolution of Cu(0), as explained later).

Preliminary experiments were performed to study the (electroactive) behaviour of styrene containing THAP at a platinum ultramicro disc electrode, which was obtained as described in Chapter 1, pages 21–24. However, in the range where copper activity is observed (see later) no additional reactions of the solvent or the electrolyte were observed. Outside this potential window, oxidation of styrene and reduction of the electrolyte were observed. As these potential ranges are not interesting for the purpose of detection of Cu(II) and Cu(I), they are not further described in this chapter.

In Fig. 12.2, current–potential curves are shown which were obtained by performing cyclic voltammetry at a platinum ultramicro disc electrode in styrene solutions containing 0.11 mol l^{-1} THAP and different concentrations of $CuBr_2$ (Fig. 12.2a) and CuBr (Fig. 12.2b). The potential was swept from 0.5 to –1.1 V vs. reference electrode (RE) (forward-sweep direction) and back to 0.5 V vs. RE (backward-sweep direction) with a sweep rate of 50 mV s^{-1}. In both figures, a reduction wave resulting in a limiting-current plateau is observed in the forward-sweep direction. The starting potential of this wave is located at –0.35 V vs. RE in solutions containing $CuBr_2$ and –0.2 V vs. RE for CuBr-containing solutions. From the formation of a limiting current, it can be concluded that transport of Cu(II) and Cu(I) towards the electrode surface is rate determining, and it was found that the product of this reaction is a metallic copper layer deposited at the electrode surface. In the backward-sweep direction, two waves are observed, for solutions containing $CuBr_2$ as well as for those of CuBr. A first wave, resulting in a limiting-current plateau, is observed in the potential region of –0.4 to –0.15 V vs. RE, while a second, peak-shaped, wave starts at potentials around –0.15 V vs. RE. The second wave can be attributed to the dissolution of the copper layer by oxidation because of its peak shape (limited amount of Cu(0)). The first oxidation wave is determined by steady-state phenomena,

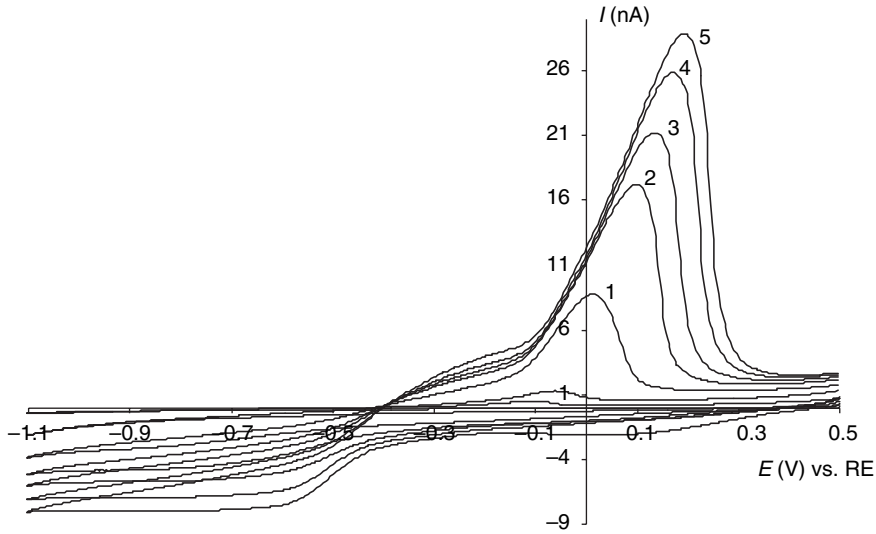

(a)

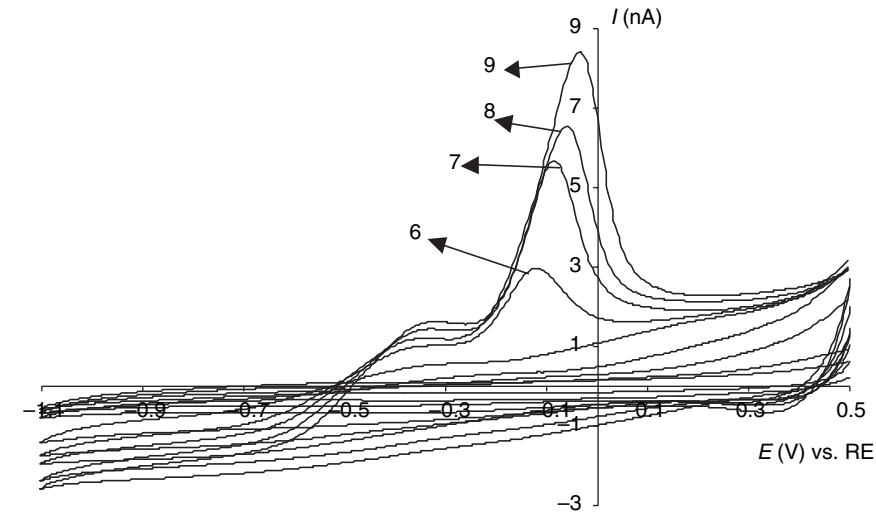

(b)

12.2 Cyclic voltammetric curves recorded at a platinum ultramicro disc electrode in a styrene solution containing 0.11 mol l^{-1} THAP and different concentrations of (a) Cu(II) and (b) Cu(I). Concentrations are (1) 1.55×10^{-3}, (2) 2.74×10^{-3}, (3) 3.91×10^{-3}, (4) 5.05×10^{-3}, (5) 6.18×10^{-3}, (6) 2.64×10^{-4}, (7) 6.99×10^{-4}, (8) 1.13×10^{-3} and (9) 1.56×10^{-3} mol l^{-1}; T=298.0 K; v=50 mV s^{-1}. (Reprinted from *Microchemical Journal*, Vol 77, De Wael et al, 'Electrochemical detection . . .', pp 85–92 (2004), with permission from Elsevier.)

probably transport of Cu(II) or Cu(I). It should be noted that the electrochemical behaviour of Cu(II) and Cu(I) in styrene is similar to that in aqueous solutions[11].

The voltammetric waves observed in Fig. 12.2 can be attributed to four reactions, partly based on literature results. It was found experimentally that the reaction product of the reduction waves observed for Cu(II) and Cu(I) reduction is metallic copper. Therefore the following reactions are suggested:

$$\mathrm{Cu(II)} + \mathrm{e^-} \leftrightarrows \mathrm{Cu(I)} \qquad [12.2]$$

$$\mathrm{Cu(I)} + \mathrm{e^-} \leftrightarrows \mathrm{Cu(0)} \qquad [12.3]$$

Equation (12.2) starts at a potential around –0.35 V, while Equation 12.3 starts at –0.2 V vs. RE. Indeed in styrene solutions containing $CuBr_2$ (Fig. 12.2a), the wave starts at –0.35 V vs. RE according to Equation 12.2. However, in that reaction Cu(I) is formed, which is reduced easily at potentials more negative than –0.2 V vs. RE. Therefore one voltammetric wave is observed corresponding to the two-electron reduction of Cu(II) to metallic copper. This wave is not initiated at –0.2 V vs. RE, because at that potential Cu(I) is not yet formed by Equation 12.2. For styrene solutions containing CuBr (Fig. 12.2b), it is now clear that the wave observed at potentials starting from –0.2 V vs. RE corresponds to Equation 12.3. However, at that potential Cu(II) is not yet reduced. In Cu(I) solutions, some Cu(II) will be present owing to homogeneous oxidation of Cu(I), which is a relatively unstable compound, and this can indeed be seen in the voltammetric curves. At potentials more negative than –0.35 V vs. RE, a slight increase of the limiting-current is observed, which can be attributed to reduction of Cu(II), present in solution in small quantities.

12.2.3 Analytical considerations

The transport-controlled limiting-current of the reduction waves can be used for electroanalytical purposes. Figure 12.3 shows a linear relationship between limiting-current at –0.80 V vs. RE and the Cu(II) (o) and Cu(I) (×) concentration. The slope for Cu(II) is twice as high as the one for Cu(I), which can be explained by the fact that Cu(II) reduction involves the exchange of two electrons (Equations 12.2 and 12.3), while the Cu(I) reduction involves only one electron (Equation 12.3). In both cases, a stable background current of 1.40±0.16 nA was found, which resulted in a detection limit of 1.4×10^{-4} and 2.1×10^{-4} mol l^{-1} for Cu(II) and Cu(I), respectively, taking into account the rule of twice the deviation of the background current (equal to 0.32 nA).

The first oxidation wave is attributed to the following reaction:

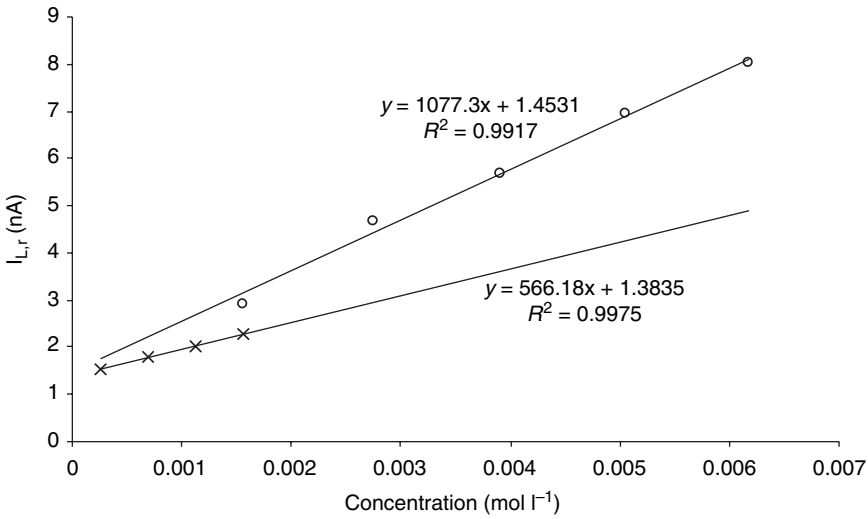

12.3 Calibration plot for detection of (o) Cu(II) and (×) Cu(I) concentration in 0.11 mol l^{-1} THAP styrene solution based on the limiting reduction current at –0.80 V vs. RE, obtained from cyclic voltammetric curves shown in Fig. 12.2a; T=298.0 K; v=50 mV s^{-1}. (Reprinted from *Microchemical Journal*, Vol 77, De Wael et al, 'Electrochemical detection . . .', pp 85–92 (2004), with permission from Elsevier.)

$$\mathrm{Cu(I)} \leftrightarrows \mathrm{Cu(II)} + \mathrm{e}^- \qquad [12.4]$$

This assumption is based on three relevant indications. First, this wave results in a limiting-current. This means that steady-state transport phenomena control the rate of this reaction, which is not compatible with a possible oxidation of metallic copper to Cu(I) or Cu(II). If the latter were to be valid, a peak-shaped response should have been obtained because of the limited available amount of metallic copper (initially deposited by reduction of Cu(II) or Cu(I) in the reduction wave). In addition, the second voltammetric oxidation wave in the backward scan direction is actually compatible with such a dissolution reaction.

Secondly, if the first oxidation wave cannot be attributed to metallic copper oxidation, only one oxidisable compound is left, namely Cu(I). Indications for this can be found in the fact that in Cu(I)-containing styrene solutions, the limiting-current of this first oxidation wave is much higher than for Cu(II)-containing solutions. As a matter of fact, the first oxidation wave is expected to be absent in Cu(II) solutions. Apparently, the presence of this wave has to be attributed to the fact that some Cu(I) is present in the vicinity of the electrode surface. When the position of the current–potential curves in Fig. 12.2 reflects the standard potentials of the

Cu(II)/Cu(0) and Cu(I)/Cu(0) redox couples, it is evident that Cu(I) is expected to disproportionate into Cu(II) and Cu(0). When originally no Cu(I) is present in a Cu(II) solution in contact with metallic copper, a reaction between Cu(II) and Cu(0) may occur until an equilibrium is attained. This would result in the presence of Cu(I) in the vicinity of the copper-covered electrode.

Additional experiments using stripping voltammetry confirmed this hypothesis. By depositing a metallic copper layer at –0.80 V vs. RE for 30, 60 and 120 s, followed by stripping off the layer with linear-sweep voltammetry from –0.7 to 0.5 V vs. RE, it was found that, for solutions containing Cu(II), the limiting-current of the first oxidation wave increased linearly with deposition time. A possible explanation would be that part of the Cu(I) formed in the second reduction wave escapes into solution, resulting in a local concentration building up in the vicinity of the electrode surface[19–20]. An increase of the deposition time then results in a higher limiting current for the first oxidation wave. Repeating the experiment with Cu(I) solutions revealed that, in this case, the limiting-current of the first oxidation wave did not change at all (Fig. 12.4). This can be explained by the fact that the concentration of Cu(I) in solution is constant and independent of deposition time, so no additional Cu(I) is formed because Cu(II) is not present in solution (or in a very low quantity only). A third item of evidence for the occurrence of Equation 12.4 was found in the literature concerning aqueous solution[11]. Finally, it is interesting to mention that the curves obtained in styrene are similar to those obtained in aqueous solution[11].

The second oxidation wave can be attributed to Equation 12.5:

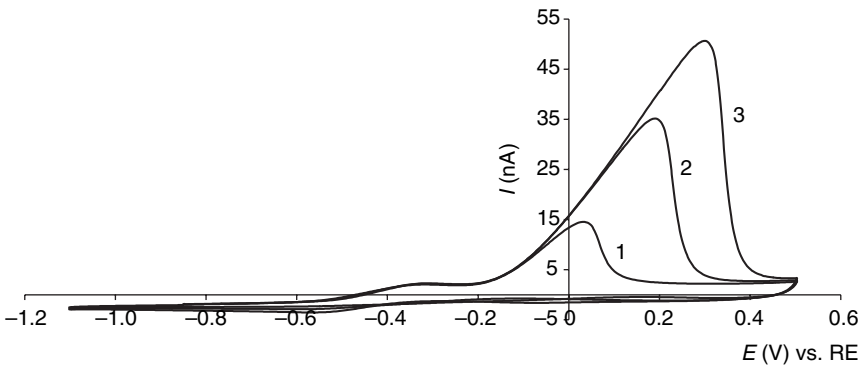

12.4 Cyclic voltammetric curves recorded at a platinum ultramicro disc electrode in styrene solution containing 0.11 mol l^{-1} THAP and 1.8×10^{-3} mol l^{-1} Cu(I) after (1) 30, (2) 60 and (3) 120 s of depositing Cu(0) at the electrode surface at a potential of –0.80 V vs. RE; T=298.0 K; v=50 mV s^{-1}. (Reprinted from *Microchemical Journal*, Vol 77, De Wael et al, 'Electrochemical detection . . .', pp 85–92 (2004), with permission from Elsevier.)

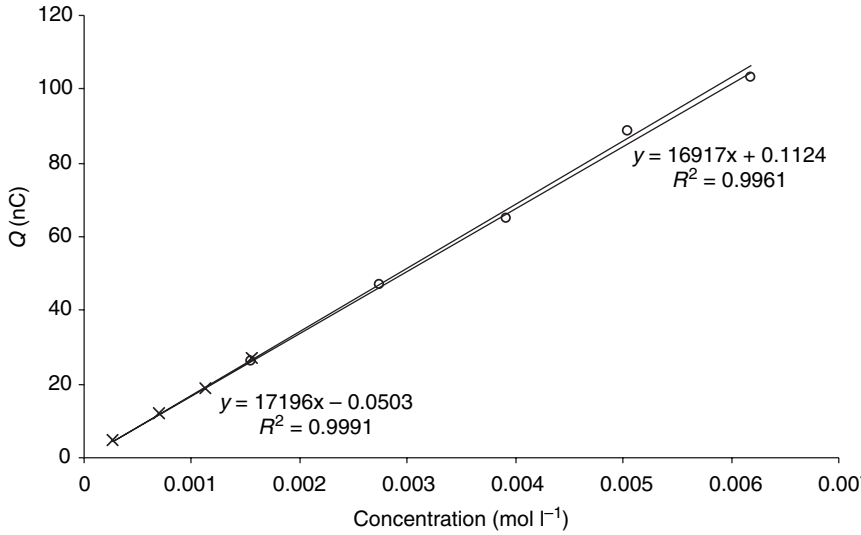

12.5 Calibration curve of Cu(0) dissolution charge as a function of (×) Cu(I) or (o) Cu(II) concentration in styrene solution containing 0.11 mol l^{-1} THAP at 298.0 K and v=50 mV s^{-1}. (Reprinted from *Microchemical Journal*, Vol 77, De Wael et al, 'Electrochemical detection . . .', pp 85–92 (2004), with permission from Elsevier.)

$$Cu(0) \leftrightarrows Cu(I) + e^- \qquad [12.5]$$

The fact that actually the reaction product was identified as Cu(II) and not Cu(I) as indicated in Equation 12.5 also confirms that Equation 12.4 corresponds to the first oxidation wave. At potentials where Cu(I) is formed (second oxidation wave), it is immediately further oxidised to Cu(II), according to Equation 12.4. The peak shape of this wave can be explained by the limited supply of metallic copper, and the current drops to zero once the copper layer is stripped from the electrode surface.

The charge under this peak is proportional to the amount of Cu(0) initially deposited, and this amount is indirectly determined by the Cu(II) and/or Cu(I) concentrations in solution. The relationship between the charge exchanged and the Cu(II) and/or Cu(I) concentration in solution is given in Fig. 12.5. It can be seen that only one calibration curve is obtained, which is expected because the slope is determined by the following reaction:

$$Cu(0) \leftrightarrows Cu(II) + 2e^- \qquad [12.6]$$

independently of whether the deposited copper layer was obtained from Cu(II) or Cu(I) reduction. This also means that, from a combination of the calibration curves in Fig. 12.3 and Fig. 12.5, it should be possible to deter-

mine Cu(II) and Cu(I) concentrations simultaneously in a mixture using the following calibration equations obtained from the data shown in Fig. 12.3 and Fig. 12.5:

$$I_{L,r} = kC_{Cu(I)} + 2kC_{Cu(II)} \quad [12.7]$$

$$Q_{p,o} = k'[C_{Cu(II)} + C_{Cu(I)}] \quad [12.8]$$

with $I_{L,r}$ the reductive limiting-current at –0.80 V vs. RE, $Q_{p,o}$ the anodic charge under the stripping peak; the constants (k and k′) correspond to the slopes of the curves shown in Fig. 12.3 and Fig. 12.5. This set of two equations contains two unknown parameters (Cu(II) and Cu(I) concentrations); therefore it is possible to obtain these concentrations using the following equations, derived from Equations 12.7 and 12.8:

$$C_{Cu(II)} = \frac{-kQ_{p,o} + k'I_{L,r}}{kk'} \quad [12.9]$$

$$C_{Cu(I)} = \frac{-kI_{L,r} + 2kQ_{p,o}}{kk'} \quad [12.10]$$

It can be seen that, from measuring the limiting-current of the reduction wave and the charge of the stripping peak, it is possible to obtain the Cu(I) and Cu(II) concentrations simultaneously after calibration (determination of k and k′).

12.3 Determination of SO_2 reactions as a function of pH and its detection at modified carbon-fibre electrodes

12.3.1 Introduction

Sulphur dioxide is used in many applications such as organic synthesis[21], in lithium batteries[22] and as a preservative. Besides detection and monitoring of sulphur dioxide in these and other applications, detection is also important for environmental reasons[23]. Sulphur dioxide is a major atmospheric pollutant and has a serious impact on buildings and vegetation as component of acid rain[23]. Depending on the pH of the solution, sulphur dioxide transforms into bisulphite and/or sulphite according to the following reactions[24]:

$$SO_2 \cdot xH_2O \underset{k_{-1}}{\overset{k_1}{\leftrightarrows}} HSO_3^- + H^+ + (x-1)H_2O \quad [12.11]$$

$$HSO_3^- \underset{k_{-2}}{\overset{k_2}{\leftrightarrows}} SO_3^{2-} + H^+ \qquad [12.12]$$

where k_1, k_2, k_{-1} and k_{-2} are rate constants, and $K_1 = 1.54 \times 10^{-2}$ mol l^{-1} [25] and $K_2 = 1.02 \times 10^{-7}$ mol l^{-1} [25] are equilibrium constants.

Various electrochemical methods based on polarography[26–28], amperometry[29–31] potentiometry[32,33] and voltammetry[31], at bare and modified electrodes[34] have been described for the detection of sulphur dioxide. Many electrolytes, particularly acidic ones like sulphuric acid and perchloric acid, have been employed. Despite many electrochemical methods that describe the detection of sulphur dioxide, there remains a problem regarding the instability of this compound and the presence of other sulphur-containing compounds in SO_2 solutions[35,36]. At gold and platinum electrodes in alkaline solution, the kinetics of sulphur dioxide oxidation and/or reduction are slow[37–39]. However, gold has been used successfully in alkaline solution[31]. Despite the relatively slow kinetics, a suitable potential window could be observed for gold where transport is the rate-determining step.

In a recent study, Rea and co-workers[40] discuss important mechanistic aspects of porphyrin electrocatalysis. Chen[41–43] presents important results for sulphite oxidation in the presence of iron, manganese and cobalt porphyrins and with electrodes modified by metal hexacyanoferrates[44]. Analytical applications involving electrodes modified with electrostatically assembled films containing cobalt tetra-rhutenated porphyrins were presented earlier[45], where detection limits below 1×10^{-6} M sulphite were attained. Similar sensors associated with a diffusion cell were explored for sulphite quantification in wines[46].

12.3.2 Fibre positioning in an electrochemical cell

A flow-through cell was developed in which to position the modified carbon fibre (see scheme presented in Fig. 12.6). Two glass tubes with an inner diameter of 50 μm are used to immobilise the carbon fibre. The fibre is sealed in the glass tubes (2) and the fibre part (1) between the two glass tubes is exposed to the solution to be analysed in a flow-though pipeline (4). This tube is made of metal in order to act also as counter electrode (5). Besides the carbon fibre, a reference electrode (3) is also positioned in the flow-through pipeline. In the work described below, this electrochemical cell was not really used as flow-through system during analysis, as once the analysis experiment starts, the solution in the pipeline is stationary. Only between two experiments is a flow rate applied in order to refresh the solution in the pipeline in which the carbon fibres are positioned.

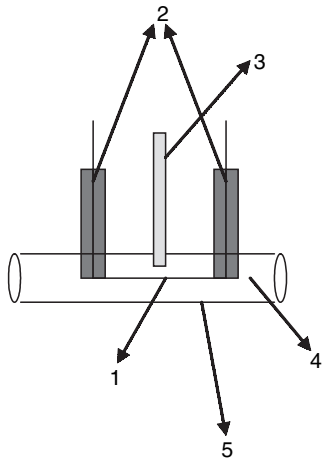

12.6 Scheme of the flow-through cells with (1) [Fe(II)TSPc]$^{4-}$ modified carbon-fibre electrode, (2) glass tubes to immobilise the carbon fibre, (3) reference electrode, (4) flow-through pipeline and (5) metallic tube acting as counter electrode.

12.3.3 Electrodeposition of [Fe(II)TSPc]$^{4-}$ in pH=7.4 buffer at carbon fibres

In Fig. 12.7, the electrodeposition of [Fe(II)TSPc]$^{4-}$ (Fig. 12.8) is shown as a function of scan number and was carried out in a 1×10^{-3} mol l^{-1} [Fe(II)TSPc]$^{4-}$ solution. Five peaks could be observed during this experiment; all of them were increasing with scan number (some of them increased weakly). This means that indeed [Fe(II)TSPc]$^{4-}$ is being deposited onto the surface of the carbon fibre. Extensive research on [Fe(II)TSPc]$^{4-}$ can be found in the literature[47–53]. The paper by Zecevic *et al.*[50] was used as reference work to identify the observed peaks. However, their study showed that no peaks were observed in the first scan using [Fe(II)TSPc]$^{4-}$. Around 0 V vs. Ag|AgCl in Fig. 12.7, a broad oxidation peak was obtained attributed to Fe^{II}/Fe^{III} oxidation. The return peak for this oxidation was observed at –0.5 V vs. Ag|AgCl (A). A second weak redox couple (B) is attributed to ring oxidation in the [Fe^{III}TSPc(-2)]$^{3-}$, giving [Fe^{III}TSPc(-1)]$^{2-}$. A relatively large irreversible reduction peak (C), centered around 0.2 V vs. Ag|AgCl, could be identified as the reduction of oxygen. Despite the fact that the experiments were carried out in solutions purged with nitrogen, oxygen was produced at the fibre surface at the most positive applied potentials. Scanning the potential to a value less positive than the oxygen-evolution reaction (up to 1.25 V vs. Ag|AgCl) did not result in peak C. Therefore, it could be concluded that this peak was due to oxygen reduction.

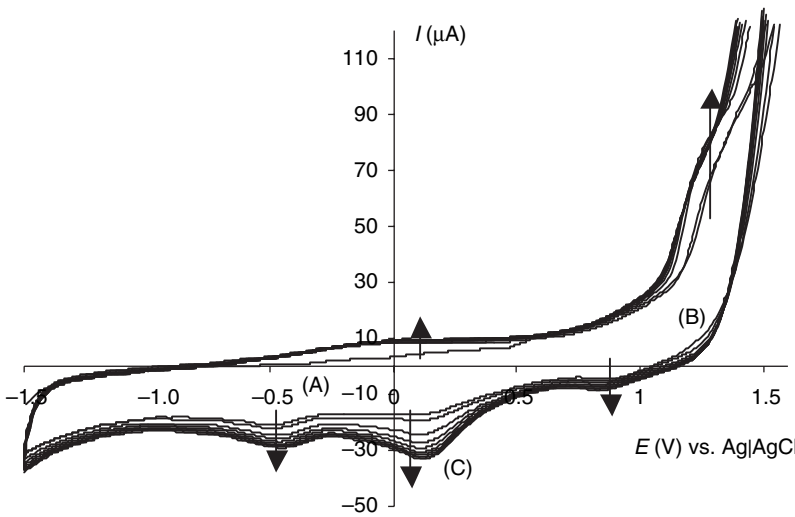

12.7 Voltammetric curves of the electrodeposition of $[Fe(II)TSPc]^{4-}$ at a carbon-fibre electrode in pH=7.4 buffer containing 1×10^{-3} mol l^{-1} $[Fe(II)TSPc]^{4-}$; $v=100$ mV s^{-1}; number of scans is 25.

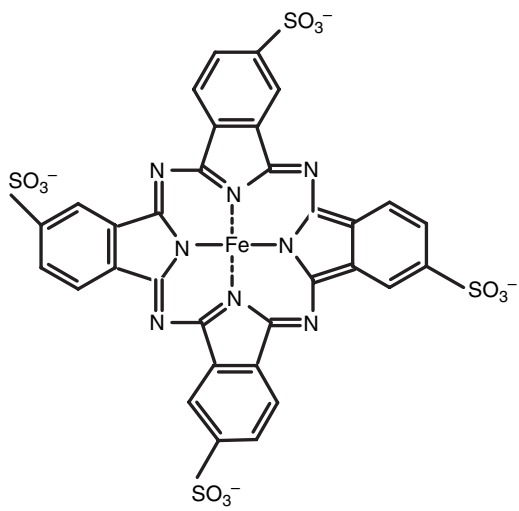

12.8 Scheme of the structure of $[Fe(II)TSPc]^{4-}$.

12.3.4 Sulphite and sulphur dioxide in 1.0 mol l^{-1} H_2SO_4

Figure 12.9 shows current–potential curves, recorded at carbon-fibre electrodes modified with $[Fe(II)TSPc]^{4-}$, with increasing concentrations of sulphur dioxide in a 1.0 mol l^{-1} H_2SO_4 solution. Similar curves were obtained

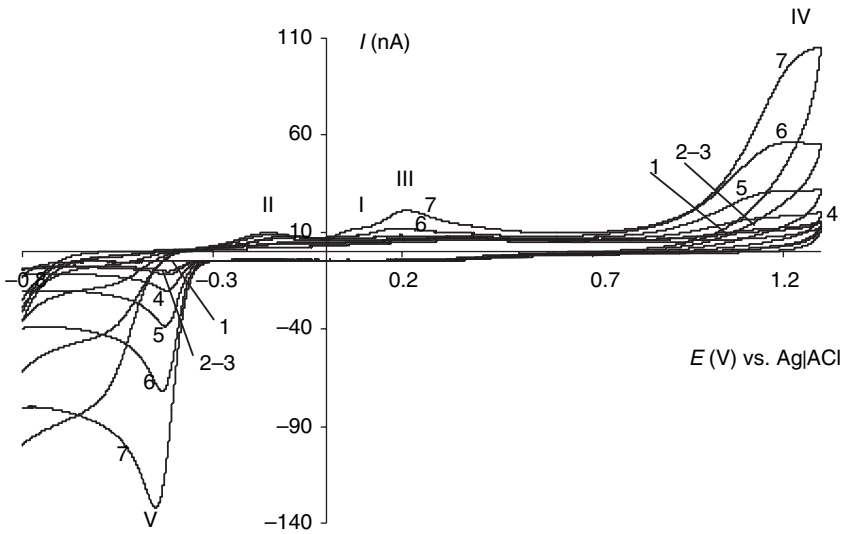

12.9 Current–potential curves recorded in 1.0 mol l^{-1} H_2SO_4 solution for increasing SO_2 concentrations at a carbon-fibre electrode modified with $[Fe(II)TSPc]^{4-}$. SO_2 concentrations are (1) 0, (2) 8.34×10^{-5}, (3) 1.00×10^{-4}, (4) 3.37×10^{-4}, (5) 6.42×10^{-4}, (6) 1.21×10^{-3} and (7) 2.20×10^{-3} mol l^{-1}; $v = 100$ mV s^{-1}.

Table 12.1 Actual fraction of SO_2, HSO_3^- and SO_3^{2-} in solution as a function of pH

K_1	K_2	C_{H^+}(mol l^{-1})	pH	Fraction SO_2^-	Fraction HSO_3^-	Fraction SO_3^{2-}
1.54×10^{-2}	1.02×10^{-7}	1	0	9.85×10^{-1}	1.52×10^{-2}	1.55×10^{-9}
1.54×10^{-2}	1.02×10^{-7}	10^{-1}	1	8.67×10^{-1}	1.33×10^{-1}	1.36×10^{-7}
1.54×10^{-2}	1.02×10^{-7}	10^{-2}	2	3.94×10^{-1}	6.06×10^{-1}	6.18×10^{-6}
1.54×10^{-2}	1.02×10^{-7}	10^{-3}	3	6.10×10^{-2}	9.39×10^{-1}	9.58×10^{-5}
1.54×10^{-2}	1.02×10^{-7}	10^{-4}	4	6.45×10^{-3}	9.93×10^{-1}	1.01×10^{-3}
1.54×10^{-2}	1.02×10^{-7}	10^{-5}	5	6.42×10^{-4}	9.89×10^{-1}	1.01×10^{-2}
1.54×10^{-2}	1.02×10^{-7}	10^{-6}	6	5.89×10^{-5}	9.07×10^{-1}	9.26×10^{-2}
1.54×10^{-2}	1.02×10^{-7}	10^{-7}	7	3.21×10^{-6}	4.95×10^{-1}	5.05×10^{-1}
1.54×10^{-2}	1.02×10^{-7}	10^{-8}	8	5.80×10^{-8}	8.93×10^{-2}	9.11×10^{-1}
1.54×10^{-2}	1.02×10^{-7}	10^{-9}	9	6.30×10^{-10}	9.71×10^{-3}	9.90×10^{-1}
1.54×10^{-2}	1.02×10^{-7}	10^{-10}	10	6.36×10^{-12}	9.79×10^{-4}	9.99×10^{-1}

for sodium sulphite, which means that in strongly acidic solution, sulphite is almost completely transformed to $SO_2\cdot xH_2O$ (Table 12.1). This also means that k_{-1} and k_{-2} in Equations 12.11 and 12.12, respectively, are high. Indeed, by dissolving sodium sulphite in 1.0 mol l^{-1} H_2SO_4, the typical smell

of SO_2 was detected. However, if a bare-carbon fibre is used, ill-defined and poorly visible waves were obtained. This is a first indication that $[Fe(II)TSPc]^{4-}$ electrocatalyses the observed reactions.

Two main waves (IV and V) can be observed in Fig. 12.9 and are attributed to oxidation (Equation 12.13) and reduction of sulphur dioxide, respectively. (The latter reaction is discussed later.)

$$SO_2 + 2H_2O \leftrightarrows SO_4^{2-} + 4H^+ + 2e^- \qquad [12.13]$$

Besides these main waves, three other waves are observed in Fig. 12.9. Waves I and II are attributed to oxidation of reaction products formed in wave V. This was proved by cycling the potential between –0.3 and 0.6 V vs. Ag|AgCl where waves I and II were absent. By addition of sodium dithionite to the solution, waves I and II again appeared, indicating that the reaction product formed in wave V is dithionite. Waves I and II were also observed at a bare-carbon-fibre electrode after addition of sodium dithionite. Therefore, it is not clear whether these reactions are electrocatalysed by $[Fe(II)TSPc]^{4-}$. However, when cycling between –0.3 and 0.6 V vs. Ag|AgCl, wave III still occurred under these conditions, indicating that this wave can be attributed to a species in solution.

Both waves IV and V in Fig. 12.9 correspond to diffusion-controlled reactions, because a linear relationship is obtained between the peak current and the square root of the scan rate. However, the slope of the relationship between the peak current and $SO_2 \cdot xH_2O$ concentration is slightly higher for the reduction than for the oxidation (Fig. 12.10, curves 1 and 2, respectively). A different number of electrons exchanged in both reactions cannot explain the small peak-current differences between these waves. As pointed out earlier, wave III (corresponding to curve 3 in Fig. 12.10) was attributed to a species present in solution. Moreover, it can be seen that the sum of the peak currents of waves III (curve 3) and IV (curve 2) is equal to the peak current of wave V (curve 1 in Fig. 12.10). Therefore, it is presumed that wave III corresponds to the oxidation of bisulphite (reaction 4), which is present at about 1.5% of the analytical sulphur dioxide concentration (Table 12.1). This wave is observed at similar potentials as those for the oxidation of the Fe–metal ion in $[Fe(II)TSPc]^{4-}$. Therefore, it is assumed that the bisulphite oxidation is electrocatalysed by the central metal ion of the $[Fe(II)TSPc]^{4-}$:

$$HSO_3^- + H_2O \leftrightarrows SO_4^{2-} + 3H^+ + 2e^- \qquad [12.14]$$

However, an additional condition, that k_1 in Equation 12.11 is relatively small, needs to be fulfilled. This is indeed the case and is confirmed by two additional experiments. In a first experiment, the pH was varied from 0 to 2 in five steps. The peak height of wave III in Fig. 12.9 increased while the one of wave IV decreased with increasing pH value, due to formation of

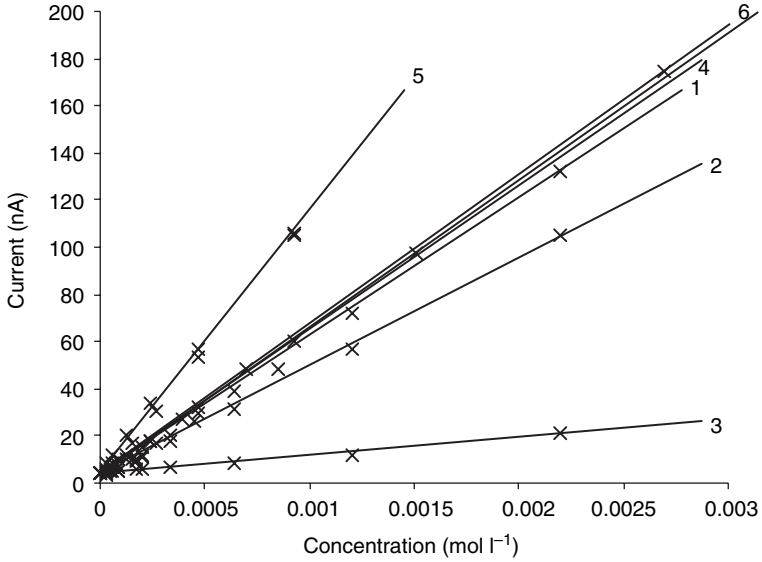

12.10 Calibration plots of the oxidation and reduction of SO_2 and its related compounds at a carbon-fibre electrode modified with [Fe(II)TSPc][4]. (1) SO_2 reduction in 1.0 mol l^{-1} H_2SO_4, (2) SO_2 oxidation in 1.0 mol l^{-1} H_2SO_4, (3) HSO_3^- oxidation in 1.0 mol l^{-1} H_2SO_4, (4) HSO_3^- oxidation in pH = 4 buffer, (5) HSO_3^- reduction in pH = 4 buffer, (6) SO_3^{2-} oxidation in pH = 8 buffer and (7) SO_3^{2-} oxidation in pH = 10 buffer.

HSO_3^- with increasing pH. In a second experiment, a preconditioning of the electrode at a potential of +0.6 V vs. Ag|AgCl was applied prior to cycling from +0.6 to +1.3 V vs. Ag|AgCl. With increasing preconditioning time, the peak height of wave IV decreased, indicating that during the preconditioning $SO_2 \cdot xH_2O$ is transformed (however slowly) to HSO_3^-, which is in turn oxidised at the preconditioning potential. Despite the fact that k_1 in Equation 12.11 is relatively small, reaction of $SO_2 \cdot xH_2O$ to HSO_3^- still occurs. Indeed, a much higher ratio of $I_{p,III}/I_{p,IV}$ is obtained than was found for the actual concentration ratio of $[HSO_3^-]/[SO_2 \cdot xH_2O]$ in solution (Table 12.1). This shows that, during the oxidation of HSO_3^-, fresh HSO_3^- is produced by Equation 12.11. This result also suggests that the peak current of waves III and IV in Fig. 12.9 cannot be attributed to the actual concentrations of bisulphite and sulphur dioxide in solution. However, the sum of these peak currents is proportional to the analytical concentration of sulphur dioxide and can therefore be used for analytical purposes.

Another possibility is to make use of the reduction wave V. No reduction prewave of HSO_3^- was observed, and since k_{-1} in Equation 12.11 is high, it can be concluded that HSO_3^- is transformed rapidly into $SO_2 \cdot xH_2O$, during

sulphur dioxide reduction. As was pointed out earlier, dithionite is supposed to be the reaction product, therefore wave V is attributed to:

$$2SO_2^- + 2e^- \leftrightarrows S_2O_4^{2-} \qquad [12.15]$$

Based on the reduction of $SO_2 \cdot xH_2O$, a detection limit of $8.5 \pm 0.1 \times 10^{-5}$ mol l^{-1} is obtained, which is lower than the one obtained by using waves III and IV ($1.2 \pm 0.1 \times 10^{-4}$ mol l^{-1}). The determination of the detection limit was based on the criterion that the detection limit corresponds to an electrode signal of twice the background current. However, an advantage of using the oxidation is that sulphate is formed as a reaction product instead of dithionite. The latter species itself is electroactive and relatively unstable; decomposition occurs easily into sulphite and related products. Dithionite can therefore become an influencing species in continuous measurement or for measurements in small-volume cells.

12.3.5 Sulphite and sulphur dioxide in pH=4 buffer at a carbon fibre

In Fig. 12.11, current–potential curves are shown for different sulphur dioxide concentrations, recorded in pH=4 buffer at a $[Fe(II)TSPc]^{4-}$-

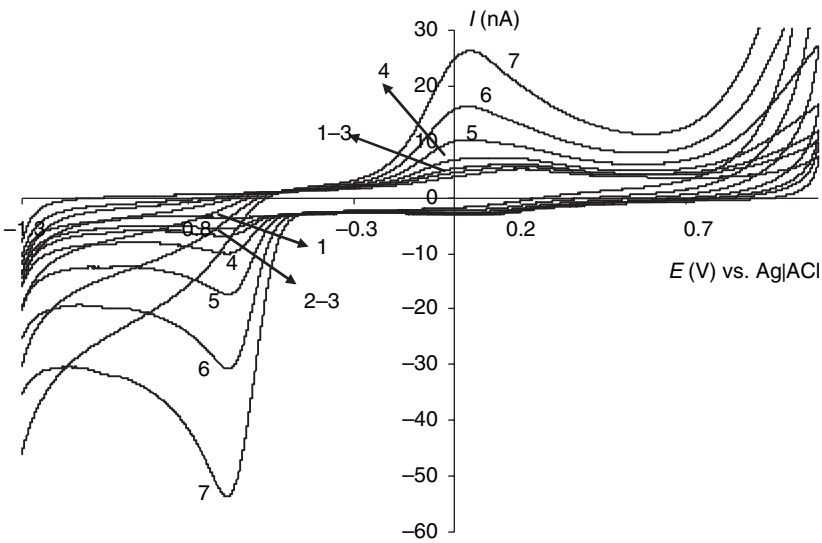

12.11 Current–potential curves recorded in pH=4 buffer solution for increasing SO_2 concentrations at a carbon-fibre electrode modified with $[Fe(II)TSPc]^{4-}$. SO_2 concentrations are (1) 0, (2) 3.89×10^{-5}, (3) 6.02×10^{-5}, (4) 8.79×10^{-5}, (5) 1.51×10^{-4}, (6) 2.71×10^{-4} and (7) 4.71×10^{-4} mol l^{-1}; $v = 100$ mV s^{-1}.

modified carbon fibre. Two waves can be detected: an oxidation wave centered around 0.05 V vs. Ag|AgCl and a reduction wave with a peak potential of –0.65 V vs. Ag|AgCl. Based on the results obtained above in 1.0 mol l^{-1} H_2SO_4, the oxidation wave corresponds to electrocatalytic oxidation of HSO_3^- catalysed by Fe in $[Fe(II)TSPc]^{4-}$, which is oxidised at the same potentials. No wave for $SO_2 \cdot xH_2O$ is observed, because SO_2 is transformed almost totally into HSO_3^- (Table 12.1) at this pH. A similar voltammogram, as shown in Fig. 12.11, was obtained with sodium sulphite as starting species. The oxidation wave corresponds to Equation 12.14 with exchange of two electrons, and is proportional to the analytical concentration of sulphur dioxide and sulphite (Fig. 12.10, curve 4).

The reduction wave cannot be attributed to reduction of $SO_2 \cdot xH_2O$ or HSO_3^- with exchange of two electrons. Its slope is twice as high as the one for the oxidation (Fig. 12.10, curve 5). Therefore, this wave is assumed to be the reduction of HSO_3^- (because this is the only compound in solution) to $S_2O_3^{2-}$ (Equation 12.16) with exchange of four electrons, because $S_2O_3^{2-}$ does not show electroactive properties over the entire potential region and is a relatively stable species:

$$2HSO_3^- + 2H^+ + 4e^- \leftrightarrows S_2O_3^{2-} + 3H_2O \qquad [12.16]$$

Owing to the higher slope obtained for the reduction, a lower detection limit can be obtained. Detection limits of $3.8 \pm 0.1 \times 10^{-5}$ and $7.4 \pm 0.1 \times 10^{-5}$ mol l^{-1} were obtained for the reduction and oxidation of $SO_2 \cdot xH_2O$, respectively, with HSO_3^- as electroactive species.

12.3.6 Sulphur dioxide and sulphite at pH=8 and pH=10 buffer at carbon fibre

In a buffer of pH=8, completely different results were obtained for sulphur dioxide and sodium sulphite as starting species. Starting from sulphite, only one oxidation wave is obtained around 0.7 V vs. Ag|AgCl. From Table 12.1 it can be seen that sulphite itself is the main compound in solution, therefore it is clear that this wave can be attributed to Equation 12.17. Its slope (Fig. 12.10, curve 6), obtained by plotting the peak current versus concentration, is situated in the range that allows exchange of two electrons:

$$SO_3^{2-} + H_2O \leftrightarrows SO_4^{2-} + 2H^+ + 2e^- \qquad [12.17]$$

Starting from sulphur dioxide, only one wave around 0.7 V vs. Ag|AgCl is observed at concentrations lower than 1×10^{-4} mol l^{-1}. At concentrations higher than this value, this wave disappears and two new oxidation waves with E_p=–0.2 and +1.1 V vs. Ag|AgCl and a reduction wave are observed. It is well known that SO_3^{2-} reacts to form $HS_2O_5^-$ in an excess of SO_2[24]. This

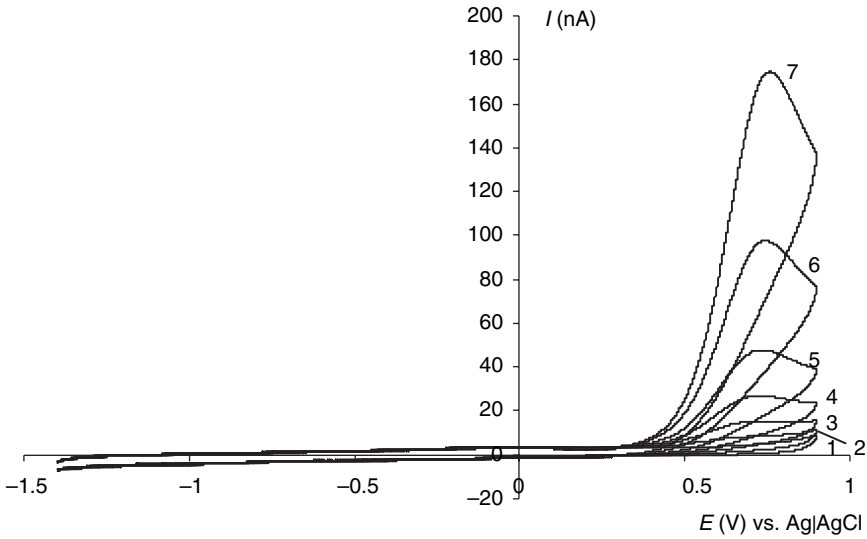

12.12 Current–potential curves recorded in pH=10 buffer solution for increasing SO_2 concentrations at a carbon-fibre electrode modified with $[Fe(II)TSPc]^{4-}$. SO_2 concentrations are (1) 0, (2) 7.47×10^{-5}, (3) 2.02×10^{-4}, (4) 3.92×10^{-4}, (5) 6.95×10^{-4}, (6) 1.51×10^{-3} and (7) 2.70×10^{-3} mol l^{-1}; $v=100$ mV s^{-1}.

excess is temporarily present during dissolution of SO_2. It is expected that this indeed occurs, but $HS_2O_5^-$ decomposes further. However, the new waves occurring are not proportional to the SO_2 concentration. Moreover, the peak current of the new reduction wave shifts to less negative potentials with increasing sulphur dioxide concentration. Similar results were obtained in buffer solutions from pH=7.5–9.0. Since these results are not suitable for analytical purposes, no experimental curves are shown and they are not further investigated. Therefore SO_2 cannot be detected in the pH range from 7.5–9.0 owing to the instability of $SO_2 \cdot xH_2O$ or its related compounds HSO_3^- and SO_3^{2-}. However, sulphite can be detected in the absence of SO_2 in pH=8 buffer.

In Fig. 12.12, current–potential curves are shown of increasing SO_2 concentration, recorded in a pH=10 buffer at a carbon fibre modified with $[Fe(II)TSPc]^{4-}$. It can be seen that in alkaline solution only one wave is obtained at 0.75 V vs. Ag|AgCl, which is identical to the one obtained when started from sodium sulphite. Therefore, it can be proposed that SO_3^{2-} is the main (Table 12.1) electroactive compound in solution. As expected, the slope between peak current and SO_2 or Na_2SO_3 concentrations corresponds to exchange of two electrons (Fig. 12.10, curve 7), and a detection limit of $7.3\pm0.1\times10^{-5}$ mol l^{-1} was obtained.

12.3.7 Conclusion

It can be concluded that the electrocatalytic detection of SO_2 is not simple and is strongly dependent on pH. However, in this study it became clear that the influence of the pH on the curves is not caused by variations in carbon-fibre electrode properties, but purely by transformation and shift of equilibrium conditions in solution. From this study, it can also be concluded that weakly acidic or alkaline solutions should be used as electrolyte in SO_2-sensing applications. For an optimal detection limit, a buffer of pH=4 should be used in combination with the reduction reaction of HSO_3^-, the main compound in solution related to SO_2. In other cases, advantage should be given to oxidation of SO_2 (and related compounds) to sulphate because reduction causes formation of possible interfering and poisoning products. Except for the pH range from 7.5–9, a detection limit of about $7.5 \pm 0.1 \times 10^{-5}$ mol l^{-1} is obtained for SO_2 or its related compounds (HSO_3^- and SO_3^{2}). However, in a pH=4 buffer, a detection limit of $4.0 \pm 0.1 \times 10^{-5}$ mol l^{-1} is obtained. The carbon fibres used in this study can also be used for detection of SO_2-related compounds such as sodium dithionite and sulphite. Thus, these fibres positioned in a flow-through cell can be an alternative for the previously discussed wall-jet electrode configuration (Chapter 6), or the results discussed in Chapter 7 can be adapted to a gold fibre positioned in a flow-through cell.

12.4 Gold-fibre textile electrodes obtained through chemical modification for the detection of Ce(IV) during polymerisation reactions of bio-polymers

12.4.1 Introduction

During the past few decades, polymers have found wide applications, and some synthetic polymers have become important components of the industrial society[54,55]. As well as these synthetic polymers, there are also a large number of naturally occurring polymers such as polysaccharides, polypeptides and proteins[56–59]. All polymerisation reactions, including both the 'synthetic' and 'natural' polymerisations, can be divided into three main classes, depending on the active species present in the reaction mixture: anionic, cationic and radical polymerisations. In recent years, our research group has been working on the development of synthetic cationic polymers that can be used as non-viral vectors for gene therapy[60–62]. Recently, the synthesis and evaluation of a series of polymers containing polyethyleneoxide (PEO) blocks and PEO grafts was reported[62]. Both types of polymers were prepared by radical chain reactions. The block co-polymers, containing a PEO

block and a vinyl block, were synthesised using cerium ammonium nitrate/PEO as redox initiator system.

Polymerisations of vinyl compounds, initiated by ceric salts in combination with reducing agents such as alcohols, aldehydes and ketones, have been described by several authors[63–70]. Ce(IV) salts are also well-known initiators for grafting vinyl monomers on naturally occurring compounds such as cellulose[71] and starch[72] and for the synthesis of block co-polymers containing a polyethyleneoxide[73,74] or polypropyleneoxide block[75]. The most commonly used ceric salts are cerium ammonium sulphate, cerium perchlorate, cerium sulphate and cerium ammonium nitrate[76]. Other frequently used metal ions in redox polymerisations are Mn(VII), V(V), Co(III), Cr(VI) and Fe(III). Redox polymerisations can be carried out both in aqueous and non-aqueous media, depending on the solubility of the monomers used. The advantage of all the above-mentioned redox polymerisations, besides the small induction period, is the possibility of operating under very mild conditions compared with thermal polymerisations[76]. In this way, the possibility of side-chain reactions is limited.

It is now generally believed that the initiation step for a Ce(IV)/PEO system proceeds in accordance with the following general reaction scheme:

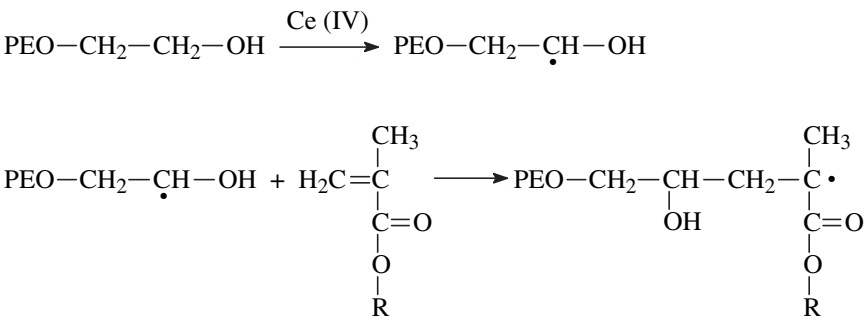

[12.18]

In the first step, a redox reaction occurs between Ce(IV) and the $-CH_2OH$ end group of PEO, generating a free radical in α-position of the –OH group of PEO. In a consequent step, the radical is transferred from the PEO chain to the vinyl monomer. The radicals formed initiate the actual polymerisation reaction (propagation):

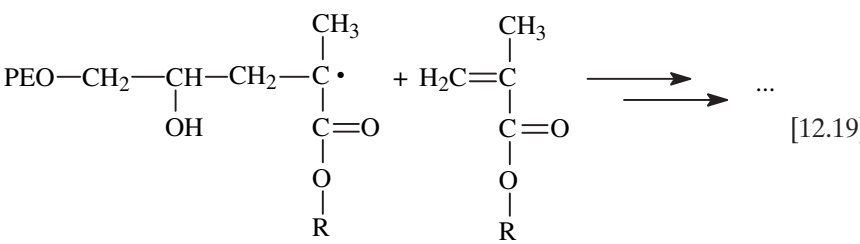

[12.19]

Several reports describe the mechanism of polymerisations using cerium compounds in combination with alcohols[77,78], diols[79,80] and polyols[81]. Only in a limited number of kinetic studies was the concentration of cerium ions measured during the polymerisation reaction. Mohanty *et al.*[80], Rout *et al.*[81], Jayakrishnan *et al.*[65] and Gupta and Behani.[67] followed the reduction of Ce(IV) ions titrimetrically.

To our present knowledge, there has been no detailed report so far studying the initiation step of the synthesis of PEO block co-polymers continuously. Here, a new method is presented that allows the determination on-line of the consumption of Ce(IV) ions in the reaction mixture by means of chronoamperometry and a flow injection analysis system using textile electrodes with a gold surface.

12.4.2 Modification of textile fibres to obtain gold-coated fibres

Common textile fibres, such as nylon, polyester and polyaramide fibres, can be modified with a metallic layer in order to provide the modified fibre with electroconductive properties. In the literature[82–85], a respectable number of papers were found to modify such fibres with polypyrrol, starting from the adsorption of pyrrol, followed by the oxidative induced polymerisation of pyrrol to polypyrrol. This initiation was obtained with $FeCl_3$. In the work described here, a polyaramide woven structure was modified. The adsorption step was accelerated by using ultrasound to promote the impregnation of pyrrol into the woven structure of the polyaramide fibres. Polypyrrol forms a suitable substrate for further deposition of a metallic layer. Similarly with chemical copper deposition[82–85], gold was deposited on the polypyrrol substrate. This gold-modified structure was finally used as an electrode.

These electrodes were positioned in electrochemical cells as described in Chapter 9, with the difference that the modified gold electrode was positioned at one side of the tube (working electrode), a platinum net at the other side (counter electrode) and a reference electrode in the middle of the tube. The solution was pumped through this cell in order to obtain a steady-state current signal (time-independent signal).

12.4.3 Electrochemical behaviour of Ce(IV) at the gold-coated textile structure

The electrochemical behaviour of Ce(IV) at a gold-coated textile structure was investigated by cyclic voltammetry in a 1.0 mol l^{-1} H_2SO_4 solution (Fig. 12.13). The potential is swept in positive direction from an initial potential of –0.2 V vs. Ag|AgCl to a vertex potential of 1.7 V vs. Ag|AgCl and in the

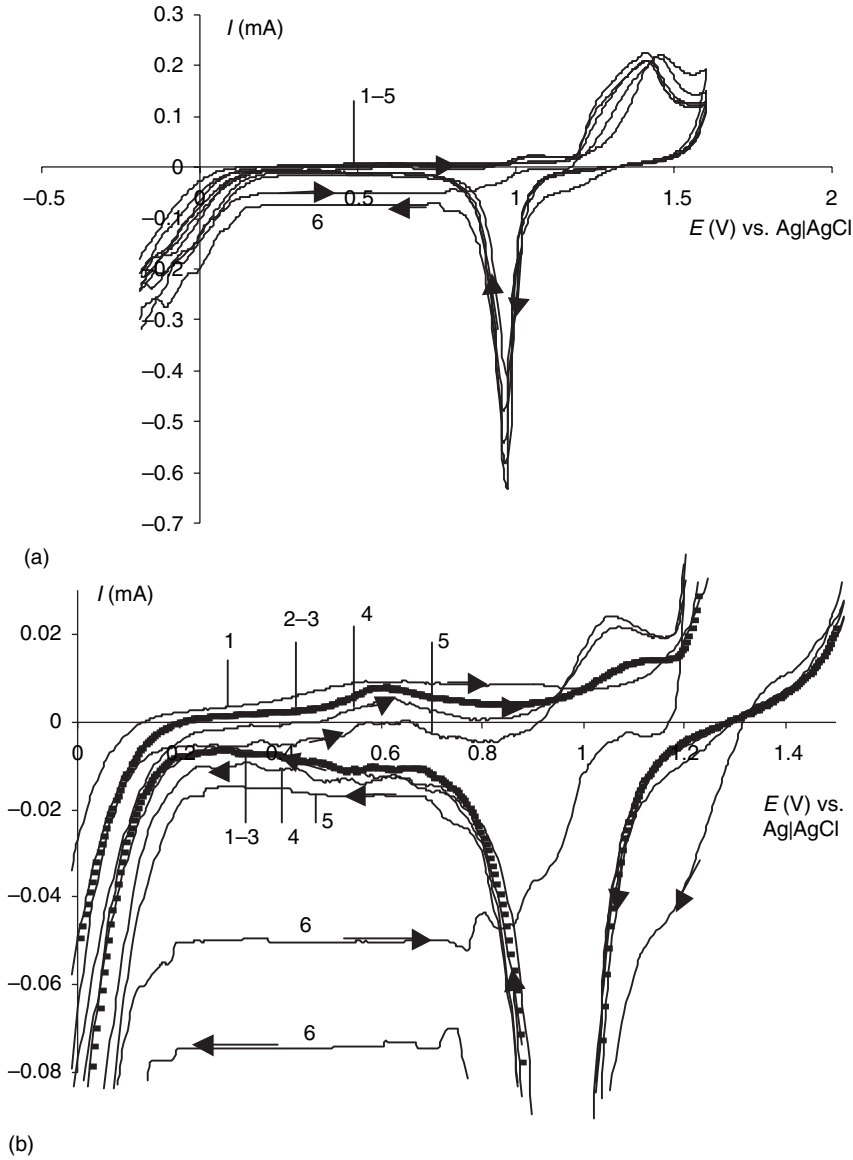

12.13 Cyclic current–potential curves (a) and a more detailed view of part of it (b), recorded at a gold-modified PPy-polyaramide woven textile structure in a 1.0 mol l^{-1} H_2SO_4 solution with a flow rate of 2.36 ml min^{-1} at 298.0 K. The Ce(IV) concentrations are (1) 0, (2) 5×10^{-6}, (3) 1×10^{-5}, (4) 3×10^{-5}, (5) 1×10^{-4} and (6) 5×10^{-4} mol l^{-1}.

opposite sweep direction back to the initial potential. Curve 1, recorded in the absence of Ce(IV), shows that over a potential range from about 0.2 to 0.4 V vs. Ag|AgCl, no electrochemical reaction of the gold surface is observed. From a potential of about 0.4 V vs. Ag|AgCl, a voltammetric wave with a relatively small limiting-current is observed (Fig. 12.13). According to Burke and O'Sullivan.[86], this wave could be attributed to the oxidation of Au adatoms (Au*) to Au(I). The slow kinetics of the equilibrium between Au and Au* explain why the limiting-current is low. From a potential of 1.1 V vs. Ag|AgCl, a relatively broad peak is observed resulting from the formation of Au(III). This peak is composed of several peaks, but is not considered further here because it is beyond the scope of this book. At a potential of 1.55 V vs. Ag|AgCl, the current starts to increase exponentially, corresponding to the oxygen-evolution reaction.

In the cathodic sweep direction, a sharp reduction peak (E_p=0.95 V vs. Ag|AgCl) is observed, which can be attributed to the reduction of the Au(III) formed in the anodic-inclined branch. Up to a potential of 0.2 V vs. Ag|AgCl, again an electro-inactive region is observed. Finally, the onset of the reduction reaction of H^+ is observed from a potential of 0.2 V vs. Ag|AgCl. Curves 2–6 of Fig. 12.13, recorded with increasing amounts of Ce(IV) present in solution, show a Ce(IV) reduction wave. The formation of a limiting-current plateau indicates that in the 0.2–0.7 V vs. Ag|AgCl potential region, transport of Ce(IV) determines the overall reaction rate. This limiting-current is proportional to the Ce(IV) concentration. Curve (6), recorded at the highest Ce(IV) concentration, clearly shows the presence of an hysteresis effect. Transport as rate-determining step in the 0.2–0.7 V potential region was confirmed by carrying out the same experiment at a gold rotating-disc electrode. The limiting Ce(IV) reduction current is proportional to the square root of the rotation rate of the disc electrode as expected from the Levich equation[87]. Cyclic voltammetry at a stationary-disc electrode showed that the peak current is proportional to the square root of the polarisation rate (Sevcik–Randles equation[87]).

The results obtained and presented in Fig. 12.14 show that chrono-amperometry, with an applied potential situated in the limiting-current plateau of the Ce(IV) reduction reaction, can possibly be used for on-line measurement of the concentration of Ce(IV). In Fig. 12.14, the current signal of Ce(IV) reduction is given as a function of concentration in a 1.0 mol l^{-1} H_2SO_4 solution at an applied potential of 0.25 V vs. Ag|AgCl and a flow rate of 2.36 ml min^{-1}. It can be seen that the current signal is relatively stable, and not dependent on time. It shows a linear relationship with the Ce(IV) concentration. This experiment was repeated eight times. Taking into account that the faradaic current I is superimposed on a time-dependent background current I_{bg}, this resulted in the following empirical equation for the relationship between current and Ce(IV) concentration. In the electrode

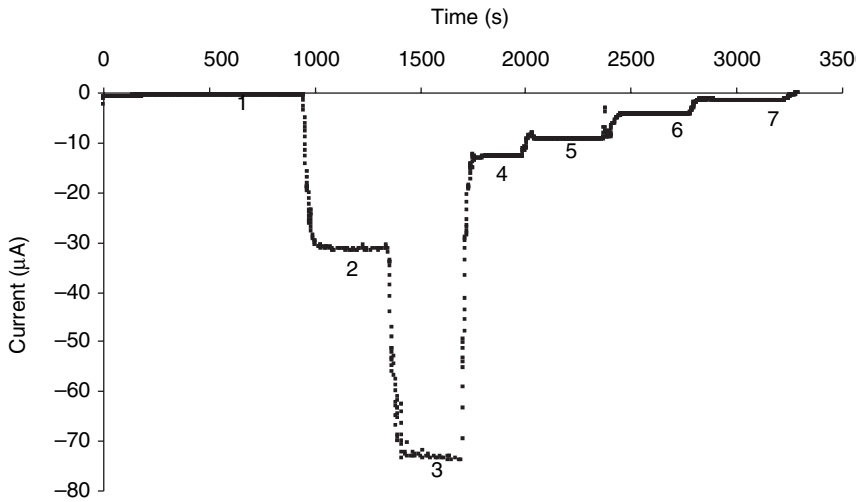

12.14 Chronoamperometric current signal of the Ce(IV) reduction at $E = 0.25$ V vs. Ag|AgCl, recorded as a function of time at a gold-modified PPy-polyaramide woven textile structure with a 2.36 ml min^{-1} continuous flow of 1.0 mol l^{-1} H_2SO_4 containing (1) 0, (2) 2×10^{-4}, (3) 5×10^{-4}, (4) 1×10^{-4}, (5) 6×10^{-5}, (6) 3×10^{-5} and (7) 1×10^{-5} mol l^{-1} Ce(IV) at 298.0 K.

configuration used, the numerical value of k_1 was 14 800 if the currents are expressed in microampere, with the Ce concentration in mol l^{-1}:

$$I = k_1 C_{Ce(IV)} + I_{bg} \qquad [12.20]$$

The decay of the background current with time, not visible in segment 1 of Fig. 12.14 owing to current scale, is shown in Fig. 12.15. It is clear that the time dependence of the background current will have a greater effect on the detection limit of the method at shorter times. When the detection limit is defined as the Ce(IV) concentration corresponding to a current signal that is twice as high as the background current I_{bg} (segment 1, Fig. 12.14), limits of 3×10^{-6}, 1×10^{-6} and 1.5×10^{-7} mol l^{-1} are obtained after 60 s, 3600 s and 14 h, respectively. For longer times, the background current remains nearly constant (75 nA cm^{-2}), resulting in a constant detection limit of about 1.5×10^{-7} mol l^{-1}.

The influence of solution flow rate on the steady-state limiting current at a constant potential of 0.25 V vs. Ag|AgCl was also investigated, using a 1.0 mol l^{-1} H_2SO_4 solution containing 6×10^{-5}, 2×10^{-4} and 5×10^{-4} mol l^{-1} Ce(IV). A logarithmic plot shows that the current is proportional to the square root of the flow rate. However, this is not valid for flow rates lower than 0.15 ml min^{-1}, where a less-stable current signal is obtained. It is likely that a steady-state transport of Ce(IV) to the electrode surface is no longer

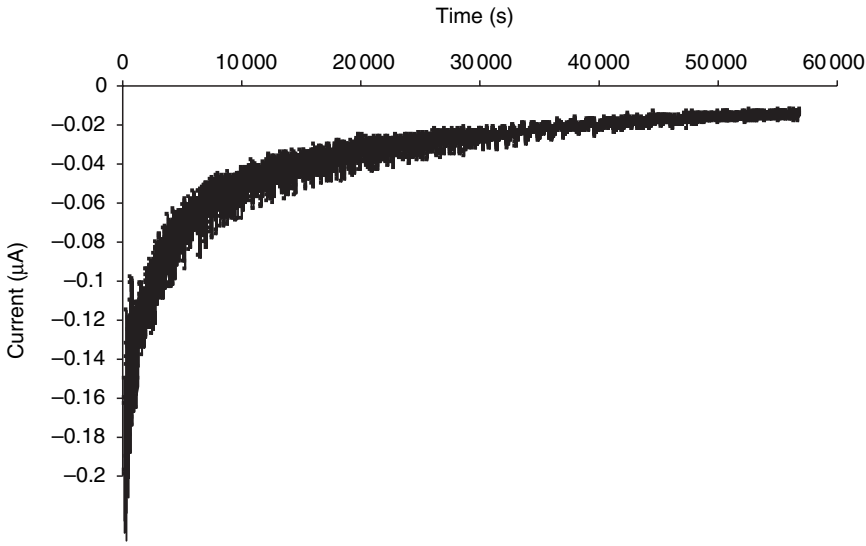

12.15 Decay of chronoamperometric background-current signal with time recorded at a gold-modified PPy-polyaramide woven textile structure (E=0.25 V vs. Ag|AgCl) in a flow-through cell with a continuous flow (2.36 ml min^{-1}) of a 1.0 mol l^{-1} H_2SO_4 solution.

attained. At higher flow rates (>3.7 ml min^{-1}), the risk of leakage of the flow-through cell increases. Therefore an optimal flow rate of 2.36 ml min^{-1} was further used.

12.4.4 Stability of the Ce(IV) solution as a function of pH

It is well known from redox titrimetry that oxidations with Ce(IV) require a strongly acidic solution, as was used in the experiments described above (1.0 mol l^{-1} H_2SO_4). At higher pH values, the risk of precipitation of basic salts increases[88]. The influence of increased pH on the chronoamperometric current signal in the flow-through cell is shown in Fig. 12.16. When the pH is in excess of about 1.5, the Ce(IV) reduction current at 0.25 V vs. Ag|AgCl starts decaying a short time after applying the potential, possibly because of precipitation or adsorption of basic salts.

A possible solution to the pH problem is to make use of the FIA principle. Samples of Ce(IV) solutions of different concentration (1×10^{-5}, 3×10^{-5}, 6×10^{-5}, 1×10^{-4} and 2×10^{-4} mol l^{-1}) and pH (0, 1.0, 2.0, 3.0, 4.0, 5.0 and 6.0) were injected in a 1.0 mol l^{-1} H_2SO_4 continuous-flow solution and analysed by chronoamperometric detection at 0.25 V vs. Ag|AgCl. Figure 12.17 shows the amperometric responses by injection of Ce(IV) samples at a pH of 3.0. Solutions with pH values higher than 6 were not investigated

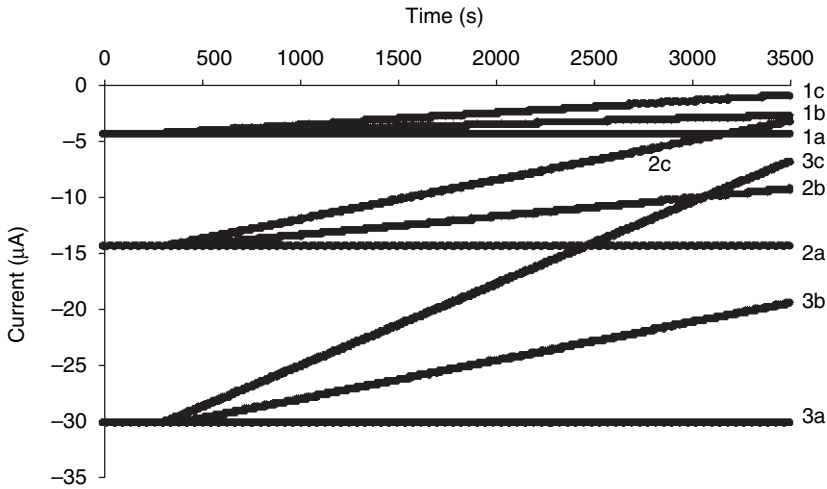

12.16 Chronoamperometric current signals recorded as a function of time at a gold-modified PPy-polyaramide woven textile structure (E=0.25 V vs. Ag|AgCl) positioned in a flow-through cell with a continuous flow of (a) 0.5 mol l^{-1}, (b) 0.05 mol l^{-1} and (c) 0.005 mol l^{-1} H_2SO_4 containing (1) 3×10^{-5}, (2) 1×10^{-4} and (3) 2×10^{-4} mol l^{-1} Ce(IV).

because, during their preparation, an immediate precipitation of Ce(IV) was observed. Comparison of the peak currents obtained at different pH values (between 0 and 6) for a constant concentration of Ce(IV) revealed that the peak signal is not dependent on pH. This depends on both the flow rate of the H_2SO_4 solution and the volume of the injected sample. For the flow rate (2.36 ml min^{-1}) used in this investigation, the maximum volume of a solution of pH 6 that may be injected is 260 µl. Higher volumes did give rise to pH-dependent signals. Smaller values resulted in smaller peaks, which negatively influenced the precision and detection limit of the method. For the optimal condition of injection volume and a flow rate of 2.36 ml min^{-1}, the relationship between peak current and Ce(IV) concentration is given by Equation 12.21. A detection limit of about 1×10^{-7} mol l^{-1} was obtained.

$$I_p = k_2 c_{Ce(IV)} \qquad [12.21]$$

where k_2 is 197 000 for the electrode configuration used, when I_p and the concentration were obtained in microamperes and mol l^{-1}, respectively.

12.4.5 Analytical and kinetic considerations

Finally, the method was applied to determine the Ce(IV) concentration during the polymerisation of polyethyleneoxide. A mixture of linear

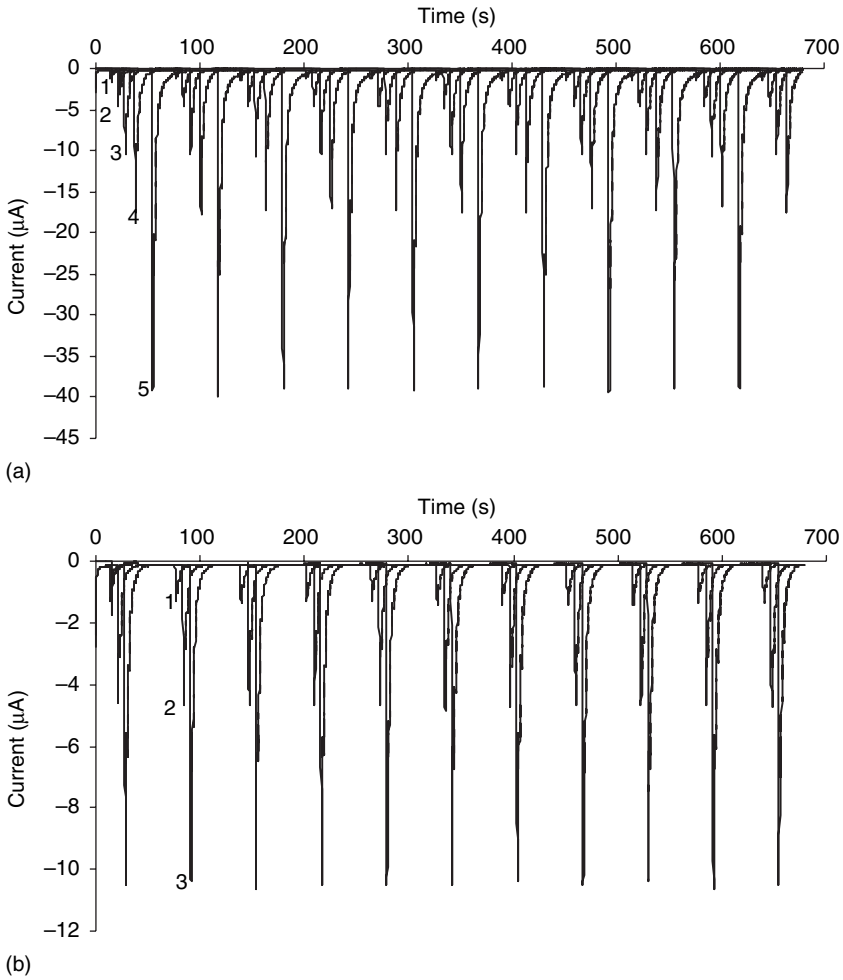

12.17 (a) and (b) Chronoamperometric current signals recorded at a gold-modified PPy-polyaramide woven textile structure positioned in a flow-through cell, by injection of 257 μl of Ce(IV) solutions at pH = 3 in a 2.36 ml min^{-1} continuous flow of 1.0 mol l^{-1} H_2SO_4 at 298.0 K. Ce(IV) concentrations are (1) 1×10^{-5}, (2) 3×10^{-5}, (3) 6×10^{-5}, (4) 1×10^{-4} and (5) 2×10^{-4} mol l^{-1}.

polyethyleneoxide and dimethylaminoethylmetacrylate (80 ml) was added to 20 ml of an aqueous solution containing 5×10^{-2} mol l^{-1} Ce(IV) at a pH of 4 in order to initiate radicals according to Equation 12.18.

When Ce(IV) is consumed during polymerisation its concentration will drop. The amount consumed is expected to be inversely proportional to the number of radicals formed in the solution. Samples from the cell solution in which the polymerisation reaction takes place were periodically injected

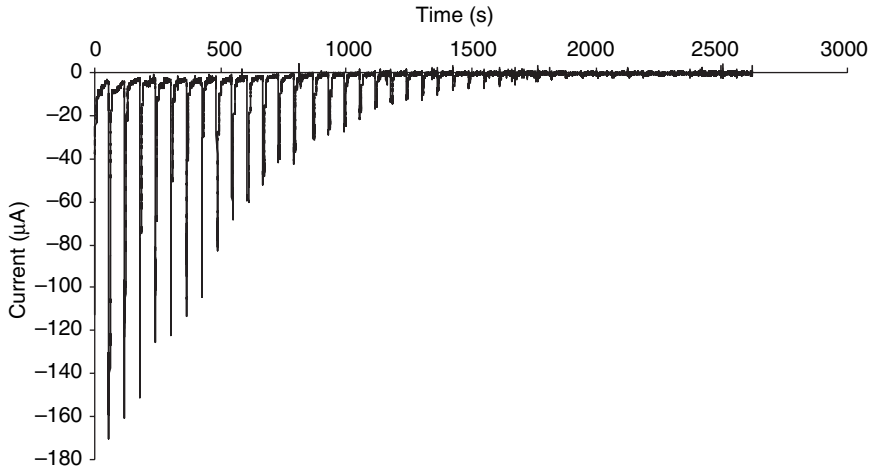

12.18 Chronoamperometric current signals of Ce(IV) reduction (at 0.25 V vs. AgIAgCl) recorded at a gold-modified PPy-polyaramide woven textile structure in a flow-through cell by injection of 257 μl samples from a polymerisation mixture at 298.0 K in a continuous flow of an aqueous solution containing 1.0 mol l^{-1} H_2SO_4.

in a 1.0 mol l^{-1} H_2SO_4 flow with a frequency of 1 min. A typical result is shown in Fig. 12.18. After approximately 40 min, the formation of radicals is apparently complete because the Ce(IV) signal is almost equal to the background current (final peaks in Fig. 12.18). However, an off-line analysis of the polymerisation product showed that the polymerisation reaction was complete after approximately 24 h. This means that the measurement of Ce(IV) during polymerisation is a powerful tool in the investigation of its kinetics and mechanism. Indeed, analysis of the polymerisation product reveals information concerning the overall reaction rate, which is determined by the slowest elementary step in the mechanism.

The continuous measurement of the concentration of Ce(IV) revealed that information can be obtained concerning the kinetics of the initiation step (Equation 12.18), which appears not to be the rate-determining step. This shows that additional information can be obtained about the rate of formation of radicals, which in turn can be an important factor in the unravelling of the mechanism of the polymerisation reaction. Repetition of the polymerisation experiments showed that results are reproducible within a margin of 3%.

12.5 References

1. Matyjaszewski K., Patten T.E., Xia J., *J. Am. Chem. Soc.*, **119** (1997) 674.
2. Matyjaszewski K., Kajiwara A., *Macromolecules*, **31** (1998) 548.

3. Kajiwara A., Matyjaszewski K., *Macromolecules*, **31** (1998) 5695.
4. Wang J., Grimaud T., Matyjaszewski K., *Macromolecules*, **30** (1997) 6507.
5. Kajiwara A., Matyjaszewski K., *Polymer J.*, **31** (1) (1999), 70.
6. Odian G., *Principles of Polymerization*, 3rd edn, Wiley, New York, 1991.
7. Bamford C.H.,'Radical polymerization' in *Encyclopedia of Polymer Science and Engineering 13*, Wiley, New York, 1990, 708.
8. Moad G., Solomon D.H., *The Chemistry of Free Radical Polymerization*, Pergamon, Oxford, 1995.
9. Osipova E.A., Kamenev A.I., Sladkov V.E., Shkinev V.M., *J. Anal. Chem.*, **52** (1997) 242.
10. Wu Z.J., Zhang Z.B., Liu L.S., *Electrochim. Acta*, **42** (1997) 2719.
11. Westbroek P., Twagiramungu F., De Strycker J., Vanmoortel I., Temmerman E., *Anal. Lett.*, **33** (2000) 2243.
12. Egashira N., Iwata D., Ohga K., *Anal. Sci.*, **6** (1990) 781.
13. Geraldo M.D., Montenegro M.I., Pletcher D., *Talanta*, **42** (1995) 1725.
14. Geraldo M.D., *J. Electroanal. Chem.*, **418** (1996) 41.
15. Evans D.H., Geraldo M.D., *J. Electroanal. Chem.*, **439** (1997) 115.
16. Chen C.-Y., *J. Electroanal. Chem.*, **487** (2000) 51.
17. Pérez-Alonso F.J., Agui L., Yánez-Sedeno P., Pingarrón J.M., *Analyst*, **125** (2000) 2006.
18. Qiu J., Matyjaszewski K., Thouin L., Amatore C., *Macromol. Chem. Phys.*, **201** (2000) 1625.
19. Van Den Bruwaene J., Kiekens P., Temmerman E., *Bull. Soc. Chim. Belge*, **92** (1983) 935.
20. Van Den Bruwaene J., Temmerman E., *Bull. Soc. Chim. Belge*, **101** (1992) 663.
21. Reich H.J., Rigby J.H., Cerfontein H., Bakker B.H. (eds), in *Handbook of Reagents for Organic Synthesis*, *Acidic and Basic Reagents*, Wiley, Chichester, 1999.
22. Potteau E., Levillain E., Lelieur J.P., *J. Electroanal. Chem.*, **476** (1999) 15.
23. Boyd C.E. (ed.) *Water Quality*, Kluwer Academic, New York, 1999.
24. Cotton F.A., Wilkinson G., Gaus P.L. (eds) *Basic Inorganic Chemistry*, Wiley, New York, 1987.
25. Weast R.C., *CRC Handbook of Chemistry and Physics*, 64th edn, CRC Press, Boca Raton, 1983.
26. Sawyer T., George R.S., Rhodes R.C., *Anal. Chem.*, **31** (1959) 2.
27. Belanger G., *Anal Chem.*, **46** (1974) 1576.
28. Garber R.W., Wilsons E., *Anal Chem.*, **44** (1972) 1357.
29. Chachulski B., *Analyst*, **123** (1998) 1141.
30. Rios A., Lucque de Castro M.D., Valcarel M., Mottola A., *Anal. Chem.*, **59** (1987) 666.
31. Hodgson A.W., Jacquinot P., Hauser P.C., *Anal. Chem.*, **71** (1999) 2831.
32. Rios J.W., Risemann J.H., Krueger J.A., *Pure Appl. Chem.*, **36** (1973) 473.
33. Yang Y., Zhang X.X., Korenaga T., Hitguchi K., *Talanta*, **45** (1997) 445.
34. Nikolov I., Petrov K., Vitanov T., *J. Appl. Electrochem.*, **26** (1996) 703.
35. Cardwell T.J., Christophersen M.J., *Anal. Chim. Acta*, **416** (2000) 105.
36. Carvalho L.M., Schwedt G., *Anal. Chim. Acta.*, **436** (2001) 293.
37. Gasana E., Westbroek P., Temmerman E., Thun H.P., *Anal. Commun.*, **36** (1999) 387.

38. Gasana E., Westbroek P., Temmerman E., Thun H.P., Twagiramungu F., *Electrochem. Commun.*, **2** (2000) 727.
39. Westbroek P., Van Uytvangh K., De Strycker J., Temmerman E., *J. Electroanal. Chem.*, **516** (2001) 83.
40. Rea N., Loock B., Lexa D., *Inorg. Chim. Acta*, **312** (2001) 53.
41. Chen S.M., *J. Electroanal. Chem.*, **407** (1996) 123.
42. Chen S.M., Chiu S.W., *Electrochim. Acta*, **45** (2000) 4399.
43. Chen S.M., *J. Electroanal. Chem.*, **432** (1997) 101.
44. Chen S.M., *J. Electroanal. Chem.*, **417** (1996) 145.
45. Azevedo C.M.N., Araki K., Angnes L., Toma H.E., *Electroanal.*, **10** (1998) 467.
46. Azevedo C.M.N., Araki K., Toma H.E., Angnes L., *Anal. Chim. Acta*, **387** (1999) 175.
47. Weber T.H., Busch D.H., *Inorg. Chem.*, **4** (1965) 469.
48. Nevin W.A., Liu W., Melnik M., Lever A.B.P., *J. Electroanal. Chem.*, **213** (1986) 217.
49. Hadasch A., Sorokin A., Rabion A., Meunier B., *New J. Chem.*, **22** (1998) 45.
50. Zecevic S., Simic-Glavaski B., Yeager E., Lever A.B.P., Minor P.C., *J. Electroanal. Chem.*, **196** (1985) 339.
51. Sanchez M., Chap N., Cazaux J.B., Meunier B., *Eur. J. Inorg. Chem.*, **7** (2001) 1775.
52. McLendon G., Martell A.E., *Inorg. Chem.*, **16** (1977) 1812.
53. Simic-Glavaski B., Zecevic S., Yeager I., *J. Phys. Chem.*, **87** (1983) 4555.
54. Streitwieser A., Heathcock C.H., Kosower E.M., *Introduction to Organic Chemistry*, 4th edn, Macmillan Publishing, London, 1991.
55. Young R.J., Lovell P.A., *Introduction to Polymers*, 2nd edn, Chapman & Hall, Los Angeles, 1991.
56. Brock T.D., Madigan M.T., Martinko J.M., Parker J., *Biology of Microorganisms*, 7th edn, Prentice Hall, Illinois, 1994.
57. Wagner E., Cotton M., Mechtler K., Kirlappos H., Birnstiel M.L., *Bioconjugate. Chem.*, **2** (1991) 226.
58. Adami R.C., Collard W.T., Gupta S.A., Kwok K.Y., Bonadia J., Rice K.G., *J. Pharm Sci.*, **87** (1998) 678.
59. Grove R.I., Wu G.Y., *Adv. Drug. Deliv. Rev.*, **30** (1998) 199.
60. Vanderkerken S., Vanheede T., Toncheva V., Schacht E.H., Wolfert M.A., Seymour L.W., Urtti A., *J. Bioactive Compatible Polymers*, **15** (2000) 115.
61. Dekie L., Toncheva V., Dubruel P., Schacht E.H., Barret L., Seymour L.W., *J. Control Rel.*, **65** (2000) 187.
62. Dubruel P., Schacht E.H., *J. Bioactive Compatible Polymers*, **15** (2000) 279.
63. Subramanian S.V., Santappa M., *Macromol. Chem.*, **6** (1968) 112.
64. Subramanian S.V., Santappa M., *J. Polymer Sci.*, **A1** (1968) 493.
65. Jayakrishnan A., Haragopal M., Mahadevan V.J., *J. Polymer Sci.*, **19** (1981) 1147.
66. Fernandez M., Fernandez T., Fernandez M.J., Guzman G.M., *J. Polymer Sci.*, **22** (1984) 2729.
67. Gupta K.C., Behari K., *J. Polymer Sci.*, **24** (1986) 767.
68. Fernandez M.N., Guzman G.M., *J. Polymer Sci.*, **27** (1989) 2427.
69. Fernandez M.N., Guzman G.M., *J. Polymer Sci.*, **27** (1989) 2703.
70. Fernandez M.N., Pelayo A., Otero T.F., Guzman G.M., *J. Polymer Sci.*, **23** (1985) 79.

71. Galioglu O., Soydan A.B., Akar A., Sarac A.S., *Angew. Macromol. Chem.*, **19** (1994) 214.
72. Okieimen F.E., Egharevba F., Jideonwo A., *Angew. Macromol. Chem.*, **184** (1991) 1.
73. Lee K.K., Jung, J.C., Jhon M.S., *Polymer Bull.*, **40** (1998) 455.
74. Topp M.D.C., Dijkstra P.J., Talsma H., Feijen J., *Macromol.*, **30** (1997) 8518.
75. Arslan H., Hazer B., *Eur. Polymer J.*, **35** (1999) 1451.
76. Sarac A.S., *Progr. Polymer Sci.*, **24** (1999) 1149.
77. Hanna S.B., Carrol W.R., Attiga S., Webb W.H., *Naturforschung*, **30** (1975) 409.
78. Renders G., Broze G., Jerome R., Teyssie P.H., *J. Macromol. Sci. A, Chem.*, **16** (1987) 1399.
79. Mohanty N., Pradhan B., Mohanta M.C., *Eur. Polymer J.*, **15** (1979) 743.
80. Mohanty N., Pradhan B., Mohanta M.C., *J. Macromol. Sci. A*, **19** (1983) 283.
81. Rout A., Rout S.P., Singh B.C., Santappa M., *Macromolecul. Chem.*, **178** (1977) 639.
82. Zhitariuk N.I., Le Moël A., Mermilliod N., Trautmann C., *Nucl. Instr. Methods Phys. Res. B*, **105** (1995) 204.
83. Freund M.S., Karp C., Lewis N.S., *Inorg. Chim. Acta*, **240** (1995) 447.
84. Shen Y., Wan M., *Synth. Metals*, **96** (1998) 127.
85. Zouaoui A., Stephan O., Cariier M., Moutet J.C., *J. Electroanal. Chem.*, **474** (1999) 113.
86. Burke L.D., O'Sullivan J.F., *Electrochim. Acta*, **37** (1992) 585.
87. Bard A., Faulkner L. (eds), *Electrochemical Methods*, *Fundamentals* and *Applications*, Wiley, New York, 1980.
88. Petzold W., *Die Cerimetrie*, Verlag Chemie, Weinheim, 1995.

Index